

DRAFT
EIC PDR
October 10, 2024

Electron Ion Collider Preliminary Design Report

Contributors:

E-C. Aschenauer¹, R. Ent², S. Joosten³, M. Żurek³, ADD NAMES AND INSTITUTIONS

¹Brookhaven National Laboratory, USA

²Thomas Jefferson National Accelerator Facility, USA

³Argonne National Laboratory, USA

Contents

0	Style Guide	2
0.1	Chapter Abstract	2
0.2	Wordsmithing	3
0.2.1	Passive voice	3
0.2.2	Verb tenses	3
0.2.3	Apostrophes	3
0.2.4	Capitalization and names	3
0.2.4.1	Pieces of EIC	3
0.2.4.2	Internal phrases	3
0.2.4.3	Discipline-specific approaches or “guiding principles” or buzz phrases	4
0.2.4.4	Formal group names	4
0.2.4.5	Headings	4
0.2.5	Captions	4
0.2.6	Spelling	4
0.2.6.1	Exceptions to U.S. spelling	4
0.2.6.2	Capitalization	4
0.2.7	Commas	5
0.2.7.1	Commas in numbers	5
0.2.8	Plurals and possessives	5
0.2.9	Abbreviations	5
0.2.9.1	Textual treatment of Figures and Tables	5
0.2.9.2	Radio frequency	5
0.2.9.3	etc., et cetera	6
0.2.10	Hyphenation of multi-word adjectival phrases	6
0.2.11	Double letters	10
0.2.12	Mathematical symbols, subscripts and superscripts	10
0.2.13	Quotation marks	10
0.2.14	Citations, references and the bibliography	10
0.2.15	Miscellaneous	11
0.2.15.1	“Calculations show that...”	11
0.2.15.2	“Should”, “must”, and reference to future studies	11
0.2.15.3	“Enable”	11
0.2.15.4	Reporting technical results without a clear statement of their import	11
0.2.15.5	Excessive and inconsistent use of lists	11
0.2.15.6	Cross-references	12
0.2.15.7	Isotopes	12
0.2.15.8	*** asterisks in comments	12
0.3	Dimensions and units	12
0.4	Numbering – chapters, sections, and subsections	13

0.4.1	This is the heading of a subsection	13
0.4.1.1	A subsubsection heading like this has no period at the end	13
	This paragraph heading ends with a period.	13
0.4.2	More formatting rules and standards	14
0.4.2.1	Clearpages and Pagebreaks	14
0.5	Equations, Tables, Figures, and plots	14
0.5.1	Equations	14
0.5.2	Tables	14
0.5.3	Converting between LaTeX and Excel table formats	14
0.5.4	Figures	17
0.5.5	Plots	17
0.6	Italics and bold face type	17
0.7	Issues that this Style Guide does not yet address	18
2	Physics Goals and Requirements	19
2.1	EIC Context and History	19
2.2	The Science Goals of the EIC and the Machine Parameters.	20
2.3	Reconstruction Tools and Special Probes	20
2.3.1	Kinematic reconstruction	20
2.3.2	Electron identification and event selection	21
2.3.3	Jets: a versatile probe	22
2.4	The EIC Science (ePIC performance for key observables)	22
2.4.1	Origin of Nucleon Mass	22
2.4.1.1	Inclusive neutral current cross sections	23
2.4.1.2	Upsilon production	23
2.4.2	Origin of Nucleon Spin	25
2.4.3	Multi-Dimensional Imaging of the Nucleon	26
2.4.3.1	Imaging in Momentum Space	26
2.4.3.2	Imaging in Transverse Position Space	28
2.4.4	Properties of Nuclear Matter	31
2.4.4.1	Gluon Saturation	31
2.4.4.2	Nuclear Modifications of Parton Distribution Functions	32
2.4.4.3	Passage of Color Charge Through Cold QCD Matter	32
8	Experimental Systems	34
8.1	Experimental Equipment Requirements Summary	34
8.2	General Detector Considerations and Operations Challenges	35
8.2.1	General Design Considerations	35
8.2.2	Backgrounds and Rates	35
8.2.3	Radiation Level	35
8.3	The ePIC Detector	35
8.3.1	Introduction	35
	The Context	35
	The Detector	36
	Technological Synergistic Aspects of the Detector Design	40
8.3.2	Magnet	41
	Requirements	41
	Justification	41
	Implementation	42
	Additional Material	42
8.3.3	Tracking	42

8.3.3.1	The silicon trackers	43
	Requirements	43
	Justification	44
	Implementation	48
	Additional Material	62
8.3.3.2	The MPGD trackers	62
	Requirements	62
	Justification	64
	Performance	70
	Implementation	70
	Additional Material	76
8.3.4	Particle Identification	76
8.3.4.1	The time-of-flight layers	80
	Requirements and Justifications	80
	Implementation	88
	Additional Material	99
8.3.4.2	The proximity focusing RICH	100
	Requirements	100
	Justification	102
	Implementation	107
	Additional Material	114
8.3.4.3	The high performance DIRC	114
	Requirements	114
	Justification	115
8.3.4.4	The dual radiator RICH	117
	Requirements	117
	Justification	117
	Performance	124
	Implementation	126
	Additional Material	140
8.3.5	Electromagnetic Calorimetry	145
8.3.5.1	The backward endcap electromagnetic calorimeter	146
	Requirements	146
	Justification	146
	Implementation	149
	Additional Material	153
8.3.5.2	The barrel electromagnetic calorimeter	154
	Requirements	154
	Justification	154
	Implementation	163
	Additional Material	169
8.3.5.3	The forward endcap electromagnetic calorimeter	175
	Introduction	175
8.3.6	Hadronic Calorimetry	187
8.3.6.1	The backward endcap hadronic calorimeter	187
	Requirements	187
	Justification	188
	Implementation	191
	Additional Material	194
8.3.6.2	The barrel hadronic calorimeter	200

	Requirements	200
	Justification	201
	Performance	204
	Implementation	205
8.3.6.3	The forward endcap hadronic calorimeter	220
	Requirements	220
	Justification	220
	Implementation	224
	Additional Material	231
8.3.7	Far forward detectors	233
8.3.7.1	The detectors in the B0 bending magnet	233
	Requirements	233
	Justification	234
	Implementation	235
	Additional Material	237
8.3.7.2	The roman pots and the off-momentum detectors	237
	Requirements	237
	Justification	238
	Implementation	239
	Additional Material	242
8.3.7.3	The zero degree calorimeter	242
	Requirements	242
	Justification	243
	Implementation	243
	Additional Material	244
8.3.8	Far backward detectors	244
8.3.8.1	The luminosity system	245
	Beam Size Effect -	245
	High rate of BH radiation and SR background -	247
	Beam Polarisation -	248
	Physical Constraints -	248
	Systematic Uncertainties -	249
	Design and Components	249
	Additional Material	254
8.3.8.2	The low Q^2 taggers	254
	Requirements	254
8.3.8.3	TCS	255
8.3.8.4	Vector Meson production	255
8.3.8.5	Spectroscopy	255
	Justification	257
	Performance	260
	Implementation	261
	Additional Material	264
8.3.9	Polarimeters	264
8.3.9.1	The electron polarimeters	265
	Requirements	265
	Justification	265
	Implementation	265
	Additional Material	266
8.3.9.2	The proton polarimeters	266
	Requirements	266

	Justification	266
	Implementation	266
	Additional Material	267
8.3.10	Readout Electronics and Data Acquisition	267
	Requirements	267
	Device Concept and Technological choice: Streaming Readout	271
	Subsystem Description (components)	272
	Readout Electronics and ASICS	272
	Scope of the Effort	276
	FEB components	276
	RDOs	280
	DAM - Data Aggregation and Manipulation Hardware	282
	GTU - Global Timing Unit	283
	Protocols	284
	DAQ/Online Computing - Echelon 0	286
	Slow Controls	289
	Implementation	289
	Status and remaining design effort:	290
	Environmental, Safety and Health (ES&H) aspects and Quality Assessment (QA planning):	290
	Construction and assembly planning:	290
	Collaborators and their role, resources and workforce:	291
8.3.11	Software and Computing	292
	Requirements	292
	Justification	292
	Implementation	292
	Additional Material	293
8.4	Detector Integration	293
8.4.1	Installation and Maintenance	293
8.5	Detector Commissioning and Pre-Operations	293

List of Figures

1	Example of a non-graphical figure.	17
2.1	y Resolutions.	21
2.2	PLACEHOLDER (Left) Jet energy scale and (Right) jet energy resolution as a function of particle-level jet energy for backward (blue squares), mid (red triangles), and forward (green diamonds) rapidities.	23
2.3	Projected ep neutral current reduced cross sections at 5×41 GeV. Statistical uncertainties assume an integrated luminosity of 10 fb^{-1}	24
2.4	Projected ep neutral current reduced cross sections at 10×100 GeV. Statistical uncertainties assume an integrated luminosity of 10 fb^{-1}	24
2.5	Projected ep neutral current reduced cross sections at 18×275 GeV. Statistical uncertainties assume an integrated luminosity of 10 fb^{-1}	25
2.6	The reconstructed mass distribution of the Y three states in the electron channel from the electron-proton collisions at $18 \times 275 \text{ GeV}$, utilizing the tracker with realistic seeding. The top left plot shows the invariant mass distribution of the Y three states in the rapidity range from -3 to 4. The other plots display invariant mass distribution for specific rapidity intervals: (top middle) $-3 < y < -1$, (top right) $-1 < y < 0$, (bottom left) $0 < y < 1$, (bottom middle) $1 < y < 2$, and (bottom right) $2 < y < 4$. The resolution of the Y three states is indicated on each plot as σ	26
2.7	Projected measurements of A_1^p	27
2.8	Left: Expected statistical and total uncertainty of un-polarized TMD PDFs for π^+ in the $Q^2 - x_B$ plane. The inner (colored) circle shows the statistical uncertainty, while the outer circle provides the total uncertainty for each $Q^2 - x_B$ bin. The color shows the beam energy configuration which provides the highest statistics in a specific bin. Right panel: Expected uncertainties of valence down (green) and sea quark (orange) TMD PDFs at $x = 0.1$ (left) and $x = 0.001$ (right) as obtained based on the MAP24 [1] global TMD fit. The lighter shaded regions show the uncertainties based on existing data while the darker shaded regions show the expected uncertainties after including ePIC data.	28
2.9	Expected uncertainties in three example x - Q^2 bins for the Collins asymmetries as a function of the momentum fraction z in three bins of hadron transverse momentum relative to the virtual photon direction.	29
2.10	Collins asymmetries for hadrons in jets	29
2.11	Generated and reconstructed t -distributions for fully-exclusive DVCS events.	30
2.12	Reconstructed minus generated track θ for all reconstructed DVCS photons (left), as well as as a function of the generated photon θ (right). Note that the left plot is on a logarithmic scale.	30

2.13	Left: differential distribution of the momentum transfer $ t $ of coherent ϕ meson electroproduction in electron-gold collisions with 18x110 GeV. The Monte Carlo model is provided by Sartre and the reconstructed distribution is obtained from full ePIC simulation with the official August 2024 simulation campaign. Right: the momentum transfer t reconstruction resolution as a function of the true t	31
2.14	Left: Differential cross-section of momentum transfer t distribution for coherent (blue) and incoherent (black) exclusive J/ψ production in ePb collisions. Right: Differential measurement of t and the residue distributions after each veto based on the far-forward detector system.	33
8.1	Table presenting the Experimental Equipment Requirements Summary in the YR. At present, the table is not updated and it is here as a mere space holder.	34
8.2	A schematic showing how hadrons and the scattered electron for different $x - Q^2$ are distributed over the detector rapidity coverage. THIS FIGURES IS A PLACE HOLDER: IT IS FROM YR AND REQUIRES REVISION.	37
8.3	A schematic showing the ePIC central detector subsystems. THIS FIGURES IS A PLACE HOLDER	38
8.4	Cumulative material budget in radiation lengths (top row) and interaction lengths (bottom row) for the whole CD (left column) and zooming at the CD tracking region (right column). THIS FIGURES IS A PLACE HOLDER BECAUSE IT HAS TO BE COMPLETED WITH SUBSYSTEM CONTOURS AND REQUIRES GRAPHICAL IMPROVEMENTS.	38
8.5	A schematic showing the ePIC far detector subsystems. THIS FIGURES IS A PLACE HOLDER	39
8.6	Maps of simulated fluence (left) and total ionising dose (right) over the ePIC tracking envelope. This is a conservative estimate assuming 10 years of running at top luminosity with 100% efficient accelerator and detector. The black lines indicate the approximate location of the ePIC SVT detector layers.	44
8.7	Schematic layout of the ePIC SVT showing the central region consisting of the inner and outer barrel made of three and two cylindrical layers, respectively, together with the endcap regions made of five annuli each. The figure also shows the surrounding Micro Pattern Gas Detector (MPGD) layers and the envelope of the Time of Flight PID detector.	45
8.8	Sketch of the MOSAIX sensor on a 300 mm wafer showing the size of the RSU, LEC, REC and of the full sensor for the three different widths.	47
8.9	Relative momentum resolution versus total momentum for charged pions (points) together with physics requirements (curves) in different pseudorapidity ranges as indicated. The results are based on full GEANT simulations using the ePIC software stack and ACTS-based track finding and reconstruction using optimized parameters.	49
8.10	Distance of closest approach in the radial direction between reconstructed charged pion trajectories and the event origin versus transverse pion momentum (points) together with physics requirements (curves) in different pseudorapidity ranges as indicated. The results are based on full GEANT simulations using the ePIC software stack and ACTS-based track finding and reconstruction using optimized parameters.	49
8.11	A close-up of a beam telescope constructed from two times three single-RSU sensors from ITS3 Engineering Run 1 with a seventh sensor (DUT) under an angle at the center of the telescope (left) and (right) results from beamtests at FNAL and from simulations for the cluster extent as a function of the beam incident angle onto the DUT.	50
8.12	Schematic overview of data and slow control lines to a group of four EIC-LAS.	51

8.13	Top left: CAD representation of the frame supporting the IB. Bottom left: IB half-barrel CAD view with sensors and cable routing. Right: Exploded CAD view of IB from the h-side and the e-side. The orange element is the kapton shield. In blue the air conveyors are shown.	53
8.14	Left: OB staves for L3 and L4. Two staves per layer are shown. Right: Exploded view of an OB stave.	54
8.15	CAD model of the preliminary (half-) disk design. Modules are shown in alternately inward (dark gray) and outward (white) facing orientations. Common bus FPCs are shown in orange. RDOs (green) are arranged on the outside of the disk ring, inside of the interface to the SVT global support structure.	55
8.16	First L4 quarter length stave prototype.	57
8.17	(Left) First test piece of the carbon composite corrugated disc core made in the LBNL composite shop. Heaters with two different heating zones that can mimic the sensor power density are placed on the carbon composite facesheet and are used for thermal measurements. (Right) Observed ΔT on the LEC section of the test heater versus coolant air velocity using corrugated carbon fiber veil prototype test piece. Measurements taken with various sizes of PGS placed underneath heater.	58
8.18	An example of a low technology readiness level prototype for the FPC of the outer barrel (layer4). Prototype made by RPE LTU.	59
8.19	ePIC Tracking Subsystems	63
8.20	Nhits	63
8.21	Radiation dose	64
8.22	CyMBaL CAD model	66
8.23	μ RWELL-BOT in ePIC central detector frame	67
8.24	Hadron and lepton beam pipes and μ RWELL-ECT disks layout.	68
8.25	Hybrid GEM- μ RWELL detector and 2D readout scheme	69
8.26	Integration of the MPGD-ECT disks in the ePIC detector	72
8.27	Design details of MPGD-ECT disks	73
8.28	MPGD General Timeline	75
8.29	The histogram shows the relative yield of charged hadrons from Pythia simulations for 18×275 GeV ep collisions as a function of momenta and pseudorapidity, η . The contours indicate the 3σ separation region of the different ePIC PID subsystems for π/K (a), K/p (b), and e/π (c), respectively.	77
8.30	EPIC magnetic field map with the PID detector envelopes overlaid. Shown is the 1.7 T setup.	78
8.31	(a) Estimates of the 1-MeV neutron equivalent fluence in $\text{cm}^{-2}/\text{fb}^{-1}$ and (b) the sum of electromagnetic and charged-hadron doses in $\text{rads}/\text{fb}^{-1}$ integrated in 1 fb^{-1} equivalent Pythia events for 10×275 GeV ep collisions. The values shown are averaged over the azimuthal angle.	79
8.32	Geometries of BTOF with insert of sensor and charge sharing distribution (left), and the layout of sensor modules and service hybrids of FTOF on one side (right). . . .	81
8.33	BTOF $1/\beta$ as a function of momentum (p) in the simulation performance with PYTHIA DIS events (left). Upper limits on the 3σ particle separation from BTOF and FTOF as a function of pseudorapidity (right).	81
8.34	Fluence accumulated for 6 months at 100% time, corresponding to one year of data taking, the fluence has to be multiplied by the assumed 10 years of life time of the ePIC detector. Red squares highlight the barrel, end-cap, and B0 trackers detectors.	82
8.35	A schematic design of service hybrids for FTOF, which serves 3 modules or 12 sensors/ASICs.	85
8.36	A schematic design of the module for FTOF, which consists of 2×2 LGADs sensors and ASICs.	86

8.37	Schematic of the AC-LGAD sub-system readout chain. Each component is undergoing design, (pre-)prototyping, testing under various environments, and customization to meet the specific requirements of individual subsystems.	87
8.38	schematic drawings of one BTOF stave (left) and half of the whole FTOF (right) cooling pipes.	89
8.39	Barrel TOF supporting mechanic structure with engagement rings situated and supported by the EPIC global support tube structure (GST). The width of each of the three engagement rings is 5mm.	90
8.40	Left: Picture and beam test results for HPK strip sensor, 1 cm long, 500 μm pitch, and 50 μm metal electrode width. Right: Picture and beam test results for HPK pixel sensor, 4x4, 500 μm pitch, and 150 μm metal electrode width. Plots from Ref. [2]. . .	91
8.41	Left: Degradation of the gain layer for AC-LGADs of several wafer (with different N_+ , oxide and active thickness) from HPK latest sensor production, showing no change in gain layer doping up to 10^{13} Neq, which is an order of magnitude over the ePIC TOF radiation requirement. Sensors were irradiated at the TRIGA reactor (Lubjiana) with 1 MeV neutrons. Right: Normalized comparison of response profile of two nearby strips for two HPK 0.5 cm length, 500 μm pitch, 50 μm strip width: one before irradiation and one after 1×10^{14} Neq, even if the total signal is degraded the charge sharing profile is unchanged. Bottom: Current over voltage measurement for irradiated HPK sensors.	92
8.42	Left: FCFD Jitter measurements with 3.5 pf input capacitance and charge injection. Right: EICROC Discriminator jitter versus the injected charge, determined from data on an oscilloscope. Left: FCFD Jitter measurements with 3.5 pf input capacitance and charge injection. Plots from the erd112 and erd109 2024 reports.	93
8.43	Picture of ppRDO connected with CMS ETL module board v0 for testing.	94
8.44	Assembled stave prototype at Purdue.	94
8.45	Assembly process of BTOF stave. Note, the scale is not real.	96
8.46	Assembly process of FTOF modules. RB3 type is shown as an example. Note, the scale is not real.	97
8.47	Collaboration institutions and their responsibilities.	98
8.48	BTOF (left) and FTOF (right) project schedules (2024/10/05 version.)	98
8.49	simulation of $1/\beta$ as a function of particle momentum for BTOF and FTOF performance.	100
8.50	The proposed pFRICH detector. See the text for more details.	103
8.51	PLACEHOLDER Left: EIC HRPPD QE as a function of wavelength. Center: QE map in the full active area at a wavelength of 365 nm. Right: Single photon timing resolution (PiLas picosecond laser pulse jitter not unfolded).	104
8.52	PLACEHOLDER (Left) The reconstructed Cherenkov angle for electrons, pions, kaons, and protons as a function of momentum. (Middle) N_σ separation between the electron and pion hypotheses as a function of momentum. (Right) Same as the middle panel, for pion and kaon hypotheses.	106
8.53	PLACEHOLDER Yield ratios of π^-/e_{scat} before (open black squares) and after (black full squares) pFRICH veto on π^- in PYTHIA 6 $e+p$ collisions at 18×275 GeV for four η bins, covering full pFRICH η acceptance.	106
8.54	PLACEHOLDER Left: Aerogel transmittance as a function of wavelength for factory, BNL, and Temple University measurements. Right: Mirror sample reflectivities as measured at BNL as a function of wavelength.	107
8.55	PLACEHOLDER Institutions contributing to the pFRICH effort and their roles, resources, and participating workforce.	113
8.56	ePIC hpDIRC geometry in the Geant4 standalone simulation.	116

8.57	(Left) dRICH detector model with highlighted the major components. (Right) dRICH inside the ePIC services lines at the barrel HCAL end point.	118
8.58	(Left) CAD model of the dRICH photodetector unit (PDU) module with its major components. (Right) dRICH detector box model with 208 PDUs forming a curved active surface.	119
8.59	(Left) dRICH aerogel model. (Right) dRICH mirror model [placeholder].	119
8.60	Transverse map of the expected 1-MeV equivalent neutron fluence per 1 fb^{-1} of integrated luminosity in e+p interactions at the maximum EIC center-of-mass energy at the location of the dRICH photodetector ($210 < z < 260 \text{ cm}$). The average, maximum and minimum values within the region of the dRICH photodetector ($100 < R < 180 \text{ cm}$, indicated by the dashed lines) are reported.	120
8.61	(Left) Dark current measurements on sample SiPM sensors for the studies of repeated irradiation-annealing . (Right) Projected increase of the DCR of SiPM as a function of the integrated luminosity (delivered fluence). The "no annealing" and the "annealing limit" curves show the limits of possible operations. The dashed line indicate the desired maximum DCR threshold.	121
8.62	3D model of the dRICH FEB.	124
8.63	Block diagram of the dRICH gas system [graphically, a preliminary version].	124
8.64	(Left) Contributions to the single-photon angular resolution for aerogel. (Right) Contributions to the single-photon angular resolution for radiator gas.	125
8.65	(Left) Event display. (Center) Reconstructed mass vs momentum. (Right) Pion identification efficiency and pion to kaon mis-identification probability as a function of momentum in three bins of rapidity.	126
8.66	(Left) Service routing around the dRICH. (Center) Installation tool. (Right) Maintenance position.	128
8.67	(Left) Test stand for SiPM characterization. (Center) Performance comparison between different SiPM models. (Right) Prototype version of the SiPM carrier board (top) and FEB (bottom).	129
8.68	(Left) Fraction of residual irradiation damage measured on multiple SiPM candidate samples after "forward-bias annealing" cycles at increasing temperature and integrated annealing time. The measurements are shown for individual sensors (gray points) and as averages (coloured points, uncertainty of the average and RMS are indicated on the plot). (Right) Temperature increase of the SiPM sensor with respect to the temperature of the SiPM carrier board as a function of the "forward-bias annealing" power at different temperature values of the circulating thermostat system.	130
8.69	(Left) C_2F_6 measured transmittance. (Center) Aerogel large tiles assembling as obtained at BELLE-II [3]. (Right) Mirror demonstrator with an optimized dRICH core structure.	131
8.70	(Left) Baseline prototype with reference detector at the SPS-H8 beam line of CERN. (Center) First ePIC-drive detector box under test at the PS-T10 beam line of CERN. (Right) Real-scale prototype model mimicking the basic dRICH construction unit (sector).	132
8.71	(Left) Cherenkov angular resolution obtained for C_2F_6 as a function of the recorded number of photons. The SPE values is consistent with expectations. (Center) SPE angular resolution measured on aerogel as a function of the refractive index. The expected resolution is obtained for an index greater than $n=1.025$. (Right) Comparison in photon yield of sensor with different SPAD size. All the measurements are obtained with the dRICH prototype.	133

8.72	(Left) Prototype PDU and assembled detector plane. (Center) Cumulated ring imaging. (Right) dual-radiator interplay for a mixed hadron beam at 10 GeV/c: After the gas information is used to tag pions (clear histogram), an effective separation between kaon and proton is provided by the aerogel (shaded histogram).	134
8.73	Construction plan	137
8.74	Transmission, absorption and scattering length curves as a function of the wavelength for the tile with $n = 1.03$.	141
8.75	Transmittance as a function of the wavelength for all the tiles.	143
8.76	Transmission length as a function of the wavelength for all the tiles.	144
8.77	CAD drawing of the EEEMCAL. The small gray shapes are the scintillating crystals. The SiPM photosensor matrices are grouped over four crystals and indicated by the pink area. The green rectangles are part of the backend electronics. The dark gray rectangles and circles on the circumference are part of the cooling system.	147
8.78	Conceptual design of the ePIC electron endcap electromagnetic calorimeter support.	148
8.79	Left: waveform (top) and integrated signal (bottom) showing single photo-electron signals in Hamamatsu 15 μm pixel SiPMs. Signals are produced with a low-intensity LED. Right: Linearity measurement, showing 2% linearity up to 3500 photo-electrons.	148
8.80	EEEMCAL simulated performance using the ePIC detector framework including all materials. Left: energy resolution as a function of the incident particle energy. Right: pion rejection factor as a function of energy and different values of electron efficiency.	149
8.81	EEEMCAL integrated schedule.	151
8.82	EEEMCAL installation fixtures that allow for installing the detector safely into the ePIC detector barrel.	152
8.83	Screenshot of the EEEMCAL Risk Management Plan and registry.	153
8.84	Structure of Barrel Imaging Calorimeter and its sectors.	155
8.85	Components of Barrel Imaging Calorimeter imaging AstroPix layers.	156
8.86	Simulated energy resolution and sampling fraction for photons in different rapidity ranges of BIC.	159
8.87	Simulated angular resolutions for photons at BIC	160
8.88	Simulated performance on particle identification from BIC	161
8.89	Simulated performance on MIP response in BIC	162
8.90	Example performance of AstroPix_v3 chip	163
8.91	Barrel Imaging Calorimeter high-level schedule for design and production phases.	170
8.92	Simulated energy response of photons and electrons in Pb/ScFi and energy response tail in different rapidity range of BIC	171
8.93	Simulated energy resolution and sampling fraction for electrons in different rapidity ranges of BIC.	172
8.94	Measured energy responses in Baby BCAL to positrons and pions	172
8.95	Barrel Imaging Calorimeter org chart.	174
8.96	The front face of the ePIC hadron end-cap.	177
8.97	Matrix of scintillating fibers prepared to build production fEMCAL blocks and SEM image of tungsten powder.	178
8.98	Front and back views of LG plates with installed SiPMs.	180
8.99	Structural and installation tests at BNL.	181
8.100	Response of calorimeter vs position in hodoscope (left panel). Energy resolution for different impact angles (right panel).	182
8.101	Signal (single photon) efficiency and background (merged di-photons) contamination for different cut value of the NN output for 60 GeV (left panel). Probability of misidentifying π^0 as a single photon vs energy (right panel)	182
8.102	fEMCAL front end electronics.	184

8.103 Neutron detection efficiency vs. E and thresholds	189
8.104 Position resolution R_{xy} and cluster efficiency vs. E for different tile sizes	189
8.105 Top: Primary, generated particle E distributions in nHCal acceptance $-4.0 < \eta < -1.0$. Bottom: Primary, generated particle p distributions in nHCal acceptance $-4.0 < \eta < -1.0$	190
8.106 Top: Primary, generated particle E distributions in $-2.0 < \eta < -1.0$ range. Bottom: Primary, generated particle p distributions in $-2.0 < \eta < -1.0$ range.	191
8.107 Top: Primary, generated particle E distributions in $-3.0 < \eta < -2.0$ range. Bottom: Primary, generated particle p distributions in $-3.0 < \eta < -2.0$ range.	192
8.108 Top: Primary, generated particle E distributions in $-4.0 < \eta < -3.0$ range. Bottom: Primary, generated particle p distributions in $-4.0 < \eta < -3.0$ range.	193
8.109 Acceptance of photoproduced $J/\psi \rightarrow \mu^+\mu^-$ in $e + p$ collisions at $18 + 275$ GeV. Top left: Acceptance vs. μ_1 and μ_2 hitting different HCals. Top Right: Acceptance vs. $-t$ for different number of μ in nHCal. Bottom Left: Acceptance vs. Bjorken x_{bj} for different number of μ in nHCal. Top Right: Acceptance vs. Pomeron x_p for different number of μ in nHCal.	194
8.110 Acceptance of photoproduced $J/\psi \rightarrow \mu^+\mu^-$ in $e + p$ collisions at $20 + 100$ GeV. Top left: Acceptance vs. μ_1 and μ_2 hitting different HCals. Top Right: Acceptance vs. $-t$ for different number of μ in nHCal. Bottom Left: Acceptance vs. Bjorken x_{bj} for different number of μ in nHCal. Top Right: Acceptance vs. Pomeron x_p for different number of μ in nHCal.	195
8.111 Acceptance of photoproduced $\Phi \rightarrow K^+K^-$ in $e + p$ collisions at $18 + 275$ GeV. Top left: Acceptance vs. K_1 and K_2 hitting different HCals. Top Right: Acceptance vs. $-t$ for different number of K in nHCal. Bottom Left: Acceptance vs. Bjorken x_{bj} for different number of K in nHCal. Top Right: Acceptance vs. Pomeron x_p for different number of K in nHCal.	196
8.112 Acceptance of photoproduced $\Phi \rightarrow K^+K^-$ in $e + p$ collisions at $20 + 100$ GeV. Top left: Acceptance vs. μ_1 and μ_2 hitting different HCals. Top Right: Acceptance vs. $-t$ for different number of K in nHCal. Bottom Left: Acceptance vs. Bjorken x_{bj} for different number of K in nHCal. Top Right: Acceptance vs. Pomeron x_p for different number of K in nHCal.	197
8.113 Energy resolution of jets vs. jet energy E compared for inclusive jets(squares) and jets with neutral veto(triangles). Track only jets(blue) are also compared to track and nHCal cluster jets(red).	198
8.114 Position of the reconstructed clusters in x, y for 2-particle position resolution study.	199
8.115 Jet charged and neutral Fractions: The charged (black lines), neutral EM (blue lines), and neutral hadron (red lines) fractions of jets at the truth level in $\eta \in (-3.5, 1.0)$ (upper left panel), $ \eta < 1$ (upper right panel), and $\eta \in (1.0, 3.5)$ (lower left panel). This illustrates that while jets are dominated by charged and neutral EM particles, there are still a distinct population of jets at central rapidity with a substantial neutral hadronic component.	200
8.116 HCal Neutral Hadron Veto	201
8.117 Transverse cutaway view of an sPHENIX Outer HCal module, showing the tilted tapered absorber plates. Light collection and cabling is on the outer radius at the top of the drawing.	202
8.118 Scintillator tiles in a layer of the Outer HCal.	203
8.119 Leakage current in HCal measured once per fill as a function of total number of ZDC coincidence hits	206

- 8.120 **Muon energy deposited on tile:** energy deposited on a given scintillator tile (i.e. the sum of G4 hits for a tile) by single GeV/c μ^- with energies between 5 and 10 GeV/c as a function of μ^- pseudorapidity. Distributions were simulated using the 2023.06.1 simulation geometry. A clear MIP peak is observed. 207
- 8.121 **DIS energy deposited on tile:** energy deposited on a given scintillator tile (i.e. the sum of G4 hits for a tile) in 18×275 NC DIS events for $Q^2 > 1000$ GeV² for all particles in the events as a function of their pseudorapidity. Distributions were simulated using the 2023.07.2 simulation geometry. 208
- 8.122 **Resolution of calibrated single pion energies:** Resolution of calibrated single π^- energies. Distributions were simulated using the 2023.05.0 simulation geometry. Red markers indicate the output of the calibration using tile-based clusters from the BHCAL, while blue markers indicate the output of the calibration using tower-based clusters from the BHCAL. The closed markers indicate the resolution as obtained by comparing the mean of a gaussian fit to the calibrated energies vs. the particle energies, while the open markers indicate the resolution as obtained by directory comparing the mean of the calibrated energies vs. the particle energies. Calibration is carried out by the LD model. 209
- 8.123 **Single pion energies in only BHCAL:** reconstructed energy of leading (highest energy) BHCAL cluster for 2 (black) - 20 GeV (light blue) single π^- in the BHCAL *only*. Distributions were simulated using the 2023.05.0 simulation geometry. Clusters are formed from individual tiles. Solid lines are gaussian fits. Energies are “uncalibrated” in the sense that they have only been corrected for the sampling fraction. 210
- 8.124 **Uncalibrated single pion energies:** reconstructed energy of all BHCAL clusters for 2 (orange), 5 (pink), 10 (purple), and 20 GeV (blue) π^- with θ between 45° and 145° . Distributions were simulated using the 2023.05.0 simulation geometry. Closed markers indicate clusters formed from individual tiles, and open markers indicate clusters formed from towers (5 tiles). Solid lines are gaussian fits, but aren’t relevant for this particular plot. Energies are “uncalibrated” in the sense that they have only been corrected for the sampling fraction. 211
- 8.125 **Calibrated single pion energies:** calibrated energy of single 2 (orange), 5 (pink), 10 (purple), and 20 GeV (blue) single π^- with θ between 45° and 145° . Distributions were simulated using the 2023.05.0 simulation geometry. Closed markers indicate clusters formed from individual tiles, and open markers indicate clusters formed from towers (5 tiles). Solid lines are gaussian fits. Energies are calibrated, i.e. the output of a regression by a Linear Discriminant (LD) ML model as implemented in TMVA. The LD model is trained on the energy, pseudorapidity, azimuth, and no. of hits (constituent cells) of the leading (highest energy) BHCAL and BIC (ScFi + imaging) clusters as well as on the sum of energy in the 6 imaging (AstroPix) and 12 ScFi (Scintillating Fiber) layers of the BIC. 212
- 8.126 **Linearity of calibrated single pion energies:** Linearity of calibrated single π^- energies. Distributions were simulated using the 2023.05.0 simulation geometry. Red markers indicate the output of the calibration using tile-based clusters from the BHCAL, while blue markers indicate the output of the calibration using tower-based clusters from the BHCAL. The closed markers indicate the linearity as obtained by comparing the mean of a gaussian fit to the calibrated energies vs. the particle energies, while the open markers indicate the linearity as obtained by directory comparing the mean of the calibrated energies vs. the particle energies. Calibration is carried out by the LD model as was done in fig. 8.125. 213

8.127	Resolution of calibrated single pion energies: Resolution of calibrated single π^- energies. Distributions were simulated using the 2023.05.0 simulation geometry. Red markers indicate the output of the calibration using tile-based clusters from the BHCAL, while blue markers indicate the output of the calibration using tower-based clusters from the BHCAL. The closed markers indicate the resolution as obtained by comparing the mean of a gaussian fit to the calibrated energies vs. the particle energies, while the open markers indicate the resolution as obtained by directory comparing the mean of the calibrated energies vs. the particle energies. Calibration is carried out by the LD model as was done in fig. 8.125.	214
8.128	Uncalibrated single neutron energies: reconstructed energy of leading (highest energy) BHCAL clusters for 1 (black) - 10 GeV (violet) single neutrons with θ between 45° and 145° . Distributions were simulated using the 2023.06.1 simulation geometry. Energies are “uncalibrated” in the sense that they have only been corrected for the sampling fraction.	215
8.129	Uncalibrated single neutron energy fractions: fraction of the reconstructed energy of the leading (highest energy) BHCAL cluster to the sum of all BHCAL clusters for 1 (black) - 10 GeV (violet) single neutrons with θ between 45° and 145° . Distributions were simulated using the 2023.06.1 simulation geometry. Energies are “uncalibrated” in the sense that they have only been corrected for the sampling fraction. Demonstrates substantial cluster splitting for neutrons.	216
8.130	DIS reconstructed tile energy: the energy of reconstructed “hits” (i.e. the reconstructed energy of individual tiles) in the BHCAL in 18×275 NC DIS events for $Q^2 > 1000 \text{ GeV}^2$ for all particles in the events as a function of their pseudorapidity. Distributions were simulated using the 2023.06.1 simulation geometry. Demonstrates typical range of reconstructed energies on a tile-by-tile basis.	217
8.131	Jacquet-Blondel variables in CC DIS: DIS kinematic variables calculated using the Jacquet-Blondel method in 18×275 CC DIS events. The black lines indicate the distributions at the truth (“vertex”) level, and the blue/red lines indicate the distributions at the reconstructed level: blue indicates a detector with an acceptance of $ \eta < 3.5$, while red indicates a detector with an acceptance of $ \eta < 4$. Detector simulation and reconstruction was carried out using a fast simulation using Delphes. Figure 8.21 from the EIC Yellow Report.	217
8.132	Truth vs. reconstructed E_T^{miss}: the truth (x-axis) vs. reconstructed (y-axis) E_T^{miss} for 10×275 CC DIS events. Detector simulation and reconstruction was carried out using a fast simulation using Delphes. Figure 4 from arXiv:2006.12520.	218
8.133	JES/R for full (tracks + ECal + HCal): The $\text{JES} - 1 = \langle \Delta p/p \rangle$ (open markers) and JER (closed markers) plotted as a function of p_{jet} in the lab frame for jets in $\eta \in (-3.5, 1.0)$ (red points), $ \eta < 1$ (black points), and $\eta \in (1.0, 3.5)$ (blue points). In the barrel region, jets are constructed from reconstructed tracks and ECal clusters <i>without</i> a nearby track. Neutral hadrons are included in the jets by smearing the particle energy by the measured energy resolution of the sPHENIX OHCAL. Jets are reconstructed via the Centauro algorithm ($R = 0.8$) and transformed back into the lab frame. Jets are required to have at least 2 particles, and exclusively charged or neutral jets are rejected. From ECCE responses to the EIC DPAP Panel; received from John Lajoie in private communication.	219
8.134	Renderings of the forward calorimeter assembly (top left), tile assembly of 8 scintillator tiles of the LFHCAL with the SiPMs sitting in a dimple on each tile, detailed stacking example (middle right) and 8-tower module design (bottom).	222
8.135	Renderings of the absorber structure for the insert modules surrounding the beam pipe (top) and their individual layer composition (bottom).	223

8.136 Left: Visualization of 8M-scintillator assembly with its individual components. Right: Samples of the individual components used for the 2024 test beam campaign.	223
8.137 Combined energy resolution of the forward calorimeter system as a function of pseudo rapidity η for single pions, evaluated within the primary LFHCal acceptance.	225
8.138 Combined position resolution of the forward calorimeter system as a function of pseudo rapidity η for single pions, evaluated within the primary LFHCal acceptance.	225
8.139 Visualization of the individual components of an 8M module.	226
8.140 Visualization of the full LFHCal in its cradle (top) and details of its moving mechanism (bottom).	227
8.141 General timeline of the LFHCal design, construction and assembly.	229
8.142 Organizational chart of the LFHCal & insert consortium, indicated by the numbers are the associated WBS structures.	232
8.143 All four far-forward subsystems in the outgoing hadron beam direction. The green cylinders are accelerator dipole and quadrupole magnets.	233
8.144 Left: The B0 tracker's acceptance of protons ($E=110$ GeV), as a function of θ_x and θ_y . PLACEHOLDER NEEDS TO BE REMADE W/REAL B FIELD Right: The p_T resolution for protons reconstructed in the B0 tracker. PLACEHOLDER NEEDS TO BE REMADE WITH FINAL LOCATIONS, FINAL TRACKING, PROPER LABELLING ETC	235
8.145 The B0 EM calorimeter's acceptance of photons with a substantial (for now half their energy) deposit in a calorimeter crystal.	235
8.146 The energy reconstructed and associated resolution for the B0 EM calorimeter of photons with $\theta < 13$ mrad in the soft (left) and hard (right) energy reconstruction regimes.	236
8.147 Summary of transverse momentum resolutions for the Roman pots and Off-Momentum Detectors. Contributions are separated by those induced by intrinsic detector choices (e.g. pixel sizes) and those from beam effects (e.g. angular divergence), which have an outsized impact on momentum measurements at very-forward rapidity. Will be replaced with DD4HEP version	239
8.148 Strawman concept for the layout of the RP and OMD sensor staves. A 1x3 configuration is also being consider to reduce the size of the necessary Samtech connector for the staves, but more study is needed to assess impact of either choice, both in terms of construction feasibility and performance.	240
8.149 Strawman concept a readout board concept to communicate with and readout RP and OMD sensor staves. Work needs to be done to solve the issue of power distribution, and to ensure the EICROC ASIC can indeed be readout by the LpGBT.	240
8.150 The layout of the luminosity monitor in the ZEUS experiment [?].	245
8.151 Relative suppression due to the BSE $(d\sigma_{corr}/dy)/(d\sigma_{BH}/dy)$ is shown as a function of $y = E_\gamma/E_e$ for three cases of collider parameters, HERA, EIC 1 & EIC 2. The corresponding beam energies and Gaussian lateral beam sizes at the interaction point are listed [?].	246
8.152 Rate of single and coincidence events for the PS detectors calculated by Dr. Gan-gadharan	248
8.153 The layout of the luminosity monitor in the ePIC experiment of the EIC.	248
8.154 Unpolarised and polarised Bethe-Heitler Cross-Section. [?]	249
8.155 DD4hep implementation of PS Calorimeters.	253
8.156 Left: Low- Q^2 taggers in relation to beamlines and central detector. Right: Tagger module with calorimeter and tracker from recent CAD model.	254

8.157	Acceptance ranges of the Central Detector and Low- Q^2 Trackers as function of Q^2 and x .	255
8.158	Low- Q^2 tagger coverage.	256
8.159	Hit rates on tracker layers for Quasi Real (Top) and bremsstrahlung (bottom) electrons, incident on Tagger 1 (left) and Tagger 2 (right), This design is based on layers with three carrier boards, each containing twelve Timepix4 hybrid sensors. The dashed lines indicated the centre lines of the Timepix4 ASICs, where the vertical columns terminate.	258
8.160	Maximum and integrated rates for Low- Q^2 trackers.	259
8.161	Layout of SciFi calorimeter.	260
8.162	Energy resolution for Cherenkov fiber calorimeter.	261
8.163	Top - Reconstruction of the initial electron energy, θ and ϕ angles from fitted tracks. Bottom - Integrated reconstruction difference.	262
8.164	Reconstruction of the initial electron as a function of Q^2 .	263
8.165	Acceptance as a function of Q^2 and $E_{e'}$.	264
8.166	ePIC DAQ component count summary	268
8.167	ePIC DAQ component counts	269
8.168	Expected worse case data rates contributions for the ePIC detector	270
8.169	Maximum data volume per RDO with noise estimates.	270
8.170	Schematic of the ePIC Streaming DAQ	271
8.171	Components of the ePIC Streaming DAQ System	272
8.172	ePIC Electronics and ASICs summary	273
8.173	Discrete block diagram	273
8.174	Discrete Adapter (left) and digitizer FEB PCBs	274
8.175	Discrete key specifications	274
8.176	CALOROC block diagram	275
8.177	CALOROC Key Specifications	275
8.178	EICROC block diagram	276
8.179	EICROC timing performance	277
8.180	EICROC Key Specifications	277
8.181	FCFD block diagram of the frontend	278
8.182	FCFD timing performance	278
8.183	FCFD Key Specifications	278
8.184	ALCOR Si Die (left) and block diagram	279
8.185	ALCOR Key Specifications	279
8.186	Scope of the electronics and ASICs developments	279
8.187	TOF pre-prototype RDO	281
8.188	3D model of dRICH RDO	282
8.189	Schematic layout based for the GTU	284
8.190	Physical concept for the fiber distribution for the GTU	284
8.191	Operation of firmware trigger under assumption that the trigger decision for the dRICH depends upon data from fHCAL	286
8.192	Proposed ePIC slow controls network topology	289
8.193	DAQ/Computing schedule	290
8.194	Electronics and DAQ Resources	291

List of Tables

1	Table illustrating “rules”	15
2	Short top-level parameters caption.	15
3	A parameter table made available for export, using the /Tables subdirectory	15
4	A table with fixed third column width, enabling text filling.	15
5	Two ways to squeeze tables.	16
6	A third way to squeeze tables.	16
2.1	Event composition in incoherent J/ψ production before and after full event selection	32
8.1	Physics requirements on the relative momentum measurement, dp/p at the event vertex for different ranges in pseudorapidity, η , and on the determination of the radial distance of closest approach, DCA_r , of the particle trajectory to the event vertex with its dependence on transverse momentum, p_T	43
8.2	Radius, length and material budget of the SVT IB and OB layers.	46
8.3	Position along the beam pipe, outer radius and material budget for the SVT layers in the EE and HE regions.	46
8.4	Summary of power and readout services for the different regions of the sPIC SVT (slow control and data links are differential pairs of wires).	50
8.5	Maximum dose of radiation by different sources at MPGD tracker layers for e+p minimum-bias event at 500 kHz event rate for 10 years EIC running with 6 months run time per year and 100% efficiency [4].	64
8.6	Hit rate per unit area of various MPGD trackers for e+p DIS events at 10×275 GeV with $1.54 \times 10^{34} \text{cm}^2 \text{s}^{-1}$ luminosity scaled from e+p DIS events at 18×275 GeV and $1.54 \times 10^{33} \text{cm}^2 \text{s}^{-1}$ luminosity, 10 GeV electron beam gas and 275 GeV hadron beam gas	65
8.7	Maximum hit rate by a single channel of various MPGD trackers for e+p DIS events at 10×275 GeV with $1.54 \times 10^{34} \text{cm}^2 \text{s}^{-1}$ luminosity scaled from e+p DIS events at 18×275 GeV and $1.54 \times 10^{33} \text{cm}^2 \text{s}^{-1}$ luminosity, 10 GeV electron beam gas and 275 GeV hadron beam gas	65
8.8	The ECT disks geometrical envelope and active areas dimensions.	68
8.9	The ECT disks angular and pseudorapidity acceptance.	68
8.10	Services requirements for the three MPGD tracking subsystems.	71
8.11	Main equipment required in the production site and availability at sites	76
8.12	Required performance for physics and proposed configurations for the TOF detector system.	80
8.13	RAW and NEQ fluence per system for the lifetime of the ePIC experiment, assuming 10 years of data taking at 50% time.	82
8.14	Summary of BTOF and FTOF low voltage and high voltage powersupply cables to distribution panels and then to the detector FEE (the exact numbers are being checked at the time of writing).	88

8.15	BTOF is designed with a barrel geometry surrounding the beam pipe and interaction point, while FTOF is a disk geometry perpendicular to the beam direction on the hadron side (positive z).	89
8.16	List of the voltage services to the dRICH electronics, indicating the number of primary power-supply channels and boards as well as the cross-section of the cables (AWG). The number of power-supply boards is defined assuming to use commercial 8-channel low-voltage boards.	126
8.17	Planned quality assurance (QA) stations, organized in order to provide redundancy and support specific characterization studies.	136
8.18	Main elements of the dRICH photodetector system with the indication of number of elements per sector and the total.	141
8.19	Baseline specifications of the SiPM sensor devices for the dRICH photodetector. All parameters are defined at room temperature ($T = 25^{\circ}\text{C}$) and at the operating voltage V_{op} , unless otherwise specified.	142
8.20	Tiles list. Tiles from 1 to 17 were produced at the High Energy Accelerator Research Organization (KEK) in Japan and delivered in March 2021 [5], except tiles 6-7 which belongs to a 2000 production manufactured by Matsushita Electric Works (Japan).	143
8.21	EEEMCAL WBS Structure	150
8.22	Selected BIC Parameters.	157
8.23	AstroPix chip parameters for BIC.	157
8.24	SiPM specifications for BIC.	158
8.25	Scintillating fiber specifications for BIC.	158
8.26	Energy resolution parameters for photons in BIC for different η ranges.	159
8.27	AstroPix requirements comparison.	169
8.28	Some requirements on performance of fEMCal and its parameters	176
8.29	Requirements and Technical specifications for fEMCal scintillating fibers.	179
8.30	Requirements and Technical specifications for fEMCal SiPMs.	181
8.31	Requirements for the FEB	183
8.32	Control and status registers on the FEB	185
8.33	Maximum expected background rates for backward HCal. The assumed threshold is 170 keV.	188
8.34	Properties of HCal scintillating tiles.	203
8.35	Properties of Kuraray Y-11 (200) wavelength shifting fibers.	204
8.36	Design parameters for the Barrel Hadronic Calorimeter w/o additional absorber, based on the sPHENIX Outer Hadronic Calorimeter.	205
8.37	Overview of the calorimeter design properties for the LFHCal.	221
8.38	Summary of systematic uncertainties at ZEUS DPD and PS detector. [?]	250
8.39	Noise Estimates	270
8.40	SALSA specifications.	280
8.41	Types of RDO	281
8.42	DAM/RDO Decoded Synchronous Command Structure. This structure is defined to allow continuous availability of the critical beam related bits and more rare commands. The data in the 40 bits worth of flexible command data encoding remains flexible but must contain enough control bits to select what structure it has. The "type", "type specific" division is an potential holding this flexibility	285
8.43	RDO downlink words	285
8.44	DAQ Computing Resources	287
8.45	Slow Controls data volume and network traffic	289

multi-chapters

1 Chapter 0

2 Style Guide

3 The following is the Style guild as developed for the full design report. This is the guide the
4 accelerator team is following and it will make merging the documents together much easier if
5 everyone uses this guide.

6 0.1 Chapter Abstract

7 **Summary:** Each chapter begins with a stand-alone single “punch line” page that serves as a chapter
8 abstract. Rather than simply duplicating the Table of Contents outline of the subject matter of the
9 chapter, a well-constructed abstract will lay out the key ideas and conclusions that chapter editors
10 wish to convey to readers. The Executive Summary will also describe these key ideas, in a modestly
11 longer form (perhaps $\sim 250 - 1000$ words per chapter). This sample **non-EIC** chapter abstract
12 emphasizes key ideas such as the separation of pre-existing and new subsystems, and the level of
13 technical risk.

14 **The Cryogenic System** consists of the cryoplant that provides cooling for cryomodules; the test and
15 instruments cryoplant that provides cooling for test stands and liquid helium for instruments; cry-
16 oplant that provides 16 K helium cooling for the target hydrogen moderators, and the distribution
17 system that connects the linac cryoplant to cryomodules. The linac cryoplant and test/instrument
18 cryoplant share common gas management and storage systems. The target cryoplant system is
19 completely separate due to potential for tritium contamination.

20 **The Vacuum System** provides vacuum for the linac beam line, target system and instrument lines.
21 It uses well established technology and procedures based on experience at similar facilities, includ-
22 ing RHIC, Tevatron, and LHC. It has low technical risk.

23 **Test Stands** provide testing and validation of both RF equipment (klystrons and modulators) and
24 cryomodules. Cryogenic connection to cryomodules in the test stands will prototype similar con-
25 nections in the linac tunnel. The test stand program accommodates the unavoidable uncertainty
26 in EIC construction schedule by allowing for RF equipment testing in a temporary location if nec-
27 essary. Cryomodule testing will be carried out at the EIC site. All cryomodules will be tested at
28 nominal temperatures and RF power levels before tunnel installation.

29 **0.2 Wordsmithing**

30 **0.2.1 Passive voice**

31 Authors should avoid the passive voice as much as possible – as in this sentence. This rule is
32 sometimes made to be broken – as in this sentence :). The crucial point is that authors should not
33 use passive voice to avoid identifying the specific individual or group of individuals within the EIC
34 organization which is/are (or will be) responsible for fulfilling some specific function. It’s not good
35 enough to say, “Quality management will be implemented”. The purpose of the Design Report is
36 to explain for EIC itself, and for readers outside of EIC, who will implement quality management,
37 and how they will do it. Excessive use of passive voice is not just bad writing. It communicates
38 confusion or uncertainty about the path from aspiration to reality.

39 **0.2.2 Verb tenses**

40 The simplest way to make everything consistent is to apply a general rule:

41 Use past tense for things that happened in the past, present tense for things that are
42 happening now, and future tense for things that will happen in the future.

43 If the designs call for something to happen, they call for it in the present tense. But it will happen
44 in the future tense. Avoid inconsistent usage across chapters, across authors, and even within the
45 same paragraph by a single author.

46 **0.2.3 Apostrophes**

47 Decades are written as in the 1960s and 1970s, NOT as in the 1980’s or 1990’s.

48 **0.2.4 Capitalization and names**

49 **0.2.4.1 Pieces of EIC**

50 For example, linac, accelerator, target station, test stand. For the sake of consistency these terms
51 will not be capitalized.

52 **0.2.4.2 Internal phrases**

53 Correct capitalization for specific “internal” EIC phrases and names will be accumulated here. For
54 example:

55 Pre-construction Phase NOT Pre-Construction phase
56 Decommissioning Phase NOT De-commissioning phase
57 Work Packages NOT Work-packages

58

59 **0.2.4.3 Discipline-specific approaches or “guiding principles” or buzz phrases**

60 Such as design integration, systems engineering, defense in depth. Recommend capitalizing none
61 of them, but the important thing is to be consistent.

62 **0.2.4.4 Formal group names**

63 When authors identify the parts of the EIC organization who will be responsible for doing some-
64 thing, then capitalize the formal names of that groups from the org chart. Recommend avoiding
65 informal terms such as “test stand personnel”, where possible.

66 **0.2.4.5 Headings**

67 The titles of sections and subsections should have only the first letter capitalized.

68 **0.2.5 Captions**

69 Write Figure and Table captions in a self-contained way, to carry a complete self-contained descrip-
70 tion of the figure. Define symbology in all figures, either in the text or (preferably) in the caption.
71 Captions always end with a period. Use the format:

```
72 \caption[Short caption for List of Tables or Figures.]{Long caption to carry a complete  
73 self-contained description of the figure or table, in the chapter text.}
```

74 **0.2.6 Spelling**

75 The Design Report follows American spelling rules. For example, with “z” not “s”, and “program”
76 not “programme”:

```
77     emphasize not emphasise  
78     meter not metre  
79
```

80 **0.2.6.1 Exceptions to U.S. spelling**

81 1. (None so far).

82 **0.2.6.2 Capitalization**

83 The words “Figure”, “Table”, “Chapter” and “Section” should always be capitalized in the text if
84 they occur with a number. For example, Figure 3.8 occurs in Chapter 3 and Table 5.5 is in Section
85 5.1.3, but there are many other figures and tables in other section, subsections and chapters.

86 **0.2.7 Commas**

87 The incorrect placement of a comma can change the meaning of a sentence. For example, compare
88 “Let’s eat Mom” and “Let’s eat, Mom”. And compare “Scientists, who conduct important research,
89 are well respected in the community” with “Scientists who conduct important research are well
90 respected in the community”.

91 Commas go where there is a natural pause in a long sentence, where additional information has
92 been added to a sentence and where, if removed, the sentence would still make sense. They are
93 used when listing items – between each item on the list. They are used where two shorter sentences
94 are made into one (usually with the addition of “and”), but still consist of two separate parts. And
95 they are used after “lead” words [however, therefore, consequently, in fact].

96 **0.2.7.1 Commas in numbers**

97 Write 2.4 million and not 2,4 million (as in some parts of Europe).

98 No commas in numbers below 10,000 – thus, write 1240 and 9999, but 12,400 and 99,999.

99 **0.2.8 Plurals and possessives**

100 For example, use

101 WPs not WP’s (plural)
102 EIC’s not EIC’ (possessive)

103

104 **0.2.9 Abbreviations**

105 **0.2.9.1 Textual treatment of Figures and Tables**

106 The words “Figure” and “Table” should always be capitalized in the text. Include a reference or
107 discussion of all Tables and Figures in the main text of the chapter. For example, “Figure 3.8 shows
108 thus-and-such”. The abbreviations Fig. and Tab. should not be used.

109 **0.2.9.2 Radio frequency**

110 The phrase “radio frequency” is always two words and is never hyphenated or capitalized, whether
111 used as an adjective or as a noun. Thus, the two radio frequencies used in the radio frequency
112 system are 352.21 MHz and 704.42 MHz. The upper case abbreviation “RF” is acceptable in many
113 circumstances.

114 0.2.9.3 etc., et cetera

115 It is acceptable to use “e.g.” within parentheses, but not outside. For example, Jack and Jill met
 116 many animals (e.g. Reynard the Fox) when going down the hill. It is also correct to say that Jack
 117 and Jill met many animals, for example Reynard the Fox, but no tortoise. Similar rules apply for
 118 “i.e.”.

119 The periods (i.e. the full stops) should not be dropped, for example “ie” or “eg”.

120 It is incorrect to use ok, o.k., or okay.

121 The following are acceptable:

122 e.g.

123 etc.

124 i.e.

125 RF (in many circumstances)

126

127 0.2.10 Hyphenation of multi-word adjectival phrases

128 In general, hyphenate an adjectival phrase where the second part is a past (-ed) or present (-ing)
 129 participle of a verb. Consider the following illustrative (nonsensical) paragraph:

130 This chapter describes the *beam physics design* of the *neutron-generating* spallation tar-
 131 get. Following a brief overview, the chapter presents a detailed description of the *beam*
 132 *physics* of EIC, which drive the accelerator design. The accelerator consists of several
 133 sections: the ion source, *normal-conducting* linac, *superconducting* linac and *beam trans-*
 134 *port* sections. The chapter also describes the *radio frequency* system.

135 Simplified advice available online includes: “When two or more words are combined to form a modifier
 136 immediately preceding a noun, join the words by hyphens if doing so will significantly aid the reader in
 137 recognizing the compound adjective.” Not so simple are phrases like “high-power proton beam” where
 138 “proton beam” itself is a single idea. Some judgement is involved

139 For the sake of consistency, the editors have created and are expanding a spreadsheet of words
 140 and phrases specifying hyphenation policy for the Design Repoprt. Here are somewhat-arbitrary
 141 rules for whether or not to hyphenate some common multi-word phrases, *when they are used as an*
 142 *adjective, a noun, or as a verb*. Alphabetically:

143 1D, 2D, 3D, 4D

144 accelerator-driven

145 back up (verb)

146 back-flow (noun adj)

147 backscattering

148 backup (adj noun)

149 baseline (adj or noun)

150 beam dynamics

151 beam guide

152 beam instrumentation

153	beam physics
154	beampipe
155	beam port
156	beam time
157	beam transport
158	beamline
159	bispectral
160	bottom-up approach
161	broadband
162	by-product
163	clamshell clamshell-style
164	clean room
165	cold box
166	co-chair (noun)
167	contact-less
168	cool-down (noun or adj)
169	coordinate
170	cost-saving
171	cross reference (noun)
172	cross-reference (verb)
173	cross section
174	cryo-building
175	cryo-pump
176	cryo-system
177	cryomodule
178	cryoplant
179	debunched
180	decision making (noun)
181	decommissioning
182	de-excitation
183	deionised
184	down-mix
185	downtime
186	eigenmode (noun adj)
187	equipartitioning
188	failover
189	failsafe
190	feed box
191	feedthrough
192	follow up (verb)
193	follow-up (adj and noun)
194	hands-on (adj)
195	high level
196	high- β
197	high-current (adj)
198	high-power
199	high-resolution
200	hot cell
201	<i>in situ</i> (italicize)
202	innermost
203	inrush

204	interdependency
205	interlayer
206	intra-layer
207	intra-nuclear
208	Joule-Thomson valve
209	layout (noun)
210	life-cycle (noun)
211	line-of-sight
212	long-pulse
213	lookup
214	Lorentz detuning (noun)
215	Lorentz-detuning (adj)
216	low-resolution
217	magnetoresistance
218	medium- β
219	metadata
220	micropattern
221	microphonics
222	midpoint
223	middleware
224	multi-component
225	multi-layer
226	multi-pacting
227	multi-particle
228	multi-resistant
229	nanoparticle
230	nano-sized
231	nanostructure
232	neutron-generating
233	noninvasive (seen both ways in different dictionaries)
234	normal-conducting
235	on-board
236	ongoing
237	on-site (adj)
238	outermost
239	outgassing
240	overarching
241	phase space (noun)
242	phase-space (adj)
243	pinpoint
244	plug-in
245	post mortem (noun or adj)
246	pre-cools
247	premoderator
248	prequalification
249	radio frequency
250	radionuclide
251	radiotoxic
252	ramp up (verb)
253	ramp-up (noun)
254	read-back

255	ready-made
256	requalification
257	roadmap
258	safety-critical
259	short-pulse
260	short-term
261	shut off (noun verb)
262	shut-off (adj)
263	space charge (noun)
264	space-charge (adj)
265	staff-based
266	start-up
267	state-of-the-art
268	storm water
269	stripline
270	sub-atmospheric
271	subcomponent
272	sub-cool
273	sub-millimeter
274	sub-second
275	superconducting
276	switchyard
277	systemwide
278	thermo-mechanical
279	thermo-plastic
280	thermo-responsive
281	thermosyphon
282	time-frame
283	time scale
284	time-saving
285	time-stamp (noun and verb)
286	timeline
287	timesaving (adj and noun)
288	tool-set
289	top level
290	trade-off
291	tunable
292	tune up (verb)
293	tune-up (adj and noun)
294	twofold
295	uniaxial
296	uninterruptible
297	un-irradiated
298	up-mix
299	uptime
300	von Mises
301	waste water (noun)
302	waveguide
303	work flow (noun)
304	work-flow (adj)
305	workspace

306 world-leading
 307 X-ray (upper case X)
 308 zigzag (noun or adj)
 309

310 **0.2.11 Double letters**

311 In UK spelling, both “focussing” and “focusing” are considered to be correct. In the Design Report
 312 we use single “s” spelling in all cases.

313 Note the ‘double “l” rule for UK English – label becomes labelled, travel becomes travelled, et
 314 cetera. Not so with U.S. English in the Design Report.

315 **0.2.12 Mathematical symbols, subscripts and superscripts**

316 Mathematical symbols are written in math-mode, even when they are embedded in text. For exam-
 317 ple, a longitudinal dimension L is often called a length. Descriptive subscripts and superscripts, as
 318 in L_{acc} or $L^{overhead}$, are not written in Roman font. They appear to be italics, no matter how long or
 319 short they are.

320 **0.2.13 Quotation marks**

321 \LaTeX is fussy about some things, like quotation marks. Sooner or later an author, a chapter editor,
 322 or a general editor must pay attention. This the correct way to put “a certain piece of text” inside
 323 quotation marks. The following “certain piece of text” is incorrect.

324 **0.2.14 Citations, references and the bibliography**

325 **Please use inspire hep bibtex entries and notation whenever possible.**

326 Don’t use a “pointer” (for example [4]) in place of naming a reference [6]. That is, use “Joe
 327 Blow [4] describes thus and such,” NOT, “[4] describes thus and such”. There should be a
 328 space in the text before the citation, so “Joe Blow[4]” is wrong. Multiple citations should be
 329 placed with the same square brackets. In the \LaTeX vernacular, use `Joe Blow~\cite{Blow2011}`
 330 or `Joe Blow~\cite{Blow2011,Smith2012}`.

331 We are using `bibtex` to handle the references, which are gathered into one `bib` file per chapter,
 332 although all references appear in a single bibliography at the end of the Design Report.

333 During the editing process we are (currently by default) using the \LaTeX package `showkeys`, which
 334 flags references (to Tables, Figures, sections and subsections) and citations (to references) above the
 335 text, or in the margin. This should aid in generating cross-references, for example, even though it
 336 is rather ugly. It will be turned off in the final stages of editing, before printing. (Comments and
 337 feedback, please!)

338 0.2.15 Miscellaneous**339 0.2.15.1 “Calculations show that ...”**

340 This usage, with no indication who carried out the calculations, provides no way for a reader to
341 check the work, or to build upon it in the future. Citations of internal documents, or of individuals
342 to contact to get more information would be helpful for readers, and would also convey a greater
343 sense of credibility. For example, “Relativistic Heavy Ion Collider (2021), unpublished calculations
344 by members of the XYZ working group. Contact Sven Larsson (sven.larsson@bnl.gov) for details.”

345 0.2.15.2 “Should”, “must”, and reference to future studies

346 In general, authors should convey the conviction that EIC will do what it should do. In those cases
347 where there is an ongoing internal debate, the Design Report should convey the sense that such
348 debates will be resolved on the basis of a reasoned and careful assessment of the evidence. Only
349 write about future studies in those limited cases where it is needed to show “that we know what
350 we are doing”.

351 0.2.15.3 “Enable”

352 Incorrect usage:

353 “Neutrons pass easily through most materials, enabling the study of large or bulk sam-
354 ples and buried interfaces.”

355 Correct usage:

356 “In addition, as the BLM system will be a major tool for beam tune-up, it should also be
357 designed in a way that enables it to pin-point the loss location as precisely as possible.”

358 The point is that the direct object of enable is made capable of doing something – roughly a syn-
359 onym for empower. You enable the direct object to do something (enable it to pin-point ...). You
360 could rewrite the first sentence to say, “enabling the study of large or bulk samples ... to take place.”
361 Then it would be correct – although more unwieldy than just saying “making possible the study of
362 ...”

363 0.2.15.4 Reporting technical results without a clear statement of their import

364 In general, it is a mistake to assume that “the numbers speak for themselves”. Using words to
365 summarize the meaning of results helps readers to understand them; it also signals that the authors
366 understand the implications of the results they report.

367 0.2.15.5 Excessive and inconsistent use of lists

368 Sometimes the use of lists is appropriate, but often there are too many in a draft. Authors should re-
369 work most lists into narrative form. For the remaining lists, authors should follow editorial guide-

370 lines to ensure consistent style across the entire Design Report.

371 After minimizing the number of lists, Design Report editors will convert most of the remaining lists
 372 to enumerated lists. The first letter of each item will be upper case, even when the items in the list
 373 are not formulated as complete sentences. Items will generally end with a semi-colon unless the
 374 phrases are very short, in which case a comma will be used. The last item in the list will be followed
 375 by a period. In those cases in which each item in a list consists of multiple sentences, items will be
 376 ended with a period.

377 0.2.15.6 Cross-references

378 Should be added throughout the whole Design Report, but only down to `\subsection` level, so that
 379 cross-references can be found and numbered in the Table of Contents. This implies that subsections
 380 should be reasonably balanced in length – not too many pages long.

381 0.2.15.7 Isotopes

382 Write ${}^3\text{He}$, for example, not 3He or He-3.

383 0.2.15.8 *** asterisks in comments

384 Sometimes a comment is inserted in a sentence, perhaps indicating that something needs to happen
 385 later, such as add a value, a citation, or more text. In this case please include (at least) 3 asterisks
 386 in a row `***` so that text searches (for example `grep *** *.f`) are made easier. ALSO CONSIDER
 387 WRITING IN UPPER CASE***.

388 0.3 Dimensions and units

389 Systeme Internationale (SI) units will be used wherever possible. For example, use MPa instead of
 390 bar. Some exceptions are inevitable, for example Kilpatrick units. Unusual units should be briefly
 391 explained, on their first introduction.

392 When in doubt, the `siunitx` package does the Right Thing, for example using:

- 393 • `\si{\units}` lower case si
- 394 • `\SI{numbers}{\units}` upper case SI

395 A longitudinal dimension – or length – L should be written in one of these ways:

- 396 • $L = 100 \text{ m}$ $\$L = 100\text{~m}$
- 397 • $L = 100 \mu\text{m}$ $\$L = 100\text{~}\si{\micro\metre}$
- 398 • $L = 100 \text{ km}$ $\$L = \$ \SI{100}{km}$
- 399 • $L = 10^2 \text{ km}$ $\$L = \$ \SI{e2}{km}$

400 so that the dimension (“m” or “μm” or “km”) is not in italics, and is separated from the numerical
 401 value by a non-breakable space – for example “~” in L^AT_EX vernacular. Do not write $L = 100\text{m}$,
 402 $100m$ or $100 m$. Note that text and mathematical equals signs are different in length (= and =):
 403 always use the latter.

404 Powers of ten are written in one of these ways:

- 405 • 3.14×10^{39} `3.14×10^{39}`
- 406 • 3.14×10^{39} `\SI{3.14e39}{}`

407 Complex dimensions may be written in one of these ways:

- 408 • $F = 42 \text{ J cm}^{-2} \text{ s}^{-1}$ `$F = 42$~J cm$^{-2}$ s$^{-1}$`
- 409 • $F = 42 \text{ J cm}^{-2} \text{ s}^{-1}$ `$F=$ \SI{42}{J.cm^{-2}.s^{-1}}`

410 Exceptionally, percentages are written without a space – 42% is correct but 42 % is not. In L^AT_EX ver-
 411 nacular a % sign is the beginning of a comment, so it is necessary to say % ...

412 Temperatures are written as 273 K or 100°C or 101°C, without a space between the number and the
 413 °C unit symbol.

414 Angles are preferably written $\theta = 7.5$ degrees, although 7.5° is acceptable.

415 0.4 Numbering – chapters, sections, and subsections

416 In the `\documentclass{report}` style, a “section” (such as this, with the numeric label 0.4) has two
 417 numbers associated with it.

418 0.4.1 This is the heading of a subsection

419 A “subsection” (like this, 0.4.1) is labelled by 3 numbers, namely “chap-
 420 ter_number.section_number.subsection_number”. Sections and subsections begin with a bold
 421 face font.

422 0.4.1.1 A subsection heading like this has no period at the end

423 In bold font, it has no numerical label, and sits separately from the text that immediately follows,
 424 even if there is no white space between `\subsubsection{}` and the first word of the text. It does
 425 not appear in the Table of Contents.

426 **This paragraph heading ends with a period.** Subsequent text remains in the same para-
 427 graph. The editors will use their judgement to prevent the excessive use of paragraph headings
 428 and boldface text.

429 0.4.2 More formatting rules and standards

430 0.4.2.1 Clearpages and Pagebreaks

431 As a rule there is NO `\clearpage` or `\pagebreak` before a new section (or subsection), and hence
432 no white space.

433 0.5 Equations, Tables, Figures, and plots

434 0.5.1 Equations

435 Start with a simple equation, like Equation 1:

$$H = \frac{\sqrt{3 \langle x^4 \rangle \langle x'^4 \rangle + 9 \langle x^2 x'^2 \rangle^2 - 12 \langle x x'^3 \rangle \langle x^3 x' \rangle}}{2 \langle x^2 \rangle \langle x'^2 \rangle - 2 \langle x x' \rangle^2} \quad (1)$$

436 Avoid ending a sentence with an equation, in order to avoid deciding whether or not to put a period
437 after the equation.

438 Here is a simple equation array:

$$\begin{aligned} M_{virg}(\sigma) &= M_{virg0} + k_{virg} \cdot \sigma \\ M_{rel}(\sigma) &= M_{rel0} + k_{rel} \cdot \sigma \end{aligned} \quad (2)$$

439 0.5.2 Tables

- 440 • Table 1 is a relatively complicated multi-column table, while Table 2 is a standard 3-column
441 parameter table.
- 442 • Table 3 shows how to make a table exportable, for example to the Parameter Tables appendix.
- 443 • The source text for Table 4 shows how to enable text filling in columns.
- 444 • Table 5 shows 2 ways to squeeze tables, with the `\scalebox{}` and `` commands.
- 445 • Table 6 shows a third way, using `\tabcolsep{}`.

446 The vertical spacing of Table rows is set in “preamble.tex” by the line
447 `\renewcommand{\arraystretch}{1.0}`.

448 0.5.3 Converting between LaTeX and Excel table formats

449 More than one free utility enables table conversion with a drag-and-drop interface. E.g.:

450 **Excel to LaTeX** try <https://tableconvert.com/excel-to-latex>

451 **LaTeX to Excel** try <https://tableconvert.com/latex-to-excel>

Facility	Location	Status	First oper.	Power [MW]	Instruments	Integrated flux [10^{14}cm^{-2}]	Peak flux [$10^{15}\text{cm}^{-2}\text{s}^{-1}$]
ESS	Lund	Pre-constr.	2019	5	22	–	40
J-PARC	Tokai	Re-furbish	2009			–	

Table 1: A standard Table looks like this, using “toprule”, “midrule” and “bottomrule” separation lines.

Parameter	Unit	Value
Energy	GeV	2.5
Current	mA	50
Pulse length	ms	2.86
Pulse repetition frequency	Hz	14
Average power	MW	5
Peak power	MW	125

Table 2: Long version of caption for top-level parameters.

Parameter	Unit	Value
Energy	GeV	2.5

Table 3: A parameter table made available for export, for example to Appendix E “Parameter Tables”, using input from a /Tables subdirectory file.

System	Subsystem	Test
Target	Shaft and drive	Run at up to 25 Hz.
	Target segments	Leak test at pressure.
	Target Safety System	Demonstrate trip signals generated for all defined cases.
Primary helium loop	Pump, heat exchanger, filter	Pressure and flow tests without target.
	Full loop with target	Full operational test without heat.

Table 4: A table with fixed third column width, enabling text filling.

Nuclide	Decay time [years]						
	0	6	40	100	1000	10 ⁴	10 ⁵
³ H	0.9	83.4	96.4	72	0	0	0
¹⁴ C	0	0	0	0	0.3	0.6	0
³⁶ Cl	0	0	0	0	0	0	0.7
³⁹ Ar	0	0	0	0.1	0.7	0	0
¹⁵⁴ Dy	0	0	0	0	0	0.2	4.3
¹⁶³ Ho	0	0	0	0.7	29.7	53.4	0

Table 5: Two ways to squeeze tables, with the “scalebox” and “phantom” commands.

Nuclide	Decay time [years]						
	0	6	40	100	1000	10 ⁴	10 ⁵
¹³⁷ La	0	0	0	0	1.4	8.7	57.6
¹⁴⁸ Gd	0	0.2	0.9	11.6	0.1	0	0
¹⁵⁰ Gd	0	0	0	0	0	0.3	5.6
¹⁵⁴ Dy	0	0	0	0	0	0.2	4.3
¹⁵⁷ Tb	0	0.1	0.6	9.3	7.2	0	0
¹⁵⁴ Dy	0	0	0	0	0	0.2	4.3
¹⁶³ Ho	0	0	0	0.7	29.7	53.4	0

Table 6: A third way to squeeze tables, with the “tabcolsep”.

452 0.5.4 Figures

453 Many figures, like Figure 1, are non-graphical images – perhaps a photograph, drawing or sketch.



Figure 1: This is an example of a non-graphical figure. We need to address the means by which we can give “all” graphs the same look and feel.

454 0.5.5 Plots

455 It is clear that for the ePIC detector sections we will mostly be using ROOT and Python, while the
456 accelerator team most likely will be using a different package; so as soon as a figure style is agreed
457 on, we will need to make style packages for ROOT and Python so all figures in the manuscript look
458 stylistically the same.

459 As teams develop initial plots, please be sure to each the codes available so that they can be remade
460 in a common style.

461 0.6 Italics and bold face type

462 In general, retrain the use of *italics* and **bold face**.

463 Long quotations will be set in italics. Italics will also be used (sparingly) for traditional purposes
464 of emphasis (e.g. “when she was good, she was *very* good.”)

465 Occasionally, authors wish to draw attention to the subject matter being addressed in a block of text.
466 Usually, this should be done by headings and subheadings. In those limited instances in which use
467 of altered type face is appropriate within the body text, the editors will use bold face, rather than
468 italics. One such situation is for short introductory phrases at the beginning of paragraph-long
469 items in an enumerated list.

470 **0.7 Issues that this Style Guide does not yet address**

471 This Style Guide addresses “consistency of style” issues. Here is a numerical list of issues that
472 could or should be significantly expanded:

- 473 1. the use of pronouns
- 474 2. specialized terminology
- 475 3. acronyms
- 476 4. the use of italics
- 477 5. the use of digits (e.g. 1) where written numbers are more appropriate
- 478 6. the overuse of capital letters (Boron vs. boron, User vs. user, etc.).
- 479 7. balancing the length of sections and subsections
- 480 8. global glossary
- 481 9. Lists
- 482 10. Plots (see placeholder 0.5.5)

483 Chapter 2

484 Physics Goals and Requirements

485 2.1 EIC Context and History

486 The Electron-Ion Collider is a major new research facility to advance the longterm vision for Nu-
487 clear Physics to discover and understand the emergent phenomena of Quantum Chromo-Dynamics
488 (QCD). The developing of the physics case for the EIC has been a tremendous community effort
489 over the last few decades.

490 A joint report on the EIC Science case was put together at the Institute for Nuclear Theory (INT) in
491 2010 [7]. This set the base for the following release in 2014 of a White Paper (WP) [8] outlining the
492 fundamental questions that would have been addressed at the EIC. In the following year, the US
493 2015 Long Range Plan for Nuclear Science recommended a high-energy high-luminosity polarized
494 EIC as the highest priority for new facility construction.

495 In 2016, the worldwide fast growing community of scientists interested in the EIC organized itself
496 under the EIC Users Group (EICUG) [www.eicug.org].

497 In 2017, the National Academy of Sciences, Engineering, and Medicine (NAS) assessed the science
498 case of the EIC as “compelling, fundamental, and timely”. Quoting from the NAS report [9] re-
499 leased in 2018, the EIC can uniquely address three profound questions about nucleons—neutrons
500 and protons—and how they are assembled to form the nuclei of atoms:

- 501 • How does the mass of the nucleon arise?
- 502 • How does the spin of the nucleon arise?
- 503 • What are the emergent properties of dense systems of gluons?

504 In December 2019, following the extremely positive assessment by the NAS, the US Department
505 of Energy (DoE) established EIC Critical Design 0 (CD0), a “mission need” declaration”, formally
506 starting the EIC Project.

507 At about the same time, in late 2019, the EICUG led an intensive, year-long consideration of the
508 EIC physics measurements and scientific equipment. This initiative yielded the EICUG Yellow
509 Report (YR) [6] defining the detector requirements needed to deliver the science case endorsed by
510 the NAS report and highlighted in the WP and all the subsequent studies and publications. The YR

511 provided the basis for further development of concepts for experimental equipment best suited for
512 EIC science needs.

513 The ePIC Collaboration, established in July 2022 at the EICUG Meeting at Stony Brook University.
514 ePIC was born as a merger of two pre-conceptual designs, ECCE [10] and ATHENA [11] and is a
515 general purpose detector to deliver the whole EIC core science program.

516 The propose of this chapter study key measurements in order to demonstrate that our current
517 detector design, is capable of delivering on its mission.

518 Processes taken into consideration are chosen for both their relevance to the core science and the
519 specific challenges that they pose to the detector.

520 All the studies contained in this pre-TDR are based on a full GEANT4 simulation of the ePIC de-
521 tector and reconstruction tools as available in the October 2024 simulation campaign. As the devel-
522 opment of both simulation and tools progresses, we will repeat our studies for the final TDR.

523 In some instances, our ability to demonstrate the detector performance for a relevant measurement
524 might be hampered by the absence of a needed tool that was yet to be developed/finalized. When
525 this occurs, it must not be taken as that the detector cannot accomplish a certain measurement or
526 that we are overlooking certain physics. Our goal is to be able to show those results by the final
527 version of the TDR (90% design completion).

528 There are many studies performed by the ePIC's Physics Working Groups that will not enter this
529 selection but that are absolutely relevant for the EIC core science and beyond. Furthermore, many
530 details that went into the physics studies, both on the analysis and the impact on the current knowl-
531 edge, will be omitted for the purpose of this TDR. The ePIC collaboration plans to separately pub-
532 lish a "science paper" containing all the missing information that cannot be given within the present
533 document.

534 2.2 The Science Goals of the EIC and the Machine Parameters.

535 We will add more on science goals and machine parameters here by version 1

536 2.3 Reconstruction Tools and Special Probes

537 2.3.1 Kinematic reconstruction

538 The DIS scattering event can be described by two kinematic variables, typically the momentum
539 transfer squared, Q^2 , and scaling variable, x_B . Although it is possible to completely reconstruct
540 neutron-current inclusive event kinematics from only the scattered electron, this does not always
541 result in the best resolution. To optimize resolution, multiple reconstruction methods can be em-
542 ployed, using various combinations of scattered electron and hadronic final state (HFS) informa-
543 tion:

- 544 • **Electron method:** uses only scattered electron
- 545 • **$e\Sigma$ method:** uses both scattered electron and HFS
- 546 • **Double-angle method (DA):** uses both scattered electron and HFS

- **Jacquet-Blondel method (JB):** uses only HFS

For more details on these three methods see Sec.8.1.1 of the YR [6]. Generally, these methods differ in the calculation of Q^2 and inelasticity y , then the scaling variable is calculated as $x_B = Q^2/sy$. Note that while JB typically does not give the best resolution, it is the only reconstruction method possible for charged-current interactions (where the outgoing DIS lepton is a neutrino).

Figure 2.1 shows the y resolution at ePIC as a function of x_B and Q^2 for 18 GeV on 275 GeV ep collisions. As can be seen, the optimal reconstruction method changes with kinematics. These resolutions result from reconstructing the electron momentum strictly from tracking detectors. The resolution could be further improved by using the electromagnetic calorimeter clusters to reconstruct the electron energy. This is particularly important for electrons scattered into the backwards ECAL.

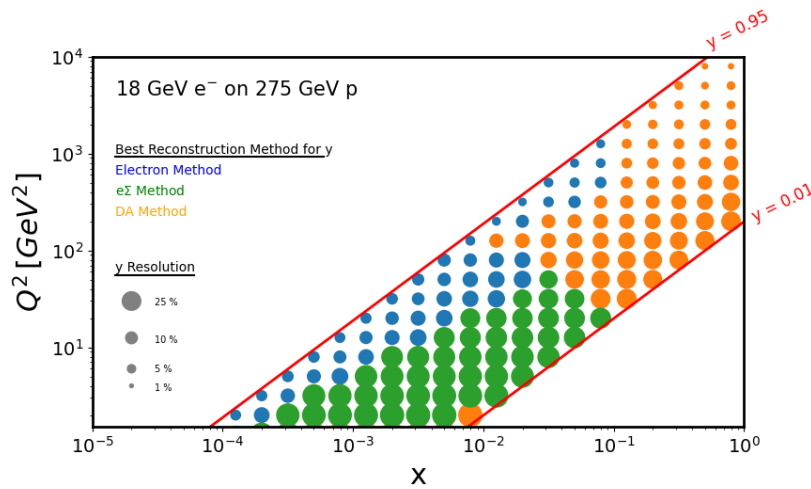


Figure 2.1: y Resolutions.

2.3.2 Electron identification and event selection

Regardless of reconstruction method used, it is important to identify the scattered electron in the event final state. It can be challenging to separate the electron signal from the large π^- background present in DIS collisions. A rudimentary electron identification algorithm has been already developed in ePIC and applied to inclusive analyses.

The first step is to separate final state electrons from pions. This is done by applying a cut on E/p , where p is the track momentum and E is the ECAL cluster energy matched to that track. Electrons will typically deposit all of their energy in the ECAL and have $E/p \approx 1$, while pions will pass through the ECAL and peak at $E/p < 1$. The current analysis uses a cut of $0.7 < E/p < 1.3$, which accounts for smearing due to electron energy and momentum resolutions.

The next step is to identify the scattered DIS electron, as other electrons may be present in the final state. All negative tracks satisfying our E/p requirement are used to calculate $\delta_h = \sum_i (E_i - p_{z,i})$, where the sum i runs over all final-state hadrons. Note that the electron candidate must be excluded in the summation. For the DIS electron, $\delta_h \approx 2E_e$, while for other particles $\delta_h < 2E_e$. The current analysis chooses the electron candidate with the highest δ_h .

573 This rudimentary algorithm is actively being improved, namely by incorporating signals from PID
 574 detectors (hpDIRC, pfRICH, TOF), applying cuts on shower shape parameters of the calorimeter
 575 clusters, and using a more rigorous treatment of δ_{η} instead of simply taking the largest value.

576 Further, kinematic cuts are applied to ensure DIS kinematics and avoid regions of poor resolution
 577 and large backgrounds:

- 578 • $Q^2 > 2 \text{ GeV}^2$
- 579 • $W^2 > 10 \text{ GeV}^2$
- 580 • $0.1 < y < 0.95$

581 2.3.3 Jets: a versatile probe

582 As demonstrated in the YR [6], jets are an important observable, bringing both complimentary and
 583 unique insight to many of the EIC science goals. In order to comprehensively evaluate the impact
 584 that they can have, jet reconstruction has been integrated into the ePIC reconstruction framework,
 585 EICrecon. It utilizes the FastJet package to implement various jet definitions. The default settings,
 586 which are used for jets saved to the shared output trees and included in the analyses below, in-
 587 clude the Anti- k_T algorithm, E-scheme recombination, a resolution of 1.0, and a minimum jet trans-
 588 verse momentum of 1 GeV/c. In addition, constituents were required to have transverse momenta
 589 greater than 200 MeV/c to be included in the clustering.

590 Due to the lack of mature algorithms for integrating information from tracking, calorimetry, and
 591 particle identification subsystems, the reconstructed jets used to benchmark the ePIC detector per-
 592 formance and evaluate physics impact are clustered exclusively from charged particle tracks.

593 The primary metrics for evaluating the quality of jet reconstruction at ePIC are the jet energy scale
 594 (JES) and jet energy resolution (JER). These quantities were calculated by comparing the energies of
 595 matched particle-level and reconstructed jets. Because the reconstruction currently uses track-only
 596 jets and we are primarily interested in quantifying the effects of the detector, only stable charged
 597 particles were used when clustering the particle-level jets. For each particle-level jet, the closest
 598 reconstructed jet in $\eta - \phi$ space was considered the matching jet as long as $\Delta R = \sqrt{\Delta\eta^2 + \Delta\phi^2}$ was
 599 less than 0.1. The quantity: [(reco - particle)/particle] jet energy was found for each set of matching
 600 jets and fit with a triple Gaussian function. A triple Gaussian was used to try to take into account
 601 the tails of the distribution. The mean of fit is taken as the JES while the sigma is taken as the JER. To
 602 get a more differential picture of the jet performance, this procedure was performed as a function
 603 of particle-level jet energy for three pseudorapidity ranges as shown in Fig. 2.2.

604 2.4 The EIC Science (ePIC performance for key observables)

605 2.4.1 Origin of Nucleon Mass

606 Nucleons are made of quarks bound together by massless gluons. The Higgs mechanism can only
 607 explain the source of the quark masses. Nevertheless, the masses of valence quarks account only for
 608 $\sim 1\%$ of a nucleon's mass and thus cannot explain the mass of all the visible matter in the universe.
 609 The remainder of the proton mass must originate from the field energy of quarks and gluons in the
 610 sea.

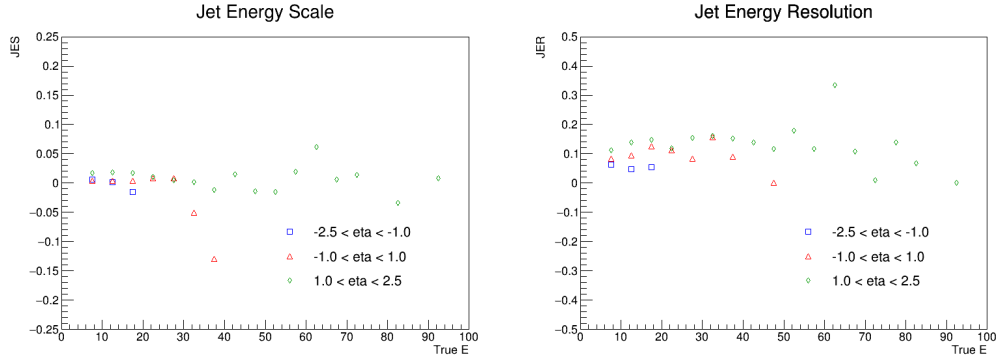


Figure 2.2: PLACEHOLDER (Left) Jet energy scale and (Right) jet energy resolution as a function of particle-level jet energy for backward (blue squares), mid (red triangles), and forward (green diamonds) rapidities.

611 The most accessible description of hadrons in terms of their constituent partons is by parton dis-
 612 tribution functions (PDFs), representing the fractional (longitudinal) momentum carried by each
 613 parton flavor. The inclusive DIS cross section is sensitive to PDFs through the structure functions
 614 F_1 and F_2 , which are linear combinations of the PDFs.

615 Tomographic images of quarks and gluons, also achievable at ePIC, will be discussed in Sec.2.4.3.

616 2.4.1.1 Inclusive neutral current cross sections

617 To extract neutral-current cross sections, corrections for acceptance and bin migration are defined
 618 by comparing reconstructed events to generated events. These corrections are then applied to the
 619 reconstructed events. Note that since the same reconstructed events are used for both the correc-
 620 tions and cross section extraction, this by definition yields the cross sections of the underlying event
 621 generator.

622 The projected neutral-current reduced cross sections for three center of mass energies are shown
 623 in Figures 2.3-2.5. These use the electron identification and event selection criteria as described in
 624 Sec: 2.3.2. However, at this stage the kinematics have been reconstructed using the electron method
 625 only. The statistical uncertainties are estimated assuming an integrated luminosity of 10 fb^{-1} for
 626 each center of mass energy.

627 2.4.1.2 Upsilon production

628 The production of the three Υ states in the electron channel was simulated in electron-proton colli-
 629 sions at a center-of-mass energy of $18 \times 275 \text{ GeV}$. The Monte Carlo samples were generated using
 630 eSTARlight, covering a range of $10^{-3} < Q^2 < 10 \text{ GeV}^2$, with no restrictions on W . The Υ states

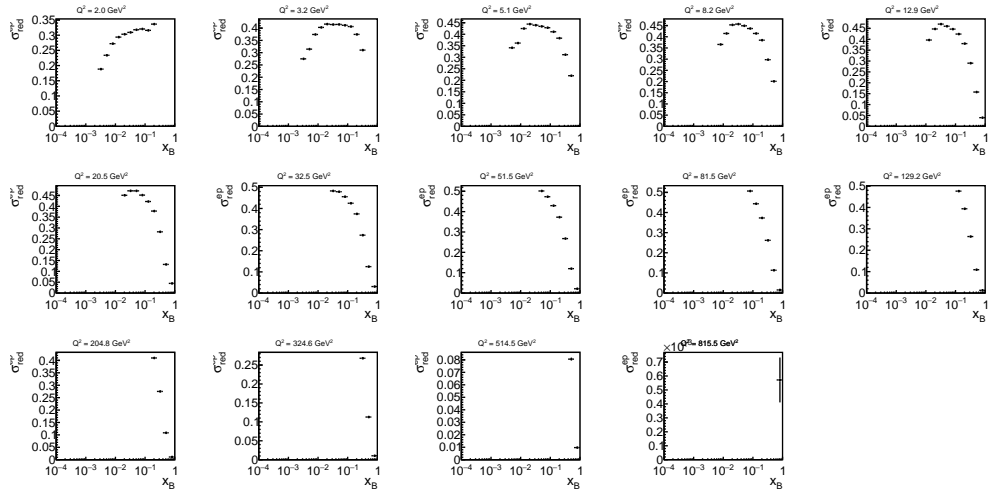


Figure 2.3: Projected ep neutral current reduced cross sections at 5×41 GeV. Statistical uncertainties assume an integrated luminosity of 10 fb^{-1} .

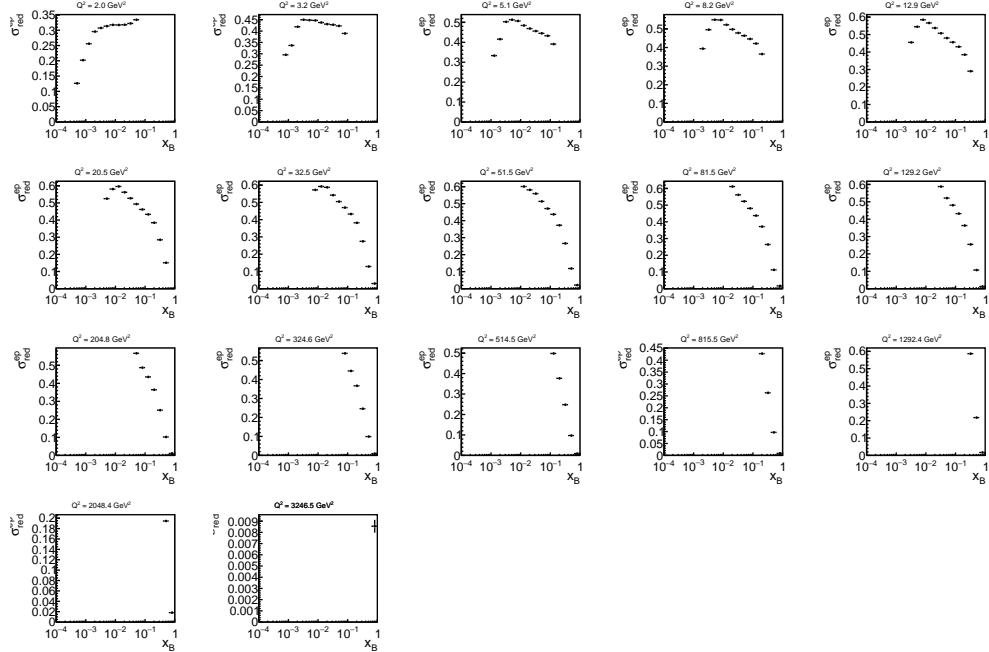


Figure 2.4: Projected ep neutral current reduced cross sections at 10×100 GeV. Statistical uncertainties assume an integrated luminosity of 10 fb^{-1} .

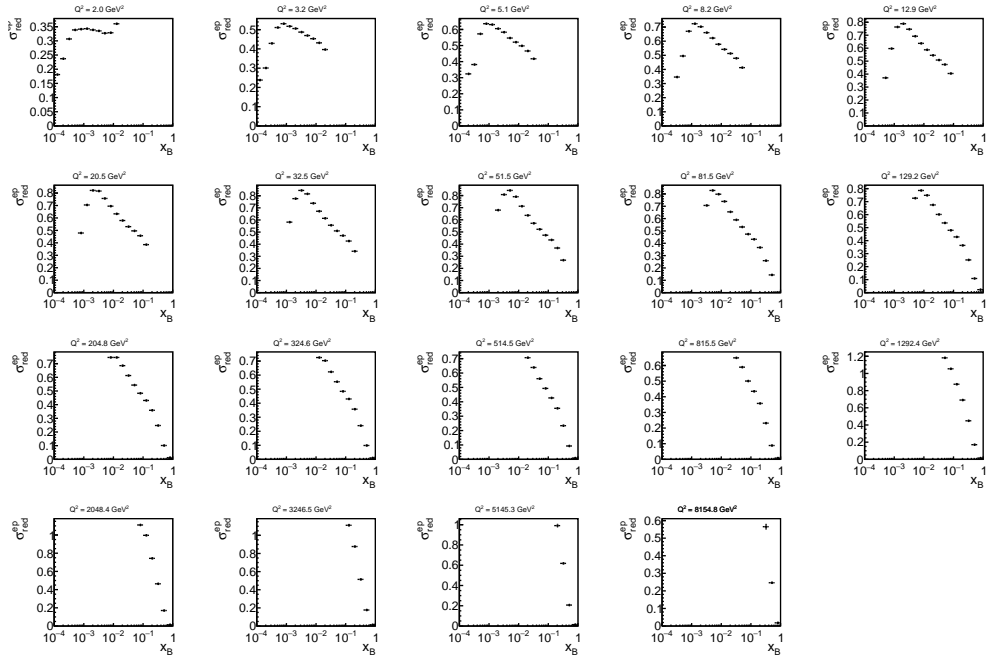


Figure 2.5: Projected ep neutral current reduced cross sections at 18×275 GeV. Statistical uncertainties assume an integrated luminosity of 10 fb^{-1} .

631 were produced according to their relative ratio based on [12] and then combined. The reconstruction of these Monte Carlo samples was simulated using EICRECON version 1.15.0. The figure
 632 showcases the momentum resolution of the ePIC tracking system in terms of separating the three
 633 Y states, which is presented across various rapidity regions for the reconstructed Y states. The top
 634 left plot in Figure 2.6 represents the resolution for all rapidity regions combined, while the other
 635 plots present results for specific intervals: $-3 < y < -1$, $-1 < y < 0$, $0 < y < 1$, $1 < y < 2$, and
 636 $2 < y < 4$. In the forward region, corresponding to $2 < y < 4$, a degradation in resolution was
 637 observed. However, in a similar study done by the muon channel (not shown), it is found to have
 638 an improvement on the resolution of approximately 1 to 8 % due to reduced final state radiation.
 639

640 2.4.2 Origin of Nucleon Spin

641 Thanks to the availability of polarized electron and hadron beams at the EIC, inclusive DIS can be
 642 used to probe the contribution of nucleon spin from quark helicity. Double-spin asymmetries be-
 643 tween different relative electron/hadron polarization states are sensitive to polarized PDFs through
 644 the spin structure function $A_1 \propto g_1 = \sum_q e_q^2 (\Delta q - \Delta \bar{q})$. The gluon contribution to nucleon spin is
 645 inferred by the Q^2 dependence of the spin structure functions, therefore it is critical for the mea-
 646 surements to cover a wide range of kinematics.

647 The projected proton double-spin asymmetries A_1^p for three center of mass energies are shown
 648 in Figure 2.7. The statistical uncertainties are estimated assuming an integrated luminosity of 10
 649 fb^{-1} for each center of mass energy, equally split between the the beam polarization configurations
 650 required for the asymmetry measurement. The reconstruction, event selection, and kinematic cuts
 651 are described in Sec. 2.3.2.

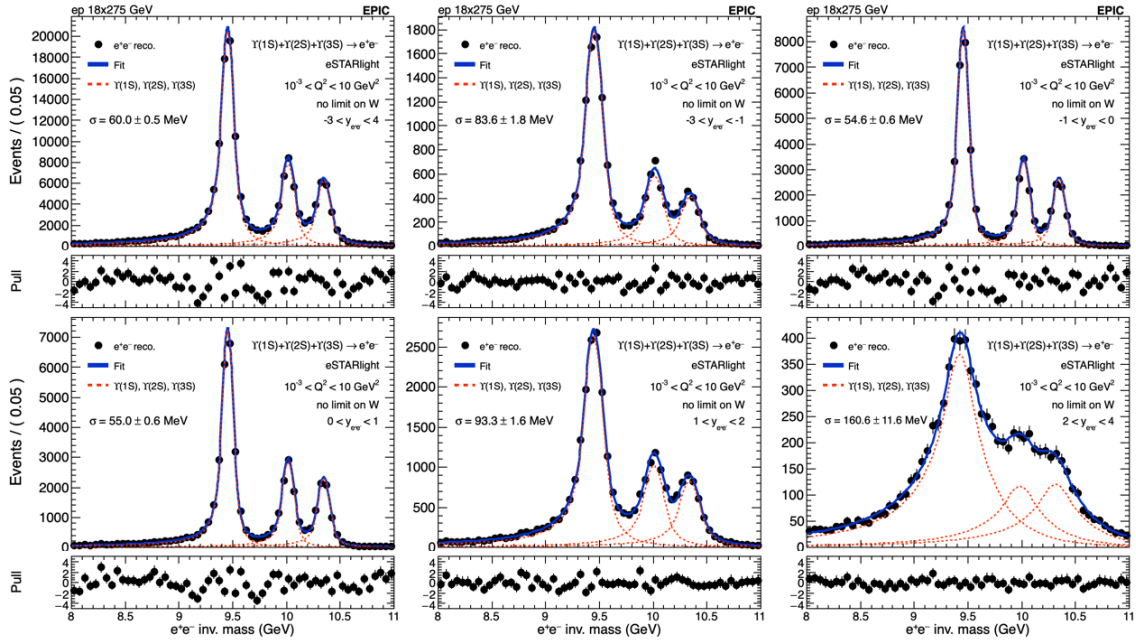


Figure 2.6: The reconstructed mass distribution of the Υ three states in the electron channel from the electron-proton collisions at $18 \times 275 \text{ GeV}$, utilizing the tracker with realistic seeding. The top left plot shows the invariant mass distribution of the Υ three states in the rapidity range from -3 to 4 . The other plots display invariant mass distribution for specific rapidity intervals: (top middle) $-3 < y < -1$, (top right) $-1 < y < 0$, (bottom left) $0 < y < 1$, (bottom middle) $1 < y < 2$, and (bottom right) $2 < y < 4$. The resolution of the Υ three states is indicated on each plot as σ .

652 2.4.3 Multi-Dimensional Imaging of the Nucleon

653 One-dimensional PDFs reveal the distribution of longitudinal parton momenta in the direction of
 654 the nucleon momentum. Nevertheless, a fast moving nucleon has still sizable transverse spatial
 655 dimensions.

656 The 3D parton structure of hadrons in momentum space is encoded in transverse momentum de-
 657 pendent parton distributions (TMDs). The non-perturbative quantities that encode the spatial dis-
 658 tributions in the transverse plane are called generalized parton distributions (GPDs).

659 2.4.3.1 Imaging in Momentum Space

660 Using semi-inclusive DIS, it is possible to extract information on the three-dimensional momentum
 661 structure of the nucleon by making use of transverse momentum dependent fragmentation func-
 662 tions. These in turn provide sensitivity to the flavor and the transverse momentum of partons in the
 663 nucleon. Already with an un-polarized nucleon the ePIC experiment can provide flavor-separated
 664 transverse-momentum dependent PDFs over a large range in x and Q^2 , and for transverse mo-
 665 menta that reach from the low, TMD-dominated region into the perturbative region. The wide
 666 range of scales, as shown in Fig.2.8 will also solve the existing uncertainties in the TMD evolution
 667 where non-perturbative contributions require experimental input.

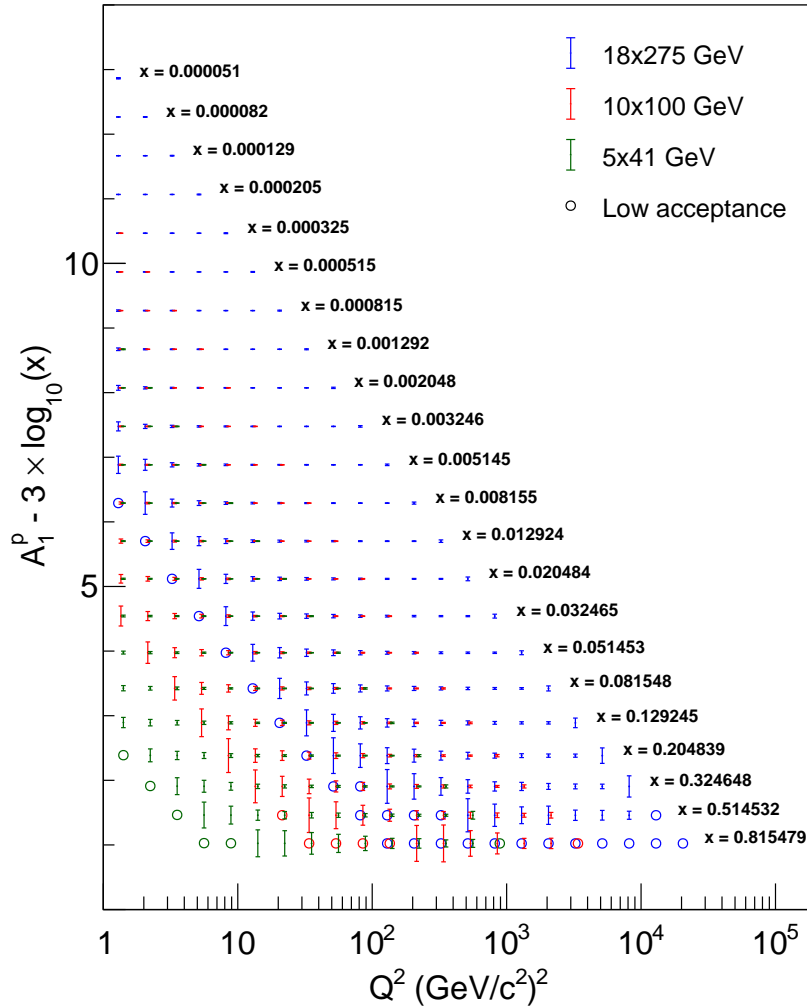


Figure 2.7: Projected measurements of A_1^p .

668 These unpolarized TMD PDFs also serve as the unpolarized baseline for any polarized TMD ob-
 669 servable which are obtained as single or double spin asymmetries. The most relevant are the Sivers
 670 function [13, 14] and the quark transversity [] which is obtained together with either the Collins
 671 fragmentation function [] or a di-hadron fragmentation function []. Examples of the expected un-
 672 certainties on these asymmetries are displayed in Fig. 2.9 where one can see that over a larger
 673 range of phase space very precise uncertainties can be obtained. Those will in turn then provide
 674 flavor-separated Transversity extractions and their first moments, the tensor charges. These ten-
 675 sor charges are of particular interest as they can relate to interactions outside the standard model.
 676 Lattice-QCD can model the tensor charges very well and any differences with the measurements
 677 would provide a hint for BSM physics.

678 Collins asymmetries of identified hadrons in jets are also sensitive to the Collins Fragmentation
 679 Function (FF), which describes the azimuthal distribution of hadrons fragmented by a transversely
 680 polarized quark as a function of the parent quark momentum fraction carried by the hadron (z)
 681 and the hadron momentum transverse to the quark direction (κ_T). Figure 2.10 illustrates projected
 682 statistical precision for Collins asymmetry measurements of charged π , K and p in jets as a function

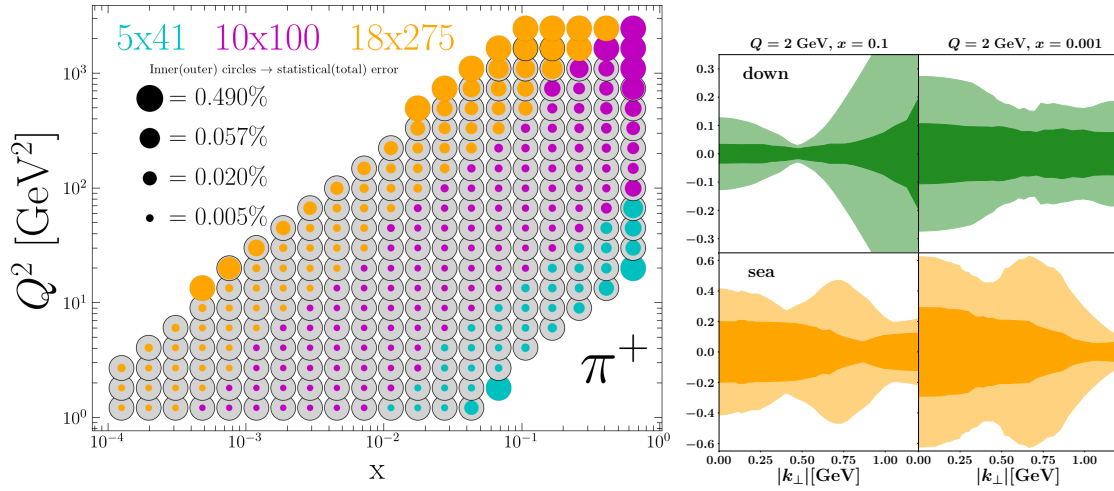


Figure 2.8: Left: Expected statistical and total uncertainty of un-polarized TMD PDFs for π^+ in the $Q^2 - x_B$ plane. The inner (colored) circle shows the statistical uncertainty, while the outer circle provides the total uncertainty for each $Q^2 - x_B$ bin. The color shows the beam energy configuration which provides the highest statistics in a specific bin. Right panel: Expected uncertainties of valence down (green) and sea quark (orange) TMD PDFs at $x = 0.1$ (left) and $x = 0.001$ (right) as obtained based on the MAP24 [1] global TMD fit. The lighter shaded regions show the uncertainties based on existing data while the darker shaded regions show the expected uncertainties after including ePIC data.

683 of hadron z and jet p_T . An absolute statistical uncertainty of less than XXX can be achieved for jet
 684 $p_T = 20$ GeV/ c for protons. When integrated over jet $5.0 < p_T < 51.9$ GeV/ c , the statistical
 685 uncertainty becomes negligible for the range of $0.1 < z < 0.8$. These high precision measurements
 686 will provide stringent constraints for quark transversity in the proton.

687 2.4.3.2 Imaging in Transverse Position Space

688 GPDs can be extracted via measurements of exclusive reactions. E.g. the exclusive production of a
 689 real photon via deeply virtual Compton scattering (DVCS) or of a meson, while the proton remains
 690 intact. Exclusivity requires all the final-state particles to be detected.

691 DVCS events have been simulated using the ePIC Monte Carlo generator [15] with a minimum Q^2
 692 of 1 GeV 2 . The analysis of such events provides a good test of a large number of subsystems within
 693 the ePIC detector, namely the scattered electron and final state photon are detected in either the
 694 central barrel or endcaps, and the scattered proton is detected in the far forward region within the
 695 B0 spectrometer or the Roman Pot detectors.

696 DVCS candidate events were identified by applying a series of cuts on the individual final state
 697 particles, as well as on the properties of the full reaction. The cuts applied were as follows:

- 698 • exactly 1 photon, scattered electron and scattered proton were reconstructed in the final state.
- 699 • the reconstructed electron and photon have momenta no more than 10% higher than the
 700 corresponding beam momentum; for this study, that corresponds to a maximum of 11 GeV
 701 for scattered electrons and 110 GeV for scattered protons.

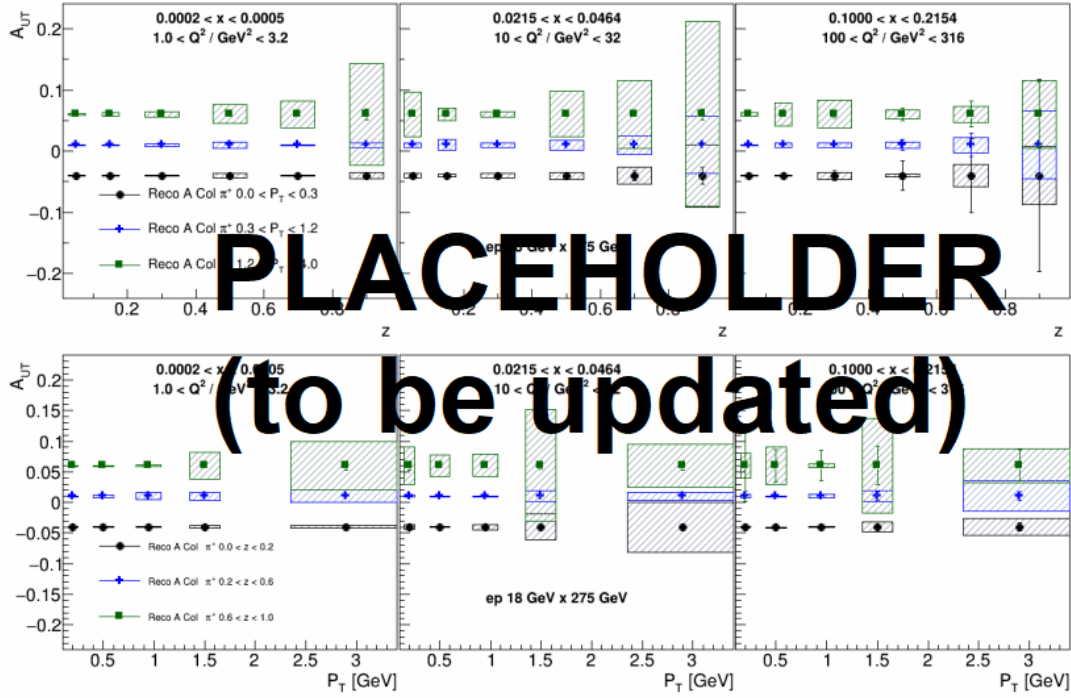


Figure 2.9: Expected uncertainties in three example x - Q^2 bins for the Collins asymmetries as a function of the momentum fraction z in three bins of hadron transverse momentum relative to the virtual photon direction.

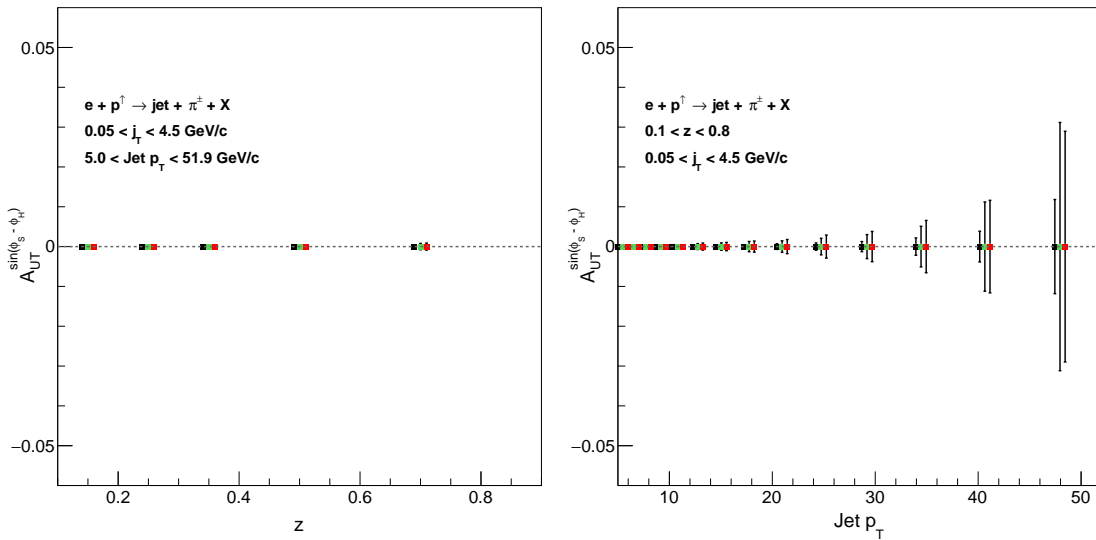


Figure 2.10: Projected statistical precision, indicated by vertical bars around data points, for measurements of Collins asymmetries of identified hadrons in jets as a function of hadron z (left) and jet p_T (right). In case the vertical bars are invisible, they are smaller than the marker size. [This figure will be updated](#)

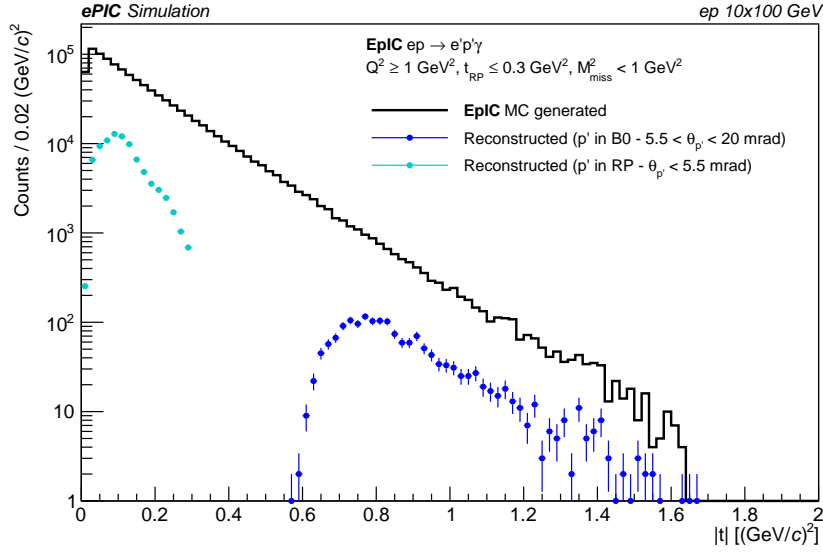


Figure 2.11: Generated and reconstructed t -distributions for fully-exclusive DVCS events.

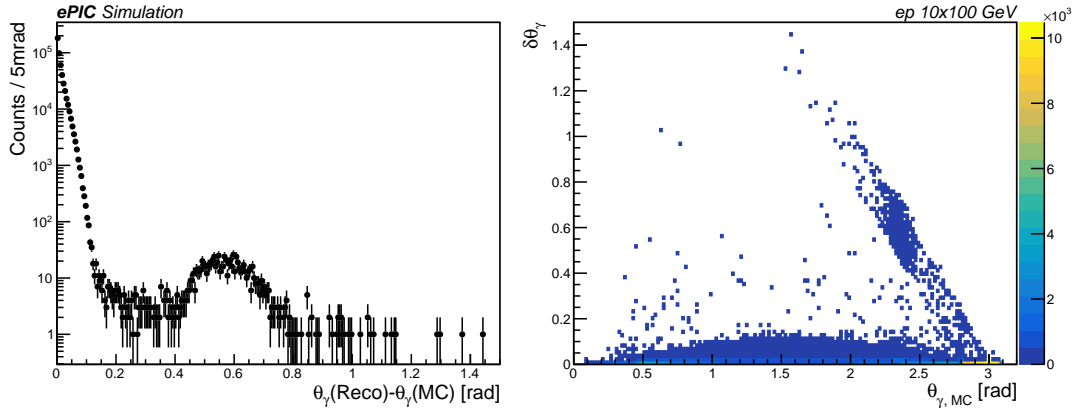


Figure 2.12: Reconstructed minus generated track θ for all reconstructed DVCS photons (left), as well as as a function of the generated photon θ (right). Note that the left plot is on a logarithmic scale.

- 702 • track θ cuts for the reconstructed proton (where θ is defined as the angle from the positive
- 703 z-axis to the track of interest) to ensure the track matches the acceptance of the detector
- 704 expected. Tracks reconstructed in the Roman Pots are required to have $\theta < 5.5$ mrad; tracks
- 705 in the B0 spectrometer are required to have $5.5 < \theta < 20$ mrad.
- 706 • a minimum Q^2 of 1 GeV^2 , to match the conditions of the initially generated events.
- 707 • a maximum t for events with the proton detected in the Roman Pots of 0.3 GeV^2 .
- 708 • a maximum missing mass of the full final state, M_{miss}^2 of 1 GeV^2 .

709 As mentioned, a key parameter on which the DVCS process depends is the Mandelstam variable t

710 of the reaction. The generated and reconstructed distributions of t , calculated for events with full
 711 exclusivity (exactly one reconstructed electron, proton and photon), are shown in figure 2.11. As
 712 well as studying the underlying physics process, DVCS can be used to test the performance of the
 713 ePIC subdetectors. Figure 2.12 shows the angular resolution of the barrel calorimeters, calculated
 714 using the detected DVCS photon. Of particular note from figure 2.12 are the following points:

- 715 • the angular reconstruction of the barrel is, on the whole, very good. No more than 0.5% of all
 716 photons are reconstructed more than 5° from their generated track, and more than 75% are
 717 reconstructed to within 1° .
- 718 • the significant majority of the generated photons are detected in the electron endcap
 719 calorimeter, in the range $2.8 < \theta < 3.1$ rad.

720 2.4.4 Properties of Nuclear Matter

721 2.4.4.1 Gluon Saturation

722 One of the three central questions highlighted in the National Academy of Science report on
 723 Electron-Ion Collider (EIC) science is to understand the properties of high parton density matter
 724 and the onset of gluon saturation. A critical observable for understanding the dynamics of gluonic
 725 matter is the spatial distribution of gluons within nuclei, particularly in systems likely to be in the
 726 saturation regime at high energy.

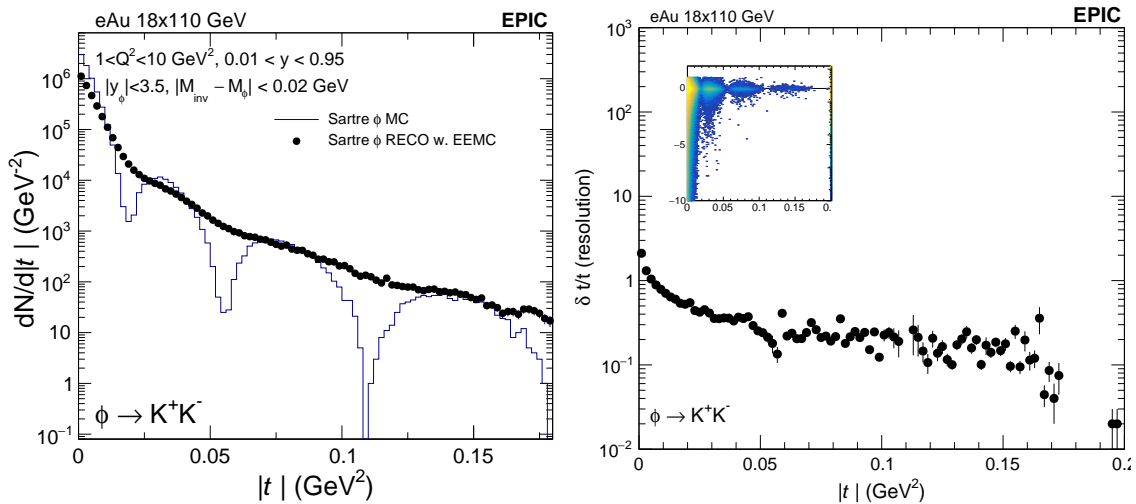


Figure 2.13: Left: differential distribution of the momentum transfer $|t|$ of coherent ϕ meson electroproduction in electron-gold collisions with 18x110 GeV. The Monte Carlo model is provided by Sartre and the reconstructed distribution is obtained from full ePIC simulation with the official August 2024 simulation campaign. Right: the momentum transfer t reconstruction resolution as a function of the true t .

727 To achieve gluon imaging of nuclei, exclusive and diffractive vector meson electroproduction involving
 728 electron-heavy nuclei collisions has been proposed [8]. In Fig. 2.13 (left), the differential

	Signal efficiency	Background efficiency
3 tracks	0.97383	0.914885
J/ψ mass window	0.898815	0.827045
Veto signals in B0	0.898805	0.429656
Veto signals in OMD	0.898805	0.29286
Veto signals in ZDC	0.898795	0.013776

Table 2.1: Event composition in incoherent J/ψ production before and after full event selection

729 cross section for ϕ meson production is shown for electron-gold collisions at an energy configura-
 730 tion of 18x110 GeV. The input is derived from the Monte Carlo model Sartre, and the reconstructed
 731 distribution is obtained after a full ePIC simulation based on the version from August 2024. The
 732 reconstruction is achieved by detecting a scattered electron in the backward calorimeter and recon-
 733 structing the two kaons from ϕ decay using tracking data.

734 As shown, the diffractive structure is barely visible in the reconstructed data due to insufficient
 735 momentum transfer (t) resolution. The main limitation stems from the electron reconstruction,
 736 where the momentum resolution is hampered by the small scattering angle relative to the electron
 737 beamline. The magnetic field in this region is insufficient to provide the necessary lever arm for
 738 achieving the required momentum resolution. More specifically, Fig. 2.13 (right) presents the mo-
 739 mentum transfer t reconstruction resolution as a function of true t . Efforts to improve the resolution
 740 are ongoing.

741 On the other hand, the incoherent vector meson production needs to be vetoed in the event in order
 742 to suppress its contamination to the coherent process. This is enabled by the far-forward detector
 743 system (B0, Roman Pot, Off-Momentum Detector, zero-degree calorimeter). By vetoing signals in
 744 the forward detectors one can reject up to two orders of magnitude of the incoherent background.
 745 Table 2.1 summarizes the fraction of signal and background events after each veto.

746 The t spectra of coherent and incoherent (before veto) are shown in Fig. 2.14 left, and the residue
 747 distribution of incoherent production events (that pass event selection) are shown in Fig. 2.14 right.
 748 Therefore, the vetoing power is sufficient to suppress the incoherent production down to a level
 749 below the first diffractive minimum but not quite for the second and third minima.

750 2.4.4.2 Nuclear Modifications of Parton Distribution Functions

751 Add text here.

752 2.4.4.3 Passage of Color Charge Through Cold QCD Matter

753 [Rongrong: performance of D^0 reconstruction with ePIC is currently under study. It is not clear if
 754 it will be available for pre-TDR, but definitely will be included in TDR.]

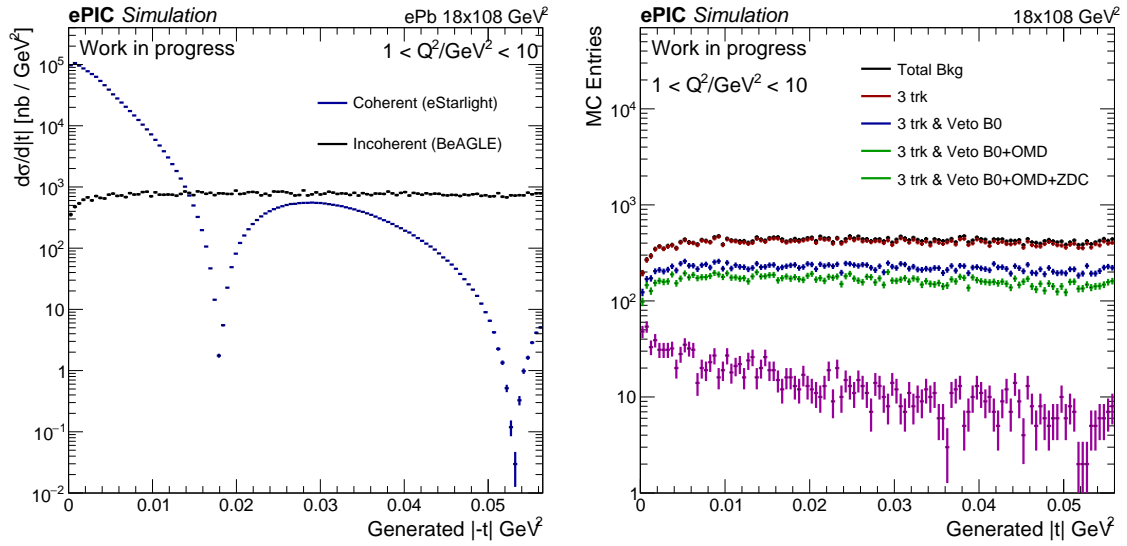


Figure 2.14: Left: Differential cross-section of momentum transfer t distribution for coherent (blue) and incoherent (black) exclusive J/ψ production in ePb collisions. Right: Differential measurement of t and the residue distributions after each veto based on the far-forward detector system.

755 Chapter 8

756 Experimental Systems

757 8.1 Experimental Equipment Requirements Summary

758 The YR table (Fig. 8.1) is being reviewed and an updated table with accompanying text will be included in the draft Version1.

Table 10.6: This matrix summarizes the high level requirements for the detector performance. The interactive version of this matrix can be obtained through the Yellow Report Physics Working Group WIKI page (https://wiki.bnl.gov/eicug/index.php/Yellow_Report_Physics_Common).

Pseudo η	Nomenclature	Tracking		Electrons and Photons				RCAL	Muons												
		Resolution	Allowed	minimum pT	SI Vertex	Resolution $\sigma_{\eta/E}$	PID			min E	p-range	Separat	Resolution $\sigma_{\eta/E}$	Energy							
6.9 to 3.8	low-Q2 tagger	$\sigma_{\theta} < 1.5\%$; 10^{-6}																			
5.0 to 4.5		$< Q^2 < 10^{-2}$ GeV ²		300 MeV/pions																	
4.5 to 4.0	Instrumentation to separate charged particles from photons			300 MeV/pions		$2\%/\eta$ (+1-3%)	50 MeV														
4.0 to 3.5		Auxiliary Det																			
3.5 to 3.0	Central Detector	Backward Calorimeter	< 100 MeV/pions, 135 MeV kaons	$\sigma_{xy} \sim 20 \mu\text{m}$, $d0(z) \sim d0(r)$ $\sim 200 \mu\text{m}$ $\mu\text{m} + 1 \mu\text{m}$	$\sigma_{xy} \sim 30 \mu\text{m} + 40 \mu\text{m}$	$2\%/\eta$ (+1-3%)	TI suppresses up to 1/E ⁴	≤ 7 GeV/c	$\approx 3 \sigma$	$\sim 50\% \eta/E \pm 6\%$	~ 600 MeV	muons useful for bkg. improve resolution									
-3.0 to -2.5													$\sigma_{pT} \sim 0.1\%$ @ 0.5%	$\sigma_{xy} \sim 30 \mu\text{m} + 20 \mu\text{m}$	$7\%/\eta$ (+1-3%)	50 MeV	≤ 10 GeV/c	$-45\% \eta/E \pm 6\%$			
-2.5 to -2.0		$\sigma_{pT} \sim 0.05\%$ @ 0.5%											$\sigma_{xy} \sim 20 \mu\text{m}$	$7\%/\eta$ (+1-3%)	50 MeV	≤ 10 GeV/c	$-85\% \eta/E \pm 7\%$				
-2.0 to -1.5		$\sigma_{pT} \sim 0.05\%$ @ 0.5%											$\sigma_{xy} \sim 20 \mu\text{m}$	$7\%/\eta$ (+1-3%)	50 MeV	≤ 10 GeV/c	$-85\% \eta/E \pm 7\%$				
-1.5 to -1.0		$\sigma_{pT} \sim 0.05\%$ @ 0.5%											$\sigma_{xy} \sim 20 \mu\text{m}$	$7\%/\eta$ (+1-3%)	50 MeV	≤ 10 GeV/c	$-85\% \eta/E \pm 7\%$				
-1.0 to -0.5		$\sigma_{pT} \sim 0.05\%$ @ 0.5%											$\sigma_{xy} \sim 20 \mu\text{m}$	$7\%/\eta$ (+1-3%)	50 MeV	≤ 10 GeV/c	$-85\% \eta/E \pm 7\%$				
-0.5 to 0.0		$\sigma_{pT} \sim 0.05\%$ @ 0.5%											$\sigma_{xy} \sim 20 \mu\text{m}$	$7\%/\eta$ (+1-3%)	50 MeV	≤ 10 GeV/c	$-85\% \eta/E \pm 7\%$				
0.0 to 0.5		$\sigma_{pT} \sim 0.05\%$ @ 0.5%											$\sigma_{xy} \sim 20 \mu\text{m}$	$7\%/\eta$ (+1-3%)	50 MeV	≤ 10 GeV/c	$-85\% \eta/E \pm 7\%$				
0.5 to 1.0		$\sigma_{pT} \sim 0.05\%$ @ 0.5%											$\sigma_{xy} \sim 20 \mu\text{m}$	$7\%/\eta$ (+1-3%)	50 MeV	≤ 10 GeV/c	$-85\% \eta/E \pm 7\%$				
1.0 to 1.5		$\sigma_{pT} \sim 0.05\%$ @ 0.5%											$\sigma_{xy} \sim 20 \mu\text{m}$	$7\%/\eta$ (+1-3%)	50 MeV	≤ 10 GeV/c	$-85\% \eta/E \pm 7\%$				
1.5 to 2.0	Forward Calorimeter	$\sigma_{pT} \sim 0.1\%$ @ 1.0%	$\sigma_{xy} \sim 30 \mu\text{m} + 40 \mu\text{m}$	$\sigma_{xy} \sim 30 \mu\text{m} + 20 \mu\text{m}$	$10-12\% \eta/E$ (+1-3%)	30 e/r	≤ 30 GeV/c	$\approx 3 \sigma$	$35\% \eta/E$												
2.0 to 2.5												$\sigma_{pT} \sim 0.1\%$ @ 1.0%	$\sigma_{xy} \sim 30 \mu\text{m} + 40 \mu\text{m}$	$\sigma_{xy} \sim 30 \mu\text{m} + 20 \mu\text{m}$	$10-12\% \eta/E$ (+1-3%)	30 e/r	≤ 30 GeV/c				
2.5 to 3.0	$\sigma_{pT} \sim 0.1\%$ @ 1.0%	$\sigma_{pT} \sim 0.1\%$ @ 1.0%	$\sigma_{xy} \sim 30 \mu\text{m} + 40 \mu\text{m}$	$\sigma_{xy} \sim 30 \mu\text{m} + 20 \mu\text{m}$	$10-12\% \eta/E$ (+1-3%)	30 e/r	≤ 30 GeV/c	$\approx 3 \sigma$	$35\% \eta/E$												
3.0 to 3.5	Instrumentation to separate charged particles from photons	Tracking capabilities are desirable for forward tagging	< 100 MeV/pions, 135 MeV kaons	$\sigma_{xy} \sim 20 \mu\text{m}$, $d0(z) \sim d0(r)$ $\sim 200 \mu\text{m}$ $\mu\text{m} + 1 \mu\text{m}$	$\sigma_{xy} \sim 30 \mu\text{m} + 40 \mu\text{m}$	$2\%/\eta$ (+1-3%)	TI suppresses up to 1/E ⁴	≤ 7 GeV/c	$\approx 3 \sigma$	$\sim 50\% \eta/E \pm 6\%$	~ 600 MeV	muons useful for bkg. improve resolution									
3.5 to 4.0																					
4.0 to 4.5																					
4.5 to 5.0													Auxiliary Detectors								
4.5 to 5.0	Neutron Detector		300 MeV/pions			$4.0\% \eta/E$ for photon energy > 20 GeV	≤ 3 cm granular by			$30\% \eta/E$ (goal), $< 50\% \eta/E$ (acceptable), $3 \text{ mrad} \eta/E$ (goal)											
> 6.2	Proton Spectrometer	intrinsic RVE $< 1\%$; Acceptance: $0.2 < p < 1.2$ GeV/c																			

Figure 8.1: Table presenting the Experimental Equipment Requirements Summary in the YR. At present, the table is not updated and it is here as a mere space holder.

760 8.2 General Detector Considerations and Operations Challenges

761 8.2.1 General Design Considerations

762 This section will discuss the detector challenges with cross-reference to the appropriate sections.
763 The Sec.s to refer to are related to machine parameters (not in chapter 8), 8.1 “Experimental Equip-
764 ment requirement Summary”, 8.2.2 “Background and Rates” and 8.2.3 “Radiation Level”. At
765 present, all these sections are not available. Therefore, for Version0, a mere list of topics that will be
766 covered is provided.

767 Discussion of challenges related to:

- 768 • Physics requirements (ref. to Sec. 8.1);
- 769 • Beams rates, polarization, luminosities (ref. to Sec.s in the machine chapters);
- 770 • Integration with the machine and hermeticity (ref. to Sec.s in the machine chapters, ref. to
771 Sec. 8.1);
- 772 • Rates and multiplicity (ref. to Sec.c in the machine chapters, to Sec. 8.2.2);
- 773 • Radiation hardness (Ref. to Sec. 8.2.3).

774 8.2.2 Backgrounds and Rates

775 Add text here.

776 8.2.3 Radiation Level

777 Add text here.

778 8.3 The ePIC Detector

779 8.3.1 Introduction

780 **The Context** The development of the EIC science and the experimental equipment required to
781 successfully implement the science as documented in the NSAC and NAS reports has been driven
782 by an international EIC community, formalized in 2016 in the EIC User Group [16], at present
783 (September 2024) formed by more than 1500 members from almost 300 institutions and 40 coun-
784 tries. Several conceptual general-purpose detectors had been elaborated. A next step effort was
785 required by the EIC project approval with the signature of CD0 in December 2019. The User Group
786 engaged in advancing the state of documented physics studies, which dictate the detector require-
787 ments, and consolidate the general-purpose detector concept matching these requirements. This
788 effort resulted in the EIC Yellow Report completed in early 2021 and then published in Nuclear
789 Physics A [17]. This document guided the two proposals for a general-purpose detector elaborated
790 in 2021, which resulted in further progress in the conceptual detector design. In 2022, a merging
791 process of the communities presenting the two proposals and of the two conceptual approaches
792 resulted in the formation of the ePIC Collaboration [18] (July 2022) and in baselining of the ePIC

793 detector as EIC project detector. At present (September 2024), ePIC has more than 850 members
794 from 177 Institutions and 25 countries, confirming the international vocation of the community
795 pursuing the EIC science and detector.

796 **The Detector** THIS DETECTOR DESCRIPTION IS AN INTRODUCTION TO THE WHOLE
797 SECTION 8.3. IT WILL BE REVISED WHEN THE SUBSYSTEM MATERIAL IS UPLOADED TO
798 ENSURE A BETTER CONSISTENCY OF THE SECTION 8.3.

799 The detector challenges and the technologies matching these challenges are discussed in Sec. 8.2.1.
800 The resulting design of the ePIC detector consists in a Central Detector (CD) surrounding the Inter-
801 action Point 6 (IP6) making optimal use of the space available at the Interaction Region (IR) com-
802 plemented by equipment situated along the outgoing beam lines, the Far Detectors (FD), which
803 complete the phase-space coverage.

804 Figure 8.2 illustrates the CD kinematic coverage; Fig. 8.3 presents a schematic overview of the CD
805 structure. The overall CD length is imposed by the constrain of the IR design. The asymmetric
806 beam energies reflect in an asymmetric design of the detector and, together with the requirements
807 from physics, imposes the choice of the different detector technologies that have been adopted. The
808 setup is designed around the solenoid providing the magnetic field for the momentum analysis.
809 The adoption of a solenoid shapes the CD in a barrel region where the subsystem have pseudo-
810 cylindrical layouts and two endcap regions, the forward one equipping the region around the out-
811 going ion beam and the backward endcap around the outgoing electron beam. The barrel sub-
812 systems cover, approximately, the pseudorapidity η region $(-1.5, 1.5)$, while the endcaps equip the
813 regions up to pseudorapidity $|3.5 - 4.0|$, the upper bound being dictated by the beampipe layout.
814 The separation in barrel and endcap region is not rigid with exceptions where the optimization
815 of the detector design suggests it. For instance, the most inner layers of the tracking system have
816 acceptance well beyond $\eta < |1.5|$, the barrel Cherenkov PID counter and the barrel electromagnetic
817 calorimeter extends in the backward endcap.

818 The CD subsystems have a layered structure, from inside to outside: tracking subsystems, parti-
819 cle identification devices, electromagnetic calorimeters, solenoid coils in the barrel, and hadronic
820 calorimeters.

821 The reference operation condition of the new **MARCO magnet** (Sec. 8.3.2), specifically designed
822 for ePIC, is with 1.7 T field intensity and it can provide up to 2 T. It has good homogeneity in the
823 central region and provides projective field lines in the forward endcap to match the requirements
824 posed by the usage of a gaseous radiator in the forward RICH. The solenoid axis coincides with the
825 electron beam line in the IR to limit the synchrotron radiation from the beam electrons. This results
826 in helicoidal trajectories of the beam ions, due to the crossing angle of the two beams.

827 The **tracking system** (Sec. 8.3.3) is the most inner subsystem in order to ensure the minimum dis-
828 tortion of the trajectories by the material crossed by the particles. It consists of pseudo cylindrical
829 layers completed by discs in the endcaps. The low material budget (Fig. 8.4) is guaranteed by the
830 selected tracker technologies, with the thin ITS3 MAPS, even in support-less arrangement in the
831 most inner layers, and MPGDs for the most external layers. The two tracker technologies support
832 each other thanks to key complementary characteristics. MAPS sensors offer extremely fine space
833 resolution, but poor timing information in the order of a few microsecond range. In-time hits can
834 be selected combining MAPS information with the measurements in the MPGDs, which have time
835 resolution of 10-20 ns. Further space and time information will be provided by the time-of-flight
836 layers in the barrel and the forward endcap and by the first layer of the barrel imaging electromag-
837 netic calorimeter equipped with AstroPix MAPS sensors. The minimization of the material budget
838 is one of the ingredients allowing fine resolution for momentum determination and vertex recon-

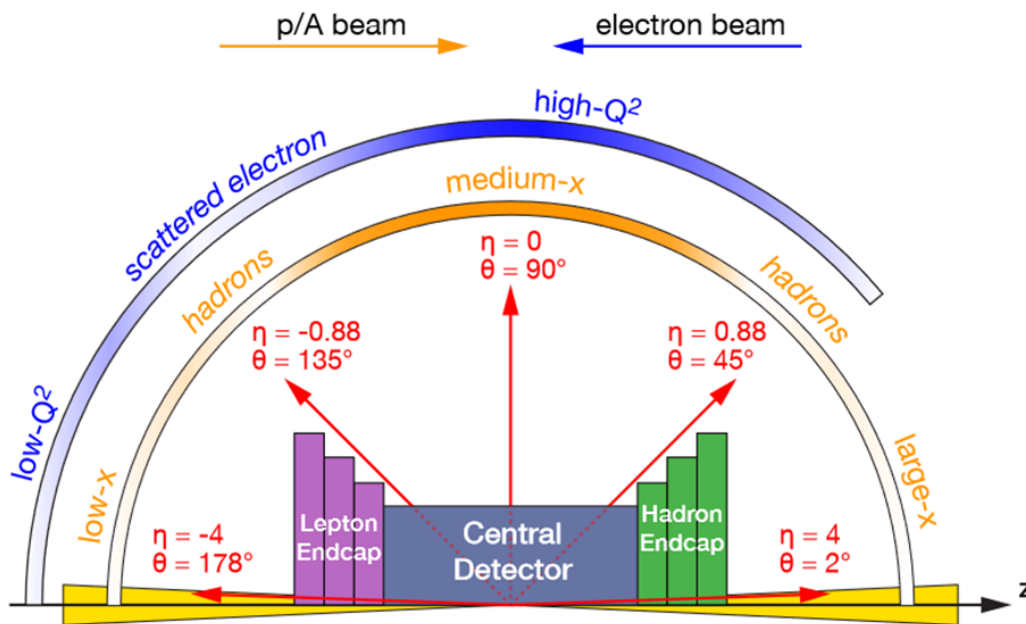


Figure 8.2: A schematic showing how hadrons and the scattered electron for different $x - Q^2$ are distributed over the detector rapidity coverage. THIS FIGURES IS A PLACE HOLDER: IT IS FROM YR AND REQUIRES REVISION.

839 struction. To this end, fine intrinsic resolution is requested for the trackers and it is provided by the
 840 ITS3 MAPS. The momentum resolution is affected by the available lever arm and the solenoidal
 841 configuration of the magnetic field, the latter having its largest impact on the very forward and
 842 backward trajectories.

843 The tracking information is also a key ingredient for the performance of the Cherenkov imaging
 844 devices; in particular, very fine resolution of the particle direction is needed for the barrel DIRC.
 845 The most external tracker layers in the barrel, positioned in front of the DIRC, further support this
 846 requirement.

847 The **particle identification subsystems** (Sec. 8.3.4) surround the tracking systems. Their mission
 848 is twofold: (i) supporting the electromagnetic calorimeters by complementing the pion/electron
 849 separation to ensure the high purity of the electron sample; (ii) identifying hadrons, as needed by
 850 a large fraction of the physics program. The coverage of the wide kinematic domain imposes the
 851 adoption of a variety of technologies with time-of-flight measurements complementing Cherenkov
 852 imaging devices. Time-of-flight dedicated layers by AC-LGADs are present in the barrel and in
 853 the forward endcap, the barrel layer being by strip sensor elements to reduce the material budget,
 854 while the forward endcap layer is by pixelized AC-LGADs. In the backward endcap, the fine
 855 time-resolution provided by the photosensors of the Cherenkov counter, which are sitting in the
 856 endcap acceptance, provide timing information via the Cherenkov light generated in the sensor
 857 window. The Cherenkov imaging counter in the backward endcap is a proximity focusing RICH
 858 with aerogel radiator and extended proximity gap to increase the resolution and, correspondingly,
 859 enlarging the momentum range for particle identification. As already underlined, the use of fine-
 860 time resolution HRPPDs by MCP technology as photosensors also provides timing information.
 861 The whole detector components are positioned in the acceptance, in front of the electromagnetic

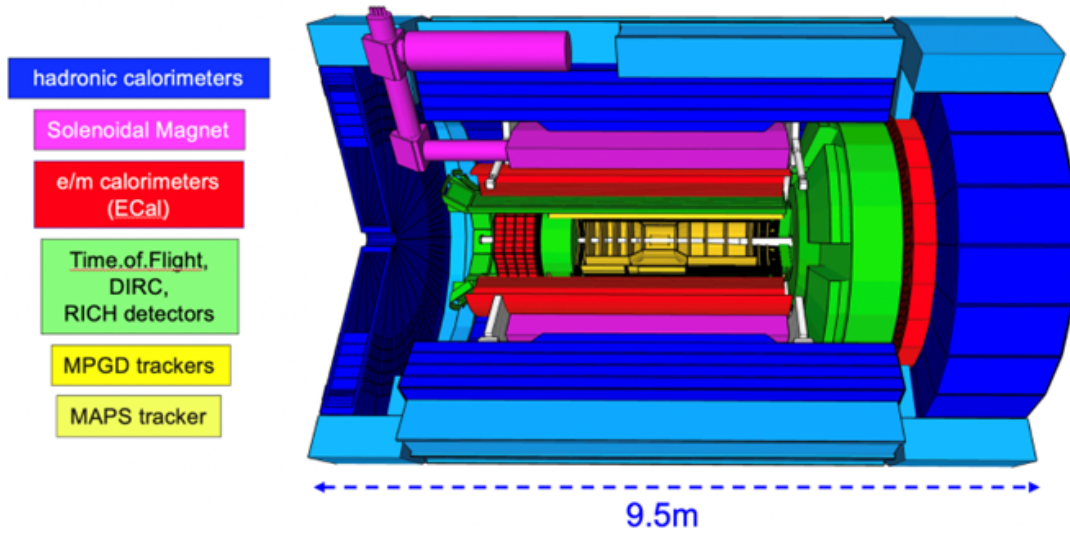


Figure 8.3: A schematic showing the ePIC central detector subsystems. THIS FIGURES IS A PLACE HOLDER

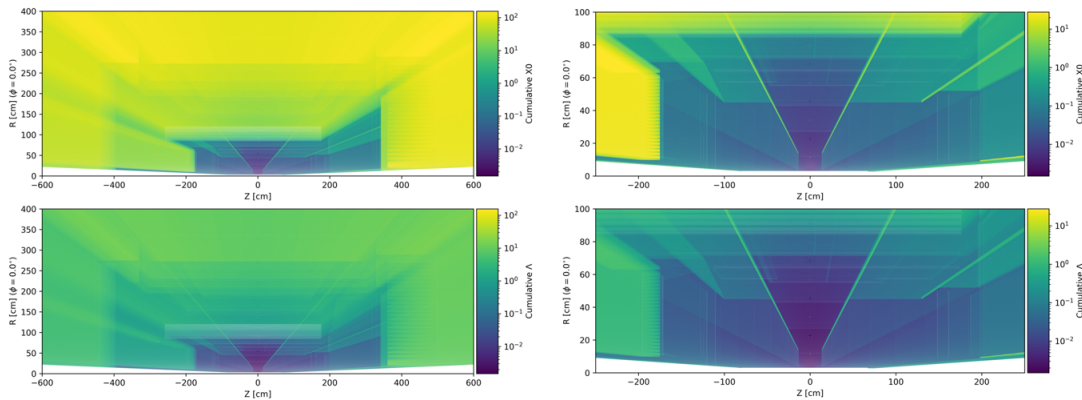


Figure 8.4: Cumulative material budget in radiation lengths (top row) and interaction lengths (bottom row) for the whole CD (left column) and zooming at the CD tracking region (right column). THIS FIGURES IS A PLACE HOLDER BECAUSE IT HAS TO BE COMPLETED WITH SUBSYSTEM CONTOURS AND REQUIRES GRAPHICAL IMPROVEMENTS.

862 calorimeter. This layout is compatible with the overall detector design; in fact, the bulky elements,
 863 namely the sensors with readout electronics and services are just in front of the calorimeter acting as
 864 a pre-shower element. In the barrel, a high performance DIRC is used, this choice being dictated by
 865 the reduced space. The DIRC fused silica bars, acting as radiator and as photon lightguides, make
 866 possible positioning the image expansion elements and the read-out electronics with its services
 867 in the backward region, outside the acceptance cone. The dual radiator RICH (Sec) in the forward
 868 endcap is equipped with two radiators, aerogel and gas, therefore acting as a couple of Cherenkov
 869 imaging counters dedicated to particle identification in two different momentum ranges, while
 870 economizing in space and single photon sensors. It is a focusing RICH with spherical mirrors as
 871 focusing elements. The photosensors and related services are placed outside the acceptance thank

872 to appropriate mirror orientation.

873 The electromagnetic calorimeters (Sec. 8.3.5) are external to the particle identification devices and,
 874 once more, the different technologies are imposed by the physics requirements, the kinematic
 875 ranges and the overall constrains. The budget of the material in front of the calorimeters is low
 876 and mainly concentrated near to the calorimeter front face. The backward endcap electromagnetic
 877 calorimeter is by fine granularity lead tungstate crystal offering very fine energy resolution.
 878 In the barrel, the electromagnetic calorimeter has a hybrid architecture combining imaging layers
 879 by AstroPix MAPS and sampling calorimetry by lead and scintillating fibers with sampling layer
 880 between the imaging layers and in the most external calorimeter portion. The layout is pseudo
 881 cylindrical with the read-out equipment at the cylinder edges minimizing the space requirement
 882 in the crowded barrel area. The electromagnetic calorimetry in the forward region is by sampling
 883 calorimetry with scintillating fibers inserted in matrices of tungsten powder embedded in epoxy.
 884 This calorimeter offer a near to 1 ratio of the signal amplitude response for electrons and hadrons
 885 and, therefore, it is design to operate in duet with the hadronic calorimeter place immediately be-
 886 hind.

887 All the **hadron calorimeters** (Sec. 8.3.6) are by iron as converter and scintillating active elements,
 888 even if with very different implementations. The forward endcap calorimeter is by SiPM-on-tile
 889 technology, with finer granularity in the central zone, near to the beam pipe, to cope with the
 890 higher rates. The barrel calorimeter, placed behind the solenoid coils, acts as a tail catcher. The
 891 backward endcap calorimeter . . . (to be completed: layout in evolution).

892 All the calorimeter subsystem in the ePIC detector make use of SiPMs as photosensors, even if of
 893 different size and pixelization, with common approach for the readout chain.

The global layout of the FDs (Sec.s 8.3.7 and 8.3.8) is illustrated in a artistic view in Fig. 8.5.

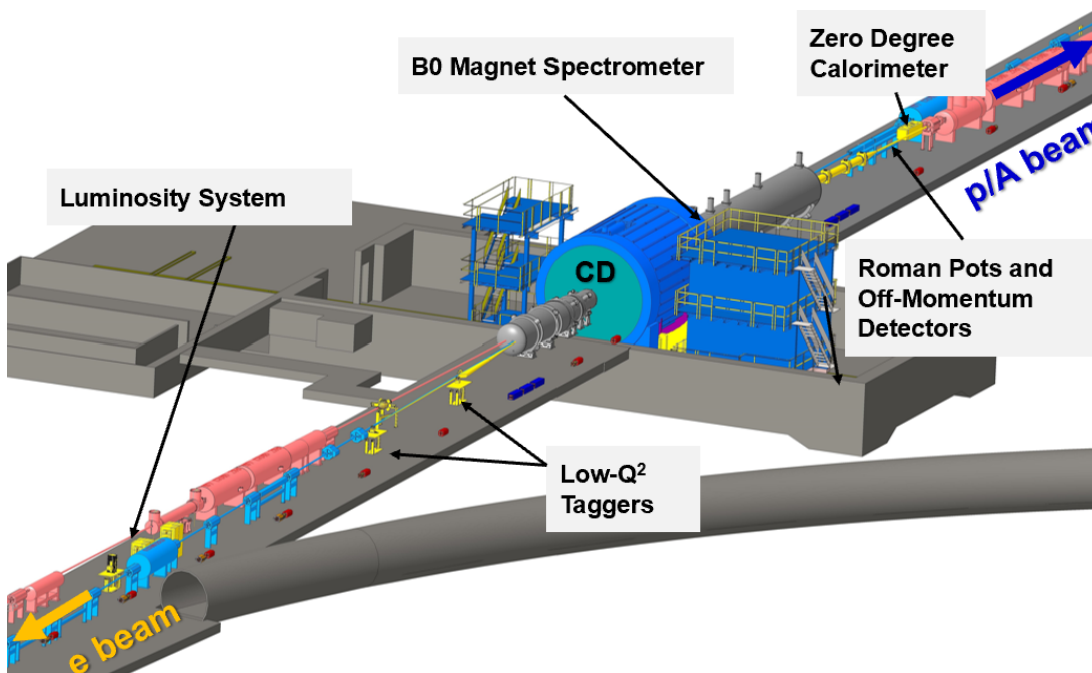


Figure 8.5: A schematic showing the ePIC far detector subsystems. THIS FIGURES IS A PLACE HOLDER

895 The **forward FDs** include tracking and electromagnetic calorimetry inserted in the first dipole of
896 the ion beam line B0, off-momentum detector trackers and roman-pot trackers and a zero-degree-
897 calorimeter. The technology for the trackers is by AC-LGADs, which have good radiation hardness.
898 The B0 electromagnetic calorimeter is by lead tungstate crystals. The zero-degree-calorimeter is
899 formed by a long SiPM-on-tile module with fine granularity adequate for photon and neutron
900 detection. A crystal layer can be inserted in front of it for those studies that require the detection of
901 low energy photons.

902 The **luminosity system** is part of the backward FD. Based on the measurement of the photons from
903 the Beta-Heitler process at IP, it consists of a high-rate calorimeter for direct photon detection and
904 a couple of pair spectrometers to detect the electrons and positrons generated by the Beta-Heitler
905 photons in the exit window. The high-rate calorimeter and the calorimeters in the pair spectrom-
906 eters are by tungstate and scintillating fibers. Tracking in the pair spectrometer is by AC-LGADs.
907 The **low- Q^2** taggers consist in tracking stations followed by an electromagnetic calorimeter. The se-
908 lected technologies must cope with extremely high rate in this kinematic region. Therefore, tracking
909 is by TimePix4 and calorimetry by tungstate and scintillating fibers.

910 Integral elements of the detector are the **electronic read-out chain**, the data acquisition system
911 (Sec. 8.3.10) and the **software implementation and computing model** (Sec. 8.3.11). The overall
912 underlining model that has guided the selection of the components and the design of the read-
913 out/DAQ/software/computing architecture is the streaming readout concept. Streaming readout
914 has been selected to simplify the readout scheme as no triggers are required and to increase the
915 information selection flexibility, to improve the event building from the holistic detector informa-
916 tion, to improve, via continuous dataflow, the knowledge of backgrounds and, therefore, enhances
917 the control over systematics. In this approach, already at the front-end level, the ASICs, which
918 are intimate related to the sensors and their performance, have been selected with architectures
919 compatible with their usage in streaming readout mode.

920 Independent setups are designed to measure and monitor the **beam polarization** (Sec. 8.3.9). Rapid,
921 precise beam polarization measurements will be crucial for meeting the goals of the EIC physics
922 program as the uncertainty in the polarization propagates directly into the uncertainty for relevant
923 observables as asymmetries. The basic requirements for beam polarimetry are non-destructive with
924 minimal impact on the beam lifetime, uncertainty at the 1% level, the capacity of measuring the
925 beam polarization for each bunch in the ring with rapid, quasi-online analysis in order to provide
926 timely feedback for accelerator setting up. The electron beam polarimetry will be based on the
927 well established Compton polarimeter techniques, where the polarized electrons scatter from 100%
928 circularly polarized laser photons. This approach offers the advantage that both longitudinal and
929 transversal polarizations are measured. Hadron polarimetry has been successfully performed on
930 RHIC polarized proton beams for nearly two decades. Through continual development a relative
931 systematic uncertainty $\pm 1.5\%$ was achieved for the most recent RHIC polarized proton run. As
932 the only hadron polarimeter system at a high energy collider it is the natural starting point for
933 hadron polarimetry at the EIC. Hadron polarization will be measured via a transverse single spin
934 left right asymmetry in the pp interaction on targets by plastic material (H-C composition), where
935 the experimental challenge is the control of the background events.

936 **Technological Synergistic Aspects of the Detector Design** The synergistic aspects of the
937 ePIC detector have been carefully maximized in view of the optimal usage of the workforce and
938 the financial resources. This is illustrated by the following examples.

939 SiPM sensors, recently introduced in calorimetry applications, are adopted for all the electromag-
940 netic and hadronic calorimeters in ePIC. They offer a cost-effective technology that can operate in
941 magnetic field, can provide wide dynamic range when the sensor type is properly chosen to tune

942 the response parameters, and present low noise level by applying appropriate thresholding. The
943 use of a common technology makes possible to access the effect of the radiation by a single effort
944 and the use of the same front-end ASIC CALOROC.

945 Also the calorimetry reconstruction software is synergistic for the overall set of subsystems.

946 In electromagnetic calorimetry, the sampling approach with tungsten and scintillating fiber is
947 adopted for the forward endcap calorimeter and in FDs: calorimetry in B0, luminosity system and
948 low- Q^2 taggers.

949 In hadron calorimetry, the SiPM-on-tile technology is used for the forward endcap calorimeter and
950 its insert in the central area, as well as for the zero-degree calorimeter.

951 In particle identification by Cherenkov imaging counters, MCP-based photosensors are used for
952 the backward endcap RICH and the barrel DIRC, that can be read by the same read-out ASIC
953 HGCROC (information to be crosschecked). The backward endcap RICH and the forward endcap
954 RICH use aerogel as radiator and the quality assessment station will be used for both batches.
955 The reconstruction software in both RICHes has large communalities and it is based on the same
956 ray-tracing algorithm.

957 AC-LGADs form the time-of-flight layers and are used for tracking in the forward FD in B0, off
958 momentum detectors and roman pots, and selected for the pair spectrometers of the luminosity
959 system.

960 In tracking by MAPS, the different sensors of the inner layers, the outer layers and the forward
961 and backward disks are all evolutions of the ITS3 sensor, therefore all based on stitching the same
962 readout chip element.

963 The same hybrid MPGD architecture with a preamplifying GEM layer followed by a μ RWELL is
964 used in the most outer tracker in the barrel and the most external discs in the endcaps. All MPGDs,
965 namely the hybrid MPGDs and the cylindrical Micromegas in the barrel are coupled to the same
966 front-end ASIC: SALSA.

967 A single integrated effort is at the basis of the tracking reconstruction with the use of the software
968 package AC.

969 **8.3.2 Magnet**

970 **Requirements**

971 **Requirements from physics:** Add text here.

972 **Requirements from Radiation Hardness:** Add text here.

973 **Requirements from Data Rates:** Add text here.

974 **Justification**

975 **Device concept and technological choice:** Add text here.

976 **Subsystem description:**

977 General device description: Add text here.

978 Sensors: Add text here.

979 FEE: Add text here.

980 Other components: Add text here.

981 **Requirements from Data Rates:** Add text here.

982 **Implementation**

983 **Services:** Add text here.

984 **Subsystem mechanics and integration:** Add text here.

985 **Calibration, alignment and monitoring:** Add text here.

986 **Status and remaining design effort:**

987 R&D effort: Add text here.

988 E&D status and outlook: Add text here.

989 Other activity needed for the design completion: Add text here.

990 Status of maturity of the subsystem: Add text here.

991 **Environmental, Safety and Health (ES&H) aspects and Quality Assessment (QA plan-**
992 **ning:** Add text here.

993 **Construction and assembly planning:** Add text here.

994 **Collaborators and their role, resources and workforce:** Add text here.

995 **Risks and mitigation strategy:** Add text here.

996 **Additional Material** Add text here.

997 **8.3.3 Tracking**

998 Add text here.

999 **8.3.3.1 The silicon trackers**1000 **Requirements**

1001 **Requirements from physics:** The Silicon Vertex Tracker (SVT) needs to meet stringent perfor-
 1002 mance requirements, set by the EIC science program, on acceptance and resolutions for charged-
 1003 particle trajectories. At a high level, the SVT needs to precisely measure the scattered electron
 1004 and charged hadrons produced in the electron-ion beam collisions. The scattered ion, if it remains
 1005 intact, is outside of the SVT acceptance. The SVT also needs to measure charged decay-particles
 1006 from hadrons containing heavy quarks and from vector meson decays. It is to aid in particle-
 1007 identification a) through determination of the displacement of the geometrical origin of the decay
 1008 particles (secondary vertex) from the collision point (event vertex) via precision reconstruction
 1009 of both vertices and b) by providing directional and impact information on charged-particle tra-
 1010 jectories through the outer gaseous tracking subsystems and into the outer particle-identification
 1011 subsystems.

1012 Table 8.1 contains the resolution requirements on the particle momentum measurement at the event
 1013 vertex for different ranges in pseudorapidity and on the determination of the radial distance of
 1014 closest approach of the particle trajectory to the event vertex with its dependence on transverse
 momentum. The SVT is the innermost subsystem of the ePIC central detector. Constraints from the

η range	dp/p [%]	DCA _r [μm]
(-3.5, -2.5)	$0.10 \times p \oplus 2.0$	$30/p_T \pm 40$
(-2.5, -1.0)	$0.05 \times p \oplus 1.0$	$30/p_T \pm 20$
(-1.0, 1.0)	$0.05 \times p \oplus 0.5$	$20/p_T \pm 5$
(1.0, 2.5)	$0.05 \times p \oplus 1.0$	$30/p_T \pm 20$
(2.5, 3.5)	$0.10 \times p \oplus 2.0$	$30/p_T \pm 40$

Table 8.1: Physics requirements on the relative momentum measurement, dp/p at the event vertex for different ranges in pseudorapidity, η , and on the determination of the radial distance of closest approach, DCA_r, of the particle trajectory to the event vertex with its dependence on transverse momentum, p_T .

1015 overall detector size and the outer subsystems limit the active volume of the SVT to $-105 < z <$
 1016 135 cm and a radius of approximately 42 cm. In combination with the 1.7 T solenoidal field, this
 1017 leads to a requirement on the point resolution of better than 10 μm as well as the need to minimize
 1018 traversed material by limiting the number of detection surfaces and minimizing their radiation
 1019 lengths.
 1020

1021 **Requirements from Radiation Hardness:** We have evaluated the radiation levels in the SVT
 1022 using the current knowledge of the beam configuration and beam backgrounds from beam gas
 1023 interactions and synchrotron radiation. Figure 8.6 shows the current estimates for fluence (in 1
 1024 $\text{MeV } n_{eq} \text{ cm}^{-2}$) and dose (in rad). The black lines indicate the approximate locations of the SVT
 1025 detection surfaces. These radiation maps have been estimated for the beam configuration with the
 1026 highest luminosity and include contributions from hadron and electron beam gas interactions. The
 1027 results assume that the machine and detector run at 100% efficiency for 6 months per year over
 1028 a period of 10 years. This is to obtain a conservative estimate. Even under these assumptions,

1029 the radiation levels in the SVT will be low to moderate. The majority of the SVT will see fluence
 1030 levels well below 10^{11} n_{eq} cm^{-2} . Innermost central layers and layers in the hadron going direction
 1031 will experience slightly higher fluence between 10^{11} and 10^{12} n_{eq} cm^{-2} , with some small regions
 1032 reaching above 10^{12} n_{eq} cm^{-2} . The dose rate map indicates that areas close to the beam pipe will
 1033 experience a total ionising dose between ten and a few hundred krad, while the rest of the SVT
 1034 remains below 10 krad.

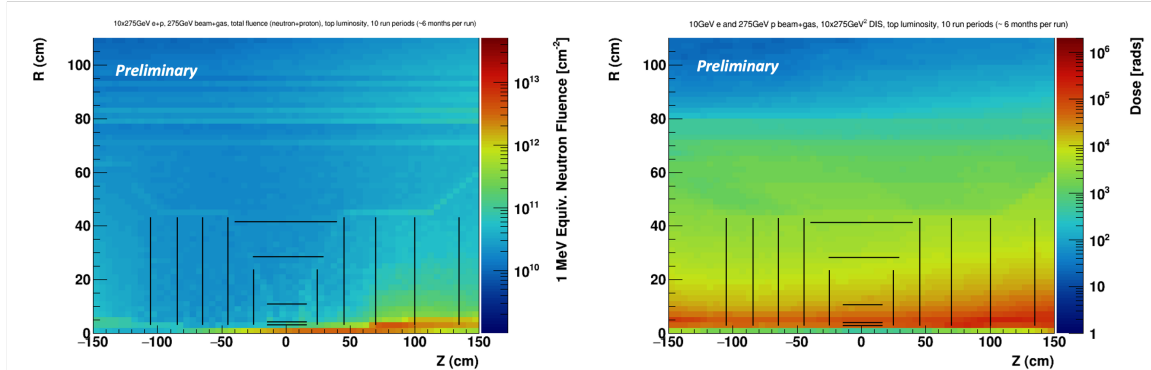


Figure 8.6: Maps of simulated fluence (left) and total ionising dose (right) over the ePIC tracking envelope. This is a conservative estimate assuming 10 years of running at top luminosity with 100% efficient accelerator and detector. The black lines indicate the approximate location of the ePIC SVT detector layers.

1035 **Requirements from Data Rates:** EIC physics rates are expected to be below 0.5 MHz. That is,
 1036 only a small fraction of the EIC beam crossings produces a physics event and physics event pileup
 1037 from within a single beam crossing is negligible. The dominant fraction of these events originate
 1038 from a region, $|z| < 80 - 100$ mm, surrounding the nominal interaction point. We thus estimate
 1039 that event pileup within the SVT is determined by its readout frame or integration window of $2 \mu s$
 1040 or a small multiple thereof. Within this window, SVT will also accumulate hits from noise and
 1041 beam backgrounds. We estimate that the associated hit load and data volume will exceed that from
 1042 physics events. Hit occupancies will be low in view of the high SVT granularity. We estimate a hit
 1043 probability per pixel per readout frame of $\mathcal{O}(10^{-7})$ and a typical total data rate at the level of 15
 1044 Gbps. The sensor and readout chain need to be efficient under these conditions.

1045 Justification

1046 **Device concept and technological choice:** To meet the stringent requirements on charged-
 1047 particle tracking and vertexing, we have designed the SVT to provide a well-integrated, large ac-
 1048 ceptance, high granularity, and low-mass tracking and vertexing subsystem. The SVT has four
 1049 regions covering a total active area of approximately 8.5 m^2 . An Inner Barrel (IB) and Outer Barrel
 1050 (OB), made of three and two detecting layers respectively, cover the mid-central pseudorapidity
 1051 range and have an active volume that extends radially to approximately 42 cm. Endcaps, each with
 1052 five detecting annuli surrounding the beampipe, are placed on either side of the nominal interac-
 1053 tion point with their active area constrained to $-105 < z < 135$ cm and an outer radius equal to
 1054 that of the OB. The Electron Endcap (EE) is positioned in the direction of the electron beam and
 1055 has acceptance for a large fraction of the scattered electrons, while the Hadron Endcap (HE) pro-

1056 vides acceptance for many of the hadrons produced in physics collisions. Figure 8.7 shows The
 1057 SVT regions and geometrical layout.

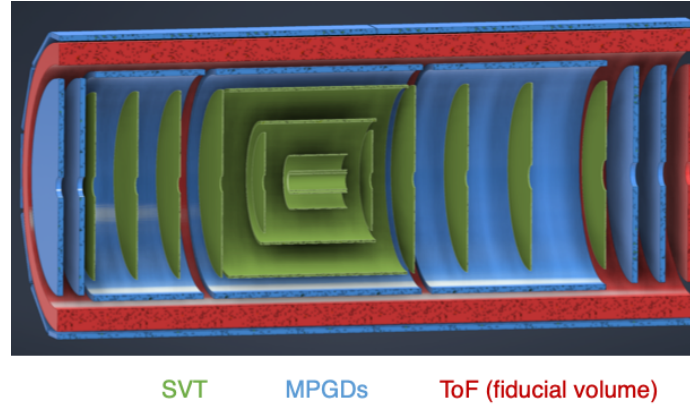


Figure 8.7: Schematic layout of the ePIC SVT showing the central region consisting of the inner and outer barrel made of three and two cylindrical layers, respectively, together with the endcap regions made of five annuli each. The figure also shows the surrounding Micro Pattern Gas Detector (MPGD) layers and the envelope of the Time of Flight PID detector.

1058 We designed the SVT to cover the required pseudorapidity range and to reach spatial resolutions as
 1059 low as $\leq 5 \mu\text{m}$ through a combination of high granularity ($\sim 20 \mu\text{m}$ pixel pitch), low power sensor
 1060 design ($\leq 40 \text{ mW cm}^{-2}$), and lightweight support structures, cooling, and electrical services. Our
 1061 development aims at achieving $0.05\% X/X_0$ in the IB, $0.25\% X/X_0$ in the innermost OB layer and
 1062 in the disks, and $0.55\% X/X_0$ in the outermost OB layer. We selected a sensor technology based of
 1063 the ALICE-ITS3 development [19] to meet our requirements. This is a new generation, large area
 1064 Monolithic Active Pixel Sensor (MAPS) in a commercial 65 nm CMOS imaging process.

1065 Subsystem description:

1066 General device description: Tables 8.2 and 8.3 show the positioning and size of the SVT de-
 1067 tecting layers, together with their material budget target. We designed the IB to provide
 1068 precise vertex reconstruction, while also contributing to momentum measurement. This is
 1069 achieved with a combination of very thin layers at optimised radii. The IB will use the AL-
 1070 ICE ITS3 wafer scale sensor [19] with a suitable adaptation of the ITS3 ultra-thin detector
 1071 concept to the large EIC beam pipe diameter. The IB design has three layers of silicon sen-
 1072 sors thinned below $50 \mu\text{m}$ and bent around the beam pipe, with minimal mechanical support,
 1073 air cooling, and no electrical services in the active area, to reach the very low material budget
 1074 target of $X/X_0 = 0.05\%$. The innermost layer is positioned as close as possible to the beam
 1075 pipe, taking into account the constraints coming from the large beam pipe radius and the
 1076 requirements from beam pipe bake-out, which will be performed with the IB installed. The
 1077 position of the second layer is chosen to maximise vertex resolution. The outermost layer of
 1078 the IB aims at maintaining the very low material budget at a radius of 120 mm and serves
 1079 both vertexing and sagitta measurements. The OB, EE and HE will be equipped with the EIC
 1080 Large Area Sensor (LAS), a modified version of the ITS3 sensor, optimized for high yield,
 1081 low cost, large area coverage. These sensors will be mounted on lightweight support struc-
 1082 tures, in the form of staves for the OB and disks for the endcaps, with integrated cooling and
 1083 electrical interfaces for power, data and slow control. The OB layers and the endcap disks are

1084 positioned to provide high precision measurements over a large level arm to improve mo-
 1085 mentum resolution and optimize acceptance at large pseudorapidity. The inner openings of
 1086 the disks will accommodate beam pipe bake-out constraints as well as beam pipe divergence.
 These translate into six different inner opening geometries over ten disks.

Region	Layer	radius [mm]	length [mm]	X/X_0
IB	L0	36	270	0.05%
	L1	48	270	0.05%
	L2	120	270	0.05%
OB	L3	270	540	0.25%
	L4	420	840	0.55%

Table 8.2: Radius, length and material budget of the SVT IB and OB layers.

Region	Disk	z [mm]	r_{out} [mm]	X/X_0	Region	Disk	z [mm]	r_{out} [mm]	X/X_0
EE	ED0	-250	240	0.25%	HE	HD0	250	240	0.25%
	ED1	-450	415	0.25%		HD1	450	415	0.25%
	ED2	-650	421	0.25%		HD1	700	421	0.25%
	ED3	-850	421	0.25%		HD3	1000	421	0.25%
	ED4	-1050	421	0.25%		HD4	1350	421	0.25%

Table 8.3: Position along the beam pipe, outer radius and material budget for the SVT layers in the EE and HE regions.

1087

1088 Sensors: The SVT will be constructed with MAPS sensors, that integrate sensing and front-
 1089 end electronics functionalities in one device. The ePIC SVT will use MAPS sensors developed
 1090 in a 65 nm CMOS imaging process based-off the ALICE ITS3 development [19]. This tech-
 1091 nology enables a high granularity and low power consumption design, and offers stitching
 1092 on 300 mm wafers for the development of large area sensors. These characteristics are key to
 1093 delivering a high precision detector through high spatial resolution and minimized material
 1094 budget.

1095 The SVT IB will use the ALICE ITS3 sensor, called MOSAIX. A sketch of MOSAIX on a wafer
 1096 is shown in figure 8.8. MOSAIX is composed of an active matrix of Repeated Sensor Units
 1097 (RSUs). Twelve RSUs are stitched along the length of the sensor. The sensor will be three,
 1098 four, and five RSUs wide for L0, L1 and L2 respectively. Each RSU is further divided into
 1099 12 tiles that can be switch off independently in case of faults to improve yield over such
 1100 large area device. A row of twelve RSUs, together with the left and right endcap (LEC, REC)
 1101 is called a segment. The LEC contains circuits for power, slow control and data. The REC
 1102 is used for power only to ensure a uniform power distribution over the full sensor length.
 1103 Data links for each segment can be configured with 3 links, plus one spare, at 10.24 Gb/s or
 1104 6 links, plus 2 spares, at 5.12 Gbps. For each segment, seven electrical links provide clock,
 1105 synchronisation and control signals, referred to here as slow control signals. The clock runs
 1106 at 40 MHz, while the other control signals will run at 5 Mbps. MOSAIX has different power

1107 domains for analogue and digital circuitry at 1.2 V, plus two more domains for specific blocks,
 1108 one at 1.2 V and one at 1.8 V [19]. The sensor's bias voltage will be in a range between -1.2
 and -4.8 V.

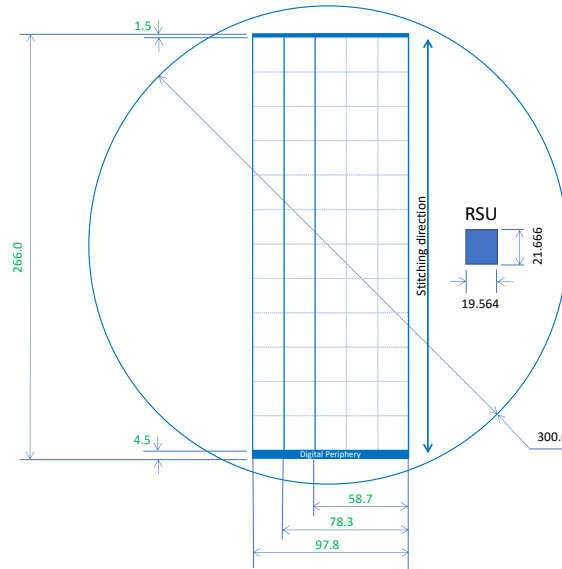


Figure 8.8: Sketch of the MOSAIX sensor on a 300 mm wafer showing the size of the RSU, LEC, REC and of the full sensor for the three different widths.

1109

1110 The SVT OB and endcaps cover an area of approximately 8 m^2 . Considerations based on
 1111 yield, cost, integration, and coverage require the use of a sensor with a smaller size. These
 1112 regions will use the MOSAIX sensor with modifications to reduce the size. This sensor would
 1113 still be large in traditional terms and is therefore referred to as the EIC Large Area Sensor
 1114 (EIC-LAS). The EIC-LAS will be one RSU wide and either 5 or 6 RSUs long. In addition
 1115 to reducing the size of the sensor, the EIC-LAS will see a reduction of the number of data
 1116 links to match the lower SVT data rate, reducing material and easing integration aspects. To
 1117 further ease the integration of the EIC-LAS in the OB and endcaps, EIC-LAS sensors will
 1118 be powered in series by a constant current and a dedicated communication protocol will be
 1119 used to reduce the number of slow control links from the counting room to the sensor. These
 1120 features will be provided by a supporting ASIC, referred to as the Ancillary ASIC (AncASIC).

1121 FEE: One AncASIC will be used per EIC-LAS. This chip includes three main features. It
 1122 integrates the SLDO regulator for serial powering. This regulator will generate the voltages
 1123 needed by the EIC-LAS from the input current. This design is adapted from the original
 1124 SLDO design for the upgrades of the ATLAS and CMS pixel detectors at the HL-LHC. One
 1125 AncASIC will integrate four SLDO regulators. The AncASIC will also contain a Negative
 1126 Voltage Generator (NVG) block. The NVG is a diode-based charge-pump circuit (Dickson-
 1127 type charge pump voltage multiplier). It will generate the sensor's negative bias voltage
 1128 from one of the regulated power supply at 1.2 V generated by the SLDO. The third block
 1129 is the Slow Control (SC). Slow control signals from the counting room will be transmitted
 1130 over I2C for multiple EIC-LAS sensors over one link. The SC block will decode them into
 1131 the MOSAIX format (i.e. into seven links). The AncASIC will be produced in a 110 nm SOI
 1132 process offering multiple MPW per year and the required transistors' ratings for the SLDO
 1133 and NVG.

1134 Other components: All components of the SVT detector are designed with the goal of achiev-
 1135 ing the low material budget target, while providing a robust, high precision system. Traditi-
 1136 tionally the bulk of the material in silicon detectors is contributed by the powering system.
 1137 The SVT will adopt a current based power distribution scheme, so called serial powering,
 1138 for the OB and disks. Groups of up to four EIC-LAS sensors are powered in series by a con-
 1139 stant current, with the electronics low voltage generated close to the sensors by the SLDO
 1140 regulators in the AncASIC. This scheme reduces cabling material and provides the only vi-
 1141 able powering solution to fit within the available space for services in the ePIC detector.
 1142 For the smaller IB system, a traditional voltage based, direct powering scheme is foreseen.
 1143 Data, slow control signals and power are routed over aluminium-based flexible printed cir-
 1144 cuits (FPC) between the SVT active elements (MOSAIX, EIC-LAS, AncASIC) and the readout
 1145 (RDO) boards. Four different RDO boards are used in the SVT. The interface board receives
 1146 data from the sensors for transmission to the counting room. The control board receives slow
 1147 control signals from the counting room to be transmitted to the AncASIC. Lightweight com-
 1148 munication between these RDO boards and the counting room is achieved by use of optical
 1149 fibers. An aggregator board achieves a reduction of the optical fiber lines through multi-
 1150 plexing via FPGA to match the number of fibers to the available channels of the FELIX data
 1151 acquisition board in the counting room. The electro-optical interface components used on the
 1152 interface and control boards are the lpGBT [20] and VTRx+ [21] devices developed by CERN.
 1153 The power board provides interface for power distribution for sensors and Anc-ASIC as well
 1154 as RDO boards. Whilst the functionality of the RDO boards and FPC remains the same, dif-
 1155 ferent designs will be needed for IB, OB and disks to accommodate the different powering
 1156 schemes, number of data links, and sensors grouping. The preferred cooling solution for the
 1157 SVT detector is air cooling, baselined for the two innermost layers of the IB and under study
 1158 elsewhere. The OB, EE and HE are designed to allow air flow through the low mass staves
 1159 and disks, made of carbon composite material, that support the sensors.

1160 **Performance** We have simulated track finding and reconstruction within the ePIC software
 1161 framework to quantify momentum and vertexing resolutions. Figure 8.9 shows the simulated re-
 1162 lative momentum resolution for single charged pions versus their total momentum for different
 1163 pseudorapidity regions, together with the requirements. The simulations show that the momen-
 1164 tum resolutions are substantially met over most of the SVT acceptance. The performance in the
 1165 range of smallest pseudorapidity, $-3.5 < \eta < -2.5$, is limited by constraints on the SVT lever
 1166 arm from ePIC's outer subsystems in this region and overall detector size. Figure 8.10 shows the
 1167 simulated radial distance of closest approach, DCA_r , for the reconstructed trajectories of simulated
 1168 charged pions to the event origin versus pion transverse momentum in different pseudorapidity
 1169 regions, together with the requirements. The simulations show that the requirements on DCA_r are
 1170 substantially met over the SVT acceptance.

1171 We have performed beamtests at FNAL with a single-RSU sensor, called babyMOSS, from ITS3
 1172 Engineering Run 1. In these tests, two times three sensors were arranged in a telescope and exposed
 1173 to the test beam. A seventh sensor, the Device Under Test (DUT), was placed at the center of
 1174 the telescope and its angle with respect to the incident beam was varied in the horizontal plane
 1175 of the telescope. Figure 8.11 shows a close-up of the telescope and results for the cluster extent
 1176 as a function of the incident beam angle onto the DUT from data and simulations. The results
 1177 demonstrate that the geometrical effect from the angle dominates over diffusion and otherwise
 1178 confirm the expected point resolution.

1179 **Implementation**

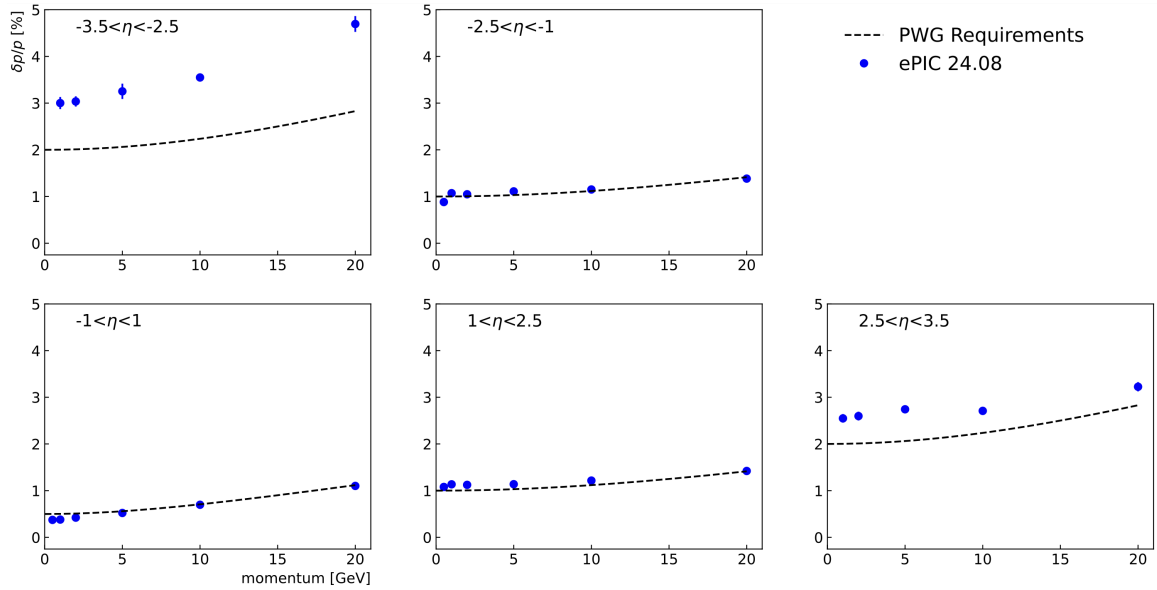


Figure 8.9: Relative momentum resolution versus total momentum for charged pions (points) together with physics requirements (curves) in different pseudorapidity ranges as indicated. The results are based on full GEANT simulations using the ePIC software stack and ACTS-based track finding and reconstruction using optimized parameters.

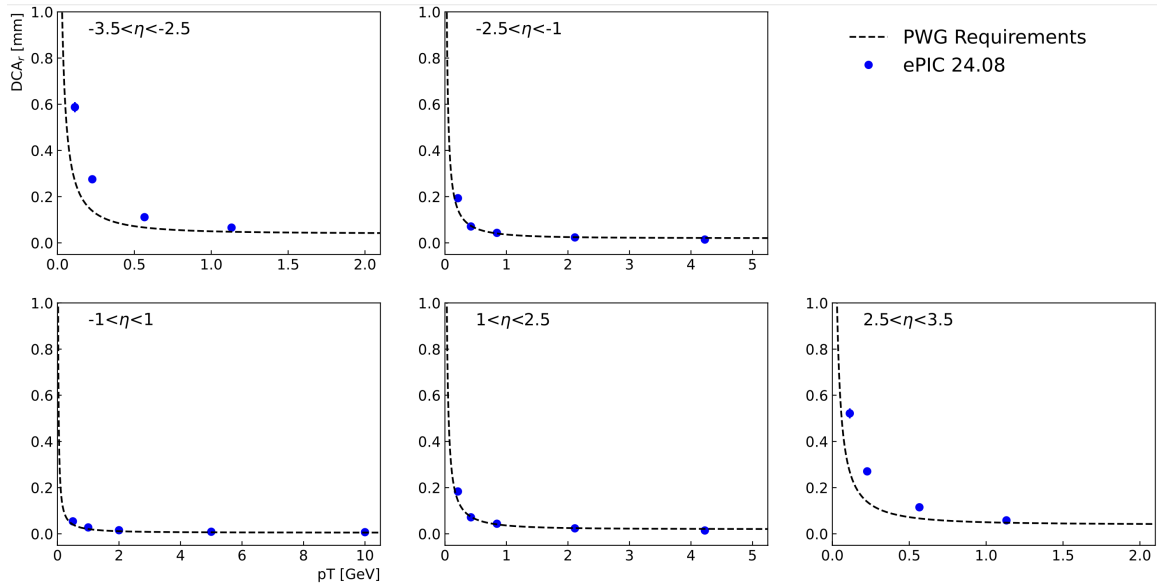


Figure 8.10: Distance of closest approach in the radial direction between reconstructed charged pion trajectories and the event origin versus transverse pion momentum (points) together with physics requirements (curves) in different pseudorapidity ranges as indicated. The results are based on full GEANT simulations using the ePIC software stack and ACTS-based track finding and reconstruction using optimized parameters.

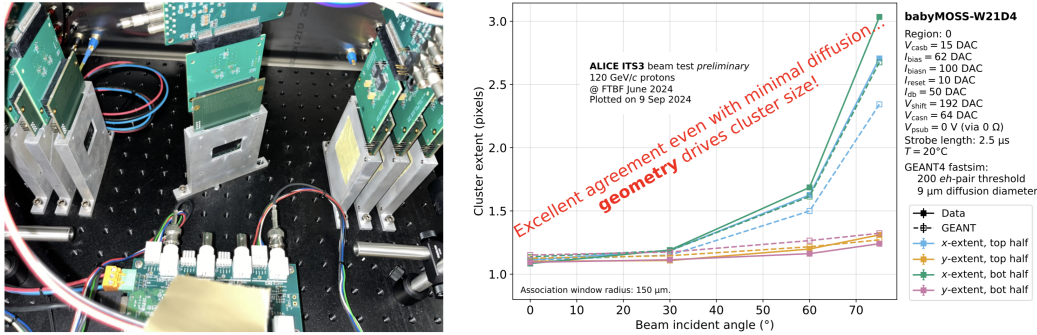


Figure 8.11: A close-up of a beam telescope constructed from two times three single-RSU sensors from ITS3 Engineering Run 1 with a seventh sensor (DUT) under an angle at the center of the telescope (left) and (right) results from beamtests at FNAL and from simulations for the cluster extent as a function of the beam incident angle onto the DUT.

1180 **Services:** Services to the SVT are of two types: electrical/fiber-optical services and cooling.
 1181 Electrical/fiber-optical services to the SVT comprise power, data and slow control. For the IB
 1182 (MOSAIX sensor and direct powering), electrical services will be by MOSAIX segment. For the
 1183 OB and endcaps (EIC-LAS and serial powering), they will be by group of up to four EIC-LAS. A
 1184 summary of the data, slow control and power lines needed in the different regions of the SVT is
 given in Table 8.4. The table illustrates the reduction in power lines using serial powering versus

Region	Sensor	Electrical services group	# power lines/group	# slow control links/group	# data links/group
IB	MOSAIX	MOSAIX segment	10	7	8
OB	EIC-LAS	Up to 4 EIC-LAS	2	3	4
ED	EIC-LAS	Up to 4 EIC-LAS	2	3	4

Table 8.4: Summary of power and readout services for the different regions of the sPIC SVT (slow control and data links are differential pairs of wires).

1185 direct powering. In the IB each MOSAIX segments will need ten lines (including the return line)
 1186 to serve the four power domains of the electronics plus the sensor bias. For each segment, the full
 1187 MOSAIX current will be transmitted. In the OB and endcaps two lines (including the return line)
 1188 will be needed to deliver the same power to up four EIC-LAS (i.e. four segments). The current
 1189 flowing on these lines will be the current needed by only one EIC-LAS, reducing the current being
 1190 transmitted to the detector of up to a factor four, and correspondingly reducing cables cross section
 1191 and material budget.
 1192

1193 Figure 8.12 shows the data and slow control distribution for a group of four EIC-LAS. Each data
 1194 line connects to one input of a VTRx+ on the interface board. Given the high speed of the data
 1195 transmission, this board will be placed at the end of each stave and disk for signal integrity. The
 1196 VTRx+ transmits the data of a group of up to four EIC-LAS over a bundle of optical fibers to the

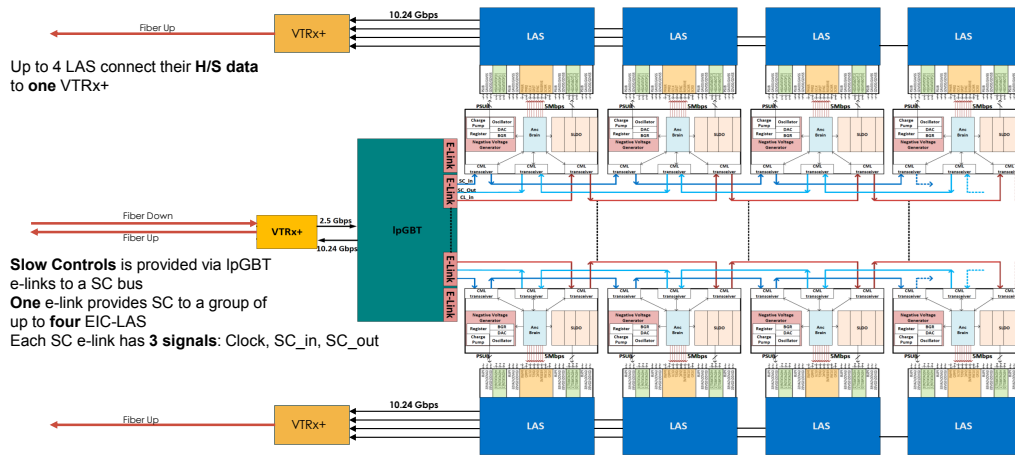


Figure 8.12: Schematic overview of data and slow control lines to a group of four EIC-LAS.

1197 counting room (each VTRx+ has a pigtail bundling up to 5 optical fibers). Slow control signals
 1198 are transmitted over optical fibers to the control board, placed along the support structure. Once
 1199 converted into electrical signals, one IpGBT elink provides the slow control signals to up to four
 1200 AncASICs. Each IpGBT has 16 elinks, meaning that each control board will serve multiple groups
 1201 of EIC-LAS. The slow control signals are transmitted between the control board and the AncASIC
 1202 either in a daisy-chain architecture (as shown in the figure) or via multi-drop. The exact configu-
 1203 ration is still being evaluated. The AncASIC converts the incoming I2C protocol to the MOSAIX
 1204 protocol expected by the EIC-LAS. As the OB and endcaps are powered in series, each EIC-LAS
 1205 is on a different ground potential. A dedicated communication scheme is thus needed. Data lines
 1206 will be AC-coupled. For the slow control, a standard DC transmission is also being investigated
 1207 with the ground difference between EIC-LAS sensors being accommodated.

1208 Flexible printed circuits (FPCs) are required to electrically connect MOSAIX sensors, EIC-LAS sen-
 1209 sors and AncASIC chips to the interface and control boards. In the IB the FPC will connect to the
 1210 REC and LEC of the MOSAIX sensor. In the OB and disks, it will run along staves and disks re-
 1211 spectively, serving groups of EIC-LAS sensors, connecting to the AncASIC. The FPCs must have
 1212 a low mass in order to maintain the low material budget of the SVT. It is therefore advantageous
 1213 to select conductive tracks made of aluminium ($X_0 = 8.9$ cm) instead of traditional copper ($X_0 =$
 1214 1.4 cm). Dielectrics like polyimide ($X_0 = 28.57$ cm) are the default solution for the manufacturing
 1215 technologies of aluminium-based FPCs deployed in scientific experiments. The selection of the di-
 1216 electric material is dependent on its loss-tangent properties versus the frequency of the signals to
 1217 be transmitted. Typically the most stringent requirements to signal attenuation are set by the high-
 1218 speed data transmission lines. In case of the ePIC SVT, it is envisaged that data links can transmit
 1219 signals as fast as 10.24 Gb/s for a length of ~ 50 cm. The baseline configuration for the FPCs as-
 1220 sumes a stack-up made of two aluminium conductive layers (each ~ 15 μm thick) separated by a
 1221 polyimide dielectric substrate (~ 35 μm), and then additional polyimide cover layers (~ 35 μm
 1222 combined thickness) to insulate the conductive tracks from external electrical shorts. This cross section
 1223 (~ 100 μm in total) would equate to a combined material budget of $\sim 0.06\%$ X_0 . The combination
 1224 of serial powering, slow control daisy-chained/multi-drop configuration and impedance matching
 1225 at 100 Ω for clock, control lines and data, enables a reduction of the number of signals to be prop-
 1226 agated. This is particularly important for staves and disks where the FPCs overlap the sensitive
 1227 area of the MAPS. By combining these power and signal distribution techniques, it is estimated
 1228 that the minimum width for the FPC can as narrow as 6 mm. This is $\sim 1/3$ of the width of the LAS

1229 (~19 mm).

1230 The transmission of the signals to the counting room will see a further stage of processing. The
1231 data fiber-optic lines will be aggregated in the aggregator board which has multiple fiber inputs, an
1232 FPGA for extracting the payload from these fibers, and one fiber output towards the FELIX board,
1233 thus reducing the number of fiber inputs at the Data Acquisition FELIX boards. It is estimated that
1234 approximately 5000 data fiber links run from the sensors to the aggregator board. Assuming an
1235 aggregation factor of 10, there will be approximately 500 fibers towards the DAQ FELIX boards,
1236 which can be accommodated by 11 FELIX boards (assuming each FELIX board will have 48 fiber
1237 inputs).

1238 Cooling adds to the service load, including the target radiation lengths in the SVT active areas.
1239 The preferred cooling solution for the SVT detector is air cooling, baselined for the two innermost
1240 layers of the IB and under study elsewhere, with liquid cooling in strategic places as necessary.
1241 We will operate the sensors at or near room temperature ($\sim 25^\circ\text{C}$), which requires a lower coolant
1242 temperature. Thermal performance of the cooling is measured with $\Delta T = T_{\text{sensor}} - T_{\text{inletairorcoolant}}$.
1243 Our target for thermal tests and simulations is ΔT of 10°C , although this is not a strict requirement.

1244 For the inner layers of the IB, the baseline is air cooling with thermally conductive foam near the
1245 LEC. Measurements from ALICE ITS3 show this is reasonable to cool the MOSAIX sensor. Air will
1246 be forced between L0 and L1. To cool L2, the possibility for natural convection with liquid cooling
1247 near the LEC is under study. The air inlet and outlet are under design, with the bulk of the material
1248 to be placed on the hadron-going side of the detector.

1249 In addition to cooling during operation, the IB will need to be kept cool during beam-pipe bake-out.
1250 The aim is for no additions to the operational cooling, i.e. no additional material (e.g. insulators)
1251 or changes (i.e. liquid instead of air). ANSYS studies at Jlab and LBNL have shown that there is a
1252 path forward to keep the detector cool. Climate chamber studies at LBNL and CERN have shown
1253 no failures up to 50°C .

1254 The target for both the OB staves and the EE and HE disks is air cooling. We are targeting a max-
1255 imum air velocity of 12 m/s within the structures of the staves and disks. Current estimates are
1256 approximately $1700\text{ m}^3\text{h}^{-1}$ total air split between the staves and disks. This will require com-
1257 pressed air to mitigate the otherwise excessive size of the air tubes coming into the detector and
1258 pressure regulation inside the detector. Studies are ongoing to reduce these numbers, including the
1259 use of thermally conductive materials (e.g. carbon foam) to help with heat dissipation. The SVT
1260 will be interlocked to turn off in the case of failure of its cooling system, including conditions so as
1261 to prevent pressurising the system beyond its design values.

1262 **Subsystem mechanics and integration:** The inner barrel (IB) layers will be made of two sym-
1263 metric half-layers, which will be the basic assembly elements of the detector. The two innermost
1264 layers (L0 and L1) will be based on four MOSAIX sensors (two for each half-layer), while the out-
1265 ermost layer (L2) will contain eight MOSAIX sensors (four for each half-layer). All the sensors
1266 equipping a given half-layer will be placed one next to the other to fully cover the half-layer sur-
1267 face and bent on a cylindrical shape at the corresponding radius (c.f. table 8.2).

1268 Each IB half-layer will consist of the following components: the MOSAIX sensors, a local support
1269 structure mainly made in carbon foam shaped as a frame along the edges of the sensors, two sets
1270 of FPCs wire-bonded to the sensor peripheries for powering and data/control transmission. The
1271 sensor cooling will be air-flow based and delivered through appropriate ducts that will be part of
1272 the local support structure and matched to the global mechanics described below.

1273 The IB global support will be the main structure supporting the MOSAIX sensors already assem-

1274 bled in half-barrels. The current design foresees a cylindrical frame structure for each layer, sup-
 1275 ported by two conical endcaps, one for L0-L1 and a second for L2, the last including a flange for
 1276 connection to the other half-cone and to the OB. The material is currently fixed in a carbon fiber
 1277 composite, whose thickness will be approximately 0.5 mm. FPC and cables from the e-side are
 1278 routed along the inner surface of the conical support. A half-cylindrical shell made of polyamide
 1279 is placed outside and close to L2 for general protection of the barrel and to constrain the airflow
 1280 on the surface of L2. Air is distributed through conveyors in the volumes between L0 and L1 and
 1281 between L2 and the outer shell. The current design of the cables (power lines) which run from
 1282 e-side to h-side need that the longerons of the local mechanics have also the role of cable trays,
 1283 the requirement of rigidity and the U-shape for cables routing suggesting carbon fiber composite
 1284 as a preferred material choice, while alternatives are being considered. Figure 8.13 shows CAD
 representations of the IB support.

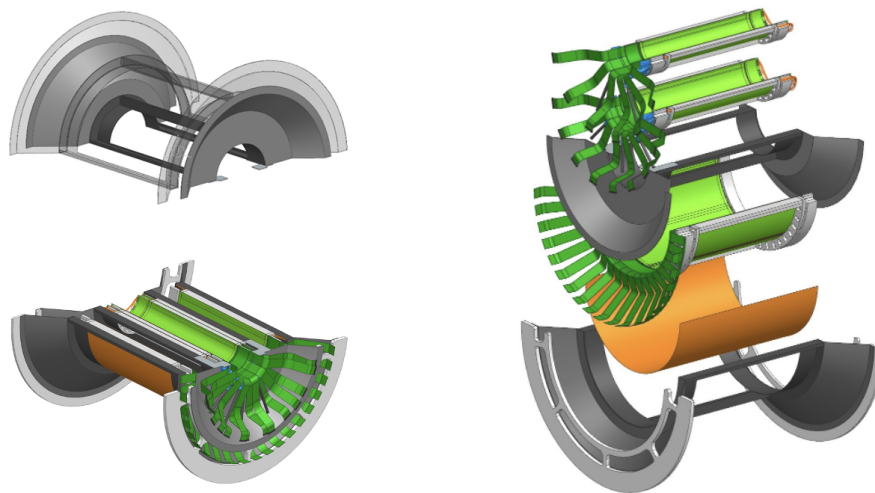


Figure 8.13: Top left: CAD representation of the frame supporting the IB. Bottom left: IB half-barrel CAD view with sensors and cable routing. Right: Exploded CAD view of IB from the h-side and the e-side. The orange element is the kapton shield. In blue the air conveyors are shown.

1285

1286 For the OB, EE, and HE, we introduced a modular approach in the SVT design to simplify the
 1287 assembly process of these complex detector elements. A modular approach reduces complexity by
 1288 breaking down the system into sub-units (i.e. detector modules) that we will pre-assemble and pre-
 1289 test and then mount/interlink in the final staves or disks. The advantage is that defects in sub-units
 1290 like detector modules are detected earlier in the production flow. This makes it easier to re-work
 1291 problems and/or discard faulty components earlier in the production flow. A modular approach
 1292 also reduces debugging complexity of the final product like a stave or disk. Overall introducing a
 1293 modular approach in the design of the OBs and Disks increases the predictability of the production
 1294 rate of the SVT in the production phase. It mitigates risks of delays by design and it increases
 1295 confidence in planning for the production phase.

1296 The goal in the definition of a detector module is to identify a coherent sub-unit from a functional
 1297 prospective, and to shape it into a design-for-manufacturing unit. Electrical and mechanical con-
 1298 straints shape the implementation of the module.

1299 The first point to consider is that the deployment of Large Areas Sensors (LASes) in the ePIC SVT
 1300 represents an unprecedented technological evolution in the field of particle trackers, without any

1301 previous, directly applicable example. The concept of a LAS is an evolution of the concept of pre-
 1302 vious detector modules where individual dies were combined into a module. The LAS combines
 1303 directly via stitching multiple repeated sensor units into a single large area silicon die. A LAS is
 1304 itself an evolution of the traditionally assembled detector modules with many single dies. Despite
 1305 this, the LAS operation depends on the ancillary ASIC (AncASIC). Therefore an electrically coher-
 1306 ent unit is represented by a LAS and its AncASIC.

1307 The two components (i.e. LAS and AncASIC) of this electrically coherent unit need to be electrically
 1308 connected via flexible printed circuits boards and micro-electronics interconnection techniques.
 1309 This electrically coherent unit needs to be supported by a mechanical frame to be interfaced with
 1310 cooling systems and to meet handling requirements.

1311 The design of a module for the outer barrel envisions two LAS with their respective two AncASIC,
 1312 once for each LAS. The mechanical frame is made of a thin film of polyimide that holds together all
 1313 the module components.

1314 The design of a module for the disks envisages one LAS and one AncASIC and a mechanical frame
 1315 made of a carbon fibre plate.

1316 We will test modules standalone after their assembly and before their assembly into staves or disks.

1317 The outer barrel (OB) layers will be segmented in staves. The staves are composite structures using
 1318 carbon fibre (CF) skins, a central CF I-beam spar and cross-ribs made of K9 foam. The side walls will
 1319 be formed by the FPCs. The structure has openings where modules will be placed. During module
 1320 mounting the modules are glued on top of these openings, forming a closed hollow structure with
 1321 large second moment of area, and thus high stiffness. The closed structure provides a contained
 1322 channel for the forced flow of air through the stave, that will remove the heat from the sensors and
 1323 ancillary ASICs. In addition to their structural function, the cross-ribs made of highly thermally-
 1324 conductive K9 foam are placed underneath high-power density components (the left endcap of the
 1325 EIC-LAS and the AncASIC) to improve the transfer of the heat into the air coolant flow.

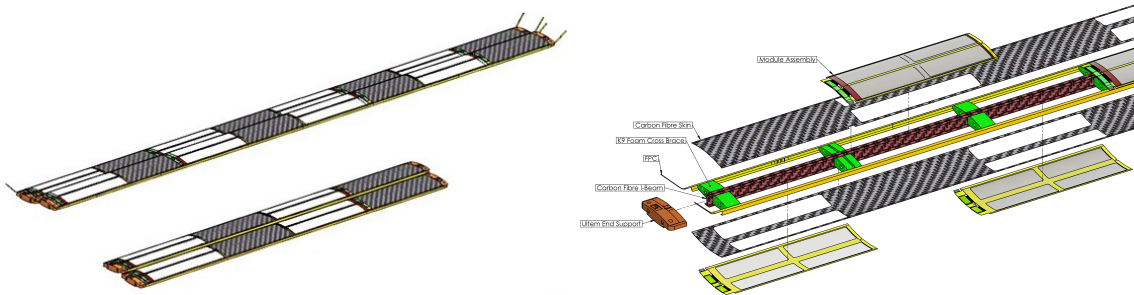


Figure 8.14: Left: OB staves for L3 and L4. Two staves per layer are shown. Right: Exploded view of an OB stave.

1326 Each stave is one OB module (two EIC-LAS) wide, and has modules on both facings, staggered in
 1327 z so that the active areas of the modules provide overlap for tracks from the vertex. L4 staves will
 1328 hold 4 modules on each facing, or 8 modules in total, while L3 staves will have half that number.
 1329 The dimensions of the staves are dictated by the layout of the SVT and we achieve the required
 1330 coverage with LAS made up of 6 RSUs in L3 and 5 RSUs in L4, respectively. L3 will consist of two
 1331 halves with 44 staves in total in a castellated layout to cover the full azimuth. L4 will consist of two
 1332 halves and have 70 staves. Our initial FEA analysis of the modal frequencies finds $f_1 = 91.6$ Hz.

1333 The staves will connect mechanically at their ends to segmented half-cones that are part of the SVT

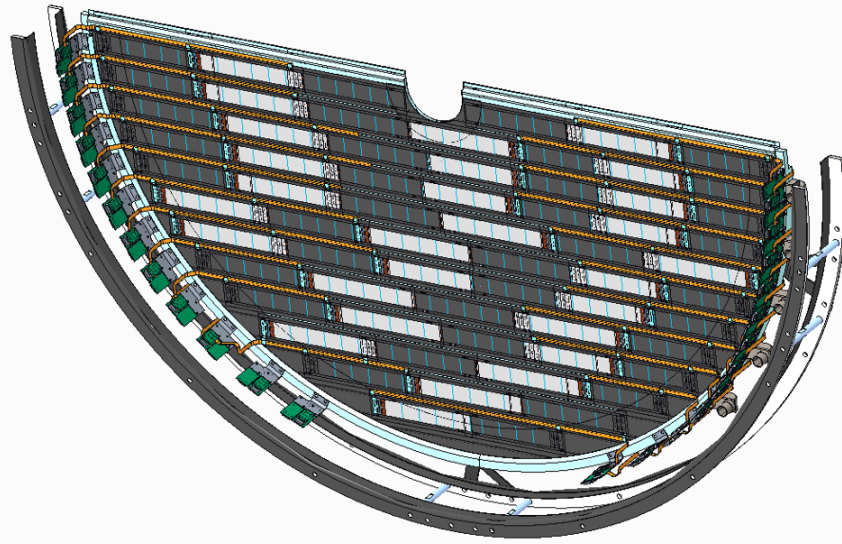


Figure 8.15: CAD model of the preliminary (half-) disk design. Modules are shown in alternatingly inward (dark gray) and outward (white) facing orientations. Common bus FPCs are shown in orange. RDOs (green) are arranged on the outside of the disk ring, inside of the interface to the SVT global support structure.

1334 support structure. This interface still needs to be detailed, but will constrain stave rotations at the
 1335 support, while allowing for limited misalignment of the support cones and thermal expansion of
 1336 components. The interface will also contain the couplings of the air channel inputs to the supply
 1337 distribution. The cones interface at their outer radius with a support tube surrounding the entire
 1338 SVT, including its services, and also connect to the the global support structure of the IB and the
 1339 innermost disks.

1340 The EE and HE disks are a two-sided design with a corrugated carbon composite core. The purpose
 1341 of the corrugation is to add strength without adding too much mass. The corrugated channels can
 1342 be used for air flow to cool the disks. It also gives options for sensor layout to maximize overlaps
 1343 of inactive area. Modules with one EIC-LAS will be tiled over the valleys of the corrugation on
 1344 either side of the disk, creating overlap along the long axis of the sensor. Modules will be placed in
 1345 an alternating inward and outward facing orientation along the corrugation which ensures that an
 1346 active area of the neighboring sensor covers the insensitive LEC.

1347 Each disk will have a ring at the outer radius that will sandwich the corrugated core to provide
 1348 mechanical support, a mounting point for the RDOs, and an inlet for air cooling. Those rings
 1349 will then connect mechanically to either the SVT support cone (ED0-1, HD0-1) or support cylinder
 1350 (ED2-4, HD2-4). This design is currently being optimized in conjunction with the global mechanics.
 1351 A CAD model of the disk design is shown in Figure 8.15.

1352 **Calibration, alignment and monitoring:** Calibration procedures are needed to optimize the
 1353 settings for the pixels in the ITS3 and EIC-LAS sensors. We anticipate these to be similar to those
 1354 used for the existing ITS2, MLR1, and ER1 sensors, and consist in data-taking scans where one
 1355 injects a charge into groups of pixels and varies their settings. We have made initial estimates of
 1356 the time required to perform such scans and anticipate that such scans can be done in a parallel
 1357 fashion in approximately half an hour with the final readout system.

1358 Alignment procedures are needed to achieve the required resolutions. We will survey the IB (half-
1359 layers, staves, and disks with precision coordinate measuring machines during their construction
1360 and will pursue a global survey during installation. Final alignment will be track-based.

1361 Monitoring will include sensor settings and other slow-control data, including temperatures, as
1362 well as analysis in near-realtime of residuals in alignment and other observables.

1363 **Status and remaining design effort:**

1364 R&D effort: The development of the MOSAIX sensor is well underway. Two submissions
1365 have already taken place in 2020 and 2022. The former, so called MLR1, included numer-
1366 ous test structures for technology exploration and to develop prototype circuit blocks for
1367 future sensors. The latter, ER1, contained exploratory designs to study stitching principles,
1368 methodology and yield. The submission of the MOSAIX sensors (ER2) aiming to satisfy ITS3
1369 requirements is planned for beginning of 2025. ePIC designers are integrated in the MOSAIX
1370 design team and contributing to the development of logic libraries, and circuitry for data
1371 transmission over the full sensor length between RSUs. The final submission (ER3) will be
1372 the MOSAIX production version for the ITS3 detector and the ePIC SVT IB.

1373 Work on the EIC-LAS has started in terms of defining the required modifications. Design
1374 work will start once the design database is available upon signature of the necessary CERN-
1375 EIC agreement.

1376 The AncASIC is in development with good progress on all functional blocks. Multi-Project
1377 Wafer (MPW) runs are foreseen until the full chip will be ready for production in 2026.

1378 E&D status and outlook – IB: We have developed a preliminary design for the two inner-
1379 most (L0 and L1) half-layers of the IB and its global support mechanics. Different solutions
1380 have been explored for bending and assembly of each half-layer: connecting two sensors
1381 in a single object and following a “half-layer” based procedure has been considered largely
1382 preferable mainly due to advantages from overlaps with the ITS3 building concept. Once
1383 the two half-layers have been individually built, they are assembled in a L0-L1 half-barrel.
1384 Blank silicon pieces with dimensions corresponding to the final MOSAIX sensors have been
1385 used to advance the design of the L0-L1 assembly and build the first half-barrel prototypes.
1386 In parallel, a preliminary design of the whole SVT IB mechanics, including an external shell
1387 to L2, has been also developed and a first mock-up has been produced.

1388 We will evolve the designs for the half-barrel assembly and for the global mechanics, towards
1389 properly engineered realistic ones. The next half-barrel assembly to be built has to integrate
1390 as much as possible all the basic components of the final detector (although in a prototyping
1391 shape) and allow for thermo-mechanical studies to finalize the cooling design. Test cam-
1392 paigns in a climate chamber and in a wind tunnel facility for ageing and cooling studies are
1393 planned. Building of a first L2 half-layer prototype, based on the guidance from the L0-L1
1394 assembly experience, is also scheduled to happen in parallel.

1395 For the SVT IB global mechanics, we will use carbon fiber composites as the main material for
1396 the support, given the low mass and excellent mechanical properties. In the coming months
1397 an engineered version is planned, with the goal of both verifying possible space conflicts
1398 within the global mechanics and matching with the SVT IB assembly procedures.

1399 E&D status and outlook – OB: We are currently prototyping the curved surface stave de-
1400 sign for L4 to evaluate tooling and assembly procedures, as well as the performance of the
1401 design. These prototypes will be equipped with mechanical dummy sensors (40 μm unpat-
1402 terned silicon) for mechanical studies, and thermo-mechanical dummy sensors (40 μm silicon

1403 encapsulated in 25 μm and 50 μm thick Kapton layers with a 5 μm thick Cu trace layer). In
 1404 particular, we will verify/measure

- 1405 – Manufacturability (co-cure), mechanical integrity and good compaction of carbon fibre,
- 1406 – Mechanical response spectrum up to 500 Hz and associated Q values,
- 1407 – Deformations with air flow up to 20 m/s,
- 1408 – Surface temperatures with thermo-mechanical dummy sensors powered up to 40 W
 1409 per stave,
- 1410 – Thermo-mechanical deformations with thermo-mechanical dummy sensors powered
 1411 up to 40 W per stave.

The results from these studies will guide us in the finalisation of the stave design. In the

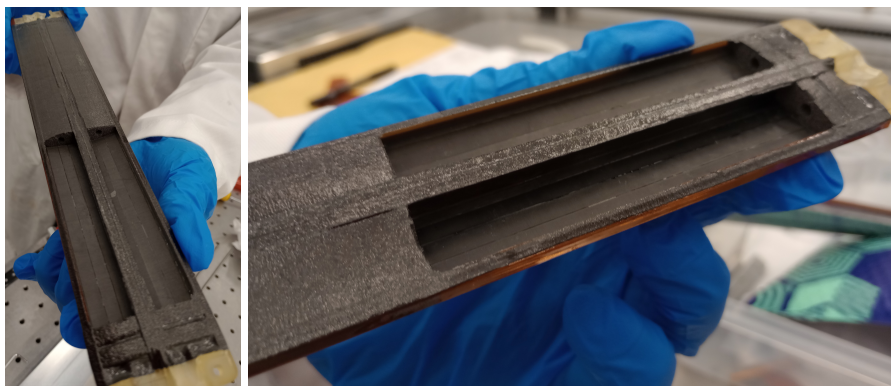


Figure 8.16: First L4 quarter length stave prototype.

1412 first phase we are prototyping the stave design with the curved facings, as this is the more
 1413 challenging to construct.
 1414

1415 Interfaces to the support cones will be designed in parallel with the design work on these
 1416 structures.

1417 E&D status and outlook – Disks: Work continues on the design and layout of the disks. We
 1418 are finalizing the carbon fiber layouts for both the corrugated core and the flat module sheets.
 1419 The first prototype was made using carbon fiber veil for the face sheets and corrugation and
 1420 had a density of 500 gsm. However, the veil is not ideal for thermal performance and can
 1421 be challenging to lay up on the corrugated tooling. New prototypes are being made with
 1422 K13CU unidirectional carbon fiber, which has a much improved thermal conductivity.

1423 The initial test piece has been tested for thermal performance using copper trace heaters. The
 1424 prototype is shown in Figure 8.17. The measured ΔT is well within 10 $^{\circ}\text{C}$ for the EIC-LAS
 1425 RSUs, but is high for the LEC, though trending in the right direction with increased air flow,
 1426 and depends on the design dissipation. The thus far high values of ΔT for the LEC region
 1427 can be due to many factors, including the low thermal conductivity of the carbon fiber veil
 1428 and the overall thinness of the contact surface. We are studying mitigation possibilities using
 1429 pyrolytic graphite sheets (PGS), which have a large in-plane thermal conductivity (upwards
 1430 of 800 W/m \cdot K) and significantly improve the thermal performance of the prototype. Results
 1431 are shown in the right of Figure 8.17. The new face sheets made with K13CU have similar
 1432 thermal conductivity to the PGS and initial tests are promising. A new, full prototype is being
 1433 assembled with the K13CU carbon fiber..

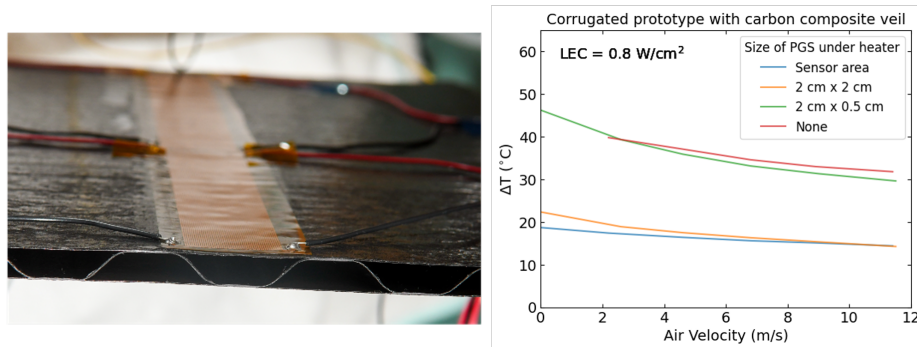


Figure 8.17: (Left) First test piece of the carbon composite corrugated disc core made in the LBNL composite shop. Heaters with two different heating zones that can mimic the sensor power density are placed on the carbon composite facesheet and are used for thermal measurements. (Right) Observed ΔT on the LEC section of the test heater versus coolant air velocity using corrugated carbon fiber veil prototype test piece. Measurements taken with various sizes of PGS placed underneath heater.

1434 We are currently developing prototypes focused on the development of assembly tooling,
 1435 module handling, and thermal and mechanical tests. Prototypes will undergo vibration tests
 1436 to understand mechanical stability. Mechanical dummy silicon ($40\ \mu\text{m}$ unpatterned silicon)
 1437 is in hand to construct a quarter disk mechanical prototype. We expect thermo-mechanical
 1438 dummies ($40\ \mu\text{m}$ silicon encapsulated in $25\ \mu\text{m}$ and $50\ \mu\text{m}$ thick Kapton layers with a $5\ \mu\text{m}$
 1439 thick Cu trace layer) at the end of the calendar year to create a thermo-mechanical prototype.
 1440 The bench tests will be paired with ANSYS structural and fluent simulations to understand
 1441 the performance under air flow and the structural integrity of the disk. This will also need
 1442 to be accompanied by bench tests and simulations that include the disc support ring and the
 1443 outer ring.

1444 E&D status and outlook – FPCs: The development of the flexible printed circuits (FPCs) for
 1445 the ePIC SVT adopts an iterative approach where a sequence of prototypes will inform the
 1446 evolutionary development of the final design. The activity on the FPC started in September
 1447 2023 and it is progressing as part of Work Package 3 “Electrical Interfaces”. The first iteration
 1448 of prototypes is underway. This started with targeting an initial design for OB L4. A defini-
 1449 tion stage captured the design requirements for powering, data transmission and geometrical
 1450 factors until March 2024. This was followed by a design stage and then by an order submis-
 1451 sion to RPE LTU (Ukraine). The first set of prototypes are currently being manufactured. The
 1452 prototypes from RPE LTU will be tested at Daresbury Laboratory and at the University of
 1453 Oxford. They will also be distributed to other interested sites. In parallel, the community of
 1454 institutes interested in FPCs started to grow. Since 09/05/2024, the WP3 community started
 1455 to have monthly meetings with representatives from BNL, Daresbury Laboratory, LANL,
 1456 LBNL and the University of Oxford. LBNL started to evaluate prototypes from Omni Circuit
 1457 Board (Canada). LANL also approached a third supplier called Q-Flex Inc. (USA) to procure
 1458 low level prototypes. The aim is to evaluate the capabilities of three different suppliers
 1459 to manufacture FPCs with aluminium conductors. Signal and power integrity of the FPCs will
 1460 be tested and the performance over samples of different suppliers compared. A key require-
 1461 ment is signal attenuation for the high speed differential transmission lines ($10\ \text{Gb/s}$). Wire
 1462 bonding and single point Tape Automated Bonding (spTAB) are being evaluated as potential
 1463 interconnection techniques in ongoing and future prototypes.

1464 E&D status and outlook – Powering: The need to regulate voltages for the MOSAIX sensors

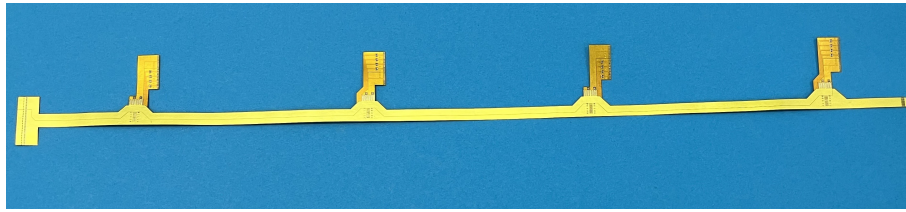


Figure 8.18: An example of a low technology readiness level prototype for the FPC of the outer barrel (layer4). Prototype made by RPE LTU.

1465 as close to the IB (to minimise losses) dictates the need for a(t least one) powering board.
 1466 Considerations for the design and development of these boards are ongoing; this includes
 1467 deciding how many regulation stages give the best balance between power losses (fewer
 1468 stages is likely to mean longer lengths of the most lossy cables, when delivering low voltage
 1469 and high current), versus additional material in the detector volume (more stages equals
 1470 more high material powering board, and the final voltage regulation is likely closer to the
 1471 active area of the IB).

1472 Conceptual powering schemes were developed and used to define specifications for the An-
 1473 cASIC and FPC designs for the OB and Disks. Requirements are being iterated based on
 1474 limitations introduced by these designs so that they can be iteratively improved. Testing and
 1475 confirmation of requirements will occur as prototypes become available; this includes:

- 1476 – Verifying output voltages and current capacity of the individual SLDOs.
- 1477 – Verifying output voltages of NVGs.
- 1478 – Daisy-chaining AncASICs to verify serial powering chain performance.
- 1479 – Quantifying performance of the FPCs in terms of current carrying capacity and voltage-
 1480 drop along the conductor lengths.
- 1481 – Combining the above elements to test full serial powering chain prototypes (1 FPC
 1482 feeding current to 4 AncASICs, each loaded with an EIC-LAS-like structure).

1483 E&D status and outlook – Powering: Work on readout electronics has mainly concentrated
 1484 on testing evaluation boards of the various components being considered for SVT readout:
 1485 lpGBT, VTRx+, radiation tolerant FPGA PolarFire, optical FireFly. As part of the ITS3 work-
 1486 package responsible for readout (WP6) we follow closely the developments in ITS3, since a
 1487 lot of the electronics for SVT is modeled after ITS3 designs. An initial prototype for the Fiber
 1488 Aggregator Board was discussed and is now under development using a commercial FPGA
 1489 board (ZCU102) mated with the optical FireFly FMC card to provide up to 8 fiber inputs and
 1490 multiple fiber outputs. The VLDB+ board from CERN (containing both lpGBT and VTRx+
 1491 was used setup a full chain starting from a Skyworks clock generator board as a stand-in
 1492 for the Global Timing Unit (GTU), a Xilinx ZCU102 board running lpGBT-FPGA firmware
 1493 as a stand-in for the FELIX board, and the VLDB+ board as the RDO. A measurement of the
 1494 jitter of the clock recovered by the lpGBT showed demonstrated adequate performance of this
 1495 chain to provide a low-jitter clock to the sensors.

1496 Together with Nikhef and Utrecht University, we are currently developing a test system for
 1497 the serializer chiplet of the ER1 prototype submission. This serializer is a prototype for the
 1498 10Gbps serializer to be deployed in the Left End Cap of the final ITS3 sensor. The test system
 1499 consists of an FMC card which contains the bonding pads for the serializer chiplet, as well as
 1500 various drivers and connectors including the possibility to drive the high-speed signal onto a
 1501 Flex-PCB to test the signal integrity over those traces. The FMC card itself will connect to a
 1502 commercial Xilinx FPGA board for pattern generation and checking.

1503 Another prototype development is the “MOSAIX Mock-up” board currently being designed
1504 at ORNL consisting of an FMC daughter card which contains the various Readout compo-
1505 nents (2 data VTRx+ and an lpGBT / VTRx+ combination for the slow controls interfaces. It
1506 will interface to a ZCU102 board where firmware will simulate the responses to slow con-
1507 trols commands, while also allowing to simulate data packets to be sent over the up to 8 fiber
1508 optic lines of the 2 VTRx+ interfaces in order to develop both data acquisition protocols and
1509 slow controls interfaces of the Readout Electronics to the MOSAIX sensor without the need
1510 of an actual MOSAIX sensor.

1511 E&D status and outlook – Cooling: Our prior work has shown that foam can be an important
1512 factor in the cooling and thermal performance of staves and disks. This is an integral part
1513 of the OB stave design and is being pursued as an option for under the LEC in the disk
1514 design. Both will be tested using thermal and thermo-mechanical dummies with upcoming
1515 prototypes.

1516 The final air cooling system will be designed based on the overall air volume of the SVT.
1517 Current estimates put the total air volume around 1000 cfm total, which would require a
1518 pressurized system. The air will be pressurized before entering the ePIC detector volume
1519 and then regulated down to various pressures as required by the different parts of the SVT
1520 (e.g. OB design requires air above 1 atm).

1521 Simulations from LBNL and Jlab have shown that during beam-pipe bake-out a 5 mm dis-
1522 tance from the beam-pipe can keep the silicon below 30 °C with air flow below 10 m/s. How-
1523 ever, air flow between the beam-pipe and L0 brings down the temperature of the beam-pipe
1524 and can affect ability to reach the 100 °C required inside. Studies are ongoing to determine
1525 what hot gas temperature is needed to bring the beam-pipe to temperature and what effect
1526 that has on the silicon. We also plan to study if airflow only between L0 and L1 is sufficient to
1527 keep the detector below the current 30 °C requirement as this will help mitigate the effect of
1528 the air cooling on the beam-pipe itself. Simulations will be paired with thermo-elastic studies
1529 in a climate chamber that will study cycling, longevity, and assess the point of failure.

1530 Other activity needed for the design completion: We are continuing our testing characteriza-
1531 tion of the products from the ITS3 sensor development sequence. We are currently preparing
1532 for the first tests on MOSAIX at CERN, in collaboration with ITS3, using a high-frequency
1533 wafer probe setup that we are jointly developing. Laboratory tests of thinned and diced
1534 wafers are also being planned, as well as beamtests and irradiation efforts.

1535 The AncASIC will be manufactured in a different process than the MOSAIX and EIC-LAS
1536 sensors. We are readying an initial MPW submission in this 110 nm process and are planning
1537 for its testing and validation. Test structures and the main functional modules of AncASIC,
1538 the SLDO, NVG and Slow Control, will undergo irradiation to verify their correct functioning
1539 in the expected radiation environment.

1540 Status of maturity of the subsystem:

1541 **Environmental, Safety and Health (ES&H) aspects and Quality Assessment (QA plan-**
1542 **ning:** We will follow and adhere to all applicable ES&H standards during the development, con-
1543 struction, installation, and ultimately commissioning and operation of the SVT. Hazards include
1544 those associated with adhesives, carbon composites, flammables, wafer-probing and wire-bonding,
1545 use of radioactive sources, testbeams, and irradiation facilities, and electrical safety. Where possi-
1546 ble, we will work across institutions to implement standardized controls and mitigations, as well
1547 as documented safety procedures.

1548 System tests in the development phase of the SVT are integral to our Quality Assessment. Quality
1549 Control forms an integral part of WBS and schedule during construction and assembly.

1550 **Construction and assembly planning:** The L0-L1 half-barrels will be manufactured in Italy
1551 by INFN: the current plan is to have a main assembly site in Bari and a second one in Padova
1552 currently being equipped. The L2 production half-layers will be built in the US. Both construction
1553 activities will include a final QC step of the corresponding complete assembly: this will include
1554 operation with air-cooling to verify thermal performance and testing of readout and control lines.
1555 After a successful pass of the QC step, L0-L1 half-barrels and L2 half-layer will be shipped to BNL.
1556 The global IB mechanics will be produced by INFN in Padova, undergo a QC step based on a
1557 metrological survey and finally shipped to BNL. At BNL the L0-L1 half-barrels and L2 half-layers
1558 will be assembled to the global mechanics to form complete IB half-barrels. All the connections to
1559 services (powering, cooling and readout) will be put in place to allow a final QC step.

1560 Modules and staves for the OB layers will be manufactured in the UK. Currently we plan to manu-
1561 facture modules at two sites, Birmingham and Daresbury Lab. This production includes electrical
1562 bonding of the sensors and ancillary ASICs to the bridge FPC. Module construction concludes with
1563 a QC on the completed module before shipping to the stave loading sites. Stave production, which
1564 comprises manufacture of the stave composite structures, and gluing of modules onto the struc-
1565 tures and electrical bonding of the bridge FPCs to the main FPCs. These production steps will be
1566 performed at Oxford and RAL. Again, the final step of the stave construction will be a QC of the
1567 completed stave. This will comprise operation with internal air cooling to verify thermal perfor-
1568 mance, operation of control lines and readout of modules. After successful pass of these QC steps,
1569 staves will be shipped individually to BNL. At BNL staves will be mounted on the support half-
1570 cones from the inside, starting with the outermost layer L4. This involves mechanical connection,
1571 connection of the air supply, and dressing of the FPCs and mounting of the RDOs on the outside of
1572 the support cones. After the mounting of the L4 staves they will be tested, and after that the same
1573 procedures will be repeated for the inner OB layer, L3.

1574 Disks and their modules will be produced and assembled in the US. LBNL, Purdue, and LANL
1575 are expected to be disk assembly sites, with LBNL and Purdue also serving as module assembly
1576 sites. Assembly of modules includes gluing of sensors to carbon composite structures, as well
1577 as electrical connection (wire or tab bonding) to a bridge FPC and the AncASIC. Modules will
1578 undergo QC before being assembled onto disk structures. The corrugated carbon composite disk
1579 structures and module flat sheets will be produced at LBNL and shipped to LANL and Purdue.
1580 Disc support rings will be produced by an outside vendor, validated at LBNL, then shipped to
1581 disk assembly sites. Disks will be assembled in halves, first on one side and then the other. Disk
1582 assembly includes gluing modules and common bus FPCs onto the front and rear sides of the discs
1583 and making electrical connections. QC is planned for each corrugated row assembly and then again
1584 after completion of the front and rear sides of each disk. Disks will be shipped in halves to BNL,
1585 where they will be installed into the larger SVT assembly. Disks are the last piece to be installed,
1586 after the IB and OB. Assembly will occur from the inner disks outward. ED0 and HD0 will be
1587 mounted to the SVT support cones. ED2-4 and HD2-4 will be mounted to the support cylinder.
1588 ED1 and HD1 could be mounted to either and will be iterated with global mechanics. Installation
1589 must include the dressing of the services, connecting of the air supply, and mounting of the RDOs.
1590 Each half disk will be tested after installation.

1591 We plan to produce the outer global support structures at Purdue and/or LBNL. Readout will be
1592 led by ORNL with testing at multiple sites.

1593 **Collaborators and their role, resources and workforce:** (Placeholder:) The SVT currently
1594 has collaborators at 20 institutions with the main institutional roles and resources outlined above.

1595 **Risks and mitigation strategy:** The SVT depends crucially on its sensors, the ITS3 sensor used
 1596 in the IB and the ITS3-based EIC-LAS used in the OB, EE, and HE, since they form the only known
 1597 way to meet the full performance requirements within ePIC. Their development is ongoing and
 1598 presents a risk. Together with the project we have identified two branchpoints, which are both
 1599 based on schedule delays:

- 1600 1. the ITS3 schedule remains compatible with the EIC project schedule, but EIC-LAS develop-
 1601 ment is delayed,
- 1602 2. the ITS3 schedule is delayed and becomes incompatible with the EIC project schedule.

1603 If the first branchpoint were triggered, the SVT OB will be replaced with two MPGD barrel layers
 1604 derived from the outer MPGD tracker, specifically its innermost (micromegas) layer. The SVT EE
 1605 and HE will in this case each be replaced with in total up to seven near-identical MPGD disks,
 1606 specifically based on the existing μ RWELL disks. If, in addition, the second branchpoint were
 1607 triggered, the SVT IB will be replaced by two or three layers based on the existing ITS2 sensor, as
 1608 used in the ALICE and sPHENIX experiments, without EIC-specific modifications.

1609 Additional Material

1610 8.3.3.2 The MPGD trackers

1611 Requirements

1612 **Requirements from physics:** Micro-Pattern Gas Detector (MPGD) technologies have been cho-
 1613 sen to complement the Si based tracking layers. MPGDs are relatively fast detectors able to provide
 1614 precision space point measurements with good timing resolution, while also maintaining the over-
 1615 all conservative material budget that is required of the ePIC detector [22]. MPGDs will play a role
 1616 in pattern recognition, ensure the central tracking system covers the required full pseudorapidity
 1617 range $-3.5 \leq \eta \leq 3.5$, and aide in PID reconstruction.

1618 The EIC collider is expected to deliver collisions with bunches crossing every ~ 10 ns [23], which
 1619 will require the MPGD detectors to provide timing resolutions $\mathcal{O}(10 \text{ ns})$ to separate events from
 1620 adjacent bunches. For ep collisions of 10×275 GeV, the DIS physics rate is expected to be around
 1621 500 kHz, while hadron and electron beam gas backgrounds rates are estimated to be 32.6 kHz and
 1622 3177.25 kHz, respectively [4]. These rates are well within the rate capabilities of MPGDs. Combin-
 1623 ing the timing information from the MPGDs with information from the Si detectors should allow
 1624 pattern recognition algorithms to discriminate between physics and background signals. In addi-
 1625 tion to providing hit information with good timing resolutions, the MPGDs will provide additional
 1626 hit points needed for robust track reconstruction. Early simulations showed that the number of
 1627 hit points used in the track reconstruction reduced from around 6 hits near $\eta = 0$, to only 3 hits
 1628 at $|\eta| > 3$, due to tracks moving out of the acceptance of some of the Si layers. ePIC endcap
 1629 gaseous trackers, (μ RWELL-ECT) were implemented to recover additional hits at larger η values.
 1630 Figure 8.20 shows the average number of hits per event in the current ePIC tracking detector as a
 1631 function of η for different momentum ranges. In this configuration the ePIC tracker measures at
 1632 least 5 hits per event over the region ($|\eta| < 3.5$).

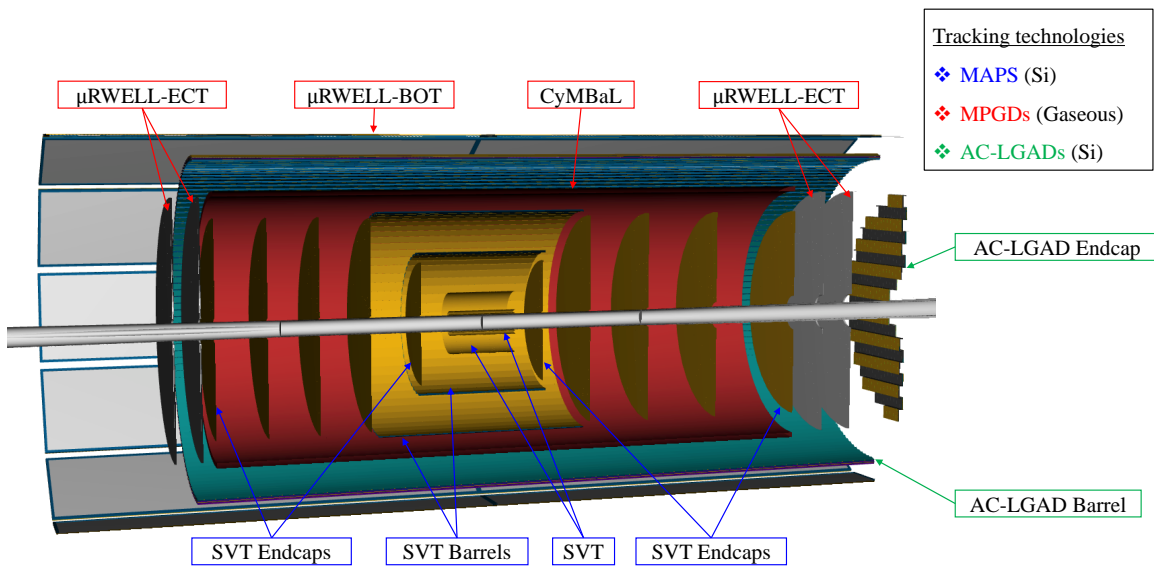


Figure 8.19: ePIC Tracking Subsystems

1633 Finally, as detailed in the Yellow Report [22], the hpDIRC requires the track entering the PID vol-
 1634 ume to have good angular resolution (0.5 mrad at $p = 6$ GeV) in order to meet its performance
 1635 requirements. This will be accomplished by providing the hpDIRC with precision hit points just
 1636 before a particle enters its volume via ePIC barrel outer tracker, (μ RWELL-BOT) and exits to the
 first tracking layer of the barrel imaging calorimeter.

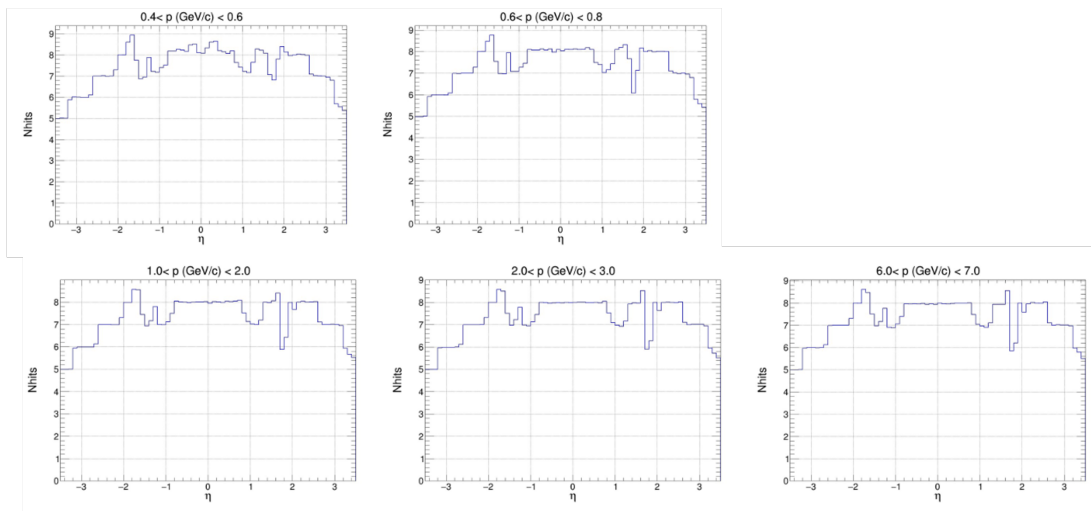


Figure 8.20: Total tracker hits vs. η for various momentum ranges.

1637

1638 **Requirements from Radiation Hardness:** Detailed simulation on radiation dose in ePIC has
 1639 been performed. Fig. 8.21 shows the estimate of hadron and EM radiation doses in ePIC simulation

1640 along with location of MPGD layers [4]. Table 8.5 shows the maximum estimated radiation dose
 1641 from various sources for MPGD trackers at various locations with 10 years of running at top ma-
 1642 chine luminosity and 100% detector and accelerator efficiency based on e+p PYTHIA simulation.

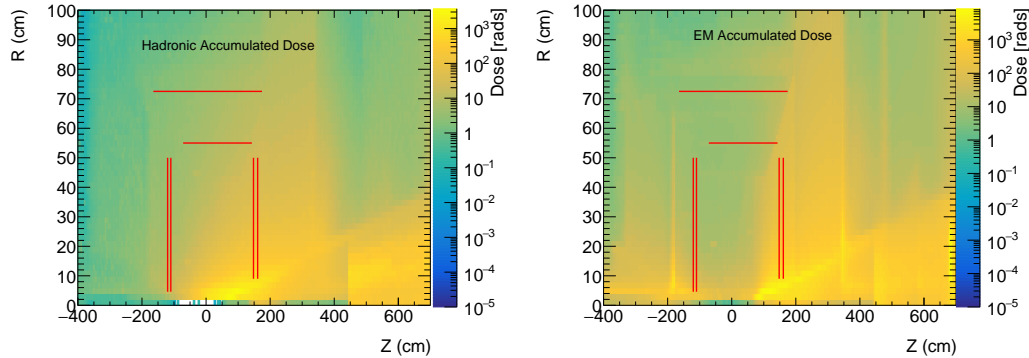


Figure 8.21: (left) EM radiation and (right) Hadron radiation dose estimate for minimum bias PYTHIA e+p events at 10x275 GeV at top machine luminosity for 6 months of running at 100% machine and detector efficiency [4]. The locations of MPGD trackers are shown by red lines [24].

1643

MPGD tracker	EM Radiation dose [krads]	Hadron Radiation dose [krads]	1 MeV neutrons equivalent fluence [cm^{-2}]	1 MeV protons equivalent fluence [cm^{-2}]
CyMBaL	0.22	0.15	2.7×10^{10}	2.0×10^{10}
μ RWELL-BOT	0.3	0.1	2.8×10^{10}	4.2×10^9
electron ECT	0.064	0.03	1.1×10^{10}	1.7×10^9
hadron ECT	0.87	0.23	3.0×10^{10}	8.5×10^9

Table 8.5: Maximum dose of radiation by different sources at MPGD tracker layers for e+p minimum-bias event at 500 kHz event rate for 10 years EIC running with 6 months run time per year and 100% efficiency [4].

1644 The MPGD trackers in ePIC will experience low radiation dose and based on past experience with
 1645 MPGD trackers in various experiments [25–27] there will be negligible aging issues. The electronics
 1646 based on SALSA and also DC-DC converter, which will be mounted on the detector back end, are
 1647 radiation hard as is shown by electronics group for ePIC in section 8.3.10 of this document.

1648 **Requirements from Data Rates:** Table 8.6 shows hit rate per unit area for each MPGD subsys-
 1649 tem in ePIC which is far lower than rate capability of MPGD detectors [28, 29]. Table 8.7 shows
 1650 the maximum hit rate experienced by a channel for various MPGD trackers in ePIC [4]. The rates
 1651 are low enough for ASIC developed for MPGDs which can handle rate of 100 kHz/channel.

1652 **Justification** The requirements cited above drives the necessity of using MPGD trackers at var-
 1653 ious locations of ePIC. MPGDs can be built over large area and their ability to handle high rates

MPGD tracker	DIS e+p rate [Hz/cm ²]	Hadron beam gas rate [Hz/cm ²]	Electron beam gas rate [Hz/cm ²]
CyMBaL	26.37	14.33	5.5
μ RWELL-BOT	9.82	5.33	1.7
electron ECT	144.68	78.63	437
hadron ECT	1326.36	720	201

Table 8.6: Hit rate per unit area of various MPGD trackers for e+p DIS events at 10×275 GeV with $1.54 \times 10^{34} \text{cm}^2 \text{s}^{-1}$ luminosity scaled from e+p DIS events at 18×275 GeV and $1.54 \times 10^{33} \text{cm}^2 \text{s}^{-1}$ luminosity, 10 GeV electron beam gas and 275 GeV hadron beam gas

MPGD tracker	DIS e+p events [Hz]	Hadron beam gas [Hz]	Electron beam gas [Hz]
CyMBaL	3.68	0.05	4.78
μ RWELL-BOT	2.76	0.04	4.78
electron ECT	9.2	3.56	102
hadron ECT	101.2	4.39	39.88

Table 8.7: Maximum hit rate by a single channel of various MPGD trackers for e+p DIS events at 10×275 GeV with $1.54 \times 10^{34} \text{cm}^2 \text{s}^{-1}$ luminosity scaled from e+p DIS events at 18×275 GeV and $1.54 \times 10^{33} \text{cm}^2 \text{s}^{-1}$ luminosity, 10 GeV electron beam gas and 275 GeV hadron beam gas

1654 with moderate spatial resolution makes them excellent candidate for large size trackers.

1655 **Device concept and technological choice:** The MPGD trackers are based on two different
1656 technology and are described in the following.

1657 **Subsystems description: CyMBaL.** The role of the ePIC Cylindrical Micromegas Barrel Layer
1658 (CyMBaL) is to wrap around the SVT in its entire length to provide an additional hit point. Conse-
1659 quently, the main requirement is to have as little as possible acceptance gaps. In order to limit the
1660 impact on particle reconstruction in the outer detectors, CyMBaL has to be light in material budget,
1661 possibly less than $X/X_0 \sim 1\%$. The requirements in space resolution are still to be finalized, but
1662 CyMBaL is expected to provide hit points with about $150 \mu\text{m}$ uncertainty. In order to help the track
1663 finding, the time resolution is expected to be of the same order of magnitude of the bunch spacing,
1664 i.e. ~ 10 ns.

1665 CyMBaL (Figure 8.22a) is composed as a set of 32 Micromegas tiles arranged in a way to ensure
1666 full coverage in φ (8 modules) and in z (4 modules). The space envelop assigned to CyMBaL spans
1667 the range between 55 cm and 60 cm in radius and it is asymmetric in the longitudinal direction,
1668 covering the range $-105 \text{ cm} < z < 143 \text{ cm}$. CyMBaL is designed in two symmetric halves that
1669 meet at $z = 19 \text{ cm}$ (due to the asymmetric keeping zone). In each half, the 16 modules are arranged
1670 in two cylinders, the inner one (in $|z|$) sitting at a radius of 55 cm and the outer one at 57.5 cm.

1671 In order to limit the complexity of the detector production, the design is aiming at limiting the

1672 differences among the modules, possibly having only a single design for the module PCBs that will
1673 be assembled with different bending radii.

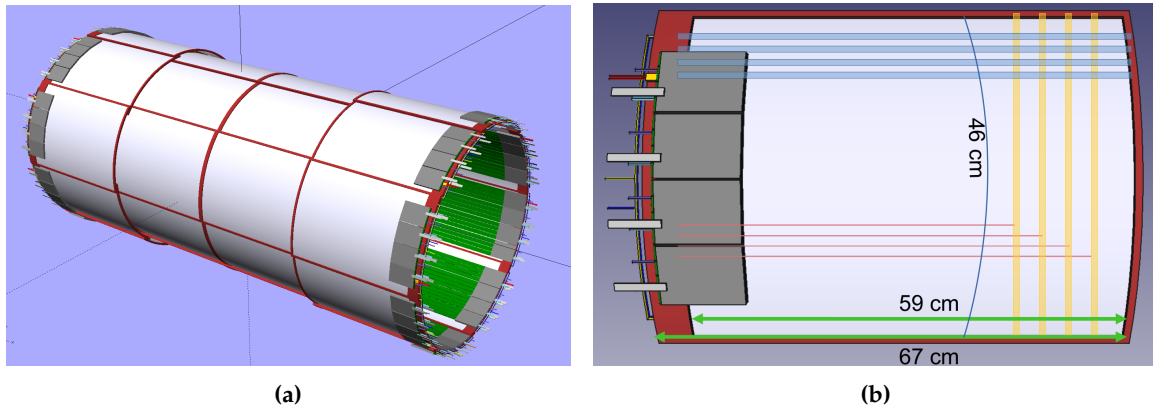


Figure 8.22: (a) CyMBaL CAD model showing the assembly of the 32 modules. (b) CAD model of a CyMBaL module. The light blue represents examples of readout strips measuring the $r \cdot \varphi$ coordinate (called Z-strips as they run along the z axis). The light yellow represents examples of readout strips measuring the z coordinate (called C-strips as they are arcs of a cylinder). The light red lines represent examples of trail lines to bring the C-strip signals to the FEBs. For the explanation of the services see the text.

1673

1674 The preliminary design of a CyMBaL module is shown in Figure 8.22b. A module is a cylindrical
1675 tile 48 cm wide (equivalent to about 50 degrees in the azimuthal direction) and 67 cm long, and the
1676 active region is about $46 \times 59 \text{ cm}^2$. The sensor is based on the bulk resistive Micromegas technology
1677 [30] with a 3 mm conversion gap. The signal will be readout by orthogonal strips to provide a
1678 two dimensional information of the position of the charged particle crossing the sensitive area.
1679 The strips running along the longitudinal direction (therefore called Z-strips) will provide the $r \cdot \varphi$
1680 measurement of the hit and they will be directly routed to the connector area. The strips running
1681 along the azimuthal direction (C-strips, C for cylindrical) will provide the z information of the hit
1682 and they will need be connected with vias to routing trails to bring the signals to the connectors.
1683 The pitch of the readout strips will be $\sim 1 \text{ mm}$ and the resistive layer will allow the charges to be
1684 shared among neighboring strips for a better centroid reconstruction. The total number of strips
1685 per module will be 1024 and they will be readout by four FEBs, each one equipped with 4×64 -
1686 channels SALSA chips.

1687 The frame will consists of carbon fiber hollow square beams and arcs of about 3 mm in size. Being
1688 hollow, these beams not only will provide the mechanical rigidity and support for the detector, but
1689 also will be used to distributed the gas inside the detector.

1690 **Subsystems description: μ RWELL-BOT.** The ePIC MPGD Barrel Outer Tracker (μ RWELL-
1691 BOT layer) is the outermost gaseous tracking layer installed in the barrel region of ePIC central
1692 tracker. The detector sits right at a radius of 72.5 cm right in front of the high performance DIRC
1693 (hpDIRC) as shown in the layout at the top left of Fig. 8.23. The tracker is split in two sectors (Z-
1694 sector) along the beam axis z . Each Z-sector is consists of 12 μ RWELL-BOT rectangular modules
1695 (φ -modules) arranged in dodecagon shape to cover 2π acceptance in the azimuthal direction (φ)
1696 as shown in the top right of Fig. 8.23. The μ RWELL-BOT φ -modules are designed to match the
1697 hpDIRC acceptance in both z and φ as shown on the bottom right of Fig. 8.23. Mechanical con-
1698 straints associated to the detector support frames as well as the very limited space available for

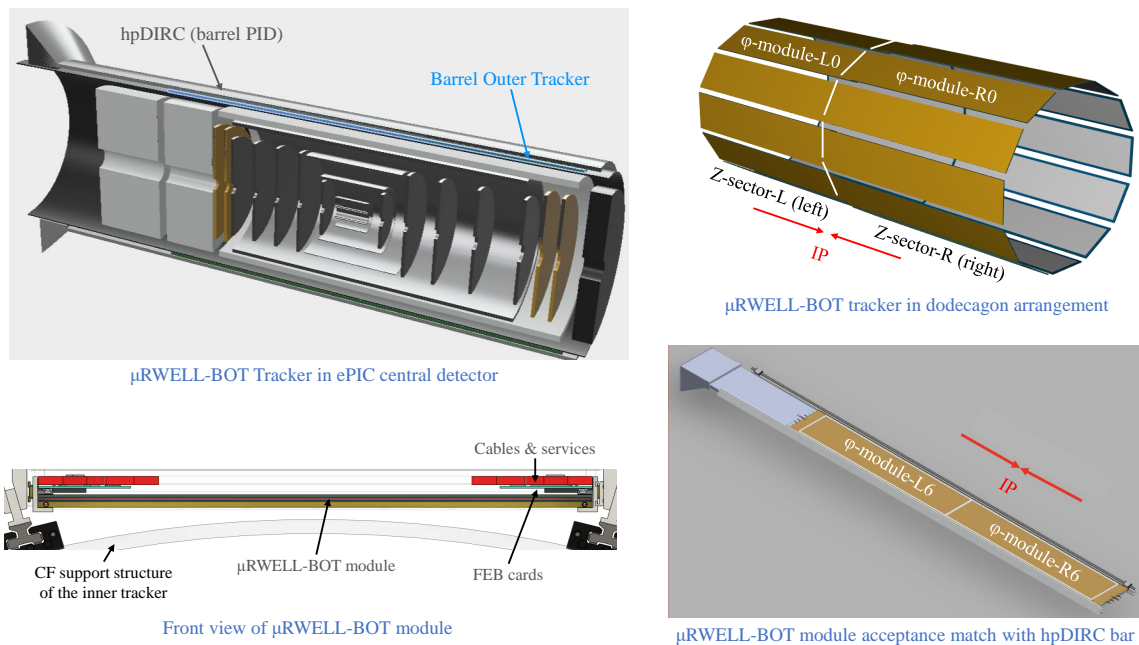


Figure 8.23: μ RWELL-BOT in ePIC central detector frame

1699 integration in the ePIC detector support frames result in an acceptance gap of $\sim 13\%$ in φ and $\sim 1\%$
 1700 in z .

1701 For the μ RWELL-BOT φ -modules, thin-gap GEM- μ RWELL hybrid detector technology (see Ap-
 1702 pendix section ??) was chosen to satisfy the detector requirement in term of position and timing
 1703 resolution as well as detector efficiency and operation stability. Proof of concept and preliminary
 1704 performance results on small size prototypes tested in beam at Fermilab in 2023 are also reported
 1705 in Appendix section ?. The design of the full size μ RWELL-BOT module prototype based on the
 1706 thin-gap GEM- μ RWELL technology is presented in Appendix section ?? as part of the Project En-
 1707 gineering Design (PED) effort to develop the engineering test article μ RWELL-BOT module based
 1708 on thin-gap GEM- μ RWELL technology.

1709 **Subsystems description: μ RWELL-ECT.** Monte Carlo simulations show that the endcap re-
 1710 gions of the ePIC detector experience the highest backgrounds in the experiment and charged par-
 1711 ticle tracking requires several hit points in the $|\eta| > 2$ region for good pattern recognition. To
 1712 optimize the ePIC baseline tracker design, two planar Micro-Pattern Gaseous Detectors (MPGD)
 1713 disks, with a central hole for the beam pipe are located both in the hadronic and the leptonic sec-
 1714 tors (see the right drawing of Figure 8.24). The ECT disks geometrical envelope is reported in Table
 1715 8.8. It takes into account the integration constraints within the ePIC detector and the beam pipes
 1716 dimensions. As shown in the left drawing of Figure 8.24, the hadron and lepton beam pipes slightly
 1717 diverge from the interaction point, therefore the ECT inner radii are calculated taking into account
 1718 the envelope radii and their center offset, the hadron beampipe forming a larger angle with the z
 1719 axis. For simplicity the inner radius is fixed by the largest of the two values calculated for the disk
 1720 located at the larger z position at each endcap region. As a result the two lepton disks located closer
 1721 to the interaction point, will have a smaller inner radius than the two hadron disks (4.65 cm vs 9 cm)
 1722 as they are located closer to the interaction point, while the outer radii of 50 cm are equal for all the
 1723 four disks and are fixed by the available volume inside the ePIC detector. The ECT disks envelope

MPGD Disk	Longitudinal location z (cm)	Outer Radius (cm)	Inner Radius (cm)	Outer Active Area Radius (cm)	Inner Active Area Radius (cm)
HD MPGD 2	161	50	9	45	10.5
HD MPGD 1	148	50	9	45	10.5
LD MPGD 1	-110	50	4.65	45	6
LD MPGD 2	-120	50	4.65	45	6

Table 8.8: The ECT disks geometrical envelope and active areas dimensions.

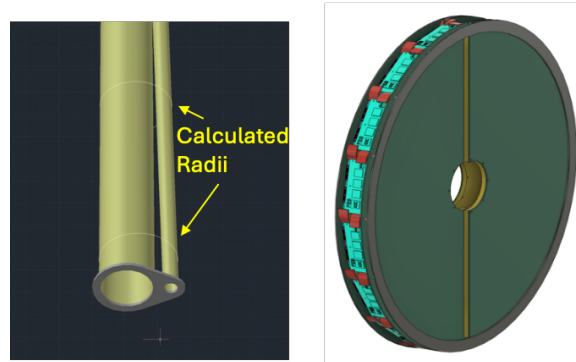


Figure 8.24: Left: Hadron and lepton beam pipes slightly diverge from the interaction point. The ECT inner radii are calculated taking into account the envelope radii and their center offset, the hadron beam pipe forming a larger angle with the z axis. Right: layout of a couple of μ RWELL-ECT disks.

1724 also includes the MPGD gas frames of 1.5 cm thickness, and a 3.5 cm outer service ring, to locate
 1725 services and electronics front-end boards. The resulting active area dimensions of the disks are also
 1726 reported in Table 8.8 and the corresponding angular and pseudorapidity acceptances are reported
 1727 in Table 8.9. The final active ranges in pseudorapidity are $2.0 < \eta < 3.3$ for the hadron sector and
 $-3.6 < \eta < -1.7$ for the lepton sector, compliant with the tracking requirements. A GEM- μ RWELL

MPGD Disk	$ \theta $ min (deg)	$ \theta $ max (deg)	$ \eta $ min	$ \eta $ max
HD MPGD 2	3.7	15.5	2.0	3.4
HD MPGD 1	4.0	16.9	1.9	3.3
LD MPGD 1	3.1	22.1	1.6	3.6
LD MPGD 2	2.8	20.4	1.7	3.7

Table 8.9: The ECT disks angular and pseudorapidity acceptance.

1728 hybrid technology with XY 2D readout has been chosen to match all the performance requirements
 1729 (see paragraph 8.3.3.2. Figure 8.25 shows the schematics of the hybrid GEM- μ RWELL detector. A
 1730 3 mm drift region, where the primary ionization charge is produced, is located between the cathode
 1731 and the GEM foil. A 3 mm transfer gap is located between the GEM foil and the μ RWELL foil. The
 1732 cathode and the 2D readout PCB are supported by a 3 mm thick honeycomb structure to minimize
 1733

1734 the detector material budget. The 2D strip read-out using a Compass-like scheme is also shown,
 1735 where the charge is collected by XY orthogonal strips located on two different printed circuit board
 1736 (PBC) layers. The strip widths of the two coordinates must be optimized (in a ratio of about 1:3) to
 1737 balance the signal amplitude in the two dimensions, since the upper layer strips screen the charge
 1738 collected on the lower ones.

1739 The XY Cartesian readout scheme was preferred over the $R\phi$ geometry for two reasons: i) the high
 1740 radial strip density at the center hole and ii) the possibility offered by the XY geometry to route all
 1741 the strips to connectors located on the outer service ring. The cathode and the 2D readout PCB are
 1742 supported by a 3 mm thick honeycomb structure to minimize the detector material budget, which
 amounts to $0.85\%X/X_0$ in the active region.

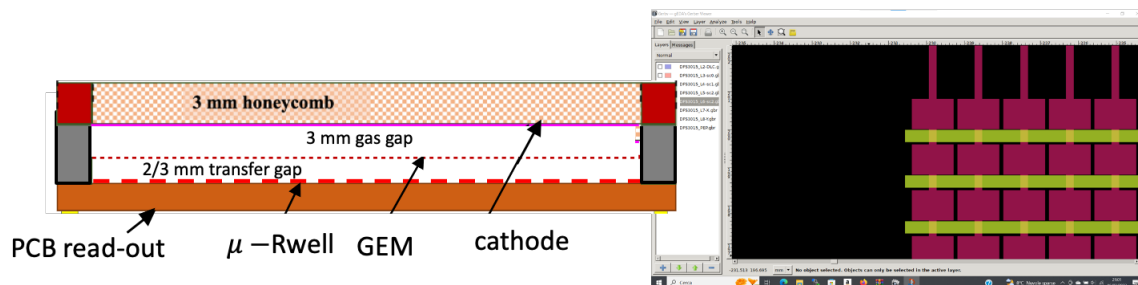


Figure 8.25: Left: schematics of the hybrid GEM- μ RWELL detector. A 3mm drift region, where the primary ionization charge is produced, is located between the cathode and the GEM foil. A 3 mm transfer gap is located between the GEM foil and the μ RWELL foil. The cathode and the 2D readout PCB are supported by a 3 mm thick honeycomb structure to minimize the detector material budget. Right: 2D strip read-out using a Compass-like scheme.

1743

1744 **Subsystems description:FEE.** To meet the requirement of streaming readout new front-end
 1745 chips for MPGD trackers in ePIC are being developed by Sao Paulo Universities and CEA Saclay
 1746 IRFU. The chip, known as SALSA, has the following characteristics :

- 1747
- 1748 • 64 channels with large input capacitance range, optimized for 50-200 pF, reasonable gain up to 1nF
 - 1749 • Large range of peaking times: 50-500 ns.
 - 1750 • Large gain ranges: 0-50 to 0-5000 fC.
 - 1751 • Large range of input rates, up to 100 kHz/ch.
 - 1752 • Reversible polarity.

1753 **Other components.** The **gas mixing unit** will be a critical component of the MPGD trackers. The
 1754 mixing unit preferably will use Mass Flow Controllers based on Proportional-Integral-Derivative
 1755 (PID) control systems. Furthermore, the mixing unit should be able to mix either two or three
 1756 different inert gases depending on the final composition of the operating gas. The preferred mixture
 1757 for CyMBaL is Ar-isobutane (95:5), however if concern is raised for flammability of this gas mixture
 1758 then a three gas mixing unit will provide the possibility of adding third gas (preferably CO_2) at the
 1759 expense of isobutane. This will help in maintaining stability (due to the isobutane component),

1760 make the gas faster and non-flammable (due to the CO_2) component. Additionally **sensors** will
 1761 be installed to monitor the temperature, pressure and humidity close to MPGD modules and if
 1762 possible also to monitor temperature of incoming and outgoing gas to give an idea of heating of
 1763 gas volume inside detector itself. The **High Voltage Power Supplies (HVPS)** are another important
 1764 component for the subsystem to bias the detector. Preferably each HV electrode associated with
 1765 each MPGDs will be powered by individual HVPS channel which will also have the capability of
 1766 monitoring current drawn by each MPGD layers, preferably having current resolution of few nA
 1767 and extremely low ripple ($< 5mV_{pp}$) to reduce noise from HVPS. There is also possibility of using
 1768 **voltage divider** to bias MPGD modules in place of using individual HV channel from HVPS to bias
 1769 the modules.

1770 **Performance** The MPGD tracking detectors share 2D spatial resolutions performances better \simeq
 1771 $150 \mu\text{m}$, timing resolutions of the order of $10 - 20 \text{ ns}$, rate capability better than $10 \text{ kHz}/\text{cm}^2$, and
 1772 detectors response not impacted by temperature instabilities, which may be compensated in the
 1773 calibration procedures. The radiation hardness of the components material is able to sustain doses
 1774 as reported in Table 8.5. The specific performances of each MPGD tracker subsystem are reported
 1775 in the following.

1776 **CyMBaL.** The CyMBaL design aims at providing complete azimuth (φ) coverage. Along the
 1777 longitudinal direction where the two halves of the system meet, only $\sim 3 \text{ cm}$ will not be covered.
 1778 CyMBaL modules are expected to provide a hit spatial resolution around $150 \mu\text{m}$ with a time reso-
 1779 lution of $10 - 20 \text{ ns}$.

1780 **$\mu\text{RWELL-BOT}$.** The barrel outer tracker will provide hit space point resolution better than 150
 1781 μm on average in the eta range of $-1 \leq \eta \leq 1$ and $100 \mu\text{m}$ in the azimuthal direction and a
 1782 timing resolution of $\sim 10 \text{ ns}$. The tracker has an acceptance gap of 15% along φ because of space
 1783 constraints imposed by the limited space in the ePIC detector. The tracker will operate at a nominal
 1784 efficiency of $\sim 95\%$. As shown in 8.6 and 8.7, the anticipated particle rate per unit area and per
 1785 readout channel is very low and will not pose any challenge in term of tracking performance, safety
 1786 operation and long term stability of the $\mu\text{RWELL-BOT}$ trackers for the lifetime of the ePIC detector.

1787 **$\mu\text{RWELL-ECT}$.** The MPGD-ECT disks are designed to provide intrinsic spatial resolution for
 1788 perpendicular tracks less than $150 \mu\text{m}$. Technological solutions and data analysis procedures exist
 1789 to guarantee similar performances also for inclined or curved tracks. The active area of the detector
 1790 has a material budget less than 1% in units of radiation length (X_0) and will cover all azimuthal
 1791 angles in the polar region specified in Table 8.9. A time resolution in the $10 - 20 \text{ ns}$ range is achiev-
 1792 able using the gas mixtures described in section 8.3.3.2. A single disk efficiency of $\simeq 96-97 \%$ is
 1793 required to provide 92-94 % combined efficiency for two disks in the same region.

1794 **Implementation**

1795 **Services.** The MPGD tracking detectors subsystem are divided in different modules, each one
 1796 requiring: gas supply lines and outlet, front end boards (FEB) connected to 5-line optical fibers
 1797 (VTRX+) for data transfer to the RDO, low voltage lines (four lines for each FEB: one pair for the
 1798 **1.8 V and one for the 3.3 V**), high voltage cables, temperature and humidity sensors and cooling in

1799 and out lines. Studies on the type of cooling and possible implementation in a serialize distribution
1800 will be done in synergy with the other subsystem of ePIC.

The service requirements for each MPGD tracking subsystem is summarized in Table 8.10.

Subsystem	CyMBaL	μ RWELL-BOT	μ RWELL-ECT
Number of Modules	32 Micromegas tiles	24 GEM- μ RWELL φ -modules	4 GEM- μ RWELL disks
Gas supply lines per module	1 in / 1 out	1 in / 1 out	8 in / 8 out
Number of FEB per module	4	14	32
Low voltage lines per module	16	56	128
High voltage lines per module	2	1 (or 4)	16
Cooling lines per module	1 in / 1 out	1 in / 1 out	4 in / 4 out
VTRX+ lines per module	4	14	32

Table 8.10: Services requirements for the three MPGD tracking subsystems.

1801

1802 Subsystem mechanics and integration.

1803 **CyMBaL.** CyMBaL integration and mechanics rely on the central tracker global support struc-
1804 tures. CyMBaL modules will be connected to the support structure.

1805 **μ RWELL-BOT.** μ RWELL-BOT integration and mechanics (see ??) rely on the outer barrel sup-
1806 port structures. Support structure connecting the carbon fiber tube and EM-Cal will serve as
1807 μ RWELL-BOT and HP-DIRC support structure.

1808 **μ RWELL-ECT.** The outer 5 cm wide ring of each disk hosts all the services listed in Table 8.10.
1809 The FEB are mounted perpendicularly to the disks, occupying the longitudinal region between
1810 them.

1811 Because of the divergence of the beam pipes, the disks cannot longitudinally slide along them but
1812 need to be shaped in sectors to be mounted around the pipes. Moreover, as the width of the Cu-
1813 kapton foil base material for the MPGD detectors restricts one dimension to about 550 mm, an
1814 implementation of the endcap trackers would consist of two half-circular disks with “D-shaped”
1815 cut-outs for the beam pipe, eventually sub segmented in four quadrants. As sketched in Figure 8.26,
1816 the disks integration and mechanics rely on the central tracker global support structures, using the
1817 same layout of the Silicon trackers. The MPGD-ECT disk are the most outer elements in the endcap
1818 region and the last to be installed in the mounting scheme of the tracking system.

1819 **Calibration, alignment and monitoring:** The three MPGD subsystems will generally follow
1820 similar calibration, alignment and monitoring procedures. There are two main calibration tasks
1821 that have been identified. The first is to determine the optimal HV settings for the MPGDs, which
1822 will be determined through efficiency scans. These scans will be performed prior to data taking
1823 campaigns and after changes in running conditions (e.g. changes in gas composition). The second

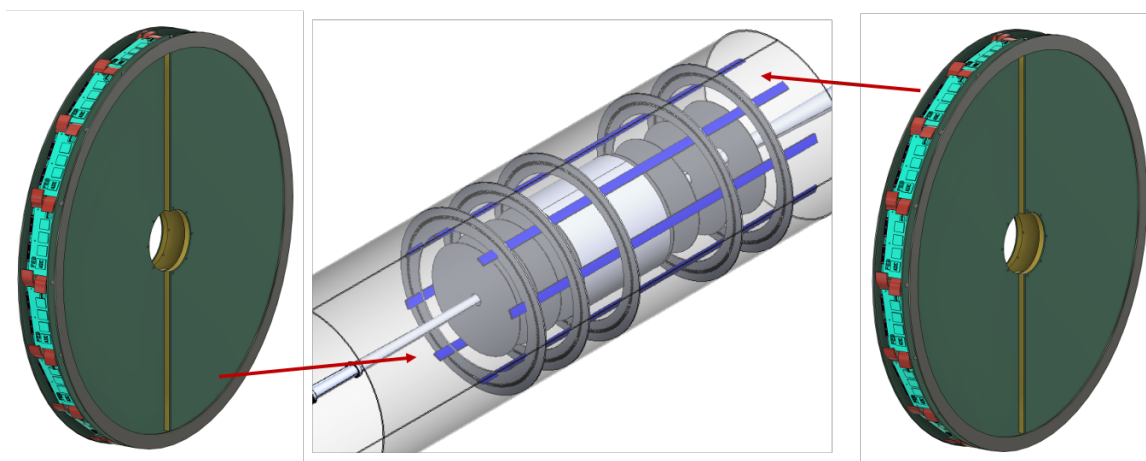


Figure 8.26: Integration of the MPGD-ECT disks in the ePIC detector

1824 calibration task is to determine pedestal values and the common noise to be subtracted from the
 1825 ADC samples, which will be determined through dedicated calibration runs. To meet the over-
 1826 all ePIC tracking performance precise knowledge of the tracking detector positions will need to
 1827 be known. The alignment of the MPGD modules will be surveyed and entered into a database
 1828 before integration. This information will be used to establish a starting point for the software align-
 1829 ment, which will be based on track reconstruction with and without magnetic field applied and
 1830 will involve all of the ePIC tracking detectors. To assure that the MPGD detectors are performing
 1831 optimally there are several criteria that will be monitored, which include the gas composition, the
 1832 environmental conditions near the MPGDs (e.g. temperature, humidity and pressure), currents
 1833 drawn by the MPGD layers from the power supply and general detector performance. Changes
 1834 in the environmental conditions can be addressed by adjusting the detector gain via a feedback
 1835 loop. The currents drawn by each high voltage channel will be read out and logged with a fre-
 1836 quency of about 1 Hz. Additionally, we will need to monitor and log the low voltage currents and
 1837 FEB temperatures. Not only will this allow us to monitor for abnormal values, but also implement
 1838 automatic safety measures should a particular value fall outside of an acceptable range. Finally,
 1839 during data taking we will monitor basic detector performance parameters such as hit occupancy
 1840 maps, 2D efficiency, signal amplitude and timing distributions will be constantly monitored.

1841 **Status and remaining design effort.**

1842 **CyMBaL.** The resistive Micromegas technology has been extensively used in nuclear and parti-
 1843 cle physics experiments. In particular, 1D-readout cylindrical Micromegas tiles are in use at JLab
 1844 in the Barrel Micromegas Tracker (BMT) of the CLAS12 experiment since 2017 [31], in experi-
 1845 mental conditions which are more challenging than those expected at the EIC. The main focus of the
 1846 ongoing R&D is to upgrade the BMT technology to 2D readout. In order to limit the number of
 1847 readout channels, the R&D also focus on exploiting the charge sharing through the resistive layer
 1848 and using ~ 1 mm pitch readout strips. Several combinations of strip readout patterns together
 1849 with layers of different resistivity have been tested in a beam test in MAMI in 2023. Further stud-
 1850 ies are ongoing with the cosmic rays test bench in Saclay and an additional beam test at CERN is
 1851 planned for 2025. The production of cylindrical tiles is being refurbished using the BMT PCBs and
 1852 a first completed detector is expected to be tested in Fall 2024. In parallel, the design of a CyMBaL

1853 module prototype has begun and its production is expected to be completed by summer 2025.

1854 **μ RWELL-BOT.** The R&D phase for the development of the μ RWELL-based trackers for EIC
 1855 detector was completed in summer 2023 and transitioned into project engineering design (PED)
 1856 effort to develop the full size thin-gap GEM- μ RWELL engineering test article as a beta version of
 1857 pre-production φ -module of μ RWELL-BOT tracker in ePIC detector. The design effort including the
 1858 CAD drawings of all mechanical parts i.e. frames and support structures as well as the sensitive
 1859 devices such as the GEM foil, the μ RWELL and the U-V strip readout PCB is in advanced stage
 1860 (see ??) and expected to be completed by the end of 2024. The fabrication of the full size engineering
 1861 test article will take place during the first half of 2025. The second half of the year 2025 will be
 1862 dedicated to a full characterization of the prototype on a cosmic test bench setup and in beam at the
 1863 CERN NA H4 beam test area including test in its 1.5 T GOLIATH magnet to study the performance
 1864 of the detector in a magnetic field strength similar to the one expected from the ePIC magnet. The
 1865 PED effort to develop the μ RWELL-BOT module including a detailed review of the design choices
 1866 and options, the timeline and outlook for the completion of the engineering test article effort in
 1867 anticipation of the module production phase is described in ??

1868 **μ RWELL-ECT.** Disk design and modules segmentation is ongoing. The choice of the connectors
 1869 will have in impact on the final strip pitch and the total number of read-out channels for each
 1870 disk: usage of Hirose connectors (140 pins for 126 channels) would limit the maximum number of
 1871 connectors and read-out channels if compared with obsolete Panasonic ones. Segmentation of the
 1872 disks in four quadrants may avoid the use of a support structure for the GEM foil. A final decision
 1873 on the final layout will be based on the results of prototype testing. Figure 8.27 shows some design
 details under investigation.

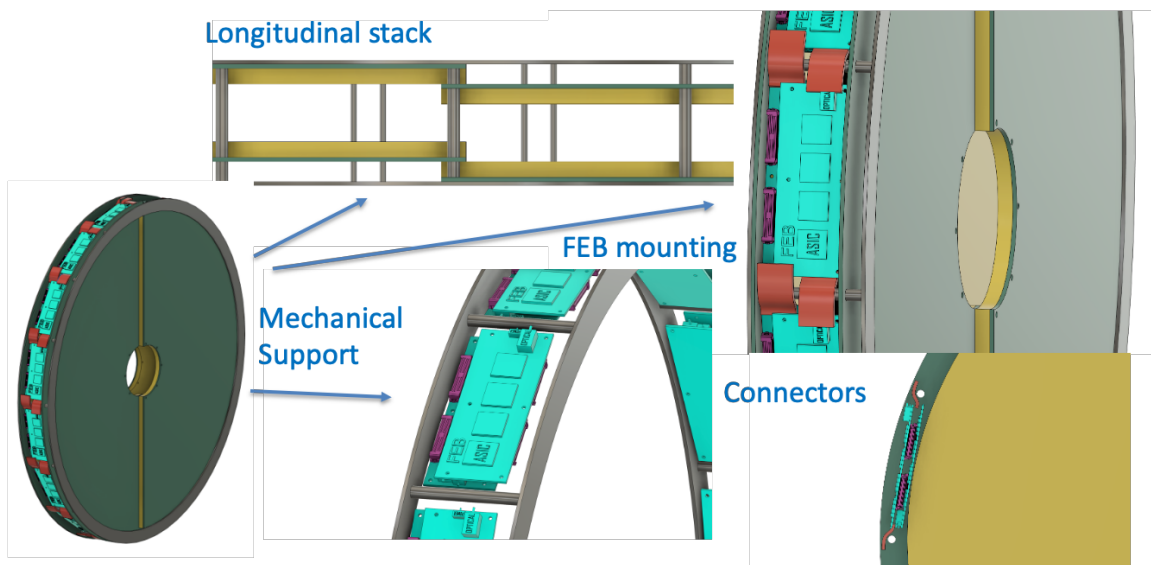


Figure 8.27: Design details of MPGD-ECT disks

1874

1875 **Environmental, Safety and Health (ES&H) aspects and Quality Assessment (QA**
 1876 **planning).** Considering MPGD consortium is composed of international collaboration so each

1877 production site for module assembly will follow guidelines of their local government to be in
1878 compliance with ES&H requirements. This include minimizing wastes during assembly procedure
1879 and disposal of harmful wastes in safe manner as directed by local government alongwith general
1880 electric and mechanical safety. During final integration of the detector subsystem at BNL , scientists
1881 and technicians will follow DOE guidelines as directed by BNL ES&H department.
1882

1883 The Quality Assessment protocol will cover the entire production lane of MPGD detectors. The
1884 readout PCBs will be assessed for mechanical precision and electrical continuity. The resistive
1885 layers will be checked for uniformity, During each step of the assembling, electrical continuity and
1886 high voltage capability of the different electrodes will be tested. Once the assembly of the module
1887 is finished, the module is checked for gas leakage and HV stability before bringing it outside of the
1888 clean rooms. Each finished detector will be then tested with cosmic rays in dedicated test benches.
1889 In these tests, the main parameters that will be studied for each module are the noise levels and the
1890 number of dead channels, efficiency and effective gain uniformity over the detector active area . A
1891 database will be used to log all the information and results for each produced module.

1892 **Construction and assembly planning.** Each of the MPGD detectors share a similar con-
1893 struction, assembly and QA timeline for having the detectors arrive at BNL in late 2029. This
1894 general timeline is shown in Fig. 8.28. More detailed timelines can be found in appendix ?? for
1895 μ RWELL-BOT
1896

1897 The construction and assembly of the MPGD subsystems will take place at various places.
1898 CEA-Saclay will be the main production site for CyMBaL modules, while the readout PCBs will be
1899 produced by industry partners. At Saclay, all the remaining parts of the production process will
1900 be realized. The resistive layer will be added using serigraphy and the low-tension micromesh
1901 will be added using the bulk process [32], which will be performed in the Saclay MPGD Lab.
1902 The curving and mechanical integration of the final detector will be done in a dedicated clean room.
1903

1904 CERN will serve as the primary source for μ RWELL and GEM foils, as well as the readout
1905 PCBs for the μ RWELL-BOT and μ RWELL-ECT detectors. Other components, such as the frames,
1906 will be produced by industry partners. The production of the μ RWELL-BOT and μ RWELL-ECT
1907 modules will be spread out over several productions sites. Jefferson Lab, Florida Institute of
1908 Technology and University of Virginia responsible for the μ RWELL-BOT modules, while INFN
1909 and Temple University will build the μ RWELL-ECT modules. A set of technical documents
1910 will be developed for each MPGD sub-detector, ensuring that all modules are produced under
1911 consistent conditions, using appropriate infrastructure, and following standardized procedures
1912 for construction and quality control testing. Each production site will procure and inspect the
1913 components separately. It is crucial that all production sites are equipped with suitable clean room
1914 infrastructure for the construction and assembly of their respective μ RWELL modules, as well as
1915 identical instrumentation for a standardized component inspection and module characterization.
1916 Each of the institutes will be responsible for the construction and characterization of their
1917 respective μ RWELL modules (+ spares). The essential equipment needed for each institute are
1918 listed in Tab. ?? of appendix ?? for the μ RWELL-BOT modules, and Tab. 8.11 for the μ RWELL-ECT
1919 modules. Each institution will leverage its existing MPGD infrastructure (clean room and detector
1920 lab and existing equipment) to minimize instrumentation costs but will upgrade where needed to
1921 meet the more demanding requirement of μ RWELL technology assembly.

1922 **Collaborators and their role, resources and workforce.**

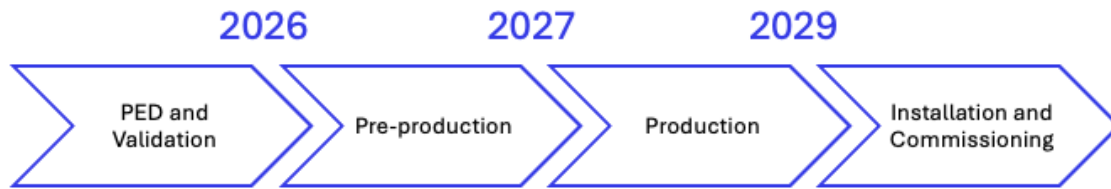


Figure 8.28: General overview ePIC MPGD tracker construction and assembly timeline.

1923 **CyMBaL.** CyMBaL design, production and tests will be lead by CEA Saclay. The details of the
 1924 workforce will be added in appendix before the next draft.

1925 **μ RWELL-BOT.** Three institutes — Jefferson Lab, Florida Institute of Technology, and the Uni-
 1926 versity of Virginia will participate in the construction, assembly, and characterization of μ RWELL-
 1927 BOT φ -modules to ensure timely mass production. They will collaborate to develop a set of techni-
 1928 cal documents, ensuring that all modules are produced under consistent conditions, using appro-
 1929 priate infrastructure, and following standardized procedures for construction and quality control
 1930 testing. All components of a μ RWELL-BOT φ -module will be designed by Jefferson Lab, how-
 1931 ever, each production site will procure and inspect the components separately. It is crucial that
 1932 all three production sites are equipped with suitable clean room infrastructure for the construction
 1933 and assembly of μ RWELL-BOT φ -modules, as well as identical instrumentation for a standardized
 1934 component inspection and module characterization. Each of the three institutes will be responsible
 1935 for the construction and characterization of eight μ RWELL-BOT φ -modules (+ spares). The essen-
 1936 tial equipment needed for each institute are listed in Tab. ?? of appendix ?. Each institution will
 1937 leverage on its existing MPGD infrastructure (clean room and detector lab and existing equipment)
 1938 to minimize instrumentation costs but will upgrade wherever possible to meet the more demand-
 1939 ing requirement of μ RWELL technology assembly. The personnel effort, expressed as a percentage
 1940 of research time over the duration of the project, at each institute is provided in tables ?, ?, ? of
 1941 appendix ?.

1942 **μ RWELL-ECT** Two institutes — Temple University and INFN Roma Tor Vergata — will partici-
 1943 pate in the design, production, assembly, and characterization of μ RWELL-ECT disks, with the
 1944 engineering support from Jefferson Lab and the collaboration of INFN LNF MPGD group lead by
 1945 Gianni Bencivenni, inventor of the μ -RWELL technology. INFN Roma Tor Vergata will focus on
 1946 the two hadron disks while Temple University will be in charge of the lepton disks. Each of the
 1947 two institutes will be responsible for the construction and characterization of 4-8 μ RWELL-ECT
 1948 modules, depending on final design. The essential equipment needed for each institute are listed
 1949 in Tab. 8.11. Wherever possible, existing equipment from the collaborating groups will be utilized
 1950 to minimize instrumentation costs.

1951

1952 **Risks and mitigation strategy.** Based on past experiences with MPGD technology following
 1953 risks and mitigation strategies are identified.

- 1954 • Delay in production of MPGD foils at CERN is the biggest risk. Considering this it has been
 1955 decided to place procurement request well in advance to provide enough time to procure

Table 8.11: Main equipment required in the production site and availability at sites

Equipment	Purpose	INFN Roma Tor Vergata	Temple bf University
ISO7 cleanroom	Inspection & Assembly	y	y
Stretcher system	Construction process	y	n
Ultrasonic Cleaner	GEM frame prep	n	y
Fume hood	GEM frame prep	y	y
Microscope	GEM visual inspection	y	y
Giga-Ohm insulation meter	GEM electrical inspection	y	n
HV box	GEM electrical cleaning	y	n
Oven	Construction process	y	n
Electronic instrumentation	Module characterization	y	n
Gas supplies	Module characterization	y	n
Shipping containers	Transport b/w sites	y	n

1956 the MPGD foils. Additionally there is possibility of using additional person power and also
 1957 prepare additional set up for assembling each module in each assembly sites so that at least
 1958 2 modules are assembled at the same time.

- 1959 • Minor risk of higher humidity content within the MPGD modules is possible however it can
 1960 be mitigated by flowing gas at higher rate.
- 1961 • It is possible that the gain provided by any of the MPGD module after installation in exper-
 1962 imental hall is lower than what has been estimated during QA. This can be mitigated either
 1963 by increasing the content of primary ionized gas in gas mixture or increasing the high voltage
 1964 on MPGD electrodes without affecting detector stability.

1965 **Additional Material** Add text here.

1966 8.3.4 Particle Identification

1967 In addition to tracking and calorimetry, Particle IDentification (PID) is a crucial component of the
 1968 ePIC experiment's physics program. The identification of stable particles is achieved either by ana-
 1969 lyzing the way they interact, or by determining their mass measuring their velocity and momentum
 1970 simultaneously. The difference in interaction is primarily used for identifying leptons, photons and
 1971 neutral hadrons, which leave very different signatures in the electromagnetic calorimeters. Charge
 1972 hadrons cannot be distinguished by their interaction in the calorimeter, but their velocity can be
 1973 measured using dedicated time-of-flight and Cherenkov detectors. All dedicated ePIC PID detec-
 1974 tors discussed in this section measure the velocity, β , of the particle and thus allow to determine its
 1975 mass. In short, they tie together \vec{p} , β , and m . In a second step this PID information can of course
 1976 also be used in a refit of the particle's trajectory. The knowledge of the particle type and its mass
 1977 does improve the multiple scattering evaluation and serve as a further constraints.

1978 ePIC has stringent requirements on its PID capabilities as detailed in the Yellow Report [6]. The
 1979 two-dimensional histogram in Fig. 8.29 illustrates the simulated yield of charged hadrons as a func-
 1980 tion of momentum and pseudorapidity, η , over the range $-5 < \eta < 5$ at the highest EIC energy

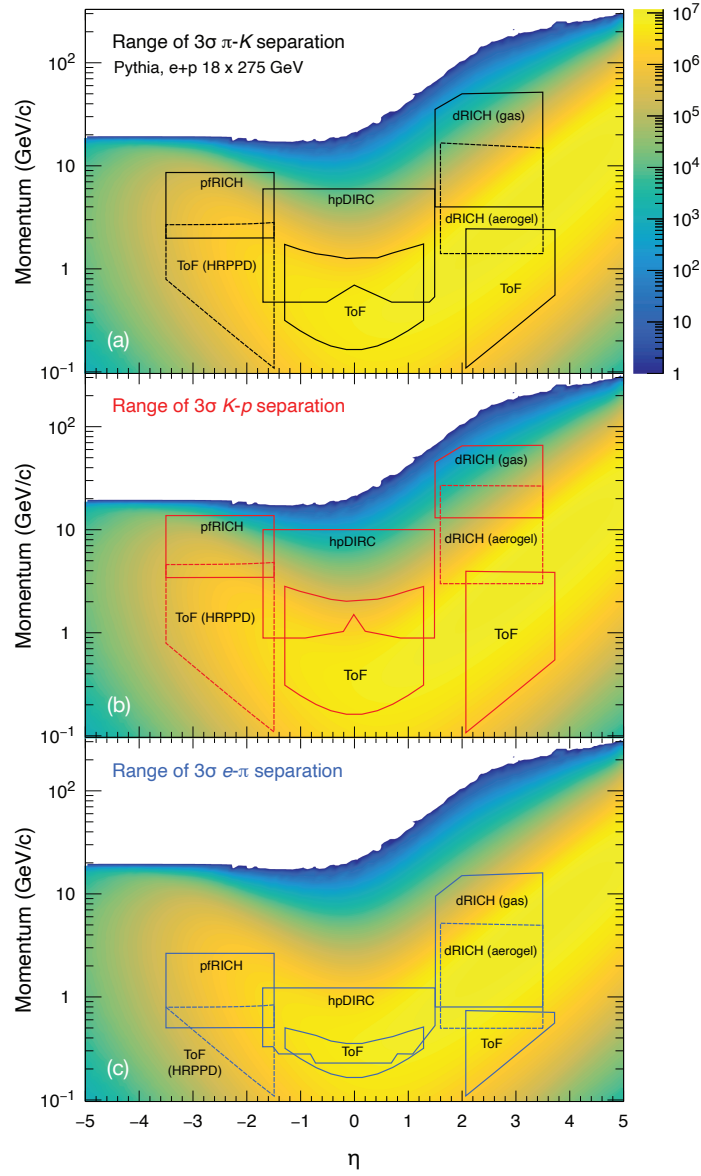


Figure 8.29: The histogram shows the relative yield of charged hadrons from Pythia simulations for 18×275 GeV ep collisions as a function of momenta and pseudorapidity, η . The contours indicate the 3σ separation region of the different ePIC PID subsystems for π/K (a), K/p (b), and e/π (c), respectively.

1981 of $\sqrt{s} = 141$ GeV. Studies of the key semi-inclusive and exclusive processes define the upper limit
 1982 requirements for 3σ separation of $\pi/K/p$ for different pseudorapidity regions [6]:

- 1983 • $p \leq 7$ GeV/c for $-3.5 < \eta < -1.0$
 1984 • $p \leq 6$ GeV/c for midrapidity $-1.0 < \eta < 1.0$
 1985 • $p \leq 50$ GeV/c for the forward region or $1.0 < \eta < 3.5$

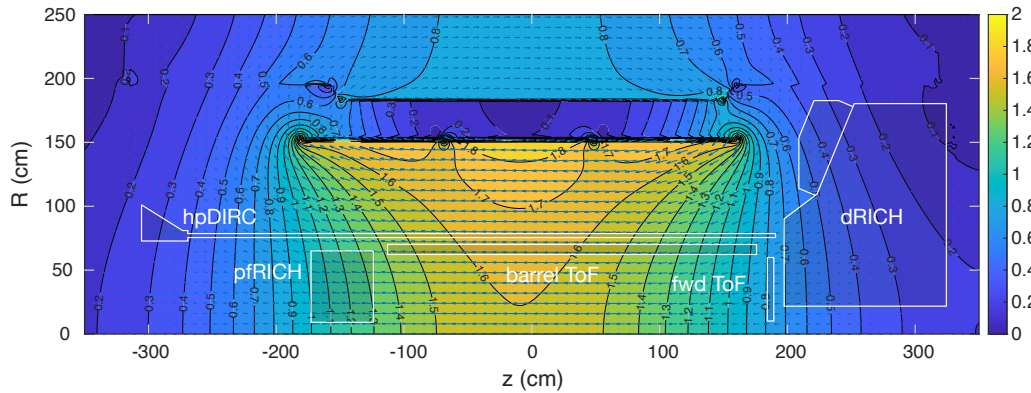


Figure 8.30: EPIC magnetic field map with the PID detector envelopes overlaid. Shown is the 1.7 T setup.

1986 Pure and efficient kaon identification is particularly relevant to semi-inclusive DIS studies, where
 1987 quark flavor tagging provides critical insights into the transverse momentum distribution and
 1988 potentially the orbital angular momentum of the strange sea quarks. Kaon identification is also
 1989 needed to reconstruct charmed hadrons, which are sensitive probes of gluon distributions in pro-
 1990 tons and nuclei.

1991 Achieving the PID goals of the ePIC experiment requires multiple detection technologies tailored
 1992 to specific momentum and pseudorapidity ranges. Cherenkov radiation detection is the primary
 1993 method at higher momenta but is limited in its low-momentum reach. After the Yellow Report,
 1994 it was realized that improving low-momentum PID is critical for light vector meson and charm
 1995 meson/baryon reconstruction. To address this, Time-of-Flight (ToF) detectors based on finely
 1996 pixelated AC-LGAD sensors were added in the barrel (0.5×10 mm pixels) and forward regions
 1997 (0.5×0.5 mm pixels). In addition to PID they will provide additional hits for tracking. The η -dependence
 1998 of the momentum spectrum along with space constraints necessitate different technologies in the
 1999 forward, backward, and barrel regions. The solution chosen by ePIC involves:

- 2000 • A dual radiator RICH (dRICH) in the forward region utilizing aerogel and gas radiators, a
 2001 set of focusing mirrors, and instrumented by SiPMs.
- 2002 • Additional low-momentum PID in the forward region is achieved by an AC-LGAD based
 2003 ToF that also provides an additional layer of tracking points.
- 2004 • A large radius high-performance DIRC (hpDIRC) in the barrel, which adds focusing to the
 2005 original DIRC design.
- 2006 • The hpDIRC is complemented by an AC-LGAD ToF detector at smaller radius. The AC-
 2007 LGAD layer provides PID information for low momentum particles that do not reach the
 2008 hpDIRC or are too slow to leave Cherenkov signal in it.
- 2009 • A proximity-focusing aerogel RICH (pfRICH) to cover the electron endcap region. This de-
 2010 sign features minimal material budget and provides additionally excellent ToF through its
 2011 novel HRPPD photosensors.

2012 Figures 8.29 illustrates the achieved coverage in the η vs. p plane of the various PID subsystems.
 2013 The contours indicate the 3σ range for e/π , π/K , and K/p -separation, respectively. This unprece-
 2014 dented wide coverage of PID in momentum and over a wide range of η makes ePIC a truly unique

collider detector. As shown, the PID systems provide, in addition to hadron PID, a significant contribution to the e -identification and its purity (e/h). When combined with the EM calorimeters, these subsystems will provide excellent suppression of the low-momentum charged-pion backgrounds, which otherwise limit the ability of the EMCAL to measure the scattered electron in kinematic region where it does not provide sufficient e/h separation.

ePIC's Cherenkov detectors, dRICH, pFRICH, and hpDIRC, must overcome various challenges related to their respective photosensors. One is the strong magnetic field that rules out the use of conventional photomultipliers. Figure 8.30 shows the realistic ePIC magnetic field for the 1.7 T setup with highlighted Cherenkov PID detectors envelopes. In the region of the hpDIRC detector plane, where the MCP-PMTs will be located, the magnetic field is at a level of 0.2-0.3 T. The field at position of the pFRICH HRPPD sensors is about 1.2 T and the field at the dRICH is 0.3-0.6 T.

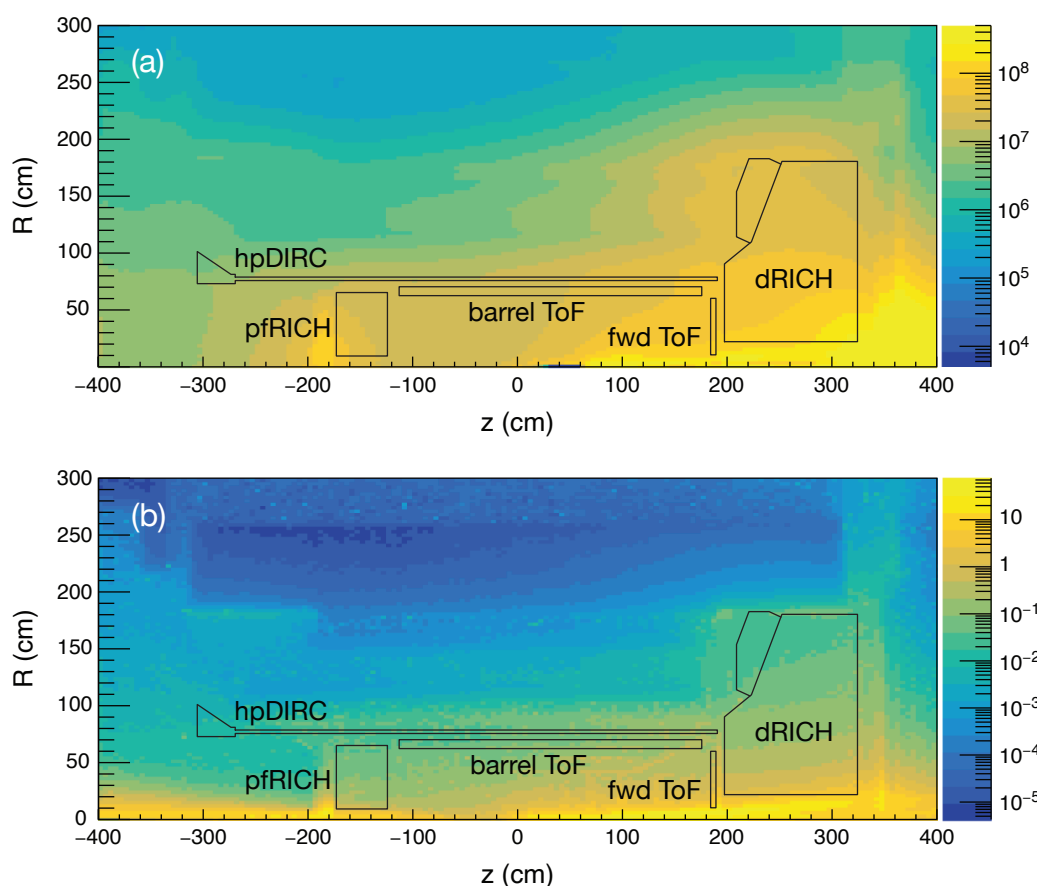


Figure 8.31: (a) Estimates of the 1-MeV neutron equivalent fluence in $\text{cm}^{-2}/\text{fb}^{-1}$ and (b) the sum of electromagnetic and charged-hadron doses in $\text{rads}/\text{fb}^{-1}$ integrated in 1 fb^{-1} equivalent Pythia events for $10 \times 275 \text{ GeV}$ ep collisions. The values shown are averaged over the azimuthal angle.

Another significant challenge is the sensors' sensitivity to radiation, particularly in the forward region where the dRICH is located. Figure 8.31 depicts the radiation map for ePIC with the PID subsystem contours. Shown are the estimates of the 1-MeV neutron equivalent fluence and (b) the sum of electromagnetic and charged-hadron dose simulated with $10 \times 275 \text{ GeV}$ ep Pythia events.

2030 SiPMs, while ideal in terms of quantum efficiency and wavelength sensitivity, do suffer from in-
 2031 creased dark currents due to radiation exposure. However, cooling during operation and thermal
 2032 annealing have been demonstrated to mitigate this issue [33, 34]. Other photosensors used, show
 2033 enough radiation hardness (HRPPD) or are situated in less radiation-intensive areas (MCP-PMT).

2034 In the following subsection the different PID subsystems in ePIC are discussed in detail. Subsection
 2035 8.3.4.1 discusses the ToF systems, followed by 8.3.4.2 on the pFRICH, 8.3.4.3 describes the hpDIRC
 2036 and we end with details on the dRICH system in 8.3.4.4.

2037 8.3.4.1 The time-of-flight layers

2038 Requirements and Justifications

2039 **Requirements from physics:** With single hit timing resolution of 35 ps from the Barrel TOF
 2040 (BTOF) and 25 ps from the Forward TOF (FTOF), the AC-LGAD TOF detector system can provide
 2041 particle identification for low momentum charged particles, e.g., π - K separation at the 3σ level
 2042 for $p_T < 1.2$ GeV/c for $-1.2 < \eta < 1.6$, and $p < 2.5$ GeV/c for $1.9 < \eta < 3.6$, respectively.
 2043 By combining the PID information for low momentum particles from the TOF detectors and high
 2044 momentum particles from Cherenkov detectors, ePIC will have excellent PID capability over a wide
 2045 momentum range in a nearly 4π acceptance, which is crucial to achieve the goals of the EIC physics
 2046 program. Besides precise timing resolution, AC-LGAD sensors can also provide precise spatial
 2047 resolution, and thus aid track reconstruction and momentum determination. The requirements on
 2048 the timing and spatial resolutions, as well as the material budgets are being evaluated in ePIC MC
 2049 simulation to find the optimal configuration without over-designing these detectors. Table 8.12
 2050 summarizes the current specifications of the timing and spatial resolutions, material budgets, the
 2051 covered area, channel counts and dimensions. Figure 8.32 shows the BTOF and FTOF layouts
 2052 with an insert showing charge sharing on a sensor. Figure 8.33 shows the performance of the
 2053 TOF detector in the form of $1/\beta$ as a function of particle momentum p for ep DIS events from
 2054 PYTHIA+GEANT4 simulation. Together with the other PID detectors, we are able to demonstrate
 2055 that the ePIC PID performance which includes the TOF detectors as one of the integral components
 2056 meets the requirements.

Subsystem	Area (m^2)	dimension (mm^2)	channel count	timing σ_t (ps)	spatial σ_x (μm)	material budget (X_0)
Barrel TOF	12	0.5*10	2.4M	35	30 ($r \cdot \phi$)	0.015
Forward TOF	1.1	0.5*0.5	3.2M	25	30 (x, y)	0.05

Table 8.12: Required performance for physics and proposed configurations for the TOF detector system.

2057 **Requirements from Radiation Hardness:** The radiation fluence and dose at ePIC are signif-
 2058 icantly less than in the LHC experiments. It is safe to assume that the maximum foreseen fluence
 2059 for the lifetime of the TOF detectors will be $< 5 \times 10^{12} n_{eq}/cm^2$, as seen in Fig. 8.34 and Tab. 8.13.
 2060 Here the highest fluence between raw and 1MeV n_{eq}/cm^2 fluence was considered, as the standard
 2061 NIEL correction is not applicable for some aspects of LGAD radiation damage.

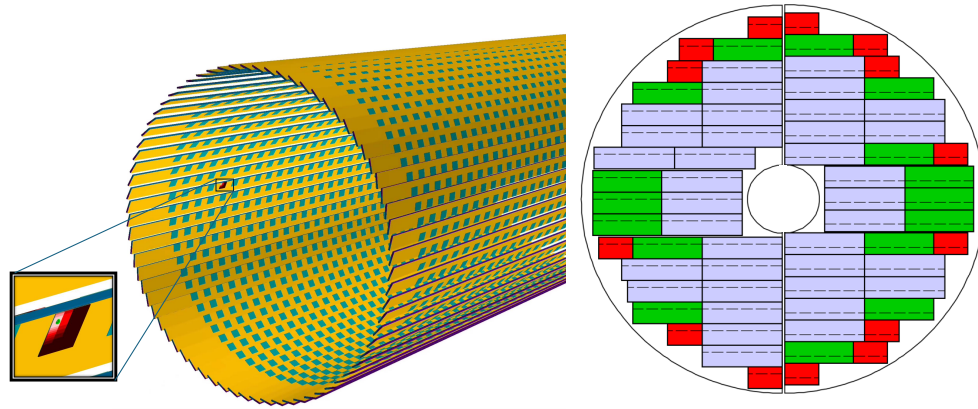


Figure 8.32: Geometries of BTOF with insert of sensor and charge sharing distribution (left), and the layout of sensor modules and service hybrids of FTOF on one side (right).

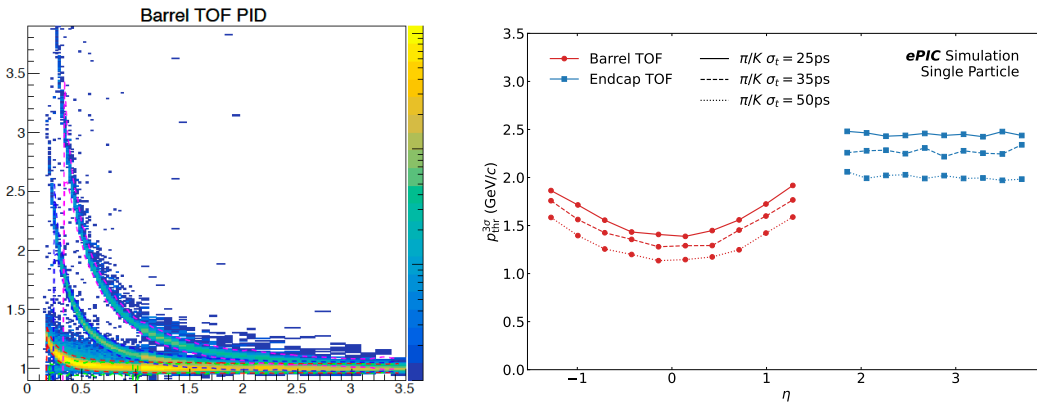


Figure 8.33: BTOF $1/\beta$ as a function of momentum (p) in the simulation performance with PYTHIA DIS events (left). Upper limits on the 3σ particle separation from BTOF and FTOF as a function of pseudorapidity (right).

2062 Much work has been done to characterize and improve the radiation resistance of LGAD gain lay-
 2063 ers to meet the requirements at the LHC [35] (up to 2.5×10^{15} $1\text{MeV } n_{eq}/\text{cm}^2$). Because of the
 2064 sensitivity of the sensor performance to the value of the N+ sheet resistance (a feature absent from
 2065 the conventional LGADs made use of for the LHC), it is possible that AC-LGADs may be signif-
 2066 icantly less radiation tolerant than their conventional cousins. Indeed, N-type doping is known
 2067 to be particularly sensitive to hadronic irradiation, with N-bulk sensors inverting to P-bulk before
 2068 exposure of even 1×10^{14} is accumulated. Furthermore, LHC LGAD detectors are designed to run
 2069 at -30C to reduce the post-radiation leakage current, while in ePIC, the sensors will be operated
 2070 at room or slightly lower temperatures for the experiment's lifetime. The leakage current increase
 2071 due to radiation damage for the fluence in ePIC has to be low enough not to trigger a thermal run-
 2072 away combined with the power dissipation from the readout chip, especially for the forward and
 2073 end-cap region where the chips are bump bonded on top of the sensors.

2074 Therefore, a radiation exposure run was performed before the ePIC LGAD design was finalized.
 2075 Several sensors from HPK and BNL were irradiated at FNAL ITA facility (400 MeV protons) and

2076 at the TRIGA reactor in Ljubljana (MeV-scale neutrons) to probe radiation effect from ionizing and
 2077 non-ionizing particles. The radiation exposure would be done in steps, allowing potential charge-
 2078 collection pathologies, should they exist, to be mapped out for the development of models and
 2079 corrections. By studying the sensor performance before and after irradiation, the change in N+
 2080 resistivity can be characterized, and this particular risk can be addressed. Sensors irradiated with
 2081 1 MeV neutrons were received in the Summer of 2024 and tested; the results are encouraging, as
 2082 seen in the following sections. Sensors were irradiated at the FNAL ITA facility but are still cooling
 2083 down from the activation; they will likely be available for testing in early 2025.

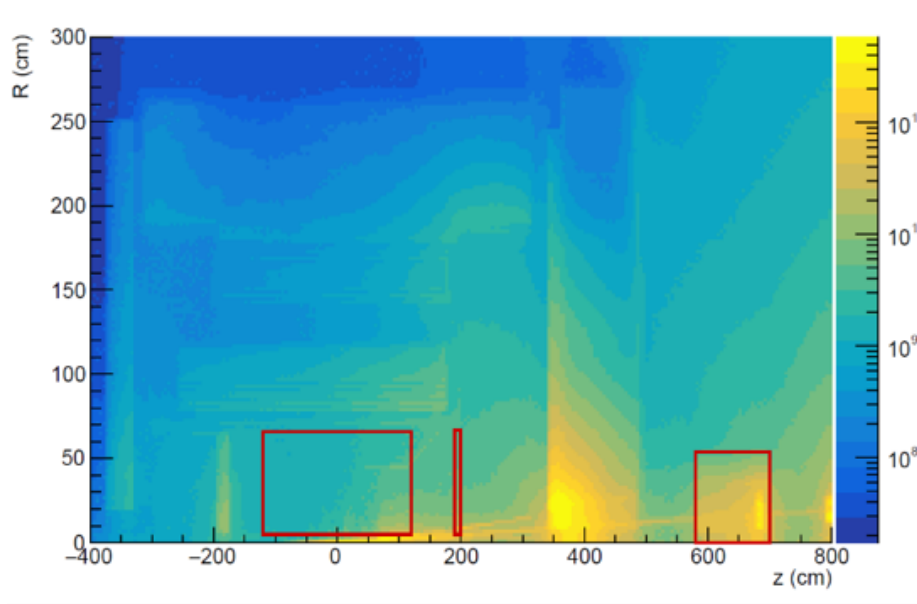


Figure 8.34: Fluence accumulated for 6 months at 100% time, corresponding to one year of data taking, the fluence has to be multiplied by the assumed 10 years of life time of the ePIC detector. Red squares highlight the barrel, end-cap, and B0 trackers detectors.

RAW fluence			
System	Average	Min	Max
Barrel	5.4×10^{10}	3.4×10^{10}	5.9×10^{11}
End-cap	1.3×10^{11}	5.1×10^{10}	1.6×10^{12}
B0 trackers	3.9×10^{11}	3.3×10^{10}	1.8×10^{12}
NEQ fluence			
System	Average	Min	Max
Barrel	3.6×10^{10}	1.1×10^{10}	1.3×10^{12}
End-cap	1.2×10^{11}	3.2×10^{10}	8.4×10^{11}
B0 trackers	4.5×10^{11}	2.7×10^{10}	4.2×10^{12}

Table 8.13: RAW and NEQ fluence per system for the lifetime of the ePIC experiment, assuming 10 years of data taking at 50% time.

2084 **Requirements from Data Rates:** As the sensors and ASICs differ between the BTOF and FTOF,
 2085 the rate requirements are presented separately for both of these sub-components. On top of that,

2086 the phase space coverage is different (mid-rapidity vs forward rapidity) which mandates different
2087 particle rate and background calculations.

2088 **BTOF:** The BTOF simulations show an average of 5 charged particles per ep collision at the highest
2089 center of mass energy. At the 500 kHz collision rate this amounts to a 2.5 MHz particle rate on the
2090 surface of the BTOF barrel. BTOF contains 2.4 million channels which give an average hit frequency
2091 per channel of 1 Hz. Due to charge sharing of the AC-LGAD strips we expect a particle to generate
2092 signals on maximum 3 strips/channels of the readout ASIC.

2093 **FTOF:** The FTOF simulation shows an average of 2 charged particles per ep collision at the highest
2094 center of mass energy. At the 500 kHz collision rate this amounts to a 1 MHz particle rate on
2095 the surface of FTOF disk. Since FTOF is expected to contain 5.8 million channels the average hit
2096 frequency per channel is 0.2 Hz. Due to charge sharing of the AC-LGAD pixels we expect a particle
2097 hit to generate signals on maximum 3×3 pixels/channels of the readout ASIC.

2098 **Electronics Noise:** Noise measurements have consistently shown a rate of 30 Hz per channel. Such
2099 a noise rate is achieved with a 5-sigma cut and is deemed to be even somewhat pessimistic but this
2100 is the number we plan to use during these calculations.

2101 **Data Rates:** We will assume a typical CERN-developed ASIC's zero-suppressed data format which
2102 is: 32 bits header, $N \times 32$ bits of channel data (ADC, TDC, ch Id) and 32 bits trailer. Such data formats
2103 are used in e.g. HGCROC which is a precursor to our expected ASICs.

2104 For BTOF the expected signal rate of bits per second per ASIC is 1 Hz (particle rate) \times 5 \times 32 (bits for
2105 3 hits) \times 64 (channels) = 10 kbps, while the noise rate is 30 Hz (noise) \times 3 \times 32 (bits for a single hit) \times
2106 64 (channels) = 185 kbps. Summing up these 2 contributions we reach the total data rate per-ASIC
2107 of 195 kbs. Since an RDO reads out 128 ASICs per half stave we expect a rate per RDO (or fiber) of
2108 24 Mbps. For the entire BTOF which contains 288 half staves we reach a total rate requirement of 7
2109 Gbps.

2110 For FTOF the expected signal rate of bits per second per ASIC is 0.2 Hz (particle rate) \times 11 \times 32
2111 (bits for 9 hits) \times 1024 (channels) = 72 kbps, while the noise rate is 30 Hz (noise rate) \times 3 \times 32 (bits
2112 for a single hit) \times 1024 (channels) = 3000 kbps. Summing up these 2 contributions we arrive at the
2113 per-ASIC data rate of 3.1 Mbps. For the worst case of 28 ASICs per RDO (or fiber) = 87 Mbs per
2114 fiber link to DAQ. For the total FTOF sub-detector of 212 RDOs we reach 18 Gbps.

2115 We note that these rates are very small and well within the reach of ASICs, interconnects as well as
2116 fiber interfaces of our electronics and DAQ. We also note that the data rates are dominated by the
2117 electronics noise which we can control by raising or lowering the various ADC or TDC thresholds
2118 of the ASIC thus adjusting the system performance even ASIC-to-ASIC if required.

2119 **Device concept and technological choice:** AC-coupled Low-Gain Avalanche Diode (AC-
2120 LGAD) is a new silicon sensor technology. Signals produced by charged particles in the sensor
2121 active volume are amplified via an internal p+ gain layer near the sensor surface. Signals induced
2122 on a continuous resistive n+ layer on top of the p+ gain layer, are AC coupled to patterned metal
2123 readout electrodes, which are on the sensor surface and separated by a dielectric layer from the
2124 n+ layer. The internal signal amplification and thin active volume enables precise timing measure-
2125 ment, while charge sharing among neighboring electrodes can provide precise position measure-
2126 ment. The AC-LGAD technology has been chosen to use for particle identification, tracking, and
2127 far-forward detectors at EIC where precision timing and spatial measurements are needed.

2128 **Subsystem description:**

2129 **General device description:** The BTOF consists of 144 tilted staves, each of which is made of
2130 two half staves with a total length of around 270 cm sitting at a radial position around 65 cm.
2131 AC-LGAD strip sensors are mounted on low mass Kapton flexible printed circuit boards
2132 (FPCs), and are wire-bonded with front-end ASICs. The FPCs are glued onto mechanical
2133 structures made from low density Carbon-Fiber (CF) materials, and bring power and in-
2134 put/output signals to the sensors and ASICs. The heat generated by the frontend ASICs are
2135 removed by an embedded Aluminium cooling tube in the CF structure. The FTOF consists of
2136 detector modules made from AC-LGAD pixel sensors bump-bonded with front-end ASICs.
2137 These detector modules are mounted from both sides onto a thermal-conductive supporting
2138 disk with embedded liquid cooling lines located around 190 cm away from the center of the
2139 experiment. Since the irradiation flux at the EIC is much smaller than that at the LHC, it is
2140 assumed that the radiation damage will not be a concern and the AC-LGAD sensors can be
2141 operated at room temperature.

2142 **Sensors:** The sensors identified for the TOF timing layer are AC-LGADs that can provide
2143 both exceptional position resolution and timing resolution [2, 36–38] while maintaining low
2144 channel density. The BTOF will employ strip sensors 1 cm long with a pitch of 500 μm and a
2145 metal electrode width of 50 μm (large pitch up to 1000 μm is also under investigation). The
2146 sensor thickness will likely be 50 μm to reduce the input capacitance to the pre-amplifiers but
2147 30 μm thick strip sensors are also under investigation. The full sensor size will be $3.2 \times 2 \text{ cm}^2$
2148 with 1 cm segments. The FTOF will employ pixel AC-LGADs with a pitch of 500 μm and
2149 metal electrode size of 50 μm (large pitch up to 1000 μm and electrode size of 150 μm are also
2150 under investigation). The thickness of the pixel sensors will likely be 20 μm to maximize the
2151 time resolution reach, as the input capacitance is not a concern for small pixels. Nevertheless,
2152 30 μm thick pixel sensors are also under investigation. The full-size sensor will be $1.6 \times 1.6 \text{ cm}^2$
2153 with $0.5 \times 0.5 \text{ mm}^2$ pixels. Studies on smaller-scale devices are presented in [2, 36] and in the
2154 following. The full-size strip sensor prototypes have been produced for the first time in the
2155 most recent HPK fabrication and received at the time of writing. Procurement of the full-size
2156 pixel sensor prototypes is still in progress. A complete evaluation of the full size prototype
2157 sensors is expected in the middle/end of 2025.

2158 **Front-End Electronics (FEE):** The FEE for AC-LGAD based detectors is focused on the de-
2159 velopment of an ASIC and service hybrids. An ASIC featuring a Constant Fraction Discrimi-
2160 nator (CFD) chip is being developed at Fermilab for the BTOF. The efforts have been focused
2161 on optimizing the analog frontend design to read out AC-LGAD strip sensors. Two versions
2162 of the ASICs, FCFDv0 and FCFDv1, featuring single- and multi-channel preamplifier and
2163 CFD, respectively, have been fabricated and tested. The new versions, FCFDv1.1 with fur-
2164 ther improvement to the frontend design tailored to 1 cm AC-LGAD strip sensors, FCFDv2
2165 with digital readout, are under development with an expected deliver date in early 2025 and
2166 2026, respectively. The EICROC project by the French group is focused on designing an ASIC
2167 for reading fine-pixelated AC-LGAD sensors, optimized pixel-based AC-LGADs detectors at
2168 ePIC such as B0, OMD, Roman Pots, and FTOF. The first version, EICROC0, is a 4×4 channel
2169 ASIC with $0.5 \times 0.5 \text{ mm}^2$ pixel size, featuring components like a transimpedance pre-amplifier,
2170 10-bit TDC for timing, 8-bit ADC for amplitude measurement, and an I2C slow control inter-
2171 face. It is designed for low capacitance and sensitivity to low charges (2 fC), operating with
2172 1 mW per channel, and targeting 30 ps timing and 30 μm spatial resolution. The prototype
2173 is currently under testing, with noise issues being addressed for future iterations. The next
2174 version, EICROC1 (expected in 2025), will feature a 16×8 channel configuration, followed by
2175 the final 32×32 channel version for full-scale implementation.

2176 The service hybrids (SH) consists of a readout board (RB) and power board (PB). A schematic
2177 design of service hybrids, which serves 3 modules or 12 sensors/ASICs, for FTOF is shown
2178 in Fig. 8.35. The readout board will aggregate data from multiple ASICs to a lpGBT (from

2179 CERN) transceiver chip via e-links, and then convert to optical signals via a VTRx+ chip (from
 2180 CERN) to be transmitted to the backend data acquisition system. lpGBT and VTRx+ are de-
 2181 signed for HL-LHC so have been proven to be sufficiently radiation hard for the EIC environ-
 2182 ment. The VTRx+ has one uplink up to 10 Gbs (for receiving clock and control signals), and
 2183 four downlinks (for data transmission), each up to 2.56 Gbs, so it can transmit data up to four
 2184 lpGBTs. The readout board also hosts interface connectors to the module board (as described
 2185 later) and power board, as well as to input LV and BV cables. The power board provide
 2186 low voltages for ASICs (1.2V), as well for lpGBT (1.2V) and VTRx+ (2.5V and 1.2V) on the
 2187 readout board via DC-DC converters. The CERN bPOL48V module is chosen as the main
 2188 converter, which takes an input of 15V and converts it into 1.2V and 2.5V. As illustrated in
 2189 Fig. 8.35, the RB is situated on top of the PB and sensor module. The PB is directly contact-
 2190 ing the cooling structure to facilitate efficient cooling of heat dissipation from DC-DC conver-
 2191 ters. The SH will have three different types with different lengths, serving 3 (12), 6 (24) and
 2192 7 (28) modules (sensor/ASICs). This will provide the most efficient coverage of a circular
 2193 shaped disk while minimizing number of cables and fibers. The example shown in Fig. 8.35
 2194 is the shortest version (about 100mm long) which serves 3 modules. The latest layout design
 2195 for FTOF disk is shown in Fig. 8.32 (right), where different colored boxes indicate different
 2196 types of SHs. Prototyping of the SH is in an advanced stage. A pre-prototype readout board
 2197 (ppRDO) has been developed and under testing, based on an Xilinx FPGA chip and a com-
 2198 mercial SFP+ optical transceiver. The first prototype RB and PB based on CERN chips will be
 2199 soon developed, especially based on similar existing design of the CMS endcap timing layer
 (ETL) detector.

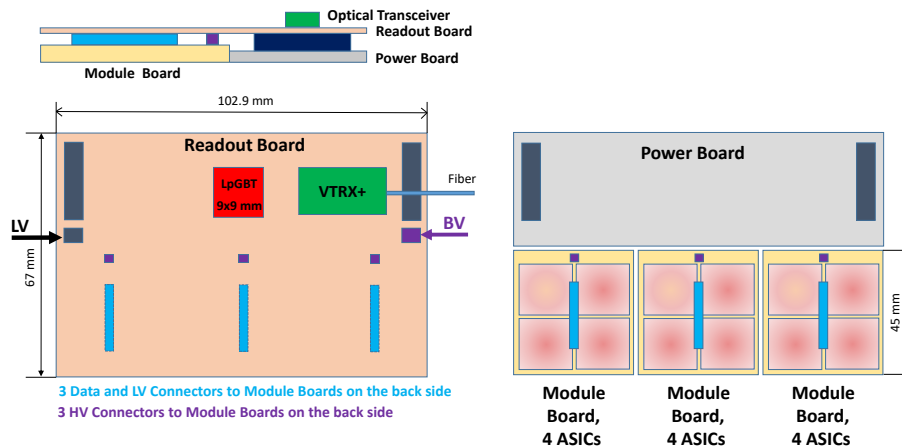


Figure 8.35: A schematic design of service hybrids for FTOF, which serves 3 modules or 12 sensors/ASICs.

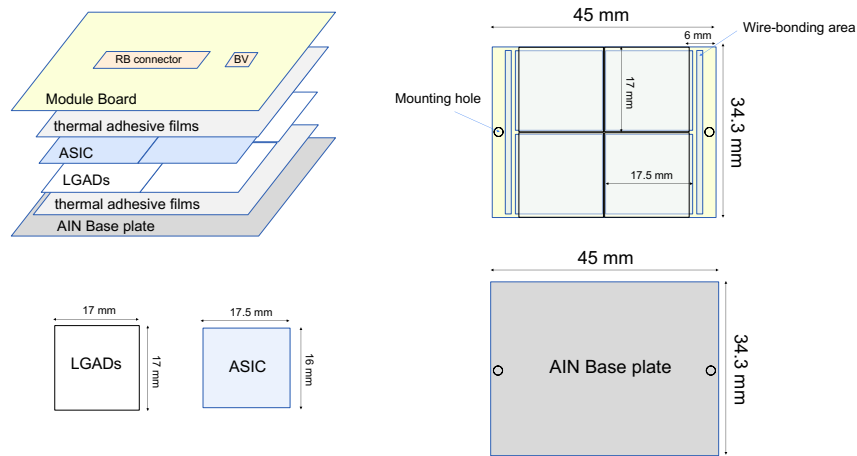
2200

2201 **Flexible Printed Circuit boards:** The Flexible Printed Circuit (FPC) is used to read out data
 2202 and distribute power to the sensors and ASICs. In the acceptance region, a material budget
 2203 of 1% X/X_0 is required, meaning the FPC material should be as minimal as possible. Ad-
 2204 ditionally, the FPC must be 135 cm in length. To meet these stringent requirements, careful
 2205 consideration of the FPC material is necessary, as signal loss is expected with such a long
 2206 FPC, especially if using polyimide, a standard material in FPCs. The sPHENIX experiment
 2207 encountered a similar challenge with their Inner Tracker (INTT), a silicon sensor tracker, and
 2208 successfully addressed it by using Liquid Crystal Polymer (LCP) instead of polyimide as the

2209 dielectric material. This technology will be adopted for our detector as well.

2210 **BTOF stave design:** Barrel staves are divided into two half-staves, with services and con-
 2211 nections coming from the outer side. The half-staves consist of a support structure with an
 2212 integrated cooling pipe, flexible printed circuit (FPC), sensors, and ASICs. Sensors and ASICs
 2213 are mounted on both the front and back sides of the half-stave, making it double-sided, with
 2214 enough overlap to achieve 100% coverage in the stave direction. The lateral overlap and tilt-
 2215 ing ensure 100% coverage in the direction parallel to the staves. In total, there are 64 sensors
 2216 and 128 ASICs on each side of the half-staves.

2217 **FTOF module design:** A schematic design of the module for FTOF is shown in Fig. 8.36.
 2218 Each module consists of 2×2 LGADs sensors and ASICs. It is covered by a module PCB
 2219 board (MB), which will provide LV power (1.2V) and transmit the data of ASICs via a board-
 2220 to-board connector to the RB. In addition, the MB also has a BV connector to the RB for
 2221 providing the BV to LGADs sensors. ASIC readout will be wire-bonded to a metal pad near
 2222 the edge of the module on the side facing the baseplate and cooling structure, as illustrated in
 2223 Fig. 8.36 (right). LGADs sensor and ASIC will be connected via bump bonding. Dimensions
 2224 shown are preliminary and will be adjusted as the prototyping progress. In the current de-
 2225 sign, the LGADs sensor is placed underneath the ASIC. The motivation is to have the sensor
 2226 as close as possible to the cooling structure to ensure lower and stable temperature, which
 2227 has been proven to be essential for achieving optimal time resolution. An alternative option
 2228 would be to swap the ASIC and sensor layer, which has the advantage of more efficiently
 2229 dissipating heat primarily generated by the ASIC. A final choice will be made as the proto-
 2230 type progress, especially after realistic thermal performance studies have been carried out.



2231 **Figure 8.36:** A schematic design of the module for FTOF, which consists of 2×2 LGADs sensors and ASICs.

2232 **Performance** The AC-LGAD systems, including the BTOF, FTOF, and far-forward systems (Ro-
 2233 man Pots, OMD, and B0 tracker), share a common readout chain currently under development.
 2234 Performance evaluations are being conducted in various laboratory environments as part of the
 2235 ongoing R&D efforts. A schematic of the full readout chain is shown in Fig. 8.37. The effort can be

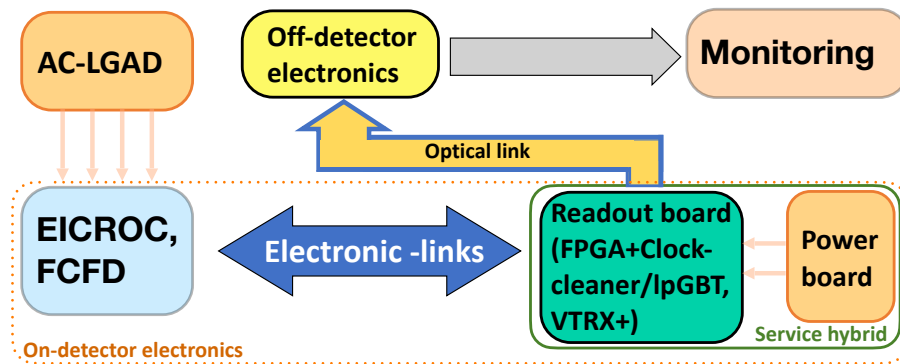


Figure 8.37: Schematic of the AC-LGAD sub-system readout chain. Each component is undergoing design, (pre-)prototyping, testing under various environments, and customization to meet the specific requirements of individual subsystems.

2236 divided into to parts: 1) integrating the sensors with ASIC, 2) development of the readout-board
2237 and power board.

2238 The Fermilab team has been developing an ASIC targeting the AC-LGAD strip sensors for BTOF.
2239 Studies showed that Constant Fraction Discriminator (CFD) could provide a better timing reso-
2240 lution with small signal amplitude from LGAD than leading edge discriminator [39]. The first
2241 single-channel CFD-based ASIC (FCFDv0) wire-bonded to a DC-LGAD sensor achieved 35 ps
2242 timing precision with beam, where the dominant contribution is expected from the intrinsic resolu-
2243 tion of the LGAD sensor. A 6-channel prototype (FCFDv1) was developed for AC-LGAD sensors,
2244 demonstrating 11 ps jitter in charge injection and 50 ps time resolution with 0.5 cm AC-LGAD
2245 strip sensor in test beam. Ongoing efforts are focused on optimizing the frontend design for 1 cm
2246 AC-LGAD strip sensors for the BTOF.

2247 Assemblies of 4x4 AC-LGAD pixel sensors with $500 \times 500 \mu\text{m}^2$ pixelation and 30 μm thickness,
2248 and 4x4 EICROC0 ASICs, were completed by the BNL, IJCLab, OMEGA, and Hiroshima groups
2249 on test-boards developed by IJCLab/OMEGA. Testing included scans of the analog and digital
2250 components using charge injection and beta particles from a Sr-90 source, resulting in a measured
2251 jitter of 8-9 ps for charges above 20 fC. Both wire-bonded and flip-chip assemblies were developed
2252 for various characterizations. Additional tests using Transient Current Technique (TCT) laser scans
2253 were conducted to map out charge distribution, and various tests are still ongoing.

2254 ORNL is developing flexible Kapton PCBs for TOF applications, where sensors and mockup ASICs
2255 will be glued, wire-bonded, and co-cured onto a composite structure at Purdue for evaluation.
2256 Flip-chip options will be available soon, aiming to support low-cost sensor-ASIC hybridization
2257 techniques.

2258 In FY24, BNL, LBNL, and Rice developed a prototype board (ppRDO) for precise clock distribution
2259 and ASIC integration for AC-LGAD systems. Key milestones, including schematic designs, part
2260 orders, PCB layout, and initial testing, were completed ahead of schedule. Firmware development
2261 and performance tests on clock-cleaning, jitter, and power distribution are ongoing. The collabora-
2262 tion aims to continue in FY25, focusing on the development of a readout board (RBv1) and power
2263 board (PBv0) for AC-LGAD systems, supporting TOF applications and ensuring DAQ compatibil-
2264 ity. The ppRDO includes three components: 1) FPGA, 2) clock cleaner, and 3) SFP+ module. Future
2265 versions will adopt lpGBT to replace the FPGA and clock cleaner, and VTRx+ to replace the SFP+
2266 module, improving performance, radiation hardness, and integration.

2267 **Implementation**

2268 **Services:** Electric power is distributed to the detector components via the Power Board (PB),
 2269 which is part of the Service Hybrid (SH). The SH also includes the functionality of the Readout
 2270 Board (RDO). In the case of BTOF, one SH supports 64 sensors and 128 ASICs, with SHs placed
 2271 on both sides of the stave. For FTOF, several types of SHs are used, covering 12, 24, or 28 sets of
 2272 sensors and ASICs. The SH is distributed on the mechanical and support disk, together with sensor
 2273 modules.

subsystem	item	quantity	diameter (mm)	lengths (m)	description
BTOF	FEE LV	24	20	15–25	Rack to Panel, 8AWG (24 AWG sense pairs)
BTOF	FEE LV	72	6.3	8	panel to detector, Alpha PN: 2424C SL005
BTOF	FEE HV	18	14	15–25	Rack to Dist. Panel
BTOF	FEE HV	144x2	1.5	8	panel to sensor
BTOF	cooling tubes	144x2	5	> 2.6	supply/return from panel to stave (Aluminum)
BTOF	cooling tubes	4x2			supply/return to panel
FTOF	FEE LV	212	9.04	25	supply/return LV from FEE to Rack
FTOF	FEE HV	14	14	25	rack to dist. panel
FTOF	FEE HV	212	2.42	10	panel to sensor
FTOF	cooling tubes	2x2	5		supply/return from panel to detector (Aluminum)
FTOF	cooling tubes	2			supply/return to panel

Table 8.14: Summary of BTOF and FTOF low voltage and high voltage powersupply cables to distribution panels and then to the detector FEE (the exact numbers are being checked at the time of writing).

2274 Low Voltage (LV) and High Voltage (HV) cables are connected to the PB, where multiple DC-DC
 2275 converters step down or adjust the voltages as needed. HV is applied to groups of multiple sensors,
 2276 rather than distributed individually to each sensor. The size of each sensor group is determined by
 2277 the design of the sensors and the electronics. Table 8.14 summarizes the service (cables and tubes)

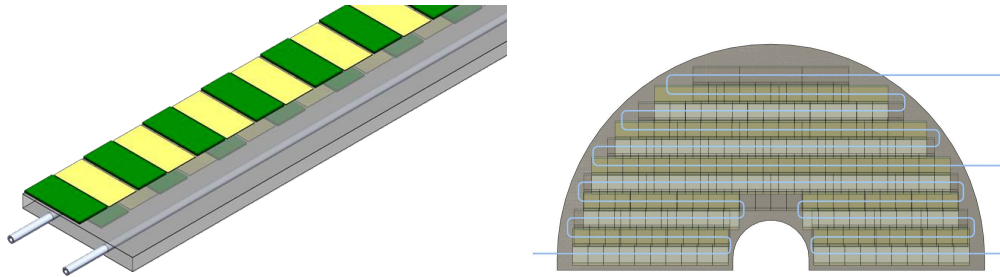


Figure 8.38: schematic drawings of one BTOF stave (left) and half of the whole FTOF (right) cooling pipes.

2278 necessary for TOF detectors.

2279 A liquid cooling system is employed to control the temperature of the detector. For the BTOF stave,
 2280 one or two cooling pipes are integrated into the stave sandwich structure, with liquid flowing in
 2281 one direction along the length of the stave. In FTOF, a winding liquid pipe is integrated into the
 2282 support sandwich structure. The flow rate and pipe diameter are determined by the amount of heat
 2283 generated and the detector's performance requirements, thermal finite element analysis determines
 2284 the design. The pressure must remain below the surrounding air pressure to ensure safe operation.
 2285 Fig. 8.38 shows a single BTOF stave with cooling pipe (left) and half of the FTOF structure with
 2286 cooling pipes (right).

2287 **Subsystem mechanics and integration:** Both the BTOF and FTOF detector systems are sup-
 2288 ported by their own support structure, which is integrated and supported by the global support
 2289 tube (GST). The BTOF is a barrel geometry time-of-flight detector system located at a radius of
 2290 63cm from $z = -117.5\text{cm}$ to $z = +171.5\text{cm}$ along the beam direction as shown in Fig. 8.39. Both
 2291 detector subsystems have 7.5cm space in radial direction for BTOF and in the beam direction for
 2292 FTOF. The three engagement rings (each of 5mm width) are made from composite materials as a
 2293 sandwich and support the BTOF detector - they are itself supported by the GST. A first concept
 2294 was developed for a BTOF stave mounting mechanism employing the engagement rings by clips
 2295 with staves at an 18 degree angle. Staves are removable individually to ease maintenance. The
 2296 FTOF detector is designed in two half disc structures, or dees, that are kinematically mounted to
 2297 the GST. Services (readout, power, cooling) of the BTOF and FTOF are routed either way and sup-
 2298 ported itself by the GST. Table 8.15 lists the positions of BTOF and FTOF relative to the global ePIC
 2299 geometry.

subsystem	z_{min} (cm)	z_{max} (cm)	inner radius (cm)	outer radius (cm)	stave angle
Barrel TOF	-117.5	171.5	62	69.5	18°
Forward TOF	185	192.5	10.5	60	0

Table 8.15: BTOF is designed with a barrel geometry surrounding the beam pipe and interaction point, while FTOF is a disk geometry perpendicular to the beam direction on the hadron side (positive z).

2300 **Calibration, alignment and monitoring:** **Calibration and alignment:** For spacial calibration
 2301 and alignment, the TOF layer is essentially treated as a layer of the overall tracking system. There-

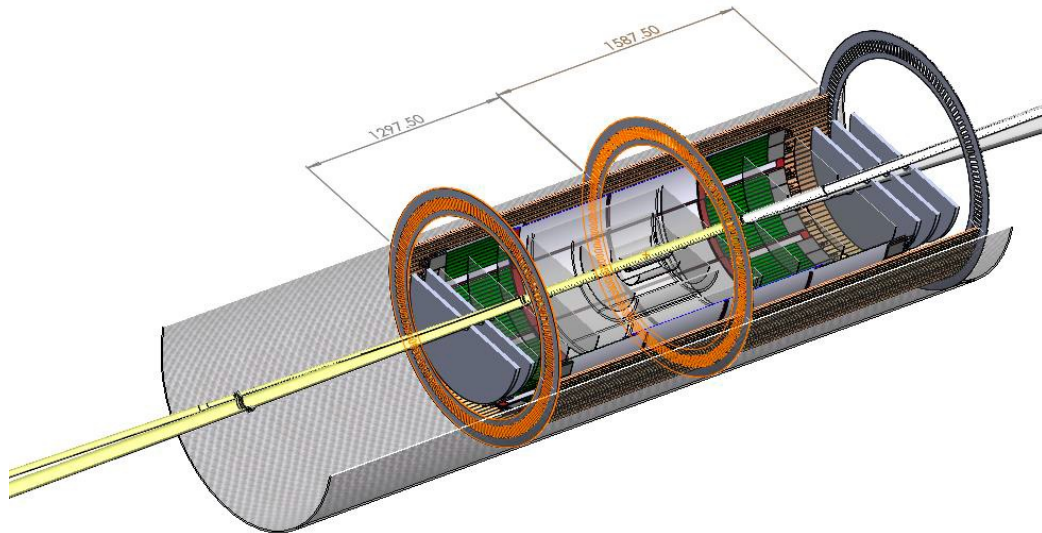


Figure 8.39: Barrel TOF supporting mechanic structure with engagement rings situated and supported by the EPIC global support tube structure (GST). The width of each of the three engagement rings is 5mm.

2302 fore, spacial alignment will be carried out as part of the entire tracker. This is typically based on the
 2303 match between tracks reconstructed in other layers of the tracking, then extrapolated to the TOF
 2304 and the hits in the TOF. By combining the information from many tracks, high precision can be
 2305 achieved.

2306 To exploit timing in the reconstruction of the charged tracks, the different TOF channels will have
 2307 to be synchronised to a precision of a few picoseconds. The absolute time calibration (or phase
 2308 shifts relative to the beam clock) is not a particular concern, as all the event reconstruction relies
 2309 on the relative time between tracks within the same collision event. The time offsets of the TOF
 2310 channels can be inter-calibrated using all the tracks collected online through a fast reconstruction
 2311 stream. The distribution of the reconstructed time at the vertex of these tracks – assuming they are
 2312 pions – should an rms spread of approximately 50 ps, including the time spread of the luminous
 2313 region and detector resolution. The mean time of this distribution over many tracks provides the
 2314 reference calibration points. Non-pion particles will contribute to the tail of the distribution, which
 2315 can be cleaned up using an iterative procedure but not necessary. These calibrations can be made
 2316 available for the prompt reconstruction of the events and updated frequently.

2317 **Monitoring:** In the readout scheme of the TOF, a common clock is distributed to the individual
 2318 channels belonging to the same service hybrid. The time stability of the clock distribution can be
 2319 monitored with a precision of a few ps every second.

2320 **Status and remaining design effort:** eRD112 and eRD109

2321 **eRD112: Sensor R&D effort** A brief summary of eRD112 activities is reported in this section, for
 2322 a more detailed review of the sensor development effort consult the 2024 erd112 report document.
 2323 HPK sensors from the latest production have been tested at the Fermilab test beam facility; the

2324 results are summarized in Ref. [2]. The summary best results are reported in Fig. 8.40. The same
 2325 HPK production was tested in laboratory with focused laser TCT and showed similar results as
 2326 reported in Ref. [37]. The presented strip sensors (Fig. 8.40, Left) show a constant time resolution of
 2327 around 35 ps, which is within the requirements for the ePIC TOF. The strip reconstructed position
 2328 resolution is between 10-20 μm , which is also within the ePIC TOF requirement of 30 μm . The best
 2329 result for pixel sensors (Fig. 8.40, Right) shows an homogeneous time resolution of 20-25 ps, well
 2330 within ePIC TOF requirements. The position resolution instead is 20-70 μm across the device; the
 2331 charge-sharing mechanism allows for precision reconstruction in between metal electrodes, but the
 2332 resolution is significantly worse for hits directly on the metal electrodes.

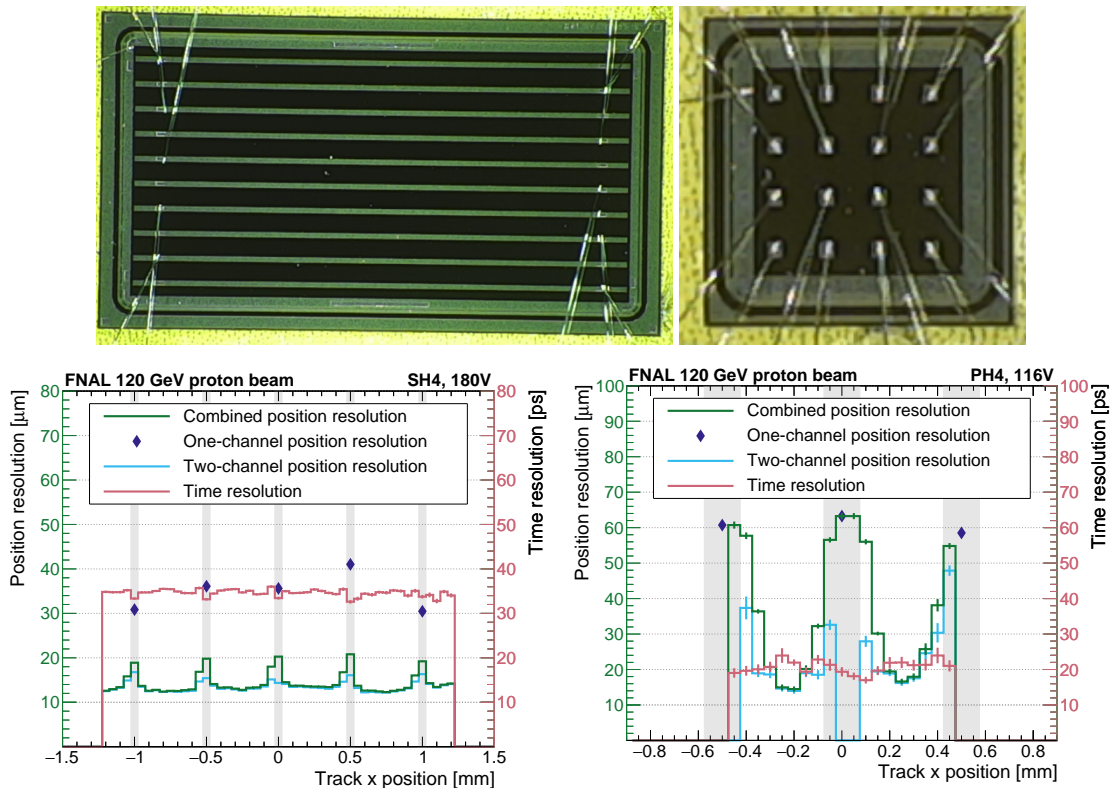


Figure 8.40: Left: Picture and beam test results for HPK strip sensor, 1 cm long, 500 μm pitch, and 50 μm metal electrode width. Right: Picture and beam test results for HPK pixel sensor, 4x4, 500 μm pitch, and 150 μm metal electrode width. Plots from Ref. [2].

2333 The position resolution requirement for the FTOF is 30 μm . Therefore, pixel technology needs to
 2334 be refined to meet the requirements. The new HPK production (expected by the end of the year)
 2335 includes smaller electrode sizes and larger gaps between electrodes that could provide good re-
 2336 construction across the sensor. However, it was observed that a larger gap decreases the total S/N
 2337 between electrodes, which might degrade the overall performance of the sensors. Results from a
 2338 BNL production provide a promising alternative to square metal pixels. The S/N is better across
 2339 the sensor for a cross-shape electrode given the same central metal shape, allowing for better re-
 2340 construction using charge sharing. HPK did not include cross-shape geometry in the latest pro-
 2341 duction, but it might be included in the next one. Another producer of cross-shaped AC-LGADs
 2342 is Fondazione Bruno Kessler (FBK). The FBK prototypes were investigated with a laser TCT, and a
 2343 similar behavior was observed for cross-shaped devices [38].

2344 The sensors irradiated at the Triga Reactor with 1 MeV neutrons were received in Spring 2024 and
 2345 characterized both for electrical proprieties (capacitance and current over voltage) and with the
 2346 laser TCT station. Gain degradation can be probed with measurements of capacitance over voltage
 2347 by identifying the gain layer depletion point (V_{GL}). Fig. 8.41, Left, shows the change in the gain
 2348 layer for the irradiated HPK AC-LGADs from several wafers, with different N_+ , oxide and active
 2349 thickness, up to 1×10^{15} Neq; in the region of interest for ePIC $< 10^{13}$ Neq the gain layer is un-
 2350 changed. The charge-sharing proprieties after irradiation were tested using a focused IR laser in
 2351 the laboratory. As seen in Fig. 8.41, Right, the spatial response of the sensor is unchanged after
 2352 irradiation up to 5×10^{14} Neq. The current increase in the irradiated HPK sensors is also negligible
 2353 until $< 10^{13}$ Neq, as shown in Fig. 8.41, Bottom. The measurements were done at room temper-
 2354 ature; therefore, no cooling will be necessary to reduce the dark current, which would increase
 2355 the sensor power dissipation in ePIC. In conclusion, no change in the behavior of the sensors is
 2356 expected during the lifetime of the ePIC detector due to radiation damage.

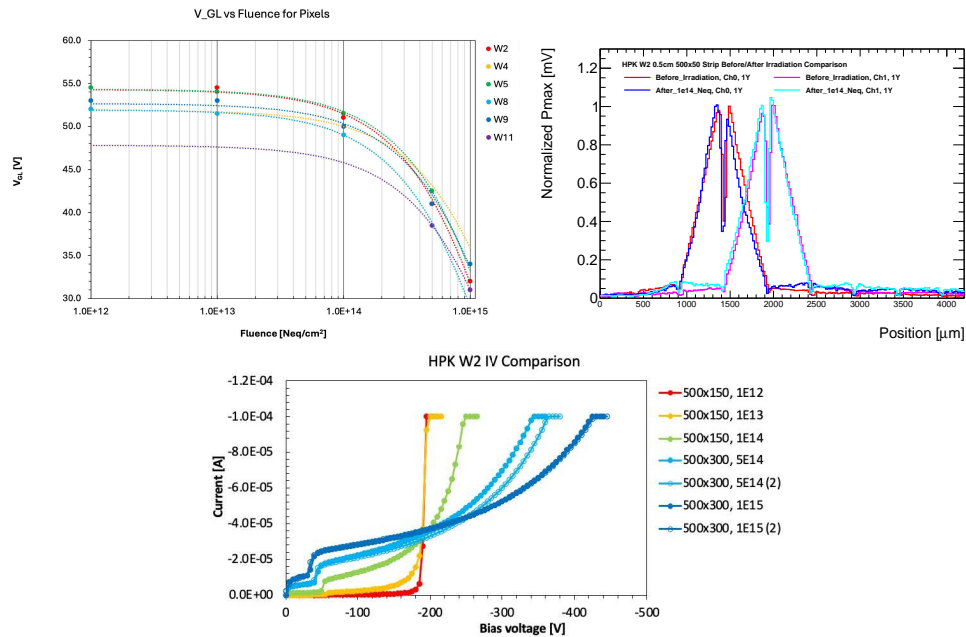


Figure 8.41: Left: Degradation of the gain layer for AC-LGADs of several wafer (with different N_+ , oxide and active thickness) from HPK latest sensor production, showing no change in gain layer doping up to 10^{13} Neq, which is an order of magnitude over the ePIC TOF radiation requirement. Sensors were irradiated at the TRIGA reactor (Ljubiana) with 1 MeV neutrons. Right: Normalized comparison of response profile of two nearby strips for two HPK 0.5 cm length, 500 μm pitch, 50 μm strip width: one before irradiation and one after 1×10^{14} Neq, even if the total signal is degraded the charge sharing profile is unchanged. Bottom: Current over voltage measurement for irradiated HPK sensors.

2357 **eRD109: readout R&D effort** A more detailed review of the electronics development effort can
 2358 be found in the 2024 eRD109 report document. In the following section, a brief summary will be
 2359 provided.

2360 The Fermilab team has continued the development of the FCFD ASIC prototype and, in FY23, has
 2361 designed the first multi-channel prototype with this approach, labeled as FCFDv1. Numerous tech-
 2362 nical improvements were implemented based on the experience with FCFDv0, aimed at addressing
 2363 the stability and performance of the system. The FCFDv1 ASIC was submitted for production in

2364 September 2023, and received in January 2024. A specialized readout board was designed to ac-
 2365 commodate the FCFDv1 connected to a 0.5 cm HPK AC-LGAD strip sensor. Initial measurements
 2366 of the performance were done using internal charge injections performed with an LGAD-like sig-
 2367 nal. With input capacitance ~ 3.5 pF a jitter of around 11 ps was achieved, as shown in Fig. 8.42,
 2368 left. Test beam campaigns have been performed to study the performance of the FCFDv1 in June
 2369 2024. The newly introduced amplitude readout was found to function well, and results show 100%
 2370 efficiency when combining neighboring strips. The time resolution measured from the beam test
 2371 was around 50 ps. A further design improvement is foreseen in FCFDv1.1 to accommodate 1 cm
 2372 AC-LGAD strip sensor and improve the timing resolution.

2373 The development of the EICROC0 chip is proceeding as planned. In 2024, an updated PCB (“2024”
 2374 PCB), has been designed by OMEGA. This updated PCB features improved testability and ground-
 2375 ing, as well as the removal of supplementary PLLs. The chip shows good homogeneity between
 2376 channels and Jitter < 35 ps for an injected charge of > 4 fC, both for the pre-amplifier and for the dis-
 2377 criminator output, as seen in Fig. 8.42, Left. A large correlated noise still remains with the updated
 2378 “2024” PCBs (already observed in the “2023” PCB), which leads to large TDC jitters, over 50 ps,
 2379 when by design, the TDC jitter is expected to be of the order of 10 ps. Nevertheless, the intrinsic
 2380 performance of the preamplifier, the TDC, and the ADC, taken individually, is confirmed to be in
 2381 agreement with the design and within the ePIC detector specifications.

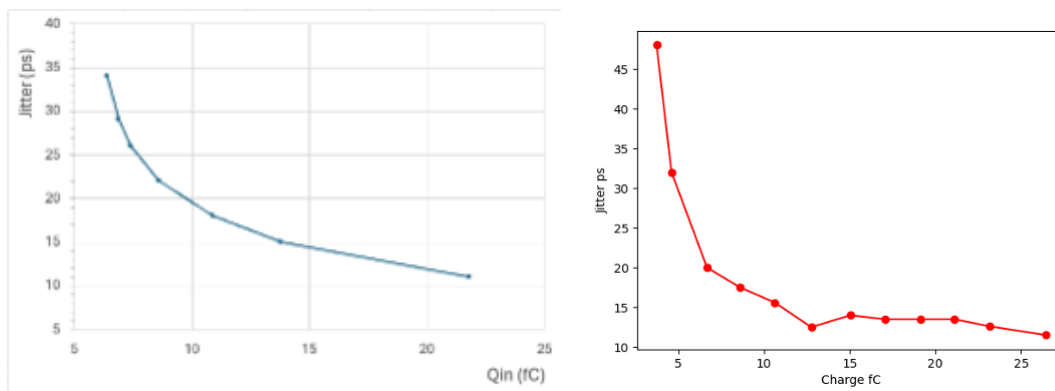


Figure 8.42: Left: FCFD Jitter measurements with 3.5 pf input capacitance and charge injection. Right: EICROC Discriminator jitter versus the injected charge, determined from data on an oscilloscope. Left: FCFD Jitter measurements with 3.5 pf input capacitance and charge injection. Plots from the erd112 and erd109 2024 reports.

2382 The development of pre-prototype readout board (RDO) with high precision clock distribution has
 2383 been completed. Figure 8.43 shows a picture of the ppRDO. It is connected with the CMS ETL
 2384 module board v0, which consists of the full-sized ETROC2 chip for testing purpose. The ppRDO
 2385 will be evolved into the prototype RB for FTOF next that consists of lpGBT and VTRx+ chips,
 2386 instead of FPGA and SFP+. Those efforts will be carried out under engineer designs as described
 2387 later.

2388 **E&D status and outlook:** E&D activities

2389 **Thermo-Mechanical demonstrator:** The fabrication of a demonstrator stave following the double-
 2390 sided design, as seen in Fig. 8.45, is ongoing. The demonstrator will be a thermal/mechanical
 2391 demonstrator of the assembly procedure and chip/sensor power dissipation. A mock-up stave,

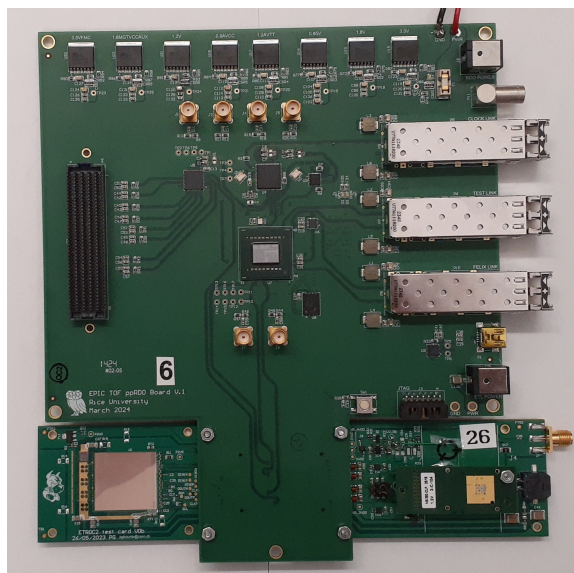


Figure 8.43: Picture of ppRDO connected with CMS ETL module board v0 for testing.

2392 example in Fig. 8.44, will be co-cured with a readout flex with a cooling pipe in the center, and a
 2393 series of Si heaters and full-size HPK sensors from the latest production will be glued to the stave, then
 2394 wire-bonded together and to the readout flex. The demonstrator will be used to probe the power
 2395 dissipation, the temperature gradient across the stave, and the mechanical assembly procedure.
 2396 Demonstrator results are expected by Q1 2025.



Figure 8.44: Assembled stave prototype at Purdue.

2397 **Environmental, Safety and Health (ES&H) aspects and Quality Assessment (QA plan-**
 2398 **ning:** We also carried out QA long-term and stress-test reliability studies of LGADs as a stepping-
 2399 stone towards studies on AC-LGADs. The tests were conducted in an ambient chamber at various
 2400 environmental conditions. We kept the sensors under bias voltage over periods of weeks, at differ-
 2401 ent temperatures, ranging from -60 to +80 degrees Celsius and under different humidity conditions.
 2402 Under these extreme conditions we carried out I-V scans. At intervals of time between tempera-
 2403 ture cycles, we also collected signals from beta particles from a Sr-90 source at room temperatures
 2404 to study any deterioration in noise or charge collection. The results were presented at IEEE confer-
 2405 ence: While we saw an impact of humidity and temperature on current and breakdown voltage, the
 2406 sensors recovered their original performance in subsequent cycles. In addition, we also studied the
 2407 impact of passivation on sensors to minimize charge build-up and early mortality. We confirmed
 2408 that passivation is critical to minimise the impact of humidity on sensors and prevent early mor-
 2409 tality. Such tests were critical after issues have been observed in silicon sensors used for tracking
 2410 detectors in other experiments, such as those at the HL-LHC. As part of our QA strategy, we also
 2411 sent to colleagues of UNM BNL-made AC-LGADs to have them irradiated at various fluences in a

2412 proton beam at ITA, in a gamma beam at SANDIA and with neutrons at the TRIGA reactor. The
2413 first results are shown in the previous sections.

2414 For both sensors and readout chips, it is imperative to evaluate the yield of the test productions to
2415 adjust the final production orders. The QA plans to evaluate the yield of the sensor productions
2416 are as follows: each produced sensor will be tested in the laboratory in a probe station with simple
2417 current over voltage (IV) and capacitance over voltage (CV) tests. AC-LGADs have a single point
2418 of DC connection on the N+, so only 1 or 2 needles are necessary for the test; a probe card is not
2419 necessary for QA. The IV test will allow us to check the current level and the breakdown voltage
2420 for each produced device; the current level has to be $\ll 1\mu A$ to not introduce power dissipation
2421 issues. The breakdown voltage of all devices has to be within 10%? to avoid issues in the HV
2422 distribution. The CV test will allow to probe the gain layer depletion voltage and demonstrate that
2423 all devices have homogeneous gain; for LHC prototypes [35], the gain homogeneity was within
2424 1%. A selection of devices from the full production will be characterized by mounting them on
2425 analog front-end boards with laser TCT and at test beam facilities to ensure the homogeneity of the
2426 charge-sharing response.

2427 To evaluate the yield of the chip (EICROC, FCFD) productions, a sample of chips from each batch
2428 will be tested and probed for homogeneity in all the channels using a calibration input. All channels
2429 have to be within 10%? of homogeneity. A selection of chips will be coupled (wire bonded or bump
2430 bonded) with a matching working sensor and mounted on a prototype PCB to probe correct and
2431 homogeneous operation in a realistic configuration. Then the boards will be tested with a laser TCT
2432 or at test beam facilities.

2433 Once the state of sensors, readout chips, and flex is advanced, a fully loaded demonstrator stave
2434 is envisioned. The mounting procedure will already be tested during the assembly of the thermo-
2435 mechanical demonstrator. The full demonstrator will then be tested with radioactive sources in
2436 laboratory or at test beams.

2437 **Construction and assembly planning:** The BTOF detector has a cylindrical shape, consisting
2438 of 144 tilted staves. These staves are assembled at designated sites within class-7 or higher clean
2439 rooms before being transported to BNL for final construction. Each stave is approximately 270 cm
2440 long and is divided into two half-staves of 135 cm. A half-stave includes a support structure with
2441 an integrated cooling pipe, a flexible printed circuit (FPC), sensors, and ASICs. The sensors and
2442 ASICs are mounted on both sides of the half-stave, with 64 sensors and 128 ASICs on each side.
2443 Wire-bonding is used to connect the ASICs to the sensors and electronics. Only components that
2444 pass various quality inspections—such as visual checks, metrology, and electrical tests—proceed
2445 to the assembly stage. During the half-stave assembly, one FPC is glued onto the support structure
2446 (Fig.8.45 (a)). To ensure precise alignment, a specialized tool is used, featuring pins and holes that
2447 guide the placement of the FPC and the correct application of glue. After assembly, the staves un-
2448 dergo both electrical and mechanical tests. Subsequently, sensors and ASICs are installed on the
2449 FPC surface using alignment tools similar to those used during the FPC mounting process (Fig.8.45
2450 (b)). These tools help position the components and apply adhesive. Electrical connections are veri-
2451 fied, and the ASICs are bonded to the sensors using wire-bonding, followed by wire encapsulation
2452 (Fig.8.45 (c)). 2 support structure with wire-bonded sensor, ASIC, FPC which is corresponding to
2453 front and back side, are attached to each other (Fig.8.45 (d)). Upon completing the installation on
2454 both sides (Fig.8.45 (e)), the final round of testing is conducted. Fully tested staves are then shipped
2455 to BNL for integration into the global support structure of the ePIC detector, which contains 144
2456 slots for precise alignment of the staves within the global coordinate system.

2457 The FTOF is constructed in a double-sided disk shape by populating modules with dimensions
2458 indicated in Fig. 8.36. Each module includes 4 sensors, 4 ASICs, a module board, and an Aluminum

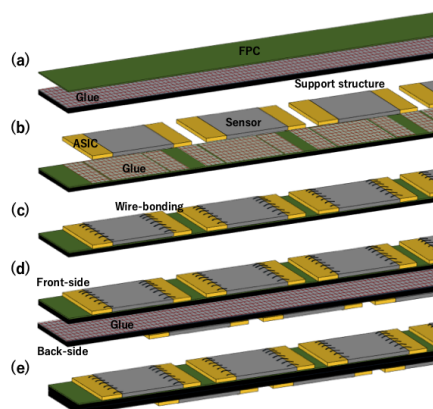


Figure 8.45: Assembly process of BTOF stave. Note, the scale is not real.

2459 Nitride (AlN) base plate, which acts as a thermal conduit to the cooling system. The modules are
 2460 connected to a service hybrid (SH) that consists of a power board (PB) and a readout board (RB).
 2461 As mentioned earlier, three different configurations of SH are used, depending on the number of
 2462 modules being supported: 3 modules (RB3), 6 modules (RB6), and 7 modules (RB7). There are
 2463 about 780 modules in total to patch the disk shape. Sensor and ASIC are connected by bump-
 2464 bonding. The module board is connected to the ASICs through wire bonding and has a connector
 2465 to interface with the RDO. Assembly of the modules occurs in class-7 (or higher) clean rooms,
 2466 while the PB and RB can be assembled under standard conditions. The assembly of each module
 2467 begins with the connection of one sensor to one ASIC using bump-bonding technology (Fig.8.46
 2468 (a)). Automated machines are used for sensor and ASIC placement, alignment, and bonding. After
 2469 bonding, the electrical performance of the sensor-ASIC hybrids is tested. Following this, 4 sensor-
 2470 ASIC hybrids are mounted on the module board, using a dedicated tool to ensure precise alignment
 2471 (Fig.8.46 (b)). Thermal adhesive films are placed between the hybrids and the module board to
 2472 ensure efficient heat dissipation. Once mounted, the ASICs are wire-bonded to the module board,
 2473 and the wires are encapsulated for protection. After the bonding process, the AlN base plate is
 2474 attached to the opposite side of the hybrid (Fig.8.46 (b)), with thermal adhesive films again used
 2475 between them to aid heat transfer. The thermal adhesive films are also put between them. The
 2476 modules undergo thorough quality checks before moving on to SH assembly. The RBs and PBs
 2477 are manufactured using standard circuit board techniques and come with dedicated connectors for
 2478 integration. SHs are available in configurations supporting 3, 6, or 7 modules, with the RB and
 2479 PB connected via dedicated interfaces (Fig.8.46 (c)). Once assembled (Fig.8.46 (d)), the modules
 2480 and SHs are tested for connectivity and performance. After passing all tests, the modules and SHs
 2481 are shipped to BNL, where they are attached to the disk-shaped support structure. Specialized
 2482 tools ensure the accurate placement of the components. Modules and SHs are mounted on both
 2483 sides of the support structure to eliminate acceptance gaps between sensors. When installing the
 2484 modules and SHs on the opposite side, a fixture is used to maintain the required clearance between
 2485 components. Finally, the fully assembled disk is installed into the ePIC detector.

2486 **Collaborators and their role, resources and workforce:** Table 8.47 shows the participating
 2487 institutes with their role, the contact person and potential commitments. This shows substantial
 2488 participation by the international collaborators outside of the U.S.. We also anticipate substantial
 2489 funding support from the international collaborators for the BTOF detector as well.

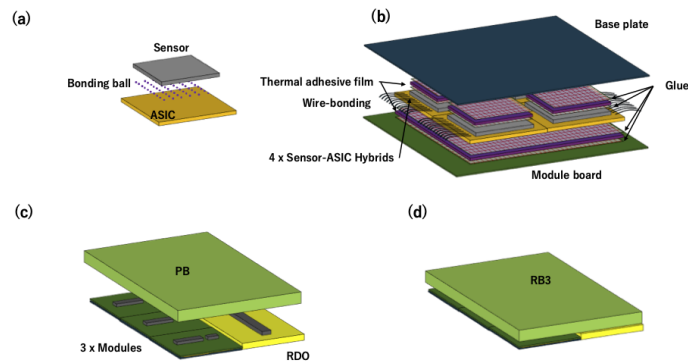


Figure 8.46: Assembly process of FTOF modules. RB3 type is shown as an example. Note, the scale is not real.

2490 **Schedule** The schedules for BTOF and FTOF projects are shown in Fig.8.48. A major inter-
 2491 dependence of the schedule is the sensor and ASIC designs. In the preproduction phase, 10%
 2492 will be made in six months while quality and procedures are being confirmed in this period. Then,
 2493 during the Production phase, the remaining 90% will be produced in two years.

2494 **Risks and mitigation strategy:** Our R&D results (eRD112) show that the performance of the
 2495 sensors would meet physics requirements for TOF subsystems. Those studies were done with
 2496 smaller chip dimension. The production for R&D study with full-size sensor chip is underway.
 2497 There is a potential risk that the performance of sensors with larger size would be worse. The
 2498 mitigation is to reduce the sensor size.

2499 The HPK sensors for R&D (eRD112) is of small quantity. A mass production would be a risk in
 2500 terms of chip yield and schedule delay. The mitigation is to explore other possible production sites
 2501 (Taiwan/FBK).

2502 FCFD ASIC design (eRD109) currently only has analog signal readout. The design and test of
 2503 the digitization component is underway and expected to have first pass early next year. Addi-
 2504 tional resource may be need to mitigate potential schedule delay and cost increase. In addition to
 2505 the baseline chips EICROC and FCFD, third-party ASICs are also taken into consideration: FAST
 2506 (INFN Torino), AS-ROC (Anadyne Inc. + UCSC), and HPSoC (Nalu + UCSC). The most advanced
 2507 one is the High-Performance System-on-Chip (HPSoC) ASIC, designed by Nalu Scientific [40], in
 2508 close collaboration with SCIPP, and fabricated in 65 nm CMOS by TSMC. HPSoC comprehends a
 2509 fast analog front end and, unique to all other current LGAD readout ASICs, will capture the full
 2510 signal waveform at a sampling rate of 10-20 GS/s. Together, these are expected to address the EIC
 2511 goal of 25 ps timing resolution or better per measured space point. V2b of the chip has a working
 2512 digital back-end and is currently under review.

2513 We have performed heat conductivity and cooling simulations, and R&D test on cooling capacity
 2514 (currently with PED funding). Those show promising outcome for meeting the cooling needs. The
 2515 potential risk is that the cooling capacity is not sufficient to maintain a stable and relatively uniform
 2516 temperature. A possible mitigation strategy is to use different material for cooling pipe with better
 2517 heat conductivity and higher flow rate.

Institute	Contact Person	NOW (TDR->Project)
Brookhaven National Laboratory	Prithwish Tribedy tribady@bnl.gov	DAQ readout chain readout, sensor-ASIC integration, sensor with FF AC-LGAD; EICROC testing
Fermi National Accelerator		FCFD ASIC (no ePIC)
Los Alamos National Laboratory	Xuan Li xuanli@lanl.gov	
Rice University	Wei Li w133@rice.edu	B/FTOF FEE?, Backend electronics (postdoc), simulation and reconstruction
Oak Ridge National Laboratory	Oskar Hartbirsch hartbricho@ornl.gov	sensor-ASIC integration, frontend electronics (waffle probing), module assembly
Ohio State University	Daniel Brandenburg Brandenburg.89@osu.edu	BTOF/FTOF: module assembly; backend electronics
Purdue University	Andreas Jung anjung@purdue.edu	Module assembly
Univ. of California, Santa Cruz	Simone Mazza simazza@ucsc.edu	Sensor, sensor-ASIC integration, module assembly (no in-kind)
University of Illinois at Chicago	Olga Evdokimov mailto:evdoiga@uic.edu	
Hiroshima University	Kenta Shigaki shigaki@hiroshima-u.ac.jp	FTOF EICROC testing, sensor testing (30%), simulation
RIKEN	Yuji Goto goto@bnl.gov	BTOF: module assembly
Shinshu University	Kentaro Kawaide kawaide@shinshu-u.ac.jp	Sensor testing, simulations
University of Tokyo	Taku Gunji gunji@cns.s.u-tokyo.ac.jp	DAQ streaming readout
South China Normal University	Shuai Yang syang@scnu.edu.cn	
Univ of Sci. and Tech. of China	Yanwen Liu	
Indian Institute of Tech., Mandi	Prabhakar Palni prabhakar.palni@unigoa.ac.in	FTOF Module Assembly/QA, sensor testing
National Inst. of Sci. Edu. Res.	Ganesh Tambave ganesh.tambave@niser.ac.in	Module Assembly
National Central University		FF AC-LGAD (sensor QA)
National Cheng-Kung University	Yi Yang yiyang@ncku.edu.tw	Mechanics and cooling systems
National Taiwan University	Rong-Shyan Lu rslu@phys.ntu.edu.tw	FF AC-LGAD; module assembly
Univ. Técnica Federico Santa María		Simulations
LBNL	Zhenyu Ye yezhenyu2003@gmail.com	BTOF ASIC testing; SH
Kent State University	Zhangbu Xu zxu22@kent.edu	Simulation, readout test, machine shop (in-kind)
Nara	Takashi Hachiya hachiya@cc.nara-wu.ac.jp	BTOF module assembly/validation/FPCB

Figure 8.47: Collaboration institutions and their responsibilities.

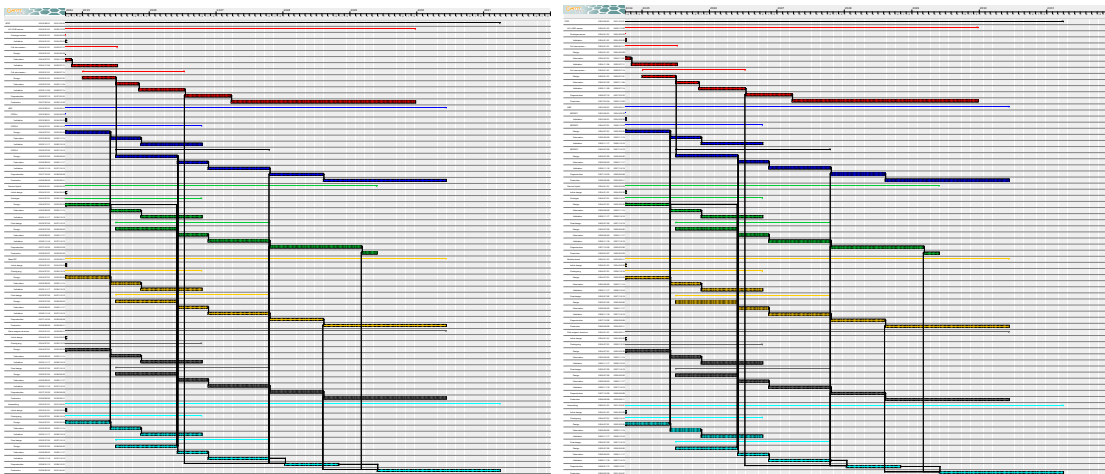


Figure 8.48: BTOF (left) and FTOF (right) project schedules (2024/10/05 version.)

2518 **Additional Material**

2519 **Low-voltage and High-Voltage powersuplies** Each service hybrid module will be powered
2520 by a radiation and magnetic field tolerant DC-DC regulation board as part of the hybrid module
2521 and mounted to the cooling plate. The minimum efficiency of the regulator board should be \geq
2522 70.0%. Input power to the DC-DC board is delivered from rack-mount Wiener PL500 series power
2523 supplies to source 15 Volts DC \pm 3.0%. The current demand from the rack-mount PSU should not
2524 exceed 80.0% of the manufacturers rating. Each channel of the PSU will have over-current fuse
2525 protection. The power cabling size is selected to operate at 125% of the total continuous maximum
2526 load. The estimated power consumption and LV cable feed size for each detector is designated
2527 as follows: Forward TOF system LV power: 6.0KW (400 Amps). LV power feeds from platform:
2528 Custom two-conductor 12AWG tray rated cabling with embedded low voltage sense twisted pair
2529 wires.

2530 Barrel TOF system LV power: 15.0KW (1,000 Amps). LV power feeds from platform: Custom
2531 two-conductor 8AWG or 10AWG (depending on LV segmentation) tray rated cabling with embed-
2532 ded low voltage sense twisted pair wires. Custom enclosed LV power distribution PCBs will be
2533 installed at the detector side and outside of the inner detector volume. A disconnect is required
2534 for each LV output port of the distribution box. Power distribution to the service hybrids will be
2535 configured to not exceed 10.0% channel segmentation from the rack-mount power control. Multi-
2536 channel ISEG ESH series power modules will provide up to negative 500VDC bias at a current of
2537 10ma per channel. Multiconductor cables terminated with REDEL connectors or individual coax
2538 cables terminated with SHV connectors will feed an enclosed HV distribution box. The HV bias
2539 cabling to the detector hybrids will be carried over a multi-drop cable configuration to service the
2540 sensor hybrids in small groups.

2541 **Schedule** Although there are still many uncertain elements at this stage, the latest schedule is
2542 shown in this section. The overall progress of development depends heavily on the advancement
2543 of the sensor. For instance, since the ASIC blueprint is based on the sensor's features, the ASIC
2544 design cannot be completed before the sensor development is finalized. This was the first principle
2545 we used to set up the schedule.

2546 At least three sensor prototypes will be produced. The first prototype, the full-size sensor pro-
2547 totype, has already been manufactured by HPK. Based on the characteristics of this sensor, the
2548 FCFDv2 and EICROC2 ASICs will be developed. Based on our experience, we can also expect that
2549 the time required to fabricate the sensor and the ASIC will be 4 months from the submission of
2550 the design. Additionally, prototypes of the the Service Hybrid (SH), electronics (FPC for BTOF and
2551 module board for FTOF), and support structure will be created based on this sensor and ASIC.

2552 Next, the design for the second full-size sensor prototype will incorporate improvements identified
2553 from the first prototype. The design will start 2 months later of starting the first sensor validation.
2554 The design of the next ASICs (FCFDv3 and EICROC3) will begin as soon as the sensor design is
2555 finalized. The SH, FPC, and stave support structure will also be developed in conjunction with
2556 this sensor and ASIC. Some characteristics of the sensor can be estimated based on accumulated
2557 knowledge, which might allow certain designs to be completed simultaneously.

2558 The second full-size sensor prototype will be the last sensor prototype, but we will make another
2559 prototype as a backup and make final adjustments for mass production. Depending on the budget,
2560 additional sensor and ASIC prototypes may be ordered.

2561 In the preproduction phase, 10% of the required number of prototypes are made in six months,

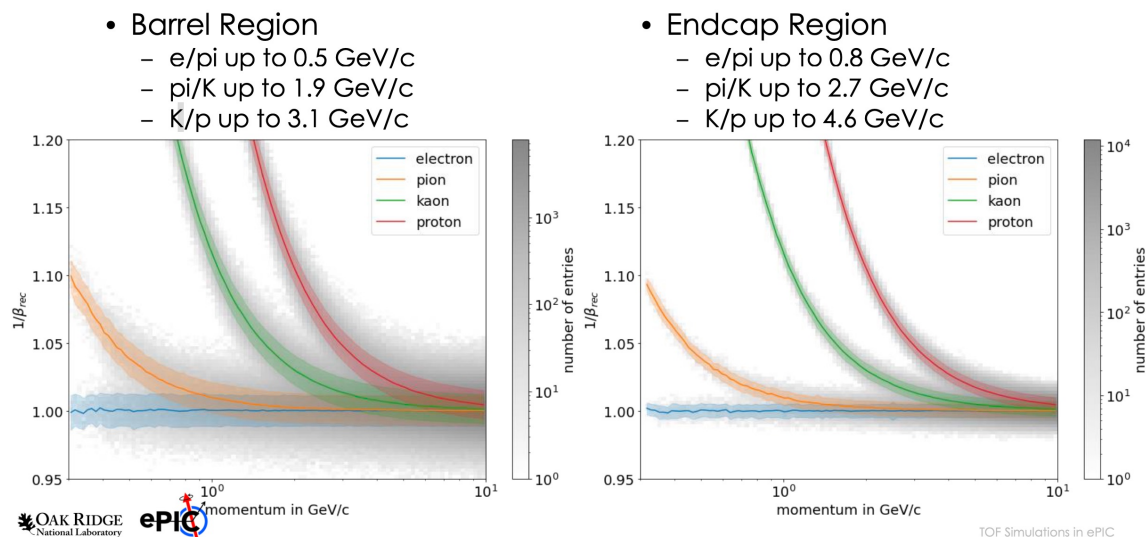


Figure 8.49: simulation of $1/\beta$ as a function of particle momentum for BTOF and FTOF performance.

2562 during which time the final confirmation for mass production is made. Then, during the Production
 2563 phase, the remaining 90% will be done in two years.

2564 During the development phase, assembly was carried out as soon as the other components became
 2565 available. However, in the preproduction and production phases, there will be a time lag between
 2566 the arrival of components and the start of assembly. This is because additional time is required for
 2567 quality assurance (QA) and quality control (QC) procedures before the components can be shipped
 2568 to the dedicated assembly sites. As a result, the preproduction and production phases will begin
 2569 two months later than other phases.

2570 **particle identification** Figure 8.49 shows an example of a single-particle response simulation of
 2571 $1/\beta$ as a function of particle momentum for BTOF and FTOF performance.

2572 8.3.4.2 The proximity focusing RICH

2573 Requirements

2574 **Requirements from physics:** The ability to identify different species of hadronic particles (pi-
 2575 ons, kaons, and protons) and to separate these from electrons will be essential for realizing much
 2576 of the EIC physics program. Particle identification capabilities in the electron going endcap region
 2577 of the ePIC detector ($-3.5 \leq \eta \leq -1.5$) will be provided by a proximity focusing ring imaging
 2578 Cherenkov detector (pfRICH). Hadrons in this region generally originate from collisions probing
 2579 low x at a given Q^2 , which is a phase space of great interest for studies in both $e+p$ and $e+A$ con-
 2580 figurations. In $e+A$ collisions this is the kinematic region where the onset of gluon saturation is
 2581 expected. Saturation generally describes novel QCD phenomena originating from the overlap of
 2582 the gluon wavefunctions, which is thought to happen at low x where gluon densities are high. This
 2583 is also a region that has never been explored by polarized $e+p$ experiments before and measure-

2584 ments of identified kaons in the backward region, for example, will provide information on the
2585 polarized strange quark distributions.

2586 Studies of physics requirements in the EIC Yellow Report define the particle identification (PID)
2587 requirements in the backwards region. Driven mostly by SIDIS measurements, the requirements in
2588 the pseudorapidity range $-3.5 \leq \eta \leq -1.5$ demand 3σ separation or better of $\pi/K/p$ for momenta
2589 $p < 7 \text{ GeV}/c$. Evaluations of particle yields and coverage of the relevant SIDIS phase space have
2590 shown that the lack of hadron PID capability for $p > 7 \text{ GeV}/c$ in the pFRICH acceptance will have
2591 little effect on the EIC physics program.

2592 The Yellow Report enumerated overall requirements on the e/h ratio and identified the need for
2593 hadron suppression on the order of 10^4 in the backward region. At high momenta, this suppression
2594 will be predominantly provided by the electromagnetic (EM) calorimeter but it is clear that at
2595 lower momenta the electron ID capabilities of the backward EM calorimeter will not be sufficient
2596 to achieve the overall required electron purity. The extra suppression power can only be met by
2597 additional PID capabilities from the RICH detector, especially in the region below $3 \text{ GeV}/c$ where
2598 the hadron distributions are at their maximum. To access low Q^2 , it is essential to provide PID in
2599 this region which includes $Q^2 = 1$ up to $\eta = -2$ and lower Q^2 up to the quasi-real photoproduction
2600 regime further backward. As low- Q^2 is correlated with low- x (at high inelasticity), e/h separation
2601 is essential to access the lowest x for the reasons outlined above.

2602 The original baseline design of the ePIC detector included ToF detectors based on AC-LGAD tech-
2603 nology in the forward, backward, and barrel regions. Their purpose was to provide PID in the
2604 momentum region below the aerogel threshold ($\lesssim 1 \text{ GeV}/c$). While physics measurements exist
2605 that require PID at low momenta in the forward and barrel region, there are no such arguments for
2606 the backward range. The main argument for the presence of a ToF detector for $\eta < -1$ was to aid
2607 in providing the start time, t_0 , for all ToF measurements in ePIC, mainly by utilizing the scattered
2608 electron. It was determined that the pFRICH, utilizing HRPPD sensors with a single photon timing
2609 resolution performance of $\sim 30\text{-}40 \text{ ps}$, could provide the same t_0 performance as a dedicated ToF
2610 system by using the copious amounts of Cherenkov photons produced as charged particles traverse
2611 the sensor fused silica windows. Thus, the dedicated backward ToF detector was removed from the
2612 ePIC baseline design meaning the pFRICH will need to provide the necessary t_0 with a resolution
2613 of $\sigma_t < 25 \text{ ps}$. This, in conjunction with vertex-time correlations, will provide a high quality t_0 for
2614 events where the scattered electron is detected in the backward region. It will also provide input in
2615 cases where the t_0 has to be derived from a bootstrap method using all timing detectors in the full
2616 ePIC coverage.

2617 **Requirements from Radiation Hardness:** The beam induced charged particle background
2618 impacts the pFRICH mainly via excess photons produced in the aerogel and fused silica windows
2619 of the HRPPD photo sensors. A fraction of the incoming photons are converted to photo-electrons
2620 (PE) by the photocathode according to its quantum efficiency. The amplification of PEs produces
2621 ions which drift towards the photocathode. These ions can react with or even sputter the photo-
2622 cathode material which leads to degradation of its quantum efficiency. HRPPD gains can also be
2623 affected by the desorption of ions from surfaces.

2624 To estimate the flux of ion back flow during the expected life span of the detector, a simulation study
2625 was performed, combining the rates from DIS events and beam gas interactions. A mass-dependent
2626 minimum energy cutoff was applied so that only particles that would produce Cherenkov radiation
2627 in the aerogel plane or HRPPD window would be considered. Each particle producing Cherenkov
2628 photons in the aerogel ($n = 1.04$) was assumed to produce ≈ 10 photons, while ≈ 100 photons were
2629 assumed from the HRPPD window ($n = 1.4$) after factoring in the QE.

2630 Convoluting an expected operating gain of 10^5 with a running period of 26 weeks/year and a
2631 luminosity of $10^{34} \text{ cm}^{-2} \text{ s}^{-1}$ yields a yearly estimate for accumulated charge of up to 0.011 C/cm^2
2632 on the photocathodes of sensors closest to the beam line. For a running period of 10 years, this will
2633 result in 0.11 C/cm^2 , or 1.1 C/cm^2 if one assume a higher gain of 10^6 to compensate the aging over
2634 time. It should be noted that the estimate of particle flux is based on realistic simulations for beam
2635 gas and DIS events. Furthermore, the rates and running period are overestimated which gives a
2636 safety factor of around 2 from the most plausible scenario. Studies to evaluate the degradation of
2637 QE with the accumulated charge are underway.

2638 **Requirements from Data Rates:** Previous data rate estimates need to be compared to rate
2639 studies above. Will add text when complete.

2640 Justification

2641 **Device concept and technological choice:** The operation of a generic proximity focusing
2642 RICH detector is based on a very simple set of principles. A charged particle passing through a
2643 thin layer of radiator (often aerogel with an appropriate refractive index) with a velocity higher
2644 than the speed of light in that medium emits Cherenkov light (photons) at an angle which is solely
2645 determined by the particle mass, momentum, and refractive index of the radiator. The 3D momen-
2646 tum of the particle is typically provided by a tracking system. If the average refractive index of
2647 the radiator is also known, measurements of the Cherenkov light emission angle can determine the
2648 particle mass, thus allowing identification of different particle species, e.g. distinguishing electrons,
2649 pions, kaons, and protons.

2650 The ePIC pFRICH was designed as a conceptually simple detector, based on proven principles,
2651 providing a high degree of performance that is practically uniform over the whole available angular
2652 acceptance in η and ϕ . In order to reach the performance requirement of 3σ separation or better of
2653 $\pi/K/p$ for momenta $p < 7 \text{ GeV}/c$, the pFRICH design was optimized in the following ways: (1)
2654 the proximity gap length was maximized as much as possible within the volume available in ePIC;
2655 (2) the radiator thickness was taken to be small enough to reduce the contribution to the single
2656 photon angular resolution to below $\sim 5 \text{ mrad}$, yet produce enough photons per track to robustly
2657 reconstruct the Cherenkov angle; (3) the HRPPD pixellation was chosen such that it contributes at
2658 most $\sim 2 \text{ mrad}$ to the angular resolution; and (4) the acrylic filter cuts off all UV light produced in
2659 the aerogel below $\sim 300 \text{ nm}$, where the $dn/d\lambda$ dependency is strongest. In addition to satisfying
2660 the PID requirements in the backward direction, the small material budget of the pFRICH design
2661 minimizes the impact on the the resolution of the endcap electromagnetic calorimeter which sits
2662 directly downstream.

2663 Subsystem description:

2664 General device description: The layout of the proposed ePIC pFRICH detector is shown in
2665 Fig. 8.50. It consists of a 1.3 m diameter and $\sim 49 \text{ cm}$ long cylindrical vessel with the outer
2666 and inner walls made from a lightweight honeycomb carbon fiber sandwich and front and
2667 rear plates made of a carbon fiber reinforced plastic (CFRP). The vessel sits 123.6 cm from
2668 the nominal interaction point. Forty-two 2.5 cm thick aerogel tiles of a trapezoidal shape are
2669 installed in individual opaque compartments in a container mounted on the upstream side
2670 of the vessel. A thin acrylic filter is installed immediately after the aerogel container. The
2671 vessel is continually flushed with dry purified nitrogen. Sixty eight HRPPD photosensors are

2672 installed in individual slots in the rear CFRP mounting plate with their fused silica windows
 2673 facing the aerogel. Inner and outer conical mirrors cover the cylindrical sides of the vessel in
 2674 order to increase the η acceptance of the Cherenkov photons produced in the aerogel radiator.
 2675 Readout boards equipped with four 256-channel EICROC ASICs are mounted on the rear
 2676 ceramic anode plates of each of the HRPPDs.

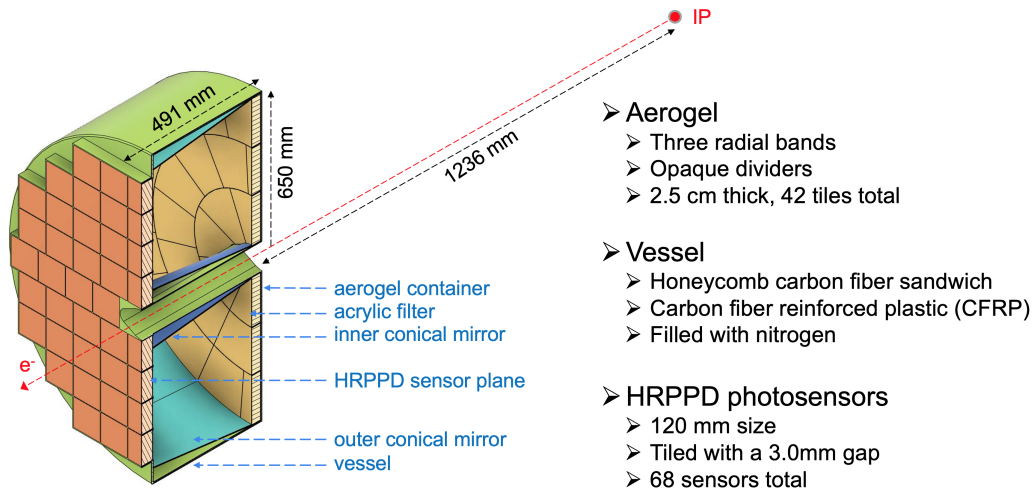


Figure 8.50: The proposed pFRICH detector. See the text for more details.

2677 Sensors: An improved version of the Micro-Channel Plate Photomultiplier Tubes (MCP-
 2678 PMTs) manufactured by Incom Inc. [41], the so-called High Rate Picosecond Photon Detectors (HRPPDs), will be used as the photosensor solution. The sensor dimensions will be
 2679 120 mm x 120 mm, with a 104 mm x 104 mm fully efficient active area in the center (75%
 2680 geometric efficiency) and will have slightly tapered 5 mm thick UV-grade fused silica win-
 2681 dows, and 3 mm thick multi-layer ceramic anode base plates. A DC-coupled variety of these
 2682 sensors will be used, with the inner side of the anode base plate patterned into 32 x 32 square
 2683 pixels, corresponding to 1024 channels per sensor, and a pitch of 3.25 mm. The sensors will
 2684 be equipped with a UV-enhanced high quantum efficiency (QE) bialkali photocathode, with
 2685 peak values exceeding 30% at 350 nm (see left and center panels in Fig. 8.51) [42]. The HRP-
 2686 PDs will be fitted with a pair of 600 μm thick MCPs with a pore diameter of 10 μm , open area
 2687 ratio in excess of 70%, and bias angle of 13 degrees in a conventional chevron configuration.
 2688 These will be operated at an amplification voltage of up to ~ 700 V to comfortably achieve an
 2689 overall detector gain above 10^6 if needed. HRPPDs will have a single photon Transit Time
 2690 Spread (TTS) of ~ 30 -40 ps (right panel of Fig. 8.51). The anode base plates will be manu-
 2691 factured from multi-layer High Temperature Co-fired Ceramic (HTCC) by Kyocera (Japan).
 2692 They will have a custom design, matching the uniform 32 x 32 pixellation on the inner (vac-
 2693 uum) side of the sensor, short shielded traces inside of the ceramic stack, and a pattern of
 2694 square pads with a smaller pitch on the outer side, matching the readout PCB design.
 2695

2696 FEE: Each sensor will be equipped with four 256-channel EICROC ASICs [43], designed by
 2697 the OMEGA group [44], each serving one quadrant of the sensor. EICROC ASICs will be built
 2698 via a 130 nm technology process, with an expected power consumption of 1-3 mW/channel
 2699 [43]. They will provide a Time of Arrival (TOA) and an ADC measurement with a dynamic
 2700 range of 1 pC for each pixel, which should be sufficient for both single photon hits (both
 2701 imaging and timing) and multi-photon hits (timing only) at a moderate HRPPD gain of a
 2702 few times 10^5 . The ASICs will be able to measure the TOA with a resolution better than 20 ps

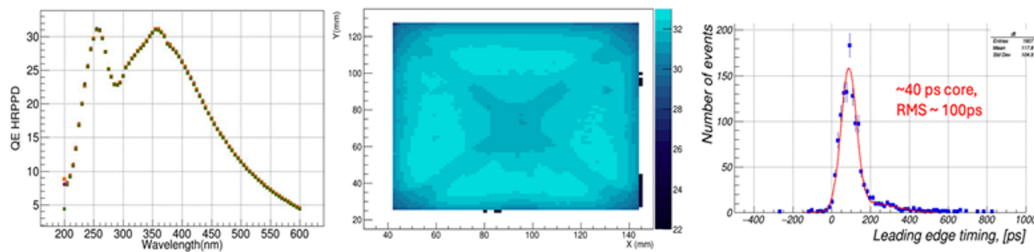


Figure 8.51: PLACEHOLDER Left: EIC HRPPD QE as a function of wavelength. Center: QE map in the full active area at a wavelength of 365 nm. Right: Single photon timing resolution (PiLas picosecond laser pulse jitter not unfolded).

2703 per pixel assuming detector capacitance on the order of ~ 10 pF, leading edge length of the
 2704 HRPPD signal below 500 ps, and collected charge of a few dozens fC achieved by tuning
 2705 the MCP gain [44]. These ballpark parameters seem to be easily within reach for pFRICH
 2706 HRPPD sensors.

2707 The ASICs will be bump bonded to the readout PCB in a “flip-chip” fashion to minimize
 2708 the parasitic capacitance of the traces inside of the PCB stack. Preliminary estimates show
 2709 that in such a scheme, where four 16×16 primary pixel arrays with a pitch of 3.25 mm are
 2710 first “compressed” to a 2.0 mm pitch inside the HRPPD ceramic base plate and then further
 2711 reduced to a $500 \mu\text{m}$ pad size in the readout PCB stack in order to ultimately match the
 2712 EICROC ASIC pitch, the combined pad and trace capacitance should not exceed 10 pF. This
 2713 is well within the expected operating range of the ASICs.

2714 Each ASIC will be connected via a dedicated copper link to its respective readout unit (RDO),
 2715 located on the outer circumference of the rear side of the pFRICH vessel. Each RDO will serve
 2716 16 EICROC ASICs, for a total of 17 RDOs. The RDOs will then be connected to a single Data
 2717 Aggregation Module (DAM). The DAM board is envisioned to be a FrontEnd Link eXchange
 2718 (FELIX) board [45] installed in the DAQ. The RDO will be connected to the DAM via a high
 2719 speed optical link capable of at least 5Gb/s throughput. The RDOs will follow the same
 2720 design used by the ePIC pixelated AC-LGAD detectors. These boards will utilize lpGBT for
 2721 aggregation of ASIC data and VTRX+ to provide the fiber interfaces. The RDO should deliver
 2722 timing signals synchronized to the beam crossings with jitter < 5 ps.

2723 Other components: In addition to the vessel structure and sensors described above, two other
 2724 components will be critical to the pFRICH: the aerogel radiators and mirrors. The pFRICH
 2725 will be equipped with aerogel tiles produced by Chiba Aerogel Factory Co., Ltd. [46] with
 2726 a nominal refractive index, $n \sim 1.040$ and a thickness of 2.5 cm. The aerogel will be cut
 2727 using a water jet technique into trapezoidal tiles providing a required radial and azimuthal
 2728 segmentation with minimal dead area. This type of aerogel will replicate the performance of
 2729 the material used in the Belle II experiment [47], and in particular, will be very transparent
 2730 in the near UV range, with an absorption length and Rayleigh scattering length in excess
 2731 of 5 mm down to ~ 275 -300 nm. The aerogel tiles will be installed in segmented containers
 2732 (slots) with $\sim 500 \mu\text{m}$ thick walls and held in place with a thin filament. The container walls
 2733 will be opaque to suppress stray photons leaking out of the aerogel tile side facets, which are
 2734 not expected to be of a high optical quality after water jetting.

2735 The pFRICH will also utilize three types of mirrors to increase the active acceptance of the
 2736 detector. The outer mirror cone consists of 12 segments approximately 40 cm in length which
 2737 sit just inside the outer wall of the pFRICH vessel. These mirrors will recover Cherenkov
 2738 photons from charged particles with large polar angles which pass through the aerogel but

2739 would exit the vessel before reaching the sensor plane. Similarly, a set of inner mirrors which
 2740 wrap around the beam pipe and surrounding support structures will reflect photons emitted
 2741 by small angle charged particles (close to $\eta \approx -3.5$) back onto the sensor plane. Finally,
 2742 small pyramidal mirrors will be placed on top of the HRPPD side walls to reflect (funnel)
 2743 photons hitting this area back into the sensor acceptance. The mirrors themselves will have
 2744 a reflectivity of approximately 90% for wavelengths between 300 and 600 nm and will be
 2745 produced at Stony Brook University using an evaporator with the CFRP substrate material
 2746 provided by Purdue University.

2747 Performance

2748 Monte-Carlo simulations: The performance of the pFRICH design was studied using a cus-
 2749 tom simulation and reconstruction software suite. The geometry of the detector, along with
 2750 other relevant characteristics such as the ePIC magnetic field map, aerogel optical properties,
 2751 mirror reflectivity, and HRPPD quantum efficiency were modeled in GEANT4 v10.05.p01 [48].
 2752 The reconstruction made use of the Inverse Ray Tracing (IRT) library, which is part of the
 2753 ePIC software stack [49], and a ROOT [50] based data structure providing access to all photo-
 2754 electron, track, and event level quantities.

2755 Parameters relevant to the performance of the pFRICH were determined by simulating sin-
 2756 gle particles thrown at a variety of energies and angles. On average, roughly 11 Cherenkov
 2757 photons were detected from particles at the saturation momentum, which is in agreement
 2758 with first principles estimates taking into account a realistic sensor quantum efficiency. The
 2759 working acceptance of the detector, defined as the region in which the ratio of tracks pro-
 2760 ducing at least one detected photon over the total number of tracks is greater than 80%, was
 2761 found to cover $-3.5 < \eta < -1.5$. Single photo-electron (SPE) and track level resolutions in
 2762 the working acceptance were also determined, with the SPE resolution being roughly 5 mrad
 2763 and independent of momentum, while the track level resolution improved with the number
 2764 of detected photons and reached a value of 1.7 mrad.

2765 The algorithm for event based reconstruction of the Cherenkov angles was validated using
 2766 multi-particle simulations. The reconstructed Cherenkov angle (in units of mrad) as a func-
 2767 tion of particle momentum (in units of GeV/c) is shown in the left panel of Fig. 8.52 and
 2768 compared to the theoretical expectations for a given mass hypothesis. It is seen that the re-
 2769 constructed angles and theoretical expectations are in good agreement, confirming that the
 2770 event based reconstruction is performing well. This plot also shows that the Cherenkov
 2771 saturation angle is approximately 295 mrad. The N_σ separation count between the electron-
 2772 pion and pion-kaon hypotheses as a function of momentum are shown in the middle and
 2773 right panels of Fig. 8.52, respectively. It is seen that 3σ separation is possible up to roughly
 2774 2.5 GeV/c for electron-pion and 9 GeV/c for pion-kaon hypotheses. Performance was found
 2775 to be relatively uniform across the whole acceptance of the detector.

2776 One of the main purposes of the pFRICH detector is to identify low momentum scattered elec-
 2777 trons in the backward direction. Specifically, it will help with separating the electrons from
 2778 π^- mesons, which are expected to dominate in the pFRICH acceptance. Using PYTHIA-6 $e+p$
 2779 collisions at 18×275 GeV, it was shown that the pFRICH will provide good π^- -electron sep-
 2780 aration for $p < 2$ GeV/c and decreasing separation power for momenta up to ~ 5 GeV/c as
 2781 seen in Fig. 8.53. The pFRICH detector therefore plays an important role in the ePIC detector,
 2782 allowing identification of the scattered electrons in kinematic region not accessible by other
 2783 detectors.

2784 Another important utilization of the pFRICH is hadron identification in the backward region
 2785 in SIDIS studies. For that reason, the ability to separate π , K , and p hadrons was studied

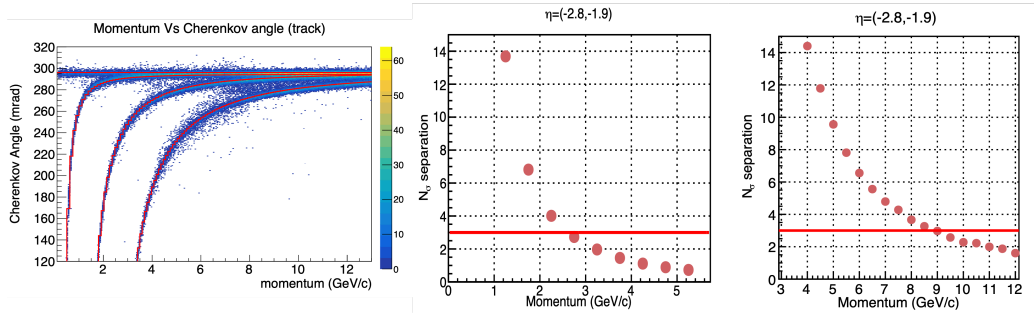


Figure 8.52: PLACEHOLDER (Left) The reconstructed Cherenkov angle for electrons, pions, kaons, and protons as a function of momentum. (Middle) N_σ separation between the electron and pion hypotheses as a function of momentum. (Right) Same as the middle panel, for pion and kaon hypotheses.

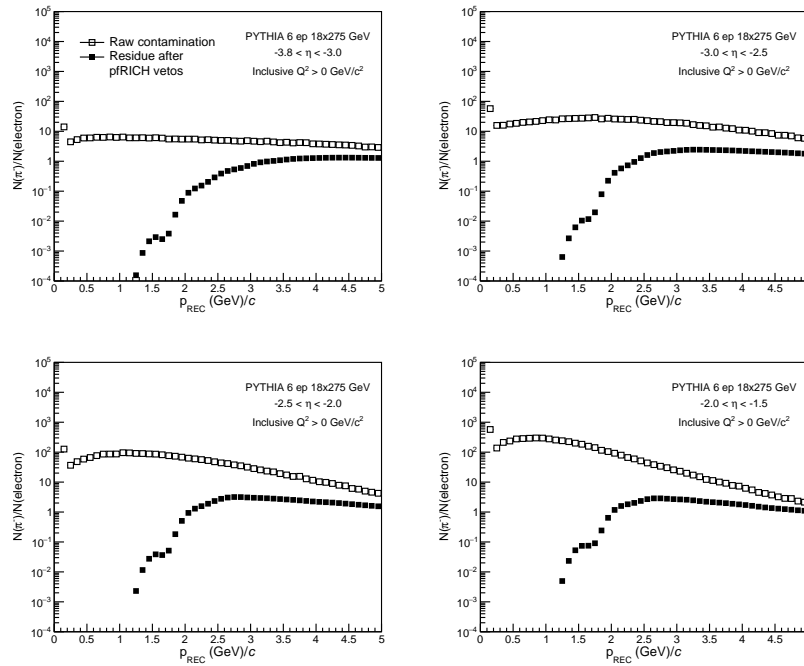


Figure 8.53: PLACEHOLDER Yield ratios of π^- / e_{scat} before (open black squares) and after (black full squares) pFRICH veto on π^- in PYTHIA 6 $e+p$ collisions at $18 \times 275 \text{ GeV}$ for four η bins, covering full pFRICH η acceptance.

2786 using simulation of $e+p$ collisions at $18 \times 275 \text{ GeV}$ in PYTHIA-8. Specifically, the expected
 2787 purity of leading K^- mesons was evaluated and was shown to be close to 100% up to hadron
 2788 momenta of $p < 6 \text{ GeV}/c$. This means that pFRICH will play an important role in SIDIS
 2789 studies as it can efficiently distinguish various hadron species in a wide momentum range.

2790 Hardware component evaluation: Hydrophobic silica aerogel manufactured by the Aerogel
 2791 Factory [46] will be used for the radiator in the pFRICH detector. Three hydrophobic aerogel
 2792 tiles, with nominal dimensions of $11 \text{ cm} \times 11 \text{ cm} \times 2.5 \text{ cm}$, density of $0.14 \text{ g}/\text{cm}^3$, and

2793 refractive index of 1.04, were ordered from the Aerogel Factory to verify and assess their
 2794 refractive index and transparency, two aerogel properties which are critical to the detector's
 2795 performance. The refractive index was determined at Temple University by measuring the
 2796 deflection of the refracted light exiting the corners of the aerogel (see QA section). The re-
 2797 fractive index measured by Temple University (n_{TU}) and the Aerogel Factory (n_{AF}) were
 2798 found to be in agreement, with a typical value of $(n_{TU} - n_{AF}) / (n_{AF} - 1) \sim 2\%$. The opti-
 2799 cal transparency was evaluated by measuring the transmittance as a function of wavelength.
 2800 Transmittance curves for each tile were measured by the Aerogel Factory using a monochrom-
 2801 ator and spectrometer (Hitachi U-4100) [51], at BNL using a monochromator and spectrom-
 2802 eter (Hitachi U-3210), and at Temple University using a LED and spectrometer setup which
 2803 provides measurements at four discrete wavelengths (see left panel of Fig. 8.54). These three
 2804 sets of measurements were found to be consistent with each other within the quoted errors.
 2805 A sufficiently high transmittance of about 68.5% at 432 nm was found when averaging the
 2806 results from three different measurements over the three produced aerogel tiles at Temple.
 2807 The wavelength dependent transmittance measurements were used to extract additional in-
 2808 formation such as clarity, transmission length, and scattering length.

2809 The mirrors will be produced by the pFRICH subsystem collaboration members, with sub-
 2810 strates fabricated at Purdue University and coating performed at Stony Brook University.
 2811 Optimization of the substrate and coating procedures is ongoing with a number of mirror
 2812 samples being produced with different substrate manufacturing techniques, coating chamber
 2813 settings, and coating material thickness. The reflectivity of the various mirror samples was
 2814 evaluated at BNL using a dedicated test stand. The best performing mirror sample, manu-
 2815 factured using a ~ 12 kilo-angstrom thickness aluminium coating, showed a measured average
 2816 reflectivity of 0.89 for wavelengths between 300 and 600 nm (see right panel of Fig. 8.54).

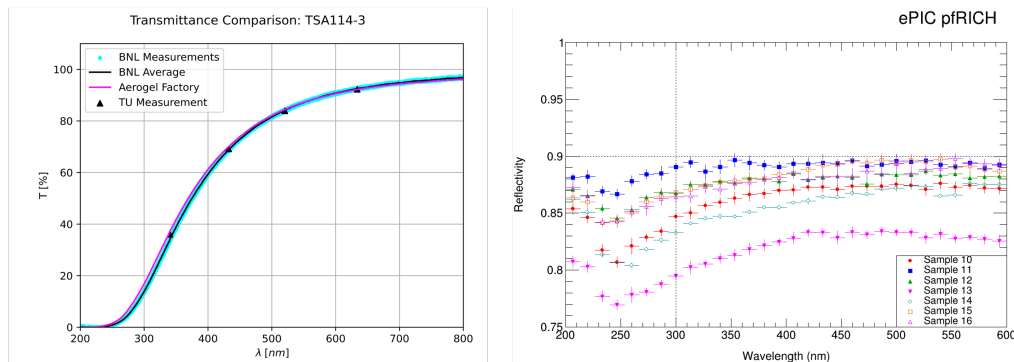


Figure 8.54: PLACEHOLDER Left: Aerogel transmittance as a function of wavelength for factory, BNL, and Temple University measurements. Right: Mirror sample reflectivities as measured at BNL as a function of wavelength.

2817 Implementation

2818 **Services:** Services relevant for the pFRICH include High Voltage (HV) and Low Voltage (LV)
 2819 systems to operate the photosensors and power the front-end electronics, respectively, a cooling
 2820 system to regulate the temperature of the electronics and sensors, and a gas system to maintain the
 2821 proper environment inside the pFRICH vessel.

2822 The HV and LV modules will be located on the electronics platform, about 15 meters away from the

2823 pFRICH detector, in a low Total Ionizing Dose (TID) environment. Therefore, standard off-the-shelf
2824 units can be used. The high-voltage system will consist of 340 individual stackable negative HV
2825 channels. Twenty three CAEN A1515BV 16-channel 1.4kV/1mA floating ground modules [52] will
2826 be used. The HV modules will be housed in a pair of CAEN SY4527 mainframes [53], equipped
2827 with additional 1200 W power module boosters. Each of the twenty three modules will be con-
2828 nected to an enclosed box distribution PCB installed on the rear side of the pFRICH vessel. The box
2829 is fed from individual 15 m long multi-conductor high voltage cables. For the HV interconnect,
2830 CERN-approved 52-pin Radiall cable connectors and receptacles will be used throughout the sys-
2831 tem. The distribution PCB will arrange five of the isolated channels of the A1515BV in a manner
2832 to provide five individual stacked voltage levels and a common ground referenced return to each
2833 HRPPD. The respective five bias levels and ground will be connected to the pads on the rear side
2834 of the HRPPDs via narrow profile Teledyne Reynolds shielded 26 AWG coaxial cables, conduc-
2835 tive vias in the Front End Board (FEB) stackup with a matching pad pattern, and custom Samtec
2836 compression interposers.

2837 The EICROC ASICs will require 1.2 V low-voltage power. Under the assumption of up to
2838 3 mW/channel power dissipation this corresponds to 3 W power (or up to 2.5A current) per pho-
2839 tosensor FEB. Accounting for other electronics components present on such a FEB, and providing
2840 a 20% safety margin, we estimate the total power consumption to be less than 300 W for the whole
2841 system. This number is used as input for designing the cooling system discussed below. We will
2842 be using a single Wiener MPOD Mini LX crate with a MPOD-C controller and four MPV4008I1
2843 4-channel LV modules [54]. One Low Voltage channel will serve four FEBs. 15 m long tray rated
2844 10 AWG jacketed cables with 20AWG (sense wires) will run between the electronics platform and a
2845 LV distribution panel on the rear side of the pFRICH vessel. From there, 18 AWG multi-conductor
2846 cables will distribute power to the individual FEB cards.

2847 The pFRICH cooling system will consist of several off-detector components and a few on-detector
2848 thermal interfaces and assemblies. The primary heat dissipating components will be the ASICs,
2849 which are anticipated to produce just over 1 W each (4 W per module), or about 300 W for the 68
2850 total modules. In addition to the ASICs, the sensors are anticipated to dissipate just under 1.5 W
2851 each or 100 W total. Conservatively, the total power output will be roughly 400 W. Following the
2852 geometry, each row of sensors will have its own pair of titanium cooling tubes directly over the
2853 ASICs. The pair of tubes that contact the same row of sensors will be in series, and all rows will be
2854 in parallel with each other. The tubes will be attached to aluminum plates with thermal epoxy, and
2855 a gap pad between the plate and ASIC will maximize thermal contact. Using a stock tube of 0.25"
2856 OD and 0.218" ID and maintaining a minimal temperature gradient in the water allows the mass
2857 flow rate to be calculated. From there the Reynolds number and pressure drop can be determined,
2858 confirming the viability of the system. Additionally, a finite element analysis (FEA) was performed
2859 to confirm the water temperature difference and determine the thermal gradient across the various
2860 components. With the described configuration, the sensors reach a maximum temperature of about
2861 32 C in the analysis.

2862 The three primary off-detector elements of the cooling system are a Polyscience chiller, Chilldyne
2863 circulator, and a distribution panel. The Polyscience chiller will allow the water to be slightly colder
2864 than room temperature, or about 15 C, which is the lowest recommended temperature without
2865 nearing the dewpoint in the interaction region. The unit is also capable of flowing about 10 liters
2866 per minute (lpm), dissipating about 800 W at that temperature and maintaining the temperature
2867 within +/-0.1 C. The Polyscience chiller would be paired with a Chilldyne negative pressure system
2868 capable of circulating water at about 8 lpm and ~10psi. It offers a significant advantage over a
2869 positive pressure solution, as if there is a leak in the system, it will draw air into the tube instead of
2870 letting water out and potentially damaging electrical components.

2871 The gas system for the pFRICH detector is designed to circulate dry nitrogen at precise pressure
2872 and flow rates to remove moisture from within the pFRICH chamber. High-purity nitrogen (H_2O
2873 $< 3 \text{ ppm}$) will be supplied from cryogenic sources. To provide secondary protection, moisture traps
2874 such as silica gel dryers will be installed near the nitrogen source. The system will maintain both
2875 the required moisture levels and gas purity by ensuring that it is sufficiently gas tight and that
2876 the chamber is kept at a slight overpressure (4 mbar) above atmospheric pressure, preventing any
2877 infiltration of ambient air. A $0.5 \mu\text{m}$ filter will be added near the source to capture dust particles. A
2878 standby nitrogen source will be available to ensure continuous operation in the event of a primary
2879 source failure. To manage fluctuations in the source pressure, a digital pressure outlet controller
2880 will be used. Additionally, nitrogen flow will be regulated by a non-pressure-limiting digital mass
2881 flow controller. The nitrogen flow rate is expected to allow several complete volume exchanges per
2882 hour, with the precise rate to be finalized later.

2883 Pressure inside the chamber will be controlled using a tank blanketing pressure regulator, which
2884 maintains a positive internal pressure relative to varying atmospheric conditions. An overpressure
2885 protection bubbler will serve as a safeguard against excessive pressure within the chamber. To
2886 ensure uniform nitrogen distribution and prevent localized air pockets, nitrogen will be introduced
2887 into the chamber at two locations near the top side of the pFRICH vessel, closer to the aerogel plane,
2888 and exhausted through two openings near the sensor plane at the bottom. All exhausted gases will
2889 be vented outside the experimental area. The entire gas system will undergo pressure testing at
2890 1.5 times the operating pressure to ensure integrity. For monitoring and troubleshooting, pressure
2891 gauges and transmitters will be installed, with critical data such as chamber pressure and flow
2892 archived for reference.

2893 **Subsystem mechanics and integration:** The shell that creates the volume of the detector will
2894 be made primarily of carbon fiber to optimize the radiation length in ePIC. Specifically, the sensor
2895 plane is intended to be made from a bulk carbon fiber layup at approximately 14.7mm thick at its
2896 thickest point. The bulk carbon fiber will be molded and CNC-cut to allow for individual sensor
2897 frames and staves to be bonded in-place to create 68 sensor pockets along this plane of the detector.
2898 Each individual HRPPD sensor will be added into the sensor plane from the outside of the vessel
2899 and sealed in each of the sensor pockets with a face seal. The overall plane will be sealed to the
2900 cylinder at the outer and inner walls using a tightly spaced bolt-pattern and an o-ring groove on
2901 the upstream end of the sensor plane to accommodate another face seal.

2902 On the upstream end of the vessel, the aerogel plane will be made from a carbon fiber honeycomb
2903 layup around $1/4''$ thick. The outer and inner circumferences of the aerogel plane will house a
2904 sealing ring made from bulk carbon fiber and an o-ring groove to create a face seal. Attached to
2905 this aerogel plane will be a web of carbon fiber that creates radial rows of pockets for the aerogel
2906 to be placed in. These tiles will be held into the pockets using a thin transparent line strung across
2907 the opening in order to contain them in place.

2908 The cylindrical portion of the vessel is comprised of identical end rings on the upstream and down-
2909 stream end that house the threaded bolt holes and sealing surfaces for the sensor plane and aerogel
2910 plane face seals. These end rings are approximately $3/4''$ (on the bolting surface) and $1''$ in thick-
2911 ness (in the z-direction). They are made from bulk carbon fiber and contain threaded inserts that
2912 are placed by CNC-machining the insert locations and bonding and threading them into place. The
2913 rest of the cylinder is made from single sheets of carbon fiber on the inside and outside of the vessel,
2914 as well as a $3/4''$ nomex honeycomb layer in between.

2915 The inner wall of the cylinder is created in a similar manner to the outer wall, namely a honeycomb
2916 construction with the end rings embedded into both ends for bolting and sealing to the aerogel and
2917 sensor planes. However, the shape of the inner wall is made such that there is 5 mm of clearance

2918 (radially) from the beam pipe flange that the pFRICH will need to pass by to be installed in ePIC.
2919 This makes the shape of this inner wall similar to an egg or an avocado.

2920 Lastly, the conical mirrors are designed such that they are attached solely to the sensor plane. This
2921 is being done to ensure that the mirrors can be controlled in relation to the sensors and will be
2922 unaffected by manufacturing misalignments and tolerance stack-up issues throughout the rest of
2923 the vessel. As such, they will hang cantilevered perpendicular the sensor plane for both the inner
2924 and outer mirrors. The outer mirrors will be concave and the inner mirrors will be convex. The
2925 construction will be a combination of a molded, bulk carbon fiber base with a bonded lexan sheet
2926 on top of it (which will have been deposited with a mirror film).

2927 Once the pFRICH has been fully assembled and ready to be placed in the overall ePIC detector,
2928 it will be moved around the assembly hall on a cart. The cart will integrate lifting eyelets for the
2929 installation of the pFRICH into ePIC, rails identical to its final location, and wheels to transport,
2930 store and work on the detector when it is out of the barrel. This tooling will allow us to lift the cart
2931 with the pFRICH secured in place with the crane in the detector hall, position it against the barrel,
2932 align the rails, and transfer the pFRICH into its final position by translating it along the z-axis.

2933 **Calibration, alignment and monitoring:** A laser-based system will be used to monitor the
2934 pFRICH performance throughout its operational life. The purpose is to monitor, on a pixel-to-pixel
2935 basis the single photon timing resolution, the single photon pulse height amplitude (HRPPD gain),
2936 HRPPD QE, and the relative delays between channels on a few ps level. The system will also
2937 monitor the reflectivity of the conical and pyramidal mirrors. To measure the timing resolution,
2938 an array of six fibers is introduced inside the detector volume from the aerogel side which casts a
2939 broad profile of low-intensity light onto the sensor plane such that each HRPPD pixel accumulates
2940 some number of single photon hits after a given number of laser pulses. The distance between
2941 a given fiber tip and an HRPPD pixel (minimum of 40 cm) defines the flight time for photons
2942 emitted from this fiber, hence the distribution of reconstructed flight times will reveal the timing
2943 resolution for this single pixel. Similarly, a separate array of six fibers is arranged such that emitted
2944 photons reflect off of the outer mirror surface before impinging on the HRPPDs. In this case, the
2945 single photon counting rate is monitored for any degradation over time, which would indicate the
2946 deterioration of either the photocathode quantum efficiency or mirror reflectivity, or both.

2947 The pFRICH monitoring system deploys a picosecond PiLas laser which produces a 405 nm laser
2948 beam with a nominal ~ 45 ps pulse width. The beam is coupled to a custom 1-to-14 optical fiber
2949 splitter by Thorlabs, that evenly distributes the light into arrays of fibers routed into the detector
2950 vessel. Two additional fibers are connected to silicon photodiodes to provide laser signal quality
2951 verification and an initial timestamp (t_0). A custom-sized 5 mm \times 5 mm engineered diffuser is used
2952 to generate a uniform 50° square pattern to optimize the intensity profile emitted from each fiber.
2953 Additionally, a fiber delay line is added to each fiber branch to provide the ability to easily separate
2954 out in time photons originating from a given fiber. In all, there are three sets (segments) of fibers
2955 downstream of the splitter that deliver photons from the laser to the detector vessel: delay fibers,
2956 long extension fibers, and fibers mounted permanently inside the detector vessel. Finally, multiple
2957 fast photodiode sensors are used to sample the laser light before and after the splitter to monitor
2958 the light output intensity and the timing performance.

2959 A relative alignment of the conical mirror segments inside of the vessel, and surface mapping will
2960 be performed on a fully assembled detector (up to the front wall removed) prior to the installation
2961 in ePIC, by using a 3D scanning system which is being built now for the purposes of first article
2962 mirrors QA assessment. The vessel as a whole will be aligned in ePIC after the installation, fol-
2963 lowing a generic procedure developed by EIC engineers for all detector subsystems. Appropriate
2964 survey targets will be mounted on the rear and barrel sides of the vessel if required.

2965 **Status and remaining design effort:** As shown in the previous text, the present pFRICH de-
 2966 sign fully meets the EIC Yellow Report requirements and subsequent amendments (see perfor-
 2967 mance section):

- 2968 • Pseudorapidity coverage from -3.5 to -1.5 in the electron-going endcap
- 2969 • π/K separation on a 3σ level up to 7 GeV/c in this whole acceptance
- 2970 • ~ 20 ps timing reference for ePIC ToF subsystems in the barrel and the forward endcap
 2971 by combining single photon signals from aerogel and signals from multi-photon flashes of
 2972 Cherenkov photons produced by charged particles in HRPPD fused silica windows

2973 R&D effort: The pFRICH design is based mostly on proven technologies, therefore, the re-
 2974 maining R&D effort is fairly small. FY25 R&D activities (partly funded through eRD110
 2975 consortium) will be limited to HRPPD aging studies, which will be performed at JLab and
 2976 INFN Trieste.

2977 E&D status and outlook: Several engineering design activities and first article productions
 2978 described earlier in the text in more detail have been performed in FY24, and will continue
 2979 into FY25:

- 2980 – Full size mirror production and quality assessment
- 2981 – First article pFRICH vessel outer shell production
- 2982 – Adjustments of the production process of CFRP-based parts, mirror substrates and
 2983 HRPPD pockets in the sensor plane in particular
- 2984 – Fine tuning of the aerogel refractive index and bulk uniformity measurement procedure
- 2985 – HRPPD sensor design modifications required after the first batch was produced
- 2986 – HRPPD performance confirmation in the ~ 1.7 T magnetic field typical for a pFRICH
 2987 location in ePIC

2988 Other activity needed for the design completion: The readout backplane design cannot be
 2989 fully completed at this stage because of the unavailability of a final design iteration of the
 2990 anticipated ASIC chip (EICROC) in either of its low channel count configurations (64, 128 or
 2991 256 channels).

2992 The performance of the pFRICH in its anticipated configuration needs to be confirmed in a
 2993 beam test for both Cherenkov photon imaging and timing in the whole momentum range re-
 2994 quired for e/π , π/K and K/p separation. Such a beam test will be performed with electron
 2995 and hadron beams at Fermilab in Spring 2025, with an extensive use of first article compo-
 2996 nents (outer vessel shell, aerogel, mirrors, HRPPDs).

2997 Status of maturity of the subsystem: The design of the pFRICH subsystem is in a fairly ma-
 2998 ture state. As described in previous sections, the pFRICH consists of a cylindrical vessel with
 2999 two endcap plates, an aerogel tile plane, an HRPPD sensor plane with onboard electronics,
 3000 mirrors and a number of subsystems (HV and LV, cooling, gas, light monitoring). Engineer-
 3001 ing design of all of these components (except for the HRPPD ASIC backplane for reasons
 3002 explained in section 3.4.3) is by now sufficiently advanced to be more than 60% ready by the
 3003 CD-2 EIC Project phase at the end of 2025.

3004 **Environmental, Safety and Health (ES&H) aspects and Quality Assessment (QA) plan-**
3005 **ning:** The environmental, safety, and health impacts of the pFRICH subsystem are expected to
3006 be minimal. When installing and integrating the pFRICH into the overall detector, all applicable
3007 safety standards (i.e. OSHA, Critical Lift procedures, etc.) will be followed and adhered to. Fur-
3008 thermore, the composition of the vessel itself consists mainly of carbon fiber, epoxy, and plastic and
3009 any (small) excess can be retained for future use or disposed of via standard waste streams. The
3010 operation of the detector will require a modest 400 watts of cooling power and the working gas is
3011 pure nitrogen which does not pose any greenhouse concerns.

3012 The individual HRPPDs, mirrors, and aerogel tiles used in the pFRICH will all undergo rigorous
3013 quality assessment (QA) checks to ensure that their operation and/or properties are within accept-
3014 able limits. Beyond the testing done by the manufacturer, the performance of individual HRPPDs
3015 will be evaluated using test stands located at BNL, JLab, and possibly Yale University. While the
3016 details of the test stands differ, they all consist of a light-tight enclosure to house the HRPPD, a
3017 fiber-coupled light source (either a pulsed laser or a monochromator), an optical assembly to focus
3018 the light onto the sensor, power supplies, and readout electronics. The gain uniformity, quantum
3019 efficiency, photon detection efficiency, and dark count rates will be determined over the entire ac-
3020 tive photosensor area. In addition, the use of a Menlo Systems Elmo 780 femtosecond laser at BNL
3021 will allow precision determination of the timing characteristics of the sensors.

3022 The reflectivity of the mirror samples produced at SBU is determined using a dedicated test stand
3023 at BNL. The setup consists of a monochromator light source, dark box, optical assembly, and mo-
3024 torized sample and sensor mount. Light from the monochromator is fed via fiber to the optical
3025 assembly where a beam splitter directs a fraction of the light to a reference photodiode and passes
3026 the remaining beam to focusing elements and then on to the mirror and measurement photodiode.
3027 The mirror sample and measurement photodiode sit on independently rotating platforms allowing
3028 measurements at a variety of angles. The mirror reflectivity is determined by taking the ratio of the
3029 photodiode current with and without the mirror present. Variations in the monochromator light
3030 source intensity are corrected using the reference photodiode. This stand is designed to evaluate
3031 mirror test samples with a maximum size of several square centimeters. Detailed QA and mapping
3032 of the detector mirrors will be performed *in situ* before the pFRICH vessel is sealed during final
3033 assembly. A dedicated 3-D scanner will be constructed for this purpose utilizing the techniques
3034 developed with the sample test stand.

3035 The aerogel quality assessment will be performed at Temple University and include assessments of
3036 the refractive index, transparency, uniformity and mechanical specifications. So far, the refractive
3037 index has been determined from the Fraunhofer method by measuring the deflection of the light
3038 passing through the corner of the aerogel tile. Work is currently underway to develop a setup and
3039 approach that is based on measuring changes in the polarization between the light incident on the
3040 aerogel and the light that is reflected from its surface. This would allow for localized refractive
3041 index measurements to ensure not only the aerogel has the proper mean refractive index, but also
3042 its uniformity across the whole tile. Transparency QA will make use of wavelength dependent
3043 transmittance measurements carried out using a newly commissioned and validated UV/VIS LED-
3044 spectrometer system. The transmittance data will be fitted with the Hunt Formula to extract aerogel
3045 properties such as the scattering surface coefficient and clarity, as well as the wavelength dependent
3046 properties which include the transmittance, transmission length, and scattering length. The density
3047 will be calculated by measuring the aerogel mass using a precision scale (100 μ g) and volume
3048 via caliper and touch probe. Reference jigs can be made to ensure that the aerogel mechanical
3049 specifications such as the side-to-side length, tile height, and surface planarity variations are within
3050 acceptable ranges.

3051 **Construction and assembly planning:** The pFRICH has been designed such that it can be
 3052 fully assembled and inserted into ePIC in one piece. Individual components such as vessel walls,
 3053 sensor and aerogel planes, mirrors, HRPPDs, and aerogel tiles will be manufactured and tested at
 3054 various locations and then shipped to BNL for final assembly. It is envisioned that final subsystem
 3055 assembly will take place in a cleanroom or dedicated lab space within the physics building at BNL.
 3056 Once assembled, the pFRICH will be transported by truck roughly 1.3 miles to the experimental
 3057 hall where it will be integrated with the other ePIC subsystems.

3058 The assembly of the pFRICH itself will proceed via the following general steps: (1) assemble the
 3059 aerogel plane by fastening it to the outer and inner walls, (2) place the sub-assembly such that the
 3060 upstream end is facing down, (3) add aerogel tiles and aerogel retaining system into the aerogel
 3061 plane, (4) pre-assemble most of the sensor plane by affixing the inner and outer mirrors and any
 3062 vessel services (i.e. inner gas tubing, laser monitoring system, etc.) to the sensor plane, (5) lift
 3063 the sensor plane over the rest of the vessel and lower the sensor plane and mirrors into place, (6)
 3064 fasten the sensor plane to the subassembly at the inner and outer walls, completing the cylindrical
 3065 vessel, (7) systematically insert and secure the individual HRPPD modules into the back of the
 3066 sensor plane, (8) lift the completed pFRICH, rotate it into its operating position, and install it onto
 3067 the transportation/storage cart.

3068 **Collaborators and their role, resources and workforce:** The pFRICH Detector Subsystem
 3069 Collaboration (DSC) member institutions, as well as other affiliated groups are listed in the table
 3070 below, along with their anticipated commitments.

Institution	Role	Workforce	Resources
Brookhaven National Lab	Project lead HRPPD and mirror testing Gas, cooling, HV & LV systems, DAQ Detector and physics simulation	5 Staff	HRPPD test stands (pico/femto-second laser, dark box with a motion control, high performance scope, waveform digitizers) Mirror test stand (monochromator) Sample temperature control chamber
Chiba University*	Connection to aerogel factory	N/A	Aerogel production equipment
Duke University	Detector modeling	1 Staff	
INFN Genova*	HRPPD B-field studies	1 Staff	
INFN Trieste*	Detector modeling HRPPD aging and B-field studies	1 Staff	HRPPD test stand (laser, dark box, waveform digitizers)
Jefferson Lab*	Mechanical design EIC Project Support HRPPD testing	2 Staff	HRPPD test stand (laser, dark box, motion control, digitizers)
Ljubljana University & JSI*	Expert input on detector design	N/A	
Mississippi State University	Laser monitoring system	1 Staff, Students	
Purdue University	Vessel and mirror fabrication	2 Staff, Students	Machine shop / fabrication lab
Stony Brook University	Vessel fabrication Mirror coating	1 Post-Doc, Students	Mirror coating chamber Vessel form
Temple University	Aerogel testing and QA	1 Staff	Aerogel test stand
University of Debrecen	HRPPD backplane design & fabrication	1 Staff	
University of Glasgow	MCP-PMT evaluation	1 Staff, Students	MCP-PMT test stand (laser, dark box, cosmic ray stand, electronics)
Yale University	Software support HRPPD QA	1 Staff, Students	HRPPD test stand (dark box with motion control, digitizers)

* No institutional commitment

Figure 8.55: PLACEHOLDER Institutions contributing to the pFRICH effort and their roles, resources, and participating workforce.

3071 **Risks and mitigation strategy:** A number of risks has been identified in the past, and mitiga-
 3072 tion strategies developed.

3073 A reliable large area highly pixellated photosensor with a high quantum efficiency and single pho-
 3074 ton timing resolution better than ~ 50 ps is a core component of the pFRICH design. The pFRICH
 3075 team, together with the EIC eRD110 consortium (Photosensors) has been routinely working with
 3076 one of the two manufacturers remaining on the market (Incom Inc.) for several years to help the
 3077 company re-design their HRPPD sensors so they fully meet EIC specifications. The ongoing evalu-
 3078 ation of the first seven EIC HRPPDs produced in 2024 shows that overall quality, as well as repro-
 3079 ducibility of parameters verified so far (quantum efficiency in particular) meet the requirements.
 3080 As a fallback photosensor solution, we consider Photek Auratek MCP-PMTs. Such a PMT has been
 3081 ordered already, and its performance will be evaluated against the pFRICH detector needs in FY25.

3082 Aerogel tiles of required quality can be produced in a very few places worldwide. The pFRICH
 3083 team, together with the EIC Project, has been routinely working with the Aerogel Factory in Japan
 3084 over the last two years, to make sure the quality and production capacity meet our requirements.
 3085 A technical lead of the Chiba Aerogel Factory in Japan is also a member of the pFRICH DSC, see
 3086 Fig. 8.55. Our simulations show, that in case Aerogel Factory cannot produce sufficiently large tiles
 3087 to cover the whole front wall of the vessel in a configuration with three radial bands as shown
 3088 in Fig. 8.50, one can resort to using tiles of a readily available size up to 145 mm in a four-band
 3089 configuration, with an acceptable loss of performance caused by additional dead area introduced
 3090 by an extra row of radial spacers between the tiles.

3091 **Additional Material** Additional material will be provided on a number of subjects, including:

- 3092 • pFRICH performance from simulation
- 3093 • π /k/p and e/h separation performance
- 3094 • Aerogel and mirror test stand results
- 3095 • Fabrication procedures
- 3096 • Test stand details

3097 8.3.4.3 The high performance DIRC

3098 Requirements

3099 **Requirements from physics:** The PID system in the central section of the ePIC detector must
 3100 provide at least 3 standard deviations of separation of π/K up to 6 GeV/c, and contribute to low
 3101 momentum e/π identification.

3102 **Requirements from Radiation Hardness:** The anticipated radiation dose in the hpDIRC op-
 3103 tics and its potentially sensitive readout electronics are predicted to be modest. These estimates
 3104 are based on minimum-bias 10×275 GeV e+p events from PYTHIA. The maximum machine lumi-
 3105 nosity over a six-month period of annual operation at 100% machine and detector efficiency for a
 3106 total of 10 years was assumed. Under these conditions, the total dose from electromagnetic and
 3107 hadronic radiation is expected to be less than 100 rad. The 1-MeV-neutron-equivalent fluence is
 3108 expected to reach 10^{10} neutrons per cm^2 .

3109 **Requirements from Data Rates:** The expected hit rate of 25 kHz per cm² for the hpDIRC
3110 was estimated using detailed Geant4 simulations, incorporating the Pythia event generator. This
3111 estimation assumes the baseline MCP-PMT sensors, which typically have a dark count rate of ap-
3112 proximately 1 kHz per mm², or 0.09 kHz per pixel.

3113 **Justification**

3114 **Device concept and technological choice:** A radially compact detector based on the DIRC
3115 (Detection of Internally Reflected Cherenkov light) principle, a specialized type of RICH counter,
3116 is appropriate. It employs solid, long, rectangular-shaped radiators made of synthetic fused silica,
3117 which also serve to guide the Cherenkov photons to outside the central region for readout. This
3118 design allows the active radiator section to remain radially compact, minimizing its impact on the
3119 performance of neighboring systems and simplifying the system integration.

3120 The photons are recorded by an array of pixelated photon sensors mounted on the back of the
3121 expansion volume. As a result of the excellent optical finish of the optical components, the emission
3122 angle of Cherenkov photons with respect to the particle track is maintained during the photon
3123 transport via the total internal reflection. This angle can be reconstructed for each track from the
3124 measured position of the photon on the detector surface and the measured arrival time of each
3125 photon.

3126 The general concept of a barrel DIRC detector was first successfully demonstrated by the BaBar
3127 DIRC and followed by several other experiments worldwide. The ePIC high-performance DIRC
3128 (hpDIRC) takes advantage of the lens-based focusing concept of the PANDA Barrel DIRC, and has
3129 also several other advancements to meet the performance requirements of the Electron-Ion Collider
3130 (EIC). The hpDIRC concept for ePIC was developed as part of the EIC generic R&D program per-
3131 formed by the EIC PID collaboration (eRD14) and direct EIC Project R&D eRD103 with the focus
3132 on extending the momentum coverage well beyond the DIRC counter state-of-the-art at that time.

3133 **Subsystem description:**

3134 General device description:

3135 The baseline design of the ePIC hpDIRC detector, as implemented in a detailed and test
3136 beam-vetted Geant4 simulation, is shown in Fig. 8.56. It is divided into twelve optically
3137 isolated sectors, each composed of a bar box and a readout box. These 12 sectors surround
3138 the beamline in a 12-sided polygonal barrel with an inner radius of about 760 cm.

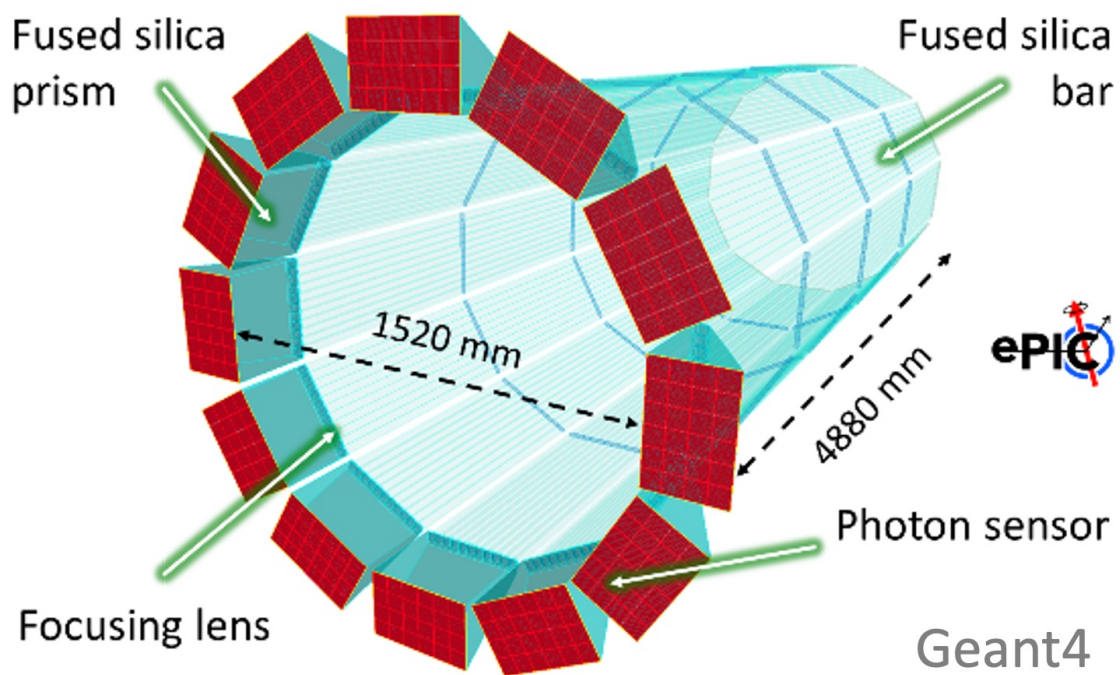


Figure 8.56: ePIC hpDIRC geometry in the Geant4 standalone simulation.

3139

8.3.4.4 The dual radiator RICH

3140

3141

3142

3143

3144

3145

3146

3147

3148

3149

Requirements The dual radiator Ring Imaging Cherenkov (dRICH) detector is part of the particle identification system in the forward (ion-side) end-cap of the ePIC detector and complements the forward time-of-flight system and calorimetry, see Fig. ???. The dRICH has to provide acceptance in the pseudo-rapidity range defined by the ePIC beam pipe and the barrel detector and to operate within the limited envelope allowed by the rest of the compact and hermetic ePIC detector. Distinctive features of the detector are: use of aerogel and gas radiators to extend the covered momentum range, usage of solid-state photomultiplier (SiPM) to ensure single photon detection capability in high and not-uniform magnetic field, non-conventional optics with curved active surfaces and compact readout electronics to fit into ePIC.

3150

3151

3152

3153

3154

3155

3156

3157

3158

3159

3160

3161

3162

3163

3164

Requirements from physics: The dRICH is required to provide continuous hadron identification from ~ 3 GeV/c to ~ 50 GeV/c, and to supplement electron and positron identification from a few hundred MeV/c up to about 15 GeV/c. Such an extended momentum range imposes the use of two radiators, gas and aerogel, with a common imaging system to ensure compactness and cost-effectiveness. The radiator gas must ensure π/K separation at $3\text{-}\sigma$ level up to 50 GeV/c in the most forward region, namely for $\eta > 2$. The aerogel radiator must cover the intermediate momentum interval, bridging the upper limit of the time-of-flight (≈ 2.5 GeV/c) to the Cherenkov threshold of the dRICH gas (≈ 12 GeV/c). These requirements dictate the prescriptions on the refractive index and the radiator chromaticity in the sensitivity region of the photosensors. The dRICH has to provide open acceptance in the ePIC forward pseudo-rapidity range $1.5 < \eta < 3.5$. To provide proper light focalization within the due volume, the dRICH active area is located behind the shadow of the barrel detector and its support ring, close to the MARCO solenoid coils. In this region, see Fig. ??, the $\approx 1T$ strong and not-uniform ePIC magnetic field imposes the use of unprecedented detectors (SiPM).

3165

3166

3167

3168

3169

Requirements from Radiation Hardness: The radiation sensitive components (sensor and front-end electronics) of the dRICH detector are concentrated in a region of moderate radiation level, below $O(10^{11})\text{ cm}^{-2} n_{eq}$ of maximum integrated fluence where n_{eq} is a 1-MeV neutron equivalent particle, see Fig. ???. Close to the beam line, where the integrated dose can reach a value of 15 krad, only radiation tolerant materials reside like silica aerogel [55].

3170

3171

3172

3173

3174

3175

3176

3177

Requirements from Data Rates: The SiPM sensor features an intrinsic significant dark count rate, currently of the order of 50 kHz/mm² at room temperature, that indefinitely increases with the radiation damage. To mitigate this effect, the dRICH sensors are operated at low temperature (less than -30 C) and regularly annealed at high temperature (up to 150 C), in order to never exceed a maximum 300 kHz dark rate per channel. The latter value corresponds to a conservative limit taken to preserve the detector performance requirements for Physics and it is supported by present simulation studies that confirm the particle-identification capabilities of dRICH are unaffected.

3178

3179

3180

3181

Justification The specifications outlined above largely define the main technological choices: the momentum range dictates radiator refractive indexes that can be reliably met only by aerogel and gas, while the ePIC environment, space and magnetic field, imposes sensor characteristics that can only be met by SiPM.

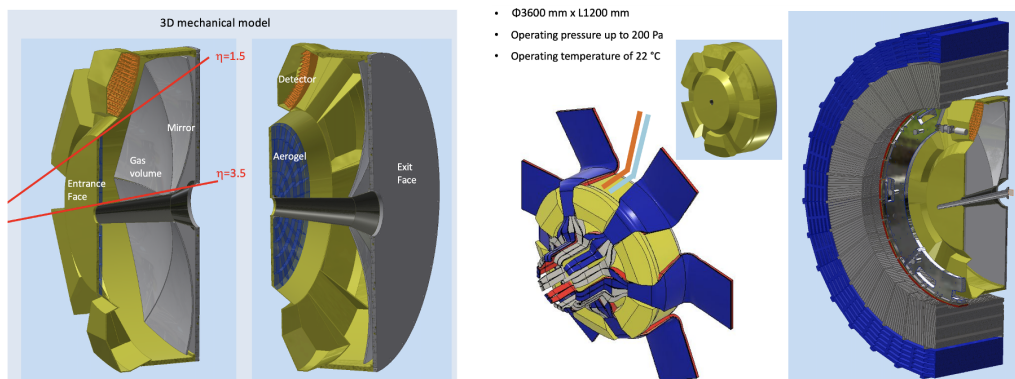


Figure 8.57: (Left) dRICH detector model with highlighted the major components. (Right) dRICH inside the ePIC services lines at the barrel HCAL end point.

3182 **Device concept and technological choice:** The dRICH is a ring-shaped detector fitting
 3183 inside the ePIC forward endcap, see Fig. 8.57. The essential components are a layer of aerogel
 3184 radiator, a volume of gas radiator, and an array of mirrors focalising the Cherenkov light into
 3185 compact areas instrumented with photo-sensors. The detector is designed in a modular way,
 3186 with 6 sectors around the beam line of equivalent mirror set and detection area.

3187 The aerogel radiator is an amorphous solid network of SiO_2 nanocrystals whose density regu-
 3188 lates the refractive index and chromaticity [3]. The use of silica aerogel for RICH detectors
 3189 is well established. It is available with refractive indices in the range 1.006–1.08 in between
 3190 gases and liquids. The current manufacturing methods succeeded in improving the attenu-
 3191 ation length Λ ($\lambda = 400 \text{ nm}$) from 20 mm (aerogel used in HERMES) to 50 mm (aerogel
 3192 for CLAS12 and BELLE-II). The selected aerogel radiator has refractive index $n = 1.026$ at
 3193 $\lambda = 400 \text{ nm}$. The chromatic dispersion has been measured during the R&D phase to be
 3194 $dn/d\lambda = 6 \cdot 10^{-6} \text{ nm}^{-1}$ at 400 nm wavelength. Aerogel is typically produced in tiles of few
 3195 cm thickness: in order to minimize edge effect, the dRICH tile side should be greater than 18
 3196 cm, approaching the world record value of 20 cm. The shape and surface flatness of the tiles
 3197 are important parameters to consider for ensuring optimal PID performance. Typically, due
 3198 to the fabrication process, aerogel tiles exhibit a slight meniscus shape. Measurements taken
 3199 during the R&D phase on aerogel samples provided by Aerogel Factory Co. Ltd revealed
 3200 deviations from the ideal parallelepiped shape by a few tenths of a millimeter, along with
 3201 a thickness variation between the center and the edges of a similar magnitude. Based on
 3202 the measurements conducted so far, this deviation from the ideal shape does not impact PID
 3203 performance. Additionally, the manufacturer, Aerogel Factory Ltd (Chiba, JP), has confirmed
 3204 that improvements in both flatness and thickness uniformity are feasible.

3205 The selected reference gas radiator is hexafluoroethane (C_2F_6) (Appendix xxx), which
 3206 matches the requirements being characterized by refractive index $n = 1.00086$ and excellent
 3207 chromatic dispersion $dn/d\lambda = 0.2 \cdot 10^{-6} \text{ nm}^{-1}$ at light wavelength $\lambda = 350 \text{ nm}$ [56].

3208 The selected refractive indexes dictates a minimum thickness of 4 cm for the aerogel and $\mathcal{O}(1)$
 3209 m for the gas in order to ensure enough photon yield. Mirror focalisation is necessary to min-
 3210 imise the consequent uncertainty on the Cherenkov photon emission point. Being inside the
 3211 detector acceptance, the mirror structure is made of carbon fiber reinforced polymer (CFRP)
 3212 to ensure the necessary stiffness while being light. In order to preserve the Cherenkov angle
 3213 information the mirror surface should have excellent optical quality, i.e. few nm roughness
 3214 and better than 0.2 mrad angular precision (reflecting in a point-like image with more than
 3215 90% of the light intensity concentrated in a disk smaller than 2.5 mm). The single mirror

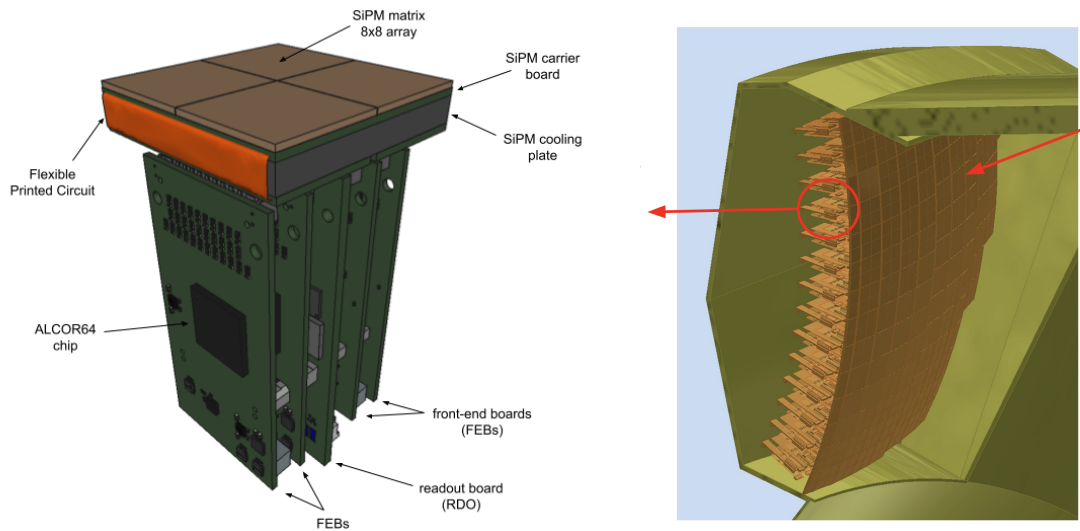


Figure 8.58: (Left) CAD model of the dRICH photodetector unit (PDU) module with its major components. (Right) dRICH detector box model with 208 PDUs forming a curved active surface.

3216 dimension is limited to a ≈ 1 m maximum diagonal when accounting for realistic forming
 3217 mandrel and coating chamber dimensions. In the dRICH mirror array, the radius of curva-
 3218 ture should be replicated within 1% of the nominal value.

3219 The dRICH photon detector surface is shaped over a sphere of radius ~ 110 cm to best
 3220 approach the 3D focal surface of the mirror array. The Silicon Photomultiplier (SiPM) sensor
 3221 technology is selected for the photon detector. It ensures superior single-photon counting
 3222 capability inside the ePIC magnetic field and compact dimensions suitable for tessellating a
 3223 shaped active surface. The single SiPM sensor has a 3×3 mm² area to provide the necessary
 3224 spatial resolution with an intrinsic time resolution better than 150 ps. The SiPM sensors are
 3225 grouped into 8×8 arrays in a buttable arrangement to minimize the dead area, which are
 3226 eventually mounted side-by-side to form a 16×16 array defining the 256 channels of the
 3227 dRICH photodetector unit (PDU). The selected front-end ASIC is ALCOR, a 64-channel chip
 3228 with coupling and rate capability optimized for SiPMs, and a ToT architecture with better
 3229 than 50 ps LSB¹ resolution in order the SiPM-ALCOR readout chain could achieve an overall
 3230 time resolution better than 200 ps RMS. To minimize the volume within the dRICH envelope
 3231 and to maximize the active area, the photodetector is organized in compact photodetector
 3232 units (PDU). The PDU integrates 256 SiPM channels with the ALCOR TDC readout provided
 3233 by four front-end boards (FEB), one readout board (RDO) to interface with the ePIC data
 3234 acquisition (DAQ) and detector control (DCS) systems. In addition, the PDU is designed
 3235 to allow sub-zero cooling of the SiPMs as well as high-temperature annealing operations.
 3236 Figure 8.58 (left) shows the conceptual design of the PDU and its main components. The
 3237 present dimensions of the PDU concept are approximately $52 \times 52 \times 140$ mm³.

Figure 8.59: (Left) dRICH aerogel model. (Right) dRICH mirror model [placeholder].

¹Least Significant Bit

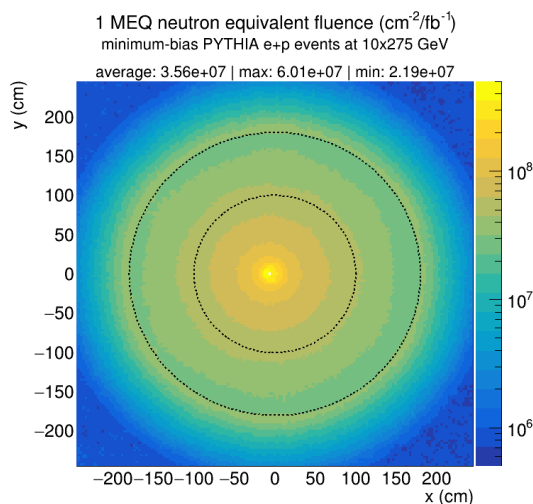


Figure 8.60: Transverse map of the expected 1-MeV equivalent neutron fluence per 1 fb^{-1} of integrated luminosity in e+p interactions at the maximum EIC center-of-mass energy at the location of the dRICH photodetector ($210 < z < 260 \text{ cm}$). The average, maximum and minimum values within the region of the dRICH photodetector ($100 < R < 180 \text{ cm}$, indicated by the dashed lines) are reported.

3238

Subsystem description:

3239

General device description:

3240

Because at ePIC the electron and hadron beam collide at an angle of 25 mrad, the common beam pipe cross-section is off-axis at the dRICH location and increasing in area with the distance from IP, imposing an asymmetric layout of the inner components, see Fig. 8.59. The aerogel wall is composed by five rings of tiles, each shaped in order to fit inside a 0.2 mm thin aluminum supporting structure. In each sector, focalization is provided by a compound of five mirrors covering a total area of about 2 m^2 with an optimized radius of curvature around 2200 mm. Six independent spherical active surfaces with curvature radius around 1100 mm, each made of 208 PDUs for a total of 53k readout channels, are mounted inside detector-boxes that provide thermal insulation, cooling for the electronics and connections to the services. Given the gas radiator open volume, the Cherenkov photons can be reflected into different detectors depending on the parent charged particle kinematics. The aerogel and photo-detector are separated from the radiator gas by transparent septa, and immersed in a dry (e.g. purged N_2) atmosphere to minimize contaminant absorption and prevent moisture formation. The mirrors are supported by a light carbon fiber structure that is mechanically decoupled from the vessel and allows fine alignment adjustments by means of pizezo-electric motors.

3241

3242

3243

3244

3245

3246

3247

3248

3249

3250

3251

3252

3253

3254

3255

3256

3257

Sensors:

3258

The silicon photomultiplier (SiPM) [57, 58] is chosen as the sensor technology for the dRICH photodetector. The main baseline specifications demand sensors with a $3 \times 3 \text{ mm}^2$ single-channel active area, single photon detection over a broad spectral range from 300 to 900 nm and very high overall photodetection efficiency $> 40\%$ at the peak sensitivity wavelength $400 < \lambda_{\text{peak}} < 450 \text{ nm}$ (see Table 8.19 in Additional Material for the full list of the baseline parameters and specifications of the SiPM sensor devices

3259

3260

3261

3262

3263

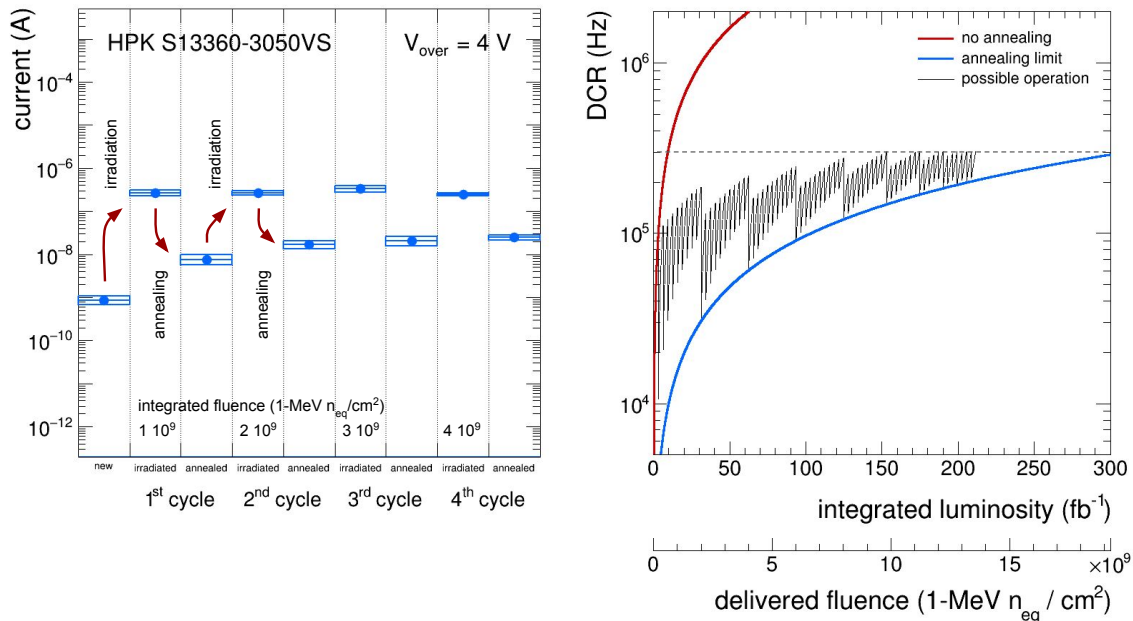


Figure 8.61: (Left) Dark current measurements on sample SiPM sensors for the studies of repeated irradiation-annealing. (Right) Projected increase of the DCR of SiPM as a function of the integrated luminosity (delivered fluence). The “no annealing” and the “annealing limit” curves show the limits of possible operations. The dashed line indicates the desired maximum DCR threshold.

3264
3265
3266
3267
3268
3269
3270
3271
3272
3273
3274
3275
3276
3277
3278
3279
3280
3281
3282
3283
3284
3285
3286

for the dRICH photodetector). SiPMs fulfil the dRICH requirements being cheap and versatile devices with excellent photodetection efficiency (PDE) and time resolution. Their single-photon performance is unaffected by high magnetic fields [59, 60], which makes SiPM the only photosensor that can efficiently operate in the field configuration at the dRICH photodetector location in the ePIC experiment, see Fig. ???. SiPM sensors on the other hand have very high dark count rates (DCR) and are not radiation tolerant. The DCR in SiPM is mostly of thermal origin and it reduces significantly by lowering the SiPM temperature, typically halving every 7-10°C in new sensors [61]. Radiation damage in SiPM is mainly due to displacement damage in silicon, which causes a significant DCR increase and reduces the effectiveness of cooling [62]. At the moderate radiation levels expected at the location in the dRICH, no significant change in the SiPM parameters (PDE, gain, quenching resistor R_{quench} , pixel capacitance C_{pixel} , breakdown voltage V_{break}) is observed [63]. SiPM cooling is important to keep the DCR low and it becomes crucial after radiation damage [64], as the increase in DCR would be such to make SiPM unusable as single-photon detectors, otherwise. In the dRICH, the SiPMs will be operated at subzero temperature of $T = -30^\circ\text{C}$, or lower. A cooling block is placed in thermal contact with the back-side of the printed-circuit board hosting the SiPMs (carrier board). Cooling fluid in the cooling block will be circulated through a closed loop by a dynamic temperature control system circulating thermostat to regulate and maintain the SiPMs at low temperature. The circulating thermostat system will also be used to circulate fluid at high temperature ($T = 100^\circ\text{C}$, or higher) to provide heat during SiPM annealing. Therefore a low-viscosity silicone fluid is particularly suitable for cold and heat transfer. The radiation damage on SiPMs increases moderately with

the integrated luminosity. At the location of the dRICH photodetector a maximum (average) fluence of $\Phi_{\text{eq}} = 6.0 (3.6) 10^7 \text{ cm}^{-2}/\text{fb}^{-1}$ 1-MeV equivalent neutrons (n_{eq} in the following) is expected from e+p interactions at the highest center-of-mass energy of the EIC (Figure 8.60). Beam-induced background from proton beam-gas events at 35 kHz are expected contribute with a maximum (average) of $\Phi_{\text{eq}} = 3.7 (1.6) 10^6 \text{ cm}^{-2}/\text{fb}^{-1}$ n_{eq} at the location of the dRICH photodetector, bringing the total maximum (average) expected radiation damage to $\Phi_{\text{eq}} = 6.4 (3.7) 10^7 \text{ cm}^{-2}/\text{fb}^{-1}$ n_{eq} . As shown by the “no annealing” curve in Figure 8.61 (right), the SiPM DCR is expected to increase with the integrated luminosity at a rate of 31.8 (18.6) kHz/fb⁻¹, reaching a DCR of 300 kHz after an integrated luminosity of approximately 9.5 (16.1) fb⁻¹. These values are based on measurements performed on Hamamatsu S13360-3050 sensors operated at $V_{\text{over}} = 4 \text{ V}$ at $T = -30^\circ\text{C}$., more details in Additional Material.

Annealing of SiPMs can be achieved exploiting the Joule effect []. When a SiPM is forward biased, the microcells composing the device behave as directly polarized diodes connected to their quenching resistors. The current flowing through the resistors eventually heat up the entirety of the sensor. In the dRICH, SiPM annealing will be performed up to temperatures of $T = 150^\circ\text{C}$ in “forward-bias mode”. The actual annealing temperature and annealing time will be tuned during detector operations according to the DCR reduction needs and available experiment down time. During the R&D phase it was shown that the “forward-bias mode” approach can cure approximately 97% of the radiation damage. It is therefore expected that a residual irreducible radiation damage (residual DCR) will build up during the dRICH lifetime. As shown by the “annealing limit” curve in Figure 8.61 (right), the SiPM residual DCR is expected to increase with the integrated luminosity at a rate of 950 (560) Hz/fb⁻¹, reaching a residual DCR of 300 kHz after an integrated luminosity of approximately 310 (530) fb⁻¹. In the dRICH, SiPM annealing will be performed with a technical implementation of the “forward-bias mode” which needs to be integrated both into the SiPM power-supply system, the front-end and control electronics, cooling and the temperature monitoring system. As previously mentioned, the circulating thermostat system used for low-temperature operation of the SiPM will be operated in heating mode to warm up the SiPM cooling plate during high-temperature annealing. This will allow one to perform the “forward-bias annealing” by delivering a lower current to the SiPM, as a fraction of the heating power is delivered by fluid. Nonetheless the required power to perform “forward-bias annealing” at once over the full dRICH detector is excessively large. Therefore annealing operations will be segmented in space and time across the dRICH detector and will be performed during periods with no Physics beam and depending on the DCR needs. As can be seen from Figure 8.60 the sensors closer to the beam line will experience a radiation damage almost a factor 3 larger than those further from the beam line and will likely require a more frequent annealing. The “possible operation” curve in Figure 8.61 (right) shows a potential scenario for the DCR evolution for SiPM sensors closer to beam pipe (worst case). This is based on an operation model where more frequent (every $\sim 3 \text{ fb}^{-1}$) softer annealing cycles at lower temperature and/or of shorter duration, delivering a DCR reduction of 10 \times , are interleaved by less frequent (every $\sim 30 \text{ fb}^{-1}$) full annealing cycles to reduce DCR as much as possible. A limit in the operation scenario is reached when the annealing is not capable to keep the DCR below the desired threshold or when the annealing frequency becomes too high. As it can be seen from Figure 8.61 (right), beyond an integrated luminosity of $\sim 200 \text{ fb}^{-1}$ to keep the DCR below the 300 kHz threshold requires to perform full annealing cycles every $\sim 5 \text{ fb}^{-1}$, which is not obviously a practical operation scenario anymore. Some or all of the SiPM sensors might be needed to be replaced at that stage with new ones or with SiPM sensors of improved performance and radiation hardness in a future upgrade of

3338 the dRICH photodetector. One has to keep in mind though that the 300 kHz limit is a
3339 conservative value that is connected to the present level of dRICH reconstruction and
3340 could be relaxed in future. Moreover, the model shown in Figure 8.61 (right) is based on
3341 measurement on Hamamatsu S13360-3050 sensors operated at $V_{\text{over}} = 4$ V in a climatic
3342 chamber at $T = -30^{\circ}\text{C}$. Possible SiPM operation in ePIC at a lower V_{over} of 3 V and at a
3343 lower T of -40°C will allow one to achieve lower DCR overall.

3344 FEE:

3345 The ALCOR (A Low Power Chip for Optical Sensor Readout) ASIC, developed by the
3346 electronics laboratory of INFN Torino, is the baseline option for the readout of the
3347 dRICH SiPM sensors. The architecture of ALCOR and its key specifications are de-
3348 scribed in Section ??*Readout Electronics and Data Acquisition*, here only some specific
3349 EIC-driven features are discussed as well as the integration of the ALCOR ASIC in the
3350 dRICH front-end electronics. The main goal of ALCOR is to provide single-photon
3351 time tagging of the incoming signals, while being able to cope with the SiPMs inher-
3352 ently high DCR: a maximum DCR value of 300 kHz/ch is expected before an annealing
3353 cycle is performed. A good time resolution, better than 200 ps RMS, is required to per-
3354 form DCR suppression via time gating at both hardware and software levels. A pro-
3355 grammable hardware shutter, implemented inside the digital logic of ALCOR, can be
3356 enabled to filter out-of-time DCR and provide a significant bandwidth reduction to the
3357 system. The time window of interest is controlled off-chip by the RDO FPGA and can
3358 be adjusted using in-pixel programmable delays to compensate timing offsets among
3359 the 64 channels. With a time window of approximately 2-3 ns, considering that the EIC
3360 bunch crossing period is about 10.15 ns, data can be reduced by a factor of 3 or 5. One
3361 important point is that the shutter will be needed only when DCR becomes higher due
3362 to SiPMs taking radiation damage over time. Therefore, the first period of ePIC data
3363 taking can be used to optimize the shutter calibration. The ASIC will be integrated in-
3364 side a BGA package, providing a compact and robust solution to be assembled on the
3365 FEB. A 16×16 mm² flip-chip ball grid array (FC-BGA), with 256 balls and 1 mm ball
3366 pitch, is the option chosen for the ASIC packaging since it offers more interconnections
3367 and better performance w.r.t. standard packaging techniques and matches well with
3368 the pixel-matrix geometry of the ALCOR ASIC. A 3D model of the FEB is shown in
3369 Fig. 8.62. Each FEB hosts one ALCOR BGA device and several components to ensure
3370 a stable and safe operation of the system. Linear regulators are employed to provide
3371 clean power supplies to the chip and are coupled to I2C interface and current monitors
3372 to control the regulators and prevent potential damage from over-current conditions.
3373 The FEB incorporates a dedicated PCB section for SiPMs bias voltage routing and also a
3374 circuit to enable the SiPM forward-biasing when annealing cycles are carried out. AC-
3375 coupling between the SiPM sensors and ALCOR inputs has been chosen to isolate them
3376 when the SiPMs are operated in forward bias. Several connectors, mounted on the FEB,
3377 provide the interface towards the RDO and the other FEB boards of the same PDU as
3378 well as towards the SiPMs carrier board and the LV-HV services.

3379 Other components:

3380 The radiator gas in the RICH vessel is controlled by the gas radiator system (Fig. 8.63).
3381 Its main tasks are, during detector operation, (i) providing well controlled pressure con-
3382 ditions in the 12 m³ RICH vessel to avoid relevant pressure difference at the vessel walls
3383 and at the fused silica windows; (ii) removing oxygen and water vapor contaminates,
3384 in order to prevent building up impurities due to air leaks entering the gas system; (iii)
3385 performing detector vessel filling with hexafluoroethane before a data taking period
3386 and radiator gas recovery at the end of the period; the filling/recovery is from/to the
3387 storage tank. The main components of the radiator gas system are two oil-free compres-

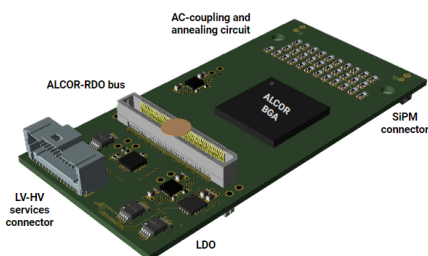


Figure 8.62: 3D model of the dRICH FEB.

3388 sors, working in parallel, which continuously extracts gas from the vessel at constant
 3389 rate in order to ensure the gas circulation, a pressure sensor installed on top of the ra-
 3390 diator vessel for continuous monitoring of the internal relative pressure and to dictate
 3391 the opening level of a flow control valve on the input line, adjusting the opening so
 3392 to preserve the relative pressure inside the vessel. Oxygen and water vapor traces are
 3393 removed by filtering cartridges with molecular sieves and Cu-catalyst, which are per-
 3394 manently in series in the circulation system. The vessel is flushed with nitrogen during
 3395 the shutdown periods. Nitrogen and hexafluoroethane separation during filling and
 3396 recovery is under study and two options can be envisaged: (i) the use of osmosis via
 3397 dedicated membranes or (ii) via a two-step procedure: replacing nitrogen with carbon
 3398 dioxide and then performing distillation at -35°C . Hexafluoroethane is a greenhouse
 3399 gas and, therefore, the residual C_2F_6 present in the nitrogen/carbon dioxide cannot be
 3400 vent out: it must be collected and trapped for disposal with a dedicated recovery sys-
 3401 tem. The control of the whole radiator gas system is performed via a Programmable
 3402 Logic Controller (PLC). More details are provided in Additional Material.

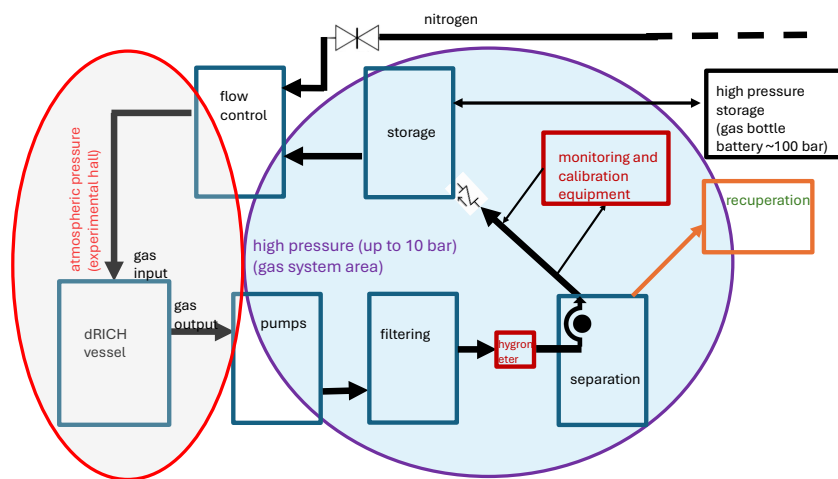


Figure 8.63: Block diagram of the dRICH gas system [graphically, a preliminary version].

3403

Performance

3404

For each recorded dRICH hit, the photon path is reconstructed taking into account the charged particle trajectory and the focalsing optics of the detector, in order to provide an

3405

3406 estimate of the Cherenkov angle at the emission point. The combined information of all
 3407 the Cherenkov photons associated to a charged particle concur to a precise determination of
 3408 its velocity (beta) and, knowing the momentum from the ePIC spectrometer, its mass. The
 3409 dRICH model is part of the ePIC simulation framework and allows complete performance
 3410 studies taking into account quality of the track reconstruction, bent trajectories (by magnetic
 3411 field) and multiple scattering. To bypass the complexity of such a framework, some specific
 3412 study can be anyway performed with private or simplified simulation chain. The laboratory
 3413 characterization and the numerous test-beams have provided detailed inputs for modeling
 3414 in a realistic way the single components and global detector response. In the dRICH, the
 3415 contributions to the single-photon (SPE) angular resolution have a different weight depend-
 3416 ing on the radiator. The dRICH has been designed in order to keep most of the contribu-
 3417 tions to the SPE angle resolution below 0.5 mrad, see Fig. 8.64, a value dictated by the tiny
 3418 Cherenkov angle difference between pions and kaons at 50 GeV/c in the radiator gas. The
 3419 single SiPM readout channel has been limited to $3 \times 3 \text{ mm}^2$ area. The MARCO coils and
 3420 the dRICH position has been optimized in order to minimize the bending inside the radiator
 3421 gas volume. The tracking resolution is assumed to cope with the same constrain. Note that
 3422 combining N photons the angular precision scale with a maximum $N^{-1/2}$ factor only in case
 3423 of a completely uncorrelated information, a condition that is not valid for the bending and
 3424 tracking contributions. The uncertainty on the emission point is not an issue for a few cm
 3425 layer of aerogel, but is critical for a 1 m long gas volume, especially within the limited space
 3426 available in ePIC for the optics: this remains the major contribution to the SPE resolution of
 3427 the radiator gas despite the mirror focalization and the curved dRICH detector surface. As
 3428 the present model assumes a single radius for the dRICH mirrors, optimized for the forward
 3429 rapidity region to boost the high-momentum reach, the resolution worsens with the polar
 3430 angle increase. This is not a problem, because the average particle momentum decrease as
 3431 well loosing the performance requirement. The chromatic error is well under control for gas
 3432 but is the largest contribution to the angular resolution for the aerogel. This derives from
 3433 the intrinsic nature of the radiator in conjunction with the quantum efficiency characteristic
 3434 of the photosensor. The chromatic uncertainty limits the aerogel momentum reach to some-
 3435 thing above 15 GeV/c, a value well above the Cherenkov threshold of kaons in gas, high
 3436 enough to provide the wanted overlap between the measured ranges of the two radiators.

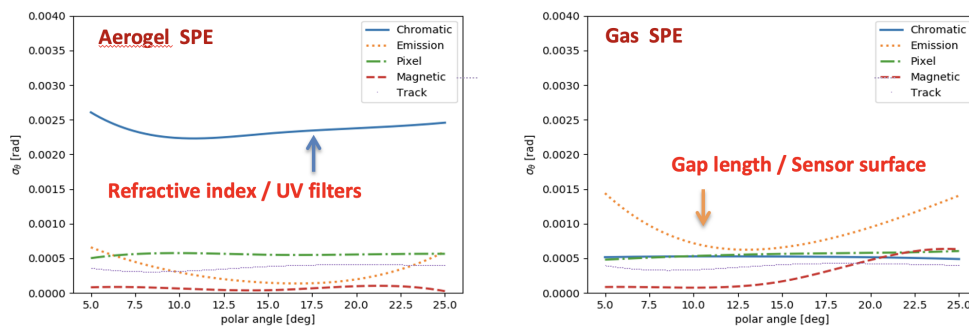


Figure 8.64: (Left) Contributions to the single-photon angular resolution for aerogel. (Right) Contributions to the single-photon angular resolution for radiator gas.

3437 The number of emitted photons varies with the pseudo-rapidity due to the different path of
 3438 the particle within the radiators. The mean number of recorded photons is about 18 for the
 3439 radiator gas and 12 for the aerogel for a particle with momentum well above the Cherenkov
 3440 threshold. In average, few charged particles per event are expected to hit the detector, see
 3441 left panel of Fig. 8.65. With a proper pattern recognition and photon path reconstruction,

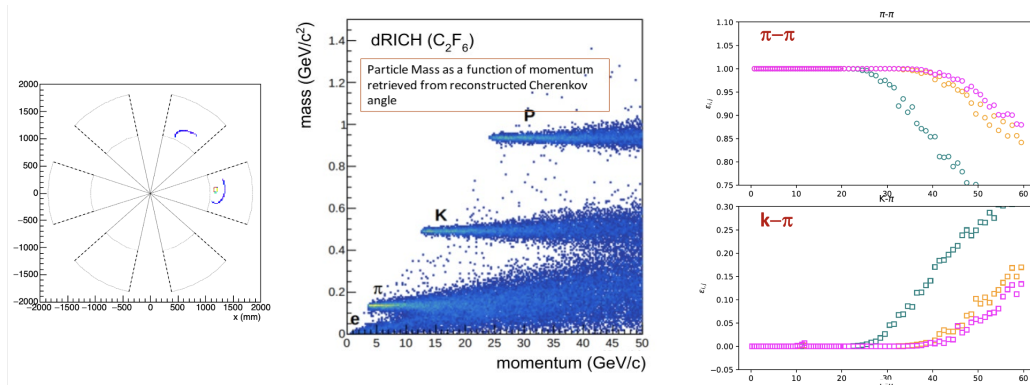


Figure 8.65: (Left) Event display. (Center) Reconstructed mass vs momentum. (Right) Pion identification efficiency and pion to kaon mis-identification probability as a function of momentum in three bins of rapidity.

3442 the information of the two radiators can be combined to extend the momentum coverage of
 3443 ePIC PID from the TOF ≈ 2.5 GeV/c upper momentum limit to above 50 GeV/c, see central
 3444 panel of Fig. 8.65. In the forward direction with optimized focalization, an identification
 3445 efficiency greater than 95 % at a corresponding 5 % percent mis-identification probability, is
 3446 achieved, see right panel of Fig. 8.65. As expected from the resolution study, the momentum
 3447 reach is reduced with the pseudo-rapidity, in accordance with the kinematics of the particles
 3448 expected from physics reactions.

3449 Implementation

3450 Services:

3451 The dRICH services are grouped into power lines for sensors, electronics and slow control
 3452 monitors, gas lines for the radiator gas volume, the aerogel inert gas volume, and cooling
 3453 lines for the sensors and electronics. Table 8.16 shows a list of the power services for the
 3454 dRICH photodetector. 18 19" wide/8U mainframes (approximately $50 \times 40 \times 70$ cm² each)
 3455 capable to host 16 boards each are needed to accommodate the low-voltage and high-voltage
 3456 boards. The primary power-supply channels will serve multiple modules at the same time,
 3457 with a typical grouping of 1024 SiPM channels. Nonetheless, further segmentation is imple-
 3458 mented on the detector electronics, reaching a low-voltage power segmentation of 64 SiPM

Name	Voltage (V)	Current (A)	Channels	Boards	AWG gauge
Analog	1.4	10.0	312	39	10
Digital low	1.4	8.5	312	39	11
Digital high	2.7	6.0	312	39	12
Master panel	5.0	5.2	6	1	13
SiPM bias	64.0	1.3	12	2	19
Annealing	12.0	3.2	1248	156	15

Table 8.16: List of the voltage services to the dRICH electronics, indicating the number of primary power-supply channels and boards as well as the cross-section of the cables (AWG). The number of power-supply boards is defined assuming to use commercial 8-channel low-voltage boards.

3459 channels and a high-voltage power segmentation of 32 SiPM channels. The circulating ther-
3460 mostat system should be capable of circulating approximately 50 l/min of fluid at a max-
3461 imum pressure of 1.5 bar in a broad temperature range (from -60°C to 120°C). Possible
3462 commercial systems are available, but more time is needed to better investigate the options.
3463 It is expected that a potential circulating thermostat system with the desired characteristics
3464 will require space in the experimental hall for a volume of approximately $1.3 \times 0.8 \times 1.6$
3465 m^3 . Manifolds are needed to split the fluid from the thermostat into 6 loops, each feeding
3466 one dRICH photodetector box. A solution without manifold and 6 smaller independent ther-
3467 mostat unit for each dRICH sector will be investigated as a possible optimization. Insulated
3468 pipes will be needed to transport the fluid from the thermostat to the detector, and back. The
3469 insulation must guarantee no frost and no water condensation on the pipes when operating
3470 at the lowest temperatures and is also required to limit transport losses in heating/cooling
3471 capacity. Cooling for the front-end electronics is required to remove the approximately 15
3472 kW of heat generated by the dRICH photodetector (≈ 2.5 kW in each of the six photodetec-
3473 tor boxes). Force-air circulation in the boxes with diffusers are being studied as a possible
3474 effective solution. It is important that the air-cooling system for the FEE electronics provides
3475 dry air with a dew point of $T = -70^{\circ}\text{C}$ or lower, well below the SiPM operating tempera-
3476 ture. A system based on forced circulation of gaseous nitrogen might be well suited also
3477 to ensure an inert environment inside the detector boxes. Gaseous nitrogen will be used
3478 to maintain the aerogel in a clean and inert environment. The radiator gas system and its
3479 related monitoring equipment require a surface of about 15 m^2 , in order to host 5 racks of
3480 instrumentation, the gas storage tank and a support for the spectrophotometer. This surface
3481 includes the space needed by the operators. Various sections of the gas system operate at a
3482 2-3 bar pressure, while the cell to measure and monitor the gas transparency operates at 10
3483 bar. Some gas bottles at typical high pressure (100-150 bar), organized in a battery, have to
3484 be included to provide the radiator gas at filling and house it when recovered. The pipelines
3485 connecting the gas system to the vessel are 70 m long with a diameter of 10 cm.

3486 **Subsystem mechanics and integration:**

3487 The dRICH structure can be described by two disks, one entrance window of 0.9 m radius
3488 supporting the aerogel radiator and one exit window of 1.8 radius mounting the mirror sys-
3489 tem, connected by two ring-shaped structures, one shell that mounts the six detector boxes
3490 and one inner pipe surrounding the ePIC beam pipe. All the elements are made in composite
3491 materials. The pipe and shell are made by a carbon fiber reinforced polymer (CFRP) bulk to
3492 provide support strenght. The two windows are a sandwich of two carbon fiber skins and
3493 a core honeycomb to limit the material budget to about 1% of radiation length each. The
3494 shell and detector boxes are shaped in order to allow the passage of all the services of the
3495 inner barrel detectors, see left panel of Fig. 8.66. The dRICH services are concentrated on the
3496 shadow of the detector boxes and do not interfere with the routing of the others. A dedi-
3497 cated scaffolding would be realized to allow the installation of the detector, and the roll-in
3498 and roll-out movements to the service position without interference with the beam pipe to
3499 preserve the beam vacuum, see central and right panel of Fig. 8.66. The dRICH is suspended
3500 inside ePIC via brakets connected to the HCAL barrell.

3501 **Calibration, alignment and monitoring:**

3502 Dark counts in SiPMs are indistinguishable from photon-induced signals and owing the large
3503 SiPM DCR there is no need of a dedicated system to evaluate the functioning of any given
3504 readout channel. A measurements of the DCR as a function of the front-end electronics dis-
3505 crimination threshold can provide information on the signal amplitude. This technique can
3506 be used at different bias voltages. Using solely the dRICH readout system it is possible to

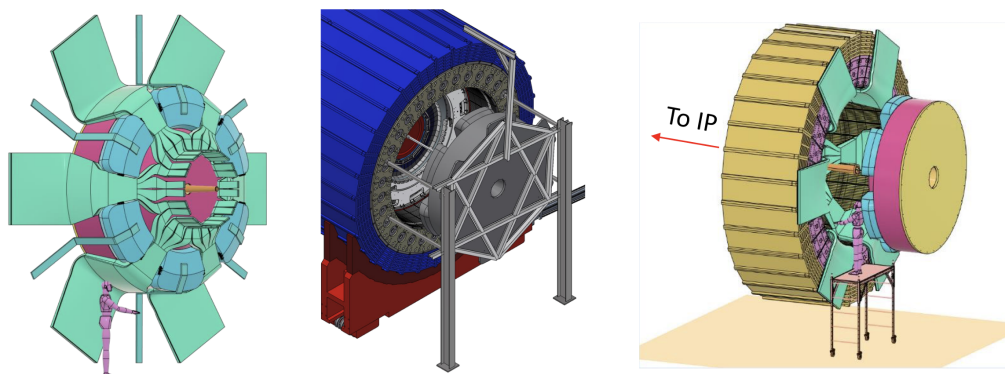


Figure 8.66: (Left) Service routing around the dRICH. (Center) Installation tool. (Right) Maintenance position.

3507 measure the signal amplitude as a function of the bias voltage, hence to obtain information
 3508 on sensor functioning and its breakdown voltage at different operation conditions. Timing
 3509 calibration of the SiPM sensors can be achieved with a picosecond pulsed laser light sys-
 3510 tem. The light from the laser is brought inside the dRICH volume via optical fibres. The
 3511 light from the laser directly impinges on a diffuser that eventually illuminates the full area of
 3512 one dRICH photodetector sector. At least one laser-fibre-diffuser system is needed for each
 3513 dRICH sector. The time delay due to the different path of photons from the diffuser to the
 3514 SiPM that detects the light is known and can be corrected to achieve a relative calibration of
 3515 the times of SiPMs within the same sector. Absolute timing calibration can then be achieved
 3516 with collision data. Samples particles from physics reactions can be used to perform fine
 3517 adjustment of the calibration constants. Electron particles identified by other ePIC subsys-
 3518 tems can be used to correct residual misalignment or calibrate the radiator refractive index
 3519 thanks to the saturated Cherenkov rings. Known particles from meson decays ($\Lambda, \phi, K_S, \dots$)
 3520 identified by kinematics criteria can be used to verify the parameters of the dRICH recon-
 3521 struction and the consequent PID performance. The calibration and monitoring equipment
 3522 of the radiator gas and gas system (see Additional Materialism) includes a set of temperature
 3523 sensors placed inside the dRICH vessel and equipment on-line in the gas circulation loop.
 3524 A commercial hygrometer and a commercial oximeter, a transparency measurement system
 3525 by a commercial spectrophotometer equipped with a high pressure (≈ 10 bar) cell and a
 3526 Jamin interferometer setup complete the set of the equipment. The interferometer, comple-
 3527 mented with temperature and pressure sensors, will provide in real-time the refractive index
 3528 of the gas in the vessel. The refractive index measurement has a twofold role: during fill-
 3529 ing/recovery, it monitors the hexafluoroethane level in the vessel, during operation it will
 3530 provide in real time the refractive index of the radiator gas to make possible quasi on-line
 3531 data reconstruction as foreseen in the ePIC streaming read-out model.

3532 Status and remaining design effort:

3533 R&D effort:

3534 **SiPM sensors.** A station has been realized to characterize the SiPM sensors inside a
 3535 climatic chamber to control the working temperature, see left panel of Fig. 8.67. The
 3536 readout chain is based on ALCOR to reproduce the ePIC configuration. Such a station
 3537 allowed detailed performance comparison between SiPMs of different manufacturers
 3538 and types, and different ageing due to radiation and annealing, e.g. see central panel

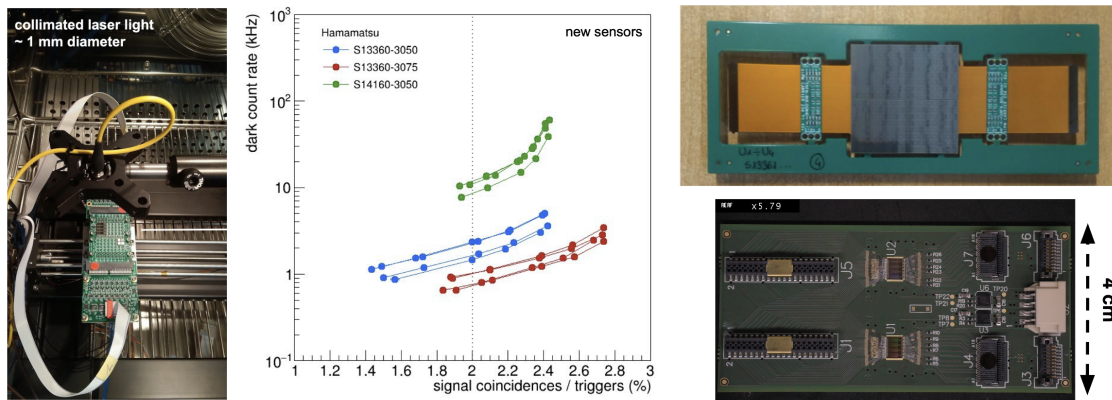


Figure 8.67: (Left) Test stand for SiPM characterization. (Center) Performance comparison between different SiPM models. (Right) Prototype version of the SiPM carrier board (top) and FEB (bottom).

3539 of Fig. 8.67. The R&D results on photosensors reported here are those obtained with
 3540 Hamamatsu S13360-3050 sensors operated at $V_{\text{over}} = 4$ V in a climatic chamber at $T =$
 3541 -30°C , unless otherwise specified. Nonetheless, the qualitative features of the results
 3542 are valid also for other types of sensors. Irradiation tests and laboratory measurements
 3543 on SiPM candidate samples show that after irradiation with a fluence of $\Phi_{\text{eq}} = 10^9 \text{ cm}^{-2}$
 3544 n_{eq} the DCR increases by approximately 500 kHz with respect to the DCR measured
 3545 when new [34]. The dark current and the DCR of irradiated SiPM decreases by almost
 3546 two order of magnitudes when placed in a thermostatic chamber at $T = 150^{\circ}\text{C}$ for 150
 3547 hours (“oven annealing”). Further tests performed to simulate a realistic experimental
 3548 situation where SiPMs experience repeated irradiation and annealing cycles (see left
 3549 panel of Figure 8.61) show that each irradiation cycle produces a consistent DCR in-
 3550 crease (approximately 500 kHz for a $10^9 \text{ cm}^{-2} n_{\text{eq}}$ irradiation) and a consistent residual
 3551 DCR (approximately 15 kHz for a $10^9 \text{ cm}^{-2} n_{\text{eq}}$ irradiation) remains after an “oven
 3552 annealing” cycle. The fraction of damage cured by the “oven annealing” cycle is of ap-
 3553 proximately 97% of each newly-produced irradiation damage. The residual damage of
 3554 15 kHz/ $10^9 n_{\text{eq}}$ builds up after each irradiation-annealing cycle and seems to be irre-
 3555 ducible within the details of this annealing protocol. The “oven annealing” protocol is
 3556 not a practical approach for a central-barrel detector in a collider experiment, because
 3557 of the limited access and because it would entail the removal of the sensors from the
 3558 photodetector to place them the thermostatic chamber to perform annealing. Irradia-
 3559 tion tests and laboratory measurements show that the “forward-bias annealing” mode
 3560 can cure radiation-induced damage on SiPM (see left panel of Figure 8.68) to the same
 3561 effectiveness level as the one measured for the “oven annealing” with a residual dam-
 3562 age of approximately 3%. The benefit of the “forward-bias annealing” is significant: an
 3563 extended SiPM sensors lifetime that can be achieved over the delivered radiation dam-
 3564 age without the need to directly access the detectors in the experimental cavern. The
 3565 fraction of damage, measured as dark current reduction, depends on the annealing tem-
 3566 perature and the duration of the annealing. Higher temperatures and longer annealing
 3567 times lead to more effective annealing. On the other hand, a limit seems to be reached
 3568 already at $T = 150^{\circ}\text{C}$ and annealing at a higher temperature of $T = 175^{\circ}\text{C}$ does not lead
 3569 to improved current reduction. Self-heating of the SiPM happens also when reverse
 3570 biased, although given that the reverse I-V characteristics of SiPM is non-linear and

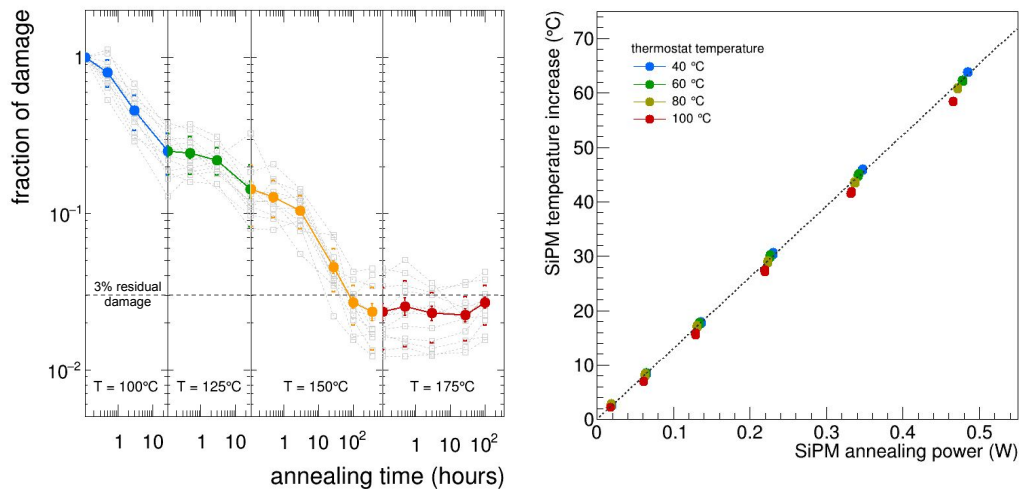


Figure 8.68: (Left) Fraction of residual irradiation damage measured on multiple SiPM candidate samples after “forward-bias annealing” cycles at increasing temperature and integrated annealing time. The measurements are shown for individual sensors (gray points) and as averages (coloured points, uncertainty of the average and RMS are indicated on the plot). (Right) Temperature increase of the SiPM sensor with respect to the temperature of the SiPM carrier board as a function of the “forward-bias annealing” power at different temperature values of the circulating thermostat system.

3571 depends on the illumination state, currents can increase with less control making the
 3572 reverse-bias annealing intrinsically more dangerous than forward-bias annealing. Labo-
 3573 ratory measurements performed so far show that one can increase the temperature
 3574 of the SiPM with respect to the temperature of the SiPM carrier board proportionally
 3575 to the power delivered by the forward-bias current. Figure 8.68 (right panel) shows
 3576 that, as expected, the increase of SiPM temperature linearly depends on the annealing
 3577 power and it is the same at different values of circulating thermostat temperature. It
 3578 is therefore sufficient to monitor the temperature of the SiPM carrier board and deliver
 3579 the needed annealing power to have control of the SiPM temperature during “forward-
 3580 bias annealing” and keep the process safely under control. Laboratory measurements
 3581 reported here are performed in an open environment at room temperature. With the
 3582 circulating thermostat temperature set at $T = 100^\circ$, we reach a SiPM annealing tem-
 3583 perature of $T = 150^\circ$ with approximately a power of 0.5 W/sensor, which corresponds
 3584 to a forward-bias current of approximately 60 mA/sensor. With the SiPM placed in
 3585 a closed environment as the in dRICH photodetector box, one would expect a lower
 3586 power needed that will be measured during detector construction. Laboratory mea-
 3587 surements of the variation of the SiPM PDE as a function of the annealing temperature
 3588 and annealing time show that for annealing temperatures up to $T = 150^\circ$ there is no
 3589 observation of a significant degradation of the PDE up to annealing times of 150 hours.
 3590 On the other hand, annealing at a temperature of $T = 175^\circ$ seem to cause a degrada-
 3591 tion of the transparency of the silicone protective window of the SiPM, which causes
 3592 a decrease in the PDE to approximately 80% of the initial value after 150 hours. As
 3593 already discussed, annealing at temperatures higher than $T = 150^\circ$ does not bring any
 3594 advantage for what concerns DCR reduction. More studies will be done, but at the
 3595 time of writing annealing at $T = 150^\circ$ can be considered safe for the expected dRICH

3596
3597
3598
3599
3600
3601
3602
3603
3604
3605
3606
3607
3608
3609
3610
3611
3612
3613
3614
3615
3616
3617
3618

operations.

FE Electronics. ALCOR has been extensively used within the ePIC dRICH Collaboration since 2021. The current version of ALCOR incorporates 32 channels, arranged in a 8×4 pixel matrix. It has been tested coupled to different SiPM models assessing its single-photon time-tagging capability and time resolution. A prototype version of the SiPM carrier and FEB board have been developed, see right panel of Fig. 8.67. The SiPM carrier provides electrical connections via thin kapton cables in order to bypass the sensor cooling plate. The prototype FEB hosts two 32-channel ALCOR chips which are directly wire-bonded on the PCB. It has been designed using specifications close to the ones for the final FEB, i.e. having the same dimensions and incorporating the same number of channels (64). It is served by a master-logic board that provide bias control and temperature monitor. These boards have been extensively used for the 2023-2024 dRICH activities, including two successful beam tests. ALCOR has been tested for radiation hardness with results showing only some small degradation on the TDC performance after a total ionizing dose (TID) of 300 krad, which is $O(100)$ times the expected TID in ePIC. These results confirm that the technology is sufficiently radiation tolerant to be used in the ePIC dRICH environment and that no special design techniques have to be adopted for the new version of ALCOR. The single-event upset (SEU) cross section has been measured to be $3.3 \cdot 10^{-15} \text{ cm}^2/\text{bit}$ for the pixel configuration registers and $8.5 \cdot 10^{-14} \text{ cm}^2/\text{bit}$ for the periphery configuration registers, which is significantly higher because these registers are not triplicated in the current version of ALCOR. From these results we can expect a mean time between failure due to SEU of about 190 hours for the entire dRICH detector.

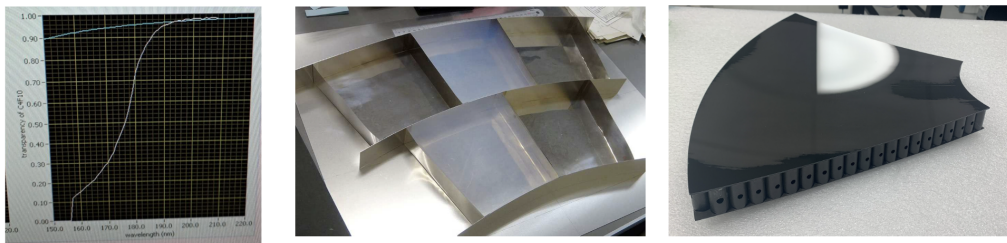


Figure 8.69: (Left) C_2F_6 measured transmittance. (Center) Aerogel large tiles assembling as obtained at BELLE-II [3]. (Right) Mirror demonstrator with an optimized dRICH core structure.

3619
3620
3621
3622
3623
3624
3625
3626
3627
3628
3629
3630
3631
3632

Radiator gas. The transparency in the near-UV benchmark region (most sensitive to the gas quality and contaminants) has been measured with a monochromator at CERN, resulting in values above 98% for a 1.6 m column of gas at wavelengths greater than 200 nm, see left panel of Fig. 8.69. The measurement has been done with a gas that was stored into bottles for about 4 years, indicating an excellent preservation with time.

Aerogel. Several measurements were performed to optically characterize the aerogel. The transmittance of silica aerogel is a measure of how much light passes through the material without being absorbed or scattered. Silica aerogel consists mostly of air. Indeed, it has a unique structure made of a three-dimensional network of interconnected nanopores, with diameters ranging from 2 to 50 nm, which allows visible light to pass through the material with minimal scattering or absorption. Specifically, in aerogel, light undergoes Rayleigh scattering, which is the elastic scattering of light by particles much smaller than the wavelength of the light. The transmittance is typically highest in the near-infrared region, where the absorption of radiation by the silica network is

3633 minimal. Its dependence on the radiation wavelength is usually defined by the Hunt
 3634 formula [65] which assumes a λ^4 -dependence of Rayleigh scattering cross section. In
 3635 silica aerogel, the low absorption is due to the absence of impurities or defects in the
 3636 silica network that could trap and dissipate the energy of the photons. Additionally, sil-
 3637 ica aerogel can be hydrophobic or hydrophilic. The tiles tested are highly hydrophobic,
 3638 which means that they repel water and other liquids. This property helps to maintain
 3639 the material's transparency even in humid or wet conditions. The aerogel scattering
 3640 and absorption capability can be assessed through the transmission length as follows:
 3641 $1/\Lambda_T = 1/\Lambda_{\text{scat}} + 1/\Lambda_{\text{abs}}$.

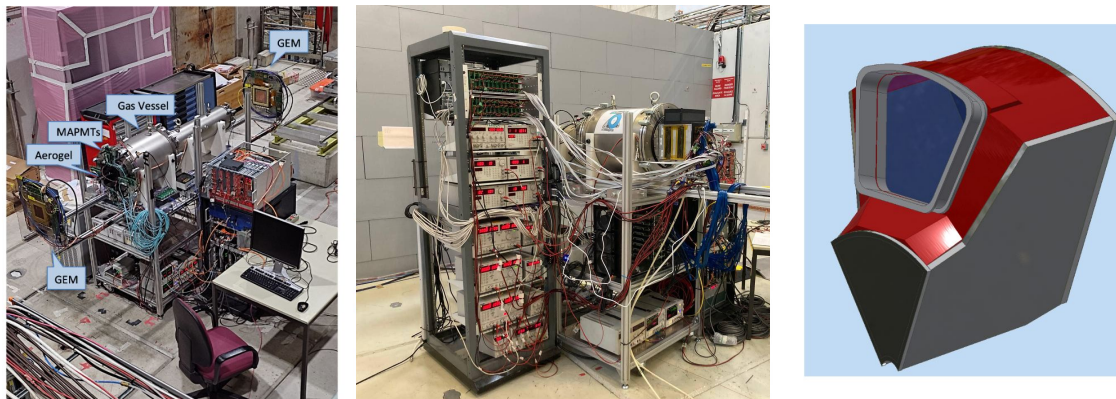


Figure 8.70: (Left) Baseline prototype with reference detector at the SPS-H8 beam line of CERN. (Center) First ePIC-drive detector box under test at the PS-T10 beam line of CERN. (Right) Real-scale prototype model mimicking the basic dRICH construction unit (sector).

3642 We have characterized several $10 \times 10 \text{ cm}^2$ and $5 \times 5 \text{ cm}^2$ aerogel tiles produced as a
 3643 spin-off the BELLE-II development in a broad range of refractive indexes. Table 8.20
 3644 reports a list of the tested samples, where for each tile its refractive index and expected
 3645 thickness in the thinnest point of its meniscus geometry are reported. On each tile trans-
 3646 mittance was measured on 15 different sampling points, to provide information on the
 3647 dependence of the transmittance on the thickness as well as on the light wavelength (in
 3648 a range from 250 to 800 nm). The maximum discrepancy along the tile is of the order
 3649 of $\approx 0.3\%$, the transparency homogeneity is quite good. Transmittance as a function of
 3650 the wavelength of a single tile was considered as the average of the transmittance value
 3651 at each sampling point. The average transmittance was fitted by the extended Hunt
 3652 formula suggested in [65] to extract scattering and absorption lengths. The results are
 3653 presented in Fig. 8.74 for a tile with $n = 1.03$, which shows that the transmission length
 3654 is nearly equal to the scattering length, whereas the absorption length is considerably
 3655 higher. Therefore, the contribution of absorption can be considered negligible. A compar-
 3656 ison of the results from all the tested tiles can provide valuable insights into the
 3657 impact of the refractive index on the optical properties of the aerogel, see Fig. 8.75. The
 3658 transmittance measurements reveal that the tiles with a refractive index close to $n=1.03$
 3659 exhibit higher transmittance length values at 400 nm compared with tiles of higher or
 3660 lower refractive index, see Fig. 8.76. In the metrology laboratory at CERN, the thickness
 3661 and flatness of the tile have been also measured. The measurement has been executed
 3662 on a tile with $n = 1.03$ using the touch probe system (force applied = 2 g). The measur-
 3663 ing system is the LEITZ PPMC with $\pm 0.3 \mu\text{m}$ of precision. There is a variation in
 3664 thickness from the center to the edges, of the order of 0.4 mm, and a different planarity

3665 in the two faces, one 0.7 mm, the other 1.27 mm. In general the tiles have the shape of a
3666 dome.

3667 **Mirror.** A mid-size demonstrator (of 60 cm diagonal) has been realized with dRICH
3668 specifications, see right panel of Fig. 8.69. The CFRP core structure has been optimized
3669 for preserving the surface shape accuracy and a light body: it adopts the light LHCb
3670 structure in the center, and the stronger CLAS12 structure on the edges. Before coating,
3671 the point-like source image test measures a D0 value, that represents a global surface
3672 quality estimator, of 1.8 mm, better than the specification of 2.5 mm. The same test
3673 indicates a radius of 2254.1 mm, slight above the request to be within 1% of the nominal
3674 2200 mm value.

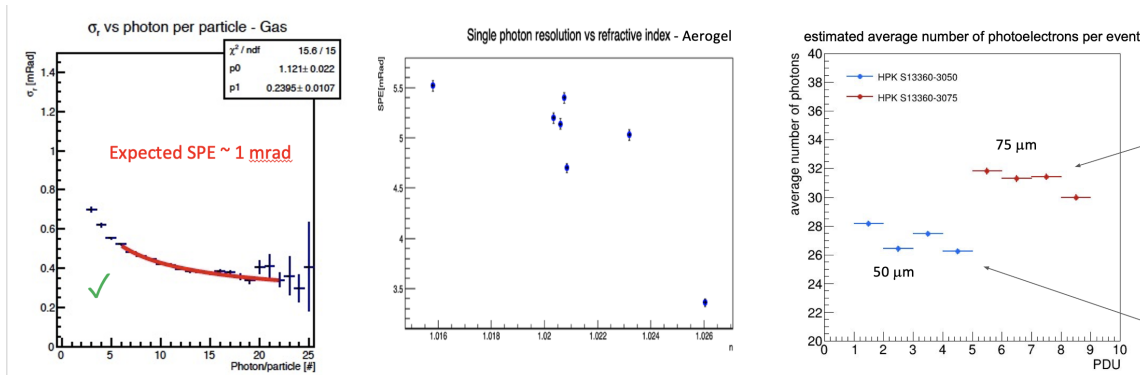


Figure 8.71: (Left) Cherenkov angular resolution obtained for C_2F_6 as a function of the recorded number of photons. The SPE values is consistent with expectations. (Center) SPE angular resolution measured on aerogel as a function of the refractive index. The expected resolution is obtained for an index greater than $n=1.025$. (Right) Comparison in photon yield of sensor with different SPAD size. All the measurements are obtained with the dRICH prototype.

3675 **Prototyping.** A baseline prototype has evolved in time to serve the dRICH R&D develop-
3676 ment for few years, see left panel of Fig. 8.70. The gas vessel is a cylinder made of
3677 vacuum standards, to allow an efficient and safe gas exchange. The entrance flange can
3678 mount an external dark box separated from the inner gas volume by a UV-transparent
3679 lucite foil (or quartz window). An aerogel tile with possible additional UV filters,
3680 plus an array of alternative sensors and readout electronics, can be inserted into the
3681 dark box. Two mirrors inside the vessel have optimized focal lengths to image the
3682 Cherenkov light from the two radiators onto the limited active surface. The major
3683 achievements obtained during several test-beams have been the validation of the dual-
3684 radiator concept, the validation of the C_2F_6 gas radiator (see left panel of Fig. 8.71), the
3685 optimization of the aerogel refractive index (see central panel of Fig. 8.71), the perform-
3686 ance study of the SiPM-ALCOR readout chain (see right panel of Fig. 8.71), and the
3687 development of an EIC-driven readout plane. A partially equipped EIC-driven plane
3688 has been realized in time for the October '23 test-beam with Hamamatsu S13360-3050
3689 SiPM sensors of standard 50 μm pixel pitch, see left panel of Fig. 8.72. The plane has
3690 been complemented for the test-beam in May 2024 with sensors of 75 μm pixel pitch,
3691 to verify the potential benefit in timing and photon detection efficiency. This has al-
3692 lowed for the first time a full ring coverage, an essential requirement for precise radi-
3693 ator performance study and effective signal over background study, see central panel
3694 of Fig. 8.72. An effective interplay between the two radiators at intermediate energies

3695 has been demonstrated, see right panel of Fig. 8.72. The new detector box has allowed a
 3696 preliminary study of the thermal gradients and possible effects on the gas performance,
 3697 indicating that the possible temperature gradient of few degrees induced into the gas
 3698 volume by the cool sensor plane can be largely mitigated by a gas re-circulation or by a
 3699 double window.

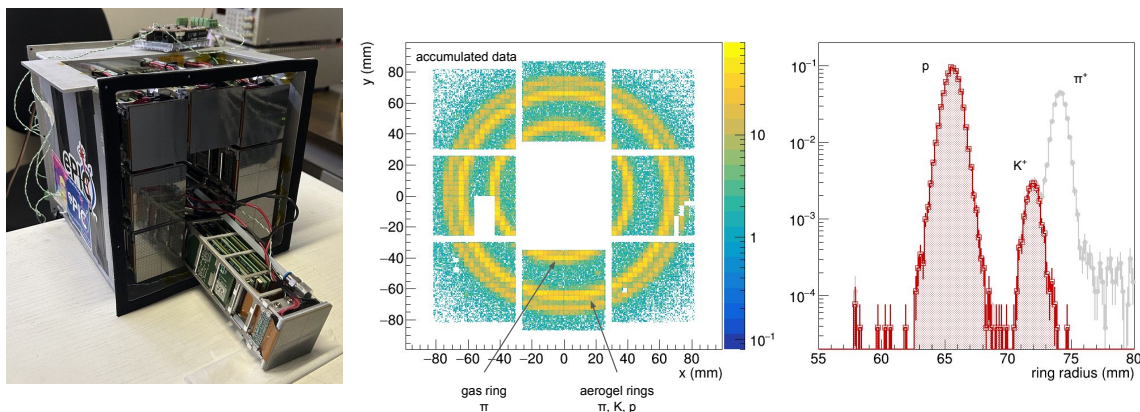


Figure 8.72: (Left) Prototype PDU and assembled detector plane. (Center) Cumulated ring imaging. (Right) dual-radiator interplay for a mixed hadron beam at 10 GeV/c: After the gas information is used to tag pions (clear histogram), an effective separation between kaon and proton is provided by the aerogel (shaded histogram).

3700 E&D status and outlook:

3701 A new version of the ALCOR ASIC is currently being designed to extend the number
 3702 of channels to 64 and integrate the chip inside a BGA package, aiming to enhance the
 3703 scalability of the readout system and meet specific EIC-driven requirements. The ASIC
 3704 package will use FC-BGA technology with 256 balls and 1 mm ball pitch. Since no
 3705 re-distribution layer (RDL) is available for the 110 nm technology in which ALCOR is
 3706 fabricated, a dedicated 10-layer 1.27 mm thick substrate in bismaleimide-triazine (BT)
 3707 resin material is currently being designed. This BT epoxy provides a more advanced
 3708 and reliable solution w.r.t. many FR4 grade materials, while being also commonly avail-
 3709 able from multiple vendors. In particular, its higher thermal conductivity and lower
 3710 z-axis coefficient of thermal expansion (CTE) values make it more suited to cope with
 3711 repeated thermal cycles, in which CTE mismatches may induce mechanical stress on the
 3712 BGA solder joints. The new version of ALCOR will also include some internal design
 3713 revisions. A programmable hardware shutter is being implemented to filter out-of-time
 3714 DCR and thus significantly reduce the data throughput. The asynchronous digital shut-
 3715 ter is implemented in ALCOR pixel logic using the external test-pulse signal and will
 3716 be provided by the RDO board. Inside the ASIC programmable delay chains, with 4
 3717 configuration bits at channel-level (LSB \simeq 350 ps) and at the chip periphery (LSB \simeq
 3718 100 ps), allow the compensation of the offsets between different pixels and columns. In
 3719 addition, the front-end will feature an increased bandwidth amplifier to improve the
 3720 system time resolution while keeping the same power consumption and also an hys-
 3721 teresis circuit in the discriminator stage to avoid unwanted re-triggering on the SiPM
 3722 signals slow tail, occurring when operating with very low thresholds. To improve its
 3723 overall SEU tolerance, the new version of the ASIC will implement triple modular re-
 3724 dundancy (TMR) also for the periphery registers as well as error-correcting Hamming
 3725 encoding for the finite-state machines (FSM). Further irradiation tests are foreseen in

3726 2025-2026 on ALCOR final version to fully validate the front-end electronics in terms
3727 of radiation tolerance for all of its components. The tape-out is scheduled during the
3728 first months of 2025. A thorough electrical characterization of this version of ALCOR,
3729 the first one assembled in a BGA package and including all the features required for
3730 the dRICH application, will be carried out to validate its new functionalities and mea-
3731 sure its performance in order to complete the E&D activity and go ahead with the ASIC
3732 mass production which is foreseen in 2026.

3733 The development of the final front-end boards takes advantage of the work done for the
3734 prototype version in terms of space constraints, readout scheme and components selec-
3735 tion. To finalize their layout several design optimization are required: define the best
3736 segmentation and routing to provide the bias voltage to the SiPMs, optimize the AC-
3737 coupling circuitry between ALCOR and the SiPM sensors, include the annealing circuit
3738 required to operate the SiPMs in forward-bias, distribute the power lines and optimize
3739 the control and monitor protocols. In addition, all components that will be mounted
3740 on these boards need to be tested to verify their radiation hardness. The design of the
3741 final version of the SiPM carrier, FEB and master-logic boards will be completed in 2025
3742 while the mass production is expected during 2026.

3743 For the radiator gas, it is required to complete the design of the gas system and finalize
3744 the layout of the monitoring equipment. Each of these activities assumes an engineer-
3745 ing study and its validation by laboratory studies. The remaining E&D activity is ex-
3746 pected to be completed by the end of 2026.

3747 An increase of the aerogel tile volume is instrumental to minimize the edge effects and
3748 contain the cost. During the R&D phase, tiles with side up to 15 cm and thickness up to
3749 2 cm were realized. A feasibility study is ongoing to increase these limits towards a side
3750 of 20 cm or a thickness of 3 cm to support the successful assembling scheme adopted
3751 at BELLE-II, see central panel of Fig. 8.69. The aerogel production efficiency should be
3752 evaluated in conjunction with the optical quality obtained. This engineering work is
3753 expected to take time and not be completed before the end of 2026.

3754 Coating of the CFRP mirror substrate should be realized and compare with the bench-
3755 mark performance obtained with the same materials at CLAS12. This work will be
3756 completed by mid 2025.

3757 A real-scale prototype is being realized with composite materials and a realistic ge-
3758 ometry (mimicking a dRICH sector). This is instrumental to validate the mechanical
3759 elements and study the assembling details (e.g. of transparent septa), the mechani-
3760 cal stability, the gas tightness, and the thermal aspects. One of the major goals of the
3761 real-scale prototype is also to reproduce the final ePIC working conditions, mount an
3762 extended readout plane with the designed RDO board, operate demonstrators of the
3763 optical components as results of the ongoing developments, and optimize the perfor-
3764 mance in a realistic off-axis optics configuration. To this end, a test-beam is planned for
3765 mid 2025.

3766 Other activity needed for the design completion:

3767 Slow control, interlock and the calibration LED/laser system design is not started yet.

3768 Status of maturity of the subsystem:

3769 The R&D activity has been focused on the most innovative aspects of the detector that
3770 present technological challenges. These are the SiPM for single-photon detection in
3771 a strong magnetic field, a compact readout electronics to fit into the ePIC envelope
3772 and the use of two radiators to extend the momentum reach. The remaining effort is
3773 substantial, but is connected to more consolidated technologies, with possibly the only
3774 exception of the gas separation system for the peculiar C_2F_6 gas.

Component	QA station 1	QA station 2	QA detail and backup
Aerogel	Temple U.	BNL	INFN-BA
Gas	BNL		INFN-TS
Mirror	JLab		Duke U.
Sensor (SiPM)	INFN CS-SA-CT	INFN-TS	INFN-BO
Readout	INFN-BO	INFN-FE	INFN-TO

Table 8.17: Planned quality assurance (QA) stations, organized in order to provide redundancy and support specific characterization studies.

3775 **Environmental, Safety and Health (ES&H) aspects and Quality Assessment (QA**
3776 **planning:**

3777 Standard slow-control and interlock procedures will be implemented to control power and
3778 cooling while monitoring gas flow, humidity and temperature. The cooling system is com-
3779 plemented by a buffer tank to allow air flow and heat removal from the detector boxes in
3780 case of a failure of the recirculating system. The gas volume is maintained at +1 mbar with
3781 respect the atmospheric pressure on the top, with a consequent +5 mbar overpressure de-
3782 fined by the hydrostatic pressure of the radiator gas on the bottom, by means of pressure
3783 regulators connected to an UPS station and a two-way bubbler. Hexafluoroethane is non-
3784 flammable and it has limited toxicity, when below 1000 ppm level and for short exposure
3785 time [ref to be added]. In case of a major damage of the supply pipeline or of the vessel
3786 itself, 12 m³ of hexafluoroethane at atmospheric pressure from the vessel (0.02% of the hall
3787 volume) will mix with the air present in the experimental hall, requiring the implementa-
3788 tion of standard ODH procedures. Hexafluoroethane has a high Global Warming Potential
3789 (GWP): 12400 for a horizon time of 100 years [66] and it is, therefore, included in the group
3790 of GreenHouse Gasses (GHG). Environment protection imposes that GHGs are not released
3791 in the atmosphere. This is obtained by using them in closed circuits, where leakages are min-
3792 imized, and by collecting and sending for disposal the fraction of gas purged during circuit
3793 filling and gas recovery at the beginning and at the end of an operation period, respectively.
3794 Both closed circuit gas circulation and purged gas trapping are characterizing elements of the
3795 dRICH radiator gas system design. The maximum expected leakage rate during operation is
3796 about 20 m³ / year assuming six-month operation. Experience in quality assurance protocols
3797 has being gained in parallel with the R&D activity. For each critical component two stations
3798 are being organized to provide essential QA and redundancy, with a (third) station able to
3799 supports in-deep characterization on samples and serve as backup, see Table 8.17. The QA
3800 activity will be supported by manpower from all the dRICH groups. Essential QA paramet-
3801 ers will be measured: integrity, refraction index, transparency, dimensions, and planarity of
3802 the aerogel; leak rate of the gas system (after completion); refractive index and transparency
3803 of the radiator gas (with the monitoring equipment of the gas system); dark count rate and
3804 PDE for the sensors; electrical connections, bias levels and data rate for the readout; dimen-
3805 sions, weight, reflectivity and D0 (point-like source image brightness) for the mirrors.

3806 Annealing of SiPM will be performed during technical stops and/or during the annual stops
3807 of the EIC machine. All the dRICH front-end electronics (FEE) will not be powered, with the
3808 exception of a few components needed to monitor and control the annealing operations. An
3809 interlock-based system will inhibit the FEE power-supply units during annealing. The circu-
3810 lating thermostat system used to cool the SiPMs will be switched to heating mode to reach a
3811 temperature of up to T = 100°C. A slow heating ramp of < 1 °C/minute will be employed to
3812 reduce thermal stress on the system. The dRICH photodetector boxes will be thermally insu-
3813 lated as much as possible to reduce heat leaks into neighbouring detectors while performing
3814 annealing. It is expected that the inner volume of the detector box can reach a temperature

3815 of $T = 100^{\circ}\text{C}$ and will be monitored with temperature sensors. Temperature sensors will be
 3816 placed on the outside of the photodetector boxes to monitor the external environment. An-
 3817 nealing of the whole dRICH photosensors at once requires up to 160 kW of power and will
 3818 not be performed as such. Only a fraction of the dRICH SiPMs will perform annealing at
 3819 a given time, to limit the total amount of power needs to about 20-40 kW. This is a similar
 3820 to the total power consumption of the FEE during normal operations and the same safety
 3821 procedures apply. Annealing power will be distributed evenly across the dRICH SiPM. In
 3822 case of a power outage, the annealing current will be promptly removed from the SiPMs and
 3823 their temperature will promptly drop to the temperature of the thermostat. The latter will
 3824 eventually slowly cool down.

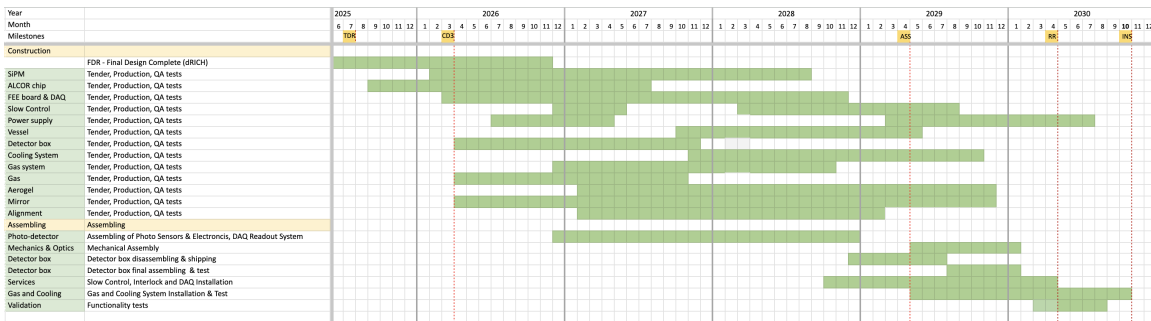


Figure 8.73: Construction plan

3825 **Construction and assembly planning:**
 3826 The construction and assembling plan assumes to compress all the necessary tasks in a short
 3827 time period in between the presently known EIC milestones: start with CD3 (at the begin-
 3828 ning of 2026) and completion 6 months in advance of installation (in October 2030). This
 3829 results in an aggressive schedule in terms of manpower and funding profile. The 6 months
 3830 contingency time before installation will be used to perform functionality tests, and complete
 3831 the services in the experimental hall at IP6. The assembling of 1248 PDUs comprising SiPM
 3832 sensors and cooling, front-end electronics and RDOs, and their integration with the services
 3833 inside six detector boxes will be staged over 2 years (mainly 2027 and 2028) by the dRICH
 3834 DSC in Italy. This organized effort requires a timely procurement, starting with the ALCOR
 3835 chip (wafer and packaging) followed by sensors, readout electronics, and box mechanics.
 3836 Cooling infrastructure and DAQ system are expected to run in parallel to the detector box
 3837 construction and be mainly covered by the EIC Project. First articles of DAQ, power sup-
 3838 ply and slow control could be used for the initial functionality tests of each single detector
 3839 box, but the main effort on such services is concentrated on a later stage of the plan during
 3840 assembling at BNL. The detector boxes will be completed in time to be shipped to BNL and
 3841 mounted on the dRICH in the second half of 2029. The dRICH vessel construction, a joint
 3842 venture of the dRICH DSC and the EIC Project, will start in 2028 in order to be ready for
 3843 detector assembling mid 2029. Mirror production is expected to take 2 years and is staged as
 3844 soon as possible, subject to the funding profile of the EIC Project, to reduce the sole source
 3845 risk. The engineering of the aerogel production is expected to extend beyond the TDR, with
 3846 the consequent production led by the dRICH DSC not happening before 2027 and lasting
 3847 for at least 2.5 years. An early procurement of the C_2F_6 gas by the EIC Project is planned in
 3848 order to reduce the risk of a market price increase. The principle design of the radiator gas
 3849 system will be completed by the end of 2026 by the dRICH DSC. The executive drawings and
 3850 the system realization by the EIC Project engineering team supported by adequate technical

3851 personnel is expected during years 2027 and 2028. The layout finalization and validation of
 3852 the monitoring equipment will be completed by the end of 2026, while its realization is by
 3853 the end of 2027 by the dRICH DSC. This equipment will be interfaced with the gas system
 3854 in 2028, via synergistic effort between the EIC Project engineering team and the dRICH DSC.
 3855 This combined group will perform the QA assessment of the gas system in 2029.

3856 **Collaborators and their role, resources and workforce:**

3857 INFN has agreed on a substantial in-kind contribution and the corresponding workforce has
 3858 taken corresponding responsibilities in the construction within the DSC. The INFN in-kind
 3859 will cover the design, production and quality assurance cost of the SiPM sensors, of front-
 3860 end ASIC (ALCOR), of the front-end board (FEB), of the readout boards (RDO) as well as
 3861 the assembly of the above components in a compact Photo Detector Unit (PDU), including
 3862 the cooling circuitry and related mechanics. It will cover the cost of the realization of the
 3863 six detector boxes (containing the PDU of each sector) with the control panels and the elec-
 3864 tronic services attached (for HV/LV/daq links routing). It will contribute to the design and
 3865 realization of the main vessel, the design/supervision of the powering and monitoring sys-
 3866 tems, the dRICH tagging system and data filtering in streaming mode, see Sec. ?? , and to the
 3867 definition of specifications and quality assurance (QA) of all the other components and ser-
 3868 vices (i.e. gas, power and cooling plants). The availability of the essential local resources as
 3869 mechanical and electronic workshops and laboratory space have been negotiated. **INFN-FE**
 3870 (IT): is coordinating the DSC activity and is leading the mechanical design. The group will
 3871 lead the design and production of the vessel in collaboration with the EIC Project and will
 3872 take care of the realization of the detector boxes and corresponding control panels for the 6
 3873 sectors. The assembly of the detector boxes is expected to happen in its laboratories. **INFN-**
 3874 **BO** (IT): the group is leading the activity on photosensors (SiPM) and data-acquisition. It
 3875 will be responsible of the procurement of SiPM, design and production the readout boards
 3876 (RDO) and coordinate the integration of the various elements of the PDU. The PDU will be
 3877 assembled in BO and tested/validated before being moved to INFN-FE for the installation
 3878 in the detector boxes. **INFN-BA** (IT): the group is leading the aerogel activity. It will coor-
 3879 dinate the mass production and the quality assurance (expected to be operated in the US at
 3880 Temple University and BNL). **INFN-CS-SA-CT** (IT): this cluster of units will work on the
 3881 QA of SiPM and front-end boards prior of the PDU assembling. They will equip test stations
 3882 in SA and CS for this purpose. **INFN-GE** (IT): is carrying out a feasibility study (and if suc-
 3883 cessful, the realization) of a dRICH tagger to filter the SiPM data stream. **INFN-LNS** (IT):
 3884 the group will contribute to the mechanical design effort. **INFN-RM1/RM-TV** (IT): the RM1
 3885 group (and one staff person of RM-TV) has extensive experience on AI algorithm running
 3886 on FPGA. They will develop algorithm for pattern recognition and data reduction on FE-
 3887 LIX cards and the interface with the signals received by the dRICH tagger or from ePIC via
 3888 GTU. **INFN-TO** (IT): the group is leading on the design, test and production of the front-end
 3889 ASIC ALCOR. The group will produce the chips and the front-end cards (FEB) mounting
 3890 the ALCOR, and coordinate the quality assurance tests of the chip and FEB. **INFN-TS** (IT):
 3891 the group is leading the radiator gas activity. It will lead the design of the gas system and
 3892 develop a continuous monitor system (critical to maintain a good chromaticity). It will also
 3893 develop a test station of SiPM (with smaller capacity with respect to the CS-SA-CT cluster).
 3894 **DUKE U.** (US) is leading the mirror activity. It will coordinate the mirror production, ex-
 3895 pected to happen in the States, the corresponding QA activity, and the coating process that
 3896 possibly will be realized at Stony Brook. **Jefferson Lab** (US) is contributing to the mechanical
 3897 design and developing tools for mirror characterization. **Brookhaven Lab** (US) is contribut-
 3898 ing to the mechanical design and integration study. It will lead the infrastructure (installation
 3899 tools, services, safety control) realization with its design authority and technical resources.

3900 **Stony Brook** (US) is developing mirror coating capability. **Temple U.** (US) is developing an
3901 aerogel quality assurance facility. **M.S.Ramaiah U.** (India) is contributing to the simulation
3902 and performance study. **NISER** (India) is contributing to the performance study. **Haryana**
3903 **and Karnataka U.** (India) have started contributing to the performance study. Secondments
3904 of personnel from all the DSC groups will be organized to support the QA activity in US and
3905 the assembling phase at BNL. The EIC Project is expected to cover the procurement effort
3906 that can be more efficiently based on US, and all the safety, infrastructural and integration
3907 aspect that require specific engineering background. This include the cost of the gas, of the
3908 mirrors, of the installation tools, of the power-supply systems, of the cooling plant and the
3909 gas plant, and of the FELIX cards receiving the data from the RDO.

3910 **Risks and mitigation strategy:**

3911 The major risk of the dRICH gas radiator is the banning of the hexafluoroethane or more
3912 severe restriction on its usage, that can also result in increased cost or difficult procurement.
3913 The only alternative option to preserve the dRICH performance would be an eco-friendly
3914 gas with very similar refractive index, an option not available in nature at atmospheric
3915 pressure. Argon at ≈ 3 bar absolute pressure mimics with great accuracy the hexafluoroethane
3916 characteristics. It is also non-expensive, non-toxic and non-flammable. R&D
3917 is being performed within the EIC generic R&D program to establish the validity of this
3918 approach as risk mitigation strategy. Radiation damage reduces the lifetime of the SiPM as
3919 good photodetector for the dRICH performance. Estimates of the radiation level on the
3920 dRICH photodetectors are expected to be accurate. The DCR model shown in Figure 8.61
3921 (right) is for the sensors experiencing the largest radiation levels (closer to the beam line) and
3922 for detector operation at $V_{\text{over}} = 4$ V and $T = -30^{\circ}\text{C}$. Operation at lower $V_{\text{over}} = 3$ V and/or
3923 lower temperature $T = -40^{\circ}\text{C}$ would reduce the DCR without loss in performance, hence
3924 allowing one to accommodate larger integrated radiation levels (up to a factor 2-3) than
3925 those reported in the figure. The addition of small thermoelectric cooling (TEC) modules will
3926 be evaluated as a potential approach to boost the cooling performance, allowing one to reach
3927 an even lower operation temperature of $T = -50^{\circ}\text{C}$ and avoid possible dishomogeneities.
3928 Current R&D on new SiPM technologies for improved performance and radiation hardness
3929 are being followed up as a risk mitigation strategy and as a potential upgrade for the
3930 dRICH photodetector in the late 2030's or in the early 2040's. For two components, optical
3931 aerogel and carbon-fiber mirror, there is only one known supplier able to deliver the wanted
3932 specifications at the present stage. An early procurement should limit the risk of a market
3933 discontinuity. Within the ePIC RICH Consortium, the recently initiated R&D on mirrors at
3934 Purdue University are being followed up as potential sources of risk mitigation in the long
3935 term period, if the adaptation to the dRICH needs will be proven feasible. DSC members are
3936 part of the recent DRD4 initiative, that aims to create a worldwide collaborative environment
3937 to favor new technological breakthroughs in Cherenkov particle identification and photon
3938 detectors. Within DRD4, there are many development areas of interest for the dRICH
3939 program, in particular gasses or mixtures alternative to the greenhouse fluorocarbon gasses
3940 and radiation hard SiPM.

3941

- 3942 **Additional Material** Planning of additional material for the gas radiator sys-
3943 tem/monitoring equipment:
- 3944 – Radiator Aerogel:
 - 3945 * aerogel characterization in lab and beam tests;
 - 3946 * details of the aerogel support and purging;
 - 3947 – Radiator Gas:
 - 3948 * Hexafluoroethane characteristics;
 - 3949 * Detailed description of the gas system;
 - 3950 * Options for gas separation during filling and gas recovery operations;
 - 3951 * Trapping system to collect hexafluoroethane in the purged gas;
 - 3952 * Jamin interferometer for refractive index measurement;
 - 3953 * Measurement of the transparency with the spectrophotometer;
 - 3954 * Oxygen and water vapor contamination: measurement and removal;
 - 3955 * High-pressure Ar R&D;
 - 3956 – Mirror:
 - 3957 * mirror characterization in lab and beam tests;
 - 3958 * details of the mirror structure;
 - 3959 * details of the mirror support;
 - 3960 * details of the mirror alignment;

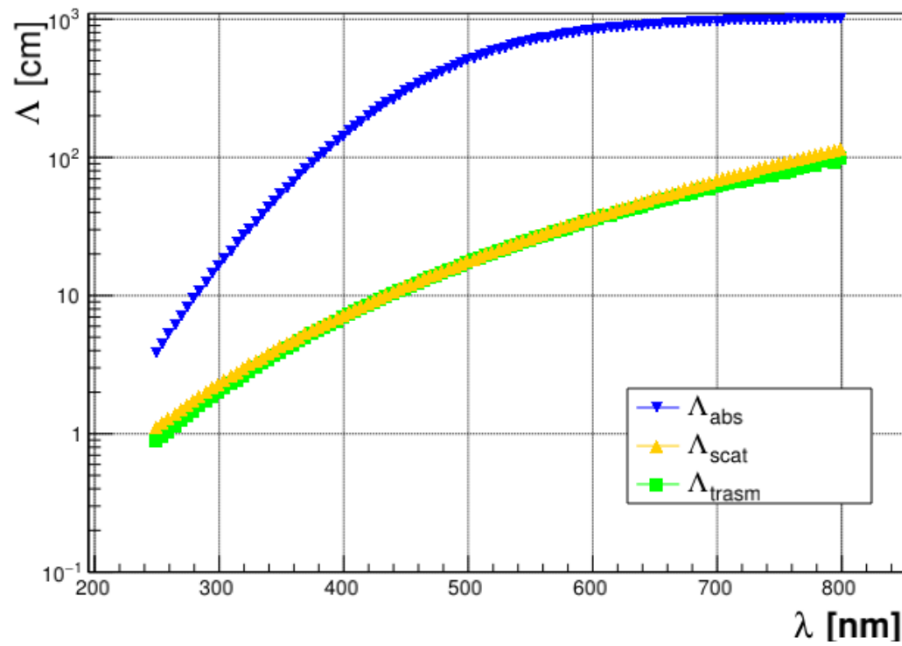


Figure 8.74: Transmission, absorption and scattering length curves as a function of the wavelength for the tile with $n = 1.03$.

3961

In the following the specifications of the main dRICH components are tabulated.

Detector element	Abbreviation	Elements/sector	Total elements
Photodetector box	PDB	1	6
Master panel board	MPB	26	156
Photodetector unit	PDU	208	1248
Silicon photomultiplier	SiPM	53248	319488
SiPM sensor arrays		832	4992
Readout board	RDO	208	1248
Front-end board	FEB	832	4992
ALCOR chips		832	4992

Table 8.18: Main elements of the dRICH photodetector system with the indication of number of elements per sector and the total.

Parameter	Value	Notes
Package type	SiPM array	
Package dimension	$< 26 \times 26 \text{ cm}^2$	
Mounting technology	surface mount	
Number of channels	64	
Matrix layout	8×8	
Channel size	$3 \times 3 \text{ mm}^2$	
Fraction of active area in package	$> 85\%$	
Microcell pitch	50 - 75 μm	
Protective window material	silicone resin	radiation & heat resistant
Protective window refractive index	1.55 - 1.57	
Spectral response range	300 to 900 nm	
Peak sensitivity wavelength (λ_{peak})	400 - 450 nm	
Photon detection efficiency at λ_{peak}	$> 40\%$	
Breakdown voltage (V_{break})	$< 60 \text{ V}$	
Operating overvoltage (V_{over})	$< 5 \text{ V}$	
Operative voltage (V_{op})	$< 64 \text{ V}$	
Max V_{op} variation between channels	$< 100 \text{ mV}$	at $T = -30^\circ\text{C}$
Channel dark count rate (DCR)	$< 50 \text{ kHz}$	
DCR at $T = -30^\circ\text{C}$	$< 5 \text{ kHz}$	at $T = -30^\circ\text{C}$
DCR increase with radiation damage	$< 500 \text{ kHz}/10^9 \text{ n}_{\text{eq}}$	at $T = -30^\circ\text{C}$
Residual DCR after annealing	$< 50 \text{ kHz}/10^9 \text{ n}_{\text{eq}}$	at $T = -30^\circ\text{C}$
Terminal capacitance	$< 500 \text{ pF}$	
Gain	$> 1.5 \cdot 10^6$	
Recharge time constant (τ)	$< 100 \text{ ns}$	
Crosstalk (CT)	$< 5\%$	
Afterpulsing (AP)	$< 5\%$	
Operating temperature range	$-40 \text{ to } 25^\circ\text{C}$	
Single photon time resolution (SPTR)	$< 200 \text{ ps FWHM}$	

Table 8.19: Baseline specifications of the SiPM sensor devices for the dRICH photodetector. All parameters are defined at room temperature ($T = 25^\circ\text{C}$) and at the operating voltage V_{op} , unless otherwise specified.

Tile	Refractive index @405 nm	Nominal thickness (mm)
1	1.03	20.7
2	1.03	20.8
3	1.03	20.1
4	1.03	20.5
5	1.03	20.4
6	1.03	10.0
7	1.03	10.0
8	1.04	20.3
9	1.04	20.5
10	1.04	20.3
11	1.04	20.4
12	1.04	20.5
13	1.05	20.5
14	1.05	20.7
15	1.05	20.6
16	1.05	20.6
17	1.05	20.8
18	1.005	20.0
19	1.005	20.0
20	1.005	20.0

Table 8.20: Tiles list. Tiles from 1 to 17 were produced at the High Energy Accelerator Research Organization (KEK) in Japan and delivered in March 2021 [5], except tiles 6-7 which belongs to a 2000 production manufactured by Matsushita Electric Works (Japan).

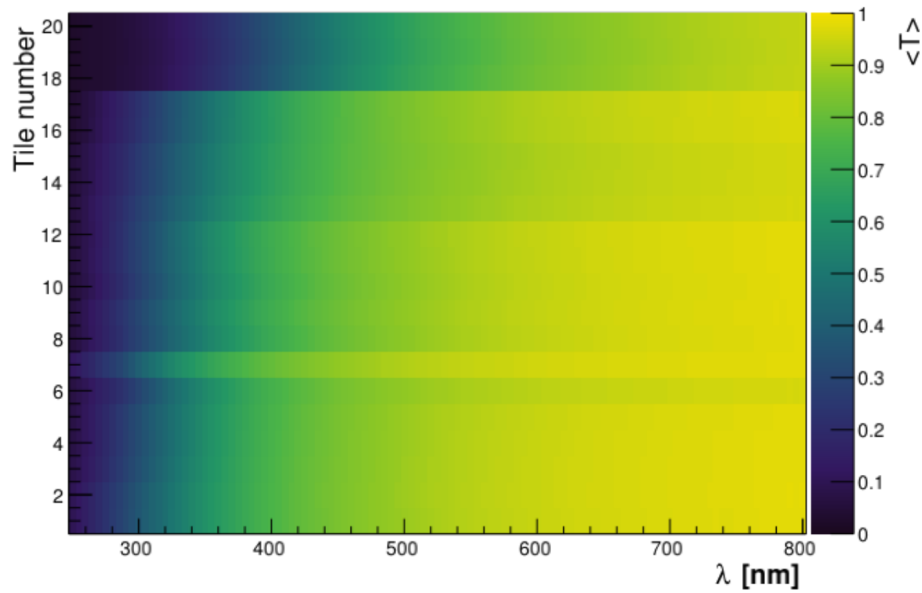


Figure 8.75: Transmittance as a function of the wavelength for all the tiles.

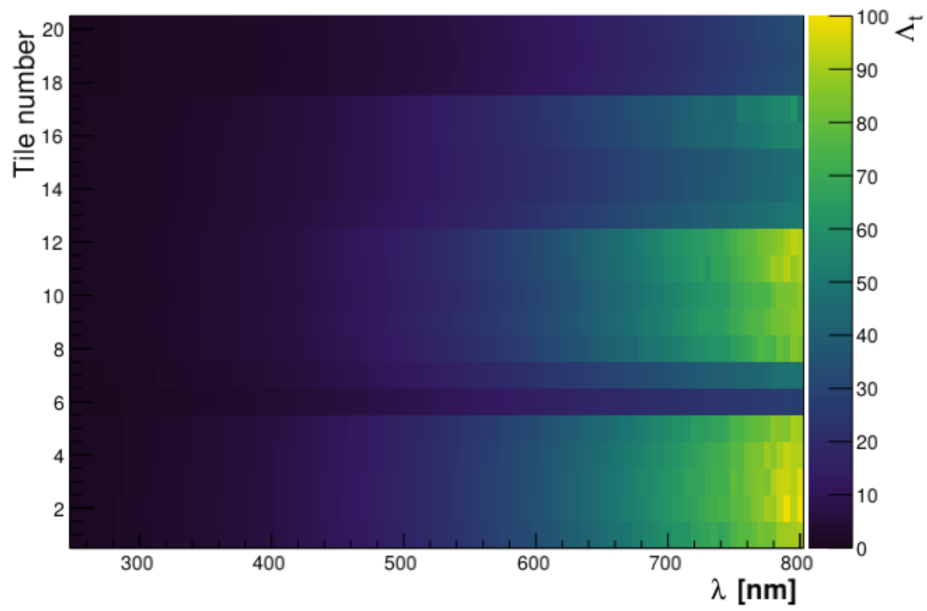


Figure 8.76: Transmission length as a function of the wavelength for all the tiles.

3962 **8.3.5 Electromagnetic Calorimetry**

3963 Add text here.

3964 8.3.5.1 The backward endcap electromagnetic calorimeter

3965 Requirements

3966 **Requirements from physics:** The electron-end-cap calorimeter will cover a dynamic energy
3967 range of 0.1–18 GeV for electromagnetic showers of the scattered electron based on e+p Pythia
3968 simulations at $18 \times 275 \text{ GeV}^2$. The EEMC is a high-resolution ECal designed for precision measure-
3969 ments of the energy of scattered electrons and final-state photons in the electron-going region. The
3970 requirements for energy resolution in the backward region is driven by inclusive DIS where precise
3971 determination of the scattered electron properties is critical to constrain the event kinematics.

3972 An excellent energy resolution of $\sigma_E/E \approx 2\%/\sqrt{E} \oplus 1\%$ is required for the backward endcap elec-
3973 tromagnetic calorimeter.

3974 **Requirements from Radiation Hardness:** The EEEMCal detector must operate at a radia-
3975 tion level of $\sim 3 \text{ krad/year}$ (30 Gy/year) electromagnetic and 10^{10} n/cm^2 hadronic at the EIC top
3976 luminosity

3977 **Requirements from Data Rates:** Add text here.

3978 Justification

3979 **Device concept and technological choice:** The EIC physics program requires high-precision
3980 detection and identification of the scattered electrons emitted in the electron-going direction, as
3981 well as final-state photons. The backward endcap electromagnetic calorimeter (EEEMCAL) pro-
3982 vides a compact solution with excellent energy resolution over a large dynamic range and with high
3983 granularity. The EEEMCAL meets the experiment requirements of fast timing to handle an inter-
3984 action rate up to $0.5 \times 10^6 \text{ Hz}$ and acceptable radiation hardness up to $\sim 3 \text{ krad/year}$ (30 Gy/year)
3985 electromagnetic and 10^{10} n/cm^2 hadronic at the EIC top luminosity. Furthermore, the EEEMCAL
3986 achieves the required clean electron identification for energies greater than 2 GeV with a rejection
3987 factor better than 10^4 when combined with other detector subsystems. The EEEMCAL has been
3988 reviewed and passed the EIC Project detector technical review of electromagnetic calorimetry in
3989 December 2022.

3990 A drawing of the EEEMCal mechanical design is shown in Figure 8.77. The EEEMCAL will be
3991 located at a distance of 175 cm from the EIC interaction point where it is installed around the beam
3992 line in a roughly cylindrical geometry. The particles of interest impinge on the front face of the
3993 detector and pass through a radiator with adapted geometrical dimensions to contain the major
3994 part of the electromagnetic shower. The produced scintillation photons are detected at the back of
3995 the radiator by means of an array of Silicon PhotoMultipliers (SiPMs) and readout with back- and
3996 front-end electronics. The entire detector is enclosed in a mechanical structure that also provides
3997 services like thermal monitoring and cooling and light monitoring. The entire assembly weighs on
3998 the order of three tons, which is consistent with the specifications of the EIC experimental area.

3999 Based on extensive simulation studies, the preferred material for the EEEMCAL radiator is lead
4000 tungstate (PWO), an extremely fast, compact, and radiation-hard scintillator providing sufficient
4001 luminescence yield (15 - 25 photoelectrons/MeV) to achieve good energy resolution. This material

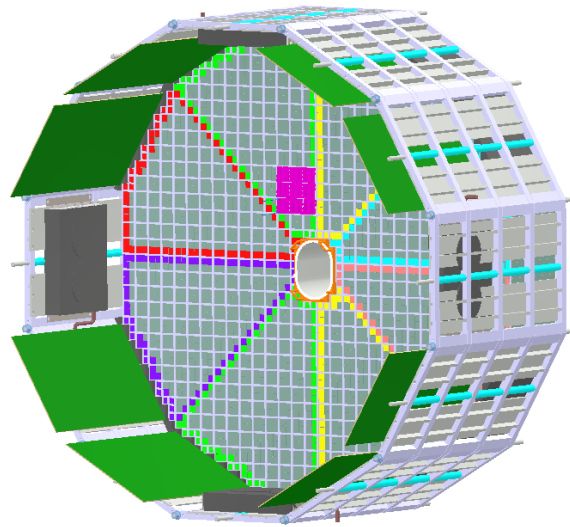


Figure 8.77: CAD drawing of the EEEMCAL. The small gray shapes are the scintillating crystals. The SiPM photosensor matrices are grouped over four crystals and indicated by the pink area. The green rectangles are part of the backend electronics. The dark gray rectangles and circles on the circumference are part of the cooling system.

4002 has been the most common precision calorimetry method of choice for hadron physics measure-
 4003 ments with electromagnetic reactions, such as at multiple setups at JLAB and also at PANDA/GSI.
 4004 To achieve good energy resolution including the so-called constant term typically requires 20 or
 4005 more radiation lengths (X_0). For PWO in the EEEMCAL we have $22X_0$ (20 cm). The transverse
 4006 block dimensions are matched to the Moliere radius to capture the major part of the transverse
 4007 shower. The measured energy resolution for PWO is $\sigma_E/E \approx 2\%/\sqrt{E} \oplus 1\%$ [67]. To pinpoint the
 4008 electron scattering kinematics, the EEEMCAL provides a position resolution of $\sim 2\text{mm}$ at 1-3 GeV
 4009 with a granularity of 2 cm. The technology for mass production of PWO crystals that guarantees the
 4010 needed homogeneity of the whole calorimeter has been well established with recent experiments,
 4011 most recently with the Neutral Particle Spectrometer at JLab [68,69].

4012 An effective way to read out the EEEMCAL is through SiPMs that offer several advantages, e.g., a
 4013 high gain and a medium photodetection efficiency of about 50%. Furthermore, SiPMs can be oper-
 4014 ated in the magnetic field of order few hundred Gauss expected at the location of the EEEMCAL.
 4015 Individual devices are grouped into an array to maximize surface coverage of the PWO blocks. In
 4016 a recent beam test campaign, the readout concept was validated to work well with a Streaming
 4017 Readout setup, the method of choice envisioned for the EIC [70].

4018 **Subsystem description:**

4019 General device description: In the EEEMCAL the PWO crystals are arranged in the mechanical
 4020 support structure (Fig. 8.78). This provides the infrastructure to attach the readout compo-
 4021 nents, cooling system, and cables, as well as the installation fixtures to mount the detector in
 4022 the experimental hall. The support for the crystals is provided by a frame that is installed in
 4023 the mechanical structure. Photosensors are located at the backend of the crystals. Mechanical
 4024 grating in the mechanical structure allows the attachment of the SiPM PCBs there. The crys-
 4025 tals are stacked with carbon fiber plates at front and back that allow one to guide the crystal

4026 into position. The cooling system provides thermal stabilization, which is important for crys-
 4027 tal performance. Based on initial thermal calculations, this stabilization can be achieved with
 4028 a combination of internal and external cooling aided by airflow.

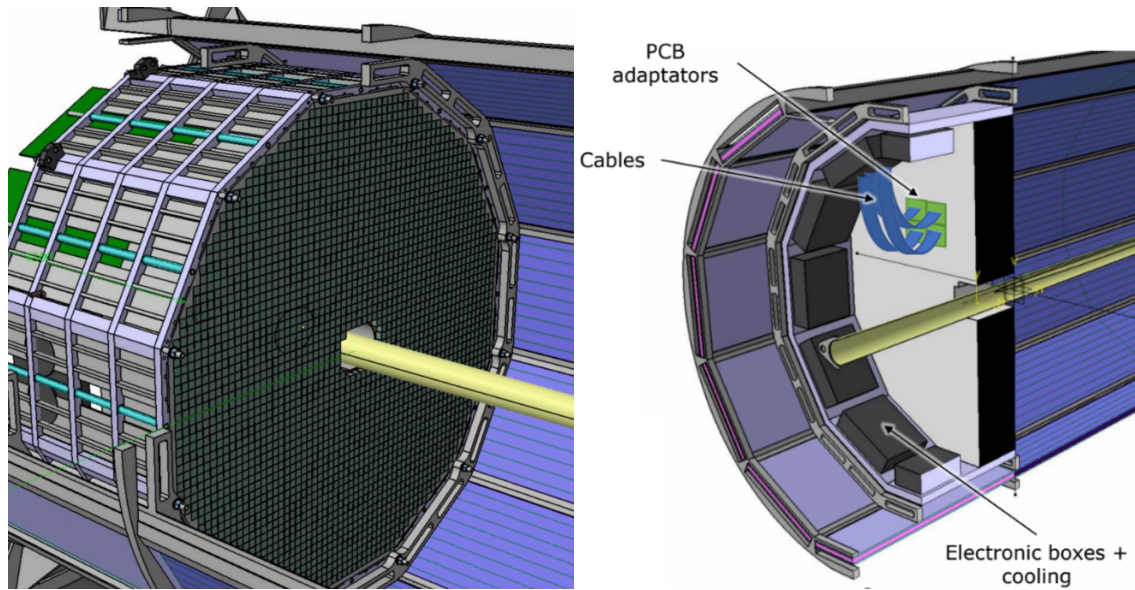


Figure 8.78: Conceptual design of the ePIC electron endcap electromagnetic calorimeter support.

4029 Sensors: Hamamatsu S14160-1315 SiPMs have been identified as the optimal choice for the
 4030 EEEMCal. Their gain of $3.6 \cdot 10^5$ and relatively low dark current rate (0.7 MHz) allow the
 4031 measurement of very small signals, close to the single photo-electron (Fig. 8.79, left), while its
 4032 high pixel density provided by a $15\text{-}\mu\text{m}$ pixel pitch provides very good linearity over several
 4033 orders of magnitude (Fig. 8.79, right).

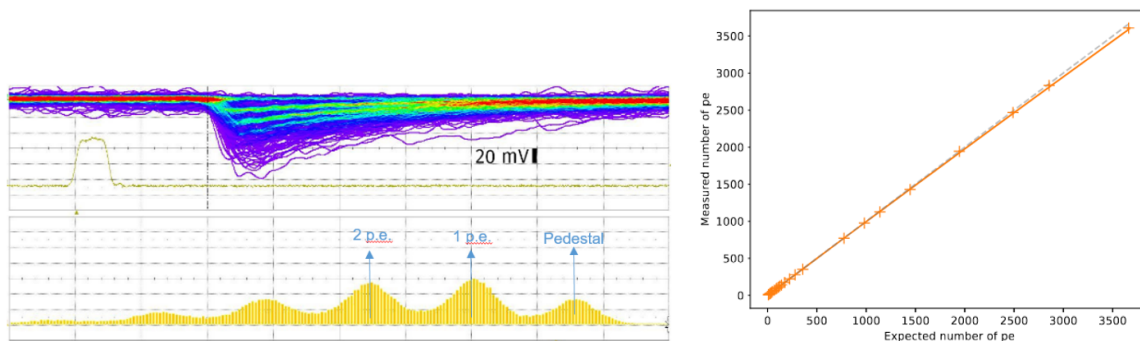


Figure 8.79: Left: waveform (top) and integrated signal (bottom) showing single photo-electron signals in Hamamatsu 15 μm pixel SiPMs. Signals are produced with a low-intensity LED. Right: Linearity measurement, showing 2% linearity up to 3500 photo-electrons.

4034 FEE: All calorimetry in ePIC will use SiPMs for their readout. However, the number of chan-
 4035 nels and input signals and capacitance varies greatly from detector to detector. The require-

4036 ments of the EEEMCal are particularly stringent in terms of energy resolution, which in par-
 4037 ticular requires the detection of low energy signals (down to 5 MeV per crystal). The readout
 4038 should provide sufficient dynamic range to accommodate for signals of energy up to 18 GeV.
 4039 A discrete readout solution based on commercial devices is currently the baseline for the for-
 4040 ward and backward ECals. However, a readout based on the existing H2GCROCv3 chip
 4041 (developed for the CMS HGCALE) is currently under investigation for the backward ECal.
 4042 It presents many advantages, in addition to exploiting the synergies with most of the other
 4043 calorimeters in ePIC. Using an ASIC in the readout of the calorimeter is a very cost effective,
 4044 more radiation tolerant and cooler (i.e. consuming less power) solution. The H2GCROCv3
 4045 chip was developed by the Omega group for the primary use for the High Granularity
 4046 Calorimeter (HGCALE) for the CMS detector at LHC, making it a great fit for any calorime-
 4047 ter readout. The ASIC requirements for the EEEMCal are very low noise level, low power
 4048 consumption and very good ($< 1\%$) linearity throughout a very large dynamic range. The
 4049 chip also has a current conveyor where each channel's bias voltage can be fine-tuned from
 4050 the ASIC itself. A variation of the H2GCROCv3 chip (CALOROC) is currently under devel-
 4051 opment by OMEGA in order to make it compatible with EIC.
 4052 Other components: Add text here.

4053 **Performance** Our group has performed extensive simulations of the detector performance in the
 4054 ePIC geometry, including a realistic material budget in front of the detector, which directly affects
 4055 its resolution and PID capabilities. Figure 8.80 shows the performance of two key parameters: the
 4056 energy resolution and the pion rejection factor. Results fulfill the physics requirements as outlined
 4057 in the Yellow Report [6] and NAS study [ref].

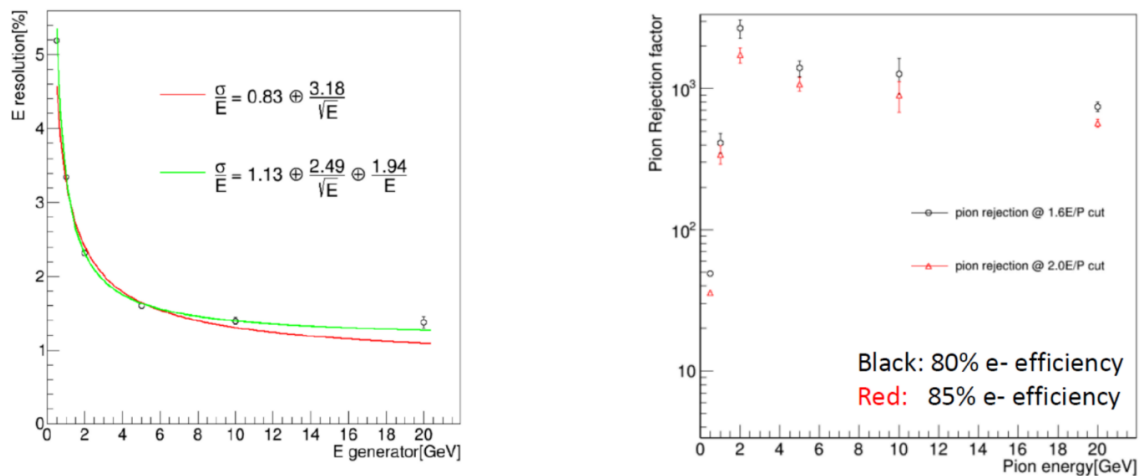


Figure 8.80: EEEMCal simulated performance using the ePIC detector framework including all materials. Left: energy resolution as a function of the incident particle energy. Right: pion rejection factor as a function of energy and different values of electron efficiency.

4058 **Implementation** The EEEMCAL project has been organized into a well-defined Work Break-
 4059 down Structure (WBS). The WBS contains the work necessary to complete the project scope and
 4060 will form the basis of planning, executing, and controlling project activities. The WBS ensures that
 4061 no portions of the estimate are omitted. The level of the WBS reflect a logical breakdown of the
 4062 work by major system as shown in Table 8.21.

WBS	WBS Title	WBS description
2.00	EEEMCAL Project	Construct the EEEMCAL. The EEEMCAL is an electromagnetic calorimeter for measurement of the inclusive process physics in the electron-going direction at the EIC
2.01	Radiator	Radiation detectors consisting of scintillating crystals (PWO) and thin reflector sheets. These provide the detection of energetic electrons
2.02	Photosensor	Photosensors consisting of multi-pixel photon counters grouped into an array to maximize surface coverage of the PWO blocks.
2.03	Mechanical	Mechanical structure including installation fixtures and a cooling system providing thermal stabilization, which is important for crystal performance.
2.04	Signal Processing/DAQ	Signal Processing/DAQ providing the front-end electronics to transmit the signals to the data analysis modules
2.05	Simulation/Software	Simulations/Software providing the software libraries and infrastructure foundation for extracting the physics from the detector

Table 8.21: EEEMCAL WBS Structure

4063 The baseline schedule for the EEEMCAL Project is shown in Fig. 8.81. The EEEMCAL project aims
 4064 at the beginning of the window of installation at BNL. The installation window dates are October
 4065 2028 to June 2030.

4066 **Services:** PbWO₄ crystals are sensitive to temperature changes with a variation of 2%/°C in
 4067 light output. Thus, the specification is to keep the crystal temperature stable within ± 0.1 °C. To
 4068 ensure this stability the additional heat generated by the electronics needs to be removed and the
 4069 following cooling structures are being considered. As internal cooling structure several machined
 4070 copper blocks with internal coolant circulation will be used around the beam pipe. To reduce the
 4071 spatial extend support structures the EEEMCAL consortium is moreover planning to use cooling
 4072 plates in between the readout cables which are linked to the support structure surrounding the
 4073 EEMC with tubes. This system is composed of 12 plates with a 5-8 mm spacing in which water can
 4074 be circulated. The cooling near the crystals will likely not be enough to meet specification. These
 4075 challenges could be overcome by outside cooling with standard cooling blocks with airflow in front
 4076 of the electronics or additional cooling added at the back of the assembly.

4077 **Subsystem mechanics and integration:** The EEEMCAL installation fixtures are shown in
 4078 Fig. 8.82. They include a mechanical structure that mounts the detector and positions it in the
 4079 EIC experimental hall at the appropriate height above ground. The structure is envisioned to ride
 4080 on rails for the installation. The rails could be on the floor as shown, but could also be within the
 4081 cylindrical structure. In the latter case the outer structure would be bolted to the floor. Having the
 4082 rails extend from the cylindrical structure has the advantage that it would not require rails on the
 4083 floor of the experimental hall, which could interfere with other hall infrastructure, e.g., the magnet.

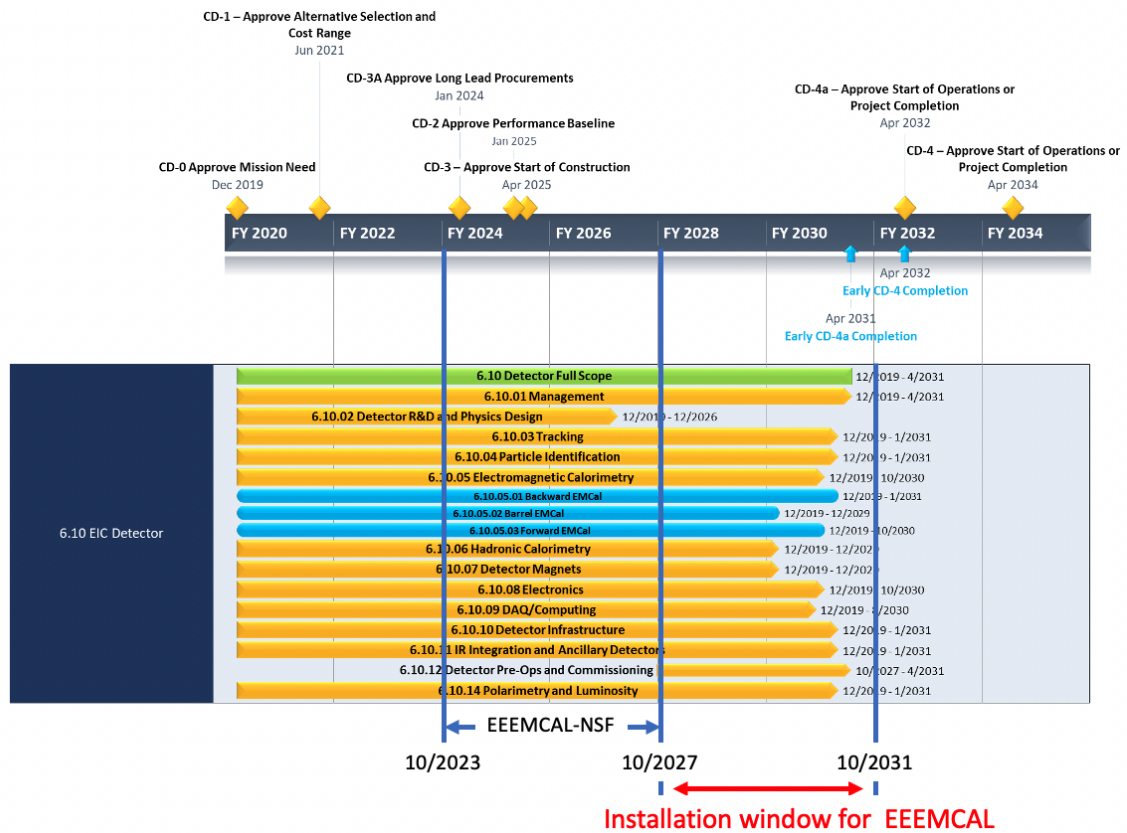


Figure 8.81: EEEMCAL integrated schedule.

4084 **Calibration, alignment and monitoring:** Add text here.

4085 **Status and remaining design effort:**

4086 R&D effort: Add text here.

4087 E&D status and outlook: Add text here.

4088 Other activity needed for the design completion: Add text here.

4089 Status of maturity of the subsystem: Add text here.

4090 **Environmental, Safety and Health (ES&H) aspects and Quality Assurance (QA) planning:** Quality Assurance (QA) is an integral part of effective project management and will be
 4091 employed throughout the design, procurement, and construction of the project. An EEEMCAL
 4092 Project-specific Quality Assurance Plan has been developed to establish all applicable QA require-
 4093 ments for the design, construction, and operation of the EEEMCAL, consistent with the EIC Quality
 4094 Assurance Plan that implements the ten criteria defined in DOE Order 414.1D.
 4095

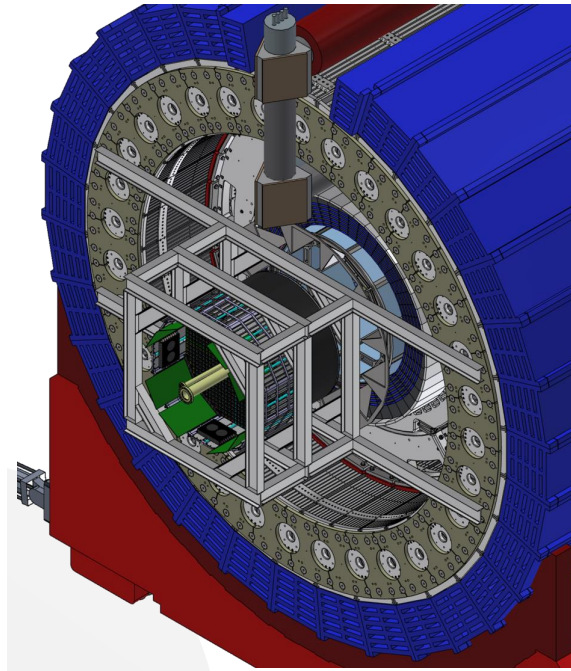


Figure 8.82: EEEMCAL installation fixtures that allow for installing the detector safely into the ePIC detector barrel.

4096 **Construction and assembly planning:** Upon completion of its construction and initial test-
 4097 ing, the EEEMCAL will be situated at BNL. The EEEMCAL collaboration leaders will coordinate
 4098 the required equipment readiness for experiment and final integration of the EEEMCAL into the
 4099 EIC beamline with the EIC Project Management, the ePIC collaboration, and the BNL and JLAB
 4100 Technical leads. This is necessary for successful integration. For example, a special external sup-
 4101 port frame will be provided, installed, and surveyed by the BNL technical staff for this purpose.
 4102 All installations and the integration of the EEEMCAL will be handled by BNL technical staff with
 4103 expert's assistance to ensure appropriate interfacing of infrastructure and fulfillment of installation
 4104 and operation protocols.

4105 Once installed in the EIC experimental hall the EEEMCAL will be operated and maintained by
 4106 the EEEMCAL team and its stakeholders in collaboration with technical teams at BNL. The nor-
 4107 mal operating resources will be provided by BNL. The physics resources to operate and maintain
 4108 the EEEMCAL will be provided through research grants. These resources are critical for tasks that
 4109 are not directly related to the construction of the calorimeter, but instead to the integration of the
 4110 EEEMCAL into the ePIC detector. Examples include developing readout software and trigger algo-
 4111 rithms, implementing online GUIs and the slow controls interfaces required to operate and monitor
 4112 the detector during data taking, as well as designing clustering algorithms and calibration tools and
 4113 integrating them into the ePIC workflow.

4114 **Collaborators and their role, resources and workforce:** Add text here.

4115 **Risks and mitigation strategy:** Risk planning details are included in the Risk Management
 4116 Plan and the Risk Registry (see Fig. 8.83). The EEEMCAL Risk Registry is a living document used

4126 8.3.5.2 The barrel electromagnetic calorimeter

4127 Requirements

4128 **Requirements from physics:** The Barrel Electromagnetic Calorimeter (BEMC) must meet the
4129 stringent physics requirements set by the EIC program. It needs to identify scattered electrons and
4130 measure their energy, particularly in high Q^2 events, and also detect decay electrons from vector
4131 or heavy flavor meson decays, and DVCS photons (G-DET-ECAL-BAR.1). Electron identification,
4132 including electron-pion separation, is required up to 50 GeV and down to 1 GeV (F-DET-ECAL-
4133 BAR.1), with an energy resolution better than $10\%/\sqrt{E} \oplus (2-3)\%$ (P-DET-ECAL-BAR.1). Addi-
4134 tionally, the BEMC must provide photon reconstruction from 100 MeV to 10 GeV (F-DET-ECAL.9,
4135 F-DET-ECAL-BAR.2). The system must also achieve photon-pion discrimination (γ/π^0 separa-
4136 tion) up to 10 GeV, with the ability to distinguish two showers with an opening angle down to 30
4137 mrad (P-DET-ECAL-BAR.3). Furthermore, the BEMC will assist with muon identification (G-DET-
4138 ECAL-BAR.3) and provide a charged tracking point behind the DIRC to help with charged hadron
4139 PID (P-DET-ECAL-BAR.4), with a spatial resolution of less than 150 μm . Lastly, the system must
4140 have sufficient dynamic range to detect MIP signals (P-DET-ECAL-BAR.5).

4141 **Requirements from Radiation Hardness:** The BEMC must be designed to operate in an en-
4142 vironment where it may experience radiation levels of up to about 3.9×10^9 1-MeV neutron equiv-
4143 alent per cm^2 per year of running (6 months), corresponding to full luminosity and background
4144 conditions (F-DET-ECAL.6). All components, including sensors, electronics, and structural materi-
4145 als, must be sufficiently radiation-hardened to maintain performance under these conditions. This
4146 includes ensuring that the sensor response, energy resolution, and position reconstruction capabil-
4147 ities remain stable throughout the detector's operational lifetime.

4148 **Requirements from Data Rates:** The BEMC and its readout technology must be designed
4149 to handle the high event rates expected at full luminosity, ensuring stable performance under
4150 expected background conditions, including radiation doses and neutron flux (F-DET-ECAL.6).
4151 The system must provide sufficient timing resolution to accurately discriminate between differ-
4152 ent bunch crossings (F-DET-ECAL.10), ensuring precise event separation and minimizing pile-up
4153 effects. The chosen detector and readout technologies must be capable of processing the high data
4154 rates without compromising performance or data integrity.

4155 Justification

4156 **Device concept and technological choice:** The ePIC BEMC is called the Barrel Imaging
4157 Calorimeter (BIC). The BIC combines two proven technologies to meet the stringent requirements
4158 of the EIC physics program. The first is a lead-scintillating fiber (Pb/ScFi) sampling calorimeter
4159 read by Silicon Photomultipliers (SiPMs), providing robust energy measurement through light col-
4160 lection, based on the well-established GlueX Barrel Calorimeter (BCAL) design. This technology
4161 offers a reliable solution for high-resolution energy measurements, benefiting from its extensive
4162 use in other experiments.

4163 The second is a silicon tracker comprising AstroPix, a monolithic active pixel sensor (MAPS) based
4164 on an HV-CMOS technology, which is interleaved with the Pb/ScFi layers to provide precise 3D

4165 imaging of calorimeter shower development. This hybrid approach enables excellent spatial reso-
 4166 lution and position reconstruction, critical for separating particle showers and achieving the neces-
 4167 sary photon and electron identification capabilities. The AstroPix sensors, developed for the NASA
 4168 space mission AMEGO-X, offer low power consumption, radiation tolerance, cost-effectiveness,
 4169 and scalability, making them ideal for large-area applications in a high-radiation environment.

4170 This combination of Pb/ScFi for energy resolution and AstroPix for spatial resolution was chosen to
 4171 balance performance, cost-effectiveness, and long-term reliability under the expected operational
 4172 conditions at the EIC.

4173 **Subsystem description:** The Barrel Imaging Calorimeter (BIC) consists of 48 trapezoidal sec-
 4174 tors, with End-of-Sector Boxes (ESBs) at each end for readout. The calorimeter spans 17.1 radiation
 4175 lengths (X_0) at central pseudorapidity, with the first layer being an AstroPix imaging layer, which
 4176 provides a tracking point behind the DIRC. Each sector has six slots for AstroPix imaging layers,
 4177 separated by $1.45 X_0$ of Pb/ScFi at $\eta = 0$. In the baseline configuration, slots 1, 3, 4, and 6—count-
 4178 ing radially outward—are filled with AstroPix sensors, while slots 2 and 5 are designated for future
 4179 upgrades. Figure 8.84 presents the overall structure of BIC and its sectors and Fig. 8.85 shows the
 4180 imaging AstroPix layers components.

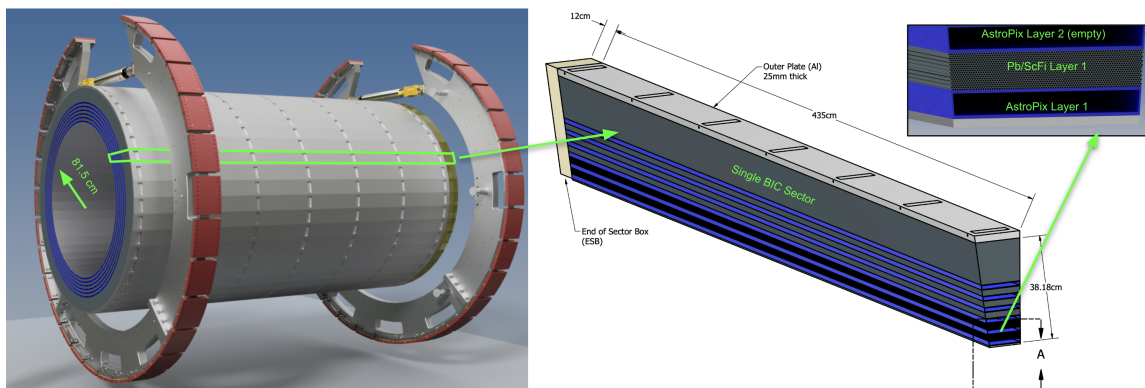


Figure 8.84: Drawing of the Barrel Imaging Calorimeter with its 48 sectors. The central drawing shows the structure of a single sector, featuring interleaved Pb/ScFi layers and slots for trays holding AstroPix chips, followed by the Pb/ScFi bulk section. On the right, a zoomed view of the first radially layers is presented.

4181 **Scintillating fibers for Pb/ScFi:** The Pb/ScFi calorimeter system is based on the GlueX model
 4182 with fibers positioned parallel to the z-direction with 2-sided readout for energy measurement
 4183 and position reconstruction along the fiber. We will use single-clad scintillating fibers with 1
 4184 mm diameter embedded in lead and glue to provide reliable energy measurement through
 4185 light collection. For the scintillating fiber parameters refer to Tab. 8.25.

4186 **Sensors for Pb/ScFi:** The light from the scintillating fibers is subdivided into 12 rows of
 4187 5 columns per sector-end by light guides, which are optically coupled with cookies to the
 4188 SiPMs. These sensors have a $50 \mu\text{m}$ pixel pitch to optimize dynamic range and photon detec-
 4189 tion efficiency. For the SiPMs parameters refer to Tab. 8.24.

4190 **FEE for Pb/ScFi:** The FEE for the Pb/ScFi system, based on the CALOROC ASIC, processes
 4191 the signals from the SiPMs. It provides sufficient time resolution for determining the z-
 4192 position of events within the scintillating fiber, while maintaining low noise and high ra-
 4193 diation tolerance.

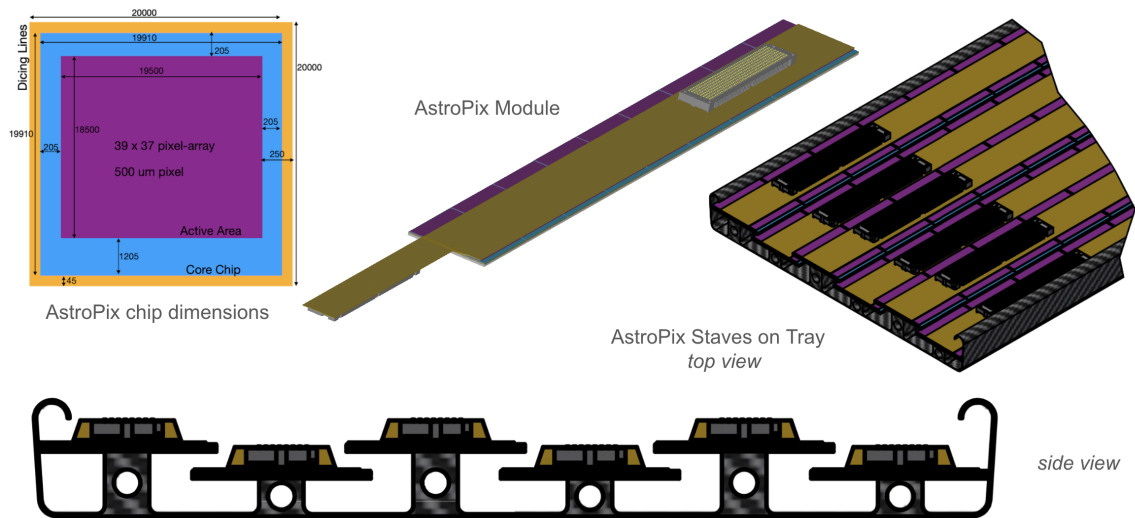


Figure 8.85: Components of Barrel Imaging Calorimeter imaging AstroPix layers.

4194 **Sensors and modules for imaging layers:** The imaging layers use AstroPix monolithic silicon
 4195 sensors with a 500 μm pixel pitch, interleaved with the Pb/ScFi layers. The 9 daisy-chained
 4196 AstroPix sensors are glued on a base plate and read out on a flexible PCB to form a module,
 4197 providing high-resolution spatial information for 3D imaging and particle identification. For
 4198 the AstroPix chip parameters refer to Tab. 8.23.

4199 **Staves and trays:** Each stave is formed by daisy-chaining 12 AstroPix modules. A tray holds
 4200 6–7 staves based on the layer position, with each tray being half of the sector length and read
 4201 out at its respective end in the ESB. This modular structure allows for flexible scaling and
 4202 future upgrades to the system.

4203 **End-of-Tray Card (ETC):** The ETC functions as the RDO unit in the ePIC DAQ scheme. It
 4204 manages signal processing, data formatting, and communication with the DAM, ensuring
 4205 efficient and reliable data flow from the sensors. Note that within the module-stave-tray
 4206 design, the ETC communicates directly with each 9-chip module.

4207 **Performance** The BIC has been designed to meet the stringent energy and particle separation re-
 4208 quirements of the EIC scientific program. The performance of the BIC and its components has been
 4209 simulated through a combination of detector simulations, beam tests, and bench measurements.
 4210 Key metrics, such as energy resolution, angular resolution, and particle identification have been
 4211 carefully studied to ensure the detector meets or exceeds the required specifications. The results
 4212 presented here highlight the detector’s capabilities and its ability to operate efficiently under EIC
 4213 conditions.

4214 **Energy resolution:** We estimated the energy resolution of the Pb/ScFi layers based on de-
 4215 tailed simulations in various rapidity ranges and photon/electron energies. The energy reso-
 4216 lution for photons extracted from the Gaussian core of a Crystal Ball fit to the expected energy
 4217 losses in Pb/ScFi is presented in Fig. 8.86 (a) and the results of the fitted stochastic and con-
 4218 stant terms a and b of the energy dependence $\sigma/E = a/\sqrt{E} \oplus b$ are presented in Tab. 8.26.
 4219 The stochastic term of around $5.8\text{--}6.6\%/\sqrt{E}$, with the constant term of $0.6\text{--}1.2\%$, depending

Detector parameters	Value
Active length (z-direction)	435 cm
Inner radius	82.5 cm
Number of sectors	48
η coverage	$-1.71 \lesssim \eta \lesssim 1.31$
Radiation Length X_0	1.45 cm
Total depth in X_0	from 17.1 ($\eta = 0$) to 42 ($\eta = -1.55$)
Molière radius	4.5 cm
Total sampling fraction of Pb/ScFi layers	about 9.5%, see Fig. 8.86
Total sampling fraction of AstroPix layers	< 0.4%
Scintillating fibers	\varnothing 1 mm, single clad fibers
Light guide length	5 cm
Number of light guides	60 per sector per side
Monitoring system	Blue LED, one LED per light guide
SiPMs	1.2×1.2 cm ² arrays, 50 μ m pixel
Number of SiPMs	60 arrays per sector per side

Table 8.22: Selected BIC Parameters.

Parameter	Specification
Pixel size	500 μ m x 500 μ m
Power usage	< 2 mW/cm ²
Energy resolution	10% @ 60 keV
Dynamic range	25-700 keV
Passive material	< 5% on the active Si area
Time resolution	3.125 ns
Si Thickness	500 μ m

Table 8.23: AstroPix chip parameters for BIC.

4220 on rapidity, satisfy the detector requirement of energy resolution better than $10\%/\sqrt{E} \oplus 2\text{--}$
4221 3% . The sampling fraction, defined as energy deposited in the scintillating fibers divided by
4222 the true energy of generated photons is presented in Fig. 8.86 (b). Our energy performance
4223 results align well with beam test data using a positron beam at Jefferson Lab. See the Addi-
4224 tional Material for more details, including results on the contribution of the low-energy tail of
4225 the energy loss.

4226 **Angular resolution:** We estimated the angular resolution for photons using the AstroPix
4227 layers, based on detailed detector simulations for various rapidity ranges and photon en-
4228 ergies. We extracted the difference between the true and reconstructed azimuthal (θ) and
4229 polar (ϕ) to estimate the FWHM resolution. In the current reconstruction algorithm, the an-
4230 gles are reconstructed from the hit with the maximal energy deposit in the AstroPix layer
4231 where the shower started. The resolutions for θ and ϕ are presented in Fig. 8.87. The re-
4232 sults indicate a small dependence of the angular resolution on η . In all regions, the angu-

Parameter	Specification
Active Area	3 mm x 3 mm (4 x 4 array) Preassembled array covering 1.2cm x 1.2cm
Pixel Size	50 μ m
Package Type	Surface Mount
Peak Sensitivity	450 nm
PDE	$\sim 50\%$
Gain	$> \sim 2 \times 10^6$
DCR (Dark Count Rate)	Typ.: ~ 500 kHz / SiPM Max: < 1.5 MHz / SiPM (DCR applies to each SiPM in the 4 x 4 array)
Temperature Coefficient of Vop	< 40 mV/C
Direct Crosstalk Probability	$< \sim 7\%$
Terminal Capacity	~ 500 pF / SiPM (Applies to each SiPM in the 4 x 4 array)
Vop Variation within a Tray	< 200 mV
Recharge Time	< 100 ns
Fill Factor	$> 70\%$
Protective Layer	Silicone (n ~ 1.5 -1.6)

Table 8.24: SiPM specifications for BIC.

Parameter	Specification
Light yield	> 3.5 photoelectrons (measured using Sr-90 source with blackened opposite end)
Diameter	1.00 ± 0.01 mm (RMS ≤ 0.02 mm)
Attenuation length	> 4 m (for blue light)
Batch-to-batch variation of light yield	$< 15\%$
Batch-to-batch variation of attenuation length	$< 10\%$
Emission spectrum	Blue-green light
Scintillation decay time	< 3 ns
Total length	4900 km
Delivery method	In canes, length of fibers 4.55 meters ± 0.01 m

Table 8.25: Scintillating fiber specifications for BIC.

4233 lar resolution remains well below 0.1 degrees, which is on the level of single pixel resolu-
4234 tion. The example fit of the θ resolution in the rapidity region of $-0.88 < \eta < -0.4$ gives
4235 (0.040 ± 0.004) deg/ $\sqrt{E} \oplus (0.016 \pm 0.003)$ mm. The ϕ resolution is worse than the θ resolu-
4236 tion due to the smearing of shower particles by the magnetic field. Overall, the results show
4237 significantly better performance than what can be achieved with any tower-like calorimetry
4238 systems and fulfills the requirements for the barrel electromagnetic calorimetry for the EIC.

η range	a/\sqrt{E} [%]	b [%]
$(-1.7, -1.3)$	6.60 ± 0.03	0.66 ± 0.04
$(-1.3, -0.88)$	6.11 ± 0.01	1.24 ± 0.01
$(-0.88, -0.4)$	5.91 ± 0.02	1.24 ± 0.02
$(-0.4, 0)$	5.85 ± 0.01	0.88 ± 0.02

Table 8.26: Fitted energy resolution parameters for photons in BIC for different η ranges.

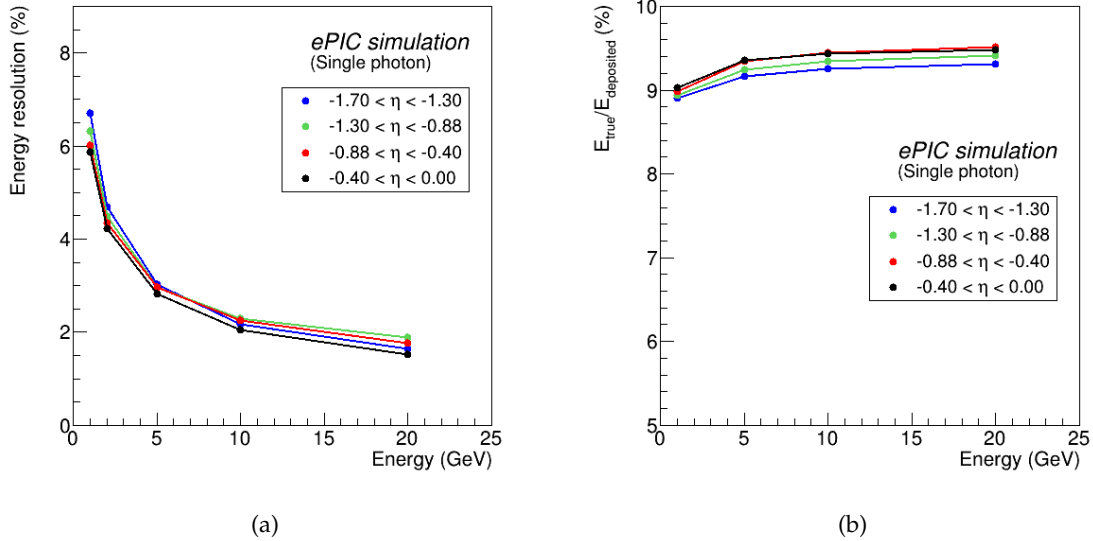


Figure 8.86: (a) Simulated energy resolution in from Pb/ScFi extracted as a σ of the Gaussian core of the Crystal Ball fit to the energy deposits of photons in different rapidity ranges at BIC. Repository to be added. (b) Sampling fraction for photons, defined as energy losses in scintillating fibers divided by the true photon energy, as a function of photon energy in different rapidity ranges. Repository to be added.

4239
4240
4241
4242
4243
4244
4245
4246
4247
4248
4249
4250
4251
4252
4253

Electron-pion separation: The design of the barrel calorimeter aims to provide high π^-/e^- separation, particularly in the momentum region below 5 GeV. The AstroPix layers capture snapshots of electromagnetic and hadronic showers, allowing for the reconstruction of a 3-dimensional profile of the shower development, supported by the longitudinal energy profiles from the Pb/ScFi layers. Charged pion rejection is carried out in a two-step process. First, an E/p cut is applied to the cumulative energy deposit in the Pb/ScFi layers. This cut is deliberately loosened to ensure high electron efficiency. The “cleaned” samples, following the E/p cut, are then fed into a classification neural network for inference. We used a 10-layer Visual Geometry Group-style Convolutional Neural Network using the combined AstroPix and Pb/ScFi detector response. The network utilizes energy and position features from both technologies capturing energy and spatial shower details. Future improvements may come from using more advanced reconstruction techniques based on Graph Neural Networks or Point Clouds. The charged pion suppression factor for $\eta = 0$ rapidity is shown in Fig.8.88 (a), for a target 95% electron efficiency. The rejection exceeds 10^3 at low to mid energies, where rejection is most critical. For comparison, results where all six imaging layers are instrumented

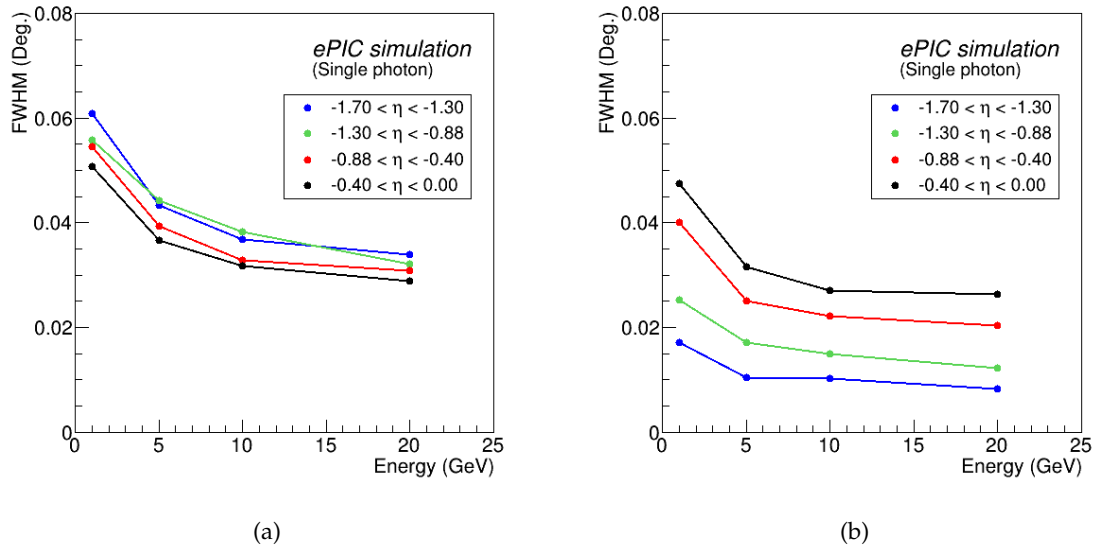


Figure 8.87: Simulated angular resolution for photons at different energies for the ϕ (a) and θ (b) angles reconstructed from the maximal-energy pixel from the first AstroPix layer where the shower started. The resolution is taken as FWHM from the distribution of the difference between true and reconstructed angle. Repository to be added.

4254 are also presented.

4255 **Photon- π^0 separation:** The upper limit of the probability of merging two γ s from a π^0
 4256 decay into one cluster at $\eta = 0$ is shown in Fig. 8.88 (b). Neutral pions decaying into two γ s
 4257 were simulated with various momenta. In different calorimeter technologies based on tower
 4258 geometry, as outlined in the EIC Yellow Report [6], the separation criterion requires that the
 4259 two γ s be separated by at least one tower size. However, for the BIC technology, which uses
 4260 granular position information from AstroPix, a different criterion has been established. The
 4261 probability of merging two γ s was determined using a separation of 6 times the FWHM of the
 4262 shower profile, measured at the third imaging layer (where more than 90% of photons with
 4263 energies above 0.5 GeV register at least one hit), providing a conservative estimate. The upper
 4264 limit for γ/π^0 separation is expected to be well above 10 GeV, based on studies incorporat-
 4265 ing AstroPix's position resolution and shower profile data. Additionally, initial results from
 4266 a neural network approach, similar to the e/π studies but simplified for neutral pion iden-
 4267 tification, were applied using full detector simulations. Preliminary results suggest a pion
 4268 rejection rate of approximately 82% at 90% electron efficiency for 10 GeV pions, based on the
 4269 current status of model training.

4270 **Low-energy response:** We evaluated the performance of the BIC for detecting MIPs through
 4271 simulations using 5 GeV muons at various rapidities. The deposited energy per readout cell,
 4272 represented by the most probable value of the MIP peak, was extracted from simulations with
 4273 Single-Clad Kuraray fibers that meet the FDR fiber specifications. This was compared against
 4274 the 4-sigma pedestal peak from S14161-3050-04 SiPM array simulations, which also fulfill FDR
 4275 specifications. Even with the dark count rate corresponding to the irradiation level of 1×10^9
 4276 1-MeV neq/cm², the MIP signal remains well-detectable with a 4-sigma cut on the pedestal.
 4277 Figure 8.89 shows the extracted most probable value (MPV) of the MIP peak in terms of the

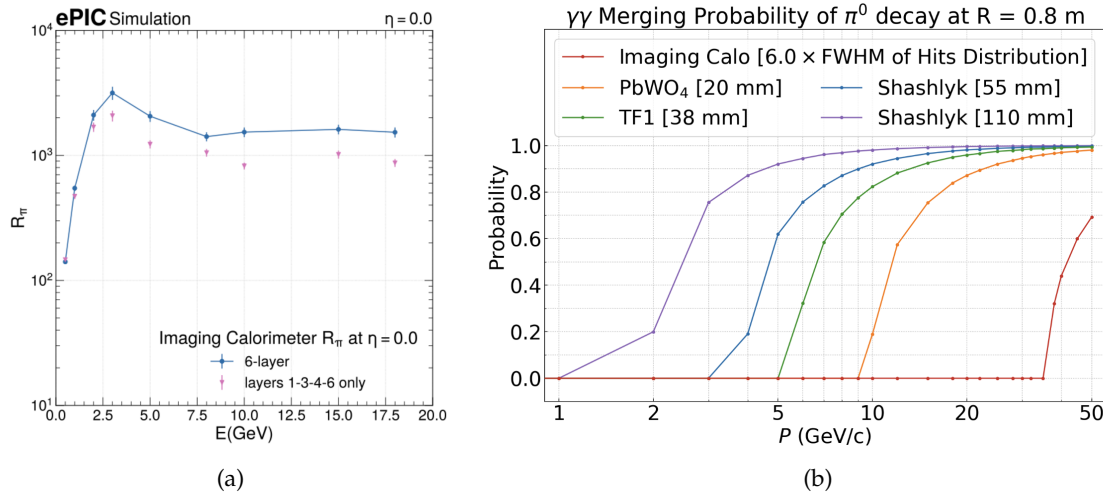


Figure 8.88: Simulated performance on particle identification from BIC. (a) The charged pion suppression factor for $\eta = 0$ rapidity for 95% electron efficiency as a function of particle energy E . Pink points show the baseline performance where slots 1, 3, 4, and 6, counting radially, of imaging layers are filled with AstroPix trays, blue points show performance with 6 imaging layers. Repository to be added. (b) Upper limit on cluster merging at $\eta = 0$ (shortest distance for particles to travel about 80 cm) from 2 photons from π^0 decay at particular π^0 momentum P . For calorimeter technologies based on tower geometry from [6] the separation by at least one tower size is required. For BIC the separation based on shower profile was assumed (see text). Repository to be added. (To be replaced by the NN results with full simulation when ready)

4278 number of photoelectrons (nphe) for muons at $\eta = 0$, which is the case where we observe the
 4279 least photoelectrons from muons due to the combination of the distance the light has to travel
 4280 in the fibers and the energy muons deposit at this angle in one Pb/ScFi layer. The pedestal
 4281 4-sigma value is marked in red. An example pedestal and MIP signal spectrum for 9 and 12
 4282 phe MIP signals, showing the worst-case scenario for the back Pb/ScFi layer of the BIC, is
 4283 also presented. The BIC demonstrates the capability to detect minimum ionizing particles for
 4284 calibration purposes in the Pb/ScFi layers, with the MIP peak from 5 GeV muons remain-
 4285 ing well-separated from the pedestal, even after irradiation doses corresponding to the first
 4286 few years of ePIC operation. This separation is maintained through careful application of
 4287 threshold cuts in each channel, ensuring that the MIP signal remains distinguishable from the
 4288 noise. Simulations investigating performance under higher irradiation levels of 1×10^{10} 1-
 4289 MeV neq/cm² are currently in progress (*will be presented in the next version of this document*).
 4290 If necessary, we can relatively lower readout thresholds, as the ASIC provides enough head-
 4291 room, and employ a coincidence logic (e.g., requiring two neighboring readout cells to fire) for
 4292 further zero suppression to ensure stable MIP performance over the lifetime of the detector.

4293 **AstroPix sensor performance:** The AstroPix chip has been extensively tested in both bench
 4294 and beam environments. The AstroPix_v3, the first full-size chip with a 500 μm pixel pitch
 4295 and row-and-column readout (35 rows and columns in a strip-like format), has demonstrated
 4296 strong performance, as summarized, for example, in [71]. Key tests included a noise study
 4297 and a radiation source test. In the noise study, less than 0.5% of the pixels exhibited a noise
 4298 rate exceeding 2 Hz, with the chip's dynamic range starting at 25 keV, allowing thresholds

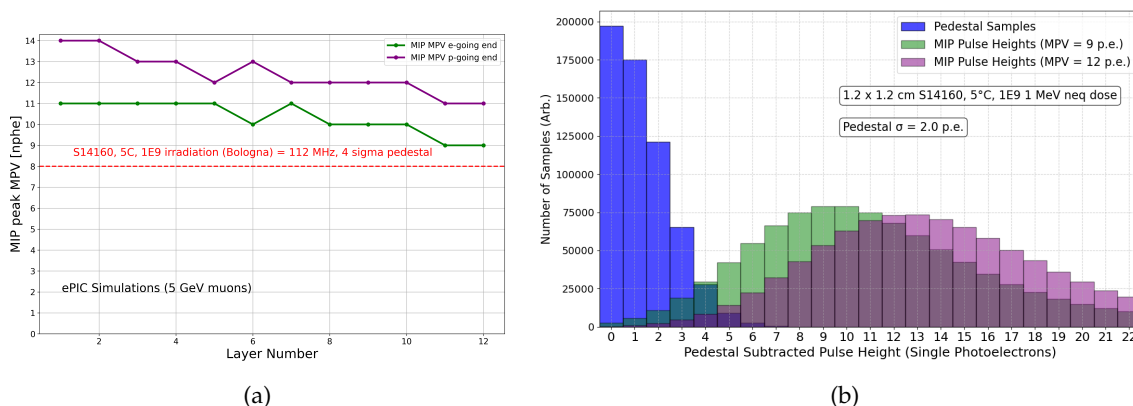


Figure 8.89: Simulated performance on MIP response in BIC. (a) The most probable value of the MIP peak in terms of the number of photoelectrons for 5 GeV muons at $\eta = 0$ at each of the BIC layers. The red line corresponds to 4 sigma of the pedestal simulated with realistic S14160 family SiPM responses at 5 degrees Celsius, irradiated with a dose of 1×10^9 1-MeV neq/cm². The green line corresponds to the electron-going end, while the purple line corresponds to the proton-going end readout cells. Repository to be added. (b) An example spectrum of the pedestal and MIP pulses at 9 and 12 phe signals, showing the worst-case scenario from plot (a) for the back Pb/ScFi layer of the BIC at $\eta = 0$. Repository to be added.

4299 over 200 mV above the baseline. These results meet the BIC's requirements for low energy
 4300 thresholds and masked pixel yield. The radiation source test, using isotopes with calibration
 4301 points ranging from 22.2 keV to 122 keV, as shown in Fig. 8.90, showed that 44% of pixels
 4302 met the 10% energy resolution requirement at 59.5 keV, and 92.4% of pixels achieved the
 4303 required 25 keV sensitivity for BIC. Although the AstroPix_v3 chip is not fully depleted, it
 4304 demonstrated promising performance. The upcoming AstroPix_v5, designed with a dynamic
 4305 range extending to 700 keV, is expected to meet energy resolution requirements for all pixels.

4306 **AstroPix beam test results:** We used beam tests at Fermilab to further validate the As-
 4307 troPix_v3 chip in both single- and double-layer configurations. In the single-layer test, data
 4308 collected with a 120 GeV proton beam was used to match corresponding row and column hits,
 4309 using matching timestamps and ToT to reveal a hit map that showed the proton beam profile
 4310 presented in Fig. 8.90. Although the AstroPix_v3 has a daisy-chained row and column readout
 4311 and does not yet have an individual pixel buffer (which is implemented in AstroPix_v4 and
 4312 higher), it demonstrated a precise hit-pixel reconstruction. In the double-layer configura-
 4313 tion, two daisy-chained layers of AstroPix_v3 were tested, successfully reading events in coinci-
 4314 dence and pinpointing hit-pixel locations, providing a proof-of-concept for layer integration
 4315 in a beam environment.

4316 The characterization of AstroPix_v3 is ongoing, with specific tests designed to meet the ePIC
 4317 detector requirements. Results show that the chip is well-suited for the BIC and aligns with
 4318 project goals. Remaining improvements, including enhanced dynamic range and energy res-
 4319 olution, will be addressed in the upcoming AstroPix_v5, which is expected to be fabricated by
 4320 early 2025.

4321 **Simulation performance validation:** We validated the simulation performance of BIC and
 4322 its components using a combination of bench tests and beam tests at the FTBF and at Hall D
 4323 in Jefferson Lab. We present more details on select benchmarks of realistic simulation results
 4324 against measurements in the supplemental material.

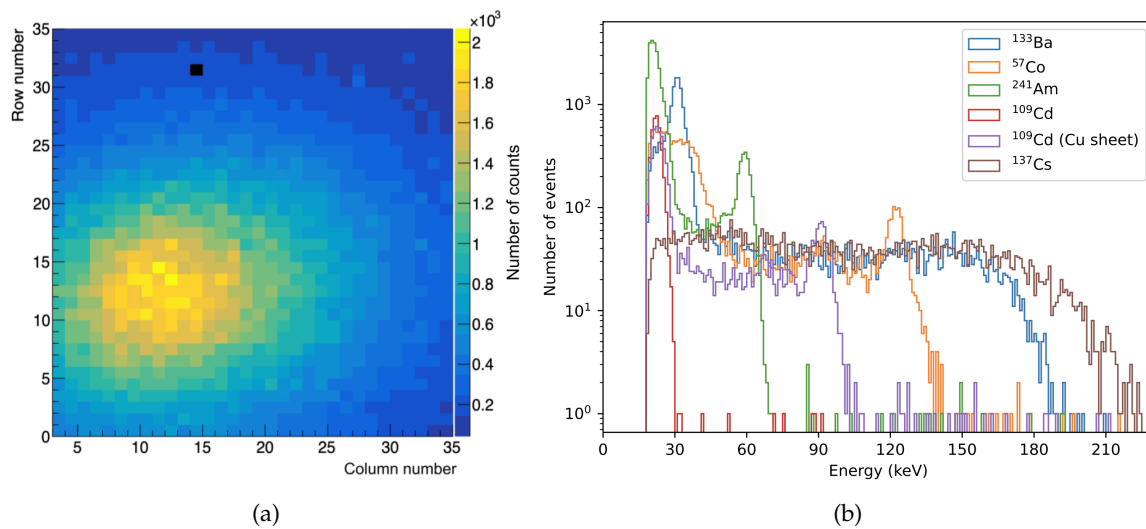


Figure 8.90: (a) Beam hit map recorded in the 120 GeV proton run in Fermilab Test Beam Facility with a AstroPix.v3 chip. The masked pixel has been marked in black. Repository to be added.(b) Calibrated energy responses form an example pixel of a AstroPix.v3 chip. Plot from [71].

4325 Implementation

4326 **Subsystem mechanics and integration:** The 48 BIC sectors are arranged in a self-supporting
 4327 Roman arch configuration. Once assembled, the full calorimeter is supported by the solenoid cryo-
 4328 stat support rings. In the hadron-going direction, a small gap must be bridged between the end of
 4329 the BIC and the support ring, while in the lepton-going direction, the system slightly overhangs,
 4330 creating a cantilevered structure.

4331 A BIC sector consists of six carbon fiber frames for the imaging layers, interleaved with five single
 4332 layers of a Pb/ScFi matrix (17 fibers tall), followed by a bulk segment consisting of seven Pb/ScFi
 4333 matrix layers. The back of the sector consists of an aluminum support plate with connectors de-
 4334 signed to link the sectors together, affix the ESB, and integrate with the global BIC support structure.
 4335 The sector is constructed as a monolith, with all components epoxied together to ensure structural
 4336 integrity.

4337 The inner face of each BIC sector consists of a 0.5 cm thick aluminum plate, designed to connect the
 4338 inner support rails to the detector. The inner support rails hold the inner detector support structure,
 4339 maximizing the use of available space while avoiding obstruction of the ESBs (the readout boxes),
 4340 ensuring that individual imaging layers can be added or removed as necessary for future upgrades
 4341 or servicing. Hence, the BIC plays a critical role in supporting the overall inner detector structure.

4342 Detailed FEA to validate the mechanical integrity of the sector design is ongoing. The design of
 4343 the support that connects the BIC to the solenoid cryostat support rings is still under development,
 4344 ensuring it meets the mechanical stability requirements while maintaining accessibility to readout
 4345 electronics and other critical components.

4346 **Calibration, alignment and monitoring:** The BIC calibration approach treats the Pb/ScFi and
4347 AstroPix imaging layers as two separate systems, each calibrated independently. For the Pb/ScFi
4348 calorimeter, we will follow well-established in-situ calibration methods, starting with MIP-based
4349 calibration, then refining with meson decays, electrons, and kinematic techniques derived from
4350 experiences with GlueX and HERA experiments. The energy calibration is further refined using
4351 decay photons from neutral pion events ($\pi^0 \rightarrow \gamma\gamma$).

4352 For the AstroPix layers, the calibration process occurs in three steps. First, an absolute pixel energy
4353 calibration is performed during stave assembly using a radioactive source. Next, in-situ position
4354 and alignment calibration will be conducted similarly to standard tracker procedures, utilizing
4355 cosmics. Finally, the overall imaging cluster energy calibration will be matched with the Pb/ScFi
4356 calorimeter, leveraging the energy reconstruction methods described above.

4357 Metrology will be used for alignment during installation, though very precise alignment is not
4358 critical, given the calorimeter's purpose. Cosmic and physics events will be used to calibrate the
4359 relative positioning of detectors and sensors, ensuring accurate reconstruction.

4360 Calibration stability during operation will be ensured by using LED-based relative light monitoring
4361 systems for continuous monitoring, along with additional checks on linearity and timing using
4362 both cosmics and dedicated calibration runs.

4363 **Services:** The Pb/ScFi part of BIC, which utilizes SiPMs, requires two LV lines (plus ground) of
4364 1.2 V and 2.5 V for each H2GCROC3-based front-end board (FEB), along with one HV line (plus
4365 ground) operating at less than 50V for biasing SiPMs. The system features a total of 5,760 readout
4366 channels distributed across 48 sectors, with one FEB per sector per side, each managing 60 readout
4367 channels. Each FEB is connected to the RDO through four lines: two data lines, one clock line, and
4368 one slow control line, and 1 RDO maintains 24 FEBs.

4369 For the AstroPix sensor layers, the LV services include two 1.8 V to power the analog and the digital
4370 part of the chip and the HV of 200-400 V distributed to each stave. Each stave within an AstroPix
4371 tray connects to the data acquisition system through an FPGA-based End-of-Tray Card (ETC, one
4372 per tray) connected to DAM via an optical link. In total, each sector will include 27 staves per side.
4373 The ETC will be powered through Power over Ethernet (PoE) within the control cable.

4374 The SiPMs require cooling to maintain a temperature of 5°C. Each ESB will have in/out lines for
4375 cooling water and a dry air system to prevent condensation. The estimated heat load per ESB is
4376 projected to be under 100 W, necessitating effective heat management. Liquid water cooling will
4377 be utilized for the SiPMs, their readout boards, and the ETCs. AstroPix sensors are highly heat
4378 efficient, consuming less than 2 mW/cm². The baseline cooling strategy involves thermal coupling
4379 to dissipate heat through the staves and trays, with cooling occurring at the edges along with the
4380 ETCs. If additional cooling is required, circulating liquid through the staves will be employed as a
4381 mitigation measure. A preliminary cooling design is expected by May 2025 as part of the Cooling
4382 FEA in the PED phase.

4383 **Status and remaining design effort:** High-level schedule for the BIC design and production
4384 phase is available in Additional Material (See Fig. 8.91).

4385 **R&D effort:** The R&D efforts for BIC focus on demonstrating the combined performance of
4386 Pb/SciFi and AstroPix in EIC-like environments. This involves measuring higher than GlueX
4387 energy response up to about 10 GeV, benchmarking high-energy electron and pion simula-
4388 tions, testing AstroPix in high-rate environments, and integrating the Pb/SciFi with AstroPix

4389 sensor layers. In FY23, responses to 6 GeV positrons in 60 cm long Pb/ScFi prototype were
4390 measured in Hall D of Jefferson Lab, showing a constant term of about 2%, consistent with
4391 simulations. The Baby BCAL was commissioned with proton, pion, and electron beams dur-
4392 ing a June 2024 FBTF test, where data collected allowed for pion simulation benchmarking.
4393 A proof-of-concept synchronization of AstroPix with Baby BCAL was achieved by triggering
4394 on the AstroPix analog signal. With extensive data from previous AstroPix tests in FY23, the
4395 R&D is ready for multi-layer beam tests, to be conducted in early FY25 pending delays at
4396 FTBF.

4397 **E&D status and outlook:** The Project Engineering Design phase of our project that started
4398 with granting the funding to the participating institutions starting Q4 2024, encompasses a
4399 detailed roadmap for the design, testing, and integration of key components for BIC. Early
4400 milestones focus on the design and development of the Pb/SciFi sector, including short and
4401 long test articles and the structural framework needed for housing these components. Along-
4402 side this, efforts are directed toward the design and prototyping of the end-of-sector box,
4403 which includes light guide and light monitoring systems integration. The tracking layer,
4404 which features AstroPix sensors, undergoes simultaneous development. This includes per-
4405 formance characterization of the AstroPix chips, module design and assembly, and testing of
4406 components such as bus tapes and end-of-tray cards. By mid-PED-phase, both the Pb/SciFi
4407 and tracking layers will undergo rigorous integration testing to ensure seamless function-
4408 ality within the full detector system. The final phase focuses on validating the designs and
4409 performing full integration testing of staves, modules, and tracking layers. Quality control
4410 procedures will be established for each component, ensuring that everything meets perfor-
4411 mance specifications before final assembly. The PED phase is expected to finish in Q1-Q2
4412 FY26.

4413 **Other activity needed for the design completion:** Within the small-scale R&D and design
4414 funding in Korea, a focused effort is underway during the period from August 2024 to April
4415 2027, covering the PED phase and pre-production phase. The primary objectives include the
4416 development of testing and assembly systems for the AstroPix chip, particularly emphasizing
4417 automatic wafer testing and module assembly. Additionally, this work involves designing
4418 the readout box for the Pb/SciFi system and producing test modules to conduct performance
4419 studies.

4420 **Status of maturity of the subsystem:** The maturity of BIC is currently estimated to be between
4421 30% and 60%, depending on the specific component. The entire BIC underwent an incremen-
4422 tal Preliminary Design Review (PDR2) in September 2024. Scintillating fibers and SiPMs have
4423 reached the final design stage, as they are classified as long-lead procurement items. Recog-
4424 nizing the extensive requirements for these materials—around 4500 km of scintillating fibers
4425 and a large quantity of SiPMs for ePIC—the project identified the need for early procurement.
4426 The Final Design Reviews (FDR) for both the scintillating fibers and SiPMs were successfully
4427 passed in September 2023. The first portion of the scintillating fibers was included in CD3a,
4428 with further procurement scheduled for CD3b. Vendor selection is nearly complete, and the
4429 first long-lead orders are expected by Spring 2025.

4430 **Construction and assembly planning:**

4431 **Pb/ScFi Sectors Construction:** The production of Pb/ScFi sectors will take place at Argonne,
4432 where there will be two production lines. The sectors will be constructed by embedding
4433 single-clad scintillating fibers in lead sheets, arranged in a stepped “Mayan pyramid” config-
4434 uration, following the GlueX model. Carbon fiber frames will be integrated with the sector
4435 as it is built, with each frame assembled from two C-channel-like sides and a top and bottom

4436 plate. The sector construction process will proceed at a pace of 0.5 to 1 matrix layer per day,
4437 with the ability to build two sectors in parallel. Once a sector is fully assembled, it will be sent
4438 to an external machine shop for precise machining. Upon return to Argonne, the sector will
4439 undergo metrology and QC before being prepared for shipment to BNL.

4440 **ESB Manufacturing:** The construction process for the ESB is still in development. ESB con-
4441 struction will include large-scale SiPM testing, SiPM mounting, light-guide manufacturing,
4442 light-monitoring system integration, construction of structural and cooling components, and
4443 manufacturing of electronics boards. There will be at least two ESB production sites: one
4444 in Canada at U. Regina and one in Korea. As the procedure is finalized, further details on
4445 assembly and integration will be specified.

4446 **AstroPix Wafers:** The AstroPix sensors will be fabricated at the AMS foundry. Due to the large
4447 scale of the detector, automatic wafer-level testing will be conducted at two sites: PNU (South
4448 Korea) and Argonne. This testing will ensure the functionality of each chip before dicing,
4449 including IV-CV measurements, ASIC performance, noise levels, and defect detection early
4450 in the production process. After testing, the wafers will be diced into individual AstroPix
4451 chips.

4452 **AstroPix Modules and Trays:** AstroPix chips will be assembled into modules at three pro-
4453 duction sites: Argonne, UC Santa Cruz, and PNU (South Korea). Each module will consist
4454 of nine daisy-chained AstroPix chips, readout on flexible PCBs. After assembly, each module
4455 will undergo initial testing to ensure proper chip-to-chip communication, pixel functionality,
4456 and noise levels. Modules that pass this stage will be integrated into staves, with 12 mod-
4457 ules per staff. To keep the production process scalable and efficient, only one flavor of staff
4458 will be used across the entire system. The staves will then undergo additional QC testing.
4459 Once validated, the staves will be integrated into trays. There are two flavors of trays: one
4460 for the first imaging layer and the other for layers 3, 4, and 6. The hadron-going side and the
4461 lepton-going side trays of the detector are mirror images of each other. Each tray will contain
4462 6 staves in layer 2 and 7 staves in the outer three layers. These trays will then undergo final
4463 QC prior to shipping to BNL. The entire production and QC procedure is designed to catch
4464 any defects early and ensure that the trays are fully operational before final integration into
4465 the BIC sectors.

4466 **Assembly Planning:** The assembly of the BIC will follow a carefully planned sequence. Upon
4467 arrival at the integration site, the Pb/ScFi sectors will be unpacked and prepared for assembly.
4468 The first step will involve attaching the light guides to the sectors. Once the initial sectors have
4469 been prepared, we can begin the barrel assembly while continuing to unpack and attach light
4470 guides to the remaining sectors. The BIC barrel will be assembled next to the solenoid and
4471 then inserted into the solenoid using existing sPHENIX tooling. Following the installation of
4472 the barrel, the imaging layer trays will be inserted using specialized tooling that is still under
4473 development. After all trays are installed, the electrical and cooling connections will be made,
4474 and the rest of the ESB will be installed to complete the installation. This phased approach
4475 ensures that all components are properly integrated before the system is brought online for
4476 testing.

4477 **Quality Control (QC) Planning:** QC will be implemented at multiple stages of the BIC produc-
4478 tion and assembly process to ensure system integrity and performance. The system, particularly
4479 the imaging layers, is designed with both modularity and scalability in mind, allowing for efficient
4480 production, easier upgrades, and reworkability. Key QC procedures include:

4481 **Pb/ScFi Sector Assembly:** The Pb/ScFi sectors will undergo thorough inspection during as-
4482 sembly. Scintillating fibers and lead sheets will be inspected for defects before embedding.

4483 After each matrix layer is completed, visual and metrological inspections will ensure proper
4484 alignment and uniformity. Final metrology checks will be performed after external machining
4485 to confirm dimensions prior to shipment.

4486 **AstroPix Wafer Testing:** Automatic wafer-level testing will be conducted to assess chip func-
4487 tionality, including chip performance, noise levels, and defect detection. Once tested, wafers
4488 will be diced, followed by additional metrology and electrical/non-electrical QC on individ-
4489 ual AstroPix chips to ensure reliability before moving to the module assembly phase.

4490 **Module and Tray QC:** Modules will be assembled from AstroPix chips and undergo func-
4491 tional tests to verify chip-to-chip communication, pixel functionality, and noise levels. De-
4492 fective modules will be identified and replaced before progressing to stave assembly. Staves
4493 will be tested for electrical continuity, power consumption, and thermal performance under
4494 load. QC for staves and trays will use the actual End-of-Tray Card (ETC) readout electronics
4495 to perform these tests. Once integrated into trays, final testing will check for alignment, elec-
4496 tronic connectivity, and cooling performance, ensuring that trays operate as intended under
4497 operational conditions.

4498 **ESB QC:** SiPMs will undergo rigorous testing to ensure proper photon detection efficiency,
4499 dark count rates, and timing precision before being integrated into the ESB. ESB integration
4500 with the sector first article will test the complete system, including electrical connections, data
4501 acquisition, and cooling systems, to ensure seamless functionality with the Pb/ScFi sectors.

4502 **Final Integration and Barrel Assembly:** After attaching light guides to the Pb/ScFi sectors,
4503 alignment and metrology checks will be conducted during barrel assembly to ensure sector
4504 and tray alignment within tolerances. Electrical and cooling system checks will be completed
4505 post-installation to confirm proper functionality. System-wide tests, including cosmic ray
4506 runs and electronic readout, will validate the entire system before commissioning.

4507 **Environmental, Safety and Health (ES&H) aspects** The BIC design incorporates standard
4508 safety and environmental practices across all production sites. We will strive for standardized
4509 safety protocols while adhering to internal work planning and control processes at each institu-
4510 tion to identify hazards, implement mitigations, and document safety procedures. Main hazards
4511 associated with the BIC include:

4512 **Lead handling:** The handling of lead sheets for the Pb/ScFi matrix requires careful consider-
4513 ation. We are working closely with experts to determine the appropriate safety steps. These
4514 steps may include specific protocols to mitigate any hazards and the potential enrollment of
4515 personnel in continuous health monitoring programs to ensure long-term safety.

4516 **Epoxy usage:** Standard procedures for handling, mixing, and applying epoxy will be fol-
4517 lowed, with work conducted in fume hoods to ensure safety. Part of our PED work aims to
4518 deploy a custom mixing nozzle to reduce air contaminants and epoxy waste while improving
4519 consistency in the application process.

4520 **Scintillating fibers:** The fibers are made of flammable polystyrene, and with the total fiber
4521 mass exceeding 3.9 tons, proper fire safety measures and storage protocols are essential.

4522 **Pinch/nip hazards:** Automated systems, such as robots for wafer probing, pick-and-place,
4523 and glue application, present pinch hazards. Controls, such as PPE, gloves, guards, and pro-
4524 cedures, will be in place to mitigate these risks.

4525 **Crush hazards:** The use of presses and swaging equipment introduces crush hazards during
4526 assembly processes. Strict safety protocols, including the use of guards and operator training,
4527 will mitigate these risks.

4528 **Radioactive sources:** The use of radioactive sources for calibration introduces additional handling requirements, and proper shielding and storage protocols will be implemented as necessary.
4529
4530

4531 **Electrical safety:** Electrical safety procedures will also be applied for all electronics and power systems associated with the BIC production tooling and detector components.
4532

4533 **Collaborators and their role, resources and workforce:** The full BIC WBS org chart is available in Additional Material (see Fig. 8.95). BIC is supported by a diverse and robust international collaboration, with institutions from the United States, Canada, Korea, and Germany. These collaborators bring together a wealth of expertise and resources, working collectively to advance the development of the BIC.
4534
4535
4536
4537

4538 In the United States, several institutions play a key role across multiple aspects of the project. Argonne National Laboratory is leading several crucial areas, including the design and assembly of modules and staves, sector production, cooling systems, and system testing and QC, while also overseeing the software, simulation, and benchmarks. Oklahoma State University leads efforts on stave bus assembly, and the University of California, Santa Cruz (UCSC) supports module design and assembly efforts. NASA Goddard Space Flight Center (GSFC) contributes via the ETC components, ensuring that electronic testing is integrated into the system.
4539
4540
4541
4542
4543
4544

4545 Canadian institutions play a critical role, especially in the production and quality control of ESB. The University of Regina contributes to multiple efforts, including the QC of scintillating fibers, SiPM integration, light guides, and electrical design, while also contributing to the system's demonstration and testing. The University of Manitoba provides leadership in cooling system development and supports the SiPM integration efforts. Mount Allison University focuses on ESB production, aiding in the overall electronics support infrastructure.
4546
4547
4548
4549
4550

4551 Korean institutions are heavily involved in various production, design, and testing processes. Collaborators from Kyungpook National University (KNU) support both electronics and SiPM integration. Yonsei University plays a key role in the sector production process and testing, while Sungkyunkwan University (SKKU) focuses on sector development and production. Pusan National University (PNU) leads efforts on wafer testing and supports software development and simulation. Additionally, Hanyang University, Korea University, and other Korean institutions provide significant contributions across assembly, installation, and testing.
4552
4553
4554
4555
4556
4557

4558 The Karlsruhe Institute of Technology (KIT, Germany) provides essential AstroPix chip support.

4559 **Risks and mitigation strategy:**

4560 A potential risk in the production of AstroPix chips is related to the feasibility of using 12-inch wafers, which offer a more modern and cost-effective solution. However, if this option proves unviable, we will need to use 8-inch wafers, increasing costs. This is budgeted in the risk registry.
4561
4562
4563

4564 The schedule has sufficient time built in to accommodate an additional iteration of AstroPix beyond v6 if needed.
4565

4566 Risks on production-delays due to the availability of scintillating fibers and SiPMs were mitigated through CD3a/b long-lead procurement ensuring the timely availability of these components.
4567
4568

4569 As outlined in the Construction and assembly planning paragraph, in the default scenario, sector production will take place at Argonne using two production lines, with one staffed
4570

4571 by Korean collaborators. ESB production and quality control will be managed by Canada
 4572 and Korea. Wafer testing will occur in both Korea and the US. AstroPix module and stave
 4573 production will be distributed across three or more sites in the US and Korea. Depending
 4574 on the level of in-kind funding, the baseline plan is to produce four to six layers. In the
 4575 unlikely event of no in-kind funding from Canada and Korea, the project will cover all sector
 4576 production labor costs, including Korean collaborators, and consolidate production to a single
 4577 ESB site (Canada) and a single wafer testing site (US). AstroPix module/stave production will
 4578 be limited to two sites in the US, requiring an increased workforce at each site or potentially
 4579 facing a one-year delay to deliver the four baseline layers.

4580 **Additional Material**

4581 **Subsystem description**

- 4582 • More detailed description of subsystems: sector, ESB, tray, module, chip
- 4583 • More details on AstroPix chip with timelines
- 4584 • More details on SiPMs
- 4585 • More details on readout scheme ETC and CALOROC

Parameter	AMEGO-X Mission Requirements	BIC Requirements
Pixel size	500 μm x 500 μm	same
Power usage	< 1.5 mW/cm ²	~ 2 mW/cm ² acceptable
Energy resolution	10% @ 60 keV	same
Dynamic range	25-700 keV	same
Passive material	< 5% on the active Si area	same
Time resolution	25 ns	3.125 ns (available in v5)
Si Thickness	500 μm	same

Table 8.27: Comparison of AstroPix requirements for AMEGO-X and BIC.

4586 **Schedule**

- 4587 • High-level BIC Schedule in Fig. 8.91.

4588 **Performance**

4589 **Realism of simulations**

- 4590 • Geometry implementation description
- 4591 • How light response is simulated: folded in measurements of nphe/GeV, fiber attenuation
 4592 length, simulations of light guides and optical cookie, SiMP PDE and simulations
- 4593 • Comparison of data from beam tests and simulations benchmarking their realism: response
 4594 to electrons and pions

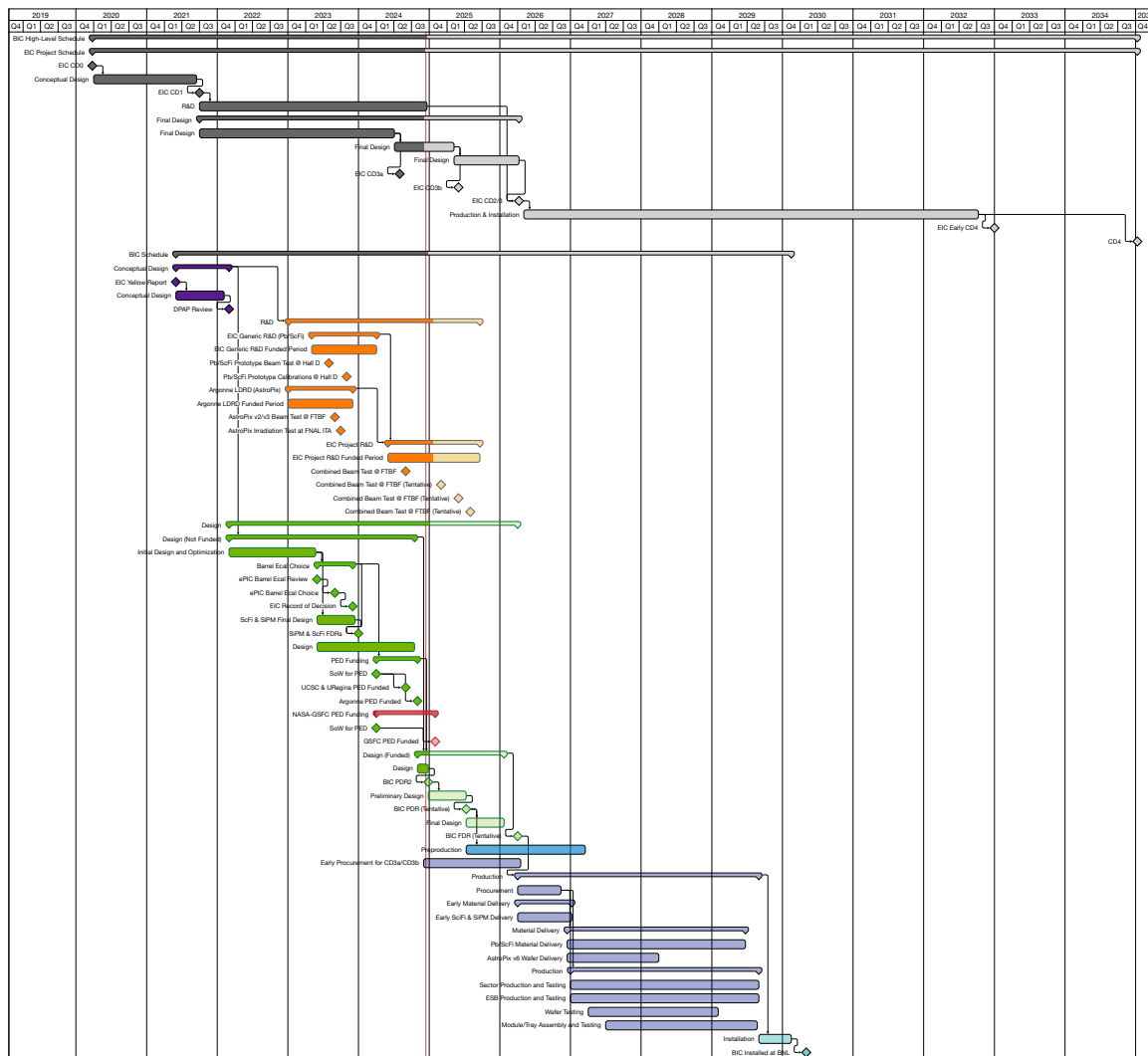


Figure 8.91: Barrel Imaging Calorimeter high-level schedule for design and production phases. (Updates expected)

4595 The realistic BIC geometry was implemented, including a detailed Pb/SciFi matrix with single
 4596 cladded fibers embedded in lead and glue, following the GlueX model. The AstroPix layers were
 4597 implemented as staves, with AstroPix chips placed in realistic dead areas, and materials accounted
 4598 for the sensors, electronics, cables, insulation, glue, and support structure. Realistic digitization and
 4599 reconstruction were applied. For the Pb/SciFi component, an effective model for light attenuation
 4600 in the fibers, photoelectron statistics, light guide efficiency, and SiPM thresholds was implemented
 4601 based on beam and bench measurements as well as optical simulations. For AstroPix, each digi-
 4602 tized readout unit corresponds to one pixel, while for the Pb/SciFi component, each readout cell
 4603 covers the area of one light guide with an attached SiPM.

4604 **Energy response**

- 4605 • Evaluation of the energy response tail
- 4606 • Simulated energy response to electrons
- 4607 • Energy resolution for low energy photons
- 4608 • Energy resolution from FTBF FY24 beam test.

4609 The contribution of the low-energy tail of the energy losses was quantified by calculating the dif-
 4610 ference between the area under the fitted Crystal Ball function and that of its Gaussian core marked
 4611 in red in Fig. 8.92 (a). The tail contribution to the overall energy loss area is shown in Fig. 8.92 (b)
 4612 and (c) for electrons and photons, respectively. The results of energy resolution and total sampling
 fraction as a function of energy for electrons is presented in Fig. 8.93.

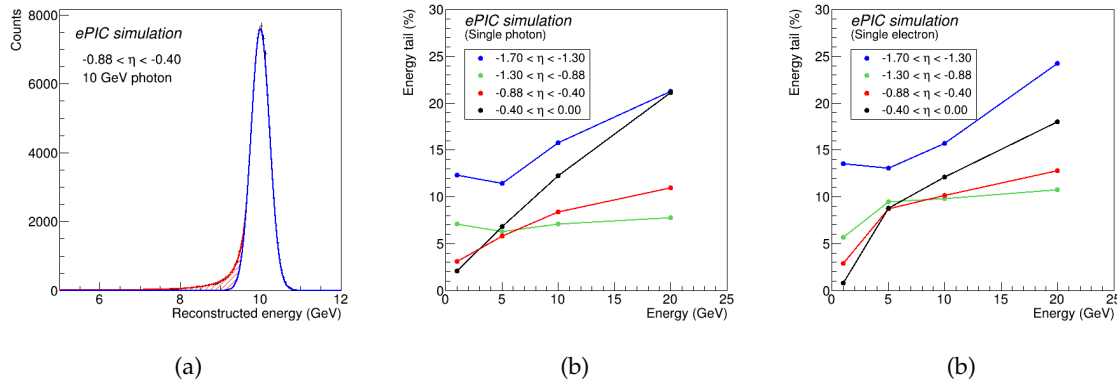


Figure 8.92: (a) Simulated energy losses in scintillating fibers of BIC for 10 GeV photons in the rapidity range $-0.88 < \eta < -0.4$. The distribution has been fitted with the Crystal Ball function; the Gaussian core of the function is marked in blue, and the power-law tail area is marked in red. (b) Percentage contribution of the low-energy tail—red area in plot (a)—to the overall area under the Crystal Ball fit to the energy losses of photon in Pb/ScFi as a function of photon energy and rapidity. (c) Same as (b) but for electrons.

4613

4614 Energy response to both electromagnetic and hadronic showers has been also tested in the beam test
 4615 environment with a 60 cm long and $15.5 X_0$ deep Pb/ScFi bulk-section prototype based on GlueX
 4616 BCAL geometry, termed *Baby BCAL*. At Hall D of Jefferson Lab, Baby BCAL was exposed to 3-6 GeV
 4617 positrons hitting it at different impact angle and position depending on beam energy. Figure 8.94
 4618 (a) presents the measured energy resolution measured in those conditions. Note that the highest
 4619 energy points reflect positrons hitting the prototype close to the end and at the impact angle that
 4620 causes partial shower leakage. At Fermilab Test Beam Facility, Baby BCAL was exposed to mixed
 4621 electron-pion-muon beam at energies of 4, 6, 8 and 10 GeV. The energy response to pion beam has
 4622 been benchmarked in simulation of Baby BCAL implemented in ePIC environment, same as used
 4623 for the BIC simulations. Fig. 8.94 (b) shows comparison between collected data and simulations
 4624 benchmarking their realism.

4625 Particle identification

- 4626 • More details about the NN methodology
- 4627 • Performance for different rapidity ranges and electron efficiencies
- 4628 • Muon detection efficiency

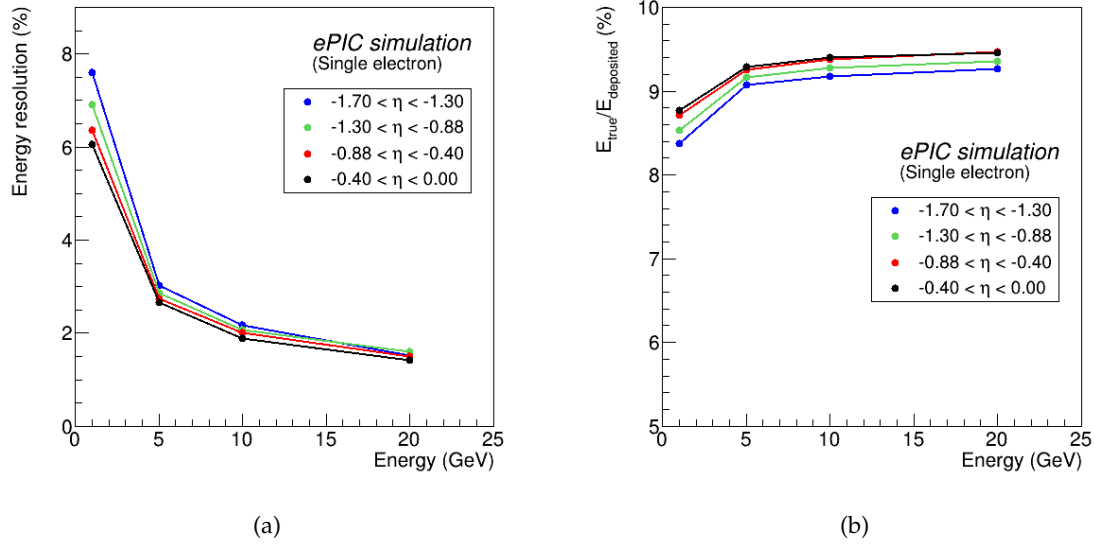


Figure 8.93: (a) Simulated energy resolution in from Pb/ScFi extracted as a σ of the Gaussian core of the Crystal Ball fit to the energy deposits of electrons in different rapidity ranges at BIC. (b) Sampling fraction for electrons, defined as energy losses in scintillating fibers divided by the true photon energy, as a function of photon energy in different rapidity ranges. (To be replaced with matching η regions and adjusted y-axis)

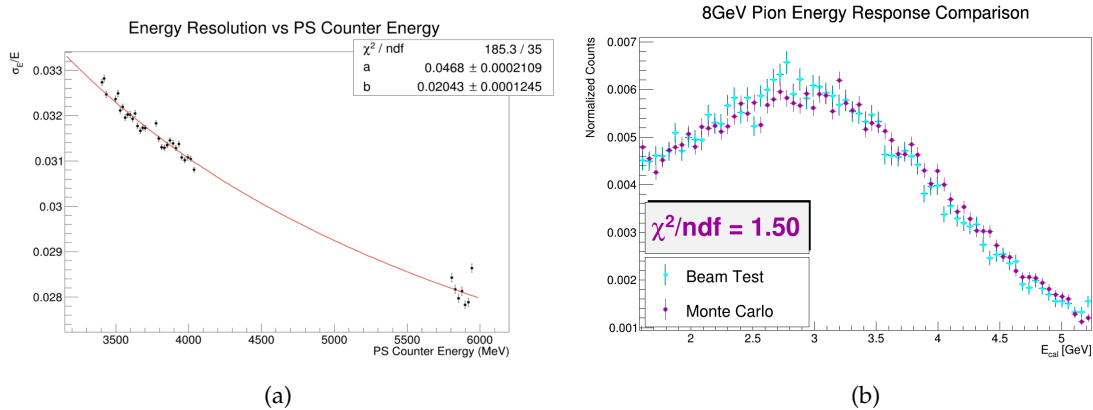


Figure 8.94: (a) Preliminary energy resolution of Baby BCAL exposed to 3–6 GeV positrons at Hall D of Jefferson Lab, with varying impact angles and positions depending on beam energy. The highest energy points correspond to positrons striking near the end of the prototype and at angles causing partial shower leakage. Red line shows the fitted function $\sigma/E = a/\sqrt{E} + b$. Repository to be added (b) Preliminary energy response of Baby BCAL to an 8 GeV pion beam at the Fermilab Test Beam Facility. The plot compares the collected data (light blue) with simulations (purple) implemented in the ePIC environment, as used for BIC simulations, benchmarking the realism of the simulation model. Repository.

4629 For our π^-/e^- separation studies, we utilized a 10-layer Visual Geometry Group (VGG)-style Con-
4630 volutional Neural Network (CNN) to process combined data from the AstroPix and Pb/ScFi parts
4631 of the calorimeter. This CNN architecture consists of 5 convolutional layers interspersed with 2
4632 pooling layers, followed by 3 fully connected (dense) layers. Each event is formatted into an input
4633 array with dimensions $N_{\text{layers}} \times N_{\text{hits}} \times N_{\text{features}}$, where 4 primary features: energy deposit, η , ϕ ,
4634 and radial position of the hit inside the calorimeter, to capture both energy deposition and spatial
4635 information about the particle shower.

4636 We trained the network using supervised learning with a data set composed of a 10:1 ratio of pions
4637 to electrons. This ensured a sufficient number of pions remained after applying the energy-over-
4638 momentum (E/p) cut, which was crucial for training accuracy. Each training cycle consisted of 20
4639 epochs, with data split into 70% for training, 10% for validation, and 20% for testing. On average,
4640 between 100,000 and 200,000 events were included in each training set, drawn from over 2TB of
4641 official singles productions simulations.

4642 The CNN's performance is measured with uncertainties based on binomial statistics, providing ro-
4643 bust estimates of classification accuracy. A similar but simplified approach was used for neutral
4644 pion identification. Initial results demonstrate promising pion rejection rates, which could be fur-
4645 ther enhanced by implementing algorithmic improvements. Future iterations of the model may
4646 explore Graph Neural Networks or Point Clouds to better capture the spatial and relational data
4647 inherent in these complex events.

4648 **MIP measurement capability**

- 4649 • More details about the SiPM simulations
- 4650 • Performance for different rapidity ranges

4651 **Services and subsystem mechanics and integration**

- 4652 • More details about integration and services

4653 **Calibration, alignment and monitoring**

- 4654 • More details about calibration

4655 **Status and remaining design effort:**

- 4656 • Detailed timeline on R&D and PED efforts

4657 **Environmental, Safety and Health (ES&H) aspects and Quality Assessment (QA plan- 4658 ning:**

- 4659 • Remaining details on ES&H

4660 **Construction and assembly planning:**

- 4661 • Full construction plan with sites, FTEs, yields, etc

4662 Collaborators and their role, resources and workforce:

- 4663 • Full org chart

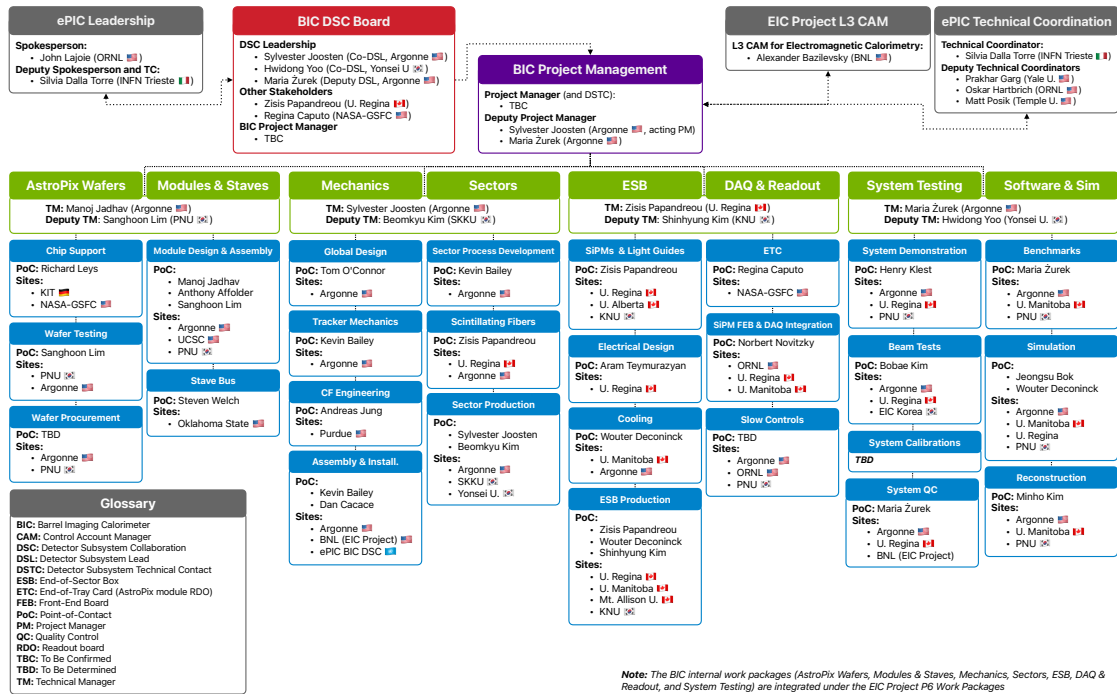


Figure 8.95: Barrel Imaging Calorimeter org chart. (Updates expected)

4664 8.3.5.3 The forward endcap electromagnetic calorimeter

4665 **Introduction** The ePIC forward electromagnetic calorimeter (fEMCal) is part of the hadron end-
 4666 cap calorimeter system, complementing the forward hadronic calorimeter. Complete calorimet-
 4667 ric coverage in ePIC is essential for detecting photons and electromagnetically decaying mesons,
 4668 which are crucial for reconstructing parton-scattering kinematics through jets and to identify DVCS
 4669 photons. fEMCal provides full azimuthal coverage within a pseudorapidity range of approxi-
 4670 mately $1.4 \lesssim \eta \lesssim 3.9$. At lower pseudorapidity, fEMCal overlaps with BEMC, ensuring contin-
 4671 uous coverage by electromagnetic calorimeters in the hadron side of the ePIC detector. Coverage
 4672 at higher pseudo-rapidity is restricted due to mechanical limitations (clearance required to accom-
 4673 modate the accelerator beam pipe).

4674 The design requirements for the fEMCal were established through extensive studies of various
 4675 detector concepts proposed for the EIC over the past decade. These concepts originated from the
 4676 designs presented in the EIC White Paper [7] and Yellow Report [6], evolving through the ECCE
 4677 [10] and ATHENA [11] proposals and culminating in the ePIC detector concept discussed here.
 4678 It was concluded that an energy resolution of approximately $12\%/\sqrt{E} \oplus 2\%$, along with high
 4679 granularity needed to distinguish single photons from DVCS events and photon pairs from π^0
 4680 decays up to 50 GeV, would meet the EIC’s measurement objectives.

4681 Though numerous electromagnetic calorimeter technologies were considered, as noted in the EIC
 4682 Yellow Report [6], the stringent space limitation in ePIC detector (an integration length of only 27
 4683 cm along the Z-axis for fEMCal) ruled out all but one technology for the fEMCal: WScFi. This
 4684 technology, developed during the generic EIC detector R&D program [72], has also been success-
 4685 fully implemented in the recently constructed barrel electromagnetic calorimeter of the sPHENIX
 4686 experiment [73], which is comparable in scope with the ePIC fEMCal.

4687 Some of the key requirements and parameters for the fEMCal are summarized in Tab. 8.28. The
 4688 most critical challenges include the limited integration space and the need for a very large dy-
 4689 namic range, approaching 7000:1. Radiation doses and neutron fluxes are not expected to pose
 4690 significant challenges for current technologies. For instance, the forward calorimeter system (FCS)
 4691 constructed for the STAR experiment at RHIC has been successfully operational since 2021 under
 4692 conditions—both in terms of radiation and neutron flux—similar to those anticipated at the high-
 4693 est luminosities of the EIC. The choice of photodetectors and front-end readout electronics for the
 4694 fEMCal is partially based on the readout system developed for the STAR FCS.

4695 **Device concept and technological choice:** Figure. 8.96 depicts the front face of the ePIC
 4696 hadron end-cap in its closed position, which is divided into two halves to allow access to the inner
 4697 ePIC detectors in its open position. The end-cap features 1,145 fEMCal installation blocks, each of
 4698 which is mounted to a one-inch-thick steel plate situated between the hadronic and electromag-
 4699 netic calorimeters. Each installation block comprises 16 fEMCal towers and weighs approximately
 4700 18 kilograms, bringing the total weight of the fEMCal to around 21,000 kilograms. A 0.250 mm air
 4701 gap separates each fEMCal installation block to accommodate production and installation fixtures
 4702 tolerances. The readout system for the fEMCal is located at the front face of the blocks, ensuring
 4703 easy access to the electronics. Cables and utilities run horizontally along each row of blocks to the
 4704 perimeter of the fEMCal, where they bunched and passed through few openings in the light-tight
 4705 external shell and connected to the RDOs positioned on the sides of the hadron end-cap.

4706 Each fEMCal installation block is composed of four “production blocks,” with each production
 4707 block consisting of a 2×2 arrangement of towers. All production blocks are identical, and precise
 4708 mechanical tolerances are ensured by using identical production molds fabricated to high toler-

Table 8.28: Some requirements on performance of fEMCal and its parameters

Parameter	Requirements	Comments
Geometrical Acceptance	$1.4 \lesssim \eta \lesssim 3.9$	$R_{out} \sim 190$ cm, $Z_{frontface} \sim 341$ cm Hole for the beam pipe 30×30 cm ²
Integration envelope	$R_{max}=205$ cm, Depth = 27 cm	
E_{min} in a single tower	15 MeV	Minimal shower energy 50 MeV
E_{max} in a single tower	100 GeV	18×275 GeV, ep
Maximum rate in a single tower	10 kHz	$E_{thr}=15$ MeV, 10×275 GeV ep 500 kHz collision rate
Radiation doses	15 kRad	Integrated over 10 years
Neutron fluxes	4×10^{11} n/cm ²	1 MeV eq, integrated over 10 years
Energy resolution	$\lesssim 12\%/\sqrt{E} \oplus (2)\%$	Verified in the test beams
γ/π^0 separation	up to 50 GeV	$\sim 5\%$ mis-identification at 50 GeV
Depth	$23 X_0$	Minimize leakages
Detector parameters	Units	Comments
X_0, R_m	7 mm, 19 mm	Rad. length, Moliere radius
f_{samp}	2%	$e/h \simeq 1$ above 10 GeV
Scintillating Fibers	$\varnothing 0.47$ mm	Single clad sc. fibers
Light yield	~ 1600 pixels/GeV	Test beam results.
Transverse size of tower	2.5 cm \times 2.5 cm	Matches R_m
Transverse size of installation block	10 cm \times 10 cm	Block of 16 towers
Total number of towers	18320	
Photodetector	S14160-6015PS	Four 6×6 mm ² SiPMs per tower 15 um pixels size
Monitoring system	Blue LED	LED integrated on SiPM board. One LED per four towers

4709 ances, within a few tens of micrometers. The epoxy layer between production blocks is typically
 4710 less than 100 micrometers thick. These thin epoxy layers, along with air gaps between installa-
 4711 tion blocks, represent the only dead material within the fEMCal volume. These dead zones have a
 4712 negligible impact on the overall performance of the fEMCal.

4713 The primary reason for using tungsten powder and scintillating fiber technology for fEMCal is that
 4714 it is the only practical method to meet the stringent requirements outlined in Tab. 8.28. Specifically,
 4715 the desired energy resolution with extremely compact tower dimensions can only be achieved by
 4716 combining a small sampling fraction with a high sampling frequency. This high sampling fre-
 4717 quency is attained by using 780 thin, 0.47 mm diameter scintillating fibers in each tower, arranged
 4718 in a staggered pattern with a center-to-center distance of approximately 0.955 mm. Both the fiber
 4719 diameter and spacing were optimized through Monte Carlo simulations to ensure fEMCal is nearly
 4720 compensated and maintains the required energy resolution. Tungsten powder is used as the base
 4721 material for the absorber structure to make the technology viable in practice. A set of specifications
 4722 for tungsten powder and scintillating fibers for ePIC were established during generic detector R&D
 4723 program for EIC and experience of constructing sPHENIX barrel EMCal utilizing WScFi technol-
 4724 ogy.

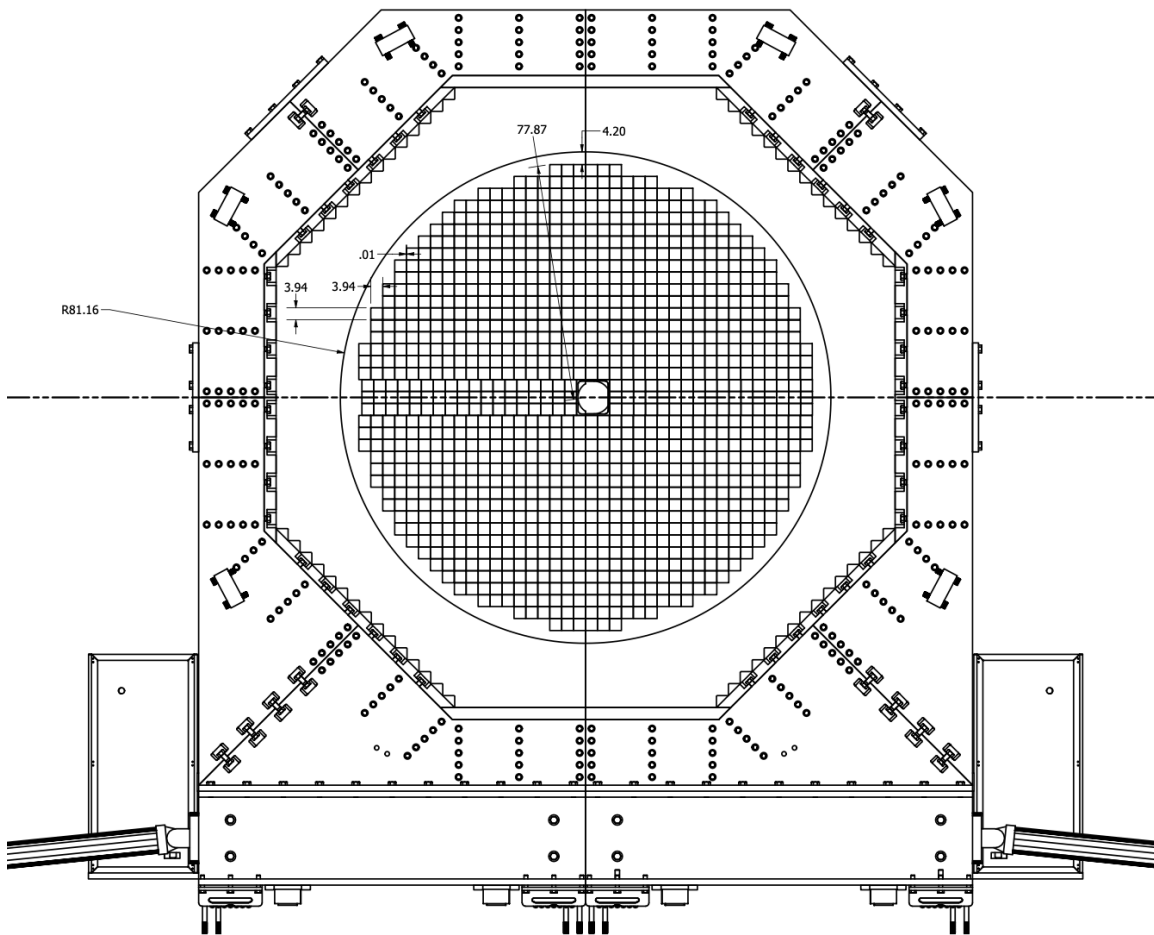


Figure 8.96: The front face of the ePIC hadron end-cap.

4725 Despite the apparent simplicity of fiber calorimeters, constructing them is not straightforward.
 4726 Detector components must be produced with extremely tight tolerances to maintain uniformity.
 4727 Historically, techniques like extrusion, machining, or rolling were used to manufacture absorber
 4728 plates, but these processes were complex and often required the creation of specialized machinery
 4729 and tools. Building fiber calorimeters has traditionally been a labor-intensive process, with indi-
 4730 vidual detector elements being handled one at a time, driving up costs compared to scintillating
 4731 plate detectors. Moreover, traditional methods face challenges with increasing sampling frequency,
 4732 as thinner absorber layers and fibers become more difficult to produce and manage. For example,
 4733 construction and assembly techniques for H1 fiber calorimeter detailed in [74].

4734 Our approach differs in that we first create a matrix of fibers and then pour the absorber material
 4735 into the matrix. Unlike previous methods, this technique eliminates the need to handle individual
 4736 calorimeter elements separately. Fig. 8.97 shows a matrix of scintillating fibers and image of tung-
 4737 sten powder used to build fEMCal prototypes. This powder has a particle size distribution of 90%
 4738 between 70 and 160 microns, a tap density of 11.5 g/cm^3 , and a purity of $W \geq 99.9\%$, with Fe, Ni,
 4739 and Co combined at $\leq 0.1\%$. Additionally, this tungsten powder exhibits excellent fluidity, a crucial
 4740 property for our application. The only operation required for the absorber material is measuring
 4741 the correct amount of powder before pouring it into the fiber matrix.

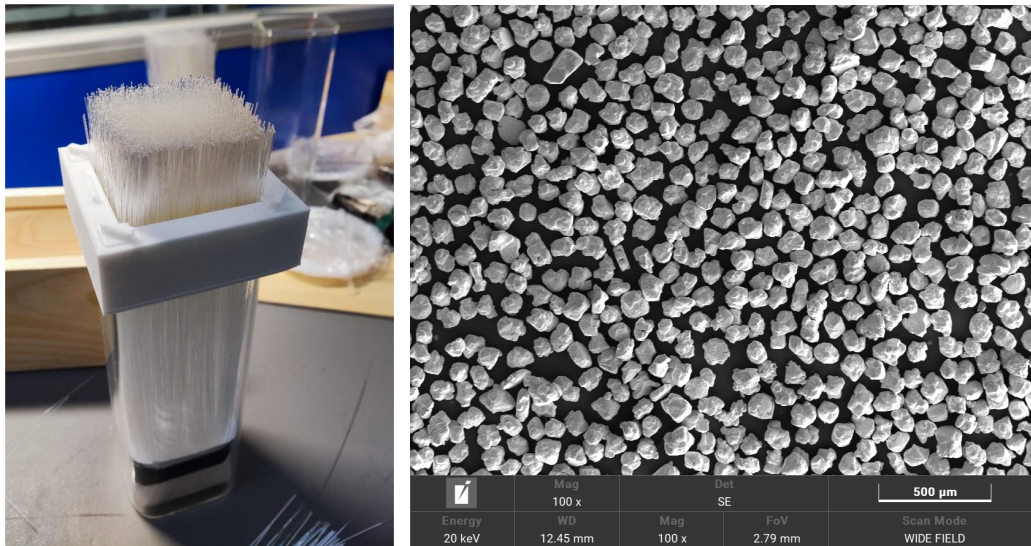


Figure 8.97: Matrix of scintillating fibers prepared to build production fEMCal blocks and SEM image of tungsten powder.

4742 The second key element is a straightforward method for forming the scintillating fiber matrix. This
 4743 matrix is defined by a set of precision brass meshes produced via photo-etching. These meshes have
 4744 mechanical tolerances of 30 microns on their overall dimensions for 300-micron thick meshes and
 4745 about 15 microns for the center-to-center distances between the holes for the scintillating fibers. The
 4746 fibers are cut to the desired length using a thermo-cutter, which melts the fiber ends to form small
 4747 drops that act as stoppers, preventing the fibers from slipping through the mesh holes. Once the
 4748 meshes are stacked, approximately 500 fibers at a time can be dropped into the container holding
 4749 the meshes, and with slight tapping, the fibers will flow through the set in seconds. For our recent
 4750 prototypes, a trained student could form a fiber matrix for a 2x2 tower production block with 3,120
 4751 fibers in around 30 minutes.

4752 The total production volume of scintillating fibers for the forward EMCal (fEMCal) is 3,000 km.
 4753 Only two companies, KURARAY and Luxium (formerly St. Gobain, BICRON), are capable of
 4754 producing the necessary fibers. Both companies' fibers were previously used to construct and
 4755 beam-test several WScFI EMCal prototypes for the EIC, with St. Gobain fibers also utilized by
 4756 the sPHENIX collaboration for their barrel EMCal. Recently, Luxium optimized the composition
 4757 of their standard BCF-12 fibers specifically for the shorter 17 cm fibers required for fEMCal, re-
 4758 sulting in a 20% improvement in light yield compared to their standard fibers. This was achieved
 4759 by adjusting the concentrations of primary and wavelength-shifting fluors, bringing them to the
 4760 same performance level as KURARAY fibers. Tab. 8.29 outlines the technical specifications and
 4761 requirements for the fEMCal fibers.

4762 To create a scintillating fiber matrix, it is essential that the fibers remain straight when placed into
 4763 the mesh framework. Fibers processed from spools tend to retain a bend due to "memory," which
 4764 leads to significant friction between fibers flowing through a set of meshes, which complicates the
 4765 assembly process. Among suppliers, only Luxium agreed to a delivery method that addresses this
 4766 issue, making them the sole provider of fibers for the fEMCal. These scintillating fibers are a long
 4767 lead procurement item, with a pre-production batch expected to arrive at ePIC by the end of 2024,

Table 8.29: Requirements and Technical specifications for fEMCal scintillating fibers.

Parameter	Requirements	Comments
Light Yield (LY)	≥ 8000 photons per MeV	Acceptance QA with Sr90 source Compared to a standard sample
Nominal Diameter	$0.47 \text{ mm} \pm 0.0094 \text{ mm RMS} \leq 0.02 \text{ mm}$	QA sampled on 10% boxes 100% at ramp-up prod. stage
Attenuation Length	$\geq 3 \text{ m}$	QA with UV LED
Batch-to-batch LY variation	$\leq 10\%$	QA with Sr90
Emission spectrum	Blue-green light	To match QE of SiPMs
Scintillation Decay Time	$\leq 3 \text{ ns}$	Bunch structure at EIC
Delivery Method	In cans, length of fibers +2%, -0%	Length $\geq 1 \text{ m}$, increment 20 cm

4768 followed by monthly deliveries of the remaining fibers. Both the production and acceptance sites
 4769 will adhere to agreed-upon QA and acceptance protocols to ensure that the fibers meet fEMCal
 4770 specifications. Some of these QA steps are outlined in Tab. 8.29.

4771 The concept of using tungsten powder as an absorber was briefly explored by the UCLA group in
 4772 2003, when they constructed and tested a small electromagnetic prototype at SLAC. At the time,
 4773 the tower structure required a thin-walled brass container to hold the dry powder and fibers in
 4774 place. However, this assembly technique proved imperfect, leading to significant transverse non-
 4775 uniformities in detector response due to variations in the sampling fraction and potential displace-
 4776 ment of fibers during packing. A compact calorimeter demands strict mechanical tolerances and a
 4777 highly uniform internal structure to achieve theoretical energy resolution. To address these issues,
 4778 we introduced intermediate meshes to secure fibers along the towers and developed a vacuum-
 4779 assisted method to infuse epoxy into the tungsten powder/fiber assembly. Once assembled, the
 4780 structure becomes rigid, eliminating the need for external containers and dead material in the
 4781 tower. The homogeneity of the WScFi structure was verified by cutting multiple samples on small
 4782 pieces which were analyzed and was found to exceed 1%. The mechanical properties of the WScFi
 4783 structure were measured and they are comparable to construction steel.

4784 This refined technique, with slight variations, was then employed in constructing the sPHENIX
 4785 barrel EMCal and all recent fEMCal R&D prototypes.

4786 **Light Collection scheme and Photosensors** The light collection scheme and photosensor
 4787 setup adhere to the general requirements outlined in Tab. 8.28. The back of each installation block
 4788 features a thin layer of optical epoxy (1.8 mm thick) mixed with 10% TiO_2 , which acts as a diffuse
 4789 optical reflector for the scintillating fibers and provides a surface for bonding the 13 mm-thick alu-
 4790 minium “strong back.” This strong back plate is then bolted to the steel interface plate connecting
 4791 the EMCal and HCal. On the front side of the installation block, a 21 mm-long light guide (LG)
 4792 plate is attached. Made from a single piece of optically clear cast acrylic, this LG plate has 64 trape-
 4793 zoidal light guides to direct light from the fibers to the SiPMs. The front and back views of the LG
 4794 plate with SiPMs attached can be seen in Fig. 8.98. The light collection efficiency of this setup is
 4795 approximately 80%, which is sufficient to detect 15 MeV in a single tower, corresponding to 24 fired
 4796 pixels. However, due to the short length of the light guide (typically much longer in fiber calorime-
 4797 ters), light “mixing” from individual fibers is minimal, resulting in spatial non-uniformities in light
 4798 collection at the 10% level, as measured with a point light source.

4799 The chosen photodetector for the fEMCal is the SiPM (Silicon Photomultiplier). Over the past 15

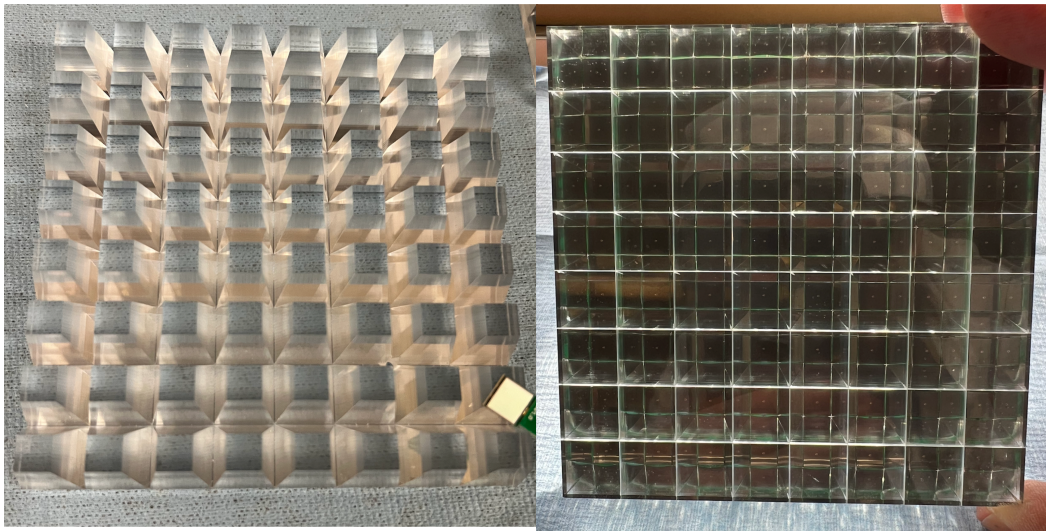


Figure 8.98: Front and back views of LG plates with installed SiPMs.

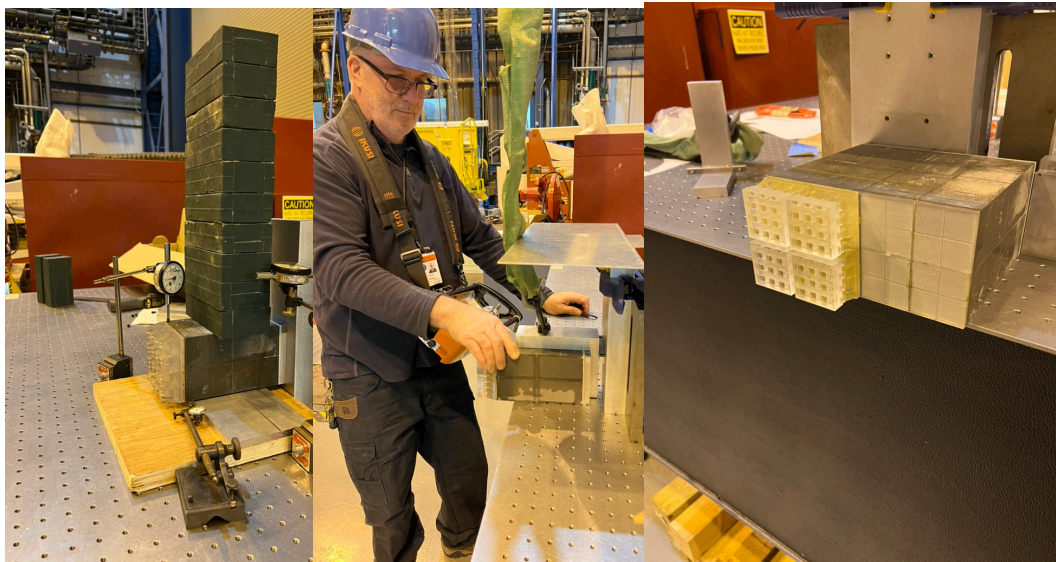
4800 years, extensive R&D programs across the globe—including the generic detector R&D program for
 4801 the EIC—have worked to bring SiPM technology to a mature and reliable level. Today, hundreds
 4802 of thousands of SiPMs are in use in various high-energy physics and nuclear physics experiments.
 4803 These detectors are extremely compact, robust, and well-suited for calorimetry readout in moderate
 4804 radiation environments, such as the forward region of the ePIC detector, as shown in Tab. 8.28. The
 4805 failure rates of SiPMs in calorimeter operations at facilities like JLab, BNL, and CERN have been
 4806 remarkably low, typically less than 0.1%. Notably, the STAR Forward Calorimeter System (FCS)
 4807 experienced zero SiPM failures during three years of operation under conditions similar to those
 4808 expected in the high-luminosity EIC. Although neutron-induced damage will lead to increased
 4809 leakage current and noise levels, these effects remain within tolerable limits. For example, it is
 4810 anticipated that the equivalent noise level for fEMCal at ePIC will rise to around 6 MeV after 10
 4811 years of operation, particularly in areas near the beam pipe. This projection is based on scaling
 4812 from the results observed in the STAR FCS. After this period, replacement of some of the SiPM
 4813 boards near the beam pipe may be necessary. These considerations informed the design of the
 4814 fEMCal readout system, ensuring a straightforward integration with the detector. The technical
 4815 specifications and performance details of the SiPMs for the fEMCal are summarized in Tab. 8.30.

4816 **Mechanical Integration** The mechanical integration, installation procedures, and structural
 4817 tests for the fEMCal were validated using installation blocks at BNL. These blocks were produced
 4818 following the final production protocols and using the same components that will be used for the
 4819 actual installation. Structural tests on smaller samples demonstrated that the safety factor for the
 4820 proposed mounting scheme is greater than 48. A full structural test Fig. 8.99 was conducted by
 4821 mounting an installation block on a mockup plate and applying five times the expected load. The
 4822 deflections at the readout end of the fEMCal block were measured to be less than 100 μm , confirm-
 4823 ing that each installation block is self-supporting and does not exert any load on the blocks beneath
 4824 it. Simple installation fixtures were designed, and the installation procedures were verified to en-
 4825 sure safety. Specifically, it was crucial to confirm that the fEMCal blocks could be safely installed
 4826 with the SiPM-carrying boards glued to the LG plates. The tests confirmed that the blocks can be

Table 8.30: Requirements and Technical specifications for fEMCal SiPMs.

Parameter	Requirements	Comments
Active Area	6 mm × 6 mm	Efficiency of light collection, E_{min} 15 MeV
Pixel Size	15 or 20 μ m	Dynamic Range, E_{max} 100 GeV
Peak Sensitivity	~ 420 nm	Match scintillating fibers spectra.
PDE	$\geq 30\%$	Efficiency of light collection, S/N
Gain	$\sim 2 \times 10^5$	at 3 V overvoltage, S/N
DCR	≤ 3000 kcps	at 3 V overvoltage, 25 C, S/N
Temperature Coefficient	≤ 40 mV/C	Stability, Uniformity
Direct Cross Talk	$\leq 1\%$	
Terminal Capacitance	≤ 2.5 nF	FEE coupling
Packing Granularity	Multiple of 4 per tray	4 SiPMs per tower at same V_{op}
V_{op} variation within a tray	± 0.02 V	Uniformity of response

4827 safely mounted onto the hadron end-cap without causing any damage to the SiPM boards.

**Figure 8.99:** Structural and installation tests at BNL.

4828 **Performance** The performance of the fEMCal prototypes has been tested in several test beams
 4829 at FNAL over the past few years, initially as part of the generic detector R&D for the EIC and later
 4830 as part of the ePIC R&D program. In the summer of 2024, one installation block featuring the latest
 4831 version of the light guide (LG) and SiPM readout was tested at FNAL. Energy scans were conducted
 4832 at various impact angles covering the entire fEMCal acceptance range. As expected, some variation
 4833 in response across the surface was observed, as shown in Fig. 8.100, due to the compact nature
 4834 of the LG. However, this variation represents an improvement compared to earlier versions [75].
 4835 Position-dependent corrections, based solely on the data from fEMCal, were applied to account
 4836 for non-uniformities. This method is similar to the approach used in the 2014 test [75] and for

4837 the sPHENIX barrel EMCal. As anticipated, the uniformity of response improves with shallower
 4838 impact angles. The energy resolution, shown in Fig. 8.100, corroborates previous measurements
 4839 with this type of electromagnetic calorimeter [75] and aligns with the performance requirements
 4840 outlined in Tab. 8.28. The measured absolute light yield is 1580 pixels/GeV.

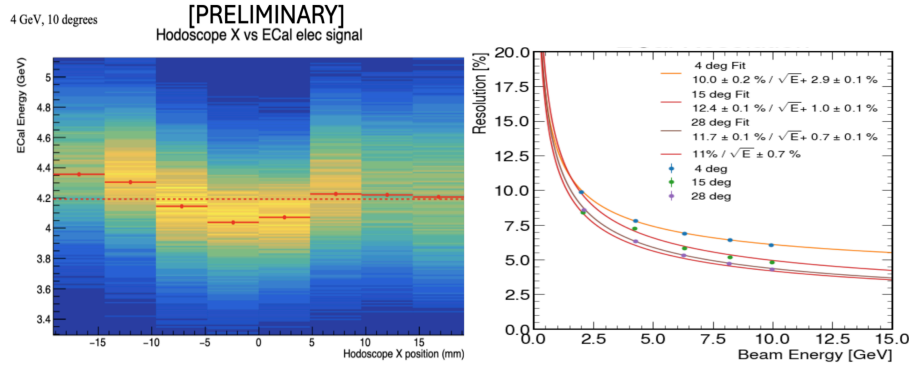


Figure 8.100: Response of calorimeter vs position in hodoscope (left panel). Energy resolution for different impact angles (right panel).

4841 The remaining performance parameters were extensively tested using MC simulations, incorporat-
 4842 ing the full ePIC simulation chain with the latest detector geometry updates. A material scan indi-
 4843 cated the presence of approximately $0.2 X_0$ of “dead” material in front of the fEMCal in ePIC, but its
 4844 impact on performance was found to be negligibly small. Simulations conducted with PYTHIA8,
 4845 using minimal Q^2 cuts for all energy configurations at the EIC, examined occupancy, rates, and
 4846 dynamic range. These studies informed the set of requirements listed in Tab. 8.28.

4847 An initial investigation into γ/π^0 separation, based on the traditional shower shape analysis
 4848 method outlined in the EIC Yellow Report (Fig. 11.46, [6]), revealed potential for improvement.
 4849 A significant enhancement in γ/π^0 separation was achieved by applying machine learning algo-
 4850 rithms. As shown in Fig. 8.101 (left panel), the misidentification rate at 60 GeV dropped to approx-
 4851 imately 10%, compared to 80% with traditional methods [6].

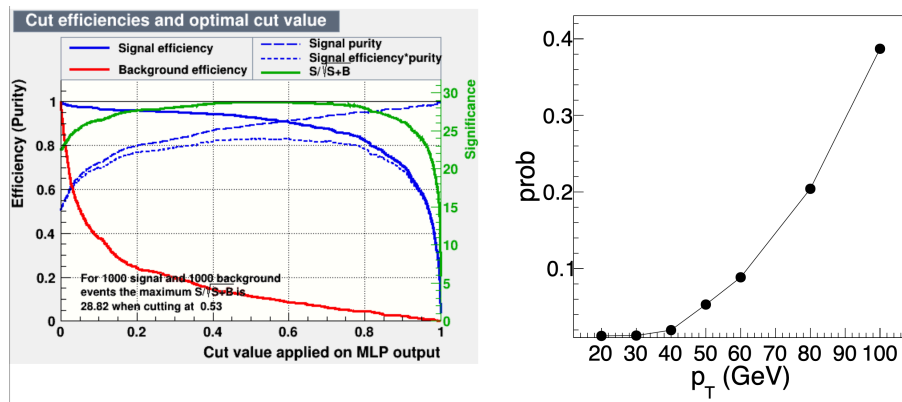


Figure 8.101: Signal (single photon) efficiency and background (merged di-photons) contamination for different cut value of the NN output for 60 GeV (left panel). Probability of misidentifying π^0 as a single photon vs energy (right panel)

4852 **Readout Electronics** The fEMCal readout electronics face three primary challenges: achieving
 4853 a large dynamic range of 7000:1, ensuring precise discrimination for streaming small signals (24
 4854 pixels) amidst dark counts of up to 45 GHz caused by radiation damage to SiPMs, and integrat-
 4855 ing everything within a compact space—around 5 cm for SiPM boards, front-end boards (FEBs),
 4856 cooling, and cables. Tab. 8.31 summarizes requirements for the FEB.

Table 8.31: Requirements for the FEB

Parameter	Requirements	Comments
SiPM & overvoltage	4xS14160-6015PS, 2-3V	
Min signal	15 MeV (@ 1.6 pix/MeV)	
Max signal	100 GeV	
Hit rate	10 kHz	per channel
Charge reso.	$\sim 210\%/\sqrt{npix} \oplus (0.9)\%$	contribute $\leq 10\%$ of fEMCal resolution
Charge nonlinearity	$\leq 1\%$	
Time resolution	$\ll 10$ ns	for ≥ 100 MeV signals only
SiPM bias voltage stability	≤ 10 mV	including T compensation
Bias voltage setting range	33 to 47 V	sufficient for meaningful IV curve
Bias current range & mon. resolution	2 mA, ≤ 200 nA	4 SiPMs per tower at same V_{op}
LED drive control	var. amplitude, masks	fired by global command

4857 Building on the successful design of the STAR FCS readout, fEMCal’s readout system transfers
 4858 SiPM signals to a low impedance load, shapes and amplifies the resulting voltage, and digitizes the
 4859 waveform. Hits are detected in the digital waveform via threshold crossing (which may be filtered).
 4860 In streaming readout mode, regions of interest in the digital waveform are identified, timestamped,
 4861 and sent to an output FIFO/merging scheme, before being transmitted to the readout (RDO) board.
 4862 At the RDO, data from up to 16 FEBs are buffered, merged, and sent to the DAM. Feature extraction,
 4863 converting raw waveform samples to estimated pulse amplitude and timing, may be done either
 4864 at the FEB or RDO level to reduce data volume. If hardware feature extraction is not used, this will
 4865 be performed during preliminary online analysis.

4866 Waveform digitization for fEMCal will operate at either 39.4 MSPS or 49.25 MSPS. The digitization
 4867 clock must be phase-locked to the beam bunch crossing clock at 98.5 MSPS to extract hit timestamps
 4868 in real-time within the streaming DAQ system. Sampling at 98.5 MSPS is not feasible due to power
 4869 and FPGA resource constraints. To meet the 15 MeV readout threshold and achieve the dynamic
 4870 range, the ADC resolution must be 14 bits. The analog waveform will be shaped before digitization
 4871 to achieve a peaking time of approximately $2.8/f_{SAMPLE}$, which ensures less than 1% error in pulse
 4872 amplitude measurement while minimizing noise from dark count pileups. For instance, a 57 ns
 4873 peaking time is optimal at 49.25 MSPS.

4874 The FEB will individually regulate bias voltage for each tower, providing temperature compensa-
 4875 tion for each SiPM board (covering 2×2 towers) and monitoring current with built-in protective
 4876 current limits. Each tower’s four SiPMs will be connected in parallel, sharing a common bias volt-
 4877 age, requiring precise matching of the breakdown voltages (V_{BR}) among the four SiPMs to ensure
 4878 uniform gain. The bias regulation circuits, developed from the STAR Forward Calorimeter, have
 4879 proven effective, though radiation sensitivity in a voltage reference IC was noted. To mitigate this,
 4880 fEMCal’s bias regulator will use a remote reference on the power distribution boards, ensuring the
 4881 required 0.03% stability. Less critical internal voltage references require only 1% stability. The bias
 4882 regulation channels provide sharp current limiting to protect the SiPMs from overload, maintaining
 4883 10 mV bias voltage stability up to the current limit (2 mA).

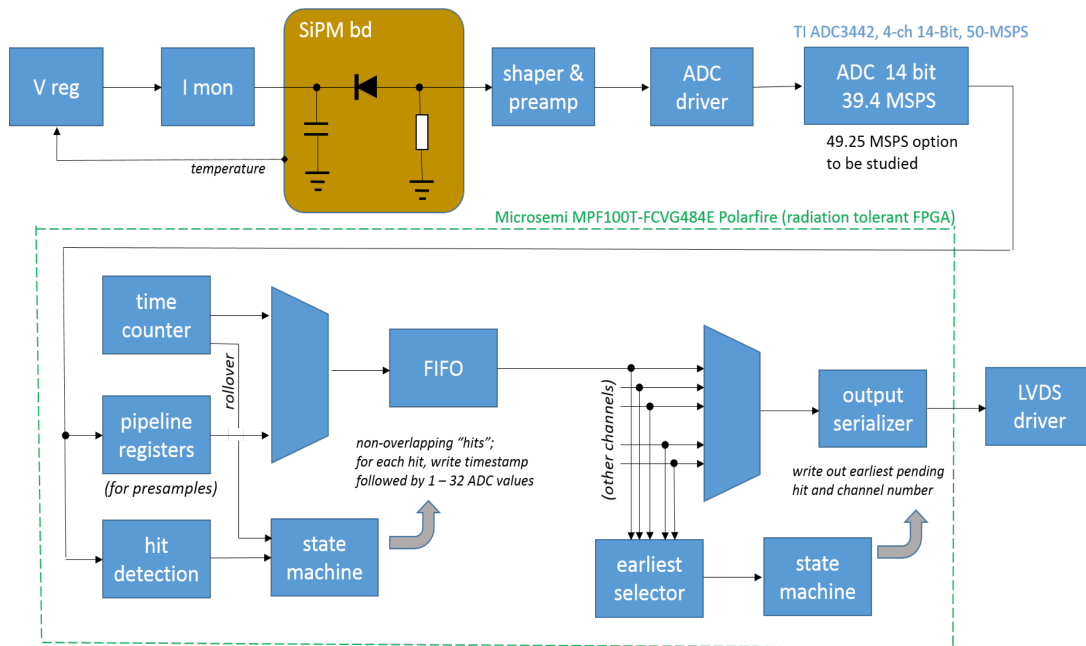


Figure 8.102: fEMCal front end electronics.

4884 Signal routing from the SiPM boards to the FEBs is achieved through board-to-board connectors,
 4885 eliminating the need for cables. These connectors can accommodate mechanical tolerances of +/-
 4886 0.5 mm between the FEB and SiPM boards and overlap with space allocated for the cooling water
 4887 tube. Should radiation damage impact the innermost FEBs, a backup plan would route SiPM sig-
 4888 nals via 2m coaxial cable bundles to FEBs mounted at the block periphery.

4889 Connections between the FEBs and RDO will use shielded Cat6 Ethernet cables, routed horizontally
 4890 through the FEB rows and out of the magnet to racks housing the RDOs. One rack will be placed
 4891 north of the north detector half, and another south of the south detector half. Cable lengths are
 4892 estimated at 15 meters, and it has been confirmed that LVDS signals can be properly received at
 4893 200 Mb/s over this distance, meeting performance requirements.

4894 Each rack will also house a Wiener MPOD crate with low-voltage (LV) power supplies, with one
 4895 crate serving the north half and one for the south half of the detector. Each FEB will require approx-
 4896 imately 250 mA at +16 V, 180 mA at -2 V, and up to 67 mA (depending on SiPM radiation damage)
 4897 at +50 V.

4898 The FEBs will be cooled conductively via a copper bracket attached to the main board (housing the
 4899 ADCs, FPGA, and power supply circuits) and connected to a water cooling line. The water line
 4900 will consist of standard 1/4 inch (potentially 3/16 inch) diameter copper tubing. A negative pressure
 4901 system will mitigate the risk of water leaks. Two rows of FEBs will be served by a single water
 4902 line in a U-shaped loop, with no fittings at each FEB, only at the loop ends. Reliable flare fittings
 4903 will be used for the connections. Custom water manifolds, located in the “service gap” at the outer
 4904 perimeter of the calorimeter blocks, will manage water distribution. The arrangement will likely
 4905 consist of two supply and return manifold sets—one for the upper and one for the lower half of the
 4906 detector.

4907 Each water circuit will need to cool about 750 W of power from 148 FEBs, requiring chillers with at
 4908 least 1.5 kW capacity for each half of the detector. One chiller will serve the north half and another

4909 the south, cooling two water circuits each.

4910 Slow controls for fEMCal will fall into two categories: hardware registers on the FEBs (communi-
 4911 cated through DAQ software and the DAM/RDO) and controls for commercial equipment such as
 4912 the water chillers and power supplies (Wiener MPOD), connected via Ethernet. SoftIOCs interfaces
 4913 will manage EPICS variables, providing GUI control, logging, and alarms.

4914 Tab. 8.32 summarizes the control and status registers for the FEB.

Table 8.32: Control and status registers on the FEB

Function/description	Qty per FEB	R/W	Notes
SiPM bias voltage (base)	32	R/W	
Bias temp. comp. slope	1	R/W	
actual compensation	8	R	i.e. temperature
SiPM current monitor	32	R	extra diagnostic info
input LV supply monitor	2	R	
FEB temperature monitor	3	R	
FEB & SiPM board serial numbers	9	R	read once at startup
firmware revision	1	R	read once at startup
firmware update interface	1	R/W	maintenance use only
hit threshold channel mask	32	R/W	
hit detection options registers	4	R/W	
LED firing mask	1	R/W	
hit scalers	32	R	
fifo overrun scalers	32	R	
ADC configuration interface	1	R/W	might be internal use only

4915 **Calibration** The fEMCal faces the hadron beam, and at mid to high energies, its signals will
 4916 predominantly come from photons produced by π^0 decays. Tower-by-tower absolute energy cali-
 4917 bration of the forward electromagnetic calorimeter will be performed by reconstructing π^0 mesons
 4918 through the invariant mass of two photons from π^0 decays. It is expected that π^0 calibration
 4919 for each tower can be achieved in approximately one day of data collection, followed by semi-
 4920 online analysis using only forward fEMCal data. The method involves associating reconstructed
 4921 π^0 mesons with the tower showing the highest response, adjusting the tower's gain based on the
 4922 π^0 mass location, and repeating the process over several iterations. This technique has been suc-
 4923 cessfully implemented in forward calorimeters at RHIC, including the STAR FCS.

4924 Electrons from DIS events, combined with tracking information, can be used to cross-check the
 4925 calibration. However, this approach requires a large dataset and will be performed offline. Addi-
 4926 tionally, Minimum Ionizing Particle (MIP) signals from hadrons can be utilized for calibration at the
 4927 low-energy end. For high energies, where the two photons from π^0 decays are too close together
 4928 for the forward EMCal to distinguish them, η mesons can be used to verify energy non-linearity.

4929 **Monitoring system** An LED system will be installed on the FEE boards to illuminate four tow-
 4930 ers using a trigger pulse. The LEDs will be preselected to provide equal light output to the towers,
 4931 serving as a critical monitoring system. This will be essential for initial testing during installation,
 4932 verifying mapping, and ensuring long-term stability of the detector, SiPMs, and FEE board gain,

4933 as well as detecting any potential radiation damage. A dedicated short LED run will be performed
4934 daily to monitor the calorimeter's performance.

4935 Additionally, the current and voltage on the FEE boards will be continuously monitored. Periodic
4936 I-V curve measurements will be conducted, on a weekly or bi-weekly basis, to assess the health of
4937 the SiPMs and FEE boards.

4938 **Status and remaining design effort:**

4939 R&D effort: eRD106 will be completed in early 2025 with finalizing analysis of the test beam
4940 data.

4941 E&D effort: Detailing of mechanical design, and formalizing production drawings.

4942 Other activity needed for the design completion: Produce and test first versions of final design
4943 FEB and SiPM boards.

4944 Status of maturity of the subsystem: $\sim 70\%$

4945 **Environmental, Safety and Health (ES&H)** The project will strictly adhere to all Environ-
4946 ment, Safety, and Health (ES&H) regulations to ensure the safety of personnel, the integrity of
4947 the equipment, and the protection of the environment throughout the construction and operation
4948 phases. Comprehensive risk assessments will be conducted for all activities, including the han-
4949 dling of hazardous materials, electrical components, while implementing proper controls to min-
4950 imize exposure to risks. Personnel will receive specialized training in safety protocols and emer-
4951 gency response procedures, and regular audits will be conducted to ensure compliance with ES&H
4952 standards. Additionally, the design of systems such as power management will prioritize envi-
4953 ronmentally friendly practices, incorporating energy-efficient technologies and minimizing waste
4954 and emissions. Continuous monitoring of environmental impact and adherence to radiation safety
4955 guidelines will be maintained to ensure the long-term safety and sustainability of the project.

4956 **Collaborators and their role, resources and workforce:** Collaboration plays a pivotal role
4957 in the success of this project, as it brings together a diverse group of experts from various institu-
4958 tions, each contributing specialized knowledge and skills. The development of the fEMCal detec-
4959 tor, for instance, relies on coordinated efforts between physicists, engineers, and technicians work-
4960 ing on different aspects such as design, testing, and integration. Collaborative efforts ensure that
4961 challenges in areas like electronics, cooling systems, and data acquisition are addressed through
4962 shared expertise and innovative problem-solving. Additionally, partnerships with other research
4963 labs, such as BNL and international institutions, allow for the exchange of ideas, the pooling of
4964 resources, and the sharing of key R&D advancements. This collaborative environment fosters a
4965 culture of learning and inclusivity, which is critical for the project's long-term success, allowing it
4966 to meet both scientific and technical goals.

4967 8.3.6 Hadronic Calorimetry

4968 Add text here.

4969 8.3.6.1 The backward endcap hadronic calorimeter

4970 The backward hadronic calorimeter, here called **nHCal** meaning **Negative-eta/Neutral Hadronic**
 4971 **Calorimeter** is a tail catcher calorimeter to be installed in the electron going negative-z direction. As
 4972 illustrated in the ePIC detector schematic REFERENCE, the nHCal is surrounded by an outer collar,
 4973 backed by a flux return plate and an oculus ring placed in front. Experience from H1 experiment
 4974 at HERA shows the need for such a calorimeter for low- x measurements [76,77].

4975 Requirements

4976 **Requirements from physics:** The main requirements for nHCal originate from physics pro-
 4977 cesses in events with low Q^2 and low $x \sim 10^{-3} - 10^{-2}$ as well as high inelasticity y . This requires
 4978 the acceptance of $-4.14 < \eta < -1.18$.

4979 The processes of interests include diffractive vector meson overproduction $J/\psi \rightarrow \mu^+\mu^-$, $\phi \rightarrow$
 4980 $K_L K_S$, $\phi \rightarrow K^+K^- \rightarrow \mu^+\mu^-$ and diffractive dijets. It will be also used as a veto for jet studies with
 4981 neutral energy component and help in scattered electron identification along with backward EMcal.
 4982 Finally, it will be used as a hadron beam background veto for dRICH in conjunction with LFHCAL
 4983 for which a good timing resolution is required. In order to measure vector meson production
 4984 with muons a good μ/π separation of tracks with MIP signal in calorimeters is required. The low
 4985 energy neutron detection for neutral jet identification requires low hit thresholds to achieve more
 4986 than 90% detection efficiency for 2 GeV neutrons. Furthermore neutral clusters have to be identified
 4987 after charged hadron correction which require a track matching and cluster position resolution to
 4988 distinguish showers which are 30 cm apart. This is achievable with tiles of up to 25 cm size.

4989 **Requirements from Radiation Hardness:** In general, the radiation dose in the electron end-
 4990 cap area is expected to be low. A study was performed and is summarized here: [https://wiki.](https://wiki.bnl.gov/EPIC/index.php?title=Radiation_Doses)
 4991 [bnl.gov/EPIC/index.php?title=Radiation_Doses](https://wiki.bnl.gov/EPIC/index.php?title=Radiation_Doses)

4992 The low radiation dose compared to the forward region makes the use of SiPMs and FEE safe.
 4993 SiPMs are required to have good low dark count rate after 10 years of running. This is possible
 4994 with the selected Hamamatsu S14160-1315PS model.

4995 **Requirements from Data Rates:** Data rates were studied by considering the following sources:

- 4996 • Deep Inelastic Scattering (DIS)
- 4997 • Synchrotron Radiation
- 4998 • Electron Beam Gas
- 4999 • Hadron Beam Gas

5000 The values are taken from background studies found here:

bkg. type	hit rate in detector [Hz]	max single channel hit rate [Hz]
DIS	$\sim 10^6$	1233.24
Synchrotron rad.	$\sim 2 \cdot 10^4$	-
e+gas	403899	6644.8
h+gas	$\sim 7 \cdot 10^5$	303.781

Table 8.33: Maximum expected background rates for backward HCal. The assumed threshold is 170 keV.

5001 • <https://wiki.bnl.gov/EPIC/index.php?title=Background>

5002 Justification

5003 Device concept and technological choice:

5004 Subsystem description:

5005 General device description: The nHCal is planned to be a sampling hadronic calorimeter with
 5006 10 layers of alternating steel and plastic scintillator of 4 cm and 0.4 cm thickness respectively.
 5007 Such arrangement provides compensation. The structure of the calorimeter will be that of
 5008 a flattened cylinder with the outer radius of 276 cm and the inner radius of 14 cm to pro-
 5009 vide room for the hadron and electron beampipes. The thickness along the beam direction
 5010 is going to be 45 cm in total. The plastic scintillator layer is going to be made of tiles with
 5011 10 cm \times 10 cm (TBD) size. Two light collection solutions are under consideration with either
 5012 the use of WLS fibers with SiPM readout or SiPM on tile design as for LFHCAL, which was
 5013 developed by CALICE [78]. The SiPM on tile is possible with smaller tiles close to the beam
 5014 ($\eta \sim -4$), while larger tiles need to use WLS+SiPM combination. Tiles and absorber plates
 5015 will be assembled into modules inspired by LFHCAL modules of 10 cm \times 20 cm \times 45 cm size
 5016 in y, x and z directions respectively.

5017 Sensors: The Hamamatsu S14160-1315PS model SiPMs will serve as light sensors. They will
 5018 either be connected to the WLS fibers or placed directly on tile.

5019 FEE: HGCROCV3 will be used as an FEE similar to their calorimetry systems in ePIC. FEE's
 5020 are going to be placed in front of the modules.

5021 Other components: Add text here.

5022 **Performance** Performance of the nHCal was studied with single particles. Thresholds for neu-
 5023 tron detection were studied vs. kinetic energy and integration time. The neutron detection ef-
 5024 ficiency is shown in Fig. 8.103 vs. energy threshold and integration time. Good performance is
 5025 achieved with 100 ns and further increase does not offer much improvement. On the other hand
 5026 already low threshold of $0.25E_{MIP}$ provides good detection efficiency of 70% at 300 MeV

5027 **Simulated DIS events** One of the basic studies is a check of energy and momentum distri-
 5028 butions going into backward HCal. This study used DIS $e + p$ events at $18 + 275$ GeV with

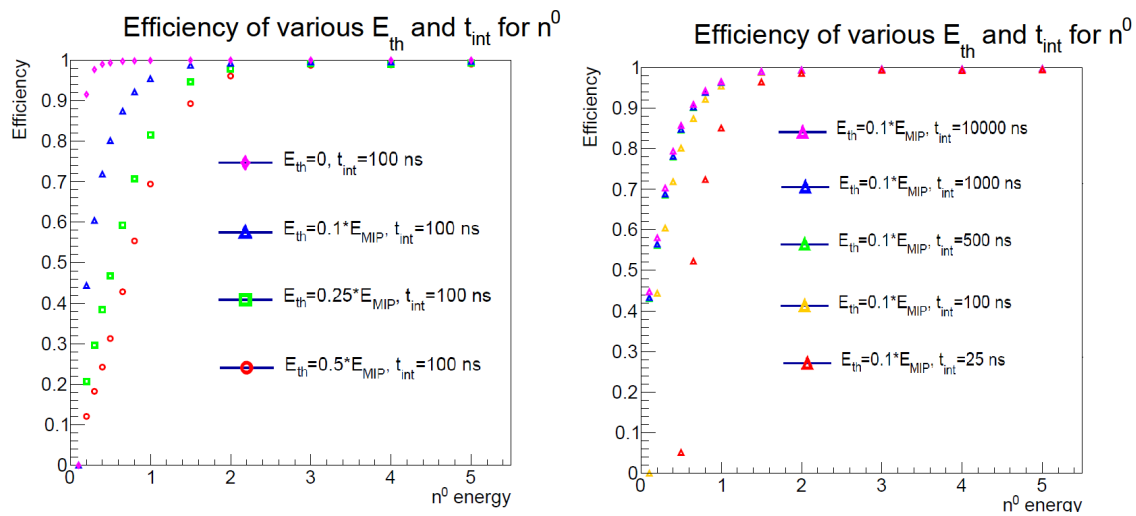


Figure 8.103: Left: Neutron detection efficiency vs. kinetic energy E_{kin} , dependence on threshold as a fraction of MIP energy deposit. Right: Same as left, but showing dependence on integration time.

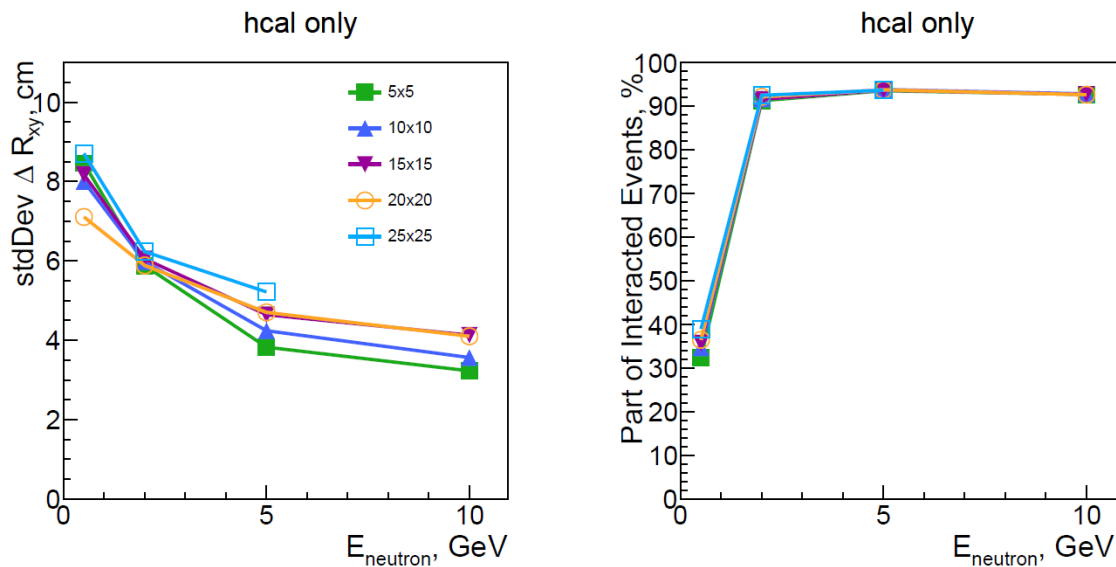


Figure 8.104: Position resolution R_{xy} and cluster efficiency vs. E for different tile sizes.

5029 $Q^2 > 1 \text{ GeV}^2$. The Fig. ?? shows total energy E and p distributions of each particle species in
 5030 nHCal acceptance $-4.0 < \eta < -1.0$.

5031 Energy and momentum distributions of particles in nHCal acceptance in $e + p$ DIS events at 18 +
 5032 275 GeV with $Q^2 > 1 \text{ GeV}^2$ was studied with the full official simulation of the ePIC detector. These
 5033 are presented in Fig. 8.105 as well as vs. η in Fig. 8.106, Fig. 8.107 and Fig. 8.108. This was used to

5034 check the average energy of neutrons and optimize the detector for measuring that.

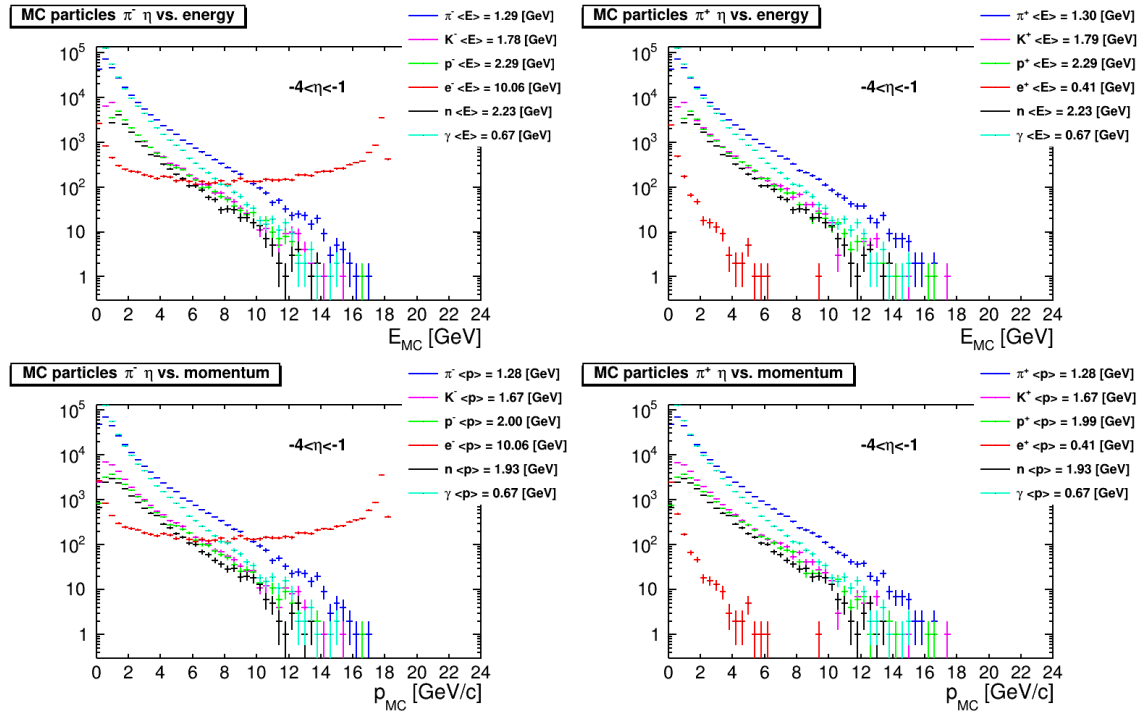


Figure 8.105: Top: Primary, generated particle E distributions in nHCal acceptance $-4.0 < \eta < -1.0$. Bottom: Primary, generated particle p distributions in nHCal acceptance $-4.0 < \eta < -1.0$.

5035 **Vector meson reconstruction** Vector meson reconstruction and acceptance was studied in $e + p$
 5036 and $e + A$ events with PYTHIA8 with the focus on exclusive diffractive photoproduction. Large
 5037 fraction of J/ψ cross section was found to be produced in the backward direction making it espe-
 5038 cially important. It has to be noted that J/ψ study is one of the major goals of EIC as listed in the
 5039 Yellow Report [?]. Acceptance of J/ψ is shown in Fig. 8.109 vs. $-t$, Bjorken x_{BJ} and Pomeron x_p .
 5040 The figure also illustrates the acceptance when decay daughters are measured in different detectors.
 5041 Similar study was performed for $e + A$ collisions and presented in Fig. 8.110.

5042 Studies of $\Phi \rightarrow K^+K^-$ were also performed as shown in Fig. 8.111 for $e + p$ and in Fig. 8.112 for
 5043 $e + A$ collisions.

5044 These studies indicate that nHCal is needed to measure J/ψ and Φ in events with $x \sim 10^{-3}$ and
 5045 lower.

5046 **Jets with neutral component** Another purpose of nHCal is to help identify jets with neutral en-
 5047 ergy component, especially low energy neutrons of around $E = 2.23$ GeV. By distinguishing these
 5048 2 samples the jet energy resolution can be improved. This was studied with full ePIC simulation
 5049 and track matching to MC particles or clusters using MC information. The jet energy resolution for
 5050 the cases of inclusive(squares) and charged-only jets(triangles) is compared in Fig. 8.113. Results
 5051 show $\sim 20\%$ improvement in jet energy resolution.

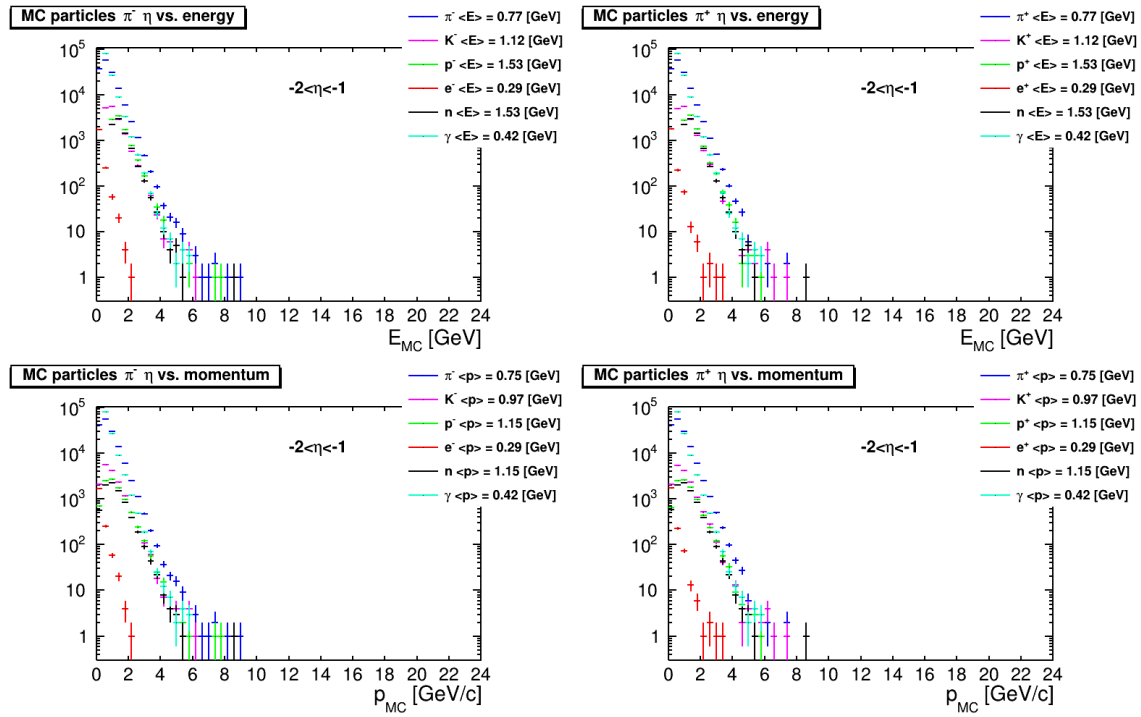


Figure 8.106: Top: Primary, generated particle E distributions in $-2.0 < \eta < -1.0$ range. Bottom: Primary, generated particle p distributions in $-2.0 < \eta < -1.0$ range.

5052 **Diffraction dijet measurement** Diffractively produced dijets are going to be studied with
 5053 nHCal. Preliminary studies indicate that 22% of diffractive dijet events contain one of the jets in
 5054 nHCal acceptance. Such events have $x \sim 10^{-3}$, so are important to study the structure of protons
 5055 and nuclei.

5056 **Cluster reconstruction** Clusters are reconstructed using standard island clustering algorithm.
 5057 In order to distinguish charged and neutral clusters track cluster matching has to be used. The
 5058 neutral energy component is obtained by subtracting the expected energy for charged particles as
 5059 provided by measurement of momentum through tracking. The overlap of clusters was studied
 5060 using 2-particle simulation of neutrons and pions with $E = 1$ GeV. This is shown in Fig. 8.114 vs.
 5061 x, y position of the reconstructed clusters. The legends indicate angles of emission of neutrons and
 5062 pions.

5063 **Implementation**

5064 **Services:**

5065 **Subsystem mechanics and integration:** Backward HCal modules will be stacked on top of
 5066 each other in a similar way to the LFHCal. All the services will be provided through the service
 5067 gap in front of the endcap. These include power supply cables for the FEEs and SiPMs as well as

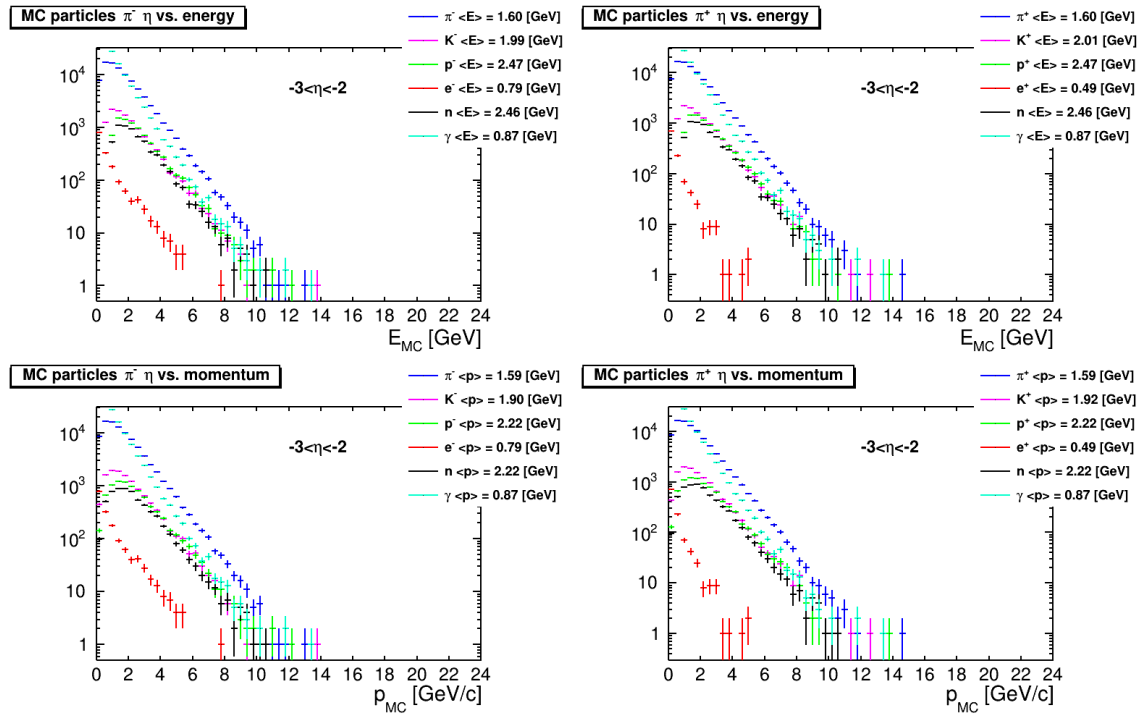


Figure 8.107: Top: Primary, generated particle E distributions in $-3.0 < \eta < -2.0$ range. Bottom: Primary, generated particle p distributions in $-3.0 < \eta < -2.0$ range.

5068 data connections to the FEEs. Communication with the calibration system will be handled by the
 5069 HGCROCv3 ASIC on FEE board through I^2C .

5070 **Calibration, alignment and monitoring:** Calibration will be performed with the use of LEDs
 5071 on tile or additional clear fibers to guide the laser/LED light(similar to STAR EEMC calibration
 5072 system) to the scintillator tiles. The system will allow for simulation of custom shower shapes in
 5073 a similar way as for LFHCAL. The response will be studied and used to calibrate the gains of the
 5074 SiPMs by adjusting bias voltage to compensate for variation and difference in response as well
 5075 as potential radiation damage to SiPM and tiles. This allows for monitoring the system during
 5076 operation.

5077 Alignment will be performed during assembly. During operation, physics events and cosmic rays
 5078 will be used to study the relative position of the calorimeter with respect to trackers. We will follow
 5079 standard alignment procedures performed at many collider experiments.

5080 Since SiPM gains are sensitive to temperature variations, temperature monitoring system using
 5081 thermocouples will be employed. These need to be only coarsely placed, because SiPMs generate
 5082 very little heat. In addition the absorber steel with large heat conductivity will allow to spread the
 5083 heat evenly over a large volume.

5084 **Status and remaining design effort:**

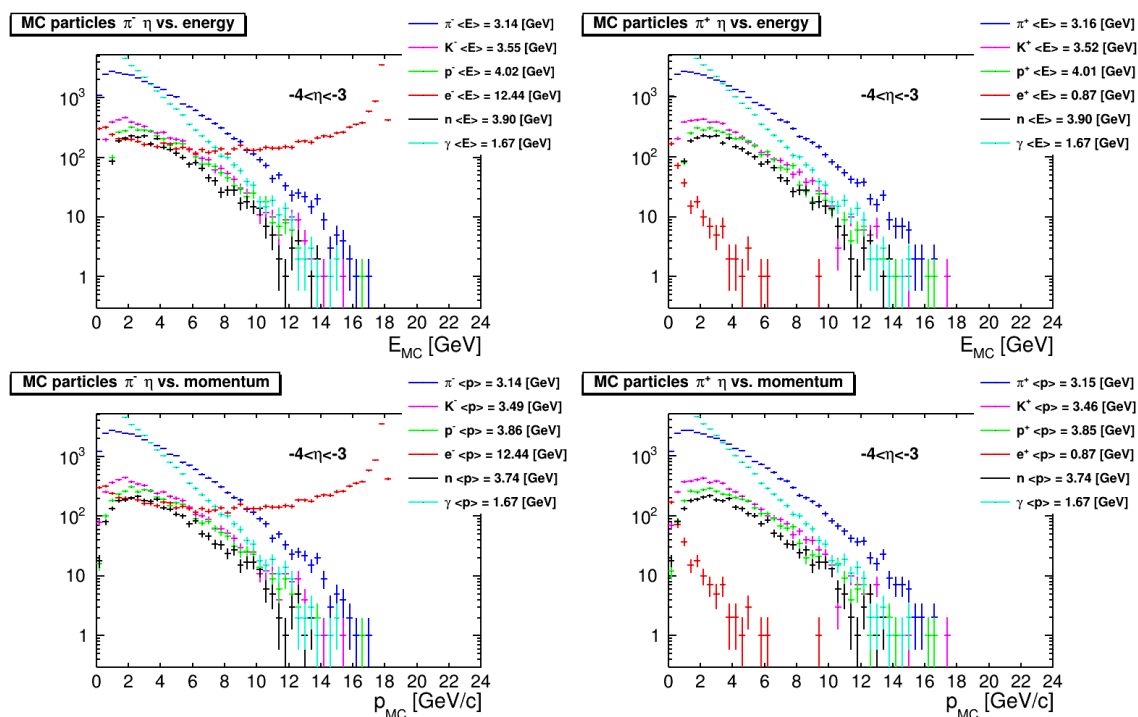


Figure 8.108: Top: Primary, generated particle E distributions in $-4.0 < \eta < -3.0$ range. Bottom: Primary, generated particle p distributions in $-4.0 < \eta < -3.0$ range.

5085 R&D effort: Finalize simulations and confirm optimal tile size.
 5086 E&D status and outlook: Design of support structures to follow the confirmed tile design.
 5087 Other activity needed for the design completion: Finalize simulations to confirm the tile size
 5088 and design.
 5089 Status of maturity of the subsystem: Technologies and design are mature. Dependent on the
 5090 outcome of performance simulations.

5091 **Environmental, Safety and Health (ES&H) aspects and Quality Assessment (QA plan-**
 5092 **ning:** We will follow standard ES&H procedures observed at all participating institutions. Qual-
 5093 ity of the tile, fiber and SiPM interfaces as well as optical isolation will be tested after assembly of
 5094 individual modules. This will be performed with the calibration system of the nHCal.

5095 **Construction and assembly planning:** Add text here.

5096 **Collaborators and their role, resources and workforce:** Add text here.

5097 **Risks and mitigation strategy:**

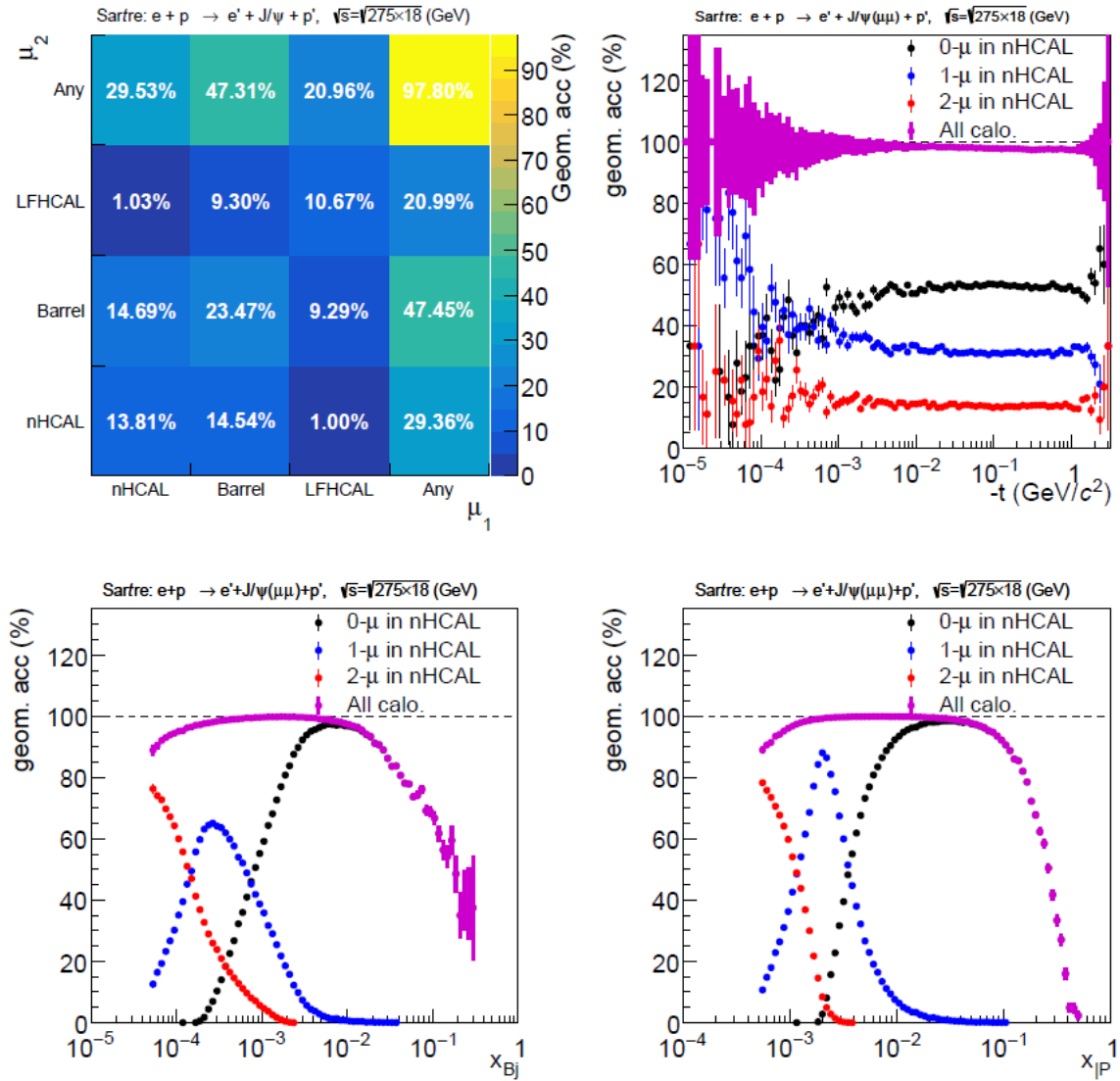


Figure 8.109: Acceptance of photoproduced $J/\psi \rightarrow \mu^+\mu^-$ in $e + p$ collisions at 18 + 275 GeV. Top left: Acceptance vs. μ_1 and μ_2 hitting different HCals. Top Right: Acceptance vs. $-t$ for different number of μ in nHCal. Bottom Left: Acceptance vs. Bjorken x_{bj} for different number of μ in nHCal. Bottom Right: Acceptance vs. Pomeron x_p for different number of μ in nHCal.

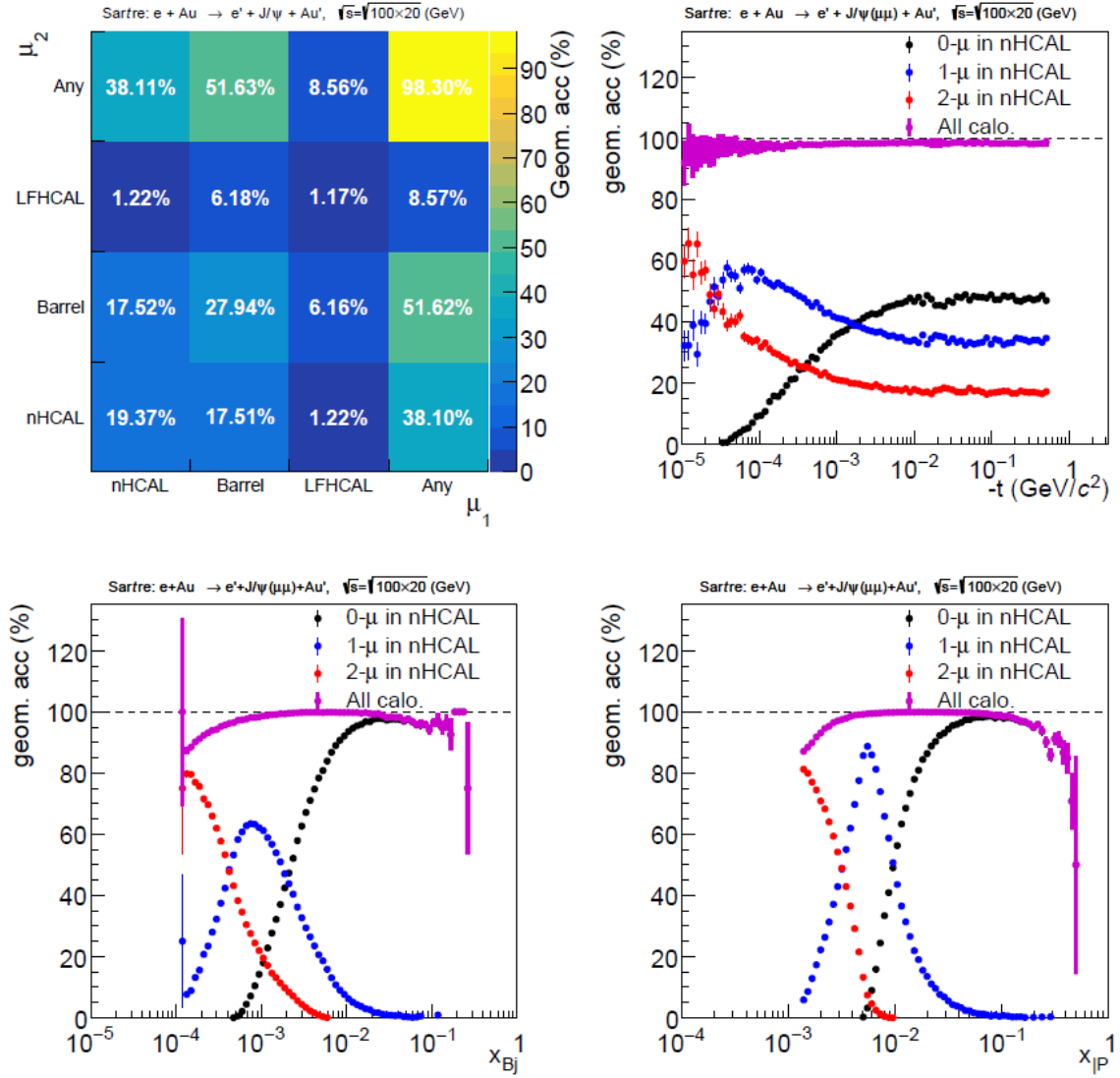


Figure 8.110: Acceptance of photoproduced $J/\psi \rightarrow \mu^+\mu^-$ in $e+p$ collisions at 20 + 100 GeV. Top left: Acceptance vs. μ_1 and μ_2 hitting different HCals. Top Right: Acceptance vs. $-t$ for different number of μ in nHCAL. Bottom Left: Acceptance vs. Bjorken x_{bj} for different number of μ in nHCAL. Top Right: Acceptance vs. Pomeron x_P for different number of μ in nHCAL.

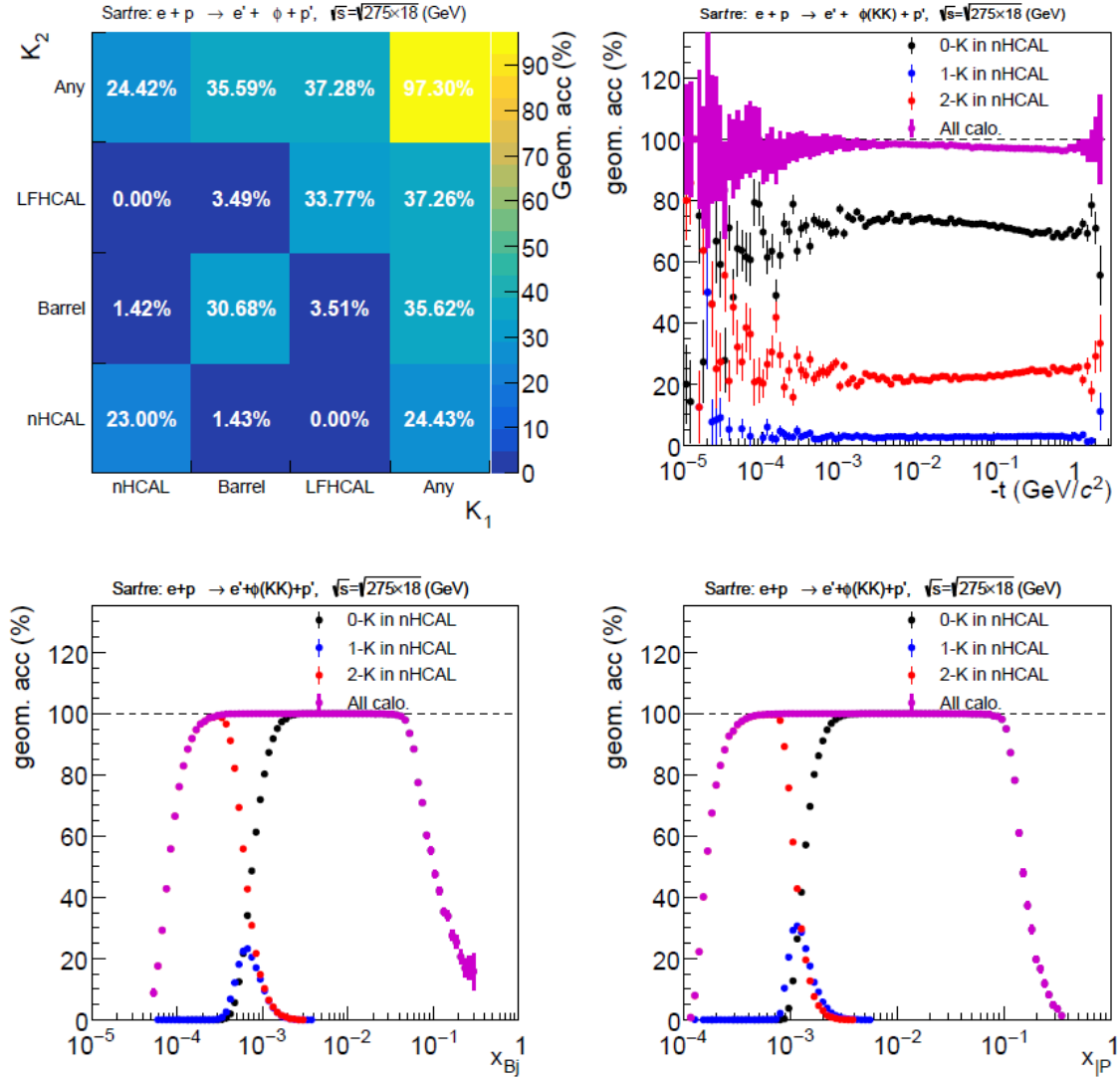


Figure 8.111: Acceptance of photoproduced $\Phi \rightarrow K^+K^-$ in $e + p$ collisions at 18 + 275 GeV. Top left: Acceptance vs. K_1 and K_2 hitting different HCals. Top Right: Acceptance vs. $-t$ for different number of K in nHCAL. Bottom Left: Acceptance vs. Bjorken x_{Bj} for different number of K in nHCAL. Top Right: Acceptance vs. Pomeron x_P for different number of K in nHCAL.

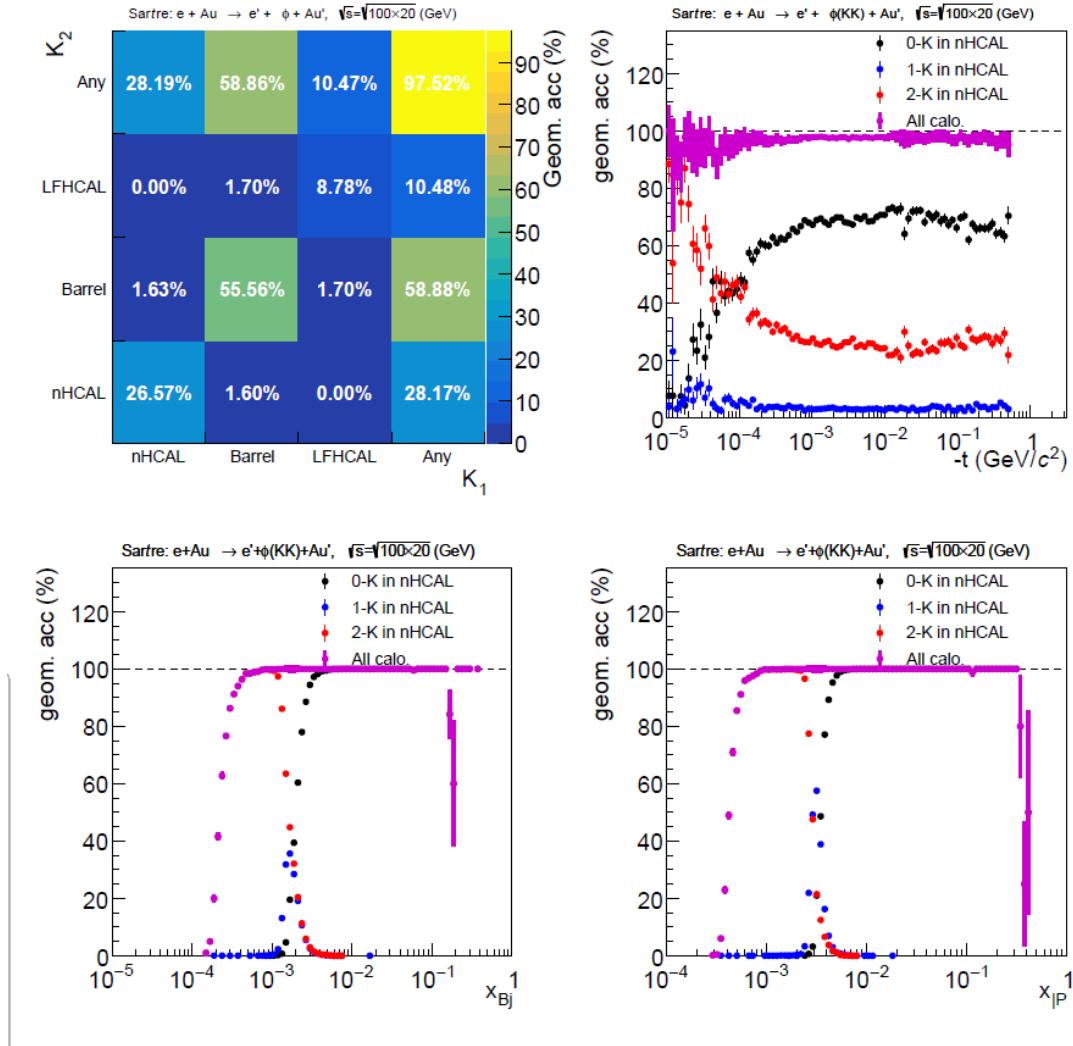


Figure 8.112: Acceptance of photoproduced $\Phi \rightarrow K^+K^-$ in $e + p$ collisions at 20 + 100 GeV. Top left: Acceptance vs. μ_1 and μ_2 hitting different HCals. Top Right: Acceptance vs. $-t$ for different number of K in nHCAL. Bottom Left: Acceptance vs. Bjorken x_{bj} for different number of K in nHCAL. Top Right: Acceptance vs. Pomeron x_p for different number of K in nHCAL.

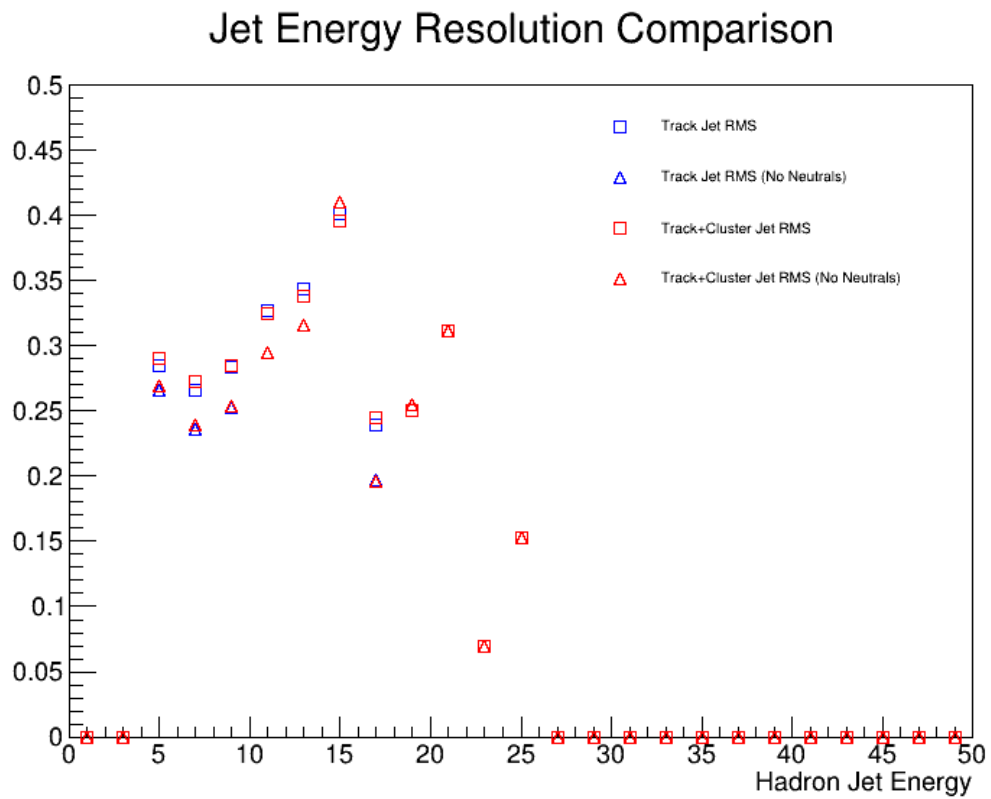


Figure 8.113: Energy resolution of jets vs. jet energy E compared for inclusive jets(squares) and jets with neutral veto(triangles). Track only jets(blue) are also compared to track and nHCal cluster jets(red).

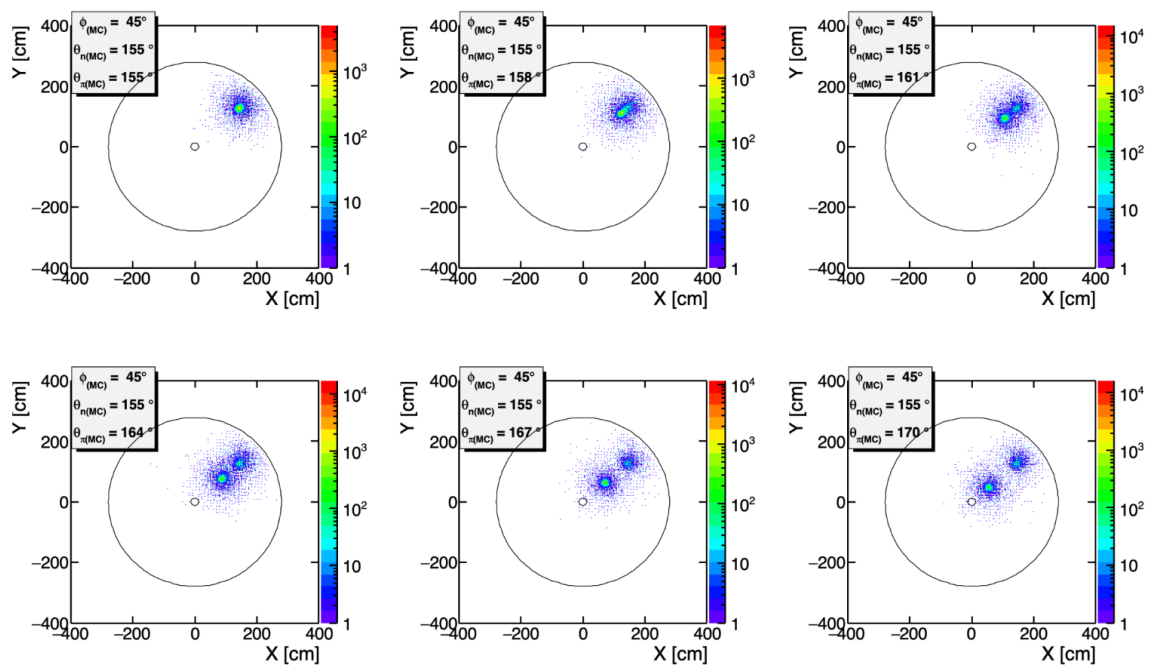


Figure 8.114: Position of the reconstructed clusters in x, y for 2-particle position resolution study.

5099 **8.3.6.2 The barrel hadronic calorimeter**

5100 **Requirements** The yellow report states the energy resolution of the mid-rapidity hadron
 5101 calorimeter should be $85\%/\sqrt{E/\text{GeV}} + 7\%$. This requirement is driven by single jet measurements.
 5102 While approximately 90% of the jet energy will be measured in the high precision tracking and
 5103 electromagnetic calorimetry, the hadronic calorimeter is crucial for capturing the neutral hadron
 5104 contribution. Figure 8.115 demonstrates the significance of the neutral hadron component.

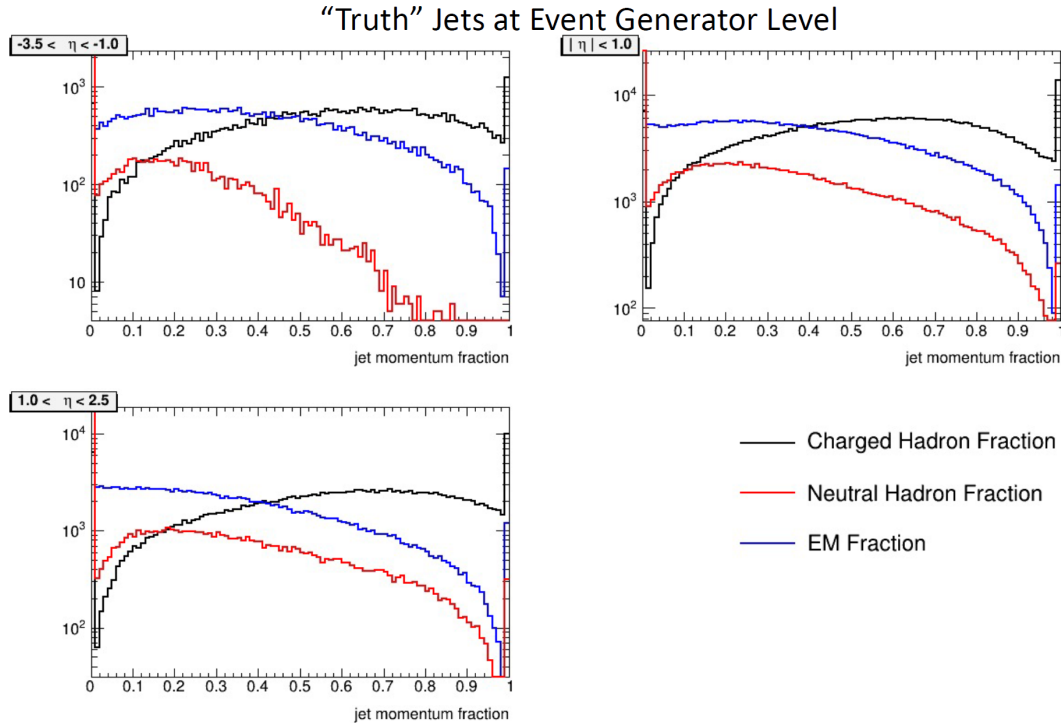


Figure 8.115: Jet charged and neutral Fractions: The charged (black lines), neutral EM (blue lines), and neutral hadron (red lines) fractions of jets at the truth level in $\eta \in (-3.5, 1.0)$ (upper left panel), $|\eta| < 1$ (upper right panel), and $\eta \in (1.0, 3.5)$ (lower left panel). This illustrates that while jets are dominated by charged and neutral EM particles, there are still a distinct population of jets at central rapidity with a substantial neutral hadronic component.

5105 A simple inclusion of the HCal energy does not necessarily improve the energy measurement. This
 5106 is because of energy smearing of neutral particles. However, the HCal can be used as a neutral veto
 5107 to select jets that do not contain neutral hadrons. This will provide the best energy resolution as
 5108 demonstrated in Fig. 8.116.

5109 **Requirements from Radiation Hardness:** Compared to LHC detectors, the various subsys-
 5110 tems of the ePIC detector have moderate radiation hardness requirements. The Yellow Report
 5111 states that at the calorimeters, the radiation level will be up to ≈ 3 krad/year electromagnetic and
 5112 $10^{11}n/\text{cm}^2$ hadronic at top luminosity. However at the BHCAL, the radiation level will be only

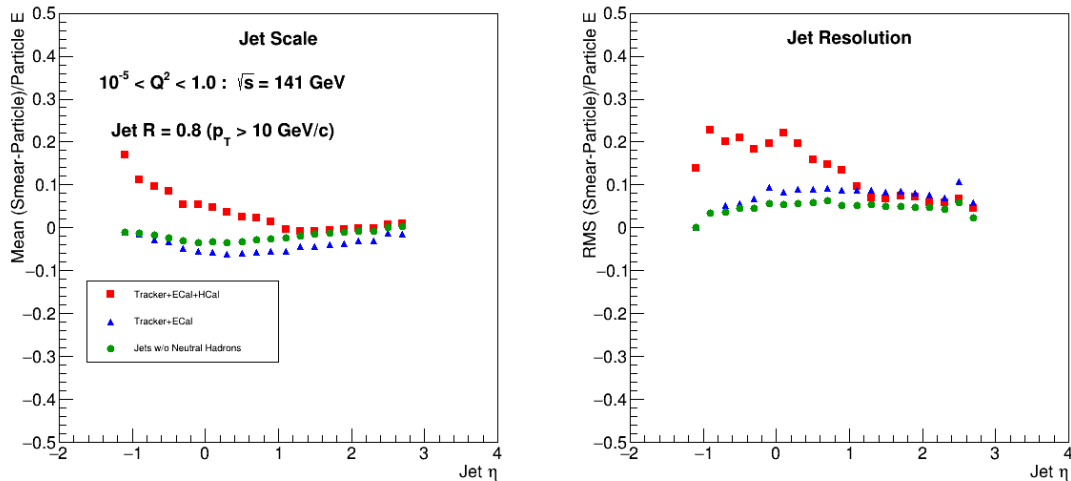


Figure 8.116: Demonstration of the effect of selecting only jets which do not contain a neutral hadron (green circles) on the jet energy scale (left) and resolution (right) as compared to the cases when all subsystems are used in jet finding (red squares) and when HCal information is excluded (blue triangles). Detector simulation and reconstruction was carried out using a fast simulation using Delphes. Figure 8.57 from the EIC Yellow Report.

5113 10 rad electromagnetic and 0.1 rad hadronic, orders of magnitude lower than, *e.g.*, at the fHCal.
 5114 The on-detector electronics (SiPMs, H2GCROC3) are radiation tolerant. While the read-out boards
 5115 (RDOs) contain FPGAs and therefore are radiation sensitive, they will sit well outside the detector,
 5116 and therefore there is no concern for single-event upsets (SEUs). The neutron fluence will be low
 5117 enough that it is not an issue for SiPMs. The neutron fluence is lower than in sPHENIX, where
 5118 the dark current increase after the first year of running is consistent with expectations. Since the
 5119 H2GCROC3s are used for the other calorimeter systems as well, there is no concern for the BHCal.

5120 Justification

5121 **Device concept and technological choice:** The sPHENIX outer HCal, which was demon-
 5122 strated to have a single particle energy resolution of $75\%/\sqrt{E} \oplus 14.5\%$, will be repurposed for
 5123 the EIC. It generally satisfies the requirements described in the previous section. The constant term
 5124 of the energy resolution may be further improved by reading out the individual scintillator tiles
 5125 instead of in towers.

5126 The absorber material for the central hadronic calorimeter will also serve as the flux return for the
 5127 solenoid magnet. Additional absorber will be added to the existing sPHENIX HCal steel plates to
 5128 further contain the magnetic field.

5129 Subsystem description:

5130 General device description: The sPHENIX Outer HCal will be used as the basis of the ePIC

5131 Barrel HCal. The sPHENIX OHCAL design was developed and optimized through a series
 5132 of simulation and prototype studies. The sPHENIX hadronic calorimeter system consists of
 5133 two longitudinal compartments of calorimeter, one inside the solenoid, which serves both to
 5134 measure the longitudinal development of electromagnetic showers thus providing additional
 5135 discrimination between electrons and hadrons beyond determination of E/p in the electro-
 5136 magnetic shower, and as the first nuclear interaction length of the hadronic calorimeter. In
 5137 the ePIC design the electromagnetic calorimeter will fill the space before the magnet. There-
 5138 fore only the sPHENIX Outer HCal will be adopted in ePIC.

5139 The basic calorimeter concept is a sampling calorimeter with tapered absorber plates tilted
 5140 from the radial direction to provide more uniform sampling in azimuth. Extruded tiles of
 5141 plastic scintillator with an embedded wavelength shifting fiber are interspersed between the
 5142 absorber plates and read out at the outer radius with silicon photomultipliers. The tilt angle
 5143 is chosen so that a radial track from the center of the interaction region traverses at least four
 5144 scintillator tiles as shown in Figure 8.117.

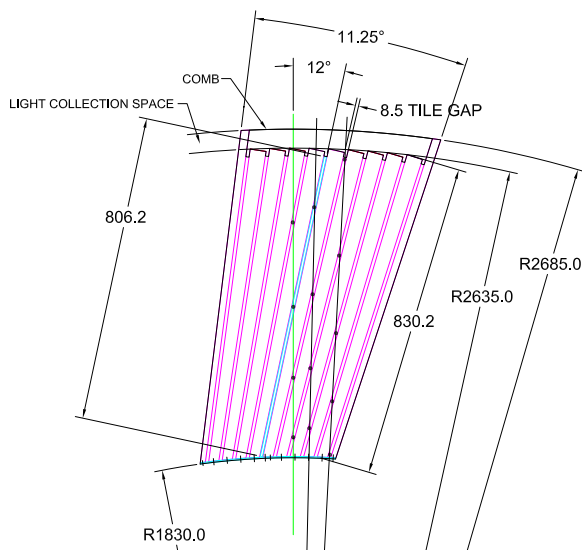


Figure 8.117: Transverse cutaway view of an sPHENIX Outer HCal module, showing the tilted tapered absorber plates. Light collection and cabling is on the outer radius at the top of the drawing.

5145 Each tile has a single SiPM. In the sPHENIX design, the analog signal from five SiPMs are
 5146 ganged to a single preamplifier channel to form a calorimeter tower. In ePIC, each SiPM will
 5147 be read out directly. Twelve tiles span 1.1 units of pseudorapidity in each direction as shown
 5148 in Figure 8.118. Therefore the overall segmentation is $\Delta\eta \times \Delta\phi \sim 0.1 \times 0.02$.

5149 Scintillator description:

5150 The properties of the HCal scintillating tiles are listed in Table 8.34. There are 12 different
 5151 shaped tiles which span half of the η range of the detector. The detector is mirror-symmetric
 5152 in η except in the region where the chimney for the cooling of the magnet reduces the depth
 5153 of the HCal.

5154 A wavelength shifting (WLS) fiber is embedded in the tile to direct the light to the SiPM. The
 5155 Kuraray single clad fiber was selected due to its flexibility and longevity which are critical
 5156 for the multiple fiber bends in the design. The routing of the fiber was carefully designed
 5157 to maximize the uniformity of light collection across the various tile shapes and avoid light

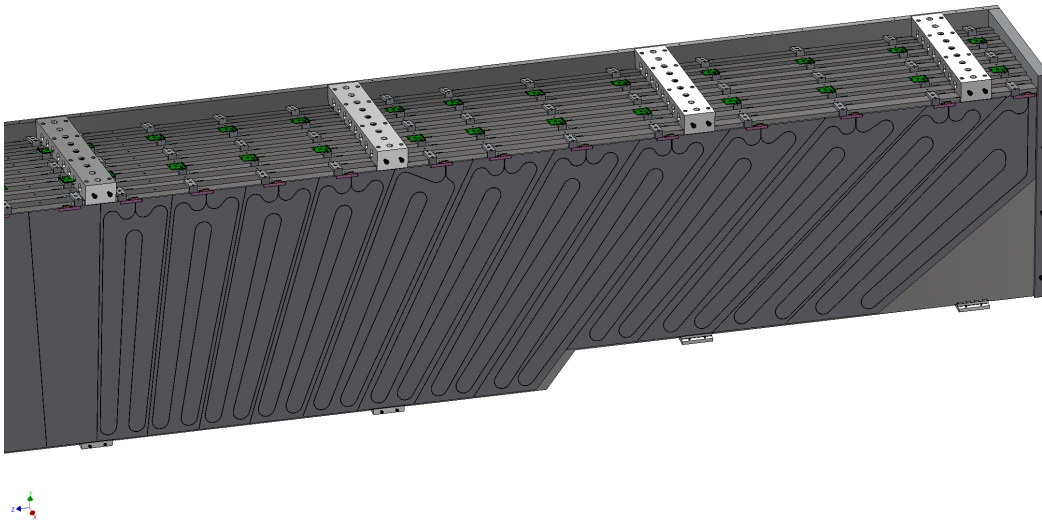


Figure 8.118: Scintillator tiles in a layer of the Outer HCal.

Component	Description
Plastic	Extruded polystyrene
Scintillation dopant	1.5% PTP and 0.01% POPOP
Reflective coating	Proprietary coating by surface exposure to aromatic solvents
Reflective layer thickness	50 μ
Wrapping	one layer of 100 μ Al foil, one layer of 30 μ cling-wrap, one 100 μ layer of black Tyvek
Attenuation length in lateral (with respect to extrusion) direction	\sim 2-2.5 m
Wavelength shifting fiber	Single clad Kuraray Y11
Fiber size	1 mm round
Fiber core attenuation length	> 2 m
Optical cement	EPO-TEK 3015

Table 8.34: Properties of HCal scintillating tiles.

5158

leaks in the bends.

5159

The Kuraray single clad fiber was chosen due to its flexibility and longevity which are critical in the geometry with multiple fiber bends. The properties of the HCal wavelength shifting fibers are listed in Table 8.35

5160

5161

5162

The fiber routing was designed so that any energy deposited in the scintillator is within 2.5 cm of a WLS fiber to minimize the pathlength of the light through the tile to the fiber and maintain uniformity in the response of energy depositions throughout the tile and across various tile shapes. In addition, the bend radius of any turn in the fiber has been limited to 35 mm based.

5163

5164

5165

Property	Description
Fiber diameter	1.0 mm
Formulation	200, K-27, S-Type
Cladding	single
Cladding thickness	2 percent of d (0.02 mm)
Numerical Aperture (NA)	0.55
Emission angle	33.7 deg
Trapping Efficiency	3.1 percent
Core material	polystyrene (PS)
Core density	1.05 g/cc
Core refractive index	1.59
Cladding material	Polymethylmethacrylate (PMMA)
Cladding density	1.19 g/cc
Cladding refractive index	1.49
Color	green
Emission peak	476 nm
Absorption Peak	430 nm
Attenuation length	> 3.5 m
Minimum bending radius	100 mm

Table 8.35: Properties of Kuraray Y-11 (200) wavelength shifting fibers.

5166 These parameters on the fiber routing were based on T2K and the sPHENIX R&D experience
 5167 with test tiles. Since there are 12 different tile shapes, the routing for each tile shape was
 5168 uniquely designed to satisfy these conditions.

5169 The two ends of a fiber are brought to the outer radius of a tile where a small plastic holder
 5170 carries a 3×3 mm SiPM at 0.75 mm from the end of the polished fibers.

5171 Table 8.36 summarizes the major design parameters of the HCAL, which is illustrated in Fig-
 5172 ure 8.117.

5173 The Outer HCAL SiPM sensors and electronics are to be arranged on the outer circumference
 5174 of the detector which reduces the radiation exposure of the SiPMs.

5175 Sensors: The SiPMs used in sPHENIX will be replaced with newer S14160-3015PS Hama-
 5176 matsu SiPMs. The SiPMs are still 3 mm X 3 mm and will be attached to a board that will fit
 5177 in the same plastic connectors used in sPHENIX to mount the SiPM to the tile. Each SiPM
 5178 will be read out individually via the CALOROC. The electronics developed for the BHCAL is
 5179 similar to other calorimeters and are described in a separate section.

5180 LED system: Each tile has a fiber that can be illuminated by an LED. The fibers will extend to
 5181 the edges of the detector where the electronics are also stationed.

5182 **Performance** The performance of the BHCAL for ePIC has been studied in simulation as well as
 5183 tested through the experience of the HCals in sPHENIX. Thus far the sPHENIX HCAL system has
 5184 performed very well in Au+Au and p+p collisions. One concern with using SiPM sensors is the
 5185 potential radiation damage in high energy collisions. The radiation exposure causes an increase in
 5186 the leakage currents and the measured noise. The leakage current measured in the commissioning
 5187 run for sPHENIX shows that leakage currents even an extrapolated are well below the limit. This is
 5188 expected since the large amount of material in front of the SiPMs reduces their radiation exposure.

Parameter	Units	Value
Inner radius (envelope)	mm	1820
Outer radius (envelope)	mm	2700
Length (envelope)	mm	6316
Material	1020 low carbon steel	
Number of tiles in azimuth ($\Delta\phi$)		320
Number of tiles in pseudorapidity ($\Delta\eta$)		24
Number of electronic channels	$320 \times 24 = 7680$	
Number of modules (azimuthal slices)		32
Total number of absorber plates	$5 \times 64 = 320$	
Tilt angle (relative to radius)	$^\circ$	12
Absorber plate thickness at inner radius	mm	10.2
Absorber plate thickness at outer radius	mm	14.7
Gap thickness	mm	8.5
Scintillator thickness	mm	7
Module weight	kg	12247
Sampling fraction at inner radius		0.037
Sampling fraction at outer radius		0.028
Calorimeter depth	λ	3.8

Table 8.36: Design parameters for the Barrel Hadronic Calorimeter w/o additional absorber, based on the sPHENIX Outer Hadronic Calorimeter.

5189 Fig. 8.119

5190 Simulations demonstrate the energy deposition for muons and DIS events. For muons, a clear MIP
5191 peak is observed as shown in 8.120. In contrast, energy distributions for DIS events are shown in
5192 8.121.

5193 The resolution of calibrated single pion energies is shown in Figure 8.122.

5194 Additional placeholders demonstrating the BHCAL performance are included in Figures 8.123 to
5195 8.133.

5196 **Implementation**

5197 **Subsystem mechanics and integration:** The BHCAL is the outermost central detector and will
5198 need to be installed first. The steel serves as the flux return for the solenoid magnet.

5199 **Calibration, alignment and monitoring:** The sPHENIX HCal was primarily calibrated using
5200 cosmic ray measurements. In addition to cosmic ray measurements LEDs are used to monitor the
5201 tiles. These monitoring systems will be crucial for properly calibrating the detector over time to
5202 account for aging effects of the tiles and radiation damage to the SiPMs.

5203 **Status and remaining design effort:**

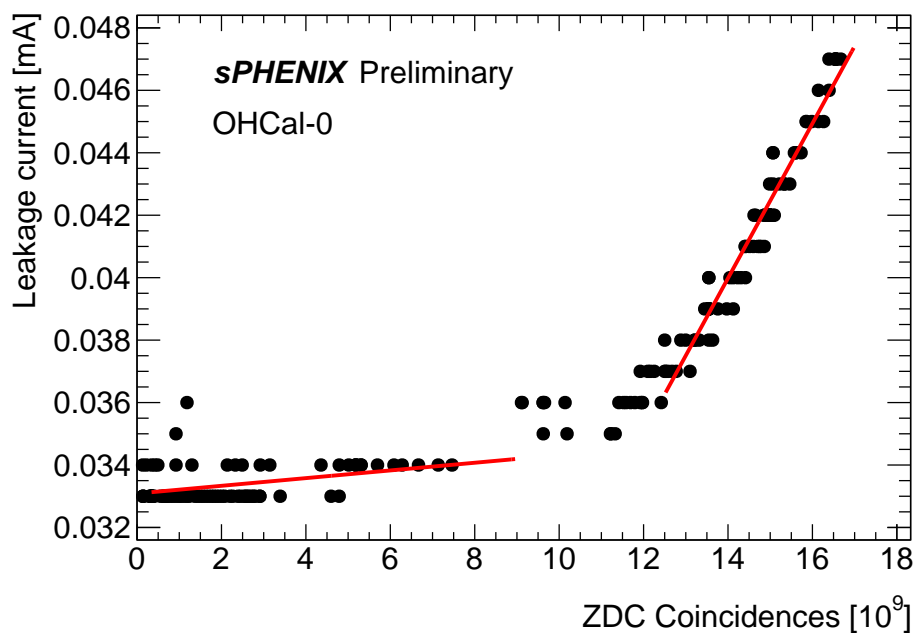


Figure 8.119: Leakage current in HCal measured once per fill as a function of total number of ZDC coincidence hits

5204 R&D effort: The basic design is set by reusing the sPHENIX outer HCal. However, the elec-
 5205 tronics and details of the LED system are still being developed. There are plans to utilize the
 5206 sPHENIX prototype, which was used to demonstrate the energy resolution from beam tests,
 5207 to test the readout of individual tiles instead of tiles. Related simulation studies are also un-
 5208 derway. Additional tests include measuring the potential noise for longer cables to transmit
 5209 the signal from the SiPM to HGCROCs located at the end of the sector.

5210 **Environmental, Safety and Health (ES&H) aspects and Quality Assessment (QA plan-**
 5211 **ning:**

5212 **Construction and assembly planning:** After RHIC running concludes, sPHENIX will be dis-
 5213 assembled. When a sector of the outer HCal is removed from sPHENIX, the tiles within the sector
 5214 will be extracted. The tiles will be shipped to Georgia State University (GSU) and University of
 5215 New Hampshire (UNH) where test stands are ready to quantify the response of the tiles to
 5216 cosmic rays and record their relative performances. These initial tests proved to be very useful
 5217 in the initial calibration procedure in sPHENIX. For sPHENIX these tests were also crucial in the
 5218 quality assessment procedure which required that the tile performance deviate no more than 20%
 5219 from the mean for that tile shape. Similar performing tiles were also grouped together into towers
 5220 for calibration purposes.

5221 After the tiles have been tested, they will be shipped back to BNL to be installed in the new sec-
 5222 tors. Additional material will have been added to the sPHENIX steel sectors. Stefan Bathe from
 5223 Baruch College will oversee the assembly process at BNL. He served as the level 3 manager for the
 5224 sPHENIX HCal and likewise oversaw the assembly of the inner and outer HCal for sPHENIX.

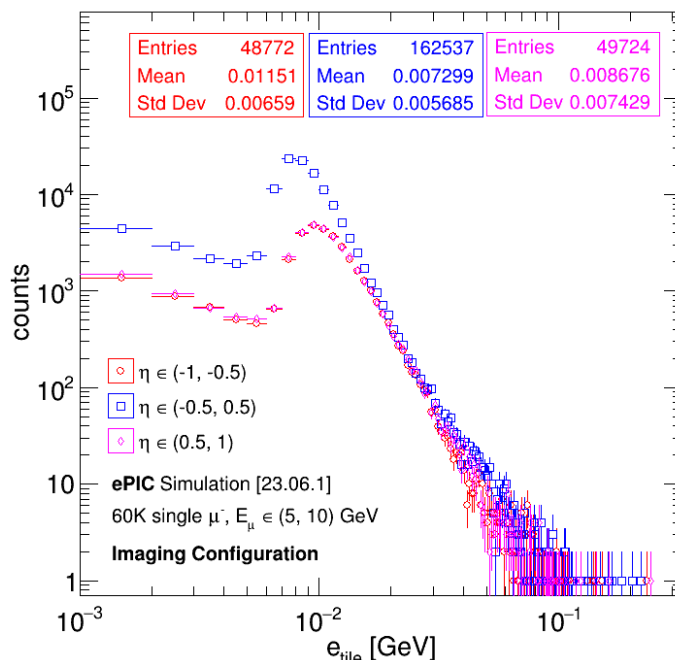


Figure 8.120: Muon energy deposited on tile: energy deposited on a given scintillator tile (i.e. the sum of G4 hits for a tile) by single GeV/c μ^- with energies between 5 and 10 GeV/c as a function of μ^- pseudorapidity. Distributions were simulated using the 2023.06.1 simulation geometry. A clear MIP peak is observed.

5225 After inserting the tiles in the proper sector locations, an SiPM will be connected to each tile. The
 5226 cables will be installed and connected to a test set up for the electronics to confirm that each tile can
 5227 be readout. Cosmic ray tests of each sector will also be performed which will confirm the relative
 5228 tile by tile calibration factors.

5229 **Collaborators and their role, resources and workforce:** Derek Anderson from Iowa State
 5230 University has been leading the simulation efforts for the BHCAL. He has held trained collabora-
 5231 tors at UNH and GSU to work on tasks associated with needed simulation studies and software
 5232 development.

5233 Baruch College and GSU groups led by Bathe and Connors respectively have extensive experience
 5234 working with the sPHENIX HCals. They will oversee the assembly and tile testing procedures for
 5235 the ePIC BHCAL as they did for sPHENIX. In addition, UNH, BNL and others will be extremely
 5236 important for ensuring the assembly timeline is achieved. Norbert Novitzky from Oak Ridge Na-
 5237 tional Lab is developing the electronics and is collaborating with members of the BNL group that
 5238 conducted the sPHENIX R&D to test the electronics with the sPHENIX HCal prototype.

5239 **Risks and mitigation strategy:** The BHCAL depends on previously tested technologies which
 5240 minimizes the risks associated with it. A limited number of spare tiles exist at Georgia State Uni-
 5241 versity in case any tiles are damaged. There are two ways we can monitor the tiles once they are

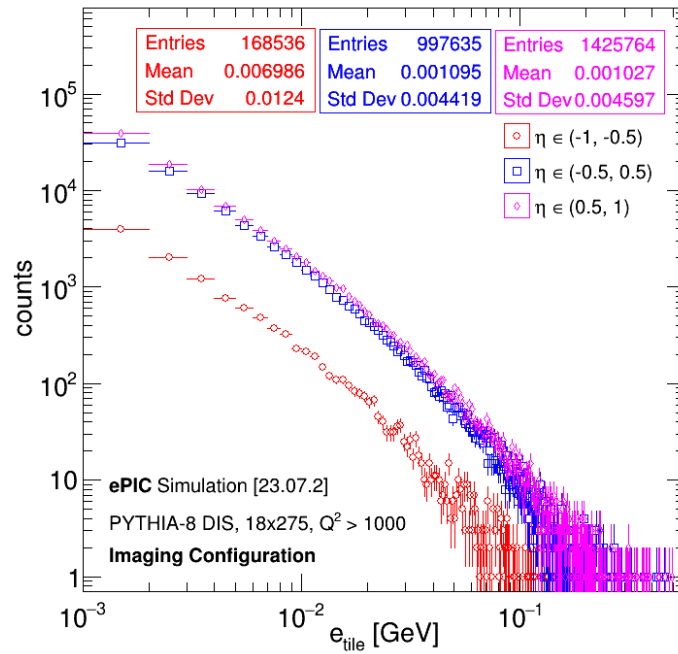


Figure 8.121: DIS energy deposited on tile: energy deposited on a given scintillator tile (i.e. the sum of G4 hits for a tile) in 18×275 NC DIS events for $Q^2 > 1000$ GeV² for all particles in the events as a function of their pseudorapidity. Distributions were simulated using the 2023.07.2 simulation geometry.

5242 installed into EPIC. The LED system is useful for quickly testing the tiles on a regular basis while
 5243 the cosmic ray studies require a long time to collect sufficient data.

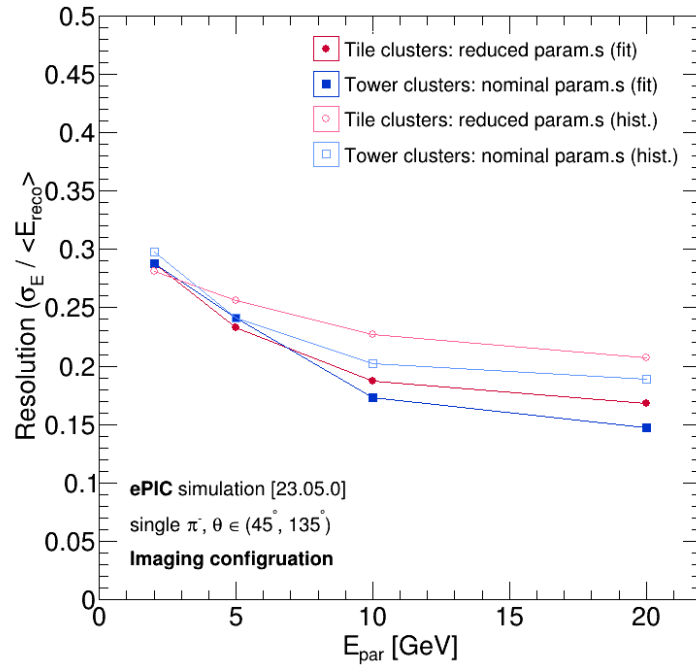


Figure 8.122: Resolution of calibrated single pion energies: Resolution of calibrated single π^- energies. Distributions were simulated using the 2023.05.0 simulation geometry. Red markers indicate the output of the calibration using tile-based clusters from the BHCAL, while blue markers indicate the output of the calibration using tower-based clusters from the BHCAL. The closed markers indicate the resolution as obtained by comparing the mean of a gaussian fit to the calibrated energies vs. the particle energies, while the open markers indicate the resolution as obtained by directly comparing the mean of the calibrated energies vs. the particle energies. Calibration is carried out by the LD model.

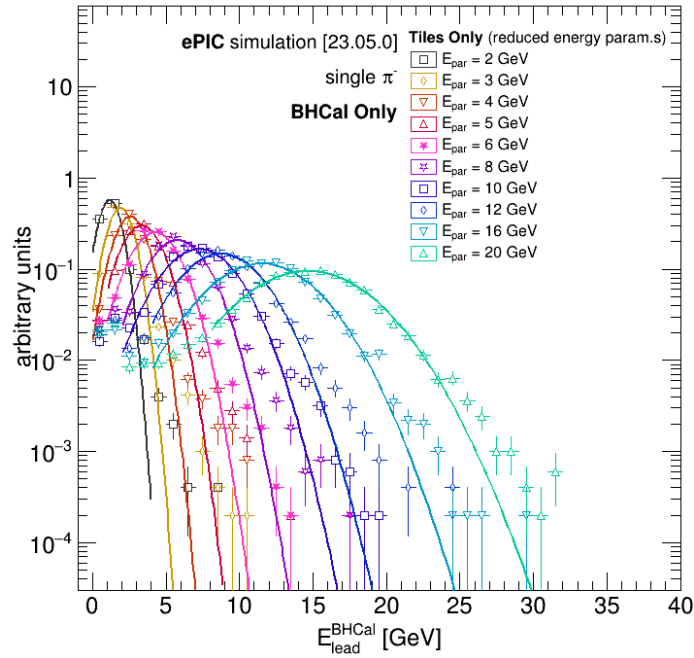


Figure 8.123: Single pion energies in only BHCAL: reconstructed energy of leading (highest energy) BHCAL cluster for 2 (black) - 20 GeV (light blue) single π^- in the BHCAL *only*. Distributions were simulated using the 2023.05.0 simulation geometry. Clusters are formed from individual tiles. Solid lines are gaussian fits. Energies are “uncalibrated” in the sense that they have only been corrected for the sampling fraction.

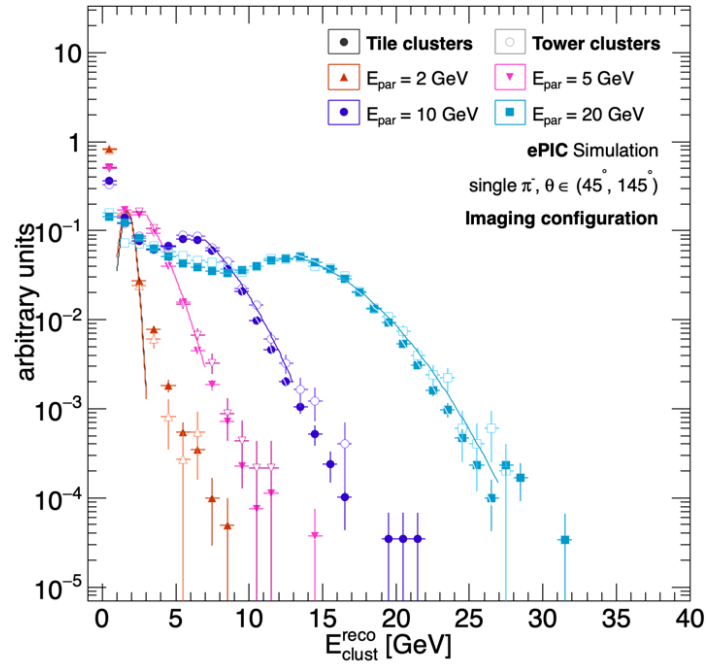


Figure 8.124: Uncalibrated single pion energies: reconstructed energy of all BHCAL clusters for 2 (orange), 5 (pink), 10 (purple), and 20 GeV (blue) π^- with θ between 45° and 145° . Distributions were simulated using the 2023.05.0 simulation geometry. Closed markers indicate clusters formed from individual tiles, and open markers indicate clusters formed from towers (5 tiles). Solid lines are gaussian fits, but aren't relevant for this particular plot. Energies are "uncalibrated" in the sense that they have only been corrected for the sampling fraction.

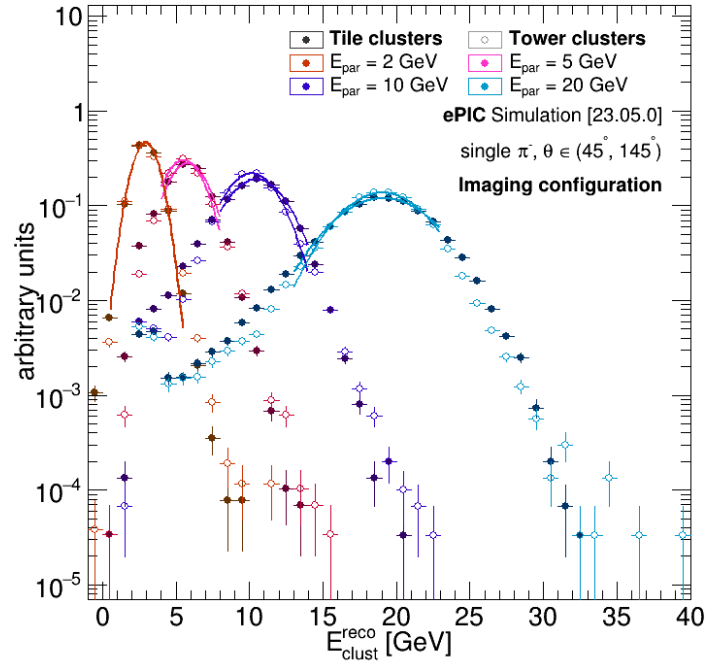


Figure 8.125: Calibrated single pion energies: calibrated energy of single 2 (orange), 5 (pink), 10 (purple), and 20 GeV (blue) single π^- with θ between 45° and 145° . Distributions were simulated using the 2023.05.0 simulation geometry. Closed markers indicate clusters formed from individual tiles, and open markers indicate clusters formed from towers (5 tiles). Solid lines are gaussian fits. Energies are calibrated, i.e. the output of a regression by a Linear Discriminant (LD) ML model as implemented in TMVA. The LD model is trained on the energy, pseudorapidity, azimuth, and no. of hits (constituent cells) of the leading (highest energy) BHCAL and BIC (ScFi + imaging) clusters as well as on the sum of energy in the 6 imaging (AstroPix) and 12 ScFi (Scintillating Fiber) layers of the BIC.

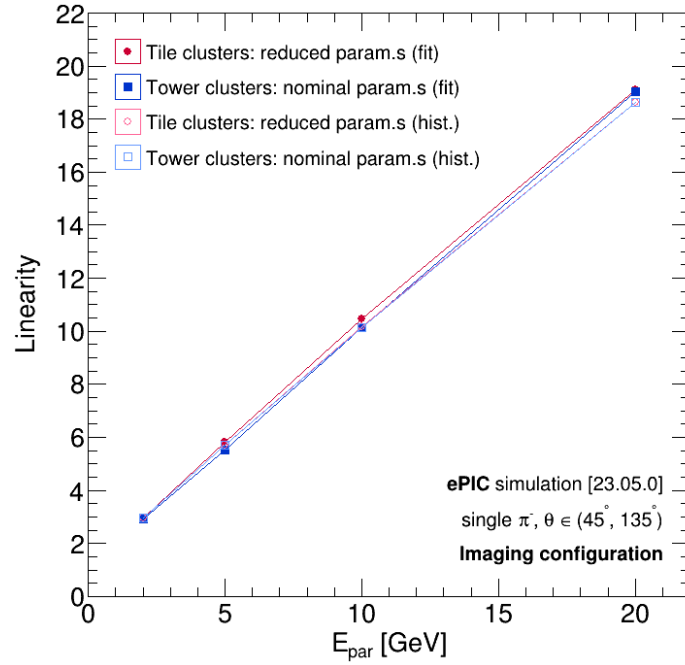


Figure 8.126: Linearity of calibrated single pion energies: Linearity of calibrated single π^- energies. Distributions were simulated using the 2023.05.0 simulation geometry. Red markers indicate the output of the calibration using tile-based clusters from the BHCAL, while blue markers indicate the output of the calibration using tower-based clusters from the BHCAL. The closed markers indicate the linearity as obtained by comparing the mean of a gaussian fit to the calibrated energies vs. the particle energies, while the open markers indicate the linearity as obtained by directly comparing the mean of the calibrated energies vs. the particle energies. Calibration is carried out by the LD model as was done in fig. 8.125.

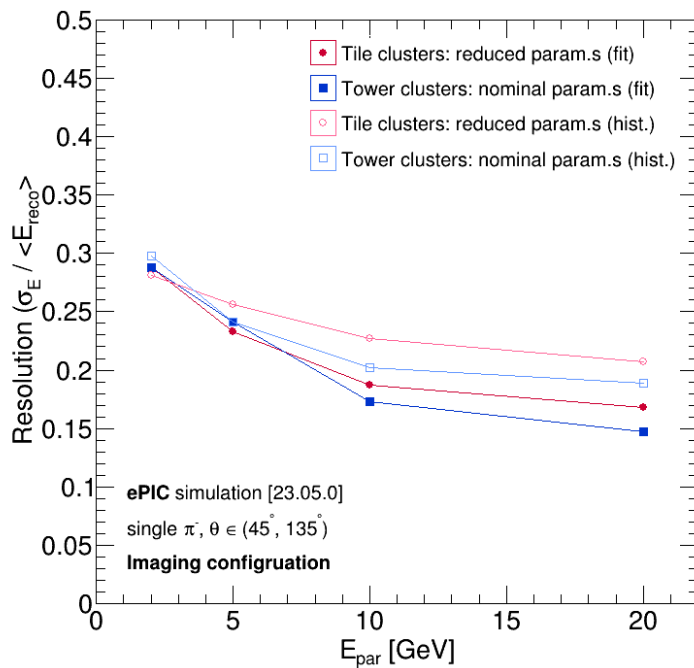


Figure 8.127: Resolution of calibrated single pion energies: Resolution of calibrated single π^- energies. Distributions were simulated using the 2023.05.0 simulation geometry. Red markers indicate the output of the calibration using tile-based clusters from the BHCAL, while blue markers indicate the output of the calibration using tower-based clusters from the BHCAL. The closed markers indicate the resolution as obtained by comparing the mean of a gaussian fit to the calibrated energies vs. the particle energies, while the open markers indicate the resolution as obtained by directly comparing the mean of the calibrated energies vs. the particle energies. Calibration is carried out by the LD model as was done in fig. 8.125.

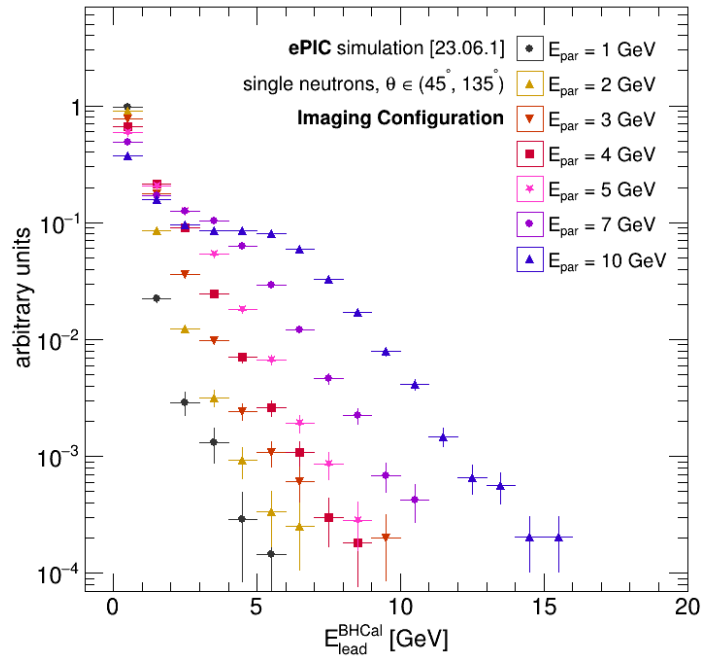


Figure 8.128: Uncalibrated single neutron energies: reconstructed energy of leading (highest energy) BHCAL clusters for 1 (black) - 10 GeV (violet) single neutrons with θ between 45° and 145° . Distributions were simulated using the 2023.06.1 simulation geometry. Energies are “uncalibrated” in the sense that they have only been corrected for the sampling fraction.

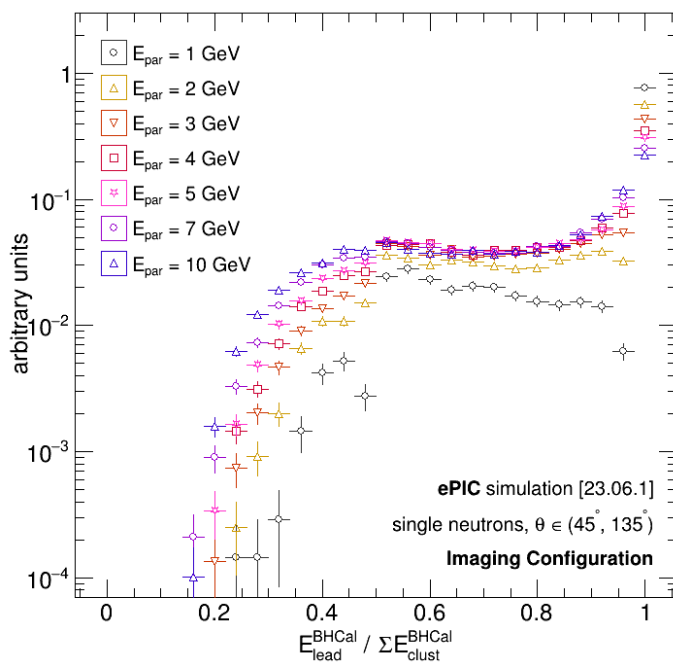


Figure 8.129: Uncalibrated single neutron energy fractions: fraction of the reconstructed energy of the leading (highest energy) BHCAL cluster to the sum of all BHCAL clusters for 1 (black) - 10 GeV (violet) single neutrons with θ between 45° and 145° . Distributions were simulated using the 2023.06.1 simulation geometry. Energies are “uncalibrated” in the sense that they have only been corrected for the sampling fraction. Demonstrates substantial cluster splitting for neutrons.

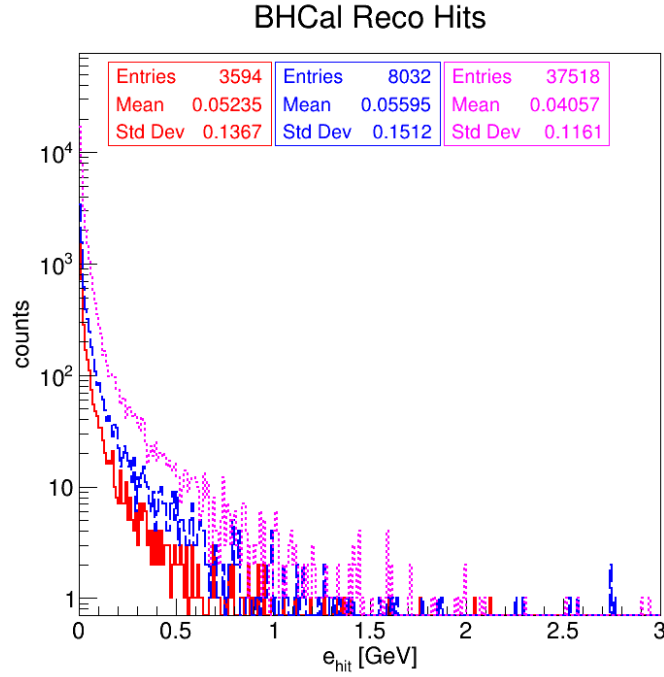


Figure 8.130: DIS reconstructed tile energy: the energy of reconstructed “hits” (i.e. the reconstructed energy of individual tiles) in the BHCal in 18×275 NC DIS events for $Q^2 > 1000 \text{ GeV}^2$ for all particles in the events as a function of their pseudorapidity. Distributions were simulated using the 2023.06.1 simulation geometry. Demonstrates typical range of reconstructed energies on a tile-by-tile basis.

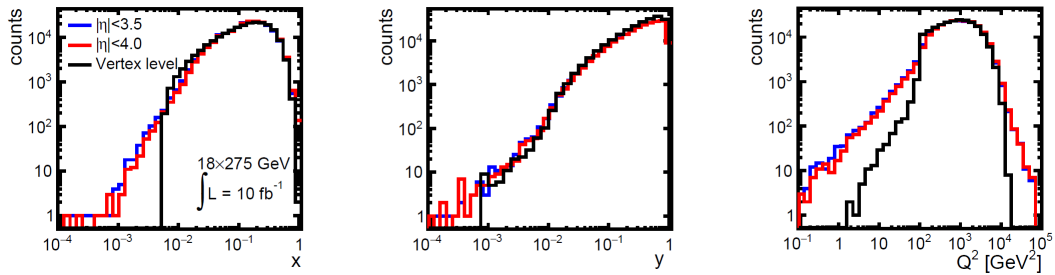


Figure 8.131: Jacquet-Blondel variables in CC DIS: DIS kinematic variables calculated using the Jacquet-Blondel method in 18×275 CC DIS events. The black lines indicate the distributions at the truth (“vertex”) level, and the blue/red lines indicate the distributions at the reconstructed level: blue indicates a detector with an acceptance of $|\eta| < 3.5$, while red indicates a detector with an acceptance of $|\eta| < 4$. Detector simulation and reconstruction was carried out using a fast simulation using Delphes. Figure 8.21 from the EIC Yellow Report.

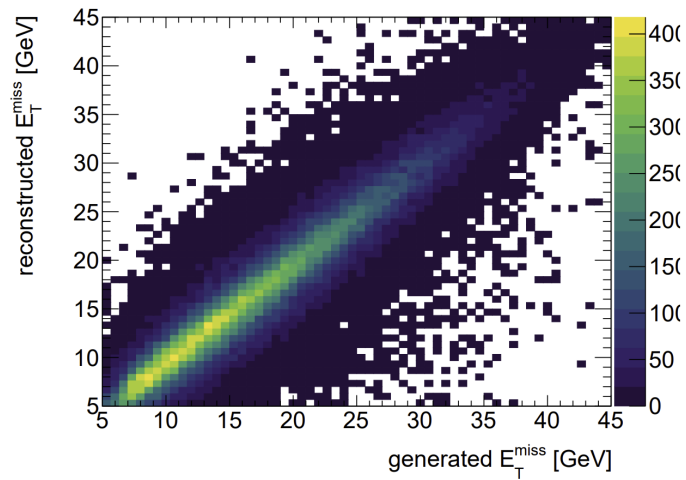


Figure 8.132: Truth vs. reconstructed E_T^{miss} : the truth (x-axis) vs. reconstructed (y-axis) E_T^{miss} for 10×275 CC DIS events. Detector simulation and reconstruction was carried out using a fast simulation using Delphes. Figure 4 from arXiv:2006.12520.

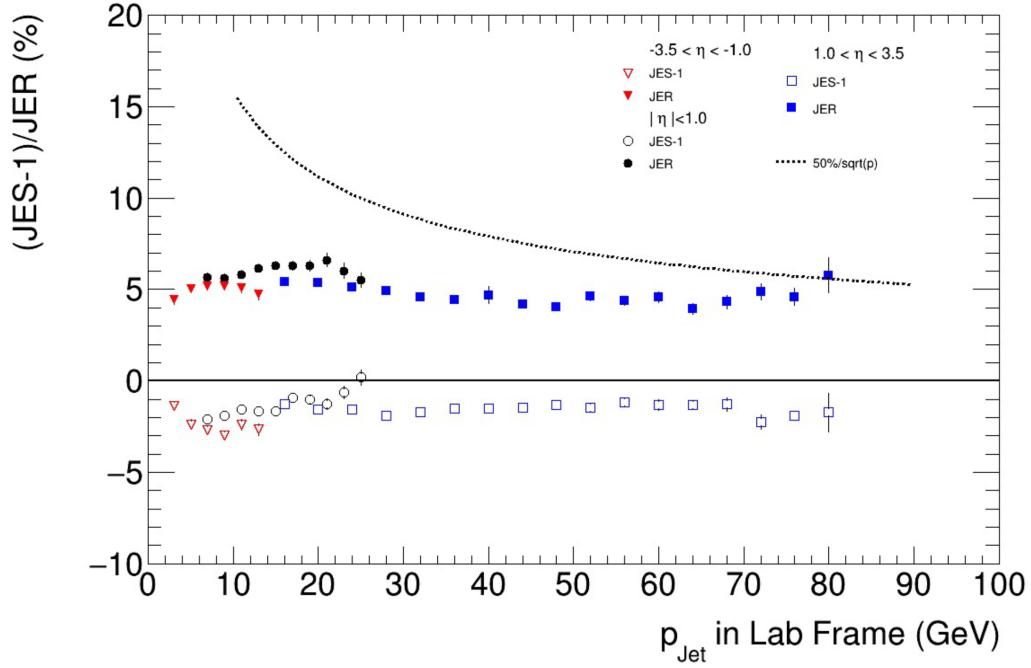


Figure 8.133: JES/R for full (tracks + ECal + HCal): The $JES - 1 = \langle \Delta p/p \rangle$ (open markers) and JER (closed markers) plotted as a function of p_{jet} in the lab frame for jets in $\eta \in (-3.5, 1.0)$ (red points), $|\eta| < 1$ (black points), and $\eta \in (1.0, 3.5)$ (blue points). In the barrel region, jets are constructed from reconstructed tracks and ECal clusters *without* a nearby track. Neutral hadrons are included in the jets by smearing the particle energy by the measured energy resolution of the sPHENIX OHCAL. Jets are reconstructed via the Centauro algorithm ($R = 0.8$) and transformed back into the lab frame. Jets are required to have at least 2 particles, and exclusively charged or neutral jets are rejected. From ECCE responses to the EIC DPAP Panel; received from John Lajoie in private communication.

5244 8.3.6.3 The forward endcap hadronic calorimeter

5245 Requirements

5246 **Requirements from physics:** In electron-proton (ep) or electron-ion (eA) collisions, many
 5247 highly-energetic hadrons are created in the process of probing the partonic structure of the tar-
 5248 get proton or ion using the electron. However, since the incoming proton/ion has a significantly
 5249 larger kinetic energy than the incoming electron, most of the hadrons are emitted in the same di-
 5250 rection as the hadron beam, into the hadron end cap, which is defined as the “forward” direction
 5251 at the EIC.

5252 Thus jets of particles, with single-particle energies of up to 150 GeV, are expected to reach the
 5253 forward hadronic calorimeter, e.g. based on simulated PYTHIA events for e+p collisions at 18×275
 5254 GeV². Typical jets consist of 10-12 particles contained within a jet radius of $R = 1$, with R being the
 5255 angular distance $\sqrt{\eta^2 + \phi^2}$. These jets also contain nontrivial substructure within this cone, which
 5256 carries important information about QCD dynamics. Unfortunately, the tracking momentum and
 5257 angular resolution worsens rapidly above $\eta = 3$. Because of this, the hadronic and electromagnetic
 5258 calorimetry in that region are required to provide both excellent energy resolution and sufficient
 5259 spatial resolution to resolve particles within the jets. Thus, the forward calorimeter system has
 5260 to be finely-segmented and built with minimal dead space in between the towers. This design
 5261 will provide shower containment for highly energetic particles while still providing good energy
 5262 resolution down to low energies.

5263 **Requirements from Radiation Hardness:** In the forward region the radiation dose the detec-
 5264 tor is exposed to varies significantly as a function of radius. Three different regions are considered:

5265 **A:** $R > 1$ m which is exposed to less than $5 \cdot 10^9$ neq cm⁻²year⁻¹

5266 **B:** 0.2 m $< R < 1$ m which is exposed to less than $10^9 - 10^{11}$ neq cm⁻²year⁻¹

5267 **C:** $R < 0.2$ m which receives around 10^{11} neq cm⁻²year⁻¹

5268 The maximum radiation dose is received closest to the beam pipe and closest to the interaction
 5269 point. Consequently, the primary concern will be the radiation hardness of the silicon photo multi-
 5270 pliers (SiPM) within each layer and a secondary concern are the ASICs used to read out their signals
 5271 and all other components for calibration or control, which will be sitting behind the calorimeter. It
 5272 is not expected that the scintillator or steel will experience significant deterioration due to the radi-
 5273 ation.

5274 Requirements from Data Rates:

5275 Justification

5276 **Device concept and technological choice:** The ePIC forward HCal (LFHCal) will be a steel-
 5277 plastic scintillator sandwich calorimeter, read out in transverse and longitudinally separated seg-
 5278 ments. The design is based on the SiPM-on-tile concept first introduced by CALICE collabora-
 5279 tion [?], which is now being further developed for the CMS HGCAL upgrade [?]. The SiPM-on-tile

5280 concept allows high readout granularities with low dead space in between scintillator tiles in a
5281 design that enables largely automated assembly of individual layer modules.

5282 The LFHCAL baseline readout granularity has been adapted to satisfy the physics performance
5283 requirements of the EIC Yellow Report [6], leading to a readout granularity of 5x5 cm in transverse
5284 direction and about 10-20 cm in the longitudinal direction. The innermost section closest to the
5285 beam pipe will be populated by an intergrated high granularity insert with higher granularity
5286 readout following the same general concept. Figure 8.134 shows an overview of the LFHCAL design
and the main parameters are given in Table 8.37.

parameter	LFHCAL	
	8M & 4M modules	insert modules
inner x,y (R)	$-20 \text{ cm} > x > 40 \text{ cm},$ $-30 \text{ cm} > y > 30 \text{ cm}$	$R > 17 \text{ cm}$
outer R (x,y)	$R < 270 \text{ cm}$	$-20 \text{ cm} > x > 40 \text{ cm},$ $-30 \text{ cm} > y > 30 \text{ cm}$
η acceptance	$1.2 < \eta < 3.5$	$3.5 < \eta < 4.4$
tower information		
x, y	5 cm	$\approx 4.2 \text{ cm}$ (layer 1-20) $\approx 6.5 \text{ cm}$ (layer 21-60)
z (active depth)	120 cm	120 cm
z read-out	$\approx 8.4 \text{ cm}$	$\approx 8.4 \text{ cm}$
# scintillator plates	60 (0.4 cm each)	60 (0.3 cm)
# absorber plates	60 (1.52 cm)	60 (1.52 cm)
interaction lengths	$5.8\text{-}6.5 \lambda / \lambda_0$	$5.8 \lambda / \lambda_0$
# towers	8752	
# modules		2
8M	1058	
4M	72	
# read-out channels	$7 \times 8752 = 61264$	≈ 7000

5287 **Table 8.37:** Overview of the calorimeter design properties for the LFHCAL.

5288 Subsystem description:

5289 **General device description:** The LFHCAL is positioned at $z = 3.68 \text{ m}$ from the interaction
5290 point, with a radius of about 2.7 m and a total depth of $\Delta z = 1.32 \text{ m}$. It is constructed in alter-
5291 nating layers of 1.52 cm steel absorber and 0.4 cm plastic scintillator, see details in Table ??.

5292 The LFHCAL is largely constructed from mechanical assemblies housing 60 layers of 2x4
5293 ("8M" modules) or 2x2 ("4M" module) tile layers. Alongside each assembly module, a multi-
5294 layer PCB picks up the electrical signals from each SiPM and passively transports them to-
5295 wards the end-face of the LFHCAL. In order to reduce the number of readout channels of the
5296 LFHCAL, SiPM signals from tiles in 5-10 consecutive layers are summed up before digitiza-
5297 tion by the readout electronics placed on the rear end of the LFHCAL, facing away from the
5298 interaction point. In order to increase the geometrical acceptance surrounding the beam pipe
5299 and allow for access to the scintillator layers during longer shutdowns to replace or anneal
5300 the SiPMs the modules surrounding the beam pipe are larger and have a conical cut-out for
5301 the beam pipe, as depicted in Figure 8.135 (left)

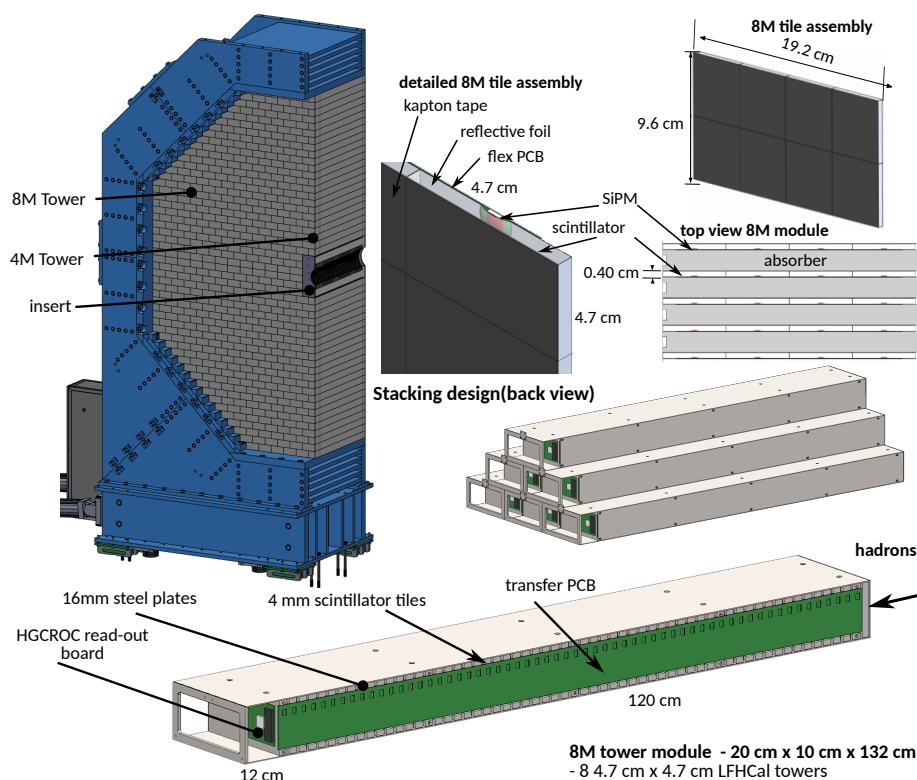


Figure 8.134: Renderings of the forward calorimeter assembly (top left), tile assembly of 8 scintillator tiles of the LFHCal with the SiPMs sitting in a dimple on each tile, detailed stacking example (middle right) and 8-tower module design (bottom).

5302 The majority of the active scintillator layers are segmented into $5 \times 5 \times 0.4\text{cm}$ tiles, individ-
 5303 ually wrapped in reflective foil, as depicted in Figure 8.136. The scintillation light generated
 5304 in each tile is detected by a SiPM placed inside a circular "dimple" depression in the center
 5305 of the tile. Tiles and SiPMs are assembled on thin, flexible printed circuit boards which
 5306 carry the electrical signal of each SiPM to the side of an assembly module. In the insert re-
 5307 gion hexagonal tiles of two different sizes are used in order to maximize the acceptance and
 5308 simultaneously reduce the number of read-out channels. Consequently, the first 20 layers are
 5309 equipped with hexagonal tiles of 4.2 cm width which are arranged in a staggered pattern re-
 5310 peating every four layers and the subsequent layers are tiled with hexagonal tiles of 6.5 cm
 5311 width. For the insert region each tile is read-out separately in order to maximize the position
 5312 resolution of individual showers.

5313 The full LFHCal consists of 68264 readout channels. Out of these about 7000 channels are
 5314 located in the insert modules and the remaining channels are contained in the 1058 "8M"
 5315 modules and 72 "4M" modules. They are grouped into 8752 towers of $5 \times 5 \text{ cm}^2$ transverse
 5316 size with each 7 read-out segments.

5317 **Scintillator:** The majority of the LFHCal will be instrumented with injection molded plastic
 5318 scintillator tiles developed and produced by the Fermilab Scintillator Manufacturing Facility.
 5319 While the lightyield of injection molded plastic scintillator is found to be 20-25% lower than
 5320 that of otherwise comparable commercially available cast sheet plastic scintillators, injection
 5321 molded scintillator tiles are at least one order of magnitude more economical on the scale of
 5322 the full LFHCal.

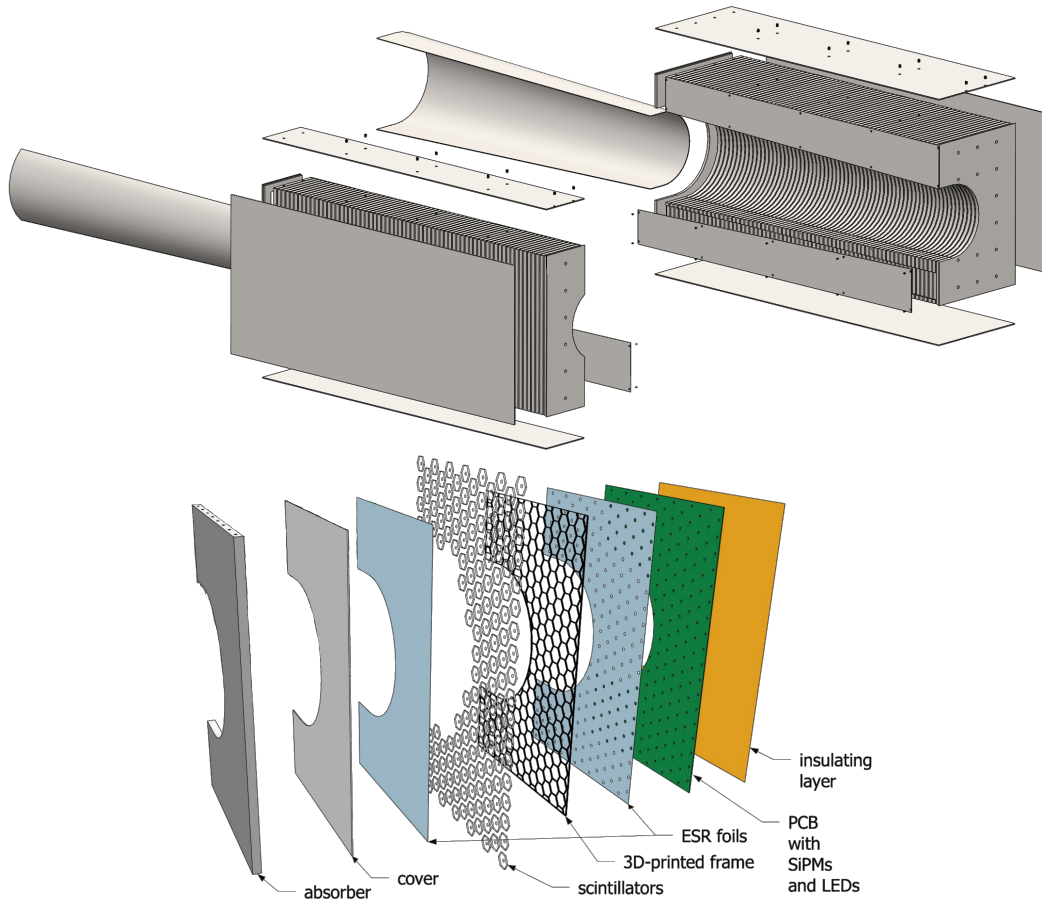


Figure 8.135: Renderings of the absorber structure for the insert modules surrounding the beam pipe (top) and their individual layer composition (bottom).

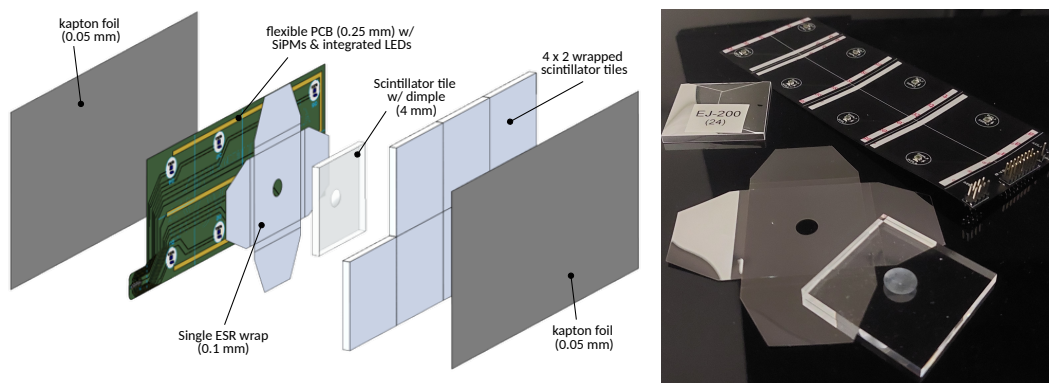


Figure 8.136: Left: Visualization of 8M-scintillator assembly with its individual components. Right: Samples of the individual components used for the 2024 test beam campaign.

5323 Only for the LFHCAL segments that will be exposed to the highest radiation doses ($R <$
 5324 1 m) and inaccessible during the yearly maintainance intervals tiles machined from cast plastic
 5325 scintillator stock will be used to increase the lightyield in order to maintain enough signal-to-
 5326 noise ratio to distinguish single MIP signals from the background noise.

5327 **Sensors:** Simulations and test bench studies have shown that SiPMs with an active area
 5328 of $1.3 \times 1.3 \text{ mm}^2$ and pixel sizes around $20 \mu\text{m}$ (i.e. Hamamatsu S13360-1325PE or S14160-
 5329 1315PS) will yield enough light yield, gain and dynamic range even after full irradiation over
 5330 the whole projected lifetime of the LFHCAL. However, as neither the scintillator tiles nor the
 5331 SiPMs are accessible after assembly, larger SiPMs with an area of $3 \times 3 \text{ mm}^2$ (ie. Hamamatsu
 5332 S13360-3025PE or S14160-3015PS) for radii below 1 m in order to provide an additional oper-
 5333 ational safety factor in the S/N ratio towards the end of its lifetime.

5334 **FEE:** The electrical signals from all SiPMs in the LFHCAL are routed towards the end-face of
 5335 the LFHCAL using a passive transfer board, where they are picked up by a summing board
 5336 that forms analog sums of 5 – 10 channels located consecutive layers of the same position.
 5337 . The summed signals are then digitized by an ASIC based on the CMS HGCROC chip de-
 5338 signed and produced by OMEGA. Each HGCROC can read out up to 72 individual SiPM
 5339 channels. It features a 12bit ADC for low amplitude hit digitization, complemented by a 16bit
 5340 time-over-threshold counter for larger amplitude signals. Individual signal arrival times are
 5341 tagged with a 20 ps time-of-arrival counter. The HGCROC chip family features trimmable
 5342 bias voltage in the range 0 – 2.5 V for each input channel, greatly reducing the number of
 5343 required high voltage power supply channels to operate the LFHCAL.

5344 While the HGCROC chip family is well advanced in its design, it is designed for the
 5345 externally triggered environment of the CMS experiment. A self-triggered variant of the
 5346 HGCROC concept named CALOROC will be developed for the use in ePIC, which will
 5347 natively support the ePIC streaming readout model. [?].
 5348

5349 **Performance** The minimum requirements for the LFHCAL performance are driven by the en-
 5350 ergy and position reconstruction of hadronic particles within a jet of 5 – 250 GeV. These require-
 5351 ments, however are to be evaluated as a combined resolution of the electromagnetic and hadronic
 5352 calorimeter response as a significant fraction of the energy might already be deposited in the elec-
 5353 tromagnetic calorimeter with its equivalent depth of one interaction length. Figure 8.137 shows
 5354 the combined energy resolution of the forward electromagnetic and hadronic calorimeter for single
 5355 pions within the primary acceptance of the LFHCAL as a function of η . It was evaluated following a
 5356 machine learning based minimization approach based on graphnet. The resulting combined energy
 5357 resolution of $\sigma_E/E = 27\%/\sqrt{E} \oplus 3\%$ exceeds the required $\sigma_E/E = (35 - 50)\%/\sqrt{E} \oplus (7 - 10)\%$ as
 5358 stated in the YR.

5359 The combined position resolution of the LFHCAL and forward electromagnetic calorimeter for sin-
 5360 gle pions can be found in Figure 8.138. Both the φ and θ resolution are found to be better than
 5361 4 mrad for pions with an energy larger than 5 GeV within the full acceptance. A mild energy de-
 5362 pendence can be observed for the θ resolution increasing as a function of energy down to 2.5 mrad.
 5363 For the φ no clear energy dependence can be claimed. While the θ resolution appears to be largely
 5364 η independent, the φ improves with increasing η to better than 2.5 mrad

5365 Implementation

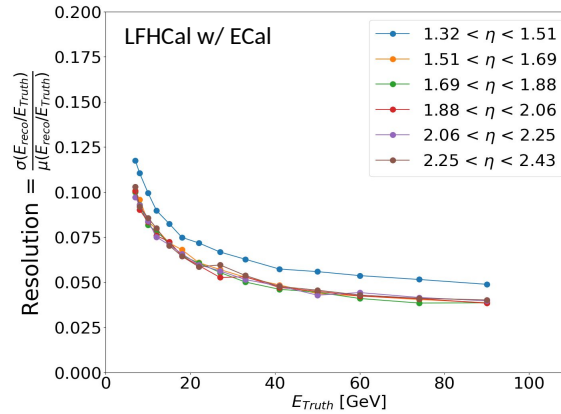


Figure 8.137: Combined energy resolution of the forward calorimeter system as a function of pseudo rapidity η for single pions, evaluated within the primary LFHCal acceptance.

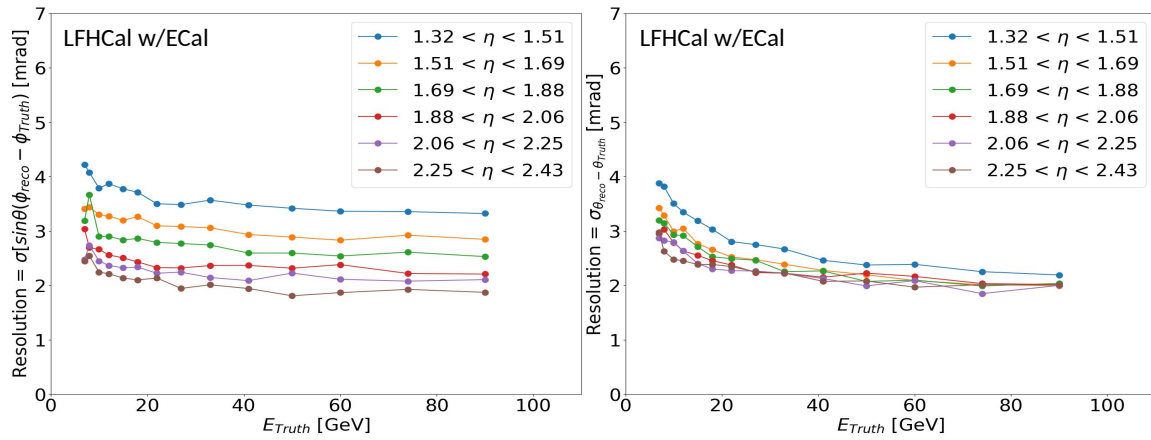


Figure 8.138: Combined position resolution of the forward calorimeter system as a function of pseudo rapidity η for single pions, evaluated within the primary LFHCal acceptance.

5366 **Subsystem mechanics and integration:** The primary construction component of the LFHCal
 5367 are the 1052 8M modules, as depicted in Figure 8.139. These modules are constructed out of an
 5368 electron beam welded and nickel-plated absorber structure out of AISI-1020 carbon steel, consisting
 5369 of the 60 absorber plates, the front and back plate and the top and bottom plate. Inside the resulting
 5370 slots inbetween the absorber plates 8M scintillator assemblies (Figure 8.136) are placed, which are
 5371 connected to a long transfer PCB running along the side of the 8M module. The module is closed
 5372 by two screwed side panels out of AISI 304 stainless steel. The read-out electronics is placed in a
 5373 rear compartment of about $19.5 \times 9.5 \times 8.5 \text{ cm}^3$, which is accessible from the rear through a cut-out
 5374 window in the back plate.

5375 The individual absorber plates are welded on the top and bottom using alternating stitch welds of
 5376 two times 63.5 mm and 88.78 mm length with a minimum penetration depth of 0.5 mm over the
 5377 full length. For the front and back plates, as well as, the those plates to which the strong back
 5378 for transportation is anchored the available maximum weld length is used to ensure maximum
 5379 stability. Afterwards, the fully welded structure is nickel electroplated to reduce the effects of
 5380 corrosion and the stainless steel side covers are installed. This production mechanisms allows for

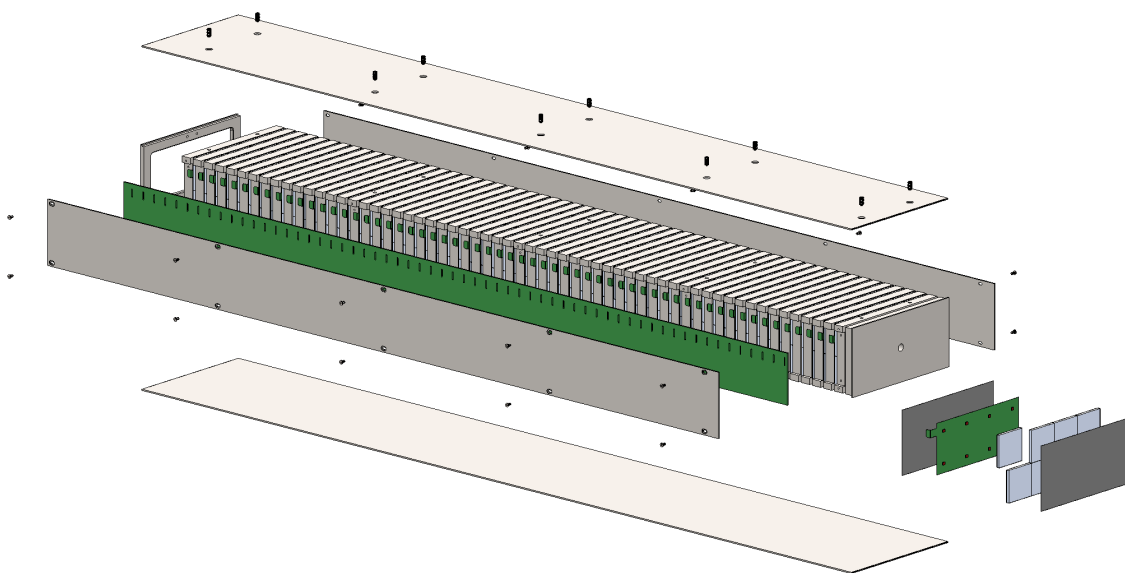


Figure 8.139: Visualization of the individual components of an 8M module.

5381 minimal distortions during construction and thus allows for a maximization of the available active
5382 detector surface.

5383 The active layers are inserted and tested together with the long transfer board at the various assem-
5384 bly locations. The FEE-cards at the rear of each module can be installed during the same assembly
5385 process or could be mounted prior to installation at Brookhaven National Laboratory depending
5386 on the production readiness of the CALOROCs.

5387 A similar construction procedure will be followed for the half sized 4M modules, where the stag-
5388 gering of the welds will not be necessary. For the two individual modules we envision the same
5389 construction technique, however, due to its weight and corresponding necessary rigidity it will most
5390 likely need to be welded also on the outer straight edge of each module to correctly disperse the
5391 load of the modules stacked on top of the respective inserts.

5392 The LFHCal will be stacked in two half shells surrounding the beam pipe, as shown in Figure 8.140
5393 (top), which are situated on rails and movable using Hillman rollers and linear actuators, which are
5394 detailed in the same drawing on the bottom. During assembly each module is lifted into place and
5395 then adjusted horizontally and vertically using different sized stainless steel shims. Afterwards it
5396 is fixated in place using bracket at the rear of each module as seen in the detailed stacking pictures
5397 in Figure 8.134. Moreover, each module is bolted to the 2.54 cm plate covering the full front face of
5398 the each half of the LFHCal. This steel plate will simultaneously serve as mounting plate for the
5399 forward electromagnetic calorimeter.

5400 **Services:** Apart from the SiPM sensors integrated into each scintillator tile layer, all active LFH-
5401 CAL electronics are located on the end-face of the LFHCAL, fully accessible in between active beam
5402 runs of the EIC. As such, there are no significant bottlenecks in terms of maximum permissible oc-
5403 cupied cross section of service channels.

5404 The total number of readout ASICs is expected to be around 1000 at a power dissipation of an
5405 estimated 2 W per ASIC distributed over the entire end-face of the LFHCAL, which is cooled with

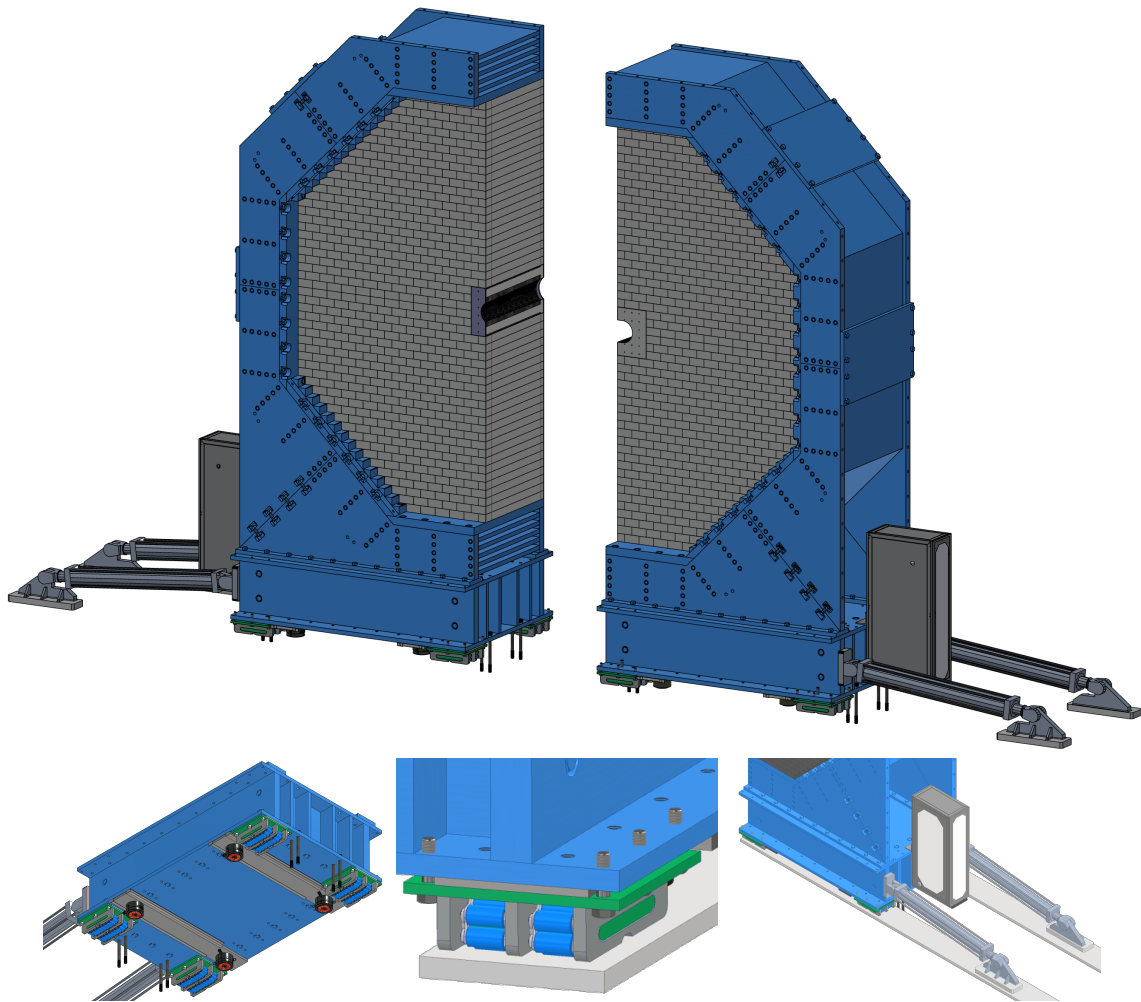


Figure 8.140: Visualization of the full LFHCAL in its cradle (top) and details of its moving mechanism (bottom).

5406 a small liquid cooling system.

5407 The overall cross section of low voltage supply cable conductors is estimated to be around
 5408 1000 mm^2 from the required current rating (up to 1 kA at 2.5 V), which can be supplied by a few
 5409 units of off-detector low voltage power supplies in a common crate area with the appropriate air
 5410 flow, mains power connection and electrical safety facilities.

5411 The HGCROC readout ASIC supports channel-individual trimming of SiPM bias voltages, reduc-
 5412 ing the overall number of required high voltage bias supply channels. For the start of the operation
 5413 of ePIC, we expect not more than 16 channels of high voltage supplies in the voltage range $50\text{--}80\text{ V}$.
 5414 When more significant adjustments to the bias voltages will have to be made due to the varying
 5415 effects of radiation damage across the LFHCAL volume, more channels might have to be added.

5416 Since the LFHCAL is planned to be assembled in two individual half-discs, all cables and other
 5417 services are separated along the same axis and cannot reach across the central separation gap of the
 5418 LFHCAL, which is either reflected in individual cable trees from the power supplies to individual

5419 halves of the LFHCAL, or potentially entirely separate power supplies located on different sides of
5420 the experimental hall.

5421 **Calibration, alignment and monitoring:** The gains of individual SiPMs will be monitored
5422 and calibrated by means of an integrated LED calibration system providing short, low amplitude
5423 flashes of light into each sensor. This gain calibration scheme does not depend on the exact ampli-
5424 tude of each LED pulse and is thus robust to changes in ambient conditions and very cost effective.
5425 The front-end electronics include a charge injection mechanism that can calibrate its own ADC and
5426 ToT scales with respect to each other.

5427 Using the calibrations in sensor gain and readout electronics scales, the lightyield of each tower of
5428 summed scintillator tiles will be monitored from the deposits of minimum ionizing tracks produced
5429 in EIC collisions during the operation of the accelerator, as well as with cosmic muons in between
5430 run periods.

5431 Initial parameters for module alignment will be provided from the metrology during and after the
5432 stack-up of the LFHCAL modules into the full LFHCAL detector. No significant relative movement
5433 of LFHCAL modules is expected during its lifetime, however the absolute position of each half-
5434 cradle will need to be validated each time the cradles are moved out and back into their positions.

5435 **Status and remaining design effort:**

5436 R&D effort: Add text here.

5437 E&D status and outlook: Add text here.

5438 Other activity needed for the design completion: Add text here.

5439 Status of maturity of the subsystem: Add text here.

5440 **Quality Assessment (QA) and Control (QC) planning:**

5441 **Environmental, Safety and Health (ES&H) aspects:** The LFHCAL design follow the best
5442 practices established within the national laboratories regarding standard safety and environmental
5443 concerns. We will strive to implement these practices at all production sites by standardizing the
5444 safety protocols, while adhering to local constraints and control processes specific to each institu-
5445 tion. Consequently, for each site the potential hazards will be identified, mitigation strategy will be
5446 developed and the appropriate safety procedures will be documented.

5447 The primary hazard during construction of the LFHCAL have been identified as:

5448 **Handling of absorber structure:** The different modules of the LFHCAL range in weight from
5449 74 kg up to 1.3 t. None of them should be lifted without a lifting fixture (strongback) and the
5450 appropriate lifting equipment for the respective weight. They will need to be uncrated for
5451 assembly and lifted on top an appropriate assembly table which can support the respective
5452 weight during installation and testing of the individual components. In particular, for the
5453 lifting operations specific protocols in compliance with the local safety rules will need to be
5454 established in order to prevent accidents.

5455 **Storage of absorber structure during assembly:** While the modules are being assembled a
5456 large fraction of the 8M modules will need to be stored at the different assembly sites. Thus
5457 in order to mitigate excessive space requirements a storage solution which allows stacking

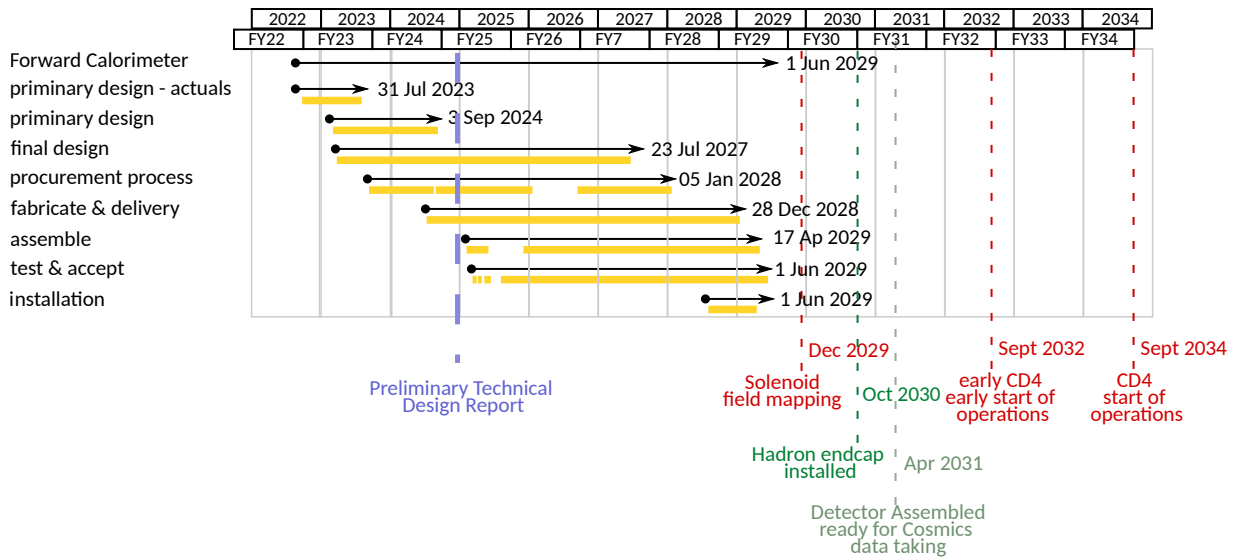


Figure 8.141: General timeline of the LFHCal design, construction and assembly.

5458 of crate modules (2-3 crates) or similar solutions will need to be pursued. This will require
 5459 additional safety measures to prevent collaps of the crates or other stacking previsions as well
 5460 as lifting the modules accordingly in their crates.

5461 **Laser operation hazards:** The ESR foil wraps will need to be cut with a laser-cutter. Controls
 5462 and measures will be implemented to ensure the corresponding device cannot be operated
 5463 without interlocks and following the laser safety guidelines of the respective institution.

5464 **Pinch/nip hazards:** Automated systems, such as robots for wafer probing, pick-and-place,
 5465 and glue application, present pinch hazards. Controls, such as guards and procedures, will
 5466 be in place to mitigate these risks.

5467 **Crush hazards:** The use of presses and swaging equipment introduces crush hazards during
 5468 assembly processes. Strict safety protocols, including the use of guards and operator training,
 5469 will mitigate these risks.

5470 **Radioactive sources:** The use of radioactive sources for calibration introduces additional handling
 5471 requirements, and proper shielding and storage protocols will be implemented as necessary.
 5472

5473 **Electrical safety:** Electrical safety procedures will also be applied for all electronics and power
 5474 systems associated with the LFHCal production tooling and detector components.

5475 **Flammable liquid handling:** For cleaning the different electrical components ethanol might
 5476 be used, these bottles will need to be handled with care and their storage will follow the
 5477 institutional safety protocols. Handling will only be done with appropriate gloves.

5478 **Construction and assembly planning:** The LFHCal construction is divided into several
 5479 phases, which are partially happening in parallel:

5480 **Absorber structure fabrication:** The individual 8M, 4M and insert module absorber structures
 5481 are assembled out of 66 individual pieces each, excluding screws, as seen in Figure 8.139.
 5482 Out of these 64 pieces are welded together using electron-beam welding after having been
 5483 preassembled and fixated in a specially designed jig for the weldment. It has been currently

5484 estimated that a maximum of 12-20 8M modules and 4M modules could be produced within
5485 a 5-day work week. The limiting factor being the availability of the large vacuum welding
5486 chamber and a full weldment cycle lasting about 2/hour per weldment. The weldments are
5487 afterwards electroplated with nickel to prevent corrosion and reduce the wearing on the outer
5488 surface due to transportation and handling. At full capacity this would require a full year of
5489 production time for the 1058 8M weldments not factoring in any delays in the supply chain.
5490 With the LFHCal also serving as flux-return for the MARCO magnet and the need to be avail-
5491 able for the powering tests currently scheduled for December 2029, has led us to acquire the
5492 LFHCal modules as part of CD3-A and CD3-B long lead procurement starting in fiscal year
5493 2024. In order to reduce the storage needs at the respective vendors and allow for a staggered
5494 further assembly the delivery of these modules will be done in badges of 50-100 modules
5495 during 2025 and 2026.

5496 **Scintillator layer assembly:** The assembly of the individual scintillator layers for the 8M and
5497 4M modules can be completely decoupled from the absorber structures fabrication. In order
5498 to assemble a single 8M-scintillator layer one fully equipped flexible SiPM-carrier board, 8
5499 wrapped tiles and two layers of Kapton foil will be needed. For the main body of the LFHCal
5500 (1058 8M and 72 4M) modules a total of 63480 8M scintillator layers and 4320 4M scintillator
5501 layers will be required, leading to at least 525120 wrapped scintillator tiles.

5502 About 10 – 12% of the tiles will be produced out of cast sheets, while the remaining $\approx 90\%$
5503 of the tiles will be injection molded out of scintillator plastic using the facilities at Fermilab.
5504 Producing all tiles out of cast material is cost and schedule prohibitive, despite having an
5505 about 20% higher light yield. The production time at Fermilab has been estimated to be about
5506 6/month of nominal operations, which can be done in batches in order to reduce the storage
5507 overhead. The tiles produced using injection molding have to be degraded and subsequently
5508 wrapped in highly reflective foil (i.e. ESR foil). Given the tight tolerances of the LFHCal
5509 modules and the amount of tiles to be wrapped it is currently envisioned to perform the
5510 wrapping using a specifically designed tile-wrapping setup similar as for the CMS HGCAL.

5511 Afterwards, the wrapped tiles are assembled into 4×2 or 2×2 scintillator assemblies backed
5512 by a flexible SiPM-carrier board and sandwiched into two adhesive sheets of thin kapton foil,
5513 as seen in Figure 8.136. The assembled layers are subsequently tested and packaged into
5514 groups of 60 assemblies to ease storage and assembly during the module assembly.

5515 For the two insert modules each layer will need to be assembled individually due their unique
5516 shape and hexagonal tile arrangements. The around 7000 hexagonal will need to be painted
5517 on their edges individually with TiO_2 -paint and then subsequently embedded in their 3D
5518 printed frame for each layer. The frame is mounted to a kapton backed SiPM carrier board
5519 which is covered with a precut ESR sheet in order to accommodate the SiPMs and LEDs for
5520 each tile. After installing another sheet of ESR-foil on top of the scintillator layer the assembly
5521 is completed by a thin cover. Due to their unique shapes and placements the insert module
5522 layers have to be assembled manually and then tested. These layers are constructed with a
5523 significantly larger rigidity than the 8M assemblies in order to allow for removal during the
5524 extended year end shutdowns and possible replacement of annihilation.

5525 **Module assembly and testing:**

5526 **LFHCal assembly:**

5527 **Collaborators and their role, resources and workforce:** The full LFHCal WBS organizato-
5528 rial chart is available in the additional material (Figure 8.142). The LFHCal consortium consists
5529 of a diverse list of institutions under the leadership of Oak Ridge National Laboratory (ORNL).
5530 Currently the majority of the leadership team is situated at ORNL, in particular regarding mechan-
5531 ical, electrical and read-out design as well as scintillator testing. System testing and Software and

5532 Simulation design are headed by Brookhaven National Laboratory (BNL) and the University of
5533 Riverside, respectively.

5534 **Risks and mitigation strategy:**

5535 Each LFHCAL scintillator tiles has to be wrapped in a suitable foil, ensuring the wrapping
5536 fulfills the requirement in light-tightness as well as geometric tolerances after wrapping. The
5537 LFHCAL tiles for lab tests and testbeam studies so far have been wrapped manually. The
5538 CMS collaboration is developing an automated wrapping machine, following two similar
5539 concepts at Northern Illinois University and DESY, Germany. We are in close contact with
5540 these groups and plan to adapt one of their designs to the needs of the LFHCAL design. If
5541 their final designs turns out to be unsuitable to wrap LFHCAL tiles, we will require additional
5542 R&D efforts to adapt the existing design to the LFHCAL or potentially develop our own. If all
5543 automated wrapping developments fail to produce reliable results, all tiles can be manually
5544 wrapped with the help of already existing 3d-printed and a sufficient number of e.g. students
5545 to perform the wrapping under supervision.

5546 The readout ASIC of the LFHCAL (as well as other ePIC detectors) is expected to be based on
5547 the HGCROC design with modifications enabling a self-triggered streaming readout named
5548 CALOROC. In case the CALOROC developments are not successful, HGCROC can be oper-
5549 ated to be quasi self-triggering by adding additional FPGA logic close to the readout electron-
5550 ics that locally generates external triggers based on the streaming trigger output that already
5551 exists in the HGCROC. This mitigation would require additional electronics on the LFHCAL
5552 end-face and greatly increase the number of differential data links required, which increases
5553 system complexity and cost.

5554 Stacking the 1168 LFHCAL modules into two coherent half-discs requires each module to
5555 adhere to the defined tolerances after assembly. Ongoing tests of the electron-beam welding
5556 procedures achieve tolerances very close to the requirements, but scaling the production to the
5557 required volume still needs to be demonstrated and validated. If the tolerances for individual
5558 modules can not be ensured, more shimming is required during the module stackup.

5559 A number of critical components of the LFHCAL are not accessible after the modules are
5560 stacked up into the full LFHCAL. All connectors and PCBs buried into the LFHCAL volume
5561 must thus be thoroughly validated for electrical and mechanical functionality and longevity. If
5562 certain connector types are found to be unsuitable e.g. in past and future testbeam campaigns,
5563 different connectors need to be selected or, if not possible, additional fastening mechanisms
5564 need to be introduced to ensure no readout channel is lost to bad or worsening connectors
5565 over the lifetime of the LFHCAL.

5566 **Additional Material**

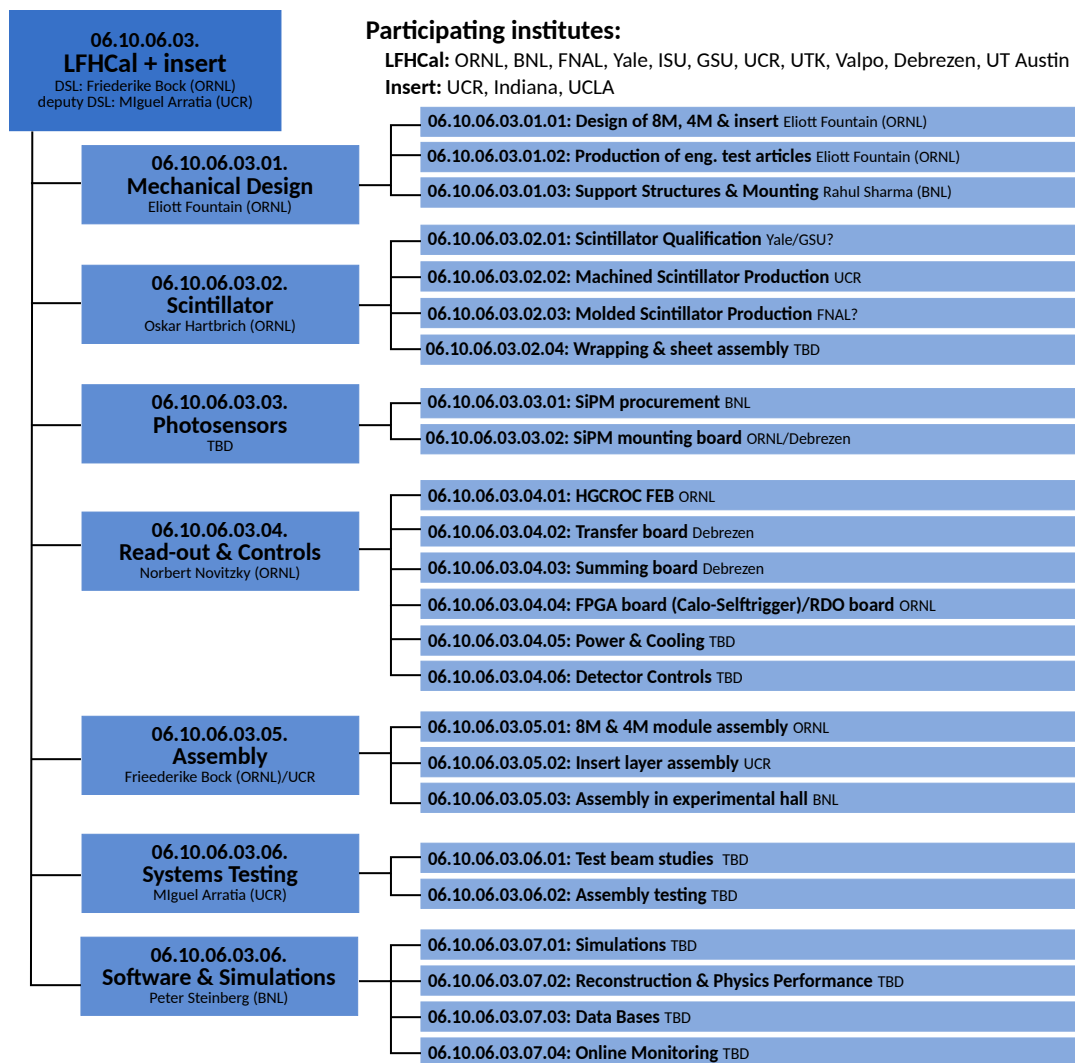


Figure 8.142: Organizational chart of the LFHCal & insert consortium, indicated by the numbers are the associated WBS structures.

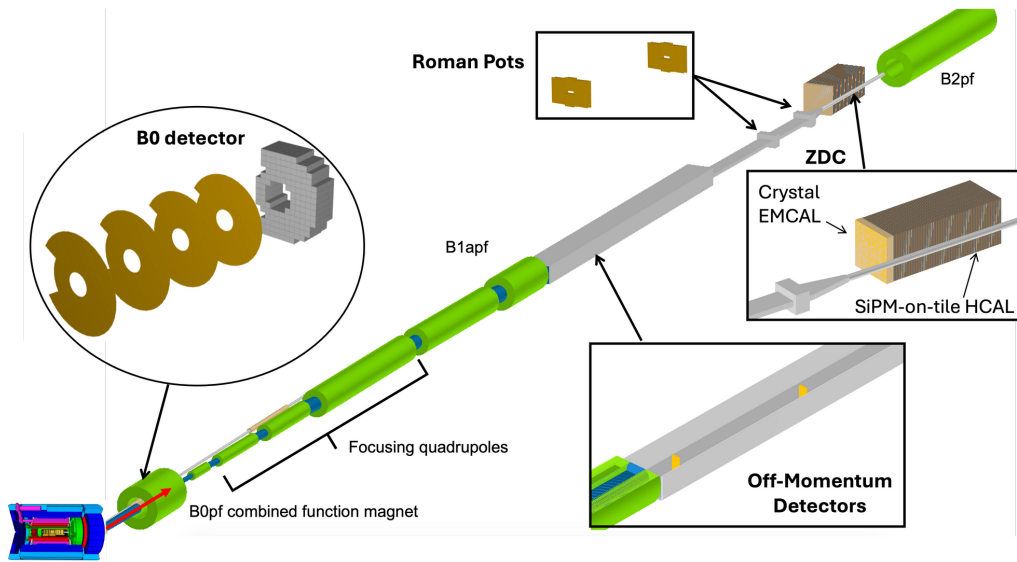


Figure 8.143: All four far-forward subsystems in the outgoing hadron beam direction. The green cylinders are accelerator dipole and quadrupole magnets.

5567 8.3.7 Far forward detectors

5568 The ePID far-forward detectors are required to enable essentially the entirety of the exclusive
 5569 physics program at the EIC, where final-states involve protons, neutrons, photons, and various
 5570 other particles at $\eta > 4.5$. There are four subsystems, all integrated with the outgoing hadron
 5571 beamline between ~ 5.5 and 39 meters from the interaction point. The far-forward subsystems are
 5572 summarized in Fig. 8.143, and details are presented in subsequent subsections.

5573 8.3.7.1 The detectors in the B0 bending magnet

5574 Requirements

5575 **Requirements from physics:** The B0 magnet bore will contain two detectors: a charged particle
 5576 tracker and an electromagnetic calorimeter. Both will have acceptance covering the angular region
 5577 from 5.5 to 20 mrad. Given the mechanical constraints imposed by the detectors' location in the
 5578 magnet (and respecting the beam lines themselves) the detectors will be highly asymmetric for
 5579 angles greater than ~ 13 mrad. To maximize acceptance it's required that there be minimal dead
 5580 areas in the instrumentation especially for angles less than ~ 13 mrad. The tracker should have
 5581 momentum resolution up to 6% for protons, and timing precision sufficient to deal with vertex
 5582 smearing. The calorimeter should have a large dynamic range with sensitivity to both soft, $O(100$
 5583 MeV), and hard, $O(100$ GeV), photons. The energy resolution should be less than $8\%/\sqrt{E} \oplus 4\%$,
 5584 with position resolution $\lesssim 10$ mm. We note that for some analysis use cases the calorimeter will
 5585 function as a photon 'tagger' rather than an actual calorimeter, and so in some regions of acceptance
 5586 (where the mechanical constraints are acute) this resolution may not be achieved but having the
 5587 acceptance instrumented is still valuable.

5588 **Requirements from Radiation Hardness:** The expected non-ionizing radiation dose at a lon-
5589 gitudinal distance of 692 cm from the interaction point (near the fourth tracking layer and the front
5590 of the calorimeter) is approximately 3.1×10^{11} 1 MeV neutron equivalent per square centimeter
5591 for $100 fb^{-1}$. At this location the ionizing dose can reach O(100) kRad.

5592 **Requirements from Data Rates:** Add text here.

5593 **Justification**

5594 **Device concept and technological choice:** The charged particle tracker will be composed of
5595 four layers instrumented with silicon. The layers are approximately equidistantly placed at dis-
5596 tances between 590 and 690 cm from the interaction point, which given the field inside the mag-
5597 net allows satisfactory proton measurement and momentum reconstruction. The electromagnetic
5598 calorimeter is composed of 135 scintillating $PbWO_4$ crystals, each one $2 \times 2 \times 20$ cm³ (the long
5599 direction is on the z axis). We note that the crystals are the same as those used in the EEEMCal.

5600 **Subsystem description:**

5601 General device description: Each tracking layer has a transverse layout to cover as much of
5602 the angular acceptance as possible given the mechanical constraints, as illustrated in Figure
5603 ???. The crystals of the calorimeter are arranged in a similar way for the same reason.

5604 Sensors: For the tracking detectors AC-coupled low-gain avalanche diodes (AC-LGADs) are
5605 chosen due to their capability to provide both high-precision space and time information. In
5606 order for the spatial resolution to meet the performance requirements charge sharing must
5607 be implemented in the reconstruction. We note that this technology is broadly in use within
5608 ePIC, and its particular implementation for the B0 detectors should be very similar to the
5609 Roman Pots/Off Momentum Detectors. For the calorimeter the $PbWO_4$ crystals produce light
5610 peaking at ~ 420 nm, which will be read out by SiPM. Four 6×6 mm² SiPM will be used per
5611 crystal, 3 with 15 micron pitch and one with a 10 micron pitch (likely Hamamatsu S14160-
5612 6015PS and S14160-6010PS, respectively). The larger pitch SiPM have fewer pixels but higher
5613 efficiency making them appropriate for smaller signals, whereas the smaller pitch SiPM will
5614 be utilized for the higher energy particle signals.

5615 FEE: Following the Roman Pots/Off Momentum Detectors, the ASICs will be readout using
5616 LPGBT in-place of FPGAs due to the high-radiation environment in which these detector will
5617 be located. AC-LGAD + ASIC modules will be connected to the LPGBT, which will be coupled
5618 to a VTRX+ to convert the signals to a fiber to send off to the DAW system. The electronics to
5619 process the SiPM signal are still to be worked out but expected to follow closely the scheme
5620 of the EEEMCal.

5621 Other components: Add text here.

5622 **Performance** The key physics task of the B0 tracker system is the measurement of protons, and
5623 this is summarized by the acceptance and transverse momentum resolution shown in Figure 8.144.
5624 The B0 calorimeter's acceptance for photons is shown in Figure 8.145. The calorimeter seeks to
5625 measure photons over a very large range. The performance of the detector, in particular the energy
5626 resolution, is shown separately for low and high energy photons in Figure 8.146. The higher energy

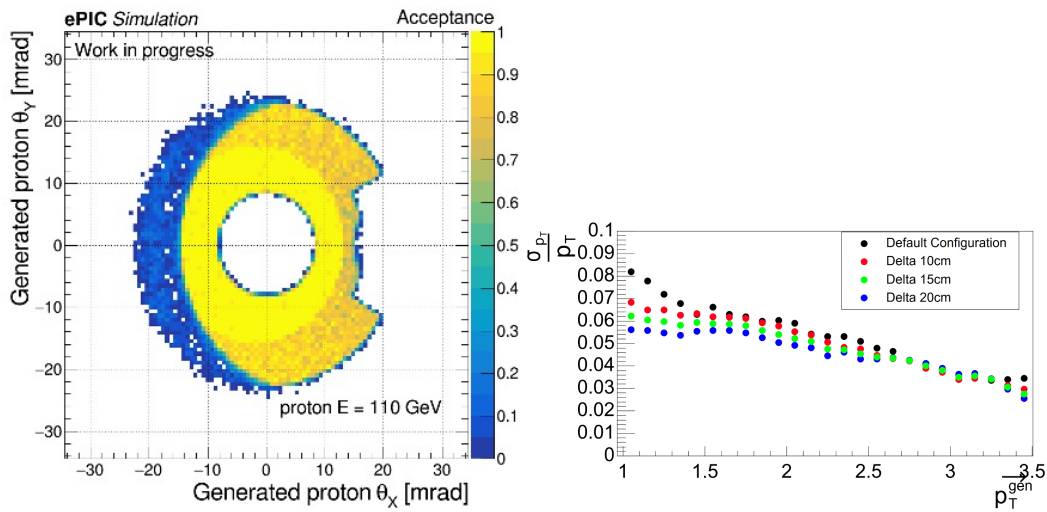


Figure 8.144: Left: The B0 tracker’s acceptance of protons (E=110 GeV), as a function of θ_x and θ_y . PLACEHOLDER NEEDS TO BE REMADE W/REAL B FIELD Right: The p_T resolution for protons reconstructed in the B0 tracker. PLACEHOLDER NEEDS TO BE REMADE WITH FINAL LOCATIONS, FINAL TRACKING, PROPER LABELLING ETC

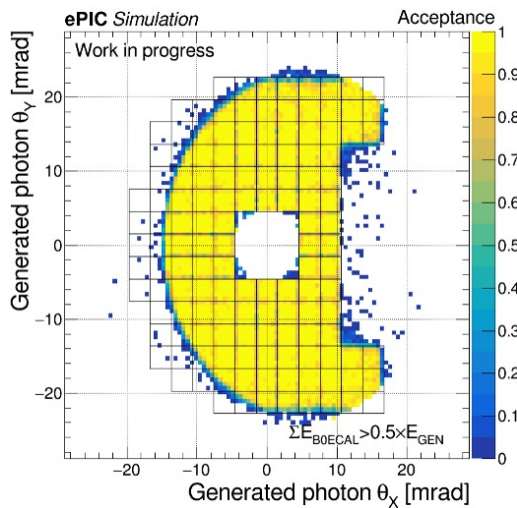


Figure 8.145: The B0 EM calorimeter’s acceptance of photons with a substantial (for now half their energy) deposit in a calorimeter crystal. PLACEHOLDER - SPLIT HARD SOFT, FIX CRYSTAL ALIGNMENT

5627 photons are evaluated based on a signal to a single 10 micron pitch SiPM, whereas the lower energy
 5628 photon performance assumes three 15 micron pitch SiPM per crystal.

5629 **Implementation**

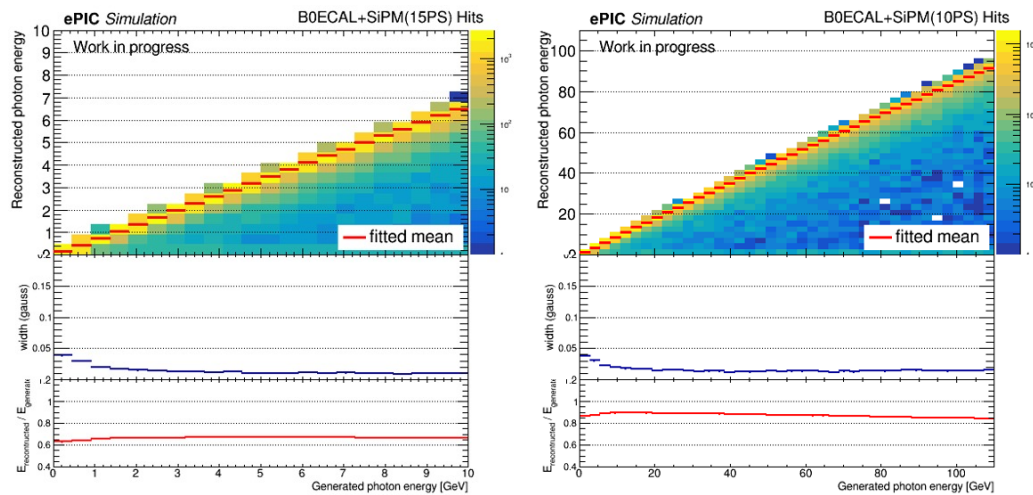


Figure 8.146: The energy reconstructed and associated resolution for the B0 EM calorimeter of photons with $\theta < 13$ mrad in the soft (left) and hard (right) energy reconstruction regimes.
PLACEHOLDER - zoom soft photon, update reflectivity

5630 **Services:** For the trackers low voltage ($\sim 3V$) and high voltage ($\sim 150V$) supplies for the operation
 5631 of the ASICs and the bias supply, as well as slow controls for the voltages and the DAQ system.
 5632 The SiPM for the calorimeter need a bias of ($\sim 5V$). The cooling system is still to be worked out, but
 5633 is expected to be air based (unlike the in-vacuum challenge of the similar instrumentation for the
 5634 Roman Pot/Off Momentum Detectors).

5635 **Subsystem mechanics and integration:** The integration of the detectors into the B0 magnet
 5636 bore is a significant undertaking. The space for the detectors (and services) is quite limited and the
 5637 installation procedure introduces more constraints. After the vacuum valve is closed there is only
 5638 about 10 cm of clearance in front of the magnet and this precludes installation of the 20 cm crystals.
 5639 To address this difficulty, the crystals will be installed prior to closing the valve closing and the
 5640 beam commissioning. At this point *only* the crystals will be installed to avoid the risk of damaging
 5641 the other components during the commissioning. Following this the SiPM and electronics of the
 5642 calorimeter will be installed. Both installations as well as the final positioning of the detectors will
 5643 be via a rail system: detector components will be loaded onto the rails system outside the magnet
 5644 and inserted in to it. We note that the detectors will be installed as sub-detectors not as monolithic
 5645 pieces covering the entire acceptance.

5646 **Calibration, alignment and monitoring:** Add text here.

5647 **Status and remaining design effort:**

5648 R&D effort: There is still work to be done for full detector operation. For the trackers es-
 5649 pecially demonstrating effective reconstruction using charge sharing and for the calorimeter
 5650 the multi-SiPM readout. For both the trackers and calorimeter this includes optimizing the
 5651 acceptance in concert with the installation procedure.

5652 E&D status and outlook: Add text here.

5653 Other activity needed for the design completion: Completion of the mechanical rail system
 5654 is underway and this includes a final scheme of subdividing the detectors into sub-detectors
 5655 accordingly.

5656 Status of maturity of the subsystem: Add text here.

5657 **Environmental, Safety and Health (ES&H) aspects and Quality Assessment (QA plan-**
 5658 **ning:** Add text here.

5659 **Construction and assembly planning:** The tracking system should benefit from the BNL local
 5660 expertise and production capabilities for AC-LGAD and from there ‘directly’ to installation readi-
 5661 ness. The calorimeter sub-components may be prepared either on or off site, but in any case the
 5662 final assembly can not be separated from the installation procedure.

5663 **Collaborators and their role, resources and workforce:** The Israeli ePIC consortium (in par-
 5664 ticular BGU and TAU) are playing the main role in the detector development and this will continue
 5665 through installation/operation. There is also very significant participation from BNL generally,
 5666 and especially for the common AC-LGAD instrumentation.

5667 **Risks and mitigation strategy:** For the trackers the largest risk is the necessity to utilize charge
 5668 sharing in the reconstruction to obtain the needed momentum resolution. Other detection tech-
 5669 nologies have been considered to mitigate this risk (with smaller pixels) but to this point none has
 5670 been identified as an appropriate alternative. For both detectors (and even more acutely for the
 5671 calorimeter) the installation challenge risks limiting the detector acceptance.

5672 **Additional Material** Add text here.

5673 8.3.7.2 The roman pots and the off-momentum detectors

5674 Requirements

5675 **Requirements from physics:** Measurement of protons at various rigidities, with rigidity de-
 5676 fined by ratio of the proton momentum to that of the beam itself, and with scattering at angles
 5677 $< 5\text{mrad}$ requires detectors integrated directly into the hadron beamline in the form of Roman pots
 5678 (RP). The Off-Momentum detectors (OMD) enable tagging and reconstruction of spectator protons
 5679 from the breakup of light nuclei (e.g. deuterons and He-3), which produce protons at rigidities
 5680 $< 65\%$, with deuterons producing protons at an average of $\sim 50\%$ rigidity. For the Roman pots,
 5681 achieving acceptance down to 0 mrad is impossible due to the presence of the hadron beam itself, so
 5682 the low- θ (low- p_T) acceptance is essentially entirely driven by the focusing quadrupoles (machine
 5683 optics) before and after the interaction point. For IP-6, the choice of low- β^* optics to maximize lu-
 5684 minosity (so-called “high divergence”) means the transverse beam size, $\sigma_{x,y} \approx \sqrt{\beta_{x,y}(z_{RP}) \times \epsilon_{x,y}}$,
 5685 where $\beta_{x,y}(z_{RP})$ are the beta-functions in (x,y) at the Roman pots location and $\epsilon_{x,y}$ is the emittance
 5686 for the machine, is larger, worsening the acceptance at the expense of luminosity. Generally, $10\sigma_{x,y}$
 5687 is the average “safe distance” for the Roman pots to operate. Conversely, a choice can be made to
 5688 reduce luminosity to improve low- θ acceptance at the Roman pots location, normally referred to

5689 as “high acceptance” optics. Given this set of operational parameters for the machine itself, it is re-
5690 quired that the sensor packages have minimal dead area at the edges to take maximum advantage
5691 of the machine optics during data taking runs.

5692 For resolution, the detectors must deliver p_T -resolution better than 10%.

5693 **Requirements from Radiation Hardness:** Maximal radiation doses are shown to be $\lesssim 10^{12}$ 1
5694 MeV neutron equivalent for NIEL radiation, while ionizing doses are around 1 krad for the Roman
5695 pots region of ePIC [will add plot here, or reference section on the radiation].

5696 **Requirements from Data Rates:** Rates during normal operations, with expected vacuum of
5697 10^{-9} mbar, are a few Hz/channel. However, the beam halo could potentially provide rates of 30-
5698 50kHz at $\sim 10\sigma$ from experience of Roman pots at STAR. While the EIC hadron beam will have
5699 many differences to the RHIC hadron beam, it’s hard to estimate the full rate impact of the beam
5700 halo without an appropriate simulation. This is something to be done in the coming year as the
5701 machine develops.

5702 Justification

5703 **Device concept and technological choice:** The basic concept of Roman pots detectors for
5704 measuring protons near the beam is not new and has been employed at HERA, RHIC, and the
5705 LHC, among other collider facilities. In the case of the EIC, the Roman pots (and OMD) need to be
5706 able to make measurements with challenges different to those in previous facilities. Studies from
5707 the EIC generic R&D program, in particular eRD24, demonstrated that the RP detectors need to
5708 have both high spatial ($\sim 140\mu\text{m}$) and timing ($\sim 35\text{ps}$) resolutions, a challenge to deliver with one
5709 subsystem. As silicon detector technology has advanced, an evolved version of the DC-coupled
5710 Low Gain Avalanche Diode (DC-LGAD) sensor, normally used for high-resolution timing detectors
5711 [Add reference here later], has come to the fore in the form of an AC-coupled version, known as
5712 the AC-LGAD. The AC-LGADs allow for pixelization and can meet the requirements of the RP and
5713 OMD subsystems, as was the goal of eRD24.

5714 An additional challenge with operation of the RP and OMD systems is the operation of these de-
5715 tectors in vacuum. The subsystems themselves are large enough to prohibit use of the conventional
5716 “pot” vessels used to protect the detectors in other colliders, and therefore necessitate the inclusion
5717 of the sensor planes directly into the machine vacuum, providing unique challenges for cooling
5718 and shielding.

5719 add figures of full detector layout here later when I have a better CAD picture to use.

5720 Subsystem description:

5721 General device description: The Roman pots and off-momentum detectors are both vacuum-
5722 based silicon sensors arranged into two stations for fully reconstructing protons at various
5723 magnetic rigidities, where rigidity here refers to the fraction of the momentum the proton has
5724 with respect to the steering dipoles design orbit momentum.

5725 Sensors: AC-coupled low-gain avalanche diodes (AC-LGADs) are the technology of choice
5726 for these two subsystems due to their capability to provide both high-precision space and
5727 time information. add references here for testbeam results on SENSORS.

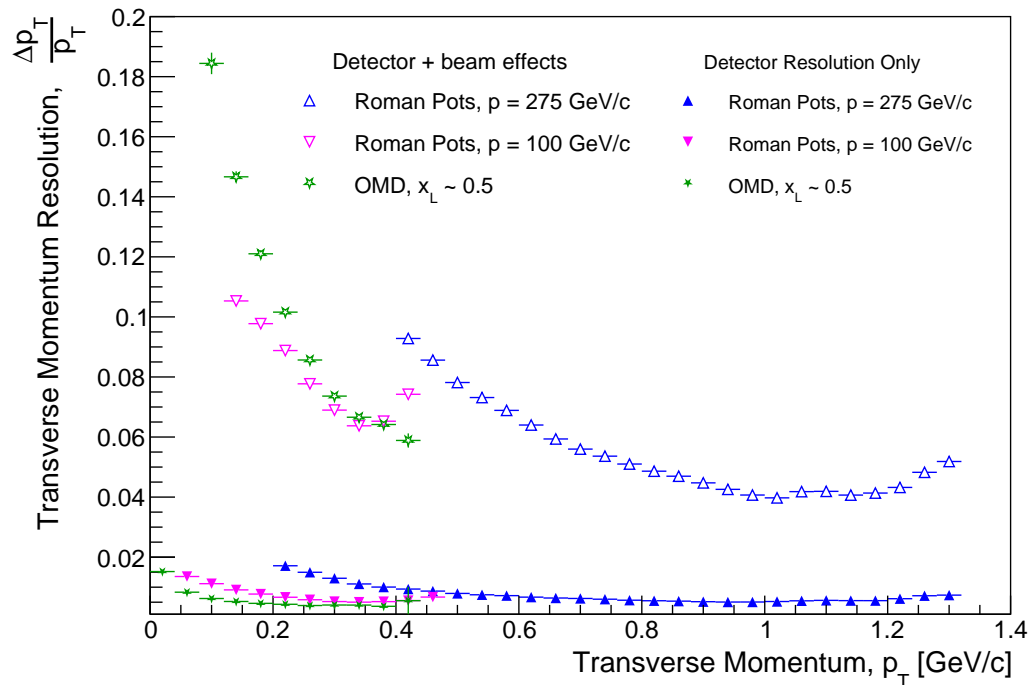


Figure 8.147: Summary of transverse momentum resolutions for the Roman pots and Off-Momentum Detectors. Contributions are separated by those induced by intrinsic detector choices (e.g. pixel sizes) and those from beam effects (e.g. angular divergence), which have an outsized impact on momentum measurements at very-forward rapidity. **Will be replaced with DD4HEP version**

5728 FEE: ASICs will be readout using LPGBT in-place of FPGAs due to the high-radiation envi-
 5729 ronment in which these detector will be located. Up to sixteen AC-LGAD + ASIC modules
 5730 will be connected to a single LPGBT, which will be coupled to a VTRX+ to convert the signals
 5731 to a fiber to send off to the DAW system. The stave design is aimed to have the minimal
 5732 amount of components inside the vacuum to ensure smooth operations and ease of access
 5733 during maintenance periods.

5734 Other components: Design of the front-end board and power distribution is still in a very
 5735 early stage for the RP and OMD systems.

5736 **Performance** The performance of the Roman pots and Off-Momentum Detectors is summarized
 5737 in Fig. 8.147. The overall momentum resolution is also affected by the detailed understanding of
 5738 the hadron magnet lattice, which is used to be able extract the normal transfer matrices used to
 5739 reconstruct momenta in Roman pots detectors. There is also a software solution in place using
 5740 deep neural networks to further improve the momentum resolution performance, especially for
 5741 the off-momentum detectors.

5742 **Implementation** The basic detector component will be a “stave” which contains 3-4 “modules”
 5743 comprised of bump-bonded AC-LGADs and ASICs attached a PCB, arranged in a 1x4 or 1x3 layout

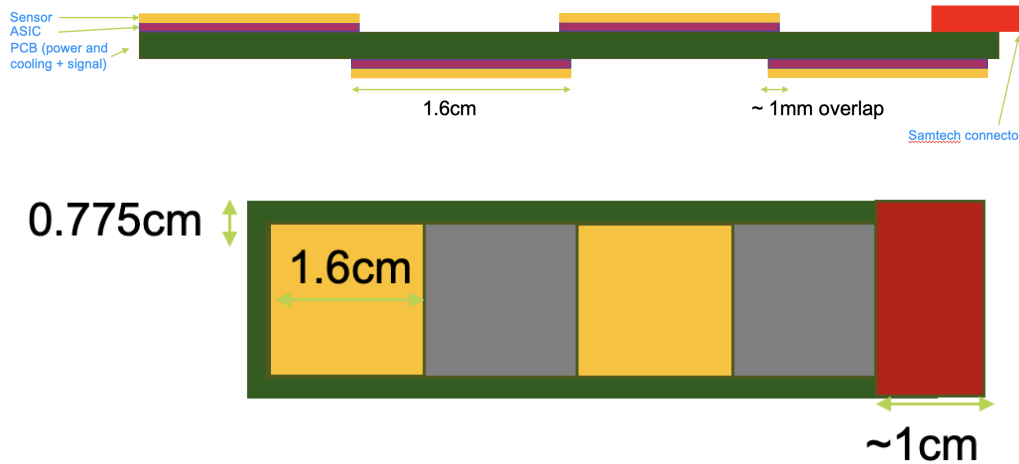


Figure 8.148: Strawman concept for the layout of the RP and OMD sensor staves. A 1x3 configuration is also being consider to reduce the size of the necessary Samtech connector for the staves, but more study is needed to assess impact of either choice, both in terms of construction feasibility and performance.

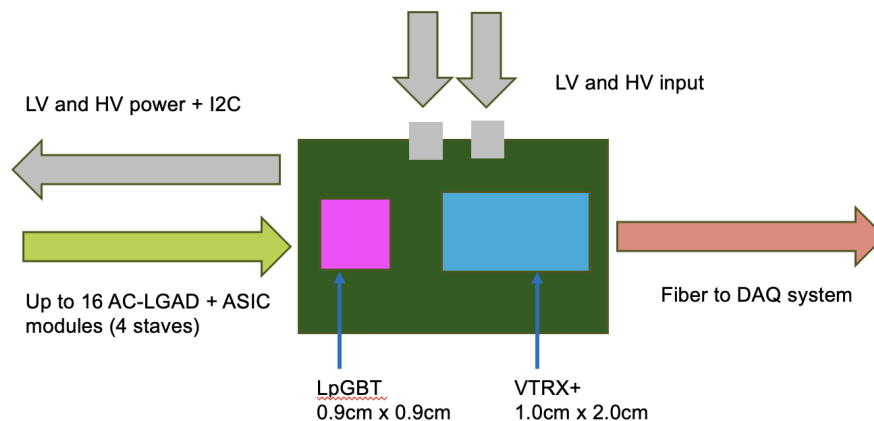


Figure 8.149: Strawman concept a readout board concept to communicate with and readout RP and OMD sensor staves. Work needs to be done to solve the issue of power distribution, and to ensure the EICROC ASIC can indeed be readout by the LpGBT.

5744 with modules on either side of the PCB to enable partial transverse overlap of the sensors to cover
 5745 the dead area at the edges (e.g. guard ring location). The staves are proposed to only contain the
 5746 sensors and ASICs, plus cooling services, with all other services coming from a readout board place
 5747 outside the vacuum which contains the LpGBT and VTRX+ components and power distribution.
 5748 The details of the this concept still need to be properly worked out with engineering support, but
 5749 strawman versions of these concepts can be found in Figs. 8.148 and 8.149.

5750 **Services:** The Roman pots and OMD have the same essential needs for services, which include
5751 cooling using conductive strips coupled to an external chiller to allow cooling in-vacuum, low volt-
5752 age ($\sim 3\text{V}$) and high voltage ($\sim 150\text{V}$) supplies for the operation of the ASICs and the HV bias supply
5753 for the sensor, and slow controls to control both voltages and the DAQ system, and also to control
5754 the moving stages necessary for the detector operations. There will also need to be communication
5755 between the slow controls and the machine for safety interlocks for fast beam abort systems, and
5756 for permits to enable motion control of the detectors when beam conditions are stabilized.

5757 **Subsystem mechanics and integration:** The primary support systems only need to be able to
5758 support very light staves with 3-4 modules per PCB. However, the entire subsystem needs to be
5759 a on motor-driven rail system to enable movement near the hadron beam, especially in order to
5760 achieve acceptance at very-low $p_T \sim 0.2 \text{ GeV}/c$.

5761 **Calibration, alignment and monitoring:** AC-LGAD sensors will be calibrated with MIPs,
5762 while alignment of the detector systems will need to be carried out using beam-based alignment
5763 with dedicated, short, very-low luminosity runs, which enable the detectors to approach the beam
5764 much closer than the standard 10σ distance such that the beam halo itself can be seen on the sensor
5765 planes. This, combined with conventional survey information used to align the motion system to
5766 the machine should enable alignment at a level much less than 1mm.

5767 **Status and remaining design effort:**

5768 R&D effort: Much work is still needed to demonstrate full system operations with full size
5769 sensors + ASICs, and the cooling concept using conductive strips. As of now, only 4x4 channel
5770 versions have been tested.

5771 E&D status and outlook: Engineering design is still very preliminary, but necessary design
5772 choices are being evaluated as engineering support becomes available.

5773 Other activity needed for the design completion: The design of the front-end PCB which
5774 carries the sensors, ASICs, and necessary services needs to be carried out. Presently, only a
5775 strawman concept which will meet our requirements exists.

5776 Status of maturity of the subsystem: The design maturity of the system will be at $\sim 60\%$ by
5777 Q2 of FY25.

5778 **Environmental, Safety and Health (ES&H) aspects and Quality Assessment (QA) plan-**
5779 **ning:** Since these detectors are embedded directly into the machine vacuum, special considera-
5780 tions must be made for integration with the machine. We expect that the detectors will be inter-
5781 locked against operation until permits are received from the machine, pending stable operations
5782 of the machine in terms of stable beam losses, collisions at the IP, and background conditions. The
5783 cooling system will also have to be integrated with the machine envelope and likely must pass an
5784 evaluation from the machine group.

5785 **Construction and assembly planning:** Sensors and EICROC ASICs will be manufactured in
5786 different foundries, but bump-bonding of the sensors + ASICs can be done for the far-forward at
5787 BNL, since these detector subsystems are very small compared to other ePIC sub-systems. The
5788 assembly will have to take place in stages which include the following steps. First, preparation of
5789 stave printed circuit boards and quality assurance testing to ensure traces pass continuity tests to

5790 the Samtech connectors will have to be carried out. In parallel, diced sensors need to be tested to
5791 ensure they can maintain bias voltage safely, and other electrical tests. ASICs will undergo similar
5792 tests to ensure they are ready for bonding into full modules. Once sensors and ASICs are prepped,
5793 modules of 32x32 channel size (one sensor, one ASIC) will be bump-bonded. Once sensors are
5794 bump-bonded, QA will need to be performed on the final modules before they are integrated into
5795 stave PCBs.

5796 **Collaborators and their role, resources and workforce:** BNL and JLAB will take the primary
5797 role in constructing the Roman pots and Off-Momentum Detectors, with engineering support for
5798 cooling possibly supplied by IJCLab in France.

5799 **Risks and mitigation strategy:** The primary risks to the successful construction of the Ro-
5800 man pots and OMD are late receipt of the final 32x32 channel EICROC ASICs and issues with the
5801 bump-bonding and construction of the final staves. There are additional risks related to machine
5802 integration.

5803 **Additional Material** Will add sufficient reference to support documents as they are compiled.

5804 8.3.7.3 The zero degree calorimeter

5805 Requirements

5806 **Requirements from physics:** The Zero-Degree Calorimeter (ZDC) plays an important role in
5807 many physics topics. The production of exclusive vector mesons in diffraction processes from
5808 electron-nucleus collisions is one of the important measurements. For the coherent processes,
5809 where the nucleus remains intact, the momentum transfer (t) dependent cross section can be re-
5810 lated to the transverse spatial distribution of gluons in the nucleus, which is sensitive to gluon
5811 saturation. In this case, however, the coherence of the reaction needs to be determined precisely.
5812 Incoherent events can be isolated by identifying the break-up of the excited nucleus. The evapo-
5813 rated neutrons produced by the break-up in the diffraction process can be used in most cases (about
5814 90%) to separate coherent processes. In addition, photons from the de-excitation of the excited nu-
5815 clei can help identify incoherent processes even in the absence of evaporated neutrons. Therefore,
5816 in order to identify coherent events over a wide t range, neutrons and photons must be accurately
5817 measured near zero degrees.

5818 The geometry of the collision is important to understand the characteristics of each event in
5819 electron-nucleus collisions. It has been proposed that collision geometry can be studied by tagging
5820 it with the multiplicity of forward neutrons emitted near zero degrees. Determining the geometry
5821 of the collision, such as the “travel length” of the struck partons in the nucleus, which correlates
5822 with the impact parameters of the collision, is very useful in the study of nuclear matter effects.
5823 Determining the geometry of the collision will allow us to understand the nuclear structure with
5824 greater accuracy.

5825 **Requirements from Radiation Hardness:** In the ePIC radiation doses and particle fluences,
5826 ZDC neutron fluence is smaller than 10^{12} neutron/cm² for 6 month operation. It is not demanding,
5827 but degradation may occur for crystals and/or photon sensors due to radiation

5828 **Requirements from Data Rates:** Dynamic range of the crystal calorimeter is a clear challenge.
5829 ~ 100 MeV photons from e+A “quasi-coherent” reactions and ~ 10 -100 GeV photons possible from
5830 other exclusive processes (Λ decay, u -channel DVCS) should be covered.

5831 **Justification**

5832 **Device concept and technological choice:** Add text here.

5833 **Subsystem description:**

5834 General device description: The Crystal calorimeter needs a good measurement of low-energy
5835 photons. The first part of ZDC is designed to use a layer of crystal calorimeter towers which
5836 is $8X_0$ in thickness. The layer consists of 2×2 cm² crystals in an array of 30×30 . LYSO
5837 is considered as the material choice for the crystal. SiPM and APD are considered as photo-
5838 sensors. The FEE and other components are also under consideration.

5839 Sensors: Add text here.

5840 FEE: Add text here.

5841 Other components: Add text here.

5842 **Performance** Test beams for crystal calorimeter prototype have been performed and its data
5843 analysis is underway. Its prototype modules have been made by Taiwan group. Two simulation
5844 calculations and evaluations have been ongoing; Λ identification and low-E photon identification.
5845 Angular resolution is a common thread. They have been less-emphasized early-on, but absolute
5846 requirements for successful exclusive physics program should be given.

5847 **Implementation** ZDC implementation would have a benefit from a creative approach; poten-
5848 tially non-static configuration which can be “changed” for different running conditions. The crystal
5849 calorimeter need depends on physics channel; some level of conflict in the final states and associ-
5850 ated requirements. Having the ability to bring the crystal calorimeter in/out of configuration, as
5851 needed, would provide clear benefit to specific physics needs.

5852 **Services:** Add text here.

5853 **Subsystem mechanics and integration:** In the current crystal calorimeter prototype module
5854 made by Taiwan group, by glueing modules together, 4×4 crystals are made, and then 4 modules are
5855 put 64 crystals together. Support and mechanical structure need to communicate with US experts.

5856 **Calibration, alignment and monitoring:** Add text here.

5857 **Status and remaining design effort:**

5858 R&D effort: Add text here.

5859 E&D status and outlook: Add text here.

5860 Other activity needed for the design completion: Add text here.

5861 Status of maturity of the subsystem: Add text here.

5862 **Environmental, Safety and Health (ES&H) aspects and Quality Assessment (QA plan-**
5863 **ning:** Add text here.

5864 **Construction and assembly planning:** Add text here.

5865 **Collaborators and their role, resources and workforce:** Add text here.

5866 **Risks and mitigation strategy:** Add text here.

5867 **Additional Material** Add text here.

5868 **8.3.8 Far backward detectors**

5869 The luminosity system at the Electron-Ion Collider plays a critical role in achieving high-precision
5870 measurements in nuclear physics experiments. By determining, monitoring and optimizing the
5871 number of particle collisions, the luminosity system ensures that the collider operates at peak per-
5872 formance, enabling detailed exploration of the structure of matter. When electrons collide with
5873 protons or nuclei, Bremsstrahlung (BH) photons are generated, with a well know cross section [].
5874 This process thus provides us with the mean to indirectly determine the luminosity by accurate
5875 and precise determination of the Bremsstrahlung photons generated in the interaction region of
5876 the collider.

5877 Accurately determining luminosity is essential for addressing the fundamental physics questions
5878 that underpin the construction of the Electron-Ion Collider. The Yellow Report specifies the EIC
5879 requirements for luminosity determination to be 1% in absolute uncertainty and 10^{-4} in relative
5880 luminosity [?]. This requirement will be fulfilled by two complementary detectors in the lumi-
5881 nosity monitoring system: the Pair Spectrometer (PS) and the Direct Photon Detector (DPD). It was
5882 demonstrated at HERA – the first electron-hadron collider – that the bremsstrahlung process can be
5883 successfully used to precisely measure the luminosity of high-energy ep collisions (ZEUS achieved
5884 an absolute uncertainty of 1.7% [?, ?]). The luminosity monitors designed for the EIC utilise the
5885 same approach with implementation that mitigates large systematic uncertainties.

5886 The two subsystems, Pair Spectrometer, and Direct Photon Detector, are sensitive to different sys-
5887 tematic effects; on one hand the Direct Photon detector is placed downstream the photon beam with
5888 full acceptance, but within the synchrotron radiation fan and needs to be shielded. In addition,
5889 at nominal luminosities planned for the EIC several photons will hit the DPD in each bunch cross-
5890 ing. Thus the counting of bremsstrahlung photons is done through the total energy determination
5891 deposited in DPD and is associated with systematic uncertainties related to gain stability. On the
5892 other hand, the PS is outside the synchrotron radiation fan and overall rates can be controlled
5893 with a dedicated converter. The luminosity determination from the PS is sensitive to systematic
5894 effects related with the acceptance determination.

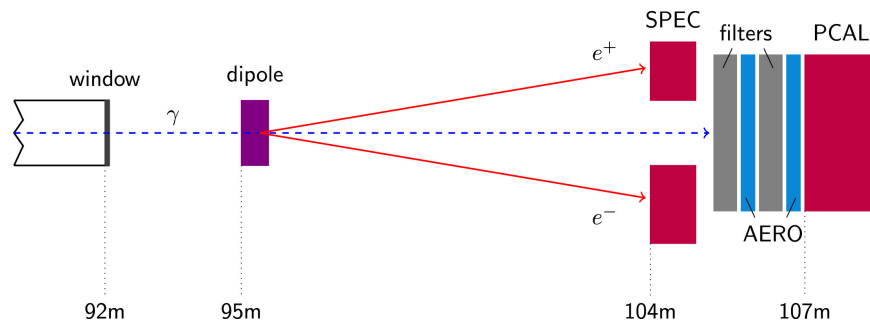


Figure 8.150: The layout of the luminosity monitor in the ZEUS experiment [?].

5895 The PS and DPD detectors in the ZEUS luminosity monitor are shown in figure (8.150). The PS system
 5896 consists of an analysing dipole magnet and two electromagnetic calorimeters, while the DPD
 5897 system includes absorbing plates and an electromagnetic calorimeter. BH photons generated in
 5898 the interaction region exit the vacuum chamber through a thick exit window. About 10% of these
 5899 photons (depending on the window's thickness) undergo pair conversion into electron-positron
 5900 pairs, which are then detected by the PS calorimeters. The remaining unconverted photons are
 5901 detected by the downstream DPD. Additionally, the luminosity monitor includes a collimator posi-
 5902 tioned just after the exit window to produce a uniform, narrow cone of photons and pair-converted
 5903 particles. This simple steel block also protects the PS system components from direct synchrotron
 5904 radiation (SR), BH radiation, and unwanted stray particles.

5905 The PS was needed at ZEUS due to challenges introduced by upgrades to the HERA accelerator,
 5906 which significantly increased luminosity and, consequently, the rate of BH events [?]. The stronger
 5907 beam focusing and increased synchrotron radiation (SR) — radiation resulting from the bending
 5908 of electrons by the magnet—led to a higher pile-up of photons in the DPD, increasing the uncer-
 5909 tainty in luminosity measurements from 1% to 3% [?]. The PS, positioned outside the SR fan and
 5910 unconverted photon flux, experienced a lower pile-up due to fractional pair conversion. This intro-
 5911 duction reduced the uncertainties in rate measurement to 2% [?], and additionally both detectors
 5912 were utilized to monitor real-time detector inefficiencies and manage systematic uncertainties.

5913 8.3.8.1 The luminosity system

5914 This ZEUS luminosity monitor design serves as a baseline for EIC but the expected luminosity
 5915 at EIC will be about 10^2 to 10^3 times that of ZEUS [?]. This directly leads to several challenges
 5916 faced during the upgrade of HERA, such as beam size effects (BSE), increased SR backgrounds,
 5917 and higher pile-up from BH radiation, becoming much more pronounced at the EIC. In addition
 5918 to these, the EIC will also feature electron beams colliding with a diverse range of hadron species,
 5919 from protons to heavy nuclei like gold, lead, and uranium. This in turn dramatically increases the
 5920 BH rates by a factor of Z^2 , making pile-up at detectors even more difficult to manage. Furthermore,
 5921 both the electron and light hadron beams will be polarized, adding another layer of complexity. In
 5922 the following section, we will discuss these challenges in more detail and outline how the "up-
 5923 graded" luminosity monitor of EIC will overcome them.

5924 **Beam Size Effect -** The BH process in electron-proton collisions is notable for its extremely
 5925 small momentum transfers between the radiating electron and the proton. It is kinetically possible
 5926 for both particles to continue along their initial paths without angular scattering, while the BH

5927 photon is emitted in the direction of the electron's momentum. This specific configuration results
 5928 in the smallest virtuality (Q_{\min}^2) of the exchanged photon [?]. At high-energy colliders, this minimal
 5929 photon virtuality becomes incredibly small. For instance, at HERA, the Q_{\min}^2 for a photon energy
 5930 of 1 GeV can be as low as 10^{-8} eV². Consequently, the typical transverse momentum transfer (q_{\perp})
 5931 reaches values around 10^{-4} eV/c. Since the BH differential cross section is proportional to Q^{-4} ,
 5932 photon virtualities near Q_{\min}^2 dominates the process and allows for the approximation,

$$Q^2 = Q_{\min}^2 + q_{\perp}^2$$

5933 and not to forget the scenarios with $q_{\perp} = 0$ is also feasible. Analyzing the process in impact
 5934 parameter space reveals that these small q_{\perp} values correlate to large impact parameters ($b = \hbar/q_{\perp}$),
 5935 explaining the precision of Bethe-Heitler cross-section calculations in the Born approximation.

5936 The derivation of the two-particle rate (R) relation with the collision luminosity (L) and cross-
 5937 section (σ)

$$R = L\sigma \quad (8.1)$$

5938 assumes both beams to be modeled as simple plane waves with a uniform impact parameter dis-
 5939 tribution. However, this assumption falls short when beams are strongly focused at the interaction
 5940 point, as focusing suppresses large impact parameters. Consequently, the BH differential cross sec-
 5941 tion is predominantly "over-sampled" at low impact parameters where the cross-section value is
 5942 smaller. This results in an effective suppression of BH. This is particularly pronounced at lower
 5943 photon energies, since typical q_{\perp} is proportional to E_{γ} .

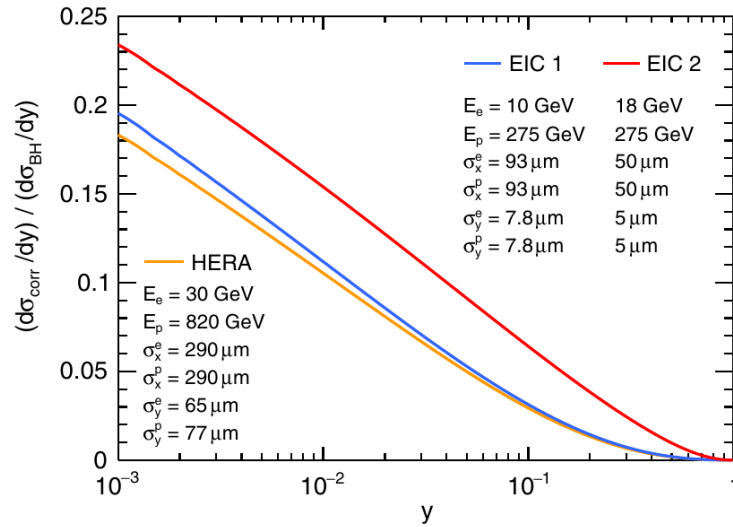


Figure 8.151: Relative suppression due to the BSE $(d\sigma_{corr}/dy)/(d\sigma_{BH}/dy)$ is shown as a function of $y = E_{\gamma}/E_e$ for three cases of collider parameters, HERA, EIC 1 & EIC 2. The corresponding beam energies and Gaussian lateral beam sizes at the interaction point are listed [?].

5944 Relative corrections to the standard Bethe-Heitler cross-sections due to the BSE is shown in figure
 5945 (8.151). Here the observed suppressed BH cross-section is related to the Bethe-Heitler cross-section

5946 as $(d\sigma_{obs}/dy) = (d\sigma_{BH}/dy) - (d\sigma_{corr}/dy)$. It is worth noting that even after higher beam energies
 5947 at HERA, the BSE will be higher at EIC due to a stronger focused beam as evident from beam size
 5948 parameters. In a recent study, the BSE is proposed to be corrected by a precise measurement of
 5949 the BH spectra as a function of lateral beam displacements (indirectly the impact parameter) at the
 5950 interaction point. This will be achieved using Van der Meer scans, commonly performed at hadron
 5951 colliders. This involves systematically varying the beam positions and crossing angles to find the
 5952 L as a function of lateral beam displacement, which can be described by the formula

$$L(B) = L(0) \exp\left(-\frac{B^2}{2(\sigma_1^2 + \sigma_2^2)}\right)$$

5953 Here, B represents the lateral displacement of one of the beams within either the horizontal or
 5954 vertical plane, σ_1 and σ_2 are the two Gaussian widths in a given plane, often assumed to be equal,
 5955 and $L(0)$ corresponds to the luminosity of nominal, head-on collisions. However, in the case of BH,
 5956 its photon spectrum will also be modified in a very specific manner, reflecting the BSE.

5957 **High rate of BH radiation and SR background -** The bunch crossing rate at EIC will be set
 5958 to 100 MHz for 5 and 10 GeV electron beam and 25 MHz for 18 GeV electron beams [?]. When this
 5959 rate is multiplied by the BH photon production rate per bunch crossing, as illustrated in Figure
 5960 (8.152), the resulting photon rates reaching the detectors looks substantial. For instance, with a 5
 5961 GeV electron beam and a 41 GeV proton beam, the coincidence rate (the rate when both the pair
 5962 converted pairs are detected simultaneously) at the Photon Spectrometer (PS) can reach approxi-
 5963 mately 90,000 photons per second. The BH photon rates during electron-nuclei interactions will be
 5964 proportional to the square of nucleus's atomic number. Therefore for the same setup but 41 GeV
 5965 Gold nuclei beams will result coincidence rate equivalent to $79^2 \times 90000 = 56 \times 10^7$ photons per
 5966 second.

5967 SR, similar to BH radiation, is emitted at very small angles ($\sim m_e/E_e$) relative to the instantaneous
 5968 direction of an electron beam's motion. At the EIC, the electron beam exiting the interaction region
 5969 passes through two quadrupole magnets, Q1eR and Q2eR, followed by a dipole magnet, B2eR. The
 5970 electron beam passes through the center of the quadrapoles and consequently, the B2eR magnet is
 5971 the sole source of direct SR impacting the far-backward region. **[Calculation of SR rates at EIC?**
 5972 **Comment quantitatively on how much sweeper helps in subsequent paragraph.]**

5973 To address the issue of high photon flux and its associated pile-up, as well as to mitigate the high
 5974 SR background, the luminosity monitoring system has been redesigned to include two new com-
 5975 ponents: a sweeper magnet and a thin converting foil, both positioned between the EW and the
 5976 spectrometer magnet, as illustrated in Figure (8.153). The enormous BH radiation and SR pass
 5977 through the exit window, resulting in substantial pair conversions. These converted particles are
 5978 deflected by the Sweeper magnet, leading to a reduced photon flux, with a large percentage be-
 5979 ing BH photons. These photons then encounter a thin converter made of the same material as the
 5980 exit window. This setup results in fewer pair conversions reaching the PS and an overall reduced
 5981 photon flux to the DPD.

5982 For electron beams at 10 and 18 GeV, the SR flux is substantial, with power reaching the exit win-
 5983 dows potentially exceeding 4 kW. To mitigate this, it was proposed to divide the dipole magnet into
 5984 two segments. The first segment, relevant to luminosity detectors, has a magnetic field about four
 5985 times weaker than that of B2eR. This modification is crucial to minimize the direct SR flux, which
 5986 is vital for accurate luminosity measurements, as it influences both PS and DPD readings [?].

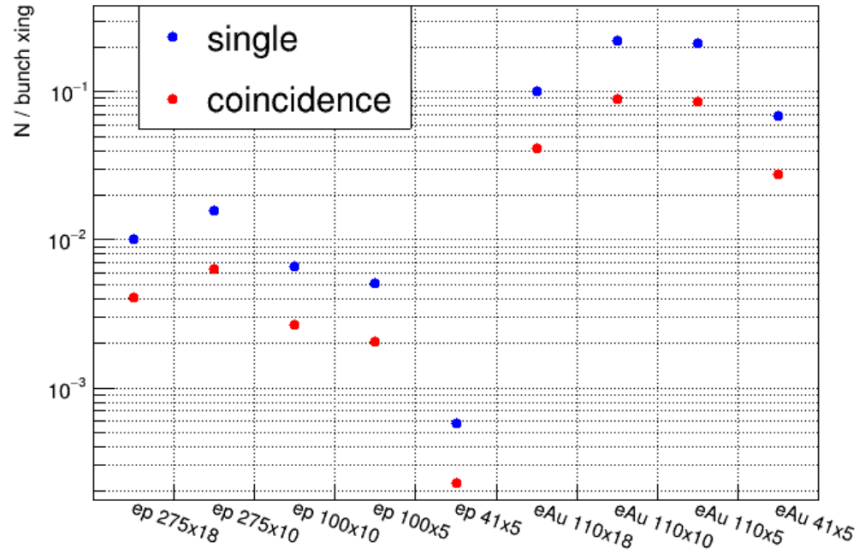


Figure 8.152: Rate of single and coincidence events for the PS detectors calculated by Dr. Gangadharan

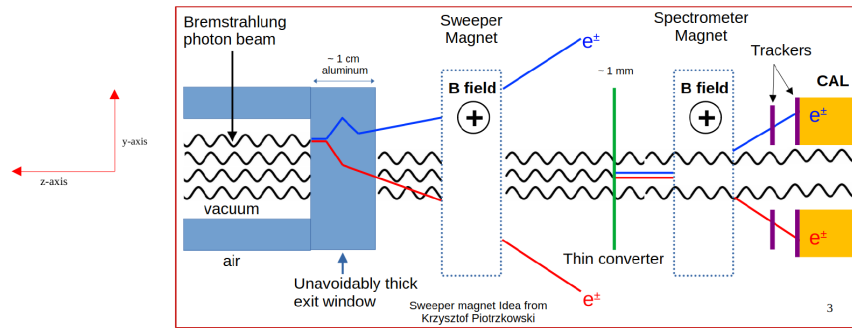


Figure 8.153: The layout of the luminosity monitor in the ePIC experiment of the EIC.

5987 **Beam Polarisation** - The electron and light ion beams at the EIC will be polarized both longi-
 5988 tudinally and transversely. A recent study investigated the impact of longitudinal beam polariza-
 5989 tion on the Bremsstrahlung cross-section in the low- q^2 region [?]. Numerical calculations revealed
 5990 that the polarized component is significantly suppressed compared to the unpolarized component,
 5991 by a factor of $m_e^2 / E_e E_p$. Figure (8.154) illustrates the unpolarized component first calculated by
 5992 Bethe-Heitler, alongside the polarized component. However, no calculation exists for transversely
 5993 polarised beams and also with the effect of nuclear recoil.

5994 **Physical Constraints** - The components of the luminosity monitoring system are placed within
 5995 the beam tunnels and are therefore constrained by the beam pipes and the equipment required to
 5996 maintain the beam, such as magnets and cooling systems. The majority of the system is located
 5997 sixty meters back from the interaction region to provide sufficient space for the magnets and detec-
 5998 tors to operate without interfering with the beam. The long air column between the exit window
 5999 and the PS calorimeters is approximately 46 meters. The “unconverted” photon beam from the

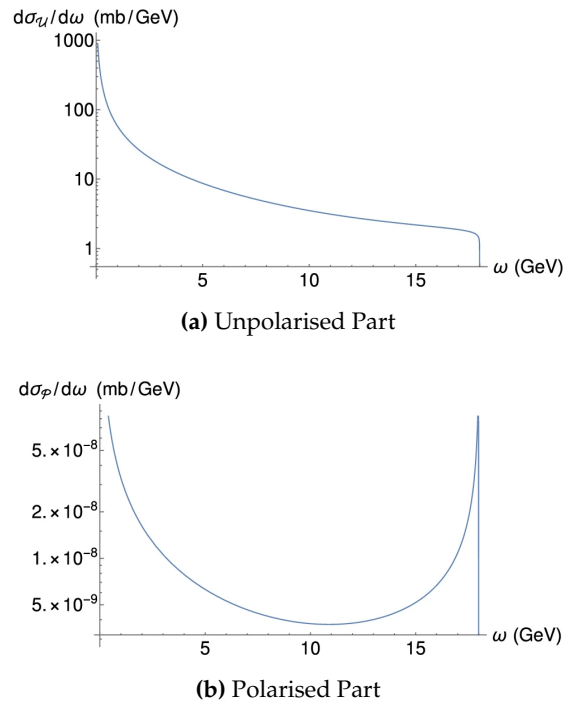


Figure 8.154: Unpolarised and polarised Bethe-Heitler Cross-Section. [?]

6000 exit window undergoes pair conversions, which are quite significant (approximately 10%) and in-
 6001 determinate during experimentation due to variability in air composition. Most of the unwanted
 6002 pair conversions occur between the exit window and the sweeper magnet and are swept away by
 6003 the sweeper. To reduce pair conversions in the air column between the sweeper magnet and the
 6004 spectrometer magnet, a helium or partial vacuum chamber will be installed between the magnets.
 6005 The thin converter will remain at the same location but will be placed inside this vacuum chamber.

6006 **Add paragraph outlining requirements on magnets imposed by physical space limitations.**

6007 **Systematic Uncertainties -** The systematic uncertainty in the luminosity measurement at ZEUS
 6008 was 1.7 %, and our goal is to reduce this value to below 1 %. Table 8.38 summarises the main
 6009 systematic uncertainties that contributed to the ZEUS luminosity determination. In our current
 6010 design, we ensure we mitigate the largest of these sources with the introduction of trackers for the
 6011 PS, that would enable an accurate determination of the detector acceptance and beam size effects,
 6012 and a sweeper magnet that allows us to have more control on the converted pair rates in the PS.

6013 **Design and Components** A two-level review of all the components of luminosity monitor is
 6014 presented below. First, a short review on the component's material, location & dimension, and
 6015 a longer version with detailed description of each component requirement, design with simula-
 6016 tion or test-beam results. Note that all length measurements are in centimeters unless otherwise
 6017 mentioned.

- 6018 • Exit Window
- 6019 – Material - Aluminum

Source	DPD detector (%)	PS detector (%)
Acceptance	1.0	1.0
x-position of photon beam	1.2	1.2
Pair conversion in EW		0.7
RMS Cut Correction		0.5
Pedestal Shifts	1.5	
Pile up	0.5	
Total	2.2	1.8

Table 8.38: Summary of systematic uncertainties at ZEUS DPD and PS detector. [?]

- 6020 – Location - (0.0, 0.0, - 1850.5)
- 6021 – Dimension - (4.0, 4.0, 1.0)
- 6022 • Collimator
- 6023 – Material - Stainless Steel
- 6024 – Location - (0.0, 0.0, - 2260.0)
- 6025 – Hollow Structure, Outer Dimension - (6.5, 6.5, 30.0), Inner Dimension - (4.832, 4.832, 30.0)
- 6026 • Sweeper Magnet
- 6027 – 0.5 T horizontal magnetic field.
- 6028 – Location - (0.0, 0.0, - 5600.0)
- 6029 – Main Body Structure, Outer Dimension (75.972, 94.0, 120.0), Inner Dimension - (42.032, 61.262, 120.0)
- 6030 – Magnetic Coils Structure (How to describe ?)
- 6031
- 6032 • Photon Vacuum Chamber
- 6033 – Material - Pipe : Aluminum & End caps : Beryllium
- 6034 – Location - (0.0, 0.0, - 5800.0)
- 6035 – Pipe Structure, Outer Dimension (6.3119, 2π rad, 555.0), Inner Dimension (6.119, 2π rad, 555.0)
- 6036
- 6037 • Converter Foil
- 6038 – Material - Aluminum
- 6039 – Location - (0.0, 0.0, - 5800.0)
- 6040 – Disk Dimension - (6.119, 2π , 0.1)
- 6041 • Spectrometer Magnet
- 6042 – Location - (0.0, 0.0, - 6000.0)
- 6043 – Main Body Structure, Outer Dimension (75.972, 94.0, 120.0), Inner Dimension - (42.032, 61.262, 120.0)
- 6044 – Magnetic Coils Structure (How to describe ?)
- 6045
- 6046 • PS Trackers
- 6047 – Type - AC-LGAD
- 6048 – Locations
- 6049 * Module 1 : Top (0.0, 15.76, - 6397.6) and Bottom (0.0, - 15.76, - 6397.6)
- 6050 * Module 2 : Top (0.0, 15.76, - 6407.6) and Bottom (0.0, - 15.76, - 6407.6)
- 6051 – Dimension - (18.06, 18.06, 0.044)

- 6052 • PS Calorimeters
 - 6053 – Type - Electromagnetic sampling (spaghetti) calorimeter
 - 6054 – Material - Active : Scintillating Fiber (ScFi) and Passive : Tungsten (W)
 - 6055 * Tungsten as powder, held together with optical epoxy.
 - 6056 – Location - Top (0.0, 15.76, -6408.6) and Bottom (0.0, - 15.76, - 6408.6)
 - 6057 – Dimension - (18.06, 18.06, 17.2)
- 6058 • DPD Calorimeters

6059 **Exit window**

- 6060 • Needs exact study of its composition and irradiation studies.

6061 **Collimator**

- 6062 • Do we need any further study ?

6063 **Sweeper and Spectrometer magnet**

- 6064 • Mapping the magnetic field. Need info from magnet experts

6065 **Photon Vacuum Chamber**

- 6066 • need info from accelerator

6067 The thickness of the exit window for electrons and positrons must be minimized to reduce material interactions. However, if a vacuum chamber is selected instead of helium filled, a minimum
 6068 thickness of the exit window is required to withstand a pressure difference of 1 atm. The minimum
 6069 thickness of beryllium should exceed 3 mm to ensure structural integrity under these conditions.
 6070

- 6071 • Mapping the Pressure
- 6072 • Study of exact composition and thickness of two end caps.

6073 **Converter Foil** The converter foil is expected to operate in a vacuum, necessitating heat removal
 6074 due to synchrotron radiation (SR). Heat removal from the converter can be achieved through the
 6075 holder, utilizing one of two options: passive cooling or circulation of a coolant.

- 6076 • Study of exact composition, thickness and radiation dose.
- 6077 • Study of pair conversion percentage.
- 6078 • How this will reduce the error in position resolution.
- 6079 • Heat removal due to SR radiation.

6080 **PS Trackers**

- 6081 • PS trackers are required to reconstruct the vertex position at the conversion foil, which has a
6082 direct impact on determining acceptance. A vertex resolution of less than 6 mm is necessary
6083 to achieve an acceptance determination uncertainty of less than 1%.
- 6084 • This has not been studied yet; however, since the PS system is located away from the IP and
6085 positioned behind collimators and magnets, and not within the BH cone, the radiation levels
6086 are expected to be manageable.
- 6087 • AC-LGADs are chosen for their excellent position and timing performance. Due to the rela-
6088 tively small detection area and the fact that this technology is planned for FTOF, PS trackers
6089 will utilize a similar design.
- 6090 • Initial studies with the nominal 500 μm pitch are expected to provide a 2 mm resolution at the
6091 vertex (conversion foil).

6092 The tracking layers for the PS system are based on AC-LGAD technology with pixelated sensors.
6093 Each side will consist of two tracking layers, resulting in a total of four layers. AC-LGAD sensors
6094 will be placed on modules similar to the FTOF design. The pitch between the readout pads, set at
6095 500 μm , is expected to provide approximately 70 μm position resolution at the detector plane and
6096 around 2 mm at the vertex (conversion foil). Current estimations indicate that, in order to achieve
6097 acceptance uncertainties below 1%, the vertex resolution in the dispersive direction must be less
6098 than 6 mm. With a 500 μm pitch, the number of readout channels is estimated to be about 130,000
6099 per plane. To minimize the number of DAQ channels, the number of pixels in the non-dispersive
6100 direction could be combined.

6101 **PS Calorimeters** The two electromagnetic calorimeters (CALs) used for the PS are of the sam-
6102 pling type, colloquially known as spaghetti CALs. The active component of the CAL consists of
6103 plastic scintillating fibers (ScFi), while the passive, or "hard," component is tungsten (W). The vol-
6104 umetric ratio of W to ScFi in each CAL is 4:1. The CALs are composed of 20 layers, with the fibers
6105 in alternate layers oriented parallel to either the x-direction or y-direction in the transverse plane.
6106 This alternating orientation in 10 layers along each direction aids in reconstructing the shower pro-
6107 file of hits, thereby enhancing the position resolution of hits. Each layer has a thickness of 0.86 cm
6108 and a transverse size of $18.06 \times 18.06 \text{ cm}^2$. Additionally, the layers are segmented into three mod-
6109 ules, each with a width of 6.02 cm. Each module contains well-distributed 448 ($14 \times 2 \times 16$) fibers.
6110 Finally, a group of 16 fibers forms a single channel for readout. Each readout will be associated
6111 with a silicon photo-multiplier (SIPM).

6112 The two PS CALs are symmetrically positioned in the vertical plane, perpendicular to the photon
6113 flux i.e., along the y-axis. The gap between the two CALs is approximately 3σ , which is sufficient
6114 for the detectors to not obstruct the final photon flux from reaching the DPD. The PS CALs serve
6115 the purpose of measuring the energy and the transverse coordinates of the pair-converted photons,
6116 which enables the reconstruction of the photon energy spectrum and thus the determination of the
6117 beam luminosity.

6118 The acceptance of PS system is effected by four major parts of the PS system.

- 6119 • The collimator which obstructs some part of BH photons.
- 6120 • The sweeper magnet which removes the pair-conversions from EW.
- 6121 • The front end cap of the vacuum chamber whose pair-conversions are not detected in CALs.
- 6122 • The fiducial areas of the CALs whose signals are rejected.

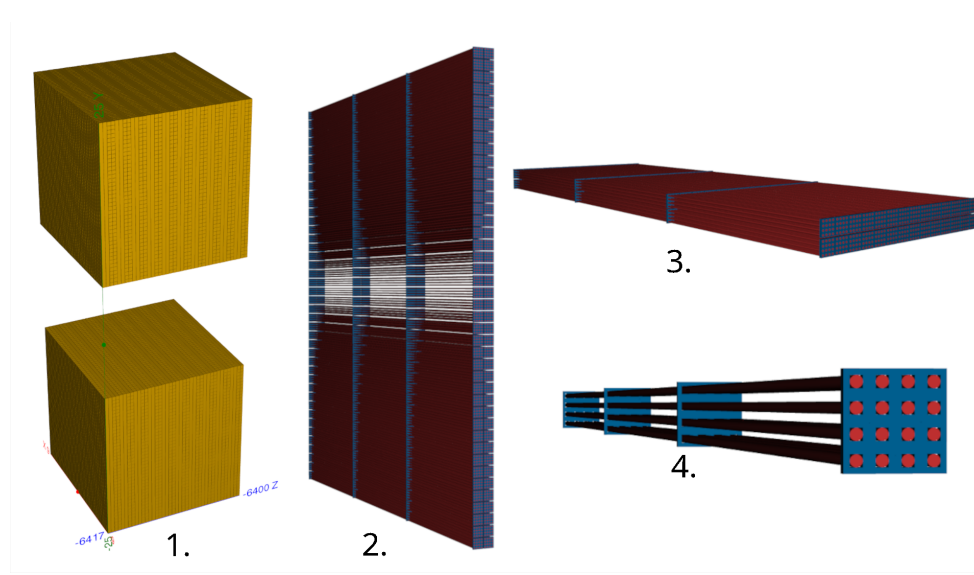


Figure 8.155: DD4hep implementation of PS Calorimeters.

6123 Plot the acceptance curve.

6124 **DPD**

6125 **Collaborators and their role, resources and workforce:** The main collaborating institutions
6126 for the PS calorimeter are York and Houston. The roles of each institution are outlined below -

- 6127 • University of York, United Kingdom
 - 6128 – Design and construction of calorimeters
 - 6129 – Calorimeter simulation
 - 6130 – Calorimeter reconstruction and analysis
 - 6131 – DAQ and electronics for calorimeter
- 6132 • University of Houston, Texas, USA
 - 6133 – Calorimeter simulation
 - 6134 – Calorimeter reconstruction software
 - 6135 – Calorimeter design support
- 6136 • Tel Aviv University, Israel
 - 6137 – Design and integration of PS trackers.
 - 6138 – Simulation.

6139 The workforce at each institution is comprised of -

- 6140 • University of York, United Kingdom
 - 6141 1. Dan Watts, academic staff (20-25 % FTE)
 - 6142 2. Nick Zachariou, academic staff (25-30% FTE)

- 6143 3. Mikhail Bashkanov, academic staff (10-15% FTE)
 6144 4. Stephen Kay, PDRA (100% FTE)
 6145 5. Alex Smith, PG Student (100% FTE)
 6146 6. Pankaj Joshi, academic support staff (5% FTE)
 6147 7. Julien Bordes, Geant4/simulation support (10-15% FTE)
 6148 8. Technical Support Staff
 6149 – Electrical engineering
 6150 – Mechanical engineering
 6151 – CAD support
- 6152 • University of Houston, Texas, USA
 - 6153 1. Dhevan Gangadharan, academic staff (X% FTE)
 - 6154 2. Aranya Giri, PG Student (100% FTE)
 - 6155 • Tel Aviv University, Israel
 - 6156 1. Igor Korover, academic staff (15% FTE)
 - 6157 2. Avishay Mizrahi, Mechanical engineer (50% FTE).

6158 Note that where an FTE range is presented, this represents a min/max value.

6159 **Risks and mitigation strategy:** Add text here.

6160 **Additional Material** Add text here.

6161 8.3.8.2 The low Q^2 taggers

6162 **Requirements** The Low- Q^2 Tagger sits close to the electron beamline and consists to two mod-
 6163 ules - each with silicon trackers and a calorimeter. This is shown in Figure 8.156.

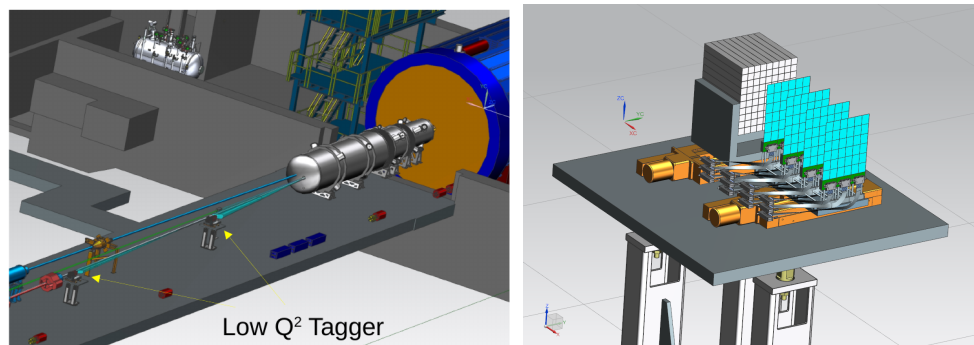


Figure 8.156: Left: Low- Q^2 taggers in relation to beamlines and central detector. Right: Tagger module with calorimeter and tracker from recent CAD model.

6164 **Requirements from physics:** The acceptance for the low- Q^2 tagger should complement the
 6165 central detector to reach the coverage close to the limits given by the divergence of the beam and
 6166 beamline magnets. Low- Q^2 tagger will have one or more stations to cover the maximum momen-
 6167 tum acceptance.

6168 The Low- Q^2 tracking system shall have a spatial resolution providing a momentum resolution $<$
 6169 5% with Q^2 acceptance between 0 and 0.1 GeV^2 . The acceptance ranges of the Central Detector and
 6170 Low- Q^2 Trackers as function of Q^2 and x are shown in Figure 8.157, and the positions and angular
 6171 acceptances of the tracker are illustrated in Figure 8.158.

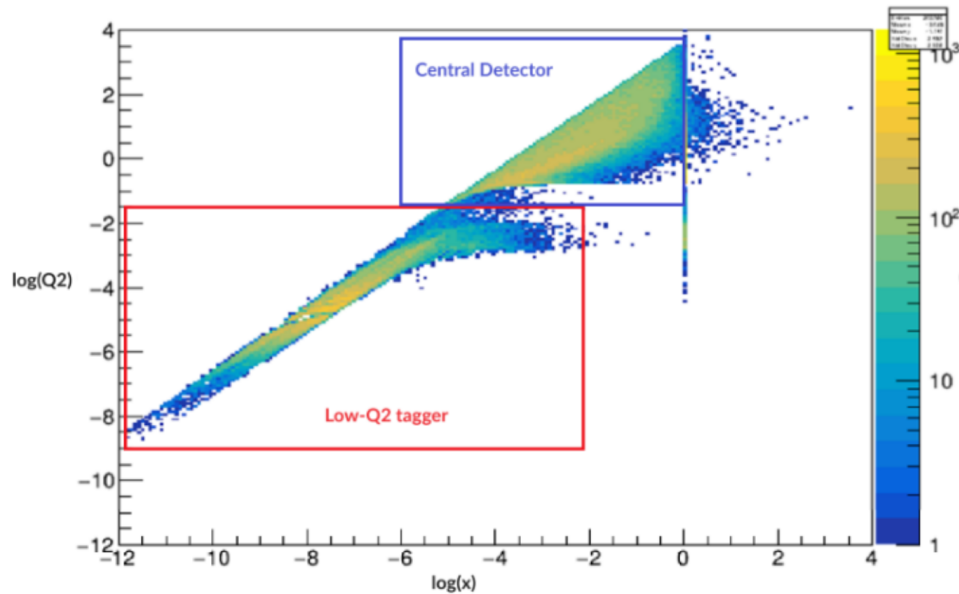


Figure 8.157: Acceptance ranges of the Central Detector and Low- Q^2 Trackers as function of Q^2 and x .

6172 *More on resolution here? Too much here on spectroscopy - maybe reduce and more from the ArXiv*
 6173 *paper blurb. Or add other sections with other physics titles. I added two.*

6174 8.3.8.3 TCS

6175 Add text

6176 8.3.8.4 Vector Meson production

6177 Add text

6178 8.3.8.5 Spectroscopy

6179 *Reduce - only want to know how it influences the detector requirements.* Electron-ion collisions,
 6180 where the electron is scattered through a very shallow angle, correspond to the case where the

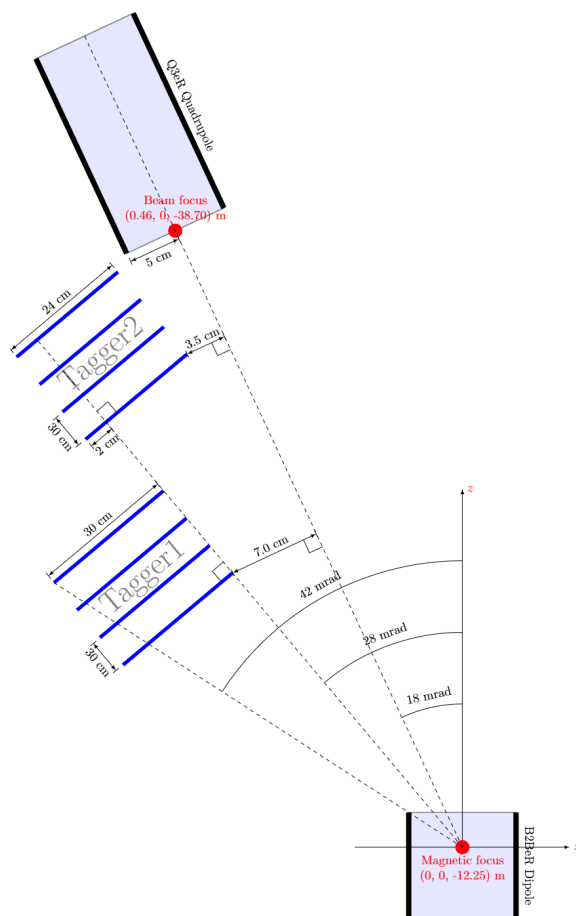


Figure 8.158: Low- Q^2 tagger coverage.

6181 exchanged photon is almost real. Such photoproduction processes are of interest in their own right,
 6182 but also can enable a program of hadron spectroscopy. Furthermore, as the virtual photon flux is
 6183 highest in this region, yields may be relatively high or rare states may be searched for.

6184 A topic of particular interest is the photoproduction of exotic charmonium-like mesonic states.
 6185 Commonly referred to as XYZ spectroscopy, these states were originally seen in decays containing
 6186 J/ψ mesons and additional products. Despite there being many missing charmonium states these
 6187 states do not fit the quark model expectations in terms of numeracy, masses or widths. While the
 6188 Z_c^+ states were manifestly exotic as their charge required additional constituent quarks to a $c\bar{c}$ pair.

6189 The production cross section of these states is expected to be low, of order 1 nb and branching ratios
 6190 to particles that can be detected can also be small. Therefore tagging a large fraction of the virtual
 6191 photon flux is essential for making measurements of exclusive production of these states. The
 6192 energy of the tagged photon can be used to determine the reaction invariant mass, W , and provide
 6193 exclusivity discrimination when combined with the measured meson state from the central detector
 6194 and hadron from the far-forward region.

6195 Reconstruction of the azimuthal angle for the electron would provide an effective linearly polarised
 6196 photon beam, with polarisations up to 1 when the tagger electron energy is close to the beam en-
 6197 ergy. Reconstructing this angle will be challenging and probably only possible with sufficiently

6198 high scattering angles. Provided this information alongside the virtual photon degree of polari-
 6199 sation, which will mainly depend on the measured energy, would allow additional constraints to
 6200 be used in partial wave analysis of the meson decay allowing the production amplitudes to deter-
 6201 mined.

6202 The Q^2 of the scattering is not directly of use for these reactions, however ultimately it can be used
 6203 to reject bremsstrahlung electrons which would improve the analysis.

6204 Count rate estimates were performed for a number of exotic states in [?] including branching ra-
 6205 tio through to detected particles and using the models developed in [?] . To summarise for the
 6206 charmonium-like XYZ states they are expected to be of the order 1000 per day at luminosities of
 6207 $10^{34} \text{cm}^2 \text{s}^{-1}$, while for double J/ψ or Z_b decays there may be 10s per day.

6208 Given just providing evidence of the existence of these states in photoproduction would be a great
 6209 result, as few of these states have been seen in more than one production mechanism, tagging
 6210 efficiencies of 10% would be sufficient. However to perform detailed physics studies to determine
 6211 quantum numbers and production amplitudes, which may provide insight into their exotic nature,
 6212 or to measure rarer states such as the Z_b , large data samples would be required.

6213 **Requirements from Radiation Hardness:**

6214 The Low- Q^2 trackers are in the far backward region, where the incident flux is predominantly
 6215 from bremsstrahlung electrons (MIPS). This means there is no requirement for a radiation hard
 6216 classification for the trackers. However, the intensity is focused on a narrow band in the bend
 6217 plane (see Figure 8.159), particularly close to the beam line, and trackers should be designed to
 6218 *spread the load* by period vertical translation, and exchange of modules.

6219 **Requirements from Data Rates:**

6220 The Low- Q^2 system must operate at a full projected EIC luminosity.
 6221 The Low- Q^2 system must operate in extreme background conditions (synchrotron radiation,
 6222 bremsstrahlung events and beam gas) at the levels specified by the simulation studies.
 6223 The Low- Q^2 trackers shall provide timing resolution sufficient to resolve 10 ns beam buckets.
 6224 The Low- Q^2 tagger will be able to measure the momentum of more than 10 electrons per bunch
 6225 crossing.
 6226

6227 The rate distributions, based on simulation, are illustrated in Figure 8.159. It is clear that the raw
 6228 rates on the detectors are dominated by bremsstrahlung, with increasing intensity closer to the
 6229 bend plane, and to the beam line. These results can be used to calculate the integrated data rates
 6230 for DAQ and storage, and the bottom right plot can be used to estimate the maximum rate which
 6231 the tracker must be able to handle, in terms of pixel, column, sensor and board. The rates are
 6232 summarised in Figure 8.160.

6233 **Justification**

6234 **Device concept and technological choice:** As described above, the Low- Q^2 detector will con-
 6235 sist of two separate taggers, each with a silicon tracker and a calorimeter. For the trackers, the
 6236 positions and layer spacing are still to be optimised on the basis of simulations. The essential char-
 6237 acteristics are angular resolution (since all other quantities are derived from polar and azimuthal
 6238 angles), rate capability and background rejection. For pixel detectors, the angular resolutions relate

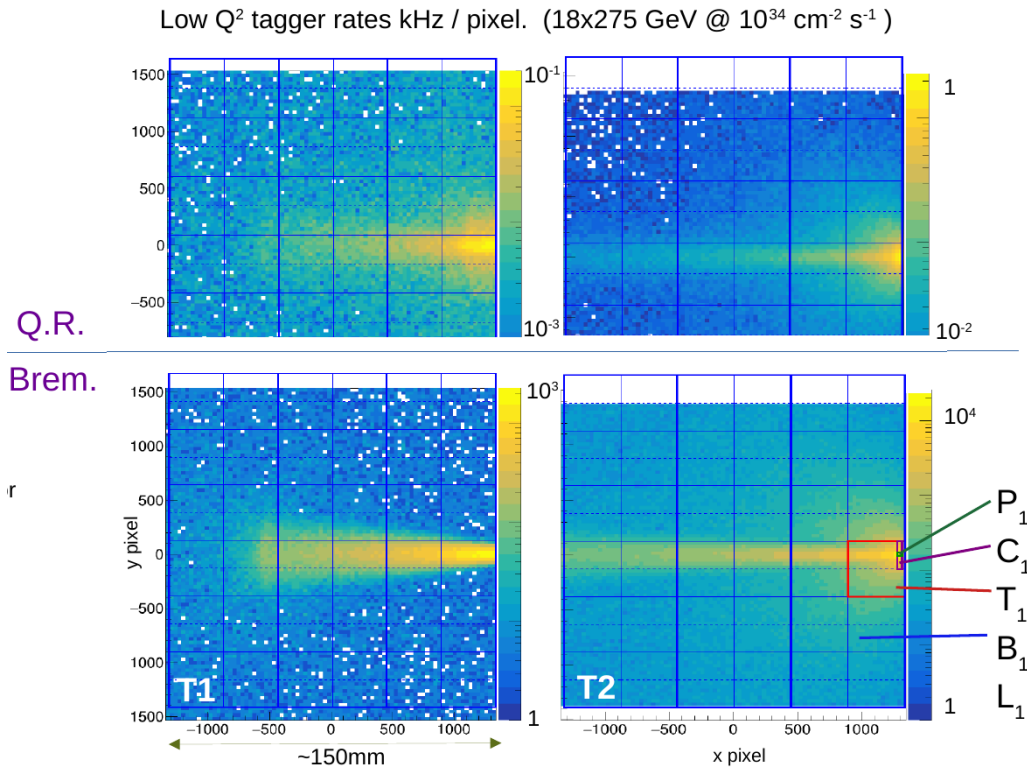


Figure 8.159: Hit rates on tracker layers for Quasi Real (Top) and bremsstrahlung (bottom) electrons, incident on Tagger 1 (left) and Tagger 2 (right). This design is based on layers with three carrier boards, each containing twelve Timepix4 hybrid sensors. The dashed lines indicated the centre lines of the Timepix4 ASICs, where the vertical columns terminate.

6239 to pixel size, or, more precisely, to the position resolution of the centroids of pixel clusters. From the
 6240 simulations it is clear that $55 \mu\text{m}$ pixels (Timepix4 pixel size) would provide very good resolution.
 6241 Bigger pixels would still provide acceptable resolution, but high segmentation is even more im-
 6242 portant for rate capability, where the efficiency for separating multiple tracks within a single event
 6243 needs to be as high as possible: For an electron-proton collision event, at maximum luminosity
 6244 there are typically ten background bremsstrahlung electrons within the same beam bucket, each
 6245 passing through all layers of a tagger and creating hits. Furthermore, in each layer there will be
 6246 *singles* resulting from rescattering, or synchrotron radiation, together with hits from detector noise.
 6247 However, we already have enough information to set some constraints on detector and readout
 6248 technologies. We have used Timepix4 as the template for much of the development, and have had
 6249 its dimensions, readout and rate capabilities as a strong influence in the development of the cur-
 6250 rent design. However, where possible, we used *generic* pixel detectors - particularly in the Geant4
 6251 simulations, with the aim of being able to evaluate other current, or emerging, technologies.

6252 It is already clear, both from a basic knowledge of the kinematics of bremsstrahlung and quasi-
 6253 real events, and from preliminary simulations, that the intensity of electrons passing through the
 6254 trackers will be distributed in a highly non-uniform way, with the bulk of the events close to the
 6255 plane of the accelerator, and the flux increasing strongly towards the electron beamline. In particu-
 6256 lar, the rates on Tagger 2 are significantly higher than Tagger 1, with the hottest zone closest to
 6257 the beamline (Figure 8.160). For an estimate of the relevant rates we focus on the bremsstrahlung

Maximum rates		
Pixel (P1)	70 kHz	
2 column (C1)	8 MHz	
Tpix4 (T1)	600 MHz	38 Gb/s
Board (B1)	1500 MHz	96 Gb/s
Layer (L1)	2500 MHz	160 Gb/s
Total integrated rates		
Tagger 1	2 GHz	130 Gb/s
Tagger 2	7 GHz	480 Gb/s
Total	9 GHz	600 Gb/s
Data buffered & filtered:	need a hadron in main detect	
Trigger rate: 500 kHz:	99.4% rejection (brem only)	
Data rate (signal):	4 Gb/s	
Data rate (incl BG and rand sample)	<20 Gb/s To tape	

Figure 8.160: Maximum and integrated rates for Low- Q^2 trackers.

6258 distribution in Tagger 2 and superimpose a tracking layer geometry based on three boards, each
 6259 consisting of 12 Timepix4 hybrids, as shown in Figure 8.159. The six Timepix4 detectors running
 6260 across the centre of Tagger 2 take the bulk of the events, with the very highest on the one closest
 6261 to the electron beam (T1). The small vertical offset between the centre of the board and the accel-
 6262 erator plane is to ensure that the centre line (dashed), where the top and bottom vertical 255 pixel
 6263 columns meet, does not coincide with the very high rate band. The maximum rate estimates can be
 6264 obtained by integrating over the relevant bins of the 2D histogram, and are shown in Figure 8.160.
 6265 Although the dimensions of pixels and sensors are from Timepix4, these rates are *detector agnostic*,
 6266 in the sense that they merely quantify numbers of electrons passing through the $55\mu\text{m}$ pixels in the
 6267 tracking plane. After comparison with other technologies with other technologies proposed for
 6268 the ePIC detector (MAPS, AC-LGAD) it became clear that Timepix4 is the only solution which can
 6269 provide the required combination of rate capability, timing resolution and position resolution. **The**
 6270 **calorimeter paragraph.**

6271 The final configuration and position of the Low- Q^2 tagger is still to be decided, since it depends
 6272 on the position and structure of the magnets and beamline configuration in the backward regions.
 6273 These are not yet finalised.

6274 Subsystem description Tracker :

6275 There are two trackers, each consisting of four layers on pixel sensors. The sensors are
 6276 mounted on carrier boards (12 sensors per board) which connect to a readout modules. Read-
 6277 out modules perform some presorting and pass data to cluster and tracking modules and data
 6278 buffers. Tracks which are in coincidence with a hadron in the central detector are saved in the
 6279 main DAQ readout.

6280 Sensors: Timepix4 ASIC with Silicon sensor.

6281 FEE: SPIDR4 readout to custom FPGA clustering and tracking modules.

6282 Other components: Frame / infrastructure with cabling and cooling for layers with removable
 6283 carrier boards. Cabling from boards to readout modules (housed below on platform).

6284 **Subsystem description Calorimeter:** Main purpose of the calorimeter is direct energy mea-
 6285 surement for cross check with energy obtained from trackers, where it is measured indirectly via
 6286 ML methods. Also alignment and fake-track reduction will benefit from the use of the calorimeter.

6287 General device description: In the initial running at lower luminosity when in-bunch pileup
 6288 from Bethe-Heitler bremsstrahlung is relatively small it is assumed to share the same technol-
 6289 ogy as luminosity pair spectrometer, i.e. scintillating fibers embedded in tungsten-powder
 6290 epoxy (SciFi), read-out by SiPMs. General layout of the SciFi calorimeter is indicated in
 6291 Fig. 8.161, giving tower arrangement of 4 layers. Total perpendicular size is given by the track-
 6292 ers. The towers are arranged perpendicular to shower axis. Fibers inner radius is 0.25 mm,
 6293 fiber spacing is 1 mm. Optical photons are detected by SiPMs, shown as yellow rings at the
 6294 end of each fiber. It is assumed that groups of 4x4 fibers in the same cell act as a single SiPM.
 6295 Opposite ends of the fibers are ended by aluminum mirrors, shown as green caps.

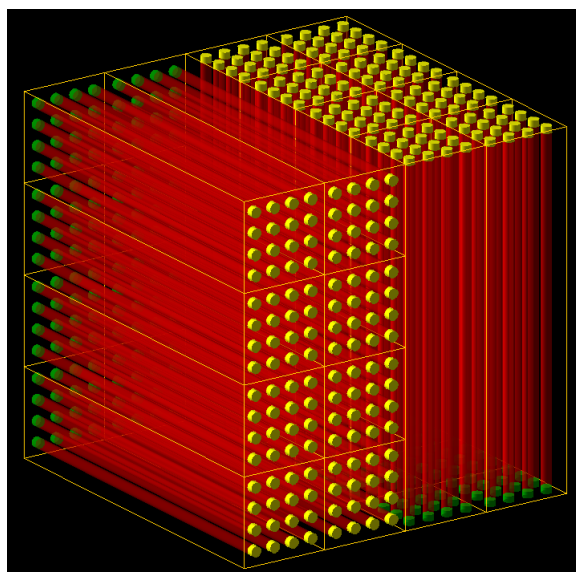


Figure 8.161: Layout of SciFi calorimeter.

6296 For the case of nominal collider luminosity, reached in later runs, the in-bunch pileup from
 6297 Bethe-Heitler bremsstrahlung will cause calorimeter rates to reach bunch crossing frequency,
 6298 giving some signal every 10 ns at top luminosity for 10x100 GeV beams. Calorimeter technol-
 6299 ogy will be shared with luminosity direct photon detector, where only Cherenkov fibers can
 6300 fulfill the rate requirement. Expected energy resolution is shown in Fig. 8.162

6301 Diameter for quartz fibers 1.5 mm, fiber spacing is 2.5 mm. The resolution is mainly driven
 6302 by limited Cherenkov photon yields. Photon detection efficiency of 0.41 is included.

6303 Sensors: SiPM, specific SiPM with fast capacitive coupling is required for nominal luminosity,
 6304 possible example is Onsemi 30035 series.

6305 FEE: fADC250 (flash ADC, 250 MSPS, 12 bit) for nominal luminosity

6306 Other components: Add text here.

6307 **Performance** Figures 8.163, 8.164 and 8.165 show the performance of the Trackers based on cur-
 6308 rent simulation.

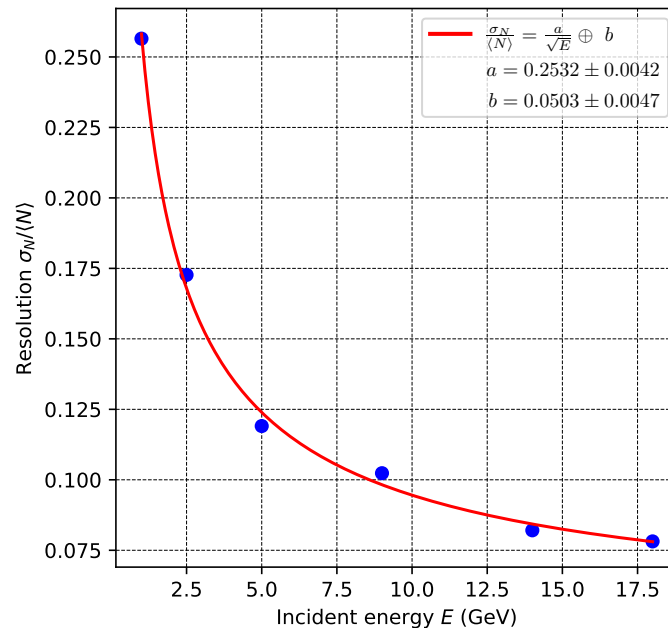


Figure 8.162: Energy resolution for Cherenkov fiber calorimeter.

6309 Implementation

6310 **Services:** No special services.

6311 **Subsystem mechanics and integration:** The taggers are housed on platforms which need to
 6312 be movable in vertical and horizontal (towards beamline) directions. Lower platform for readout
 6313 modules in close proximity for readout modules. Bias and LV per board (24 total). Chiller (800W)
 6314 per tagger.

6315 **Calibration, alignment and monitoring:** Procedures for calibration and equalisation of indi-
 6316 vidual sensors are already well established within the Medipix collaboration. These will be mapped
 6317 to a dedicated Slow Controls interface for the tracker. Alignment and timing calibrations require
 6318 tracks; they can be developed locally using cosmic rays and more rigorously tested in beam at Jlab
 6319 or one of the European facilities.

6320 Status and remaining design effort:

6321 **More a total effort not just R&D**

6322 R&D effort:

6323 Electron tracker

6324 Total expected from UK Infrastructure project in FTE years:

6325 Academic 1.5

6326 Senior Researchers 2.5

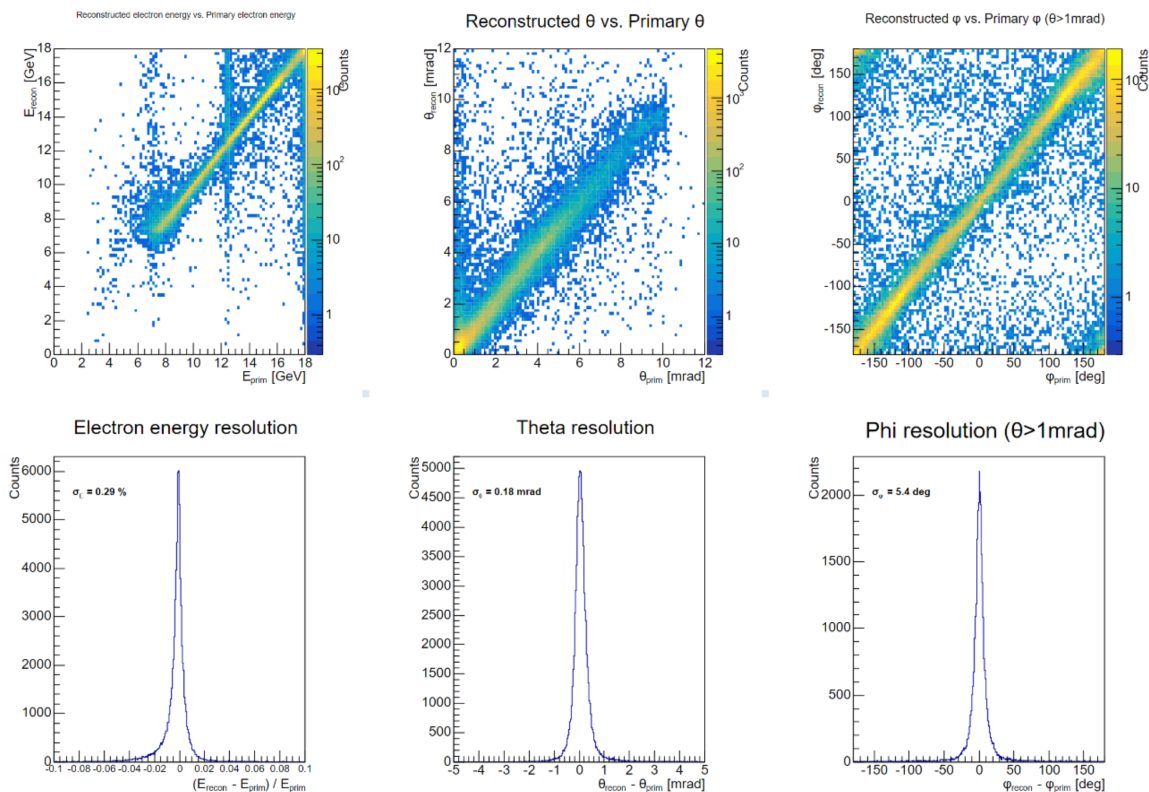


Figure 8.163: Top - Reconstruction of the initial electron energy, θ and ϕ angles from fitted tracks. Bottom - Integrated reconstruction difference.

6327 Postdocs 10.0
 6328 Technical 3.0
 6329 PhDs 10
 6330 Additional Requirement: Postdoc 6 FTE Years
 6331

R&D status and outlook:

Electron tracker:

6332 A test rig with SPIDR4 and Timepix4+Si sensors is complete, and fast readout tested. The
 6333 development of prototype tracker with single sensor layers in progress. To be tested in stand-
 6334 alone mode in Mainz, Dec24, with a further test using preliminary ePIC DAQ at Jlab in 2026.
 6335 Carrier board for 12 x Timepix4 sensors to be developed and approved by Dec 2027. Pro-
 6336 curement and fabrication of layers from Jan 2028 - 2030. Completion of taggers including
 6337 mechanical infrastructure, cooling, readout to be completed in Glasgow by Dec 2030 with
 6338 delivery to BNL Jan 31.
 6339

Other activity needed for the design completion

6340 Final decision on positioning, layer dimensions and spacing is still to be made. The requires
 6341 completion of designs for magnets, beamline and vacuum windows in the backward region.
 6342

Status of maturity of the subsystem:

Electron tracker

6343 The Timepix4 sensor is well established, and is the latest in a series of detectors by the CERN
 6344
 6345
 6346

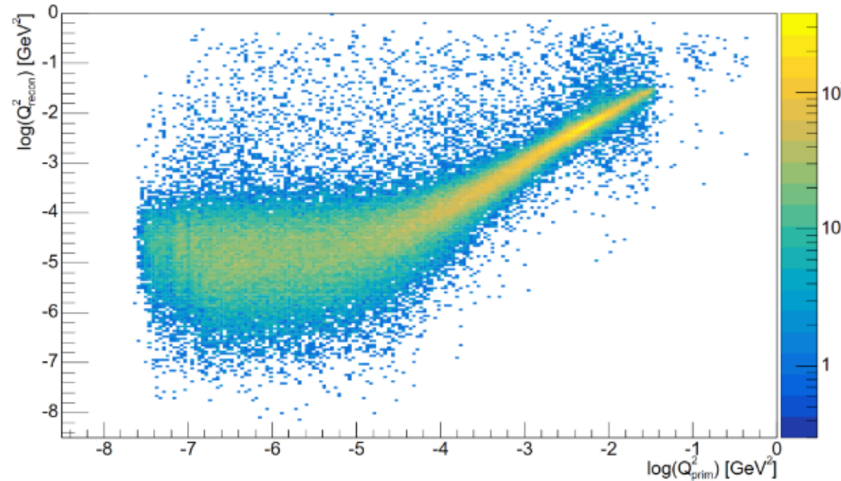


Figure 8.164: Reconstruction of the initial electron as a function of Q^2 .

6347 Medipix collaboration. Current applications used the wire-bonded readout mode, but the
 6348 TSV (through silicon vias) mode is in fast development, and we anticipate having a test setup
 6349 within the next few months. The TSV mode is required to allow 4-side buttability, and fabri-
 6350 cation of the layers with no dead space. The current readout uses SPIDR4 from the NIKHEF
 6351 group in Amsterdam. We will collaborate with the developers to make an upgraded version
 6352 of their carrier boards and readout to handle the data from the 12 sensor layer modules.

6353 **Environmental, Safety and Health (ES&H) aspects and Quality Assessment (QA plan-**
 6354 **ning:** We will follow all procedures laid out by BNL and other labs where production test and
 6355 development are carried out. During the engineering design phase, we will include production of
 6356 mockups and engineering test articles to insure the proper functionality and quality, and will have
 6357 full production chain tests for each sub-system.

6358 For operation with HV and cooling we will ensure that these are mechanically secure and not a
 6359 trip hazard, have proper warning signs and follow the lab procedures for electrical safety, and
 6360 for operation near the beam-pipe and vacuum, anyone working near the far-forward/backward
 6361 detectors will wear ear protection, and will post signage to that effect.

6362 **Construction and assembly planning:** The tracker modules will be constructed assembled
 6363 and tested in Glasgow as Work Package 2 (WP2) of the UK's EIC Infrastructure project. We will
 6364 follow closely the fabrication and quality control procedures developed for the LHCb Velopix and
 6365 ATLAS ITK detectors by the Glasgow experimental particle physics group.

6366 **Collaborators and their role, resources and workforce:** The electron trackers are a *deliver-*
 6367 *able* within the UK's EIC Infrastructure project. The resources for constructing and delivering the
 6368 trackers are expected to be mostly met by this. However, the project is still to be passed through a
 6369 peer review panel and the costings for the tracker work package officially approved. As outlined
 6370 above, we anticipate that we need an additional 6 FTE postdoc years for simulation, analysis and



Figure 8.165: Acceptance as a function of Q^2 and E_e' .

6371 thermal modelling relating to detector development.

6372 **Risks and mitigation strategy:** The Timepix4 tracker is being developed in close collaboration
6373 with colleagues in the Medipix collaboration. We will use suppliers and services recommended
6374 by them for wafers and production. For local production, fabrication and testing we have a team
6375 trained in bonding and quality control in case of staff changes. Our maximum rates have been
6376 calculated on the basis of EIC maximum proton luminosities, so in the initial running we will be
6377 well below capacity.

6378 **Additional Material** Add text here.

6379 8.3.9 Polarimeters

6380 Add text here.

6381 **8.3.9.1 The electron polarimeters**

6382 **Requirements**

6383 **Requirements from physics:** Add text here.

6384 **Requirements from Radiation Hardness:** Add text here.

6385 **Requirements from Data Rates:** Add text here.

6386 **Justification**

6387 **Device concept and technological choice:** Add text here.

6388 **Subsystem description:**

6389 General device description: Add text here.

6390 Sensors: Add text here.

6391 FEE: Add text here.

6392 Other components: Add text here.

6393 **Performance**

6394 **Implementation**

6395 **Services:** Add text here.

6396 **Subsystem mechanics and integration:** Add text here.

6397 **Calibration, alignment and monitoring:** Add text here.

6398 **Status and remaining design effort:**

6399 R&D effort: Add text here.

6400 E&D status and outlook: Add text here.

6401 Other activity needed for the design completion: Add text here.

6402 Status of maturity of the subsystem: Add text here.

6403 **Environmental, Safety and Health (ES&H) aspects and Quality Assessment (QA plan-**
6404 **ning:** Add text here.

6405 **Construction and assembly planning:** Add text here.

6406 **Collaborators and their role, resources and workforce:** Add text here.

6407 **Risks and mitigation strategy:** Add text here.

6408 **Additional Material** Add text here.

6409 **8.3.9.2 The proton polarimeters**

6410 **Requirements**

6411 **Requirements from physics:** Add text here.

6412 **Requirements from Radiation Hardness:** Add text here.

6413 **Requirements from Data Rates:** Add text here.

6414 **Justification**

6415 **Device concept and technological choice:** Add text here.

6416 **Subsystem description:**

6417 General device description: Add text here.

6418 Sensors: Add text here.

6419 FEE: Add text here.

6420 Other components: Add text here.

6421 **Performance**

6422 **Implementation**

6423 **Services:** Add text here.

6424 **Subsystem mechanics and integration:** Add text here.

6425 **Calibration, alignment and monitoring:** Add text here.

6426 **Status and remaining design effort:**

6427 R&D effort: Add text here.

6428 E&D status and outlook: Add text here.

6429 Other activity needed for the design completion: Add text here.

6430 Status of maturity of the subsystem: Add text here.

6431 **Environmental, Safety and Health (ES&H) aspects and Quality Assessment (QA planning):** Add text here.

6433 **Construction and assembly planning:** Add text here.

6434 **Collaborators and their role, resources and workforce:** Add text here.

6435 **Risks and mitigation strategy:** Add text here.

6436 **Additional Material** Add text here.

6437 **8.3.10 Readout Electronics and Data Acquisition**

6438 **Requirements** The electronics and data acquisition systems are required to digitize and readout
6439 the data provided by the sensors of all ePIC detectors. The Electronics must tag hits with a time
6440 resolution sufficient to identify the bunch crossing (10.16 ns) and provide high resolution time ref-
6441 erences as stringent as 5 ps according the specific detector needs. The ePIC readout system must
6442 provide high data volume links to front end electronics up to 10 Gb/s for selected components. The
6443 readout system must provide very high live times, with the goal of zero-system wide deadtime in
6444 normal operation, despite the possibility of by-channel deadtime according the specific readout
6445 technology of each detector.

6446 The Data Acquisition will group streaming data into time frames of $O(0.6 \text{ ms})$. The readout systems
6447 are expected to digitize up to $O(2 \text{ Tb/s})$ and must be capable of reducing this data volume to an
6448 output rate of $O(100 \text{ Gb/s})$ using techniques to compress signal and remove noise with minimal
6449 impact to signal integrity. The data from all running detectors for each time frame will gathered
6450 together in a single buffer for transfer to the echelon 1 computing facilities located at BNL and JLAB
6451 for archive and analysis.

Detector Group	Channels					Det Fiber Down	Det Fiber Up	RDO	Fiber Pair (DAQ)	DAM	Data Volume (RDO) (Gb/s)	Data Volume (To Tape) (Gb/s)
	MAPS	AC-LGAD	SIPM/PMT	MPGD	HRPPD/MCP-PMT							
Tracking (MAPS)	16B					183	5863	183	183	7	15	15
Tracking (MPGD)				164k		640	2560	160	160	5	27	5
Calorimeters	500M		100k					522	522	17	70	17
Far Forward		1.5M	10k					80	80	6	36	12
Far Backward	66M	128k	4k					60	82	14	301	16
PID (TOF)		6.1M				500	1364	500	500	14	50	12
PID Cherenkov			318k		143k			1283	1283	32	1275	32
TOTAL	16.6B	7.7M	432k	164k	143k	843	9,787	2,788	2,810	95	1,774	109

Figure 8.166: ePIC DAQ component count summary

6452 **Requirements from Physics** The scientific mission of ePIC is reflected in the requirements of
 6453 the Electronics and DAQ through the scale and technology of the ePIC detectors shown in figures
 6454 8.166 and 8.167. Large channel counts combined with low occupancy lead to the need for multi-
 6455 ple levels of aggregation at the Front End Boards (FEB), the Readout Boards (RDO) and the Data
 6456 aggregation and Manipulation Boards (DAM).

6457 The performance of the EIC Collider also impacts the requirements of the readout system. The col-
 6458 lision rates and background rates are detailed in section ???. Two aspects are particularly important
 6459 for the Electronics and DAQ.

6460 The first is the maximum event rates, which we expect to be as high as 500 kHz for DIS, 3.2 MHz
 6461 for Electron Beam Gas and 32 kHz for hadron Beam Gas. These rates are of primary interest within
 6462 DAQ to estimate the data volumes which are described below.

6463 The second consideration is that individual bunch crossing can have different polarization states.
 6464 This implies that the luminosity and polarization of the beams must be tracked by bunch and
 6465 produces the requirement that events must be associated to the bunch crossing from which they
 6466 originated.

6467 **Requirements from Radiation Hardness** The electronics installed in the ePIC detector will
 6468 be subjected to significant radiation doses. Radiation doses are described in section ???. Electronics
 6469 placed in the central detector (SVT, eTOF, bTOF, and MPGDs) will utilize radiation hard compo-
 6470 nents to minimize the effect of radiation.

6471 Electronics must be chosen and placed to minimize failure rates. Transient failures such as single
 6472 bit upsets (SEUs) must have a recovery process which automatically senses, initiates, and accom-
 6473 plishes recovery while running in order to avoid downtime. There are commercial IP cores avail-
 6474 able for FPGAs that can support recovery from simple SEUs. More complex (multi-bit) failures will
 6475 require an automated reset and reload feature for FEBs and RDOs.

6476 **Requirements from Data Rates** The triggerless readout of the ePIC detector uses zero-
 6477 suppression to help manage the volume of data read out. The streaming model's sensitivity to
 6478 noise, beam background, and collision data make the understanding of these effects critical. Colli-
 6479 sion, synchrotron radiation and beam gas backgrounds from both the electron and hadron beams
 6480 have been studied extensively by the ePIC collaboration, and the methods are presented in section
 6481 ???. The hits have been converted to data volumes using our current understanding of zero sup-
 6482 pression and data formats of each detector readout. Furthermore, the distribution of hits to each

Detector System	Channels	ASIC	FEB	RDO	Gb/s (RDO)	Gb/s (Tape)	DAM Boards	Readout Technology	Notes
Si Tracking: Inner Barrel (IB) Outer Barrel (OB) Backward Disks (BE) Forward Disks (FE)	1.88 Pixels 5.08 Pixels 4.78 Pixels 4.78 Pixels	160 495 462 462	592* 1870* 1744* 1744*	24 55 52 52	2.36 3.52 4.68 4.68	2.36 3.52 4.68 4.68	1 2 2 2	ITS-3 sensors & ITS-2 staves / w improvements	ASIC corresponds to VTRX+ counts FEB corresponds to detector fiber RDO is off detector Fiber aggregator
MPGD tracking: Electron Endcap Hadron Endcap Inner Barrel Outer Barrel	16,384 16,384 32,768 98,304	256 256 512 1536	64 64 128 384	16 16 32 96	2.86 4.01 4.10 15.81	0.58 0.80 0.82 3.16	1 1 1 2	urWELL / SALSA urWELL / SALSA MicroMegs / SALSA urWELL / SALSA	VTRX+ based FEB
Forward Calorimeters: LFHCAL 8K HCAL insert ECAL W/ScFi Barrel Calorimeters: HCAL 1.536 ECAL ScFi/PB 5,760 ECAL ASTROPX 3,256 Backward Calorimeters: NHCAL 2,852 ECAL (PWO)	63,280 8K 18,320 1,536 5,760 500M pixels 3,256 2,852	1130 142 1772 28 102 500M pixels 58	1130 142 574 28 102 58 102	74 9 72 2 4 340 4 13	18.54 17.72 14.75 0.87 11.45 1.25 3.46 2.00	2.47 2.36 7.36 0.12 1.52 1.25 0.47 0.99	2 1 2 1 1 8 1 1	SIPM / CALOROC SIPM / CALOROC SIPM / Discrete SIPM / CALOROC SIPM / CALOROC Astropix SIPM / CALOROC SIPM / Discrete	CALOROC: 56 CH/CALOROC 16 CALOROC / RDO Discrete: 32 CH/FEB, 8 FEB/RDO conservative (16 estimate).
Far Forward: B0: Crystal Calorimeter 4 AC-LGAD layer 2 Roman Pots 2 Off Momentum ZDC: Crystal Calorimeter HCAL 9,216	135 688,128 524,288 294,912 900 9,216	672 512 288 30 165	168 128 72 30 165	42 32 18 4 11	2.3 12.75 14.53 3.53 2.30 0.22	2.3 2.1 2.1 0.7 4.5 .22	1 1 1 1 1	SIPM/APD / Discrete AC-LGAD / EICROC AC-LGAD / EICROC AC-LGAD / EICROC SIPM/APD / Discrete CALOROC	4 layer x 42 module x 4 EICROC x 1024 ch 2 stations x 2 layer x 32 module x 4 EICROC x 1024 ch 2 stations x 2 layer x 18 module x 4 EICROC x 1024 ch
Far Backward: 2 x Low Q Tagger 2 x Low Q Tagger Cal 3,360 2 x Lumi PS Calorimeter 128k 2 x Lumi PS tracker Direct Photon Lumi Cal 100	66M pixels 420 3,360 128k 100	3456 1000	288 250 24	24 1 64 24*	37 - 19 45 200	.3 - 7 2 7	10 1 2 2 1	Timepix4 SIPM / CALOROC SIPM / Discrete AC-LGAD: FCFD or EICROC SIPM / FADC250	Firmware Trigger to reduce output rate Low Q Calorimeter doesn't run at high luminosity
PID-TOF: Barrel Endcap	2,359,296 3,719,168	18,432 3,652	288 212	288 212	15.95 33.92	4.79 7.34	8 6	AC-LGAD: FCFD or EICROC AC-LGAD: EICROC	bTOF 128 ch/ASIC, 64 ASIC/RDO eTOF 1024 pixel/ASIC, up to 28 ASIC/RDO
PID-Cherenkov: dRICH pRICH DIRC	317,952 69,632 73,728	4968 544 576	4968 68 144	1242 17 24	1240 24 11	13.5 12.5 6	30 1 1	SIPM / ALCOR HRPPD / FCFD or EICROC MCP-PMT / FCFD or EICROC	Worse case after radiation. Includes 30% timing window. Requires further data volume reduction Firmware trigger

Figure 8.167: ePIC DAQ component counts

Summary of Data Flow

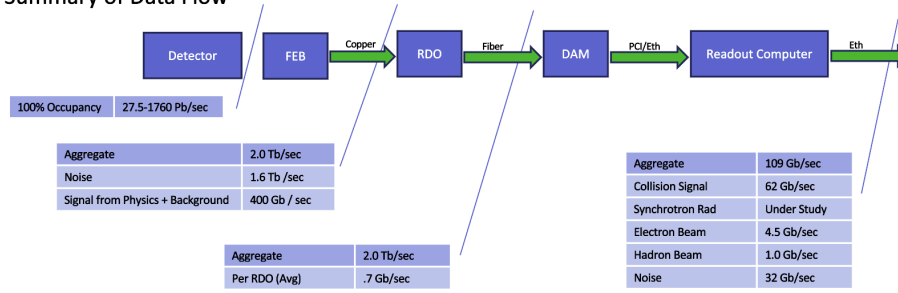


Figure 8.168: Expected worst case data rates contributions for the ePIC detector

Detector	Channel Max Hit Rate (Hz)	Noise To RDO (gbps)	Noise Per RDO (gbps)	Noise To Tape (gbps)	RDO (max) (gbps)	RDO_max / with Noise (gbps)
SiBarrelTracker	4.13E-04	3.25	0.06	3.25	0.00	0.06
SiBarrelVertex	5.22E-03	1.15	0.05	1.15	0.17	0.21
SiEndcapTracker	2.78E-03	6.02	0.06	6.02	0.23	0.29
BackwardMPGDEndcap	2.19E+02	1.74	0.11	0.35	0.42	0.52
ForwardMPGDEndcap	4.44E+02	1.74	0.11	0.35	0.86	0.97
MPGDBarrel	8.67E+01	3.26	0.10	0.65	0.04	0.14
OuterMPGDBarrel	1.29E+01	15.23	0.16	3.05	0.01	0.17
LFHCAL	2.10E+04	10.33	0.14	1.38	1.30	1.44
HcalEndcapPInsert	6.18E+04	1.31	0.15	0.17	2.78	2.93
EcalEndcapP	1.51E+05	0.78	0.01	0.35	2.69	2.70
HCcalEndcapN	7.81E+04	0.53	0.13	0.07	2.64	2.77
EcalEndcapN	8.07E+04	0.14	0.01	0.06	1.06	1.07
HcalBarrel	1.30E+03	0.25	0.13	0.03	0.08	0.21
EcalBarrelImaging	2.92E-02	0.32	0.00	0.32	0.01	0.01
EcalBarrelSciFi	1.52E+03	0.94	0.07	0.13	2.69	2.76
TOFBarrel	1.74E+00	13.59	0.05	4.53	0.01	0.06
TOFEndcap	8.34E-01	32.13	0.15	7.14	0.07	0.22
hpDIRC	2.35E+02	3.22	0.13	1.07	0.00	0.13
pFRICH	4.99E+02	3.05	0.18	1.02	0.00	0.18
dRICH	1.09E+02	1220.94	0.98	6.10	0.00	0.98
B0 Crystal Calorimeter	2.66E+05	0.00	0.00	0.00	0.00	0.00
B0 AC-LGAD	1.72E+01	5.95	0.20	1.32	0.00	0.20
RP	3.31E+01	4.53	0.21	1.01	0.00	0.21
OM	5.93E+00	2.53	0.21	0.56	0.00	0.21
ZDC Crystal Calorimeter	7.81E+04	0.02	0.00	0.02	0.00	0.00
ZDC HCAL	3.39E+01	0.20	0.02	0.20	0.00	0.02
DirectPhoton	2.00E+08	0.00	0.00	0.00	0.00	0.00
LowQ2Tracker	8.76E+00	0.04	0.00	0.04	0.00	0.00
LowQ2Calorimeter	0.00E+00	0.01	0.01	0.01	0.00	0.01
PairSpectrometerTracker	2.44E+02	0.74	0.07	0.25	0.00	0.07
PairSpectrometerCalorimeter	3.26E+04	0.07	0.07	0.07	0.00	0.07
Total		1334.01		40.67		

Figure 8.169: Maximum data volume per RDO with noise estimates.

Detector	Noise (Hz/channel)
ITS3, Astropix, Timepix	0.01
AC-LGAD	30
HRPPD	230
dRICH(initial)	3000
dRICH(Max)	300,000
All Others	4.5σ = 340

Table 8.39: Noise Estimates

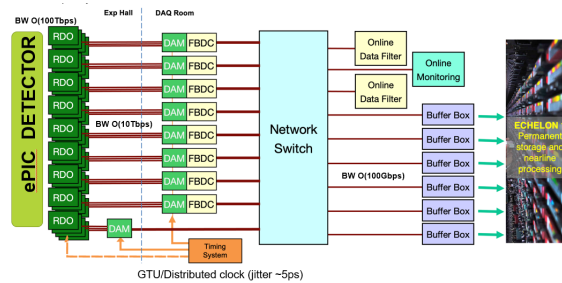


Figure 8.170: Schematic of the ePIC Streaming DAQ

6483 component has been estimated by arbitrarily assigning readout components to the sensitive planes
 6484 of the detectors in order to estimate the impact of potential bottlenecks.

6485 The hit rate for the collision signal is taken from simulated hits for DIS events generated by the
 6486 ePIC physics and detector simulations. The simulated data set was taken for 18×275 GeV collisions
 6487 with $Q^2 > 0$ with luminosity $1.54 \times 10^{33} \text{ cm}^2 \text{ s}^{-1}$. The collision rate was 83kHz, but the hit rates were
 6488 scaled to the maximum rate of the EIC collider of 500kHz. Hadron and electron beam gas events
 6489 were generated using the simulated vacuum profile after 10,000 Ah of pumping. Noise calculations
 6490 are currently based on the ePIC detector group expert estimates and shown in table 8.39.

6491 One additional factor that must be considered is dark currents in the SiPM detectors which increase
 6492 with radiation damage. In particular, this issue affects the dRICH, in which the SiPM threshold
 6493 must remain low enough to be sensitive to single photons. There are several features planned to
 6494 reduce these dark currents including annealing, and implementation of timing windows to syn-
 6495 chronise readout with collision times. These are described in section ???. The DAQ system must be
 6496 designed with the capability to manage the highest rates expected by the dRICH and must also ap-
 6497 ply filters to reduce the dRICH noise, either by applying a firmware trigger or by using specialized
 6498 AI algorithms to determine which hits correspond to a dRICH physics signal.

6499 Finally, noise is expected to be a potential issue in all other detectors as well. Generally, the noise
 6500 level can be controlled with thresholds. The acceptable noise levels by detector is planned to be set
 6501 according to the full data bandwidth requirements. The data volume expected, including collisions,
 6502 background and noise for the worse case RDO by detector, is shown in table 8.169.

6503 **Device Concept and Technological choice: Streaming Readout** The ePIC readout system
 6504 will implement a flexible, scalable, and efficient streaming DAQ as outlined by the EIC Yellow Re-
 6505 port. This design will provide the advantages of streaming include the replacement of custom L1
 6506 trigger electronics with commercial off-the-shelf (COTS) computing, virtually deadtime-free oper-
 6507 ation, great flexibility in event selection using full event data along with offline analysis, and the
 6508 opportunity to study event backgrounds in detail. These advantages come at the cost of greater
 6509 sensitivity to noise and background. A schematic of the readout system is show in figure 8.170.

6510 The components in the ePIC readout system are shown in figure 8.171. Readout will be accom-
 6511 plished using detector specific front end sensors and adaptors. Even though the organization of
 6512 the front end electronics varies by detector needs the custom electronics of each system generically
 6513 referred to as Front End Boards (FEBs). There is no global trigger system in ePIC, instead each
 6514 FEB is required to self-trigger, providing a stream of hit data. Digitization and zero-suppression
 6515 is typically handled with ASIC support. Each FEB has similar needs for clocks, configuration, and
 6516 serial data links. These needs are provided by Readout Boards (RDOs). The RDOs also aggregate

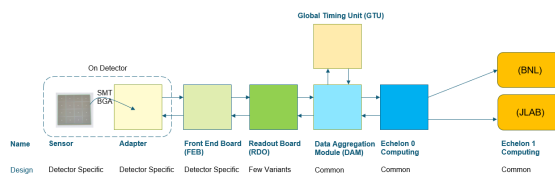


Figure 8.171: Components of the ePIC Streaming DAQ System

6517 data from the FEBs. The RDOs are driven by either FPGAs or IpGBT. The RDO serves as an interface
 6518 between custom, technology driven, readout schemes of specific detectors and the ePIC DAQ.
 6519 While there are a number of variations of the RDOs depending upon the FEB technology, all of the
 6520 RDOs support a unified ePIC DAQ fiber protocol. They distribute high-resolution time reference,
 6521 configuration, and control to the FEBs and transmit hit data and monitoring information to the
 6522 Data Aggregation and Manipulation Boards (DAM).

6523 The DAM boards have significant processing available for implementing firmware triggers and
 6524 other data reduction algorithms. They also provide further aggregation and function as the inter-
 6525 face between the electronics and the first level of COTS computers called the Frame Builder
 6526 Data Collectors (FBDC). The farm of COTS DAQ computers dedicated to readout, data reduction,
 6527 logging, monitoring, QA and data buffering and transfer to data centers is integrated in the ePIC
 6528 computing model and referred to as echelon 0.

6529 Synchronizing the front end electronics and provide high resolution time reference to beam cross-
 6530 ings is an important requirement of the streaming DAQ. The Global Timing Unit (GTU) is the
 6531 interface to EIC collider controls. It receives the 98.5Mhz bunch crossing clock, orbit information,
 6532 and beam polarization information and distributes it via the DAM boards to the RDOs and FEBs.
 6533 The GTU is the only global source of real time information provided to the FEB/RDOs, so it must
 6534 provide information a trigger system would normally provide. These functions include the ability
 6535 to synchronize data from different detectors, to send flow control signals, to pass bunch informa-
 6536 tion such as spin orientations and bunch structure, the ability to provide user defined signals for
 6537 signaling special data formatting or calibration needs, and the ability to implement a hardware
 6538 trigger for debugging or as a fallback option to solve unforeseen readout issues.

6539 The communication between the RDOs, DAM, and GTU will use an unified data protocol serving
 6540 four functions:

- 6541 • The distribution of configuration information from the DAQ System to configure the RDOs,
 6542 and to distribute configuration information to the FEBs via the RDOs using their serial links,
- 6543 • The distribution of real-time control information to the RDO and FEBs,
- 6544 • The distribution of a high-resolution beam crossing timing signal to the RDO and FEBs,
- 6545 • The high performance (~ 10 Gb) transfer of hit data and monitoring information from the
 6546 FEBs and RDO to the DAM boards.

6547 Subsystem Description (components)

6548 Readout Electronics and ASICS

Implementation	Detector/Sensor	Key Attributes
Discrete	Calorimeter/SiPM	COTS devices, 14-bit digitization
CALOROC	Calorimeter/SiPM	ASIC, 10-bit digitization
EICROC	AC-LGAD, pixel	ASIC, High-precision timing for Cd < 5 pF
FCFD	AC-LGAD, strip	ASIC, High-precision timing for Cd < 10 pF
ALCOR	dRICH/SiPM	ASIC, uses shutter for 1 p.e. sensitivity
SALSA	MPGD	ASIC, peaking time to 50 ns, includes DSP

Figure 8.172: ePIC Electronics and ASICs summary

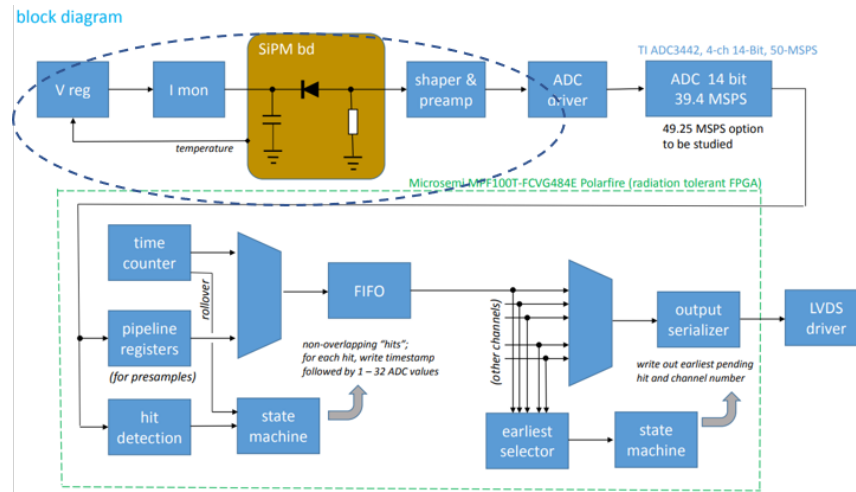


Figure 8.173: Discrete block diagram

6549 **Overview** Readout electronics is being developed based on the sensor technologies. Common
 6550 requirements among various sub-detectors have been identified to maximizing synergy. The read-
 6551 out electronics conforms to the ePIC streaming readout model with triggerless operation and serial
 6552 interfaces. To facilitate calibration and debugging, capability for triggered operation is also imple-
 6553 mented. The development of the readout electronics and ASICs are summarized in figure 8.172.

6554 **Discrete** The Discrete readout implementation addresses the readout from calorimeters with
 6555 SiPMs where high resolution digitization is required and commercial devices (COTS) are em-
 6556 ployed. The design and technologies will be validated for specific locations within the ePIC de-
 6557 tector, where radiation hardness of COTS devices will need to be verified. The block diagram is
 6558 shown in figure 8.173.

6559 The circled area in fig. 8.173 delineates the Adapter section with SiPMs and bias circuitry; the
 6560 remaining parts make up the FEB PCB, which includes signal conditioning, ADCs and readout
 6561 logic. The Adapter and FEB PCBs are located at the detector, as a stack, and CAT6 cables are
 6562 employed for serial interfaces. Key specifications are shown in figure 8.175. Prototypes of the
 6563 Adapter and FEB PCBs are shown in figure 8.174.

6564 **CALOROC** The CALOROC ASIC is currently under development to address readout from
 6565 calorimeters with SiPMs and for which a 10-bit resolution digitization with wide dynamic range ca-
 6566 pabilities is applicable. The CALOROC design is based on the existing H2GCROC ASIC for SiPMs

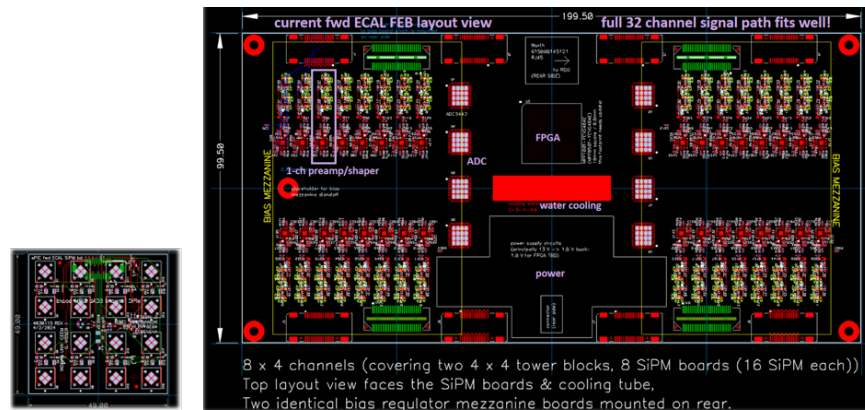


Figure 8.174: Discrete Adapter (left) and digitizer FEB PCBs

Function	Waveform digitizer with COTS devices
Channels	32
Digitizer	TI ADC 3422
Resolution	14-bit (12-bit also available)
Shaping	80 ns peaking time
Power	Microsemi MPF100T-FCVG484E Polarfire (Rad Hard)
Cooling	Liquid
Cabling	CAT6

Figure 8.175: Discrete key specifications

6567 with similar frontend and a backend, or digital section with interfaces, conforming to the needs of
 6568 the streaming readout approach at the EIC. In parallel, tests with the H2GCROCv3 chip continue
 6569 to provide input and validation into the design of the CALOROC ASIC. There are, however, two
 6570 frontend variants being considered: CALOROC1A uses an ADC, a TOA and a TOT for wide dy-
 6571 namic range, similar to the H2GCROC; CALOROC1B uses a different frontend architecture making
 6572 use of dual gain switching techniques to extend its dynamic range. The CALOROC block diagram
 6573 is shown in figure 8.176 and its specifications summarized in figure 8.177.

6574 **EICROC** The EICROC ASIC is currently under development to address readout from AC-LGAD
 6575 pixel detectors with low detector capacitance (C_{din}) and very stringent timing precision require-
 6576 ments. The EICROC design is based on the existing HGCROC ASIC for Si and PMTs with similar
 6577 frontend and a backend, or digital section with interfaces, conforming to the needs of the streaming
 6578 readout approach at the EIC, which is already being designed for the CALOROC. Main IP blocks
 6579 consist of preamp, discriminator, TOA, ADC and TDC. The EICROC block diagram is shown in
 6580 figure 8.178 and its specifications are summarized in figure 8.180. Figure 8.179 shows the EICROC
 6581 timing performance with varying charge from input signals.

6582 **FCFD** The FCFD ASIC is currently under development to address readout from AC-LGAD strip
 6583 detectors with medium detector capacitance (C_{din}) and very stringent timing precision require-
 6584 ments. The FCFD design implements the constant fraction discriminator technique for high preci-
 6585 sion timing without time-walk corrections. The backend, which is currently being considered, may
 6586 be based on the existing ETROC ASIC or the EICROC development. The FCFD block diagram is

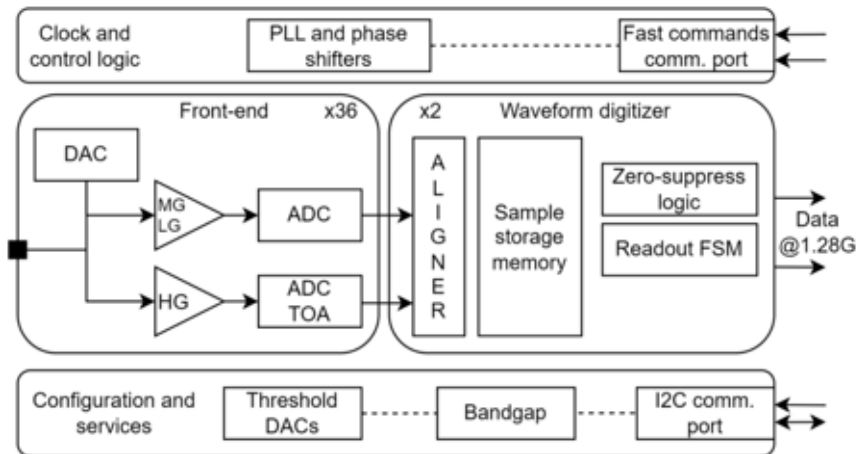


Figure 8.176: CALOROC block diagram

Function	Charge and timing digitization from SiPMs
Tech Node	130 nm CMOS
Channels	64
C _{din}	500 pF – 10 nF
Digitization	Charge: 10-bit ADC, 15-bit TOT; Timing: <500 ps TOT (1 MIP)
Dynamic Range	Up to 12 nC
Clock	39.4 MHz operation from BX 98.5 MHz
Links	1260.8 Mbps @ 39.4 MHz, multiple
Power	10 mW/ch
Package	BGA
Rad Tolerance	Radiation hard

Figure 8.177: CALOROC Key Specifications

6587 shown in figure 8.181 and its specifications are summarized in figure 8.183. Figure 8.182 shows the
 6588 FCFD timing performance with varying charge from input signals.

6589 **ALCOR** The ALCOR ASIC is currently under development specifically for the readout of the
 6590 dRICH detector with SiPMs due to its single photo-electron sensitivity requirement. The ALCOR
 6591 design includes trans-impedance amplification (TIA) with regulated common gate (RCG) bias for
 6592 low noise, inhibit or shutter operation to limit contribution from dark-rate SiPM noise and TDCs
 6593 to allow for single-photon tagging or time and charge digitization. The shutter function is a critical
 6594 aspect of this ASIC and it is programmable for width and latency. The ALCOR Die and block
 6595 diagram are shown in figure 8.184 and its specifications are summarized in figure 8.185.

6596 **SALSA** The SALSA chip is an ASIC currently under development, foreseen to do the readout of
 6597 the different MPGD trackers, namely the barrel cylindrical Micromegas, the barrel μ RWELL and
 6598 the end-cap μ RWELL detectors. The purpose of SALSA is to amplify, shape and digitize signals
 6599 coming from the MPGD detectors, and then perform basic data processing on the digitized samples
 6600 before to transmit them to the next element of the data acquisition chain. It gathers in a single
 6601 die a CSA pre-amplifier, a shaper and an ADC for each of the 64 channels, followed by a DSP
 6602 which performs baseline corrections, digital shaping and a zero-suppression in order to reduce the

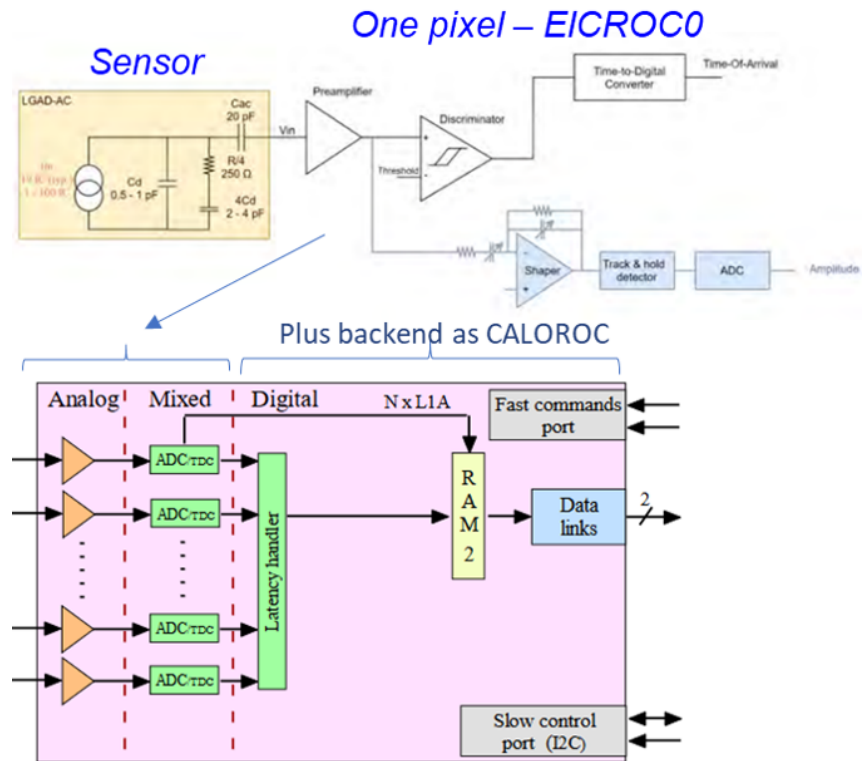


Figure 8.178: EICROC block diagram

6603 output data bandwidth. Furthermore, to reduce data output even more, a peak finding algorithm is
 6604 implemented to extract from samples information like amplitude and time of detected hits. It will
 6605 be able to work both in the streaming readout environment foreseen at EPIC, and in a triggered
 6606 environment.

6607 The characteristics, performances and configurability of SALSA are designed to make the ASIC
 6608 very versatile, being able to be adapted to several kinds of MPGD detectors and to several appli-
 6609 cations. It will be able to work with a large range of signal amplitudes, a large range of electrode
 6610 capacitance and large range of signal rise times. Its target specifications are summarized in the
 6611 Table 8.40.

6612 **Scope of the Effort** The scope of the electronics and ASICs developments is summarized in
 6613 figure 8.186, based on the number of readout channels, technologies employed and institutions
 6614 developing these readout solutions.

6615 It is noted that the pFRICH and the hpDIRC detectors benefit from the FCFD and the EICROC de-
 6616 velopments due to their timing precision requirements. The FCFD is, however, the nominal choice
 6617 due to its lower channel density packaging for these applications with higher detector capacitances,
 6618 which enable tailoring their timing performance via detector bias adjustment.

6619 **FEB components**

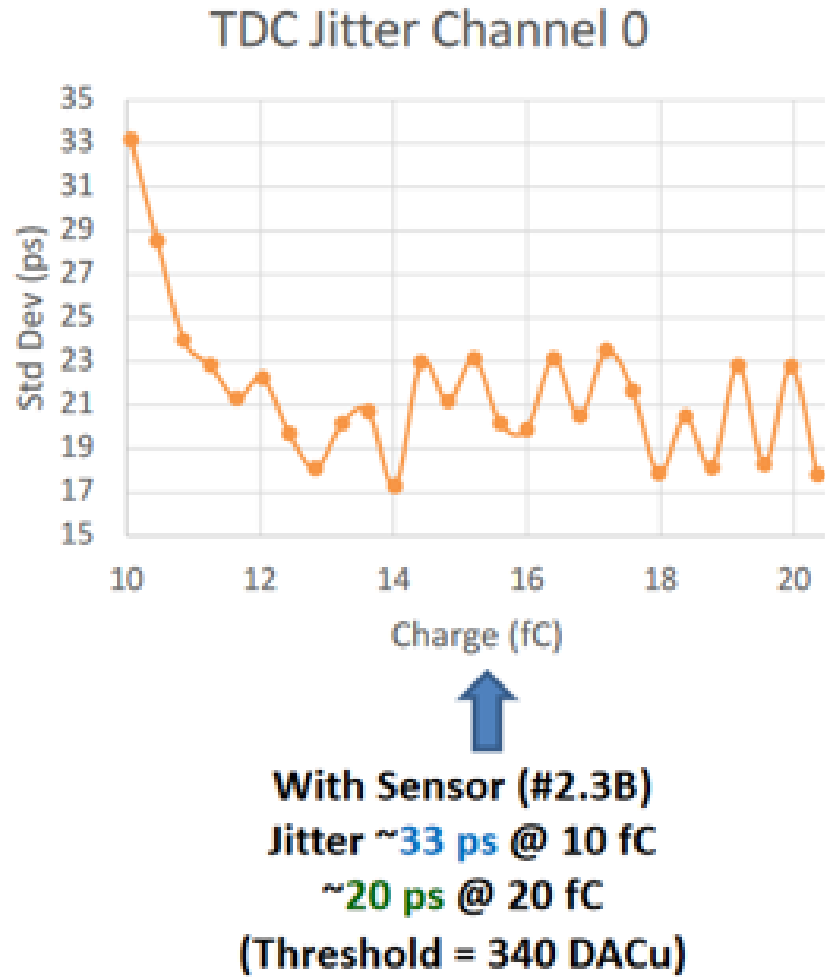


Figure 8.179: EICROC timing performance

Function	Timing digitization from AC-LGAD pixels
Tech Node	130 nm CMOS
Channels	1024 (32x32)
Cdin	1 – 5 pF
Digitization	ADC: 8-bit, TDC: 10b; Timing: 30 ps
Dynamic Range	1 – 50 fC
Clock	39.4 MHz operation from BX 98.5 MHz
Links	1260.8 Mbps @ 39.4 MHz, multiple
Power	<2 mW/ch
Package	Bump + wire bonds
Rad Tolerance	Radiation hard

Figure 8.180: EICROC Key Specifications

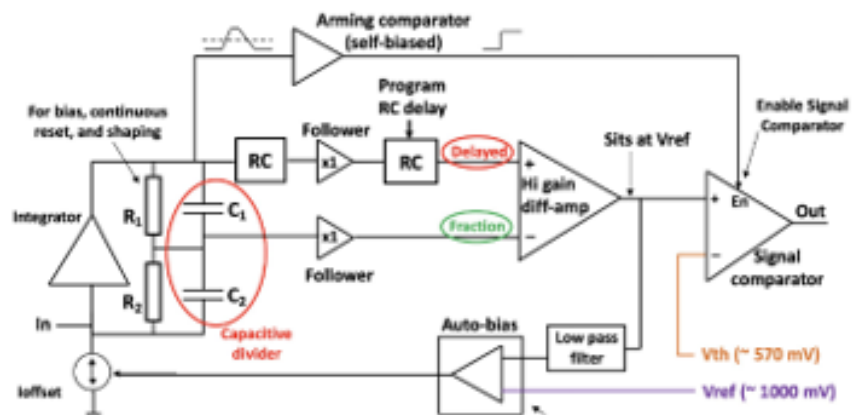


Figure 8.181: FCFD block diagram of the frontend

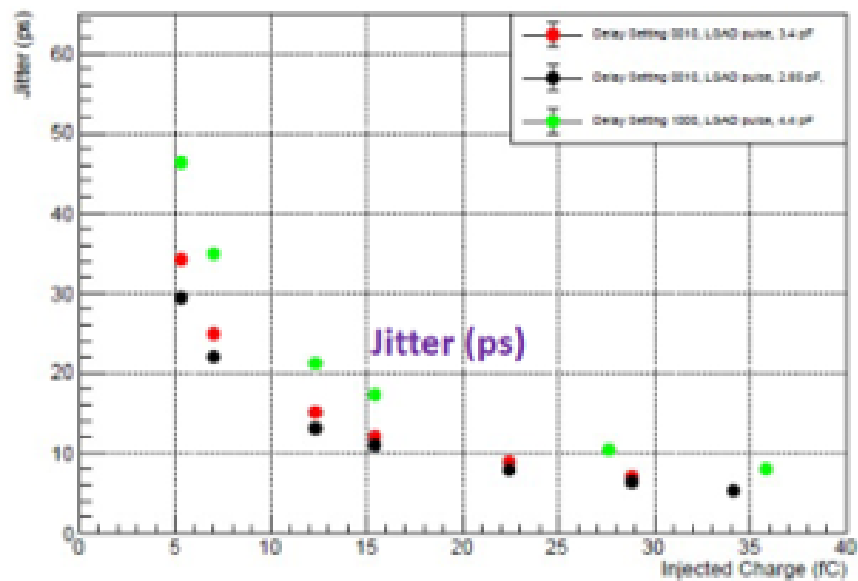


Figure 8.182: FCFD timing performance

Function	Timing digitization from AC-LGAD strips
Tech Node	65 nm CMOS
Channels	128
Cdin	<15 pF
Digitization	TBD; Timing: 10 - 30 ps
Dynamic Range	5 – 40 fC
Clock	39.4 MHz operation from BX 98.5 MHz
Links	1260.8 Mbps @ 39.4 MHz, multiple
Power	<2 mW/ch
Package	Bump + wire bonds
Rad Tolerance	Radiation hard

Figure 8.183: FCFD Key Specifications

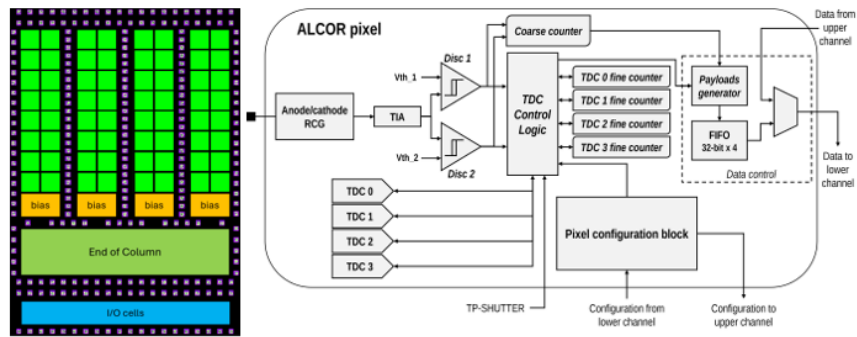


Figure 8.184: ALCOR Si Die (left) and block diagram

Function	Digitization from SiPMs with 1 p.e. sensitivity
Mode	Single-photon tagging or time and charge
Tech Node	110 nm CMOS
Channels	64 (8x8), dual polarity
C _{din}	<1 nF
Digitization	20-40 ps TDCs, TOA + TOT; Timing <150 ps
Shutter	Width: 2-3 ns, programmable latency
Input Rate	<2.4 MHz (up to 5 MHz on single channel)
Clock	394.08 MHz operation from BX 98.5 MHz
Links	788 Mbps LVDS, SPI configuration
Power	12 mW/ch
Package	BGA
Rad Tolerance	Radiation hard

Figure 8.185: ALCOR Key Specifications

6620 **DC/DC converters** DC/DC converters are employed throughout ePIC for the efficient distribution and regulation of the various sub-systems. The bPOL12V and bPOL48V DC/DC modules
 6621 are selected for their radiation hardness and high magnetic field tolerances. Designs based on the
 6622 LTC36xx family of devices will also be employed after proper validation.
 6623

6624 **IpGBT** The low power Giga-Bit Transceiver (IpGBT) chip will be extensively used in ePIC sub-
 6625 systems to provide aggregation and serial communications of up to 2.5 Gbps. The IpGBT is radiation
 6626 hard with Serializer/Deserializer (SERDES) functionality.

	# Ch	# Ch/ Unit	#ASICs/ Wafer	#Wafers	Node (nm)	Package	Institution
Discrete/COTS	24 k	32	NA	740	COTS	NA	IU
CALOROC	97 k	64	480	5	130	BGA	OMEGA/IN2P3/IJCL/ORNL
EICROC	5.2 M	1024	160	42	130	Wafer Bump	OMEGA/IN2P3/IJCL/CEA-IRFU/AGH
FCFD	2.6 M	128	180	149	65	Wire Bond	FNAL
ALCOR	318 k	64	800	8	110	BGA	INFN
SALSA	202 k	64	500	9	65	BGA	CEA-Saclay/U of Sao Paulo

Figure 8.186: Scope of the electronics and ASICs developments

Specification	Values	Remarks
Number of channels	64	
Input capacitance	50-200 pF	Reasonable gain up to 1 nF
Peaking time range	50 - 500 ns	
Max gain range	50 fC to 5 pC	
Max input rate	100 kHz/channel	Fast CSA reset
Signal polarity	Negative and positive	
ADC max sampling rate	50 MS/s	
ADC dynamics	12 bits	More than 10 effective bits
DSP processing	Baseline correction, filter, zero-suppression, peak finding	
Readout modes	Streaming readout, triggered	
Output data links	4 Gigabit links	1 only used at EPIC
Die technology	TSMC 65nm	
Die size	$\sim 1 \text{ cm}^2$	
Power consumption	$\sim 15 \text{ mW/channel}$	
Radiation hardness	Up to 300 Mrad and $10^{13} n_{eq}/\text{cm}^2$	

Table 8.40: Main specifications of the SALSAs chip.

6627 **VTRX+** The VTRX+ module is an electro-optical receiver/driver which will be extensively used
6628 in ePIC to interface to multi-mode optical fibers with MT optical connectors. One (1) receiver Rx
6629 (2.5Gbps) and four (4) transmitters Tx (10Gbps) are implemented. The VTRX+ is radiation hard
6630 and it is tolerant to high magnetic fields; it has a small footprint, has low power consumption and
6631 interfaces directly to the lpGBT transceiver devices.

6632 **RDOs** The RDO aggregates ASIC information from the multiple front end boards. The RDO also
6633 has the function of delivering a high resolution clock ($\leq 5 \text{ ps}$ jitter) to the front end boards. This
6634 clock is reconstructed from the data downlink fiber. The final function of the RDO is act as the
6635 interface between the detector specific function of the ASICs to the global ePIC DAQ fiber proto-
6636 col. This protocol labels bunch crossings, organizes time frames, uses user defined fast commands
6637 to communicate with the ASICs and provides the capabilities for firmware triggering and flow
6638 control.

6639 However, several detectors: the SVT, the MPGD based detectors, and all AC-LGAD based readouts
6640 will make use of lpGBT or lpGBT-like aggregation using VTRX+ transceivers. The lpGBT aggre-
6641 gates ASIC information, and delivers a high resolution reconstructed clock. However, it attempts
6642 to give a transparent interface to the ASICs. It does not have the capability of implementing the
6643 full ePIC protocol. For these RDOs the protocol will be implemented at the next level, either inside
6644 the DAM board or in a second level fiber to fiber RDO.

6645 There will be several versions of the RDO depending on the needs of the specific detectors. The
6646 different RDO types are summarized in table 8.41

Target Detector	Input	Output	technology
TOF Pre-Prototype, Calorimeters	copper	SFP+ fiber	FPGA
dRICH	copper	VTRX+ fiber	FPGA
SVT, MPGD, AC-LGAD second level	fiber	fiber	FPGA
AC-LGAD	copper	VTRX+ fiber	lpGBT
Imaging Calorimeter (Astropix)	copper	fiber	FPGA
Low Q^2 Tagger (Spyder3 Board)	copper	up to 12 fiber	FPGA
Direct Photon Detector	copper	fiber	flash

Table 8.41: Types of RDO



Figure 8.187: TOF pre-prototype RDO

6647 **TOF pre-prototype RDO (FPGA based copper to SFP+** The TOF pre-prototype RDO was
 6648 designed to use elements common to most ePIC detector RDOs. These elements include Xilinx
 6649 Ultrascale+ Artix FPGA, SFP+ fiber optics interface, clock cleaner PLLs, and clock recovery. The
 6650 pre-prototype has been produced and is undergoing measurements of power usage and clock jitter.
 6651 The board is shown in figure 8.187.

6652 **dRICH RDO** The dRICH RDO is part of the dRICH Photo Detector Unit PDU (see section ??,
 6653 1248 PDUs will serve the dRICH). It provides read-out of four 64-channel ALCOR ASIC, installed
 6654 each on a separate FEB. The space constraints are particularly demanding: the total RDO area is
 6655 $40 \times 9 \text{ mm}^2$ - quite similar to a credit card - requiring a devoted design, given the high integration of
 6656 data buses and services within the PDU. The FPGA providing readout of the ALCOR is an AMD
 6657 Artix Ultrascale+ AU15P-SBVB484, complemented by a PolarFire FLASH-based FPGA MPF050T-
 6658 FC5G325. The latter will support remote programming and continuous scrubbing of configura-
 6659 tion bits of the SRAM-based AMD FPGA, to protect against SEU. Given the space constraints and
 6660 the need to curb power consumption (total RDO power is expected $\approx 4 \text{ W}$) the CERN-developed
 6661 VTRX+ optical transceiver has been selected, directly connected to the AMD FPGA SERDES. The

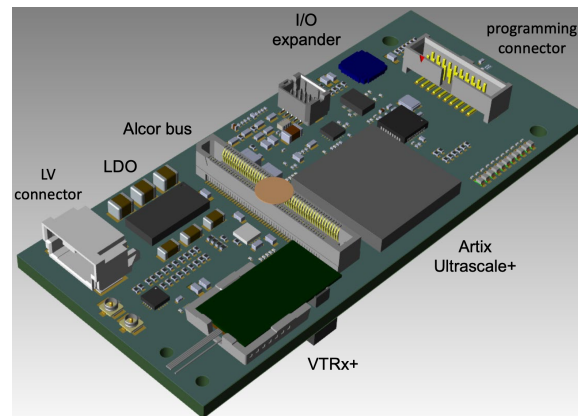


Figure 8.188: 3D model of dRICH RDO

6662 maximum throughput per link (reached at maximum radiation damage before annealing) is fore-
 6663 seen not exceeding 2 Gbps, safely within VTRX+ specifications The ALCOR will be read out at
 6664 394 MHz, with a clock multiplier and jitter-attenuator (Skyworks Si5326) deriving this clock from
 6665 the reconstructed EIC clock. A Microchip microcontroller provides power management and acts as
 6666 watchdog against SEL. The first prototype of this card is under production and will be intensively
 6667 tested during 2025, including irradiation tests. A 3D-rendering of the card is shown in Fig. 8.188.

6668 **Fiber to Fiber RDO** The fiber to fiber RDO is to be used with lpGBT-like FEBs to convert the
 6669 transparent ASIC interface to the ePIC DAQ protocol. They are also necessary to further aggregate
 6670 the fibers, particularly in the case of SVT and bTOF large numbers of low-data utilization fibers are
 6671 required.

6672 **lpGBT based copper to fiber RDO** This RDO is yet to be designed, but is required for the
 6673 lpGBT based readout of the inner detectors.

6674 **Astropix End of Stave Card (RDO)** This RDO is to be developed by NASA for use with the
 6675 Astropix sensors.

6676 **Low Q^2 RDO** This is a RDO specifically for the low Q^2 taggers. It is expected to be an updated
 6677 version of the Spyder3 board. These use the timepix sensor and have high potential data volumes,
 6678 requiring several uplink fibers per RDO.

6679 **Flash based RDO** The Flash RDO is a specialized interface for the Direct Photon Detector. This
 6680 detector has only about 100 channels, but is expected to have very high occupancy, and as such the
 6681 appropriate technology is to digitize all data at 200 MHz and stream it directly to the DAM boards
 6682 which will summarize the information, writing out only the summed energy deposited each bunch
 6683 crossing, or histograms of the bunch crossing energies according to bunch number.

6684 **DAM - Data Aggregation and Manipulation Hardware** For the ePIC DAQ system the DAM
 6685 boards will be used as the primary aggregation point for the “raw” detector data streams. Because

6686 these boards are also the final aggregation points for the front-end (hardware managed) DAQ, there
6687 will need to be some well-defined but configurable algorithms for merging streams and managing
6688 potential congestion and data loss both for the incoming detector streams and the outgoing aggre-
6689 gated streams being queued up for online processing.

6690 In Addition, the DAM boards will interface with the Global Timing Unit (GTU) hardware via a
6691 proprietary communication protocol that supports a synchronized EIC clock distribution to all sub-
6692 systems and general DAQ/Run control and configuration. Finally, the DAM will act as the slow
6693 control interface for configuration and monitoring of all detector subsystem front-end boards (e.g.
6694 ASICs and other digitizing electronics).

6695 We have identified an ideal candidate for the DAM hardware. An updated version of the FELIX
6696 board (Model FLX155) is currently being produced at BNL for ATLAS at the HL-LHC. Its features
6697 are substantial and the updated components ensure a longevity of production, performance and
6698 support that match very well with the EIC timeline. The board is built around the Xilinx Versal
6699 ACAP. This will facilitate using the board both as a PCIe device (supporting both PCIe Gen4 and
6700 Gen5 standards) in a server or as a standalone “smart” “aggregation” switch running a Linux OS.
6701 It can support up to 48 serial links to RDOs at the front-end running at speeds up to 25 Gbps as well
6702 as an LTI interface (8 fibers) supporting a high-resolution direct clock along with our GTU-DAM
6703 communication protocol. There is also a separate 100 Gb ethernet link off the board. A DDR4 RAM
6704 slot is available to support buffering and more complex algorithms for data reduction or interaction
6705 tagging. The board supports JTAG and I2C communications.

6706 We expect to procure several FLX155 boards for testing and software/firmware development in
6707 2025.

6708 **GTU - Global Timing Unit** The design of the global timing distribution system (GTU) will be
6709 central to the operation of the streaming readout model. The timing system must provide signals
6710 to ensure that the data from different detectors can be synchronously aggregated. It must provide
6711 a copy of the accelerator bunch crossing clock (running at 98.5Mhz) to all front-end systems. A
6712 subset of these systems (e.g. TOF) will require a phase aligned system clock with a jitter of <5 ps
6713 in order realize required timing resolutions for these detectors (20-30 ps).

6714 The GTU is also the only source of real time information provided to the FEB/RDOs, so it must
6715 provide information a trigger system would normally provide. These functions include the ability
6716 to synchronize data from different detectors, to send flow control signals, to pass bunch informa-
6717 tion such as spin orientations and bunch structure, the ability to provide user defined signals for
6718 signaling special data formatting or calibration needs, and the ability to implement a hardware
6719 trigger for debugging, calibration or as a fallback option to solve unforeseen readout issues.

6720 Figure 8.189 shows a schematic layout based on required functionality of the GTU. The physical
6721 concept is shown in figure 8.190. The GTU will be custom rack-mounted hardware in the DAQ
6722 room with a base board and multiple plug-in optical interface modules. It will be based on a multi-
6723 FPGA architecture including a single Zync SoC FPGA supporting gigabit ethernet and a full Linux
6724 OS to facilitate both ePIC Run Control and other user-based applications. It will include an interface
6725 for the EIC Common platform (Clock, beam orbit and other collider information) and an interface
6726 for feedback from the local IP-6 beamline to support bunch crossing clock phase corrections

6727 The jitter-cleaned and phase corrected clock then is fanned out for distribution to all DAM boards
6728 via a multi-fiber communications link (We intend to support up to 150 of these links for current
6729 needs as well as potential future requirements). In addition we plan to support up to 250 direct
6730 clock links to the RDO/FEB electronics. This is to mitigate potential limitations with the distribu-

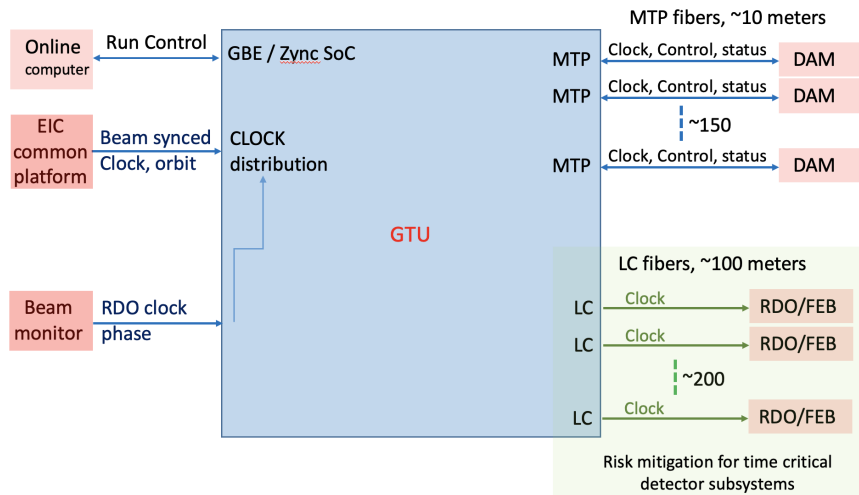


Figure 8.189: Schematic layout based for the GTU

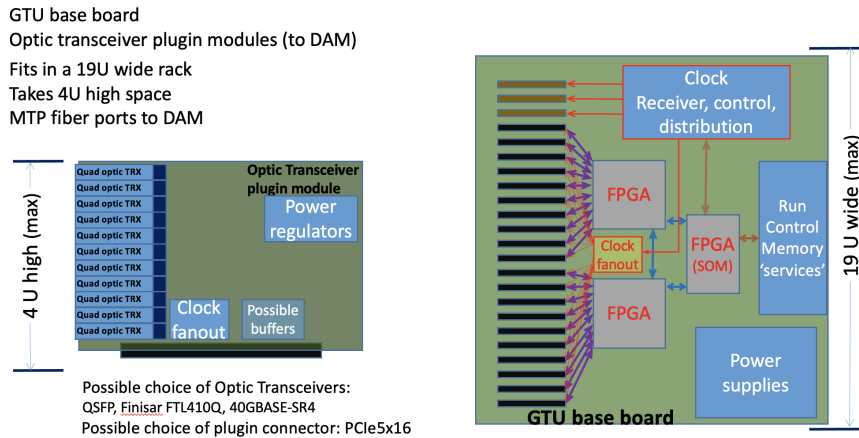


Figure 8.190: Physical concept for the fiber distribution for the GTU

6731 tion of the low jitter (<5 ps) clock via the DAM path communication protocol.

6732 **Protocols** The ePIC fiber protocol is used to communicate information between the GTU, DAM
 6733 and RDO boards. The DAM to RDO communications are limited by the type of interface, and can
 6734 be described in three categories as shown in table 8.43.

6735 The ePIC fiber protocol depends upon a synchronous command structure (table 8.42 which simul-
 6736 taneously encodes fast commands, to be delivered to the RDO or ASICs with fixed latency relative
 6737 to the bunch crossing and control information such as the current bunch crossing. The RDO acts
 6738 upon delivered synchronous commands to provide headers defining the time frames, and to im-
 6739 plement required features. The lpGBT provides a transparent fiber interface to the ASICs and does
 6740 not have features capable of implementing the full ePIC DAQ protocol, so this functionality must
 6741 be provided later in the chain, either in a second layer fiber to fiber RDO, or in the DAM board
 6742 itself.

Decoded Synchronous Command Structure							
[0:7]	[8:15]	[16:23]	[24:31]	[32:39]	[40:47]	[48:55]	[56:64]
Flexible Command Data Encoding				FAST CMD		Comma	
type	type specific			FAST CMD		Comma	

Table 8.42: DAM/RDO Decoded Synchronous Command Structure. This structure is defined to allow continuous availability of the critical beam related bits and more rare commands. The data in the 40 bits worth of flexible command data encoding remains flexible but must contain enough control bits to select what structure it has. The "type", "type specific" division is an potential holding this flexibility

type	clock (MHz)	downlink rate (Gb/s)	downlink word length (ns)	downline word width (bits)
FPGA Standard	98.5	10	10.15	64
FPGA VTRX+	98.5	2.56	10.15	16
lpGBT VTRX+	39.4	2.56	25.375	64

Table 8.43: RDO downlink words

6743 The maximum timeframe length, in bunch crossings will be defined to fit within 2^{16} , which implies
 6744 a time frame length of ≈ 0.6 ms. This is also a convenient time as it corresponds to a manageable
 6745 maximum time frame size of ≈ 10 MB. The need to support both the 10.15 ns EIC clock and the
 6746 synchronized 25.375 ns clock support by cern lpGBT and CERN developed asics demands that time
 6747 frame lengths be limited to multiples of 5 EIC clocks, if the time frame's are to be synchronized in
 6748 time.

6749 The features encoded in the Synchronous command protocol are

- 6750 1. Synchronize bunch counters among all detector readouts
- 6751 2. Define the time frame boundaries
- 6752 3. Provide RDO and DAM Data processing flags
- 6753 4. Configure ASICs and RDOs
- 6754 5. Firmware based triggering
- 6755 6. Flow control
- 6756 7. Transfer Data
- 6757 8. Transfer Slow Controls Data

6758 **Firmware Trigger** One example of the operation of the protocol is in the firmware trigger to
 6759 be implemented to reduce dRICH noise. It's important to note that the the firmware trigger under
 6760 discussion is not (or not necessarily) a global trigger that would remove full events from the readout
 6761 of the ePIC detector. Instead, this trigger is expected to affect only the data from particular detectors
 6762 with unusually high data volumes. In this example, the dRICH.

6763 The path of the commands sent is show in figure 8.191. Data arrives at DAM boards with 10us
 6764 from digitization. It is stored in the DAM boards. After 10us FPGA based algorithms provide a

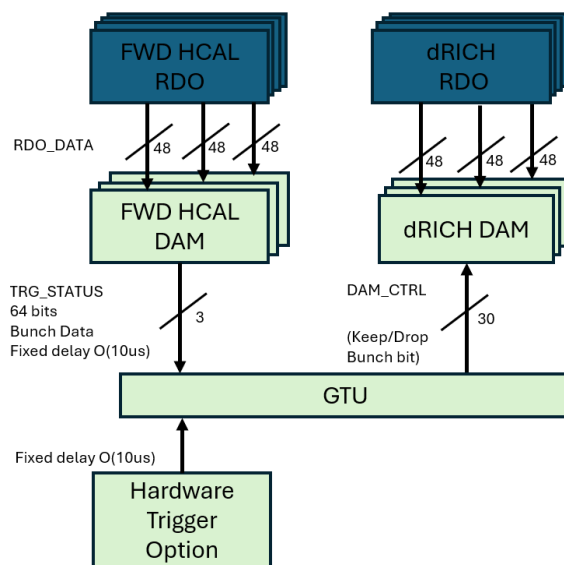


Figure 8.191: Operation of firmware trigger under assumption that the trigger decision for the dRICH depends upon data from fHCAL

6765 description of the data (for example number of hits above a specified threshold) from each fHCAL
 6766 DAM board. This information is encoded into 64 bits and sent to the GTU which aggregates data
 6767 from fHCAL DAM boards and sends the keep/drop bunch bit to the dRICH DAM boards. The
 6768 dRICH DAM boards drop or transmit data based upon this message. The decision comes after a
 6769 fixed latency of about 11us which is very small compared to the buffering available on the DAM
 6770 board.

6771 Note that a similar approach can be implemented with a hardware signal into the GTU. In this case
 6772 a fixed delay is applied to the hardware signal, but the decision mechanism uses the same data
 6773 path.

6774 **dRICH data algorithms** There are also additional schemes for implementing dRICH data re-
 6775 duction using only dRICH data or aggregated data from different sub-detectors. This is currently
 6776 under investigation by the dRICH groups at INFN. One possibility would be to perform such re-
 6777 duction on the network of interconnected dRICH DAMS using the APEIRON framework [79]
 6778 which implements a multi FPGA ML algorithm with deterministic time. The results of this cal-
 6779 culation are transmitted to the GTU in the same manner as in the previous firmware trigger. The
 6780 DAM buffering capacity is exploited in this scheme. Another possibility is to use instead, Online
 6781 Data Filter algorithms in the servers receiving the aggregated data (see Fig. 8.170), exploiting xPU
 6782 resources. Given the noise rate in the dRICH will increase with the radiation damage (see section
 6783 ??), this will provide an opportunity to develop and test carefully such systems

6784 **DAQ/Online Computing - Echelon 0** Table 8.44 outlines the planned resources for the ePIC
 6785 detector DAQ and Online computing needs. This is based on the elements shown in the DAQ
 6786 schematic in Figure 8.170. Several thousand fibers from the RDOs will be aggregated in the DAM
 6787 boards and presented to the Online Farm. To be clear each online farm node represents one multi-
 6788 core server. The expectation is that they will minimally support 32-64 cores, and selected nodes

Resource	Totals
DAM/FELIX boards	136
EBDC Servers	92
DAQ Compute Nodes	108
File Servers (Buffer Box)	6

Table 8.44: DAQ Computing Resources

6789 will support PCIe-based GPUs and/or FPGAs in addition to the DAM boards in the FBDC (Frame
 6790 Building Data Concentrator) nodes. The high performance DAQ network is expected to support
 6791 100/400 Gbps bandwidth connections. As the majority of the Online computing is expected to be
 6792 COTS hardware, much of it will be acquired as late as is reasonable in the construction phase.

6793 All Echelon 0 resources are fully dedicated to operation of the ePIC Detector and are included as
 6794 part of the EIC Project. One open question under consideration, however, is to split these resources
 6795 between the DAQ Room at IP-6 and the SDCC (BNL main data center) and to integrate them as
 6796 a single enclave under ePIC control. There are several advantages to this configuration. First it
 6797 will reduce the overall cost of infrastructure upgrades to the DAQ Room cooling systems. Also,
 6798 having a subset of ePIC computing resources available in the SDCC will allow better network
 6799 access to DAQ and electronics labs during construction (when the DAQ Room will not be available.
 6800 Finally, during operations having DAQ tiered storage of production data in the SDCC will facilitate
 6801 distribution of that data to both Echelon 1 processing sites (BNL and JLAB).

6802 At the DAM stage the aggregated data streams will have substantial buffering and available net-
 6803 work bandwidth for online processing that will be primarily focused on event identification and
 6804 background/noise reduction. While we do not currently have solid estimates on the necessary
 6805 computing resources to complete the required tasks, we have tried to provide conservative esti-
 6806 mates of computing resources that would allow a full reconstruction of a 500 kHz trigger rate of
 6807 events from similar scale detectors that exist now (e.g. GlueX and CLAS12 at Jefferson Lab and
 6808 sPHENIX at RHIC). More likely the necessary computing resources for online filtering to get the
 6809 expected data rates of $O(100 \text{ Gbps})$ to files will be somewhat smaller.

6810 **Time Frame Building** In the streaming model, the primary consideration is ensuring that
 6811 enough bandwidth and buffering will be available to handle the digitized data at each stage of
 6812 the DAQ. At the front-end stage time frames for the individual streams are created, managed and
 6813 aggregated. Given current background and noise estimates the planned bandwidth off the detector
 6814 to the DAM boards $O(10 \text{ Tbps})$ should be more than sufficient.

6815 Streams at the DAM boards will support time frames using a 16 bit bunch crossing counter which
 6816 would represent a configurable time window of up to $65536 * 10.15 \text{ ns} = 665 \text{ s}$. Although the front-
 6817 end DAQ will be synchronized using a single common clock from the EIC, not all ASICs/digitizers
 6818 at the FEBs will be running at the same frequency. Hence the timestamps coming from hits in
 6819 different detectors will need to be wrapped in smaller "time slices" within the full time frame to
 6820 establish an absolute time for each hit.

6821 Time frames buffered at the DAM boards will be able to utilize the online farm to complete a full
 6822 build of complete time frames with data from all detectors. Effectively N streams from the DAM
 6823 boards will generate $M < N$ streams of time frames containing the time frame fragments from the N
 6824 original streams. This will greatly facilitate additional event identification and processing at both
 6825 the Echelon 0 and Echelon 1 stages.

6826 **Data Processing** The ePIC readout system must support data reduction techniques. The imple-
6827 mentation of firmware based triggering has already been described, but there are many additional
6828 techniques that might be implemented in echelon 0. These include zero loss techniques like aggre-
6829 gation of headers from ASICs or DAM board data. It could include standard or ML based compres-
6830 sion techniques. It could involve analysis techniques such as cluster finding or track reconstruction.
6831 There could also be ML based noise reduction techniques. And there could be analysis done for
6832 specific purposes such as the creation of scalers for monitoring or collider feedback.

6833 The framework for the code generating these features must allow the code to be shared with the
6834 offline software, for operational transparency, and for algorithm evaluation.

6835 The results of the code must be incorporated into the time frame data using data formats that allow
6836 for independent data banks to co-exist. The policy of ePIC is expected to be to avoid dropping any
6837 data unless data volumes make it necessary. There should also be a sample of unprocessed data
6838 even if the readout of raw data banks are suppressed due to data volume limits. This implies that
6839 the write out of specific data banks be controlled by configurable prescales.

6840 **Configuration Databases** Configuration information must be stored and made accessible to
6841 the ePIC Collaboration.

6842 **Slow controls interface to RDOs/FEBs** The primary configuration and slow control com-
6843 munications interface to all the ASICs and other digitizing electronics (FEBs) will be through our
6844 proprietary data link between the DAM board and the RDOs. Our current plan is to take advan-
6845 tage of the Versal SoC FPGA dual-core ARM Cortex processor. ALL DAM boards will support a
6846 full LinuxOS and gigabit ethernet access. This will facilitate running an EPICS soft IOC as well as
6847 user-based server applications for local and remote communication with the front-end electronics.

6848 Slow control communication on the DAM-RDO link must be bidirectional which means that slow
6849 control communications must share the link with streaming data coming from the detectors. The
6850 protocol must ensure that adequate bandwidth is available for digitized hits from the detector and
6851 slow controls readouts. The flow control provisions must enforce this requirement.

6852 Software and firmware development of drivers and libraries necessary to access all the FEB "fla-
6853 vors" is supported as part of the Project. The majority of the FEBs will support standard I2C control
6854 communications.

6855 **Monitoring / Logging** A unified system for centralized logging of informational and error mes-
6856 sages is required. These messages should be ideally be available and archived in web-accessible
6857 form.

6858 A unified system for monitoring of the real time behaviour and utilization of online components is
6859 also needed.

6860 **Interface to Echelon 1** As discussed in Section X (computing), the ePIC DAQ (Echelon 0) is an
6861 integral part of the computing system, and the output of the DAQ data triggers the calibration and
6862 reconstruction pipeline in Echelon 1, located at the computing centers of the host labs. From the
6863 DAQ buffering disks, two identical copies will be sent to the buffer file system at the BNL SDCC
6864 via a dedicated fiber link and at the JLab Data Center via the 400 Gbps ESnet link, respectively.
6865 Each data center's data buffer has the capability of about three weeks' ePIC data taking to allow for

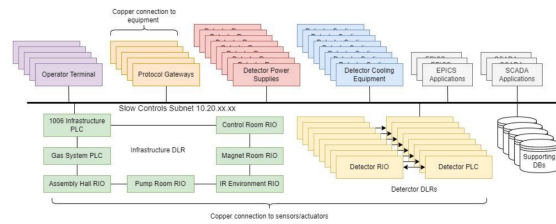


Figure 8.192: Proposed ePIC slow controls network topology

Scenario	Yearly Database Storage (TB)	Network Traffic (Mbps)
estimated	53.9	22.8
worst case	173.5	73.4

Table 8.45: Slow Controls data volume and network traffic

6866 multiple iterations of calibration jobs and reconstruction passes. Data will also be copied to perma-
 6867 nent archival storage (presumably HPSS-like tape system), one copy at each site, which allows for
 6868 reprocessing of the data in the future in case a problem identified in the prompt reconstruction pass
 6869 or an improved reconstruction becomes available in the future. Nevertheless, in a steady state, the
 6870 prompt calibration and production are expected to make the final analysis-ready data for physics
 6871 working groups within days of the data taking, significantly expedited compared to many ongoing
 6872 Nuclear Physics experiments.

6873 **Slow Controls** There will be a myriad of slow controls information associated with both the
 6874 EIC collider and the ePIC detector. These include various systems associated with the beamline,
 6875 magnets, detector biases, gas flows, temperatures, pressures, etc. . . While the design and imple-
 6876 mentation of these slow control systems will be driven by the relevant subsystems they are asso-
 6877 ciated with, it is the defined responsibility of the DAQ to provide software tools to facilitate the
 6878 integration of all this information with the streaming physics data. This will include synchronizing
 6879 the times associated with readout of slow control systems and the bunch-crossing clock that will be
 6880 driving the DAQ system. Online slow control databases to support calibration and reconstruction
 6881 processing will also be developed. Finally, a general network infrastructure in the experimental
 6882 hall and control room, independent of the high performance DAQ network, will be provided to
 6883 support integration of all slow control systems

6884 A schematic of the proposed slow controls network topology is shown in figure 8.192. The imple-
 6885 mentation uses EPICS 7 on an ethernet network to control detector operation and read and archive
 6886 conditions information. Allen-Bradley PLCs are to be used for controlling power to racks in the IR
 6887 and for detector interlocks.

6888 Resource requirements for the slow controls system were obtained by surveying detector man-
 6889 agers. These resulted in approximately 500,000 channels to be read and stored. The yearly storage
 6890 estimates and network traffic estimates are show in table 8.45.

6891 Implementation



Figure 8.193: DAQ/Computing schedule

6892 **Calibration, alignment and monitoring:** During run time, predetermined calibration and
 6893 alignment will be used in configuring the readout electronics and data reduction computing tasks.
 6894 These calibration and alignment are managed by detector groups, extracted from dedicated prior-
 6895 to-beam calibration runs, such as pedestal runs and zero field runs. When necessary, such as
 6896 changes in detector condition, new calibration will be extracted and updated to be used in data
 6897 taking. The calibration constant used will be archived in the run database and made available for
 6898 reference in the offline analysis.

6899 Constant monitoring for detector status and data pipeline healthiness is key to high-efficiency data
 6900 taking and a successful run. We expect a multi-level of monitoring that includes monitoring the
 6901 metrics on (1) detector statues (2) each stage of the data pipeline (3) sampled data content for de-
 6902 coding and analysis. In addition, in the Echelon-1 computing facility, full reconstruction will be
 6903 performed for a small fraction of time frames expediently to provide holistic feedback of the exper-
 6904 iment capability down to analysis level observable such as π^0 and K^0 s.

6905 **Status and remaining design effort:**

6906 R&D effort: ASIC R&D to continue through 2025

6907 E&D status and outlook: The bulk of the engineering design efforts still required for the
 6908 readout electronics are centered around the development of RDO and FEB designs needed
 6909 to support all the detector subsystems. This information is needed to establish baseline costs
 6910 and better define construction and testing schedules. Project Engineering design for a GTU
 6911 engineering article can be completed prior to CD2/3. Finally, we expect to procure several
 6912 FLX155 engineering articles in 2025 to support further timing and communication protocol
 6913 testing and initial firmware development.

6914 Status of maturity of the subsystem: Electronics and DAQ held a second PDR in June 2024.
 6915 We expect to hold a third PDR in 2025 on track to an FDR in 2026. There are CD-3B items in
 6916 the Electronics for VTRX+ and lpGBT. The FDR was held in June 2024, and will be presented
 6917 during the CD-3B review in January 2025.

6918 **Environmental, Safety and Health (ES&H) aspects and Quality Assessment (QA plan- 6919 ning:**

6920 **Construction and assembly planning:** Figure 8.193 shows the current project schedule for
 6921 DAQ/Computing. It is broken down into four general categories: Design/Procurement, Fabricate
 6922 and Delivery, Test and Accept and Installation. Early in the construction phase there is a heavy
 6923 focus on building and testing custom hardware (GTU, DAMs, RDOs) in order to facilitate detector
 6924 subsystem testing and DAQ firmware/software development.

Detector System		Channels	SensorTechnology	Readout Technology	Institution
SI Tracking	3 vertex layers	7 m ²	MAPS	ipGBT, VTRX+	STFC, UK, ORNL
	2 sagitta layers	368 pixels	MAPS	ipGBT, VTRX+	STFC, UK, ORNL
	5 backward disks	5,200 MAPS sensors	MAPS	ipGBT, VTRX+	STFC, UK, ORNL
	5 forward disks		MAPS	ipGBT, VTRX+	STFC, UK, ORNL
MPGD Tracking					
	Barrel, e & H Endcaps	202 k	URWELL, MicroMegas	SALSA	CEA, OMEGA, JLab
Forward Calorimeters					
	LHCAL	63,280	SIPM	CALOROC	ORNL, Debrecen
	HCal Insert	8 k	SIPM	CALOROC	ORNL, Debrecen
	pCAL W/SciFi	16,000	SIPM	Discrete	IU
Barrel Calorimeters					
	HCal	7,680	SIPM	CALOROC	ORNL, Debrecen
	ECAL SciFi/Pb	5,760	SIPM	CALOROC	U Regina, ORNL
	ECAL Imaging Si ASTROPiX	500 M pixels	Astropix	Astropix	KIT,NASA (GSFC), ANL
Backward Calorimeters					
	nHCal	3,256	SIPM	CALOROC	ORNL
	ECAL (PWO)	2,852	SIPM	Discrete	IU, EEMCAL Consortium
Far Forward					
	B0: 3 Crystal Calorimeter	135	SIPM/APD	Discrete	IU, JLab
	B0: 4 AC-LGAD layers	688,128	AC-LGAD Pixel	EICROC	UCLab, OMEGA, BNL, ORNL, Rice
	2 Roman Pots (RP)	524,288	AC-LGAD Pixel	EICROC	UCLab, OMEGA, BNL, ORNL, Rice
	2 Off Momentum (OMD)	294,912	AC-LGAD Pixel	EICROC	UCLab, OMEGA, BNL, ORNL, Rice
	ZDC: Crystal Calorimeter	900	SIPM/APD	Discrete	IU, JLab
	ZDC: HCal	9,216	SIPM	CALOROC	ORNL, Debrecen, JLab
Far Backward					
	Low Q Tagger 1	33,030,144	Timepix4	Timepix4	U. Glasgow
	Low Q Tagger 2	33,030,144	Timepix4	Timepix4	U. Glasgow
	Low Q Tagger 1+2 Cal	420 (2x210)	SIPM	CALOROC	U. York
	2 Lumi PS Calorimeter	3,360 (2x1680)	SIPM	Discrete	U. York
	2 Lumi PS Tracker	128,000 (2x64,000)	AC-LGAD Strip	FCFD/EICROcX	FNAL, OMEGA, Hiroshima, NTU, ORNL, UIC, UH, Rice, KSU, Tokyo
	Lumi Direct Photon Calorimeter	100	SIPM	Flash250	AGH Krakow, JLab
PID-TOF					
	Barrel bTOF	2,359,296	AC-LGAD Strip	FCFD/EICROcX	FNAL, OMEGA, Hiroshima, NTU, ORNL, UIC, Rice, BNL, KSU, Tokyo
	Hadron Endcap fTOF	3,719,168	AC-LGAD Pixel	EICROC	UCLab, OMEGA, BNL, ORNL, Rice
PID-Cherenkov					
	dRICH	317,952	SIPM	ALCOR, VTRX+	INFN (BO, FE, TO)
	pRICH	69,632	HRPPD	FCFD/EICROcX	BNL, FNAL, JLab
	hpDIRC	73,728	MCP-PMT or HRPPD	FCFD/EICROcX	BNL, FNAL, JLab

Figure 8.194: Electronics and DAQ Resources

6925 Once IP-6 infrastructure upgrades have been completed (DAQ and Control rooms, Wide Angle
6926 Hall), we can begin the main trunk fiber pulls into the hall and tunnels and install required patch
6927 panels and terminate fibers. At this time we can also start installation of the general IP-6 network
6928 infrastructure in the Hall, DAQ and Control Rooms.

6929 Computing hardware procurement and installation are scheduled in three phases during the course
6930 of construction. Phase I at the beginning of construction will be for a small subset of machines for
6931 development and evaluation. They will be placed in both the DAQ/Electronics development labs
6932 as well as in the SDCC. Phase II will be primarily in the DAQ Room as part of the DAQ subsystem
6933 installations and will provide the opportunity for full chain large scale testing of the DAQ as well as
6934 for detector subsystems as they begin to be installed at IP-6. Finally Phase III will be implemented
6935 at the end of the full ePIC detector installation as we have a better understanding of the required
6936 resources needed for initial Physics operation. This hardware will be installed at both the DAQ
6937 Room and in the SDCC which will define the full Echelon 0 enclave.

6938 **Collaborators and their role, resources and workforce:** The institutions specifically devel-
6939 oping the readout electronics and ASICs are listed under the electronics section. Figure 8.194 lists
6940 the institutions which have expressed interest in participating in the design of various other parts
6941 of the readout chain. Formal agreements committing engineering and technical personnel have not
6942 been officiated.

6943 **8.3.11 Software and Computing**

6944 **Requirements**

6945 **Requirements from physics:** Add text here.

6946 **Requirements from Radiation Hardness:** Add text here.

6947 **Requirements from Data Rates:** Add text here.

6948 **Justification**

6949 **Device concept and technological choice:** Add text here.

6950 **Subsystem description:**

6951 General device description: Add text here.

6952 Sensors: Add text here.

6953 FEE: Add text here.

6954 Other components: Add text here.

6955 **Performance**

6956 **Implementation**

6957 **Services:** Add text here.

6958 **Subsystem mechanics and integration:** Add text here.

6959 **Calibration, alignment and monitoring:** Add text here.

6960 **Status and remaining design effort:**

6961 R&D effort: Add text here.

6962 E&D status and outlook: Add text here.

6963 Other activity needed for the design completion: Add text here.

6964 Status of maturity of the subsystem: Add text here.

6965 **Environmental, Safety and Health (ES&H) aspects and Quality Assessment (QA plan-**
6966 **ning:** Add text here.

6967 **Construction and assembly planning:** Add text here.

6968 **Collaborators and their role, resources and workforce:** Add text here.

6969 **Risks and mitigation strategy:** Add text here.

6970 **Additional Material** Add text here.

6971 **8.4 Detector Integration**

6972 Add text here.

6973 **8.4.1 Installation and Maintenance**

6974 Add text here.

6975 **8.5 Detector Commissioning and Pre-Operations**

6976 Add text here.

References

- 6978 [1] A. Bacchetta, V. Bertone, C. Bissolotti, G. Bozzi, M. Cerutti, F. Delcarro, M. Radici, L. Rossi,
6979 and A. Signori, "Flavor dependence of unpolarized quark transverse momentum distributions
6980 from a global fit," *JHEP*, vol. 08, p. 232, 2024.
- 6981 [2] Irene Dutta and Christopher Madrid and Ryan Heller and Shirsendu Nanda and Danush
6982 Shekar and Claudio San Martín and Matías Barría and Artur Apresyan and Zhenyu Ye and
6983 William K. Brooks and Wei Chen and Gabriele D'Amen and Gabriele Giacomini and Alessan-
6984 dro Tricoli and Aram Hayrapetyan and Hakseong Lee and Ohannes Kamer Köseyan and
6985 Sergey Los and Koji Nakamura and Sayuka Kita and Tomoka Imamura and Cristian Peña
6986 and Si Xie, "Results for pixel and strip centimeter-scale AC-LGAD sensors with a 120 GeV
6987 proton beam," 7 2024.
- 6988 [3] M. Tabata *et al.*, "Silica aerogel radiator for use in the A-RICH system utilized in the Belle II
6989 experiment," *Nucl. Instrum. Meth. A*, vol. 766, pp. 212–216, 2014.
- 6990 [4] ePIC, "Summary of epic background rates," 2024.
- 6991 [5] M. Tabata, I. Adachi, H. Kawai, T. Sumiyoshi, and H. Yokogawa, "Hydrophobic silica aerogel
6992 production at kek," *Nuclear Instruments and Methods in Physics Research Section A: Accelerators,
6993 Spectrometers, Detectors and Associated Equipment*, vol. 668, pp. 64–70, 2012.
- 6994 [6] R. Abdul Khalek *et al.*, "Science Requirements and Detector Concepts for the Electron-Ion
6995 Collider: EIC Yellow Report," *Nucl. Phys. A*, vol. 1026, p. 122447, 2022.
- 6996 [7] A. Accardi *et al.*, "Electron Ion Collider: The Next QCD Frontier: Understanding the glue that
6997 binds us all," *Eur. Phys. J. A*, vol. 52, no. 9, p. 268, 2016.
- 6998 [8] A. Accardi *et al.*, "Electron Ion Collider: The Next QCD Frontier: Understanding the glue that
6999 binds us all," *Eur. Phys. J. A*, vol. 52, no. 9, p. 268, 2016.
- 7000 [9] "National Academies of Sciences, Engineering, and Medicine, An Assessment of U.S.-Based
7001 Electron-Ion Collider Science," *The National Academies Press, Washington, DC*, 2018.
- 7002 [10] J. K. Adkins *et al.*, "Design of the ECCE Detector for the Electron Ion Collider," 9 2022.
- 7003 [11] J. Adam *et al.*, "ATHENA detector proposal — a totally hermetic electron nucleus apparatus
7004 proposed for IP6 at the Electron-Ion Collider," *JINST*, vol. 17, no. 10, p. P10019, 2022.
- 7005 [12] S. R. Klein, J. Nystrand, J. Seger, Y. Gorbunov, and J. Butterworth, "Starlight: A monte carlo
7006 simulation program for ultra-peripheral collisions of relativistic ions," *Computer Physics Com-
7007 munications*, vol. 212, pp. 258–268, 2017.
- 7008 [13] D. W. Sivers, "Single Spin Production Asymmetries from the Hard Scattering of Point-Like
7009 Constituents," *Phys. Rev. D*, vol. 41, p. 83, 1990.
- 7010 [14] D. W. Sivers, "Hard scattering scaling laws for single spin production asymmetries," *Phys.
7011 Rev. D*, vol. 43, pp. 261–263, 1991.

- 7012 [15] E. C. Aschenauer, V. Batozskaya, S. Fazio, K. Gates, H. Moutarde, D. Sokhan, H. Spiesberger,
7013 P. Sznajder, and K. Tezgin, "EpIC: novel Monte Carlo generator for exclusive processes," *Eur.*
7014 *Phys. J. C*, vol. 82, no. 9, p. 819, 2022.
- 7015 [16] "The electron-ion collider user group."
- 7016 [17] R. A. Khalek *et al.*, "Science Requirements and Detector Concepts for the Electron-Ion Collider:
7017 EIC Yellow Report," *Nucl. Instr. and Meth. A*, vol. 1026, p. 122447, 2022.
- 7018 [18] "The epic collaboration website."
- 7019 [19] A. Collaboration, "Technical Design report for the ALICE Inner Tracking System 3 - ITS3 ; A
7020 bent wafer-scale monolithic pixel detector," tech. rep., CERN, Geneva, 2024.
- 7021 [20] lpGBT Design Team, "lpGBT documentation – release," 2024.
- 7022 [21] J. Troska *et al.*, "The VTRx+, an optical link module for data transmission at HL-LHC," 2017.
- 7023 [22] D. H. *et al.*, "Science requirements and detector concepts for the electron-ion collider: Eic
7024 yellow report," *Nuclear Physics A*, vol. 1026, p. 122447, 2022.
- 7025 [23] F. Willeke and J. Beebe-Wang, "Electron ion collider conceptual design report 2021," 2 2021.
- 7026 [24] EIC, "Eic detector geometry," 2024.
- 7027 [25] D. N. *et al.*, "Aging effects in the COMPASS hybrid GEM-Micromegas pixelized detectors,"
7028 *Nucl. Instrum. Meth.*, vol. 1065, p. 169511, 2024.
- 7029 [26] C. A. *et al.*, "Construction, test and commissioning of the triple-gem tracking detector for
7030 compass," *Nucl. Instrum. Meth.*, vol. A490, no. 1, pp. 177 – 203, 2002.
- 7031 [27] T. Kawamoto, S. Vlachos, L. Pontecorvo, J. Dubbert, G. Mikenberg, P. Iengo, C. Dallapiccola,
7032 C. Amelung, L. Levinson, R. Richter, and D. Lellouch, "New Small Wheel Technical Design
7033 Report," tech. rep., 2013. ATLAS New Small Wheel Technical Design Report.
- 7034 [28] M. P. *et al.*, "The μ -rwell: A compact, spark protected, single amplification-stage mpGD," *Nu-*
7035 *clear Instruments and Methods in Physics Research Section A: Accelerators, Spectrometers, Detectors*
7036 *and Associated Equipment*, vol. 824, pp. 565–568, 2016. Frontier Detectors for Frontier Physics:
7037 Proceedings of the 13th Pisa Meeting on Advanced Detectors.
- 7038 [29] E. F. *et al.*, "Resistive micromegas high-rate and long-term ageing studies at the cern gamma
7039 irradiation facility," *Nuclear Instruments and Methods in Physics Research Section A: Accelerators,*
7040 *Spectrometers, Detectors and Associated Equipment*, vol. 1042, p. 167423, 2022.
- 7041 [30] M. C. *et al.*, "Development of micromegas detectors with resistive anode pads," *Nuclear In-*
7042 *struments and Methods in Physics Research Section A: Accelerators, Spectrometers, Detectors and*
7043 *Associated Equipment*, vol. 1003, p. 165268, 2021.
- 7044 [31] A. Acker and others, "The CLAS12 micromegas vertex tracker," vol. 957, p. 163423.
- 7045 [32] I. Giomataris, R. De Oliveira, S. Andriamonje, S. Aune, G. Charpak, P. Colas, A. Giganon,
7046 P. Rebourgeard, and P. Salin, "Micromegas in a bulk," *Nucl. Instrum. Meth. A*, vol. 560, pp. 405–
7047 408, 2006.
- 7048 [33] M. Calvi, P. Carniti, C. Gotti, C. Matteuzzi, and G. Pessina, "Single photon detection with
7049 SiPMs irradiated up to 10^{14} cm⁻² 1-MeV-equivalent neutron fluence," *Nucl. Instrum. Meth. A*,
7050 vol. 922, pp. 243–249, 2019.
- 7051 [34] R. Preghenella *et al.*, "Study of radiation effects on SiPM for an optical readout system for the
7052 EIC dual-radiator RICH," *Nucl. Instrum. Meth. A*, vol. 1056, p. 168578, 2023.
- 7053 [35] "Technical Design Report: A High-Granularity Timing Detector for the ATLAS Phase-II Up-
7054 grade," tech. rep., CERN, Geneva, 2020.

- 7055 [36] C. Madrid, R. Heller, C. San Martín, S. Nanda, A. Apresyan, W. Brooks, W. Chen, G. Giacomini,
7056 O. Kamer Köseyan, S. Los, C. Peña, R. Rios, A. Tricoli, S. Xie, and Z. Ye, “First survey of
7057 centimeter-scale ac-Igad strip sensors with a 120 gev proton beam,” *Journal of Instrumentation*,
7058 vol. 18, p. P06013, June 2023.
- 7059 [37] C. Bishop, A. Das, J. Ding, M. Gignac, F. Martinez-McKinney, S. Mazza, A. Molnar, N. Nagel,
7060 M. Nizam, J. Ott, H.-W. Sadrozinski, B. Schumm, A. Seiden, T. Shin, A. Summerell, M. Wilder,
7061 and Y. Zhao, “Long-distance signal propagation in ac-Igad,” *Nuclear Instruments and Meth-
7062 ods in Physics Research Section A: Accelerators, Spectrometers, Detectors and Associated Equipment*,
7063 vol. 1064, p. 169478, 2024.
- 7064 [38] L. Menzio *et al.*, “First test beam measurement of the 4D resolution of an RSD pixel matrix
7065 connected to a FAST2 ASIC,” *Nucl. Instrum. Meth. A*, vol. 1065, p. 169526, 2024.
- 7066 [39] S. Xie, A. Apresyan, R. Heller, C. Madrid, I. Dutta, A. Hayrapetyan, S. Los, C. Peña, and T. Zim-
7067 mermann, “Design and performance of the fermilab constant fraction discriminator ASIC,” *Nu-
7068 clear Instruments and Methods in Physics Research Section A: Accelerators, Spectrometers, Detectors
7069 and Associated Equipment*, vol. 1056, p. 168655, 2023.
- 7070 [40] C. Chock, K. Flood, L. Macchiarulo, F. Martinez-McKinney, A. Martinez-Rojas, S. Mazza,
7071 I. Mostafanezhad, M. Nizam, J. Ott, R. Perron, E. Ryan, H.-W. Sadrozinski, B. Schumm, A. Sei-
7072 den, K. Shin, M. Tarka, D. Uehara, M. Wilder, and Y. Zhao, “First test results of the trans-
7073 impedance amplifier stage of the ultra-fast hpsoc ASIC,” *Journal of Instrumentation*, vol. 18,
7074 p. C02016, feb 2023.
- 7075 [41] O. H. W. Siegmund *et al.*, “Advances in microchannel plates and photocathodes for ultravi-
7076 olet photon counting detectors,” *Society of Photo-Optical Instrumentation Engineers Proceedings*,
7077 vol. 81450J.
- 7078 [42] C. J. Hamel *et al.*, “LAPPD and HRPPD: Upcoming Upgrades to Incom’s Fast Photosensors,”
- 7079 [43] “EICROC ASIC.” [https://indico.bnl.gov/event/18539/contributions/73731/
7080 attachments/46348/78403/CdLT_EICROC_6mar23.pdf](https://indico.bnl.gov/event/18539/contributions/73731/attachments/46348/78403/CdLT_EICROC_6mar23.pdf).
- 7081 [44] “Organization for Micro-Electronics desiGn and Applications.” [https://portail.
7082 polytechnique.edu/omega/](https://portail.polytechnique.edu/omega/).
- 7083 [45] J. Anderson *et al.*, “FELIX: a PCIe based high-throughput approach for interfacing front-end
7084 and trigger electronics in the ATLAS Upgrade framework,” *JINST*, vol. 11, no. 12, p. C12023,
7085 2016.
- 7086 [46] “Chiba Aerogel Factory Co., Ltd.” <https://www.aerogel-factory.jp/>.
- 7087 [47] M. Yonenaga *et al.*, “Performance evaluation of the aerogel RICH counter for the Belle II spec-
7088 trometer using early beam collision data,” *Prog. Theor. Exp. Phys.*, no. 093H01, 2020.
- 7089 [48] S. Agostinelli *et al.*, “GEANT4—a simulation toolkit,” *Nucl. Instrum. Meth. A*, vol. 506, p. 250,
7090 2003.
- 7091 [49] “ePIC IRT Package.” <https://github.com/eic/irt/tree/pfrich>.
- 7092 [50] R. Brun and F. Rademakers, “ROOT - An Object Oriented Data Analysis Framework, Proceed-
7093 ings AIHENP’96 Workshop, Lausanne,” *Nucl. Inst. & Meth. in Phys. Res. A*, no. 389, pp. 81–86,
7094 1997.
- 7095 [51] M. Tabata, I. Adachi, Y. Hatakeyama, H. Kawai, T. Morita, and T. Sumiyoshi, “Large-area silica
7096 aerogel for use as cherenkov radiators with high refractive index, developed by supercritical
7097 carbon dioxide drying,” *The Journal of Supercritical Fluids*, vol. 110, pp. 183–192, 2016.
- 7098 [52] “CAEN A1515BV 16-channel floating ground High Voltage module.” [https://www.caen.it/
7099 products/a1515b/](https://www.caen.it/products/a1515b/).
- 7100 [53] “CAEN SY4527 High Voltage mainframe.” <https://www.caen.it/products/SY4527/>.

- 7101 [54] “Wiener Mpod Low Voltage system.” [https://www.wiener-d.com/power-supplies/
7102 mpod-lv-hv/](https://www.wiener-d.com/power-supplies/mpod-lv-hv/).
- 7103 [55] S. K. Sahu *et al.*, “Measurement of Radiation Damage on Silica Aerogel Cherenkov Radiator,”
7104 *Nucl. Instrum. Meth. A*, vol. 382, pp. 441–446, 1996.
- 7105 [56] R. Abjean, A. Bideau-Mehu, and Y. Guern, “Refractive index of hexafluoroethane (C-2F-6) in
7106 the 300-nm to 150-nm wavelength range,” *Nucl. Instrum. Meth. A*, vol. 354, pp. 417–418, 1995.
- 7107 [57] C. Piemonte and A. Gola, “Overview on the main parameters and technology of modern Sili-
7108 con Photomultipliers,” *Nucl. Instrum. Meth. A*, vol. 926, pp. 2–15, 2019.
- 7109 [58] L. P. Rignanese, P. Antonioli, R. Pregonella, and E. Scapparone, “SiPMs and examples of
7110 applications for low light detection in particle and astroparticle physics,” *Riv. Nuovo Cim.*,
7111 vol. 47, no. 5, pp. 299–349, 2024. [Erratum: *Riv. Nuovo Cim.* 47, (2024)].
- 7112 [59] R. Hawkes, A. Lucas, J. Stevick, G. Llosa, S. Marcatili, C. Piemonte, A. Del Guerra, and T. A.
7113 Carpenter, “Silicon photomultiplier performance tests in magnetic resonance pulsed fields,”
7114 in *2007 IEEE Nuclear Science Symposium Conference Record*, vol. 5, pp. 3400–3403, 2007.
- 7115 [60] S. España, L. Fraile, J. Herraiz, J. Udías, M. Desco, and J. Vaquero, “Performance evaluation of
7116 sipm photodetectors for pet imaging in the presence of magnetic fields,” *Nuclear Instruments
7117 and Methods in Physics Research Section A: Accelerators, Spectrometers, Detectors and Associated
7118 Equipment*, vol. 613, no. 2, pp. 308–316, 2010.
- 7119 [61] F. Acerbi *et al.*, “Cryogenic Characterization of FBK HD Near-UV Sensitive SiPMs,” *IEEE Trans.
7120 Electron. Dev.*, vol. 64, pp. 521–526, 10 2016.
- 7121 [62] S. Merzi, F. Acerbi, C. Aicardi, D. Fiore, V. Goiffon, A. G. Gola, O. Marcelot, A. Materne, and
7122 O. Saint-Pe, “Radiation Damage on Silicon Photomultipliers from Ionizing and Non-Ionizing
7123 Radiation of Low-Earth Orbit Operations,” *Sensors*, vol. 24, no. 15, p. 4990, 2024.
- 7124 [63] E. Garutti and Y. Musienko, “Radiation damage of SiPMs,” *Nucl. Instrum. Meth. A*, vol. 926,
7125 pp. 69–84, 2019.
- 7126 [64] T. Tsang, T. Rao, S. Stoll, and C. Woody, “Neutron radiation damage and recovery studies of
7127 SiPMs,” *JINST*, vol. 11, no. 12, p. P12002, 2016.
- 7128 [65] E. Nappi, “Aerogel and its applications to rich detectors,” *Nuclear Physics B - Proceedings Sup-
7129 plements*, vol. 61, no. 3, pp. 270–276, 1998. Proceedings of the Fifth International Conference
7130 on Advanced Technology and Particle Physics.
- 7131 [66] EU, “Regulation (EU) 2024/573 of the European Parliament and of the Council on fluorinate
7132 greenhouse gases,” <https://eur-lex.europa.eu/eli/reg/2024/573/oj>, 2024.
- 7133 [67] M. Kubantsev, I. Larin, and A. Gasparian, “Performance of the PrimEx electromagnetic
7134 calorimeter,” *AIP Conf. Proc.*, vol. 867, no. 1, pp. 51–58, 2006.
- 7135 [68] T. Horn *et al.*, “Scintillating crystals for the Neutral Particle Spectrometer in Hall C at JLab,”
7136 *Nucl. Instrum. Meth. A*, vol. 956, p. 163375, 2020.
- 7137 [69] A. Asaturyan *et al.*, “Electromagnetic calorimeters based on scintillating lead tungstate crystals
7138 for experiments at Jefferson Lab,” *Nucl. Instrum. Meth. A*, vol. 1013, p. 165683, 2021.
- 7139 [70] F. Ameli *et al.*, “Streaming readout for next generation electron scattering experiments,” *Eur.
7140 Phys. J. Plus*, vol. 137, no. 8, p. 958, 2022.
- 7141 [71] Y. Suda *et al.*, “Performance evaluation of the high-voltage CMOS active pixel sensor AstroPix
7142 for gamma-ray space telescopes,” *Nucl. Instrum. Meth. A*, vol. 1068, p. 169762, 2024.
- 7143 [72] O. D. Tsai *et al.*, “Results of \& on a new construction technique for W/ScFi Calorimeters,” *J.
7144 Phys. Conf. Ser.*, vol. 404, p. 012023, 2012.
- 7145 [73] C. A. Aidala *et al.*, “Design and Beam Test Results for the sPHENIX Electromagnetic and
7146 Hadronic Calorimeter Prototypes,” *IEEE Trans. Nucl. Sci.*, vol. 65, no. 12, pp. 2901–2919, 2018.

- 7147 [74] T. Nicholls *et al.*, "Performance of an electromagnetic lead / scintillating fiber calorimeter for
7148 the H1 detector," *Nucl. Instrum. Meth. A*, vol. 374, pp. 149–156, 1996.
- 7149 [75] O. D. Tsai *et al.*, "Development of a forward calorimeter system for the STAR experiment," *J.*
7150 *Phys. Conf. Ser.*, vol. 587, no. 1, p. 012053, 2015.
- 7151 [76] F. Aaron *et al.*, "Measurement of the proton structure function $f_1(x, q^2)$ at low x ," *Physics Letters*
7152 *B*, vol. 665, no. 4, pp. 139–146, 2008.
- 7153 [77] R.-D. Appuhn *et al.*, "The h1 lead/scintillating-fibre calorimeter," *Nuclear Instruments and*
7154 *Methods in Physics Research Section A: Accelerators, Spectrometers, Detectors and Associated Equip-*
7155 *ment*, vol. 386, no. 2, pp. 397–408, 1997.
- 7156 [78] A. White *et al.*, "Design, construction and commissioning of a technological prototype of a
7157 highly granular sipm-on-tile scintillator-steel hadronic calorimeter," *Journal of Instrumentation*,
7158 vol. 18, p. P11018, nov 2023.
- 7159 [79] R. A. et al., "Apeiron: A framework for high level programming of dataflow applications on
7160 multi-fpga systems," *EPJ Web of Conferences*, no. 11002, 2024.

